

UNIVERSIDAD COMPLUTENSE DE MADRID

FACULTAD DE CIENCIAS FÍSICAS



**TESIS DOCTORAL**

**Análisis de la formación temprana de las  
galaxias masivas con datos JWST y HST**

**Analysis of the early stages in the formation of  
massive galaxies with JWST and HST data**

MEMORIA PARA OPTAR AL GRADO DE DOCTORA EN ASTROFÍSICA

PRESENTADA POR

**Ángela García Argumánez**

DIRECTORES

Pablo Guillermo Pérez González

Armando Gil de Paz

Madrid, 2023





UNIVERSIDAD  
**COMPLUTENSE**  
MADRID

## DECLARACIÓN DE AUTORÍA Y ORIGINALIDAD DE LA TESIS PRESENTADA PARA OBTENER EL TÍTULO DE DOCTOR

D./Dña. Ángela García Argumánez,  
estudiante en el Programa de Doctorado Astrofísica,  
de la Facultad de Ciencias Físicas de la Universidad Complutense de  
Madrid, como autor/a de la tesis presentada para la obtención del título de Doctor y  
titulada:

Análisis de la formación temprana de las galaxias masivas con datos JWST y HST  
Analysis of the early stages in the formation of massive galaxies with JWST and HST data

y dirigida por: Pablo Guillermo Pérez González y Armando Gil de Paz

### DECLARO QUE:

La tesis es una obra original que no infringe los derechos de propiedad intelectual ni los derechos de propiedad industrial u otros, de acuerdo con el ordenamiento jurídico vigente, en particular, la Ley de Propiedad Intelectual (R.D. legislativo 1/1996, de 12 de abril, por el que se aprueba el texto refundido de la Ley de Propiedad Intelectual, modificado por la Ley 2/2019, de 1 de marzo, regularizando, aclarando y armonizando las disposiciones legales vigentes sobre la materia), en particular, las disposiciones referidas al derecho de cita.

Del mismo modo, asumo frente a la Universidad cualquier responsabilidad que pudiera derivarse de la autoría o falta de originalidad del contenido de la tesis presentada de conformidad con el ordenamiento jurídico vigente.

En Madrid, a 4 de agosto de 2023

**GARCIA  
ARGUMANEZ  
ANGELA -  
45835615L**  
Fdo.: \_\_\_\_\_

Firmado digitalmente por GARCIA  
ARGUMANEZ ANGELA - 45835615L  
Nombre de reconocimiento (DN):  
c=ES,  
serialNumber=IDCES-45835615L,  
givenName=ANGELA, sn=GARCIA  
ARGUMANEZ, cn=GARCIA  
ARGUMANEZ ANGELA - 45835615L  
Fecha: 2023.09.04 09:57:39 +02'00'

Esta DECLARACIÓN DE AUTORÍA Y ORIGINALIDAD debe ser insertada en  
la primera página de la tesis presentada para la obtención del título de Doctor.



*A toda mi familia, por ser  
lo más bonito que tengo.*



# Agradecimientos

---

Quiero empezar agradeciendo a todas las personas que, de alguna forma u otra, han contribuido a que haya podido llegar hasta aquí. Esta tesis no hubiese sido posible sin el apoyo y cariño que he recibido a lo largo de mi recorrido académico. La contribución de todas estas personas ha sido fundamental en este viaje y les estoy sinceramente agradecida por haber hecho posible este capítulo de mi vida. Pido disculpas por adelantado por si omito a alguien que merezca estar en esta muestra de agradecimiento.

Me gustaría empezar agradeciendo a mis dos directores de tesis por haberme guiado y acompañado durante estos años, ya que sin ellos esta tesis no habría sido posible. En primer lugar, a Pablo G. Pérez González, quien a pesar de su pésimo gusto en cuanto a equipos de fútbol, me dio la oportunidad de llevar a cabo esta tesis. Le doy las gracias por su ayuda y orientación, por su disponibilidad, por todas las oportunidades que me ha dado, por su experiencia y su amplio conocimiento, los cuales han contribuido enormemente a mejorar significativamente la calidad de este trabajo. En segundo lugar, doy las gracias a Armando Gil de Paz por su apoyo y su guía durante toda la tesis, por sus excepcionales ideas y puntos de vista, por haberme ayudado a entender los conceptos más difíciles con su infinita paciencia, por su optimismo y, sobre todo, por creer siempre en mí.

Doy las gracias a mis profesores de la Sagrada Familia de Elda, pues todos ellos forjaron en mí la base que me permitió posteriormente estudiar una carrera de ciencias. En especial, a Don Mariano por enseñarme a amar las matemáticas, a Don Manuel Galindo, que al enterarse de que iba a estudiar Física dedicó desinteresadamente su mes de julio a enseñarme, entre otras cosas, a diagonalizar matrices para que llegase lo mejor preparada posible a la carrera, y, con especial cariño, a Don José Luis Cremades, que fue la primera persona que se sentó a explicarme el sentido de lo que era una derivada, que durante 4 años me dio la mejor formación posible y me enseñó a amar la Química (casi) tanto como la Astrofísica.

Agradezco también a la Universidad Complutense de Madrid el haberme permitido realizar esta tesis mediante la Ayuda Predoctoral UCM. En relación a la Facultad de CC. Físicas, estaré eternamente agradecida a Lucas Pérez, por enseñarme que no hay asignatura difícil si se cursa con él y por darme todas las oportunidades posibles para introducirme en el mundo de la investigación. También me gustaría agradecer a María Lorenza Escudero y, especialmente, a Cristina García, por acompañarme durante mis primeros pasos en la carrera investigadora, acogiéndome durante un año con los brazos abiertos. A Juan Jiménez Castellanos, por el tiempo que dedicó en primero para que aprendiese a programar, así como por su apoyo durante los momentos más difíciles de la tesis. A Nicolás Cardiel, por mostrarme lo bonita que puede llegar a ser la Astrófica, y a Elisa de Castro, por todo su apoyo y la ayuda ofrecida cuando me lesioné. Asimismo, agradezco de corazón a Mariángeles Flechoso el haberme facilitado la etapa final de mi tesis con sus buenos consejos y su voluntad para ayudar a los estudiantes. Y a Afri, por la simpatía y cercanía que siempre me ha transmitido.

También extendiendo mi gratitud al resto del Departamento de Física de la Tierra y Astrofísica, que me acogieron desde el principio como a una más. Especialmente, a todos los predocs y postdocs que he tenido la suerte de conocer, con los que he compartido tan buenos momentos durante estos años, pero que no me atrevo a enumerarlos por si me dejo alguno. A Belén Alcalde, por todos sus consejos y por estar siempre dispuesta a ayudarme (eres un ser de luz), y a Rosi, con la que he compartido tantos cafés y sufrimiento. Con especial cariño, doy las gracias a Antonio Verdet por todas las risas cómplices y todo el apoyo que me ha mostrado durante estos cinco años cuando más lo necesitaba. A Ainhoa Sánchez Penim, por haberme acompañado durante todo este tiempo como amiga y haberme permitido conocer a sus dos grandes y merecidísimas alegrías surgidas durante mi tesis.

Me gustaría agradecer también a Anna Ferré-Mateu su apoyo desinteresado y sus consejos durante este último año. Y a José María Gavira, por sus interminables (y siempre interesantes) correos, por haberme recordado lo bonita que puede ser la ciencia y por tener siempre una respuesta a mis preguntas.

Merecen una mención especial aquí Alicia Chacón y Nuria de Miguel, con las que he compartido tan buenos momentos desde que las conocí. Siempre echaré de menos los años que vivimos juntas como una familia. También tengo que agradecer a Dani, Laura y Paloma, compañeros de sufrimiento y de alegrías. A Dani, por tener siempre una sonrisa, por muy mal que fuesen las cosas. A Paloma, que aún después de tantos años, siempre descubro algo de ella que logra sorprenderme. No cambies, por favor. Y a Laura, por todos los momentos compartidos en los que hemos intentado arreglar juntas el mundo, y a quien me gustaría tener siempre cerca. A Juan y Pablo, quienes lograron que la experiencia del máster fuera enriquecedora en todos los sentidos. Y a Juan Carlos y a Javier, por todos los cafés compartidos, que espero que continúen.

Por supuesto, tengo que agradecer también a Carlos Moreno por sus largas llamadas para ponernos al día y por su maravillosa forma de ser. Y a Néstor, que aunque nuestros caminos se separaron, siempre me apoyó hasta el final y me ayudó a crecer como persona. A Irene, a quien admiro, y quien se ha convertido en una persona muy importante en mi vida que espero tener cerca durante mucho tiempo. Y, como no, a mi Moso, sin el cual no me hubiese imaginado hacer una tesis, por nuestra “relación de alto contexto” y por todos los buenos momentos que aún nos quedan por vivir juntos.

Por último, doy gracias a mis padres por creer en mí desde el principio y por darme siempre la mejor educación posible, así como por permitirme alcanzar mi sueño de llegar a estudiar Astrofísica, a pesar del esfuerzo económico que esto supuso. A ellos y a mis hermanos, les agradezco su apoyo incondicional durante los momentos más duros. Especialmente, agradezco a mi hermana pequeña Alicia que, pese a la distancia, siempre se ha mantenido cerca y a la cual admiro por su valentía. También agradezco a toda mi familia de Elda el amor que me han dado durante todos estos años y por ser los mejores en organizar fiestas. Allá donde voy os llevo siempre a todos en el corazón. Quiero agradecer también a mi madrina Paqui y a mi padrino Jose, por haber estado siempre pendientes de mí desde que nací. Por último, quiero terminar dando las gracias a Plasti, a quien quiero con todo mi corazón, y quien a pesar de intentar desanimarme para que no hiciera la tesis, ha estado a mi lado durante todo este tiempo, convirtiéndose en un pilar fundamental de mi vida y cuidándome cuando más lo he necesitado. Gracias por haberme dejado recorrer este camino de la mano contigo.



# Contents

---

<b>Summary</b>	<b>vii</b>
<b>Resumen</b>	<b>ix</b>
<b>List of Figures</b>	<b>xi</b>
<b>List of Tables</b>	<b>xxiii</b>
<b>1 Introduction</b>	<b>1</b>
1.1 From structure formation to first stars . . . . .	1
1.1.1 Structure formation . . . . .	3
1.1.2 Baryons in dark matter halos: formation of the first stars . . . . .	4
1.2 A global picture of how massive galaxies formed . . . . .	7
1.2.1 Massive galaxies: a two-stage formation scenario . . . . .	8
1.3 A further glance: the James Webb Space Telescope . . . . .	10
1.3.1 Probing the early Universe with the <i>James Webb Space Telescope</i> . . . . .	11
1.3.2 Recovering the assembly history of galaxies via 2D SPS with JWST . . . . .	13
1.3.3 Open questions in galaxy formation . . . . .	14
1.4 Main objective of this thesis . . . . .	14
<b>2 Simulated data: the Illustris Simulation</b>	<b>17</b>
2.1 Introduction to cosmological simulations . . . . .	17
2.2 The Illustris Simulation . . . . .	20
2.2.1 The Illustris Project . . . . .	20
2.2.2 The Illustris Simulation: general characteristics . . . . .	22
2.2.3 Galaxy formation model in Illustris . . . . .	23
2.2.4 Illustris halos and subhalos . . . . .	24

2.2.5	Snapshots in Illustris . . . . .	25
2.2.6	Illustris predictions and comparison with observations . . . . .	28
2.3	Synthetic images in Illustris: the “mock ultra-deep fields” . . . . .	30
2.4	Massive galaxies at $1 < z < 4$ in Illustris: building the ground-truth galaxy SFH from their stellar particles . . . . .	33
2.5	On the representativeness of the sample of massive galaxies at $1 < z < 4$ . . . . .	35
2.6	Final considerations . . . . .	37
<b>3</b>	<b>Observational data: the <i>Hubble</i> and <i>James Webb</i> Space Telescopes</b>	<b>39</b>
3.1	The Hubble Space Telescope . . . . .	40
3.1.1	General characteristics . . . . .	42
3.1.2	Scientific instruments . . . . .	42
3.1.3	HST cosmological fields . . . . .	46
3.2	The James Webb Space Telescope . . . . .	52
3.2.1	JWST general characteristics . . . . .	54
3.2.2	Scientific instruments . . . . .	55
3.2.3	Introduction to JWST cosmological surveys . . . . .	59
3.3	Final considerations . . . . .	63
<b>4</b>	<b>Recovering Star Formation Histories: Stellar Population Synthesis in 2D</b>	<b>65</b>
4.1	Stellar population synthesis modeling: an overview . . . . .	65
4.1.1	Basic ingredients of SPS . . . . .	68
4.2	Details of the SPS model used in this work . . . . .	69
4.2.1	IMF . . . . .	70
4.2.2	Isochrones . . . . .	70
4.2.3	Stellar spectra libraries . . . . .	71
4.2.4	SFH . . . . .	73
4.2.5	Dust . . . . .	73
4.3	Synthesizer code . . . . .	74
4.4	2D SPS . . . . .	76

---

<b>5 Probing the earliest phases in the formation of massive galaxies with simulated HST+JWST imaging data from Illustris</b>	<b>79</b>
5.1 Introduction . . . . .	79
5.2 Dataset . . . . .	80
5.2.1 Illustris Simulation and synthetic deep-survey images . . . . .	80
5.2.2 Sample selection . . . . .	81
5.3 Photometric data from the Illustris simulation . . . . .	84
5.3.1 Photometric broad-band filters . . . . .	84
5.3.2 Photometric measurements . . . . .	84
5.3.3 Redshifts . . . . .	89
5.3.4 Ground-truth physical properties of each galaxy . . . . .	90
5.4 Estimation of the SFH from 2D SED fitting . . . . .	91
5.4.1 Stellar populations synthesis modeling . . . . .	92
5.4.2 Estimating SFHs from HST+JWST photometry . . . . .	96
5.5 Validation of the method . . . . .	98
5.5.1 Characterization of the earliest phases in the formation of massive galaxies . . . . .	98
5.6 Expectations for the derivation of the SFH of $z > 1$ massive galaxies with HST+JWST data . . . . .	100
5.6.1 When did massive galaxies begin to form? . . . . .	100
5.7 Summary and conclusions . . . . .	113
<b>6 Earliest phases in the formation of massive galaxies at <math>1 &lt; z &lt; 4</math> from spatially-resolved Star Formation Histories</b>	<b>115</b>
6.1 Introduction . . . . .	115
6.2 Observations . . . . .	115
6.2.1 JWST imaging from CEERS . . . . .	116
6.2.2 HST imaging from CANDELS/EGS . . . . .	116
6.3 Selection of the preliminary sample . . . . .	117
6.3.1 Estimation of photometric redshifts and preliminary stellar masses . . . . .	117
6.3.2 Preliminary sample . . . . .	118

6.4	Methodology . . . . .	118
6.4.1	Photometry: measuring integrated and 2D SEDs . . . . .	118
6.4.2	SPS modeling . . . . .	122
6.4.3	Massive galaxies and SFH from the 2D SED fits . . . . .	124
6.5	Results . . . . .	124
6.5.1	CEERS final sample of massive, $1 < z < 4$ galaxies: redshift and stellar mass	126
6.5.2	The first stages of the SFH in massive $1 < z < 4$ galaxies . . . . .	126
6.5.3	On the potential impact of Pop III stars and non-universal IMF . . . . .	132
6.6	Discussion and conclusions . . . . .	135
<b>7</b>	<b>Conclusions and Future Work</b>	<b>137</b>
7.1	General conclusions . . . . .	137
7.2	Future work . . . . .	139
<b>A</b>	<b>Other combinations of parameters explored in the SED fits</b>	<b>141</b>
<b>B</b>	<b>2D-SPS method validation for a reduced number of filters</b>	<b>155</b>
<b>C</b>	<b>Flashcards of CEERS galaxies</b>	<b>157</b>
<b>D</b>	<b>Table of CEERS galaxies</b>	<b>269</b>
<b>E</b>	<b>Table with formation times for CEERS galaxies</b>	<b>279</b>
	<b>List of research publications</b>	<b>293</b>
	<b>Acronyms</b>	<b>295</b>
	<b>Bibliography</b>	<b>301</b>

# Summary

---

The most massive galaxies in the nearby Universe are generally quiescent and present relatively old stellar populations. Understanding the origins of these massive galaxies, such as the Milky Way and even more massive systems, and how they formed their stars is a primary objective in astrophysics. The reason for this is that these galaxies hold very valuable information to unravel the mysteries of cosmic evolution and the processes that govern how galaxies form and evolve.

Constraining the epoch in which these galaxies emerged and analyzing the early stages of the stellar mass assembly in their likely progenitors at higher redshifts would represent an important step forward in our comprehension of the complex process of galaxy formation and evolution. This thesis presents a comprehensive study which combines cutting-edge observational capabilities with a sophisticated analysis technique to investigate the first stages in the formation and stellar mass assembly of massive progenitors at  $1 < z < 4$  of these galaxies. This work not only addresses the question of when they began to form their stellar populations but also compares the results with predictions of current cosmological simulations to explore its potential limitations and revisions required in their cosmological and/or galaxy formation models.

This research has been conducted by combining of the exceptional optical capabilities of the *Hubble Space Telescope* (HST) and the unprecedented infrared capabilities of the *James Webb Space Telescope* (JWST). Our dataset includes optical-to-NIR broad-band observations from the Cosmic Assembly Near-infrared Deep Extragalactic Legacy Survey (CANDELS) with HST and the Cosmic Evolution Early Release Science (CEERS) Survey with JWST. These cosmological surveys enable us to access the spatially-resolved emission of a representative sample of massive galaxies at  $1 < z < 4$ . Our approach is to combine the information provided by these stellar populations in two dimensions (2D), derived from stellar population synthesis in 2D (2D SPS), and develop a methodology that allows us to infer the first stages of their integrated star formation histories (SFHs) in a more robust way than when only using integrated emission. This thesis can be divided into a first part on the development and validation of our 2D-SPS methodology with simulated imaging data, and a second part on the application of this 2D-SPS methodology to real JWST + HST observations.

The development of this 2D-SPS methodology has been performed using the Illustris numerical simulation. Illustris is a large-scale hydrodynamical simulation which reproduces the general relationships observed for galaxies at different redshifts. In addition, Illustris provides synthetic images that imitate those of real cosmological surveys from JWST and HST. We use the latter synthetic images from Illustris to develop and optimize our 2D-SPS methodology for inferring the early stages of the SFH of a galaxy, built by combining the information of their spatially-resolved stellar populations. The advantage of using Illustris is that we can access the individual simulated particles that comprise each galaxy in the simulation, which provides us with the ground-truth information regarding its formation and stellar mass assembly. This is crucial to test and evaluate our 2D-SPS-derived SFHs, especially their first stages, with the ground-truth values provided by the simulated particles belonging to the galaxies.

One of the benefits of using Illustris is that, using its merger trees and tracking galaxies in time down to  $z = 0$ , we can select only massive  $1 < z < 4$  galaxies which are *bona-fide* progenitors of the most massive ( $M_{\star} > 10^{11} M_{\odot}$ ) local galaxies. We use this sample of massive  $1 < z < 4$  progenitors to test our 2D-SPS method and to study its effectiveness in recovering the first episodes of stellar mass assembly from the SFH of these galaxies. For our analysis, we quantify the first stages of stellar mass formation by calculating the formation times at which the galaxy formed 5%, 10%, and 25% of its stellar mass, computed directly from the corresponding SFH. We evaluate the goodness of our estimations in terms of the accuracy, defined as the median relative difference between the formation times measured and those obtained for the ground-truth extracted from Illustris. Our method proves to be successful in recovering the formation times with a median accuracy below 5%. In addition, the comparison of the formation times inferred for our sample of Illustris massive progenitors at  $1 < z < 4$  with those of their descendants at  $z = 0$ , together with those inferred of the whole population of  $M_{\star} > 10^{11} M_{\odot}$  galaxies at  $z = 0$ , gives us information about the limitations and biases we may also encounter in real (naturally magnitude-limited) observations.

With our 2D-SPS method already validated, we are ready to apply it to real massive galaxies observed in the first epoch of JWST/CEERS observations executed in June 2022. These observations consist of six NIRCcam pointings which overlap the majority of the CANDELS/EGS field, for which HST data are already available. Our overall findings reveal that massive  $1 < z < 4$  galaxies in CEERS began its stellar mass assembly at very early ages of the Universe, challenging our previous assumptions regarding the formation of the first galaxies at high redshift, in line with other recent JWST works. We compare our results from the predictions for massive galaxies in Illustris and another state-of-art and improved simulation, the IllustrisTNG (The Next Generation). Both simulations exhibit significant discrepancies regarding the cosmic times at which galaxies began to form their stars when compared to the formation epochs of CEERS galaxies. Our results highlight potential shortcomings in the current galaxy formation models of these simulations at early epochs.

The research of this thesis not only advances in our comprehension of the early formation and assembly of the stellar mass in massive galaxies, but also provides observational constraints for future cosmological and galaxy formation models, adding another small piece to the puzzle of understanding of our cosmic origins.

# Resumen

---

Las galaxias más masivas del Universo cercano suelen no mostrar formación estelar actualmente y presentan poblaciones estelares relativamente viejas. Entender los orígenes de estas galaxias masivas, tales como la Vía Láctea y sistemas aún más masivos y cómo formaron sus estrellas es un objetivo primordial de la astrofísica. La razón es que estas galaxias contienen información muy valiosa de carácter cosmológico y sobre los procesos que rigen cómo se forman y evolucionan las galaxias.

Restringir la época en la que surgieron estas galaxias y analizar las primeras etapas de ensamblaje de la masa estelar en sus progenitores a mayores desplazamientos al rojo representaría un importante paso adelante en nuestra comprensión del complejo proceso de formación y evolución de las galaxias. Esta tesis presenta un estudio exhaustivo que combina capacidades observacionales de vanguardia con una sofisticada técnica de análisis para investigar las primeras etapas en la formación y ensamblaje de masa estelar de progenitores masivos a  $1 < z < 4$  de estas galaxias. Este trabajo no sólo aborda la cuestión de cuándo comenzaron a formar sus poblaciones estelares, sino que también compara los resultados con las predicciones de las simulaciones cosmológicas actuales para explorar sus posibles limitaciones y las revisiones necesarias de los modelos cosmológicos y/o de formación de galaxias.

Esta investigación se ha llevado a cabo combinando las excepcionales capacidades del Telescopio Espacial Hubble (HST, del inglés *Hubble Space Telescope*) en el óptico y del Telescopio Espacial James Webb (JWST, del inglés *James Webb Space Telescope*) en el infrarrojo. Nuestro conjunto de datos incluye observaciones en imagen de banda ancha en el óptico e infrarrojo cercano de las exploraciones Cosmic Assembly Near-infrared Deep Extragalactic Legacy Survey (CANDELS) con el HST y Cosmic Evolution Early Release Science (CEERS) con el JWST. Estos sondeos cosmológicos nos permiten acceder a la emisión espacialmente resuelta de una muestra representativa de galaxias masivas a  $1 < z < 4$ . Nuestro enfoque consiste en combinar la información proporcionada por estas poblaciones estelares en dos dimensiones (2D), derivada de la correspondiente síntesis de poblaciones estelares en 2D (2D SPS), y desarrollar una metodología que nos permita inferir las primeras etapas de sus historias de formación estelar (SFHs, del inglés *Star Formation Histories*) de una manera más robusta que cuando sólo se utiliza la emisión integrada. Esta tesis puede dividirse en una primera parte sobre el desarrollo y validación de nuestra metodología 2D SPS con datos de imagen simulados y una segunda parte sobre la aplicación de esta metodología 2D SPS a observaciones reales de JWST + HST.

Esta metodología 2D SPS se ha desarrollado y testado utilizando las predicciones del proyecto Illustris, simulación hidrodinámica a gran escala que reproduce las relaciones generales observadas para galaxias a diferentes corrimientos al rojo. Además, Illustris proporciona imágenes sintéticas que imitan las de las exploraciones cosmológicas reales de JWST y HST. Utilizamos estas últimas imágenes sintéticas de Illustris para desarrollar y optimizar nuestra metodología 2D SPS a la hora de inferir las primeras etapas de la SFH global de una galaxia, construida combinando la

información de sus poblaciones estelares espacialmente resueltas. La ventaja de utilizar Illustris es que podemos acceder a las partículas simuladas individuales que componen cada galaxia dentro de la simulación completa, lo que nos proporciona la información de partida sobre la formación y ensamblaje de la masa estelar de las galaxias simuladas. Esto es clave para evaluar la calidad (precisión y exactitud) de las SFHs derivadas mediante el método 2D SPS, especialmente en sus primeras etapas, en comparación a los valores reales (*ground-truth* en inglés) proporcionados por las partículas simuladas pertenecientes a las galaxias.

Una de las ventajas de usar Illustris es que, gracias a sus árboles de fusiones y al seguimiento de las galaxias en el tiempo hasta  $z = 0$ , podemos seleccionar únicamente galaxias masivas de  $1 < z < 4$  que son progenitoras genuinas de las galaxias locales más masivas ( $M_{\star} > 10^{11} M_{\odot}$ ). Utilizamos esta muestra de progenitores masivos  $1 < z < 4$  para probar nuestro método 2D SPS y estudiar su eficacia a la hora de recuperar los primeros episodios de ensamblaje de masa estelar a partir de la SFH de estas galaxias. Para nuestro análisis, cuantificamos las primeras etapas de formación de masa estelar calculando los tiempos en los que la galaxia formó el 5%, 10% y 25% de su masa estelar, calculados directamente a partir de la SFH correspondiente. Evaluamos la bondad de nuestras estimaciones en términos de su *precisión*, definida aquí como la mediana de la diferencia relativa entre los tiempos de formación medidos y los obtenidos para del *ground-truth* extraído de Illustris. Nuestro método consigue recuperar los tiempos de formación con una precisión media inferior al 5%. Además, la comparación de los tiempos de formación inferidos para nuestra muestra de progenitores masivos de Illustris a  $1 < z < 4$  con los de sus descendientes a  $z = 0$ , junto con los inferidos para toda la población de  $M_{\star} > 10^{11} M_{\odot}$  galaxias a  $z = 0$ , nos proporciona información sobre las limitaciones y sesgos que también podemos encontrar en las observaciones reales (limitadas en magnitud de forma natural).

Con nuestro método 2D SPS ya validado, estamos listos para aplicarlo a galaxias masivas reales observadas en la primera época de observaciones del JWST/CEERS ejecutadas en junio de 2022. Estas observaciones consisten en seis apuntados NIRCcam que cubren la mayor parte del campo CANDELS/EGS, para el que ya se dispone de datos HST. Nuestros resultados revelan que las galaxias masivas a  $1 < z < 4$  en CEERS comenzaron su ensamblaje de masa estelar en edades muy tempranas del Universo y lo hicieron de forma muy rápida, desafiando nuestras suposiciones previas sobre la formación de las primeras galaxias a alto corrimiento al rojo, en línea con otros trabajos recientes del JWST. En este sentido, comparamos nuestros resultados referentes a las predicciones para galaxias masivas en Illustris con aquellos basados en la simulación mejorada de última generación IllustrisTNG (del inglés *The Next Generation*). Ambas simulaciones muestran discrepancias significativas respecto a los tiempos cósmicos en los que los precursores de las galaxias masivas comenzaron debieron haber empezado a formar sus estrellas en comparación con la época de formación de las galaxias observadas como parte de la exploración CEERS. Nuestros resultados ponen de manifiesto posibles deficiencias en los actuales modelos de formación de galaxias incluidos como parte de estas simulaciones en épocas tempranas o bien en el contexto cosmológico general asumido por las mismas.

La investigación de esta tesis no sólo ha permitido avanzar en nuestra comprensión de la formación temprana y el ensamblaje de la masa estelar en galaxias masivas, sino que también proporciona restricciones observacionales para futuros modelos cosmológicos y de formación de galaxias, añadiendo otra pequeña pieza al rompecabezas de la comprensión del origen de las galaxias en el Universo.



# List of Figures

---

- 1.1 Large-scale structure observed with 2dFGRS (left in blue) for  $\sim 10,000$  galaxies in the local Universe, which is reproduced by cosmological simulations such as the Millennium Simulation (right in red). The Earth would be sitting at the apex of the diagram. *Credits:* Adapted from Springel et al. (2006). . . . . 2
- 1.2 Global picture of the Universe state and epochs from Big Bang to present day. Immediately following the Big Bang, the Universe began to expand adiabatically. This expansion cooled the Universe enough to enable electrons to recombine with protons. The cosmos remained dark and neutral throughout the Dark Ages period until the formation of the first stars at Cosmic Dawn, likely at  $z \approx 15 - 20$ . As the first galaxies grew in abundance, the Lyman continuum photons gradually ionized their adjacent intergalactic medium (IGM). This is the start of Cosmic Reionization, with the Universe transitioning from mostly neutral (HI) to nearly entirely ionized (HII). This transition phase is believed to have ranged from  $12 \lesssim z \lesssim 6$  (from 0.35 to 1 Gyr in age of the Universe). The maximum cosmic star formation rate density was reached at Cosmic Noon ( $\sim 2 - 3$ ) when most of the stellar mass was formed decreasing after  $z \sim 1$  until now (Madau & Dickinson 2014). *Credits:* Figure adapted from Robertson (2022) and NASA. . . . . 3
- 1.3 **a)** Minimum halo mass for star-formation as a function of redshift. The dotted line marks the limit given by the Jeans mass (see text). Below these masses (yellow area), the internal pressure of the system prevents the collapse. The dashed line marks the locus where the cooling time of the system,  $t_{\text{cool}}$ , equals the free-fall time,  $t_{\text{free-fall}}$ . If  $t_{\text{cool}} > t_{\text{free-fall}}$ , the gas will not efficiently cool (pink area). If  $t_{\text{cool}} \ll t_{\text{free-fall}}$ , the gas will effectively cool, overcome pressure support, and collapse on a timescale given by  $t_{\text{free-fall}}$  (cyan region). Solid lines shows the halo mass vs. redshift for different overdensities in which the halos are already statistically significant in abundance (the lower the  $\sigma$ , the more abundant). For halo masses below  $10^4 M_{\odot}$ , no cooling is possible since their virial temperatures cannot be lower than of the CMB (gray region). According to Bromm (2013), this simplified model is only valid for  $z \gtrsim 20$ . **b)** Schematic picture of the formation of the first stars and galaxies. The first stars would be Pop III stars formed in  $M_h \sim 10^6 M_{\odot}$  at  $z \sim 20 - 30$ . These low-mass halos would be incapable of withstanding the intense negative feedback from Pop III stars in order to form a second generation of stars and, thus, cannot be considered as galaxies. First galaxies would be formed at  $z \sim 10$  in  $\sim 10^8 M_{\odot}$  halos, composed of Pop II stars. *Credits:* Panel a) adapted from Bromm (2013). Panel b) adapted from Cimatti et al. (2020). . . . . 7

- 1.4 **a)** Two-stage formation scenario for massive galaxies (see details in the main text).  
**b)** Schematic diagram of typical processes and morphological transformations that massive galaxies can undergo. *Credits:* Panel a) adapted from Spiniello et al. (2021). Panel b) extracted from Cimatti et al. (2020). . . . . 9
- 1.5 Zoomed-in portion of dwarf galaxy Wolf–Lundmark–Melotte (WLM), in our galactic neighborhood, observed with *Webb*/NIRCam and *Spitzer*/IRAC. A significant improvement in spatial resolution is appreciated with *Webb*. The small left inset shows the dwarf galaxy observed with VLT/OmegaCAM. The filters used to create the color images are indicated inside the figures (color-coded with the corresponding colors). *Credits:* NASA, ESA, ESO, CSA, STScI, Kristen McQuinn (Rutgers University), Alyssa Pagan (STScI) for image processing. . . . . 11
- 2.1 Modified figure from Vogelsberger et al. (2020). It shows an overview of some dark matter-only (left) and hydrodynamical (right) simulations, both large-scale (bottom) and zoomed-in simulations (top). Zoomed-in N-body simulations (top left): Aquarius (Springel et al. 2008), GHALO (Stadel et al. 2009), Phoenix (Gao et al. 2012), ELVIS (Garrison-Kimmel et al. 2014), and Via Lactea (Diemand et al. 2008). Zoomed-in hydrodynamical simulations (top right): NIHAO (Wang et al. 2015), Auriga (Grand et al. 2017), APOSTLE (Sawala et al. 2016), Latte/FIRE (Wetzel et al. 2016), and Eris (Guedes et al. 2011). Large-scale N-body simulations: Millennium (Springel et al. 2005b), Millennium-II (Boylan-Kolchin et al. 2009), Millennium-XXL (Angulo et al. 2012), Dark Sky (Skillman et al. 2014), and Bolshoi (Klypin et al. 2011). Large-scale hydrodynamical simulations: Illustris (Vogelsberger et al. 2014a,b; Genel et al. 2014), EAGLE (Schaye et al. 2015; Crain et al. 2015), IllustrisTNG (Springel et al. 2018), Romulus25 (Tremmel et al. 2017), Simba (Davé et al. 2019), Massiveblack-II (Khandai et al. 2015), Horizon-AGN (Dubois et al. 2014). . . . 19
- 2.2 Example of an Illustris merger tree for  $z = 0$  descendant of a galaxy from the main high-redshift sample analyzed in García-Argumánez et al. (2023; see also Chapter 5). The descendant at  $z = 0$  is highlighted with a cyan circle, while the considered progenitor galaxy at  $z \sim 1$  is marked with a green dotted circle. Bigger circle sizes correspond to higher halo masses. The circles are color-coded by specific SFR (sSFR). We show an RGB image for the  $z = 0$  galaxy generated by Torrey et al. (2015). The two empty horizontal lines correspond to the corrupted snapshots 53 and 55. . . . . 26
- 2.3 Illustris deep survey images (or Illustris mock ultra-deep fields) from Snyder et al. 2017 (three images on top), with a zoomed-in region in Field C (cyan and yellow squares). Each field is 2.8 arcmin a side. The HST Ultra-Deep Field is shown above as a comparison. *Credit:* Adapted from <https://archive.stsci.edu/hlsp/illustris>. 31

- 2.4 Distributions for redshift, stellar mass, SFR, and stellar half-mass radius for massive galaxies at  $1 < z < 4$  in the catalogs of Illustris mock-ultra deep fields (filled histograms). These catalogs only include galaxies brighter than  $g < 30.0$  mag. With unfilled histograms, we show the distributions for the 4,295 massive galaxies in the snapshot  $z = 1$  (dotted) and the 232 massive galaxies in that at  $z = 4$  (dashed) of the simulation (not necessarily appearing in the images). The histogram for  $z = 1$  has been normalized so that its maximum coincides with that of the massive,  $1 < z < 4$  galaxies in the images. Median and quartile values are shown at the top with segments. . . . . 32
- 2.5 Ground-truth SFH for `Illustris-1_073_0141918` calculated from its stellar and gas particles within  $2r_{\text{hm}}$ . The left panel shows the stellar mass density distribution in this galaxy. Particles within  $2r_{\text{hm}}$  are located inside the green sphere. We show as zoomed-in panels the same stellar mass density distribution (cyan rectangle on top) and the gas mass density distribution (yellow rectangle at the bottom). For stellar particles inside  $2r_{\text{hm}}$ , we load their formation and formation times. We make of a histogram of the formation times (expressed as lookback times) and sum the formation masses of the stars formed in each bin to generate the SFH. We force the SFH to have an age equal to that of the first star formed in the galaxy. The SFR at the origin of lookback time is calculated by summing the SFR values of gas particles in the green sphere (marked with a blue star in the SFH figure). Finally, we normalize the resulting SFH to recover the stellar mass of all the stellar particles inside  $2r_{\text{hm}}$ . . . . . 34
- 2.6 Schematic diagram of our sample of Illustris massive  $1 < z < 4$  progenitors to be analyzed in Chapter 5. We start from all the massive (circle) and non-massive (small black dot) galaxies in the Illustris synthetic deep survey images which are located at  $1 < z < 4$  (between the two horizontal dashed lines on the left). Using Illustris merger trees, we can follow the evolution of all the galaxies in the images at those redshifts until  $z = 0$  (bottom dotted line). Those  $z = 0$  galaxies do not appear in the images. Galaxies with  $M_{\star} > 10^{11} M_{\odot}$  at  $z = 0$  are represented by a square. Our sample of massive  $1 < z < 4$  progenitors (circles with a blue star inside) is composed of massive  $1 < z < 4$  galaxies in the images which end up as a very massive galaxy at  $z = 0$ . The descendants at  $z = 0$  of this sample are shown with orange squares with a star inside. These  $z = 0$  descendants can have other progenitors different from those considered in our  $1 < z < 4$  sample. On the right, we layout the conditions fulfilled by galaxies in our sample of  $1 < z < 4$  progenitors (top) and by their  $z = 0$  descendants (bottom). . . . . 36

- 3.1 *Hubble* images. **a)** HST coupled to space shuttle *Discovery* during the third HST servicing mission (SM-3A) in December 1999, with two astronauts in the front of the image and the Earth in the background. **b)** Comparison between the core of M100 observed by HST before (left) and after (right) the spherical aberration was corrected during the first servicing mission in December 1993. The left image, taken with the original Wide Field and Planetary Camera 1 (WFPC-1), misses fine and faint details owing to the starlight blur produced by the optical aberration in the primary mirror. The right image was taken with the Wide Field and Planetary Camera 2 (WFPC-2), installed during the servicing mission, and shows the significant improvement produced by the corrective optics that compensated the aberration. **c)** HST cross section that shows the Cassegrain design of the telescope and the path that light follows when it enters the telescope until it reaches the instruments. **d)** HST field of view after SM4 with the instruments entrance apertures in the focal plane as they are projected on the sky. **e)** Wavelength ranges (in nm) covered by the current scientific instruments in HST. *Images credits:* ESA/Hubble & NASA. . . . . 41
- 3.2 Modified figure from the *ACS Instrument Handbook* (Ryon 2022). HST total system throughput as a function of wavelength for several HST instruments. The lines show the maximum throughputs for each instrument at a given wavelength. Current operating instruments are shown with solid lines, and replaced (WFPC2) or inoperable (ACS/HRC, NICMOS) instruments with dashed lines. . . . . 44
- 3.3 Throughput of ACS and WFC3 filters used in this thesis. WFC3 filters are shaded inside, and their names have been boxed. . . . . 44
- 3.4 Sky coverage of CANDELS fields: GOODS-N (**a**), GOODS-S (**b**), UDS (**c**), EGS (**d**), and COSMOS (**e**). Adapted figures from Barro et al. (2019), Guo et al. (2013), Galametz et al. (2013), Stefanon et al. (2017), and Nayyeri et al. (2017), respectively. Gray shaded zones represent CANDELS WFC3 F160W mosaic, where darker zones correspond to deeper data, except for UDS, where WFC3 data are the hatched region delimited by the red solid line and, ACS, inside the dashed red line. In EGS (**d**), ACS data are the light blue larger shaded zone enclosing the WFC3 data in the center (dark gray). See details in main text. . . . . 50
- 3.5 *Webb* images. **a)** JWST from launch to L2. The position of Sun-Earth L2 is shown on the top right. **b)** Front (left) and side (middle) view of JWST. Images show how the Optical Telescope Element (OTE) and the Integrated Science Instrument Module (ISIM) are separated from the spacecraft bus and are shaded from sunlight by the sunshield. **c)** Comparison between JWST image quality (with MIRI) with respect to that of *Spitzer* IRAC 8.0  $\mu\text{m}$ . **d)** Schematic view of the optical design of JWST, which is a three-mirror anastigmat with a primary mirror, secondary mirror, tertiary mirror, and an additional fine steering mirror. **e)** Angles in which JWST can rotate for observations. The inset shows the allowed rotation with respect to the axis pointing to the Sun direction. Adapted figure from STScI. *Credits:* AURA/S. Lifson for a), McElwain et al. (2023) for b) and d), NASA/ESA/CSA/STScI/JPL-Caltech for c), STScI for e). . . . . 53

- 3.6 Scientific instruments and NIRCam images. **a)** JWST focal plane and field of view of the scientific instruments (highlighted) and the FGS. Several observing modes for the instruments are marked in different colors. **b)** NIRCam modules and field of view for both the short wavelength (SW) and long wavelength (LW) channels. Both channels can be simultaneously observed. **c)** Total system throughputs for NIRCam broadband filters. The ones used in this work have been highlighted. The dark gray bar in the middle is approximately the dichroic cutoff between the SW and LW channels. Adapted figure from STScI.  
*Credits:* STScI for all images. . . . . 57
- 3.7 Comparison of the SED fit of a  $z > 4$  galaxy in the pre-JWST era (blue dots and green model) and using new JWST CEERS data (orange dots and red model). The object belongs to the CANDELS EGS photometric catalog (Stefanon et al. 2017). The blue dots correspond to CANDELS HST photometry, together with  $K_s$  band and the four *Spitzer*/IRAC bands from the photometric catalog. The orange dots correspond to new NIRCam photometric data. The SED-fitting-derived probability distributions for stellar mass and redshift are shown as an inset (green for the CANDELS fit and red for the JWST fit). The JWST SED fit significantly better constrains the redshift and stellar mass distributions. An RGB postage stamp of the galaxy is also shown ( $5'' \times 5''$ ), created with NIRCam F444W, F200W, and F150W images.  
*Credits:* Adapted figure from Carnall et al. (2023). . . . . 60
- 3.8 CEERS images. **a)** Layout of CEERS observations: whole program (top middle), June observations (bottom left), and December observations (bottom right). **b)** CEERS NIRCam Epoch 1 color mosaic. We have highlighted and zoomed-in four  $1 < z < 4$  galaxies with  $M_\star > 10^{10} M_\odot$ . *Credits:* D. Kocevski for a), and NASA/STScI/CEERS/TACC/S. Finkelstein/M. Bagley/R. Larson/Z. Levay for the mosaic in b). . . . . 61
- 4.1 Schematic diagram of the SPS modeling with the isochrones technique, extracted from Conroy (2013). SSPs are built from an IMF, isochrone tables, and stellar spectra libraries. These SSPs are combined with a parametrized SFH and chemical enrichment and dust models to produce the CSP spectrum (see details in the main text). The middle-left panels show an example of SFH parametrized by a time-delayed exponential, i.e.,  $SFR(t) \propto t \cdot e^{-t/\tau}$ , for two different star formation time-scales:  $\tau = 1$  Gyr (black) and  $\tau = 10$  Gyr (red), and the corresponding assumption on the evolution of the metallicity (below). The dust attenuation panel (middle right) shows the attenuation law from Calzetti et al. (2000; red line) and the MW extinction curve (Cardelli et al. 1989; O'Donnell 1994; in black). In the bottom panel, the resulting SPS spectrum is shown before (blue) and after (red) applying the dust model. Nebular emission is not included in these models. . . . . 67

- 4.2 IMF comparison: Chabrier (2003) (red), Kroupa (2001) (blue), and the canonical Salpeter (1955) (orange dashed) IMF. All IMFs have been normalized to recover  $1 M_{\odot}$  when they are integrated from  $0.1 M_{\odot}$  to  $100 M_{\odot}$  (white area). The dotted red and blue lines (in the gray shaded area) show the values of the Chabrier (2003) and Kroupa (2001) IMFs, respectively, outside the range of initial stellar masses considered in this work. . . . . 71
- 4.3 SEDs for SSP models in SB99 and BC03. Models have been created assuming a Salpeter IMF ( $0.1$  to  $100 M_{\odot}$ ) for both SB99 (dotted) and BC03 (solid), for two metallicities:  $Z = 0.004$  (left panel) and  $Z = 0.020$  (solar; right). Ages of 10 Myr, 100 Myr, 1 Gyr, and 5 Gyr are shown in different colors. . . . . 72
- 4.4 **a)** Double-burst SFH. The galaxy SFH (black solid) results from the combination of an old population (orange dashed) and a young population (blue dashed), each described by  $SFR(t) \propto t e^{-t/\tau}$ . The ages of the old and young population are  $t_{\text{old}} = 4$  Gyr and  $t_{\text{young}} = 1$  Gyr, respectively, and their time-scales,  $\tau_{\text{old}} = 1.5$  Gyr and  $\tau_{\text{old}} = 100$  Myr. This synthetic galaxy would be at  $z = 1$ , with a stellar mass of  $10^{10} M_{\odot}$ , where the young burst accounts for 10% of this mass. **b)** Calzetti (2000) attenuation law expressed as  $A_{\lambda}/A_V$  as a function of wavelength. Two different values for  $R_V$  have been adopted:  $R_V = 4.05$  (Calzetti law; black solid) and the typically adopted value of  $R_V = 3.1$  (gray dashed). . . . . 75
- 4.5 Example of galaxy SFH recovered from the 2D-SPS modeling for an Illustris galaxy. The black solid line shows the galaxy SFH obtained by adding together the individual SFHs of the spatially-resolved SEDs (thin colored lines), for which a two population SFH is assumed. The square inset shows an WFC3/F160W image of the galaxy. The grid shows the regions from where these 2D SEDs have been measured (same color code as used for their SFHs). The alternative galaxy SFH derived from the integrated SED, measured inside the integrated aperture, is shown in dotted blue, also assuming a two population SFH. The green solid line shows the ground-truth SFH for the galaxy, provided by the simulated particles belonging to the galaxy in Illustris. The figure shows how the galaxy SFH derived from the 2D-SPS modeling, unlike that of the integrated SED, is able to capture the shape of the true SFH, especially at higher lookback times. . . . . 77

- 5.1 Left panel: Main Sequence plot for those galaxies at  $1 < z < 4$  included in the mock survey presented in S+17 which are progenitors of very massive galaxies ( $M_{\star} > 10^{11} M_{\odot}$ ) at  $z = 0$ . All progenitors are color-coded by redshift. In this chapter, we concentrate on the analysis of the most massive progenitors ( $M_{\star} > 10^{10} M_{\odot}$ ), which are plotted with star symbols. The Main Sequence found for all the Illustris simulated galaxies at different redshifts (Sparre et al. 2015) has also been plotted. Middle panel: postage stamp images for some representative examples of our galaxies (size  $2.5'' \times 2.5''$ ). These RGB images are created using ACS/F1814W, NIRCcam/F200W, and NIRCcam/F277W asinh-scaled images as B, G and R filters, respectively. The position of these galaxies in the left panel has been highlighted with a white dot inside. Right panel:  $g - r$  color vs. stellar mass diagram for descendants at  $z = 0$  of all galaxies at  $1 < z < 4$  (independently of their stellar mass) in the S+17 mock survey images. Descendants of the final sample of 221 galaxies analyzed in this chapter are plotted as stars. . . . . 83
- 5.2 Histograms for our  $1 < z < 4$  sample of 221 simulated galaxies: redshift (top left panel), total stellar mass (top right), SFR (bottom left), and stellar half-mass radius (bottom right). These properties have been extracted from the Illustris-1 database. Median and quartiles are shown as segments on the top. . . . . 83
- 5.3 Top panel: histogram for the radii of the photometric apertures of the 221 galaxies in the final sample as a fraction of  $2 \times r_{\text{hm}}$  radius, the typical radius used by Illustris to compare with observations. The cumulative fraction of galaxies is shown as a red line. Bottom panel: histogram for the fraction of stellar mass enclosed by the photometric apertures (blue filled histogram) and for a radius of  $2 \times r_{\text{hm}}$  (orange hatched) with respect to the total stellar mass in the galaxy. In both cases, we neglect neighboring galaxies. These total masses have been extracted from the simulated particles belonging to each galaxy in the Illustris database. At the top of both panels, we show the median and quartiles for each histogram. . . . . 88
- 5.4 Postage stamp images (size  $2.5'' \times 2.5''$ ) for one of our galaxies: Illustris-1\_066\_0000006 at  $z = 2.192$  (Field A of S+17 images). This galaxy code stands for galaxy id 6 and snapshot 66 ( $z = 2.21$ ) in the Illustris-1 simulation. Left panel: Segmentation map, with colored regions delimiting the galaxy (in orange), three nearby galaxies (green, yellow, and red), and sky pixels (black). We also show the integrated photometric aperture (dark cyan solid line) and the starting aperture of  $r = 2 \times r_{\text{hm}}$  used to calculate the former (dotted line). Inside the integrated aperture, we show the grid where the 2D photometry is measured: the cells that are finally kept for the 2D-SPS analysis are shown in cyan, cells discarded for not fulfilling the SNR and surface brightness criterion as pink hatched squares, and cells discarded for not including any pixel from the considered galaxy as white hatched squares. Middle panel: WFC3/F160W image (already registered, PSF-matched, and sky noise-added) with the integrated aperture. Right panel: WFC3/F160W image where the values of the pixels from nearby galaxies have been masked by replacing them with the same Gaussian sky noise distribution previously added to the images. We also show the integrated aperture and the grid. . . . . 90

- 5.5 Stellar mass vs. redshift plot for galaxies in our sample, with values extracted from the Illustris database. We show the stellar mass when considering all the particles in the galaxy (total stellar masses) as light blue circles and the stellar mass obtained when only particles inside twice the stellar half-mass radius as small dark blue dots. Histograms of stellar masses and redshifts are shown at the top and on the right, with the median and quartiles marked. . . . . 91
- 5.6 Example of one integrated SED fit for one of our galaxies: Illustris-1\_062\_0004079 at  $z = 2.843$ . This galaxy code stands for galaxy id 4079 and snapshot 62 ( $z = 2.73$ ) in the Illustris-1 simulation. The best fit is shown as a red line. We also show the models corresponding to the old (green) and young (orange) stellar populations. The transmission curves of the filters have been included at the bottom of the figure. The best-fit stellar parameters for the old and young populations are also given. An RGB image (size  $1.5'' \times 1.5''$ ) with the integrated aperture is shown as an inset. . . . . 94
- 5.7 Stellar masses for the  $1 < z < 4$  sample derived from the integrated SED-fits vs. their ground-truth values calculated from the simulated stellar particles belonging to each galaxy (inside a sphere with the same radius as that of the integrated photometric aperture). The one-to-one relation is shown with the dotted black line. The histograms for both distributions are shown in different colors, with the median and the 68% intervals as horizontal segments. . . . . 95
- 5.8 Schematic diagram of the methodology followed to obtain the median SFH for a galaxy from its 2D-SPS analysis. First, we show an RGB image of the galaxy and some of the HST+JWST broad-band images (in Table 5.1) processed to imitate CANDELS and CEERS observations for HST and JWST filters, respectively. We measure the 2D photometry inside a grid (in cyan) with cell size equal to the spatial resolution element, in addition to the integrated photometry (blue aperture). As an example, we show the SEDs measured for three regions of the grid: the center of the galaxy (teal cell), an arm region (light green), and a diffuse emission zone (pink). To estimate the uncertainties and degeneracies in the derived stellar populations, each SED is fitted 300 times by performing MC simulations. We add the individual SFHs inferred from all the grid regions to obtain the SFH for the whole galaxy. The black thin SFHs in the bottom subfigure show the SFHs for the whole galaxy created by accounting for the uncertainties in the SFHs of each grid region, where the median galaxy SFH from this 2D-SPS method is shown in yellow. The blue dotted SFH is the galaxy SFH inferred from the integrated photometry. The ground-truth SFH of the galaxy, given by the stellar particles belonging to the galaxy, is the green solid SFH. . . . . 97



- 5.9 Comparison between the mass-fraction formation times (measured backwards from the redshift of observation of the galaxy) of our 2D-SPS method and their ground-truth values:  $t_5$  (upper-left),  $t_{10}$  (upper-right),  $t_{25}$  (lower-left) and  $t_{\text{mw}}$  (lower-right) calculated from our 2D-SPS-derived SFHs versus their reference values calculated from the SFHs built from the simulated stellar particles in galaxies. Each galaxy is represented by 300 vertically spread points, which correspond to the mass-fraction formation times of the 300 2D-SPS SFHs, built from the 300 MC particles in each resolution element in the grid. The median of these values for each galaxy is shown as bigger circles and error bars represent the standard deviation of these values (68% interval). All points are color-coded by galaxy redshift. On the top of each panel, we show the ratio between the  $t_k$  of our 2D-SPS method and their ground-truth values as a function of the latter. As an inset, we include the offsets of the galaxies in the sample. . . . . 99
- 5.10 Ground-truth stellar mass histograms for the different samples extracted from the Illustris-1 database: when considering all particles in galaxies (top panel) or only particles inside twice the stellar half-mass radius (bottom panel). We show our main 2D-SPS sample of progenitors at  $1 < z < 4$  in blue, massive galaxies at  $1 < z < 4$  in cyan, the descendants at  $z = 0$  of our  $1 < z < 4$  progenitors in orange, and the whole population of very massive galaxies at  $z = 0$  in green. The median and the 68% intervals are shown at the top of each panel. . . . . 103
- 5.11 Ground-truth median SFHs calculated from the simulated particles for the subsamples of galaxies: all  $M_\star > 10^{11} M_\odot$  galaxies at  $z = 0$  (green lines), all massive galaxies at  $1 < z < 4$  (cyan), our main  $1 < z < 4$  progenitors sample (blue), and the descendants at  $z = 0$  of this high-redshift sample of progenitors (orange). The results from the 2D-SPS analysis are not included in this figure. The median SFHs for the  $z = 0$  subsets have been calculated in two ways: considering all the particles in galaxies (dotted lines) or only the particles inside a sphere with radius  $2 \times r_{\text{hm}}$  to the galaxy center (solid). The median SFH of the two high-redshift samples has been built using only particles whose distance to the galaxy center is lower than the radius of the photometric aperture used for each galaxy. Shaded areas represent the uncertainty of the median. As vertical lines, we show the  $t_5$ ,  $t_{10}$ ,  $t_{25}$ , and  $t_{\text{mw}}$  calculated for each SFH shown. As a comparison, we show in purple the median SFH calculated in Iyer et al. (2020) for all galaxies at  $z = 0$  in the Illustris simulation with  $M_\star \sim 10^{11} M_\odot$ . . . 105

- 5.12 Comparison between the median SFH of our main  $1 < z < 4$  progenitors sample derived from the 2D-SED fits (in red) and from the simulated particles (in blue). We also include the median SFH of the descendants of this high-redshift sample at  $z = 0$  built with particles inside  $2 \cdot r_{\text{hm}}$  (in orange) and the median SFH of massive galaxies at  $1 < z < 4$  derived from applying the 2D-SPS method to this sample (pink). Shaded areas represent the uncertainty of the median. The SFHs have been normalized to recover the same stellar mass as the median 2D-SPS-derived SFH of our main  $1 < z < 4$  sample over the same redshift intervals ( $z \gtrsim 1$ ). The vertical lines depict the  $t_5$ ,  $t_{10}$ ,  $t_{25}$ , and  $t_{\text{mw}}$  mass-fraction formation times for each SFH. Gray diamonds show the Illustris SFMS level at  $z = 1, 2,$  and  $4$  (Sparre et al. 2015). On the top panel, we show the evolution of the integrated stellar mass at each redshift for our main high-redshift sample (2D-SPS and particles, same color code). . . . . 109
- 5.13 Histograms of  $t_5$  and  $t_1$  calculated from the SFHs of galaxies in the different samples considered. Our main  $1 < z < 4$  sample of progenitors is represented by the outlined histograms: values calculated from the 2D-SPS-derived galaxy SFHs are outlined in red, while those calculated from the ground-truth SFHs built from the database (DB) are represented with a dashed blue line. For the 2D-SPS-derived values, we only show the median  $t_5$  or  $t_1$  for each galaxy (calculated out of the 300 SFHs per galaxy). The cyan, filled histogram represents the distribution of the ground-truth  $t_5$  and  $t_1$  for massive galaxies at  $1 < z < 4$ , calculated from the ground-truth SFHs built by considering only particles inside  $r_{\text{phot}}$  in the database. The ground-truth distribution for the  $z = 0$  descendants of our main sample is shown as the orange, hatched histogram. For the whole population of very massive galaxies at  $z = 0$ , only its median and quartile values are shown (black segments). For these two  $z = 0$  samples, only particles inside  $2 \times r_{\text{hm}}$  have been considered. Median and quartiles are shown as segments on the top. . . . . 111
- 6.1 Postage stamp images ( $3.5'' \times 3.5''$ ) for a CEERS galaxy nircam1-3670 at  $z = 1.13$ . **a)** RGB image generated with NIRCcam filters (R:F356W, G:F200W, B:F115W) with asinh scaling, with the initial integrated aperture ( $a = 2r_{\text{Kron}}$ ; dashed blue). **b)** Original segmentation map, where the pixels belonging to the considered galaxy are shown in red, the sky pixels in black, and pixels belonging to other galaxies, in yellow and orange. **c)** Edited segmentation map. We add a previously non-identified neighboring galaxy (in white) and we extend the pixels belonging to the neighboring galaxy on top (yellow). **d)** Reduction of the integrated aperture to minimize pixels belonging to neighbors. The new final integrated aperture is shown in solid blue. **e)** New RGB image of the galaxy in which the flux of the pixels belonging to other sources has been replaced by random sky noise. **f)** Final photometric apertures: integrated aperture for integrated photometry (blue) and grid for 2D photometry (cyan). . . . . 121

- 6.2 RGB images ( $3.5'' \times 3.5''$ ) generated with NIRCcam filters (R:F356W, G:F200W, B:F115W) and with asinh scaling for six CEERS galaxies in our final sample. *First row (of each galaxy panel):* final integrated aperture (dashed blue) and, in case this is smaller than the initial integrated aperture ( $a = 2r_{\text{Kron}}$ ), we also show the latter (solid blue). *Second row:* Final integrated aperture and final grid. . . . . 123
- 6.3 **a)** 2D-SPS-derived galaxy SFH for nircam2-7435 (solid light blue), obtained as the median of the different galaxy SFH realizations (thin black) which result from the MC solutions obtained for each of the 2D SEDs and corresponding to the SB99 models. The galaxy SFH derived from the integrated SED is shown in dashed blue (also for SB99). The galaxy SFH obtained for BC03 is shown in dashed orange as a comparison. **b)** RGB image ( $2'' \times 2''$ ) of the galaxy generated with NIRCcam filters (R:F356W, G:F200W, B:F115W; asinh scale) with its integrated aperture **c)** and the 2D grid. **d)** Segmentation map for the galaxy. . . . . 125
- 6.4 Stellar mass *vs.* redshift for our final CEERS sample of 333 galaxies at  $1 < z < 4$  with  $M_{\star} > 10^{10} M_{\odot}$  when SB99 (blue) and BC03 (orange) models are used. The redshift and stellar mass distributions are shown at the top and on the right, respectively, with median and quartiles marked with segments on top (and right) of the corresponding histograms. As a comparison, we include the results from applying the same photometric + 2D-SPS analysis to  $1 < z < 4$  massive galaxies from the Illustris simulation (magenta; see main text). . . . . 127
- 6.5 Median SFH for CEERS massive galaxies at  $1 < z < 4$  for (SB99 in blue and BC03 in orange). As a comparison, we include the median SFH for massive,  $1 < z < 4$  in Illustris (pink) after applying the same photometric + 2D-SPS analysis to these galaxies (Chapter 5 and García-Argumánnez et al. 2023; see main text). All median SFHs have been normalized to recover the same mass as that of the median SFH for BC03. Shaded areas represent the uncertainty of the median. Vertical lines show the formation times  $t_5$ ,  $t_{10}$ , and  $t_{25}$  computed from these median SFHs. On top, we show the evolution of the integrated stellar mass for the median SFHs. . . . . 129
- 6.6 *Left panels:*  $t_5$  (top) and  $t_{10}$  (bottom) distributions calculated from each individual galaxy SFH in the sample. CEERS galaxies are shown in the filled histograms: BC03 in orange and SB99 in blue. Illustris massive,  $1 < z < 4$  galaxies, to which the same 2D-SPS method has been applied, are shown in pink. We include as a comparison the distributions for all Illustris and TNG100 massive galaxies at  $z = 4$ , for which the galaxies SFHs have been derived from their simulated stellar particles (instead of via 2D SPS; see main text). Median and quartiles are shown as segments at the top. *Right panels:*  $t_5 \times 10^8 M_{\odot}$  (top) and  $t_{10^9} M_{\odot}$  (bottom) distributions computed from each galaxy SFH as the cosmic times at which those stellar mass were formed (same color code). . . . . 133
- A.1 Method validation figure for  $\tau_{\text{young}} = 10 \text{ Myr}$  and  $\text{age}_{\text{lim}} = 60\%$  of the age of the Universe, for BC03 models. . . . . 143

A.2	Method validation figure for $\tau_{\text{young}} = 10$ Myr and $\text{age}_{\text{lim}} = 60\%$ of the age of the Universe, for SB99 models. . . . .	144
A.3	Method validation figure for $\tau_{\text{young}} = 10 - 100$ Myr and $\text{age}_{\text{lim}} = 60\%$ of the age of the Universe, for SB99 models . . . . .	145
A.4	Method validation figure for $\tau_{\text{young}} = 10 - 150$ Myr, and $\text{age}_{\text{lim}} = 60\%$ of the age of the Universe, for SB99 models. . . . .	146
A.5	Method validation figure for $\tau_{\text{young}} = 10 - 200$ Myr, and $\text{age}_{\text{lim}} = 60\%$ of the age of the Universe, for SB99 models. . . . .	147
A.6	Method validation figure for $\tau_{\text{young}} = 10$ Myr, and $\text{age}_{\text{lim}} = 50\%$ of the age of the Universe, for SB99 models. . . . .	148
A.7	Method validation figure for $\tau_{\text{young}} = 10 - 100$ Myr, and $\text{age}_{\text{lim}} = 50\%$ of the age of the Universe, for SB99 models. . . . .	149
A.8	Method validation figure for $\tau_{\text{young}} = 10 - 100$ Myr, and $\text{age}_{\text{lim}} = 50\%$ of the age of the Universe, for BC03 models. . . . .	150
A.9	Method validation figure for $\tau_{\text{young}} = 10$ Myr, and $\text{age}_{\text{lim}} = 30\%$ of the age of the Universe, for SB99 models. . . . .	151
A.10	Method validation figure for $\tau_{\text{young}} = 10$ Myr, and $\text{age}_{\text{lim}} = 40\%$ of the age of the Universe, for SB99 models. . . . .	152
A.11	Method validation figure for $\tau_{\text{young}} = 10$ Myr, and $\text{age}_{\text{lim}} = 70\%$ of the age of the Universe, for SB99 models. . . . .	153
A.12	Method validation figure for $\tau_{\text{young}} = 10$ Myr, and $\text{age}_{\text{lim}} = 80\%$ of the age of the Universe, for SB99 models. . . . .	154
B.1	Comparison between the mass-fraction formation times of our 2D-SPS method, considering only the 8 filters in Chapter 6, and their ground-truth values: $t_5$ (upper-left), $t_{10}$ (upper-right), $t_{25}$ (lower-left) and $t_{\text{mw}}$ (lower-right) calculated from our 2D-SPS-derived SFHs versus their reference values calculated from the SFHs built from the simulated stellar particles in galaxies. Each galaxy is represented by 300 vertically spread points, which correspond to the mass-fraction formation times of the 300 2D-SPS SFHs, built from the 300 MC particles in each resolution element in the grid. The median of these values for each galaxy is shown as bigger circles and error bars represent the standard deviation of these values (68% interval). All points are color-coded by galaxy redshift. On the top of each panel, we show the ratio between the $t_k$ of our 2D-SPS method and their ground-truth values as a function of the latter. As an inset, we include the offsets of the galaxies in the sample. . . . .	156

# List of Tables

---

2.1	The Illustris Project large-scale simulation runs and some relevant numerical parameters. Illustris-(1,2,3) are the hydrodynamical simulations and Illustris-Dark-(1,2,3) are their dark matter-only analogs that have the same initial conditions but do not include the baryonic component. . . . .	21
2.2	Illustris snapshots with redshifts, scale factors and ages of the Universe. The relevant snapshots for this thesis, with $1 \lesssim z \lesssim 4$ , are highlighted with a gray shade. . . . .	27
3.1	General characteristics of the ACS channels. Observations for this thesis have been taken by the WFC channel, highlighted in gray. . . . .	44
3.2	Broadband ACS/WFC filters used in this thesis. . . . .	45
3.3	General characteristics of the WFC3 channels. Observations for this thesis have been taken with the IR channel, highlighted in gray. . . . .	46
3.4	Broadband WFC3 filters used in this thesis . . . . .	46
3.5	CANDELS fields: sky positions and references. . . . .	48
3.6	CANDELS fields: HST ACS and WFC3 images. . . . .	51
3.7	General characteristics of NIRCcam channels. . . . .	58
3.8	Broadband NIRCcam filters used in this thesis. . . . .	58
3.9	CEERS NIRCcam Epoch 1 imaging data and HST broadband filters. . . . .	63
5.1	Photometric broad-band images used in Chapter 5. . . . .	85
5.2	Integrated magnitudes of our $1 < z < 4$ sample . . . . .	89
5.3	Free parameters and their ranges in the SED fitting for a double delayed-exponential SFH. . . . .	93
5.4	Mass-fraction formation times and redshifts for different samples in Chapter 5. . . . .	112
6.1	Formation times and redshifts for median SFH of massive $1 < z < 4$ galaxies in Fig. 6.5.130	
6.2	Formation times and redshifts for massive galaxies analyzed in Chapter 6. . . . .	132

A.1	Results for the validation of the 2D-SPS method for some other combinations of parameters explored for different values of $\text{age}_{\text{lim}}$ and $\tau_{\text{young}}$ . We have highlighted the best-fitting parameters presented in Chapter 5 with a gray shade. . . . .	142
D.1	Characteristics of CEERS massive galaxies at $1 < z < 4$ analyzed in Chapter 6 . . . .	270
E.1	Formation times inferred for CEERS massive galaxies at $1 < z < 4$ analyzed in Chapter 6. . . . .	280

# Introduction

---

Our Milky Way, like most of other nearby massive galaxies, is not forming stars in a significant way any more. This means that most of the stellar mass in these galaxies was formed in the past. Gaining insights into the origins of local massive galaxies, such as the Milky Way and their more massive counterparts, is crucial to achieving a full understanding of the complex process of galaxy formation and evolution. The advent of new and more powerful observatories has given us a glimpse into an increasingly early and more active star-forming Universe, allowing us to probe galaxy populations at different redshifts and, when combined with numerical simulations, have broaden our comprehension of the most important processes that govern how galaxies evolve. Recently, the cutting-edge observational capabilities of NASA’s *James Webb Space Telescope* have opened the door to look even further back, to even when the first galaxies are supposed to have started forming their stars. At the same time, its exquisite data at intermediate redshifts makes possible to analyze the most likely progenitors of local massive galaxies in an unprecedented way. In this thesis, we concentrate on investigating the initial stages of stellar mass assembly in these progenitors at high redshift with the aim to address the question of when nearby massive galaxies began to form their stellar mass.

In this introduction, we first give a general overview of the evolution of structure formation over cosmic time and the emergence of the first stars and galaxies in the Universe (Section 1.1). After that, we concentrate on discussing the importance of massive galaxies for studying galaxy formation and the possible scenarios for the formation of massive galaxies observed today such as the Milky Way or even more massive (Section 1.2). Subsequently, we outline how the *James Webb Space Telescope* is expected to shed light onto the formation of the first galaxies at very high redshift and massive galaxies later in time (Section 1.3). Finally, we present the objectives to be addressed in this thesis (Section 1.4).

## 1.1 From structure formation to first stars

The present-day Universe we observe today is highly structured and complex. As shown by redshift surveys in the nearby Universe such as the two-degree-Field Galaxy Redshift Survey (2dFGRS) or the Sloan Digital Sky Survey (SDSS), galaxies are not uniformly distributed in sky, but they tend to be located in clusters and groups forming a filamentary large-scale structure. This large-scale structure is commonly known as the “cosmic web” (Bond et al. 1996). Even early cosmological simulations (Springel et al. 2006) already predicted that the large-scale distribution of dark matter exhibited voids, walls, and filaments strikingly similar to those observed in the large-scale

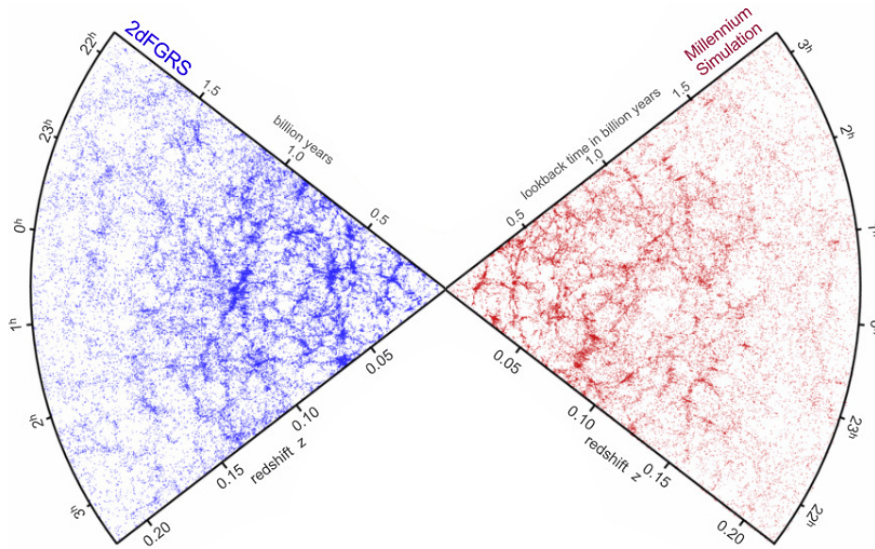


**Figure 1.1:** Large-scale structure observed with 2dFGRS (left in blue) for  $\sim 10,000$  galaxies in the local Universe, which is reproduced by cosmological simulations such as the Millennium Simulation (right in red). The Earth would be sitting at the apex of the diagram. *Credits:* Adapted from Springel et al. (2006).

distribution of galaxies (Fig. 1.1). Thanks to these cosmological simulations (discussed further in Chapter 2), we now know galaxies reside in the backbone of this cosmic web, formed by the clumpy and filamentary dark matter distribution.

This highly structured Universe that we observe today contrasts the nearly homogeneous state of the Universe at the very beginning. The latter can be inferred from the Cosmic Microwave Background (CMB) radiation observed with the *Planck* satellite, which is the thermal relic from the epoch of recombination, and which implies only tiny ripples imprinted on the density distribution at those early times. The ultimate aim of Extragalactic Astrophysics and Cosmology is to establish the physical mechanisms that connect the evolved state of the present-day Universe with the smooth initial conditions observed from the CMB measurements.

The most favored (and simple) cosmological model that fits CMB data and predicts present-day large-scale structure is the  $\Lambda$ -Cold Dark Matter ( $\Lambda$ CDM) cosmological model. This model consists of a flat Universe with an accelerating expansion governed by the so-called “dark energy”, which is commonly interpreted as due to a cosmological constant  $\Lambda$  the nature of which is still unknown. Apart from dark energy, the other components of this model are matter and radiation. Matter is composed of both baryons and dark matter. Dark matter consists of (still unidentified) weakly interacting elementary particles with negligible random velocities at early times (hence “cold” dark matter) which dominates the matter density of the Universe and, thus, the large-scale gravitational forces. The present-day matter, vacuum energy, baryon and radiation density parameters, expressed as a ratio of the critical density<sup>1</sup> of the Universe ( $\rho_{\text{crit}}$ ), are given by  $\Omega_{\text{m},0} = \rho_{\text{m},0}/\rho_{\text{crit}} = 0.3153$ ,  $\Omega_{\Lambda,0} = \rho_{\Lambda,0}/\rho_{\text{crit}} = 0.6847$ ,  $\Omega_{\text{b},0} = \rho_{\text{b},0}/\rho_{\text{crit}} = 0.0493$ , and  $\Omega_{\text{rad},0} = \rho_{\text{rad},0}/\rho_{\text{crit}} = 9.2 \times 10^{-5}$ , respectively, with a Hubble constant of  $H_0 = 100 h \text{ km s}^{-1} \text{ Mpc}^{-1}$  for  $h = 0.6736$  (Planck Collaboration

<sup>1</sup>The critical density is the average density of the Universe required for gravity to halt the expansion of the Universe at an infinite time in a Universe without cosmological constant.



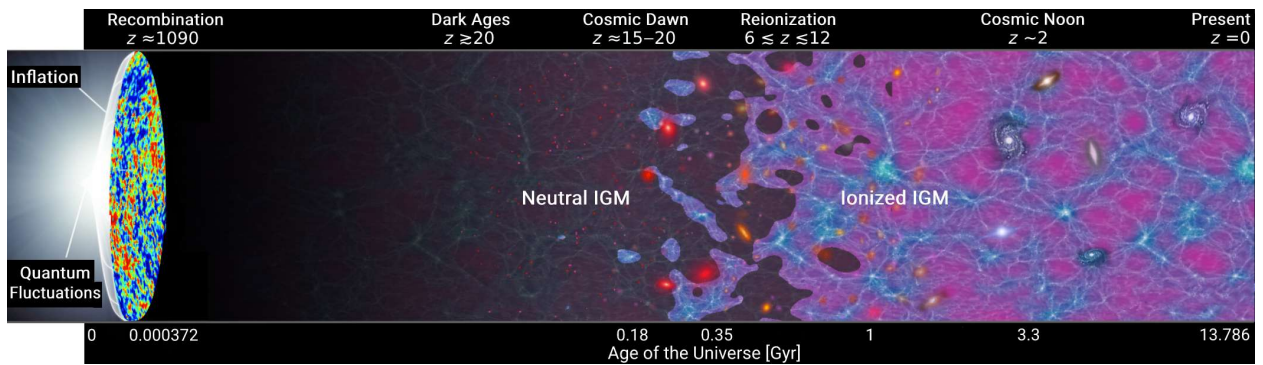


**Figure 1.2:** Global picture of the Universe state and epochs from Big Bang to present day. Immediately following the Big Bang, the Universe began to expand adiabatically. This expansion cooled the Universe enough to enable electrons to recombine with protons. The cosmos remained dark and neutral throughout the Dark Ages period until the formation of the first stars at Cosmic Dawn, likely at  $z \approx 15 - 20$ . As the first galaxies grew in abundance, the Lyman continuum photons gradually ionized their adjacent intergalactic medium (IGM). This is the start of Cosmic Reionization, with the Universe transitioning from mostly neutral (HI) to nearly entirely ionized (HII). This transition phase is believed to have ranged from  $12 \lesssim z \lesssim 6$  (from 0.35 to 1 Gyr in age of the Universe). The maximum cosmic star formation rate density was reached at Cosmic Noon ( $\sim 2 - 3$ ) when most of the stellar mass was formed decreasing after  $z \sim 1$  until now (Madau & Dickinson 2014). *Credits:* Figure adapted from Robertson (2022) and NASA.

et al. 2020). Although dark energy is the dominant component today, radiation was dominant in the beginning and up to  $z \approx 3400$ , which was followed by an epoch dominated by matter until  $z \approx 0.3$ , at which the current dark energy era started.

Fig. 1.2 shows an schematic view of the different epochs of the Universe from Big Bang to present day within this  $\Lambda$ CDM framework. By finding galaxies at the highest redshifts (i.e., searching for the first galaxies) or exploring the initial phases of stellar mass formation in lower (intermediate) redshift galaxies, as it will be done in this thesis, we should be able to gain insights into when, how, and where the first stars (and galaxies) formed, and their contribution to Reionization. This is also connected to structure formation throughout the Dark Ages and to Cosmology in general, on one side, and to baryonic processes that give rise to the formation of the first stars, on the other. In the following subsections, we give a general overview of the cosmic evolution of the early Universe, describing from the Big Bang to structure formation in Section 1.1.1, and the evolution of baryons and emergence of the first stars and galaxies in Section 1.1.2.

### 1.1.1 Structure formation

After the Big Bang, the Universe experienced a rapid inflationary epoch of exponential expansion between  $t \sim 10^{-36}$  s and  $\sim 10^{-34}$  s, known as “cosmic inflation”, and driven by the vacuum energy density of an effective scalar field called “inflaton”. Inflation froze the quantum fluctuations present in this scalar field (by causally disconnecting them as a consequence of the rapid accelerating expansion) and grew them to larger scales. This led to the emergence of almost scale-invariant primordial (presumably) gaussian density perturbations, whose power spectrum can be expressed

as  $P_{\text{prim}}(k) \propto k^{n_s}$ , with  $n_s \approx 1$ . These nearly scale-invariant<sup>2</sup> primordial density fluctuations are reflected in the almost perfect isotropy of the Cosmic Microwave Background (CMB), located at  $z \sim 1100$ , with anisotropies in temperature of  $\Delta T/T \sim 10^{-5}$ , and whose measurements constrain extremely well the initial conditions for structure formation.

After inflation, dark matter density fluctuations grew over time due to gravitational instabilities (i.e., self-gravity makes overdense regions increase their density contrast over time, while this contrast decreases in underdense regions). Baryons, however, were strongly coupled to the radiation field before recombination, and radiation pressure prevented baryonic density fluctuations from significantly growing. This, together with the fact that dark matter was (and is) more abundant, made the formation of structures governed by dark matter. This coupling of baryonic matter to the radiation field ended after recombination, after which baryons were able to fall into the potential wells generated by dark matter.

As a dark matter overdensities grows, its self-gravity makes it expand more slowly than Hubble expansion until, at some time, it stops expanding and begins to collapse on itself to form virialized system supported by the kinetic energy of dark matter particles (which cannot be radiated away). These gravitationally bound regions of dark matter that decoupled from Hubble expansion and collapsed are called “dark matter halos” and are the basic units onto which baryonic matter collapses (see below). The number density of halos with a given mass at each redshift, known as the “halo mass function” (HMF), is predicted from the extended Press-Schechter formalism (Press & Schechter 1974; Bond et al. 1991) and confirmed by the results of N-body simulations (e.g., Lacey & Cole 1994) and is a critical ingredient to establish the history of formation of galaxies of different masses. At a fixed redshift, less massive halos are more abundant, since the number density of halos decreases as mass increases. At a fixed mass, the number density of halos is higher for lower redshifts. As a consequence of this, dark matter structures grow hierarchically, from small systems that virialized first to large structures that form later, mainly as a result of mergers from smaller systems, but also by the accretion of diffuse matter non-belonging to the halo.

### 1.1.2 Baryons in dark matter halos: formation of the first stars

Before recombination (at  $z \approx 1100$ ), baryons were coupled to the radiation field, and radiation pressure prevented them from falling into the potential wells generated by dark matter. This coupling ended after recombination, and baryons were free to follow the spatial distribution of dark matter, to fall into the dark matter halos and to settle down in the inner parts of them in quasi-hydrostatic equilibrium (i.e., where the pressure of the gas compensates the gravitational force). Nevertheless, because of the different nature of baryons, these are subject to undergo physical processes that dark matter does not suffer (e.g., dissipation, heating, cooling, or star formation), which make baryons behave differently than dark matter when density overdensities are sufficiently large. On large scales, the gravitational field created by dark matter dominates and the distribution of baryons is similar to that of dark matter. In contrast, on smaller scales the balance between the gas pressure and cooling will become important.

The process that leads to the formation of stars in the Early Universe is complex. Thus, in order to form stars, the gas must first fall into an halo. For this to happen, the mass of the halo

---

<sup>2</sup>Actually,  $n_s = 0.9965$ , according to Planck Collaboration et al. (2020)

must exceed the *Jeans mass*, so that the potential well generated by dark matter is sufficiently large to overcome gas pressure and enable gas to fall into the dark matter halo. But this Jeans criterion is not enough for an halo to form stars. Once in the halo, the gas must be able cool by radiative process in order to lose pressure support and collapse to eventually form stars. As the halo collapses, frictional processes transform the potential energy of the gas into heat. In a very simple approximation, the Rees–Ostriker–Silk criterion (Rees & Ostriker 1977; Silk 1977) predicts that only gas with a cooling time ( $t_{\text{cool}}$ ) shorter than its dynamical or free-fall timescale ( $t_{\text{free-fall}}$ ) will be able to easily collapse towards the center of the halo and become denser. On the contrary, if the cooling time is longer than the free-fall time, this cooling will be inefficient, the gas will rapidly become pressure supported and the collapse will slow down (see, e.g., Bromm 2013; Klessen & Glover 2023). Fig. 1.3a shows in which halo masses cooling will be effective (cyan region) as a function of redshift of collapse assuming primordial gas of zero metallicity ( $Z \approx 0$ ). The yellow zone delimits the halos with masses below the *Jeans mass*, for which no gas has fallen into. Apart from the Rees–Ostriker–Silk criterion (dashed line) and the Jeans mass (dotted) line at each redshift, we must also consider the abundance of halos with a given mass at each redshifts. This is marked by the solid lines in Fig. 1.3a. This line shows the relation  $M_h$  vs.  $z_{\text{vir}}$ , that depends on how likely a halo can arise from the gravitational collapse of a peak within the random (gaussian) field of primordial density fluctuations. For a halo to be statistically significant, we must consider the  $3 - 4\sigma$  peaks (or lower; Couchman & Rees 1986, since higher-sigma peaks are too rare to be noticeable abundant and to have an impact on the cosmic history). From this simplified analysis shown in Fig. 1.3a, one infers that star formation could first occur in  $M_h \sim 10^6 M_\odot$  at  $z \sim 10 - 20$  (see Bromm 2013). Although this figure is a simplification, this global picture has been confirmed by simulations (e.g., Bromm et al. 2002; Yoshida et al. 2003).

Gas cooling in these high-redshift halos was different than that observed at lower redshift. The primordial gas is metal-free and cannot be cooled via metal-line transitions or lines from other heavier molecules as it does in chemical enriched regions. In the pristine gas, atomic hydrogen and helium, formed in the Big Bang Nucleosynthesis, are efficient coolants at  $T > 10^4$  K. But at  $T < 10^4$  K, the main channel to cool the gas (up to  $\sim 200$  K) is the small amount ( $n_{\text{H}_2}/n \sim 10^{-3}$ ) of molecular hydrogen (Saslaw & Zipoy 1967; Peebles & Dicke 1968), and trace amounts of other secondary molecules (e.g., deuterium, and  $\text{HHe}^+$ ). This molecular cooling allows the gas to reach the densities needed for the formation of the first metal-free Population III (Pop III) stars (see reviews of Greif 2015; Klessen & Glover 2023, and references therein). The formation of the first stars marks the end of the cosmic “Dark Ages” ( $z \sim 1110 - 30$ ; e.g., Dayal & Ferrara 2018).

As mentioned above, the first Pop. III of stars are thought to have formed in low-mass ( $M_h \sim 10^6 M_\odot$ ) dark matter halos (called “minihalos”) that virialized at  $z \sim 20 - 30$  (Couchman & Rees 1986; Tegmark et al. 1997; Schauer et al. 2019; Skinner & Wise 2020), and which correspond to  $3 - 4\sigma$  peaks in the gaussian random field of primordial density perturbations (e.g., Tegmark et al. 1997). Although no direct observation of Pop III stars in the early Universe has been achieved, according to simulations, Pop III stars are thought to be unusually massive ( $\sim 10 - 100 M_\odot$ ; Clark et al. 2008, 2011; Stacy et al. 2010, 2016; Greif et al. 2012) due to the inefficient fragmentation in the molecular cloud as a consequence of the relatively warm temperature of the collapse metal-free gas ( $\sim 100$  K vs. 10 K in low-redshift molecular clouds), with an initial mass function (IMF) that tends to be top-heavy that has a nearly flat mass distribution above  $10 M_\odot$  (Hirano et al. 2014, 2015; Stacy et al. 2016). Nevertheless, there is still much uncertainty regarding the final masses and

IMF of Pop III stars (see Klessen & Glover 2023 for a review). Although the contribution of Pop III stars in nearby galaxies is expected to be small, the actual fraction of the stellar mass budget in this population is unknown, and their contribution is even more uncertain in higher redshift galaxies.

Due to their large masses, Pop III stars were important UV emitters (Omukai & Palla 2003), capable of ionizing their surrounding IGM. Therefore, the formation of these first stars marks the beginning of the Epoch of cosmic Reionization (EoR;  $z \sim 30 - 6$ ), which approximately spans from the birth of these first Pop III stars, to when nearly all of the IGM is ionized (Bromm & Yoshida 2011; Zaroubi 2013; Wise et al. 2014; Stark 2016; Dayal & Ferrara 2018; Cooray et al. 2019). The shallow potential wells in minihalos hosting these first Pop III stars makes them highly vulnerable to their negative stellar feedback (Barkana & Loeb 2001; Bromm & Yoshida 2011), which prevents a second generation of new stars from forming in them (Fig. 1.3b). Considering a galaxy as a long-lived stellar system hosted by a dark matter halo (Bromm & Yoshida 2011) which is capable of gravitationally retaining a significant fraction of its gas, these minihalos cannot be considered as the *bona-fide first galaxies*. Instead, simulations show that  $\sim 10^8 M_\odot$  dark matter halos at  $z \sim 10$  were the hosts of the first galaxies (e.g., Wise & Abel 2007, 2008; Greif et al. 2008, 2010). These halos were already sufficiently metal-enriched (from previous Pop III stars in minihalos) to form low-mass Population II (Pop II) stars in a less bursty manner<sup>3</sup> and massive enough to withstand their feedback (see Fig. 1.3 b).

Pop III stars are the main contributors to the cosmic star formation history from their formation at  $z \sim 30$  until  $z \sim 15 - 20$ , when the contribution of the subsequent second generation of (slightly) metal-enriched Pop II stars becomes dominant (see Klessen & Glover 2023, and references therein). In fact, a recent a study by Hartwig et al. (2022) shows that although Pop III stars produce individual ionized IGM regions in their surroundings, there will not be a significant accumulation of ionizing background at large-scale until these individual regions start to overlap, and this event takes place until considerably after Pop II stars have become the dominant source of ionizing photons.

Observational advances in the last decade opened the door to start searching for galaxies at the epoch of Reionization. Deep imaging surveys performed by space telescopes like *Hubble Space Telescope* (HST) and *Spitzer*, in combination with other ground-based telescopes like Subaru, the Very Large Telescope (VLT), or Keck have provided us with numerous samples of galaxies in the EoR using several selection techniques (see, e.g., Dayal & Ferrara 2018, and references therein). Among the latter, we can cite the Lyman break technique (to look for Lyman Break Galaxies; LBGs), gravitational lensing, or the narrow-band Lyman Alpha technique (to look for Lyman Alpha Emitters; LAEs). These techniques have enabled *Hubble* to detect  $\sim 1000$  galaxy candidates with photometric redshifts of  $z \sim 7 - 9$  ( $\sim 750 - 550$  Myr after Big Bang; e.g., Finkelstein et al. 2013). Follow-up spectroscopic confirmation with Keck, VLT and the Atacama Large Millimeter/submillimeter Array (ALMA) have confirmed  $\sim 100$  galaxies at  $z \sim 7$ , but only a handful at  $z > 8$  (see Robertson 2022 for a review), with only one spectroscopically confirmed galaxy at  $z = 11.1$  ( $\sim 400$  Myr after Big Bang; Oesch et al. 2016). This redshift frontier ( $z \sim 8 - 10$ ), set by the

<sup>3</sup>The IMF is thought to change from top-heavy to the regular bottom-heavy IMF observed today when a critical metallicity of  $\sim 10^{-6} - 10^{-4} Z_\odot$  is reached (Bromm et al. 2001; Schneider et al. 2002). Pop III stars are thought to have formed from the primordial gas with  $Z \sim 5 \times 10^{-9} Z_\odot$  (according to the Big Bang Nucleosynthesis), and thus, with a top-heavy IMF, unlike the observed Pop II stars, with  $Z \sim 0.005 - 0.05 Z_\odot$  (Dayal & Ferrara 2018).

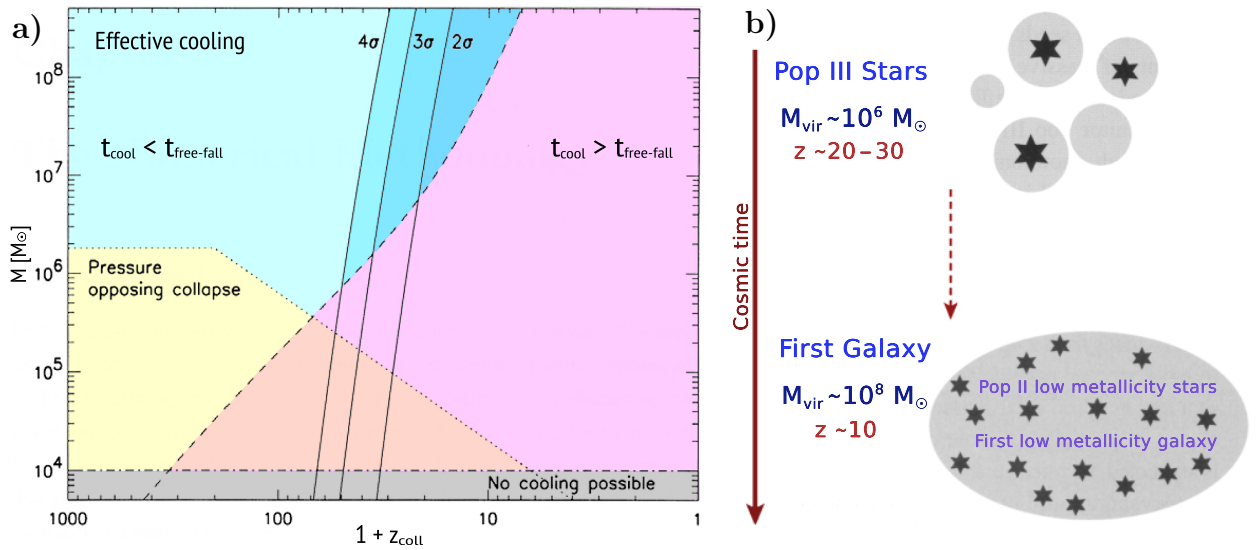


**Figure 1.3:** **a)** Minimum halo mass for star-formation as a function of redshift. The dotted line marks the limit given by the Jeans mass (see text). Below these masses (yellow area), the internal pressure of the system prevents the collapse. The dashed line marks the locus where the cooling time of the system,  $t_{\text{cool}}$ , equals the free-fall time,  $t_{\text{free-fall}}$ . If  $t_{\text{cool}} > t_{\text{free-fall}}$ , the gas will not efficiently cool (pink area). If  $t_{\text{cool}} \ll t_{\text{free-fall}}$ , the gas will effectively cool, overcome pressure support, and collapse on a timescale given by  $t_{\text{free-fall}}$  (cyan region). Solid lines show the halo mass vs. redshift for different overdensities in which the halos are already statistically significant in abundance (the lower the  $\sigma$ , the more abundant). For halo masses below  $10^4 M_{\odot}$ , no cooling is possible since their virial temperatures cannot be lower than of the CMB (gray region). According to Bromm (2013), this simplified model is only valid for  $z \gtrsim 20$ . **b)** Schematic picture of the formation of the first stars and galaxies. The first stars would be Pop III stars formed in  $M_h \sim 10^6 M_{\odot}$  at  $z \sim 20 - 30$ . These low-mass halos would be incapable of withstanding the intense negative feedback from Pop III stars in order to form a second generation of stars and, thus, cannot be considered as galaxies. First galaxies would be formed at  $z \sim 10$  in  $\sim 10^8 M_{\odot}$  halos, composed of Pop II stars. *Credits:* Panel a) adapted from Bromm (2013). Panel b) adapted from Cimatti et al. (2020).

limit of *Hubble*'s capabilities, is too low to provide a complete census of galaxies in the Reionization Epoch and at higher redshifts, when the first galaxies and stars began to form. Nevertheless, JWST is expected to expand this horizon of observability with the aim to better characterize the direct relation between the formation of first galaxies and Reionization by providing a large number of very high-redshift galaxies approaching those considered as the first galaxies (see Section 1.3).

## 1.2 A global picture of how massive galaxies formed

The study of massive galaxies at high redshift is fundamental for understanding and constraining our models of galaxy formation and evolution and, therefore, the underlying cosmology and the corresponding physical processes involved. Indeed, they are the most-likely progenitors of local massive early-type galaxies (ETGs; e.g., Swinbank et al. 2006; Ricciardelli et al. 2010; Fu et al. 2013), the most massive systems we observe today, and which host  $\sim 50 - 60\%$  of the total stellar mass in the Universe (e.g., Fukugita et al. 1998; Bell et al. 2003). Local ETGs are quiescent systems

(i.e., with no significant ongoing-star formation) that completed their formation long ago in the past (see reviews from Renzini 2006, and Blanton & Moustakas 2009, and references therein). In addition, the “downsizing” scenario states that the most massive galaxies started and completed their stellar mass formation earlier than less massive systems (e.g., Cowie et al. 1996; Heavens et al. 2004; Pérez-González et al. 2005, 2008). This means that by studying the progenitors of local massive galaxies we can access the earliest phases of star formation in the Universe. Furthermore, the advantage of observing massive galaxies is that, because of their high luminosity, they are more easily detected than lower-mass systems at any redshifts, which makes them ideal targets for galaxy surveys at high redshift such as those being pursued with JWST.

In this thesis, we will consider as “massive” those galaxies with stellar mass  $M_{\star} \geq 10^{10} M_{\odot}$ . This definition encompasses galaxies slightly less massive than the Milky Way (whose stellar mass is  $\log(M_{\star}/M_{\odot}) = 10.71 \pm 0.09$ ; Licquia & Newman 2015) and more massive galaxies, up to the most massive ellipticals, with masses in the local Universe as high as  $\log(M_{\star}/M_{\odot}) \sim 12.5$  (Erfanianfar et al. 2019).

There are two different approaches to study of the formation of Milky Way-like and more massive galaxies: 1) either to analyze in detail similar galaxies at  $z = 0$  in order to reconstruct their SFHs over the 13.7 Gyr of present age of the Universe, or 2) to study the properties of galaxies that lie at higher redshifts and try to establish evolutionary connections between progenitor galaxies and their descendants (or progenitor/descendant relationships) at different redshifts, providing us with a global picture of how galaxies have evolved through time. As discussed in Section 1.2.1, the latter approach has been extensively studied with *Hubble* in the last twenty years by studying galaxies at  $z \lesssim 4$  with the aim to provide a global picture of how massive galaxies form and evolve especially at early epochs for which the former approach provides very little information.

### 1.2.1 Massive galaxies: a two-stage formation scenario

The average size of massive galaxies at higher redshift is smaller than that of their local counterparts of similar masses. This was first discovered by Daddi et al. (2005) for seven massive, quiescent, early-type galaxies at  $z \sim 2$ , and confirmed in follow-up studies with larger samples (e.g., Trujillo et al. 2007; van Dokkum et al. 2008, 2010, 2014; Whitaker et al. 2013; Tomczak et al. 2014). These massive, compact, quiescent spheroids, commonly observed at  $z \sim 2 - 3$ , are nicknamed “red nuggets” and present typical effective radii of  $\sim 1$  kpc (Carollo et al. 2013; van der Wel et al. 2014), a factor of  $\sim 4$  smaller than local quiescent galaxies of similar mass (Trujillo et al. 2007; van Dokkum et al. 2008). This implies that they present stellar densities of up to  $\sim 1 - 2$  orders of magnitude (e.g., van Dokkum et al. 2008; Szomoru et al. 2012).

The smaller galaxy size of early-type galaxies with increasing redshift for a fixed mass is also found in star-forming galaxies (e.g., van der Wel et al. 2014), although the decrease in size with increasing redshift is less steep. There is also observational evidence for the existence of compact, star-forming galaxies at high redshift called “blue nuggets”<sup>4</sup>, whose masses and abundances are compatible with being the progenitors of red nuggets (e.g., Barro et al. 2013, 2014; Williams et al. 2014; Bruce et al. 2014; Nelson et al. 2014). Such compact systems have not been found locally

---

<sup>4</sup>In this case, *blue* does not imply color, but a star-forming system. This is because a dusty star-forming galaxy, with a redder color, still would be considered a blue nugget.

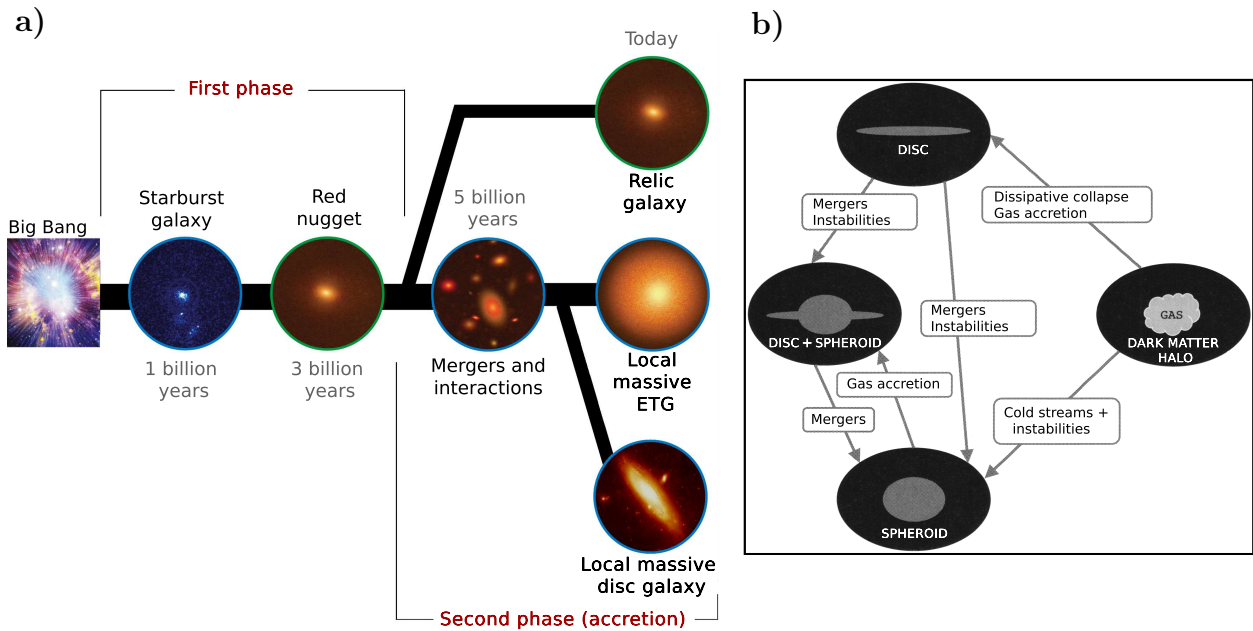


**Figure 1.4:** a) Two-stage formation scenario for massive galaxies (see details in the main text). b) Schematic diagram of typical processes and morphological transformations that massive galaxies can undergo. *Credits:* Panel a) adapted from Spiniello et al. (2021). Panel b) extracted from Cimatti et al. (2020).

yet (e.g., Trujillo et al. 2009; Taylor et al. 2010). In addition, the formation times of both massive, low-redshift galaxies and red nuggets at higher redshift similar (e.g., Daddi et al. 2005; Carnall et al. 2020).

Classically, there were two opposed models to explain the formation of spheroids or early-type massive galaxies: “monolithic collapse” (based on gravitational collapse of a single protogalaxy) and “hierarchical” (based on mergers). Nevertheless, those scenarios have been discarded in the last two decades, based on the aforementioned observational data of galaxies at  $z \sim 2 - 3$ , together with theoretical studies using cosmological simulations. These theoretical studies have analyzed the formation and assembly of massive galaxies by reconstructing their full galaxy assembly histories (e.g., De Lucia & Blaizot 2007). This kind of studies have provided strong evidence for a two-phase evolutionary scenario (e.g. Naab et al. 2009; Oser et al. 2010) in which massive galaxies would have formed most of their stellar mass at high redshift ( $z \gtrsim 2$ ) via a first main dissipative phase of *in-situ* star formation, followed by a secondary phase of multiple (dry) minor mergers that gradually increase the galaxy size (also called *ex-situ* processes). As we will see below, these two phases (or *tracks*) are not necessarily present in all galaxies.

The initial phase of rapid growth in this two-stage formation scenario is dominated by violent *in-situ* star formation at  $z \gtrsim 2$  (Oser et al. 2013) in which galaxies form the bulk of their stars in only the first billion years of cosmic time. In this phase, also known as the *fast track*, stars are formed by highly dissipative gas rich processes like major mergers or violent disc instabilities, which can result in the formation of a compact star-forming galaxy (i.e., the observed blue nuggets). Then, as star formation is quenched, or at least progressively damped (Catalán-Torrecilla et al., 2017), these systems would become massive, ultra-compact, passive galaxies (i.e., a red nugget). This is

followed by a second and more extended phase in which they experience a series of intense minor (dry) mergers with satellite galaxies that gradually extend their sizes and potentially transform them into the more extended galaxies commonly observed today. The relative contribution of this second phase seems to be more important in more massive galaxies. Recent studies based on both semi-analytical and hydrodynamical simulations have confirmed and polished this two-phase scenario by predicting the accreted stellar fractions of early-type galaxies and confirmed that the fraction of accreted material increases with lower redshift and higher stellar masses (e.g., Lee & Yi 2013, 2017; Dubois et al. 2016; Rodriguez-Gomez et al. 2016; Davison et al. 2020; Pulsoni et al. 2021; Remus & Forbes 2022). Interestingly, for a small fraction of early-type galaxies, this second phase of accretion via minor mergers apparently did not take place. This is the case of the so-called “relic galaxies” (Trujillo et al. 2009, 2014; Ferré-Mateu et al. 2015, 2017). These are ultra-compact and massive galaxies which missed the accretion phase and passively evolved until present-day without being disturbed. Thus, their stellar populations, formed in the early stages of the Universe, hold very valuable information about the earliest phases of galaxy formation, although they are limited in the local Universe by the little spectrophotometric evolution of stellar populations of  $\geq 10$  Gyr of age.

The two-phase formation scenario is valid to explain the formation of local massive spheroids and bulges, but also disc galaxies (Fig. 1.4a). In the above scenario, a disc can be formed in the second phase of accretion around the bulge grown in the previous stage (see, e.g., Costantin et al. 2021). Another possibility is that the disc galaxy is formed from the beginning in the dark matter halo. In this case, disc galaxies form when the gas in a halo conserves angular momentum during collapse (i.e., does not transfer it to the dark matter). This is known as “dissipative collapse” and allows the gas to settle into a rotating disc perpendicular to the angular momentum as it collapses. For this to happen, the gas in the halo must have previously acquired a relatively high angular momentum (like dark matter in the halo) from tidal forces of neighboring structures. Star formation in this extended disc takes place from local instabilities of molecular clouds in the disc. In either of the two formation cases, the survival of this disc will depend on the merger history of the galaxy (e.g., major mergers might likely destroy or thicken it) and the environment (e.g., if the disc galaxy enters a cluster, it will likely lose its disk due to environmental quenching). Fig. 1.4b shows the main processes and morphological transformations that may occur during the formation and assembly history of massive galaxies.

### 1.3 A further glance: the James Webb Space Telescope

As happened with *Hubble* when it was launched 32 years ago, the *James Webb Space Telescope* (JWST; Gardner et al. 2006) is expected to revolutionize our comprehension of galaxy formation and evolution (and many other fields in Astrophysics). This is primarily due to three outstanding technical characteristics of JWST when compared to those of its precursors *Hubble* and *Spitzer* in terms of:

1. Spatial resolution.
2. Depth.
3. Spectral range coverage.



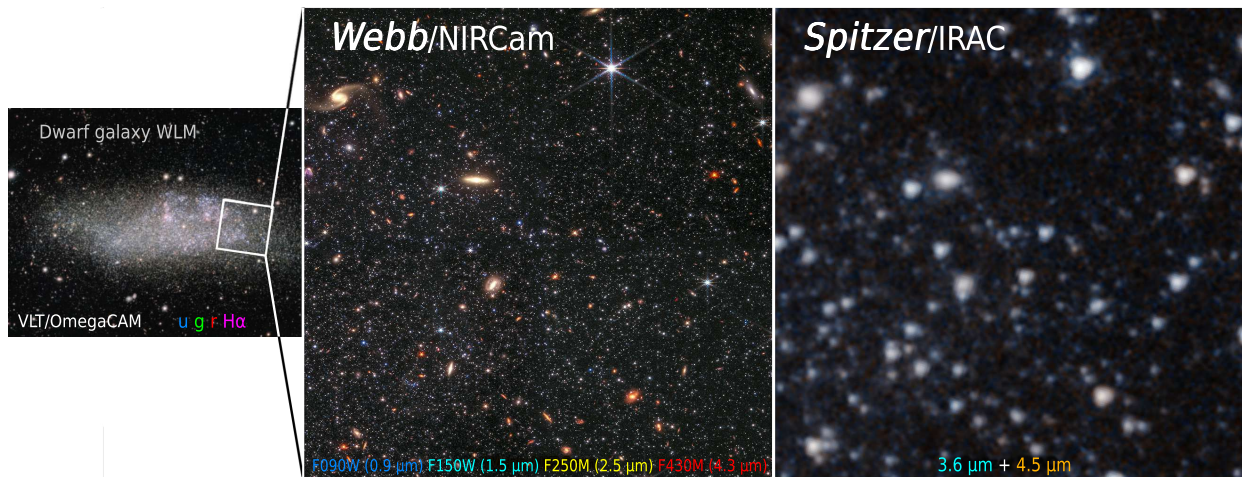


**Figure 1.5:** Zoomed-in portion of dwarf galaxy Wolf–Lundmark–Melotte (WLM), in our galactic neighborhood, observed with *Webb*/NIRCam and *Spitzer*/IRAC. A significant improvement in spatial resolution is appreciated with *Webb*. The small left inset shows the dwarf galaxy observed with VLT/OmegaCAM. The filters used to create the color images are indicated inside the figures (color-coded with the corresponding colors). *Credits:* NASA, ESA, ESO, CSA, STScI, Kristen McQuinn (Rutgers University), Alyssa Pagan (STScI) for image processing.

These technical features and its implications are discussed further in Chapter 3. Briefly, we emphasize here that before *Webb*, only HST was able to resolve different parts of distant galaxies. Unfortunately, the wavelength coverage for imaging with HST was limited (up to  $\sim 2 \mu\text{m}$ ) and unable to probe the rest-frame optical of very distant galaxies, leading to high uncertainties in the parameters derived for their stellar populations due to the poor constrain of their Spectral Energy Distributions (SEDs). This problem was usually overcome by extending the SED of galaxies with *Spitzer* data in the mid-infrared (MIR). Nevertheless, those *Spitzer*-extended SEDs could only be built for the integrated flux of galaxies (and not for regions within them) due to the poor spatial resolution of *Spitzer* ( $\sim 10$  times worse than that of *Hubble* at the same wavelength; see Fig. 1.5). On the contrary, the unprecedented spatial resolution of JWST in the near-infrared (NIR) and MIR, combined with its unmatched depth (up to 2 orders of magnitudes deeper than previous observatories) and exceptional wavelength coverage ( $\sim 1 - 28 \mu\text{m}$ ), allows us to combine its data with those of HST and to study the spatially resolved emission of distant galaxies in the optical, NIR, and MIR, and thus, providing unprecedentedly constrained photometric redshifts, stellar masses, star formation rates, or star formation histories (SFHs) of these galaxies. In addition to this, the exceptional imaging characteristic of JWST will be complemented with its spectroscopic capabilities in a wide wavelength range.

### 1.3.1 Probing the early Universe with the *James Webb Space Telescope*

The majority of the highest-redshift galaxies identified to date are LBG, and thus, they are observed based on their distinctive spectral discontinuity in the UV: the Lyman break. This consists in a cutoff in the rest-frame spectrum below the Lyman-limit at  $912 \text{ \AA}$ , which is caused by the almost complete absorption at bluer wavelengths than this limit (effectively, below  $1216 \text{ \AA}$ ) by neutral

hydrogen present at  $z \gtrsim 6$ . Observationally, these galaxies are detected using a dropout technique (the Lyman break technique) that consists in detecting galaxy with non-negligible integrated fluxes at wavelengths redder than  $(1+z) \times 1216 \text{ \AA}$ , but with no detections blue-ward than this wavelength. HST, because of its limited wavelength coverage, cannot detect  $z \gtrsim 10$  galaxies with this technique (since their Lyman break is located at redder wavelengths than those covered by the reddest filters of HST). Nevertheless, the unprecedentedly deep IR imaging provided by JWST at  $\lambda > 2 \text{ \mu m}$  is able to overcome this limitation inherent to the use of HST, being able to observe galaxies at  $z > 10$ , possibly reaching  $z \sim 15$ , therefore probing the first few hundreds megayears after the Big Bang (see Robertson 2022 for a review). In this way, JWST will provide us with more comprehensive insights of galaxy formation beyond our current  $z \sim 8 - 10$  frontier.

In this regard, there are still many uncertainties about the Dark Ages and how the Universe became completely ionized in the Reionization era where JWST could do major contributions. For instance, it is believed that the UV radiation from the first galaxies was the main cause for Reionization, but observations show that galaxies nearby and at higher redshifts absorb most of this radiation before it can even reach the IGM (Siana et al. 2010; Flury et al. 2022). The timescale in which this Reionization occurred is also a matter of debate. To match observations, it is necessary for galaxies at those high redshifts to ionize the IGM within approximately the first 700 Myr. Nevertheless, galaxies that emit enough ultraviolet radiation have not been found at those distances yet and much of what we know about Reionization relies on the extrapolation of existing trends at lower redshifts. The exceptional characteristics of JWST will help us understand these issues regarding the cause of Reionization by observing galaxies when the Universe was younger than 1 Gyr.

JWST will also open the door, for the first time, to study the extreme physical conditions of very distant galaxies (in terms of their low metallicity, high density, accretion rates, or merger rates; see reviews from Bromm & Yoshida 2011 and Stark 2016) or primordial Super-Massive Black Holes (SMBHs). For instance, galaxies observed up to  $z \sim 8 - 9$  provide evidence of Carbon and Oxygen emission, although those heavy elements are not expected to be available in the ISM of galaxies at those redshifts (Hutchison et al. 2019; Topping et al. 2021). JWST is expected to provide more insight about these  $z \sim 8 - 9$  galaxies through rest-frame optical spectroscopy, which will allow measurements of their metallicities, star formation rates, or ionization properties. Regarding the formation of the first Pop III stars, JWST is not sensitive enough to detect halos forming the first Pop III stars in the Early Universe (see Klessen & Glover 2023, and references therein), but it may be able to detect individual supermassive Pop III stars or small clusters of them through gravitational lensing if they are highly lensed. Nevertheless, the probability of this occurring is very small (Rydberg et al. 2013; Diego 2019).

Finally, with *Webb* we will also be able to validate the observed trends for  $z \sim 4 - 10$  galaxies and evaluate whether these still remain at higher redshifts. Among them, we can mention the rapid decline in the cosmic star formation rate for  $z > 9$  (e.g., Oesch et al. 2014, 2018), the increase in steepness of the faint-end slopes for both luminosity and mass functions (e.g., Bouwens et al. 2015; Song et al. 2016), or the increase in the stellar mass-halo mass ratio (e.g., Behroozi & Silk 2015; Behroozi et al. 2019).

### 1.3.2 Recovering the assembly history of galaxies via 2D SPS with JWST

From the observational point of view, the assembly history of a galaxy is imprinted on the properties of its stellar populations. Significant observational work has been conducted in the last few years (in the pre-JWST era) to study the stellar populations of the most massive galaxies at  $z > 3$  from the integrated emission of photometrically-selected (and sometimes spectroscopically-confirmed) samples through the use of the stellar population synthesis (SPS) technique (e.g. Glazebrook et al. 2017, Alcalde Pampiega et al. 2019, Forrest et al. 2020a,b, Marsan et al. 2022 and references therein). However, there are also spectroscopic and photometric studies that show that the physical properties of galaxies present systematic trends both radially, mainly, but also azimuthally in the local Universe (see, e.g., Di Matteo et al. 2013, Tacchella et al. 2015, Nelson et al. 2016, Wang et al. 2017, Ho et al. 2018, Sánchez-Menguiano et al. 2020, Abdurro'uf et al. 2022, Chamorro-Cazorla et al. 2022, Bellardini et al. 2022). For these kinds of studies, the stellar population synthesis (SPS) modeling in two dimensions (2D) has become an essential tool to derive these subgalactic-scale resolved properties by analyzing their spatially-resolved emission. If applied to massive progenitors at high redshift, this spatially-resolved analysis can provide further clues on the role of different mechanisms (e.g., internal vs. external, secular vs. fast) on the evolution of massive galaxies, since the different mechanisms proposed act at different scales and have a different impact as a function of galactocentric distance (Dekel & Burkert 2014, Zolotov et al. 2015, Tacchella et al. 2015, 2016, 2018, 2019, Akhshik et al. 2022) and for different morphological components (e.g., Méndez-Abreu et al. 2021, Johnston et al. 2022 for local galaxies, and Costantin et al. 2021, 2022 for higher-redshift galaxies). This heterogeneity of the properties of stellar populations within galaxies may have as a consequence a spatial variability in the SFH across different regions within a given galaxy, which further highlights the need to analyze stellar populations in two dimensions in our case if we aim at determining when galaxies began to form their stars.

Still, we cannot ignore that the main drawback of the stellar population synthesis is the intrinsic degeneracies associated with the study of the emission from stars, even within individual pixels. Indeed, limitations in the spectral resolution, wavelength coverage and/or signal-to-noise ratio of the data, result in strong degeneracies in the parameter space of physical properties such as age, star formation timescale, metallicity, or attenuation by dust. The correlations among these parameters are more or less difficult to disentangle depending on the value of each specific parameter (e.g., young ages, such as those expected in high-redshift galaxies, are less prone to some of these degeneracies), as well as the mentioned observational errors and wavelength coverage (see, e.g., Gil de Paz & Madore 2002). The latter problems are especially difficult to tackle as we go to higher redshifts and/or study less massive galaxies, since galaxies are generally too faint to reach their continuum level with high spectral resolution. This makes the SPS analysis of progenitors of massive nearby galaxies at high (or intermediate) redshift, ultimate goal of this thesis, rather challenging, especially when aiming at statistically representative samples of galaxies. These large samples are even harder to get when using spectroscopic (instead of photometric) data, which are resource-demanding and therefore relatively scarce. In addition, due the technological limitations of our observatories, it is hard to cover wide spectral ranges to account for different populations and effects such as dust extinction or other degeneracies. In this regard, *Webb* will play an important part in overcoming these issues, thanks to its unprecedented sensitivity, high spatial resolution, wide wavelength coverage, sensitive to stars of different ages, and variety of spectral resolutions (from spectroscopic  $R \sim 3000$  to photometric  $R \sim 7$  and spectro-photometric  $R = 100$ ).

Therefore, JWST offers us for the first time a unique opportunity to analyze spatially-resolved stellar populations at intermediate redshifts with spectral information from the rest-frame UV to the optical or even NIR, in particular when combined with HST data. That combination of circumstances allows us to explore for the first time the early epochs of star formation in galaxies in a more robust way using a novel approach. Specifically, we are able to conduct this study from a spatially-resolved analysis of the stellar populations in galaxies, at sufficiently high depths, and by accessing rest-frame wavelengths that are sensitive enough to the evolution of the ages of the stellar populations that we want to explore. In addition, we can also reach redshifts that are high enough to improve the sensitivity of the modeling to the spectrophotometric evolution of the stellar populations and, at the same time, with wavelength coverage from the rest-frame UV to the NIR when combined with HST. This thesis aims at investigating the exceptional opportunity presented by the combination of the aforementioned circumstances that have arisen from the arrival of JWST.

### 1.3.3 Open questions in galaxy formation

There are still many uncertainties regarding galaxy formation in the early Universe which are mainly related to the fact that, before James Webb, it was not feasible to conduct observations at the high redshifts that correspond to the end of the Dark Ages or the beginning of Reionization. The lack of observational evidence of galaxies at the beginning of the Reionization epoch, with very few of them confirmed belonging to this epoch, made it difficult to study the connection between the appearance of these first galaxies and stars with the process of Reionization or, of particular interest in this thesis, to constrain the epochs when those first galaxies appeared and how rapid they assembled their stellar mass. The limitations in observational capabilities of previous observatories, which were unable to directly detect a representative number of galaxies at high redshift ( $z \gtrsim 10$ ), together with the uncertainties in the complex process of galaxy formation, made it significantly challenging to address the latter open questions in the pre-JWST era.

## 1.4 Main objective of this thesis

The main objective of this thesis is to address this lack of knowledge about the early stages of galaxy formation and, more specifically, to answer the open question of when the first massive galaxies appear in the Universe, which is directly related to the question of when massive galaxies (like the Milky Way) began to form their stellar populations.

The approach followed in this thesis to address the latter question is to look further and fainter in order to search for the most likely progenitors of local massive galaxies at different redshifts, and subsequently analyze their stellar populations, especially their Star Formation Histories (SFHs). Our strategy is to combine imaging data from JWST with already existing broad-band data from HST, with the aim of extracting spatially-resolved SEDs of progenitors at high redshift of local massive galaxies. The unprecedented wavelength coverage of JWST in the NIR will allow us to cover the rest-frame emission in our galaxies from the UV to (at least)  $\sim 1 \mu\text{m}$ , a wavelength range which is particularly important to robustly constrain the properties of stellar populations. Furthermore, the high spatial resolution of JWST (and HST) enables the measurement of spatially-resolved SEDs for each galaxy and, thus, the derivation of their stellar population properties in 2D by applying a

novel 2D-SPS method developed for this thesis. This determination of stellar population parameters in 2D is essential for the identification of the evolutionary stages a galaxy can undergo regarding the evolution of its stellar content and can help determine when its assembly began. In this thesis, we will combine the information provided by the stellar population parameters in two dimensions to recover realistic integrated galactic SFHs. The power of this method lies in the fact that the observational characteristics of smaller regions within a galaxy are likely to be described by a less complex SFH, making it possible to define their characteristics with fewer parameters than those needed to describe the SFH of the entire galaxy as a whole. Therefore, by dividing the galaxy into smaller regions and deriving the SFH for these regions, we are making the problem of recovering the (more complex) integrated SFH of the galaxy simpler.

To address the main objective of the thesis and provide insight about when massive galaxies began to form, we will concentrate on determining the earliest phases of the formation of massive ( $M_{\star} \geq 10^{10} M_{\odot}$ ) galaxies at  $1 < z < 4$ . These early stages of formation for these galaxies will be inferred by analyzing their integrated SFHs built from their 2D-SPS analysis. For these massive galaxies, very high quality and spatially-resolved data will be available with JWST and are already available with HST. In addition, our redshift range ( $1 < z < 4$ ) includes the cosmic epoch known as “cosmic noon”, at which the cosmic star formation rate density history peaked ( $z \sim 2$ ) and where a considerable fraction of the local stellar mass was formed: about half of the present-day stellar mass was formed by  $z = 1.3$  (see Madau & Dickinson 2014 for a review). Our findings study should potentially help to identify the primary precursors of massive galaxies at cosmic noon, an epoch of particular interest which will be broadly studied with JWST in the forthcoming years.

We divide this thesis work into three different parts:

1. The first part of this thesis is devoted to developing a method and to assessing the robustness of using our 2D-SPS method on HST+JWST imaging data for determining the SFHs of massive,  $1 < z < 4$  galaxies, namely, the early stages (or onset) of their SFHs. For this, our first objective is to establish a methodology and evaluate its performance using synthetic deep survey images generated by cosmological simulations, in particular, the Illustris Simulation (Vogelsberger et al. 2014a,b; Genel et al. 2014). These simulated images, available in the broad-band filters from HST and JWST, imitate the conditions of real surveys, and thus, similar processing techniques can be applied to them. Moreover, the advantage of using simulations is that we can access the information of the simulated stellar particles that compose each galaxy in the simulation (what we call the “ground-truth” in this thesis). This information can be directly compared with the results inferred from our 2D-SPS analysis of galaxies in the synthetic images. This is fundamental in order to constrain the ranges of the input parameters for the SED fits that best recover the first formation stages in the SFH of our massive galaxies. We also study whether the sample of massive galaxies at the considered redshift are truly representatives of the actual progenitors of very massive galaxies at  $z = 0$ , regarding the SFH of these galaxies.
2. Once our methodology has been validated with Illustris, the second goal of this thesis is to apply our 2D-SPS method to massive,  $1 < z < 4$  galaxies observed with JWST (+ HST). By the time the first part of the thesis was accomplished, some early JWST imaging data were already available. In our case, we make use of the imaging data from the Cosmic Evolution Early Release Science (CEERS) Survey, one of the first surveys to be conducted with JWST.

These data are combined with previous HST data of the same region, namely, those from the Cosmic Assembly Near-infrared Deep Extragalactic Legacy Survey (CANDELS). The aim of the second part of the thesis is to infer the formation times of massive galaxies at  $1 < z < 4$  observed with HST + JWST imaging data by applying the already validated 2D-SPS methodology with Illustris. The formation times derived will allow us to address, from the observational point of view, the fundamental open question of when massive galaxies began to form stars.

3. Finally, and related with the latter point, the last of the objectives of these thesis is to compare the formation times inferred for observed, high-redshift galaxies with the predictions of cosmological simulations at those redshifts. Cosmological simulations have been fairly successful at reproducing the properties of the local population of galaxies and, coarsely, those at high redshift. However, these simulations rely on very scarce observational data at high redshift. Our aim is to assess the validity of the predictions of these simulations in the early Universe regarding galaxy formation and provide future simulations with new data at these redshifts to better constrain their galaxy formation models and, possibly also, the underlying cosmology.

The outline of this thesis work is as follows. In Chapter 2 we provide an overview of the Illustris Simulation and describe which information we can extract from the simulation for our study to conduct the aforementioned objectives. In Chapter 3, we present a detailed description of the technical characteristics of *Hubble* and *Webb*, together with the characteristics of the cosmological surveys to be used in this thesis work: CANDELS and CEERS. Details on our Stellar Population Synthesis (SPS) modeling are provided in Chapter 4. In Chapter 5, we present the implementation and evaluation of our 2D-SPS methodology using synthetic images of massive,  $1 < z < 4$  galaxies from Illustris (point 1 above). The last part of the thesis is included in Chapter 6. This chapter describes how our 2D-SPS method is applied to CANDELS+CEERS massive galaxies observed at  $1 < z < 4$ , the SFHs and formation times inferred for these galaxies (point 2 above), and how the latter compares with those of simulated galaxies in cosmological simulations (point 3). Finally, the general conclusions of this thesis and future work are presented in Chapter 7.

# Simulated data: the Illustris Simulation

---

In this chapter, we describe the Illustris Simulation and discuss why it constitutes the ideal testbed for the development and validation of our 2D SPS method for deriving the early stages in the formation of massive,  $1 < z < 4$  galaxies from HST + JWST observations. After a general introduction about cosmological simulations (Section 2.1), we present the Illustris Simulation (Section 2.2), describe its general characteristics, and summarize the most relevant accomplishments of the simulation in reproducing galaxy population properties, highlighting its limitations. After that, we present the Illustris synthetic deep survey images (Section 2.3) that will be used to develop our 2D SPS method (presented in Chapter 5), and from where we will derive our 2D SPS SFHs. Finally, we focus on how we can extract information about massive,  $1 < z < 4$  galaxies in the simulation, and in particular, how this information can be used to build their ground-truth galaxy SFH (Section 2.4), which will be compared with our 2D SPS SFHs derived from the Illustris synthetic images.

## 2.1 Introduction to cosmological simulations

In the past few decades, cosmological simulations have become an unquestionable tool to study galaxy formation and evolution. The major advances in computational power, the improvements in algorithms, and the better understanding of the physical process responsible for the shaping and evolution of galaxies have allowed to reach a remarkable agreement between simulations and observations over a very wide range of scales. An important aspect of these cosmological simulations is that they try to model a representative part of the Universe (typically boxes of hundreds of  $\text{Mpc}/h$ ) to produce a whole population of galaxies. Because of the richness of predictions these calculations create, they are very useful for research in galaxy and structure formation, since they allow to address some of the open questions discussed in Chapter 1, for which no observational data is still available in some cases.

The aim of these simulations is essentially to bridge the early and smooth state of the Universe observed in the Cosmic Microwave Background with the highly-complex and evolved state we observe today. The fundamental idea that lies behind these cosmological simulations is simple: the initial conditions of the simulation are set to match the initial state of the Universe, and after implementing the models and laws of physics, the initial state is evolved forward in time. In modern simulations, this is done by modeling the evolution of dark matter, dark energy and baryonic matter over time. Finally, the output of the simulation is compared to real observations (at present time

and different redshifts) and, in case of tensions between the two, the models and/or physical laws of the simulation are refined. This comparison with observations is crucial not only to verify that the implemented models are sufficiently good, but also, to better understand the physics of galaxy formation itself. This can be done by studying, for instance, the impact of any specific mechanism on the evolution of galaxies (e.g., the comparison of the output of the simulation for different feedback recipes helps us to understand how feedback produced by SMBHs or supernovae shapes the properties of galaxies).

Although cosmological simulations can also be used to study different cosmological models and how these affect the properties of the populations of dark matter halos and galaxies (see, e.g., Angulo & Hahn (2022) for a review of simulations with alternative models to cold dark matter), most of the cosmological simulations are performed within the framework of the  $\Lambda$ CDM cosmological model. In this sense, cosmological simulations have played an important role in testing and establishing this model. The positive aspect of simulations is that both the fundamental parameters of  $\Lambda$ CDM and the specific initial conditions used (i.e., the initial perturbation spectrum) are believed to be known with high-accuracy. The main difficulty, however, is the simultaneous computation of the evolution of dark matter and gas dynamics in time. For this, it is essential to (numerically) solve the coupled system of partial differential equations that describe gravity and hydrodynamics. In the case of the non-interacting dark matter particles, the collisionless Boltzmann equations coupled to Poisson’s equation must be solved in an expanding Universe whose expansion is governed by the Friedmann equations. For the modeling of the baryonic component, which is initially composed of gas alone, this is typically described by assuming an inviscid ideal gas that follows the Euler/Navier-Stokes equations (see Vogelsberger et al. 2020 for a review of the different numerical methods to solve both the baryonic and dark matter component).

Despite the baryonic matter (e.g., stars and gas) only composes the  $\sim 5\%$  of the energy/mass budget of the Universe in the  $\Lambda$ CDM paradigm (Planck Collaboration et al. 2020), the modeling of ordinary matter is extremely challenging in cosmological simulations due to the large number of physical processes that affect baryons and drive their evolution. As a consequence, the first cosmological simulations could not directly address the evolution of this ordinary matter. Instead, simulations had to be simplified to only account for dark matter. The most widely-used approach for this consists in following the trajectories of dark matter particles which comprise an N-body system: “N-body simulations”.

The predictions from these dark matter-only calculations are very important in the area of large-scale structures and the study of the geometry properties of the cosmic web. Even early dark matter-only simulations already predicted that dark matter was not completely homogeneously distributed, but exhibited nodes, filaments, walls and voids and filaments that were compatible with those seen in galaxy large-scale distributions (e.g., Springel et al. 2006). The Millennium simulation (Springel et al. 2005b) is probably the most publicly successful dark matter-only simulation, but other examples are also shown in Fig. 2.1 (left side), both zoomed-in (top panel) and cosmological (bottom). Currently, the present-day dark matter-only simulations can effectively resolve many orders of magnitude below those where galaxies are formed and where, according to cosmological models in which dark matter is assumed to be a cold<sup>1</sup> elementary particle, we should expect to find

---

<sup>1</sup>“Cold” refers to the velocity dispersion of dark matter particles at early times ( $z \sim 3400$ ), i.e., if dark matter was composed of relativistic particles or not back then. For cold dark matter, negligible (non-relativistic) random velocities are assumed.



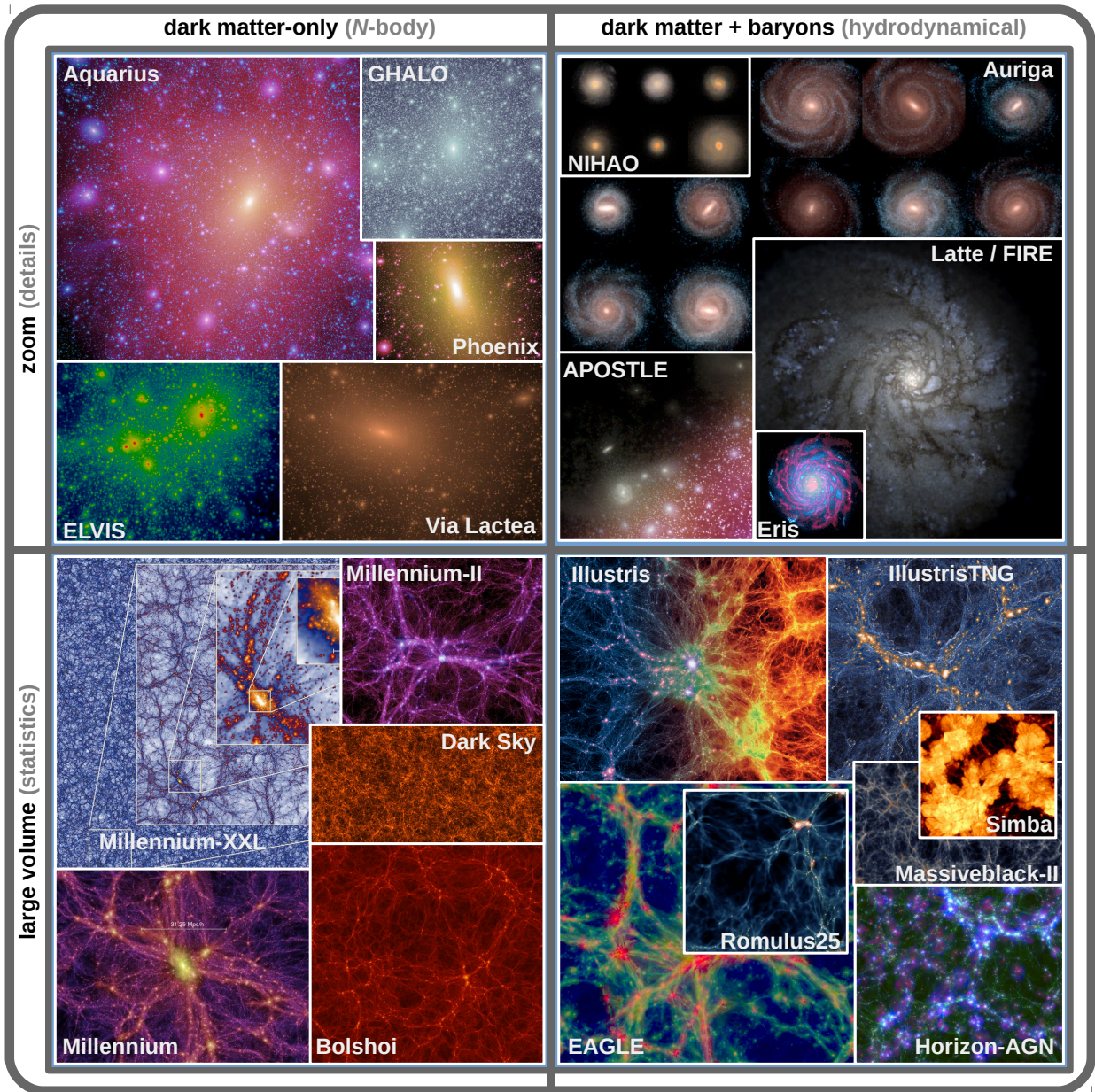


**Figure 2.1:** Modified figure from Vogelsberger et al. (2020). It shows an overview of some dark matter-only (left) and hydrodynamical (right) simulations, both large-scale (bottom) and zoomed-in simulations (top). Zoomed-in N-body simulations (top left): Aquarius (Springel et al. 2008), GHALO (Stadel et al. 2009), Phoenix (Gao et al. 2012), ELVIS (Garrison-Kimmel et al. 2014), and Via Lactea (Diemand et al. 2008). Zoomed-in hydrodynamical simulations (top right): NIHAO (Wang et al. 2015), Auriga (Grand et al. 2017), APOSTLE (Sawala et al. 2016), Latte/FIRE (Wetzels et al. 2016), and Eris (Guedes et al. 2011). Large-scale N-body simulations: Millennium (Springel et al. 2005b), Millennium-II (Boylan-Kolchin et al. 2009), Millennium-XXL (Angulo et al. 2012), Dark Sky (Skillman et al. 2014), and Bolshoi (Klypin et al. 2011). Large-scale hydrodynamical simulations: Illustris (Vogelsberger et al. 2014a,b; Genel et al. 2014), EAGLE (Schaye et al. 2015; Crain et al. 2015), IllustrisTNG (Springel et al. 2018), Romulus25 (Tremmel et al. 2017), Simba (Davé et al. 2019), Massiveblack-II (Khandai et al. 2015), Horizon-AGN (Dubois et al. 2014).

dark matter halos (White & Frenk 1991; Bertone et al. 2005). For example, Wang et al. (2020), assuming dark matter is a Weakly Interacting Massive Particle (WIMP), find a resolved population of dark matter halos with masses<sup>2</sup> ranging from  $M_{200} = 10^{15} M_{\odot}$  to  $M_{200} = 10^{-6} M_{\odot}$  (the Earth’s mass). This is achieved by using a multi-zoom technique in which the size of the highest-resolution region is only  $\sim 300$  pc across, with a particle mass of only  $\sim 10^{-11} M_{\odot}$ .

Computational advances, together with our better understanding to implement relevant physical models in the formation and evolution of galaxies, have enabled in recent years to develop the so-called “hydrodynamical simulations”. Unlike previous semianalytical simulations, which are based on a post-processing of pure dark matter-only simulations to predict the baryonic distribution from a set of assumptions and recipes, hydrodynamical simulations model the baryonic component from the beginning by solving the hydrodynamical equations and by following the baryonic particles evolution, together with dark matter. These hydrodynamical simulations are mainly focused on the study of individual galaxies in detail (zoomed-in simulations; Fig. 2.1, top right), or on large cosmological volumes (Fig. 2.1, bottom right), with typical resolutions in the kiloparsec scale and  $M_{\star} \sim 10^6 M_{\odot}$ . Since the resolution of current large-scale hydrodynamical simulations is insufficient to resolve some of the smallest physical processes that affect the evolution of galaxies, these simulations usually make use of customized sub-grid models to account for these unresolved effects. Still, recent large-scale hydrodynamical simulations like The Illustris Project (Vogelsberger et al. 2014a,b; Genel et al. 2014) or Evolution and Assembly of GaLaxies and their Environments (EAGLE; Schaye et al. 2015; Crain et al. 2015) have proven to be successful in reproducing realistic galaxy populations that reasonably reproduce several of scale relations and properties observed for real galaxies.

In particular, in this thesis, we make use of the Illustris simulation, the largest large-scale hydrodynamical simulation at the time it was released which yields a realistic galaxy population. In addition, it also publicly offered synthetic galaxy images that resembled those of deep galaxy surveys in different common HST and JWST broadband filters. This chapter aims at giving an overview of the characteristics of this simulation, as well as discussing the reason it represents an excellent scenario for implementing and testing new methods for the analysis of stellar populations in 2D to be conducted with JWST.

## 2.2 The Illustris Simulation

### 2.2.1 The Illustris Project

The Illustris Project (Vogelsberger et al. 2014a,b; Genel et al. 2014) is a series of large-scale N-body/hydrodynamical simulations, with different resolution levels and implemented physics, that follow the evolution of a periodic cubic box of  $(106.5 \text{ Mpc})^3$  from  $z \simeq 127$  ( $\sim 12$  Myr after the Big Bang) until  $z = 0$ . There are six primary simulations in the Illustris Project: three of them, Illustris-(1,2,3), include hydrodynamics and the same full baryonic physics model, and three other analogue dark-only simulations, Illustris-Dark-(1,2,3), use the same initial conditions of the former

---

<sup>2</sup> $M_{200}$  is the virial mass of the halo measured within a sphere centered at the potential minimum which encloses a mean density 200 times the critical density of the Universe.

**Table 2.1:** The Illustris Project large-scale simulation runs and some relevant numerical parameters. Illustris-(1,2,3) are the hydrodynamical simulations and Illustris-Dark-(1,2,3) are their dark matter-only analogs that have the same initial conditions but do not include the baryonic component.

Simulation name	Description	Box volume (Mpc <sup>3</sup> )	$N_{\text{baryon}} / N_{\text{DM}}$	$\epsilon_{\text{baryon}}^* / \epsilon_{\text{DM}}^{**}$ (pc)	$m_{\text{baryon}} / m_{\text{DM}}$ (10 <sup>6</sup> M <sub>⊙</sub> )
Illustris-1	full physics	106.5 <sup>3</sup>	$2 \times 1,820^3 \sim 1.2 \times 10^{10}$	710/1,420	1.26/6.26
Illustris-2	full physics	106.5 <sup>3</sup>	$2 \times 910^3 \sim 1.5 \times 10^9$	1,420/2,840	10.1/50.1
Illustris-3	full physics	106.5 <sup>3</sup>	$2 \times 455^3 \sim 1.9 \times 10^8$	2,840/5,680	80.5/400.8
Illustris-Dark-1	only DM	106.5 <sup>3</sup>	$1 \times 1,820^3$	710/1,420	-/7.52
Illustris-Dark-2	only DM	106.5 <sup>3</sup>	$1 \times 910^3$	1,420/2,840	-/60.2
Illustris-Dark-3	only DM	106.5 <sup>3</sup>	$1 \times 455^3$	2,840/5,680	-/481.3

**Notes:**

\* This is the softening length in physical units for baryonic particles at  $z < 1$ . For  $z \geq 1$ ,  $\epsilon_{\text{baryon}}$  equals that of dark matter.

\*\* The softening length of dark matter,  $\epsilon_{\text{DM}}$ , is expressed in comoving units and is constant with redshift. For Illustris-1, this corresponds to a softening length, in physical units, of 0.71 kpc for  $z = 1$ , and of 0.28 kpc for  $z = 4$ .

but do not include the baryonic component. All these simulations assume a  $\Lambda$ CDM cosmology with cosmological parameters consistent with the Wilkinson Microwave Anisotropy Probe (WMAP)-9 (Hinshaw et al. 2013):  $\Omega_{\text{m}} = 0.2726$ ,  $\Omega_{\Lambda} = 0.7274$ ,  $\Omega_{\text{b}} = 0.0456$ ,  $\sigma_8 = 0.809$ ,  $n_s = 0.963$ , and  $H_0 = 100 h \text{ km s}^{-1} \text{ Mpc}^{-1}$  with  $h = 0.704$ , where  $h$  is the present-day Hubble expansion rate,  $n_s$  is the spectral index of the primordial power spectrum, and  $\sigma_8$  is the root mean squared amplitude of the mass fluctuations inside spheres of  $8h^{-1} \text{ Mpc}$  linearly extrapolated to  $z = 0$ .

In Table 2.1 we show the main simulations of the Illustris Project, conducted all in the same box of 106.5 Mpc a side. The highest-resolution and most complete simulation of the Illustris Project in terms of physical modeling is Illustris-1, which is referred to as “the Illustris simulation” or, simply, “Illustris”. Illustris-1 was the first large-scale hydrodynamical simulation that simulated a representative portion of the Universe and produced a population of galaxies which successfully reproduced the basic properties of the ones observed. Illustris-2 and Illustris-3 are two lower-resolution versions of the Illustris simulation, with fewer resolution elements, and also higher particle masses and lower spatial resolutions (see Table 2.1). These two simulations were mainly run for resolution study purposes. In the case of the dark matter-only simulation runs, they can be useful to study the impact of baryonic effects on the dark matter distribution. In this thesis, we will only focus on the Illustris-1 simulation (hereafter, “Illustris”), the highest-resolution hydrodynamical simulation of the Illustris Project, and the only large-scale hydrodynamical simulation that, at time this thesis work began, provided synthetic deep survey images imitating mock HST and JWST observations of the Illustris simulated galaxies (see Section 2.3). The latter condition was the main reason for not using other (newer) simulations like IllustrisTNG (The Next Generation; Springel et al. 2018; Naiman et al. 2018; Pillepich et al. 2018a; Nelson et al. 2018; Marinacci et al. 2018) simulation, the successor magnetohydrodynamical simulation of Illustris<sup>3</sup>.

<sup>3</sup>TNG model implements an enhanced version of the galaxy formation model from the original Illustris Project, which integrates new physics (like the treatment of cosmic magnetism), numerical advancements, and refinements to the original model (see the TNG presentation papers cited above for more information).

The Illustris Project was publicly released (Nelson et al. 2015) and the available data products can be found on <https://www.illustris-project.org>. We have downloaded Illustris data either directly as raw files in HDF5 format or by using the web-based interface (API) that allows a wide variety of user requests to extract the desired data. For this thesis, the total amount of data downloaded in HDF5 format of  $\sim 40$  Gb (i.e., without considering those downloaded via the API). To have an estimate of the impact of this project on the scientific community, by the end of 2022, there were more than 230 published papers that made use in a direct way of any simulation from the Illustris Project, and which can be consulted on their website.

### 2.2.2 The Illustris Simulation: general characteristics

The Illustris simulation (or Illustris-1) was run using the moving-mesh AREPO code (Springel 2010), where a moving mesh is used to solve the inviscid Euler equations for hydrodynamics, and using a Tree-PM scheme (Xu 1995) to calculate gravitational forces. The AREPO code uses an unstructured Voronoi tessellation in which the mesh-generating points can freely move to easily represent the geometry of the flow in a more flexible way. In addition, Illustris includes a galaxy formation physics model (described in detail in Vogelsberger et al. 2013) comprised of a comprehensive set of modules that take into account the most relevant and crucial astrophysical processes for galaxy formation. This galaxy formation model includes, among other, the modeling of how stars and SMBHs form, evolve, and how they affect their environments (e.g., in the shape of galactic winds fueled by star formation or radio bubbles, or proximity effects caused by the radiation of Active Galactic Nuclei, AGNs). In Section 2.2.3, we further discuss the implementation of these physical models.

The different types of resolution elements in Illustris are: dark matter particles, gas cells, stellar and stellar wind particles, and SMBHs. This simulation follows the evolution of  $N_{\text{DM}} = (1,820)^3$  dark matter particles and  $N_{\text{baryon}} = (1,820)^3$  initial<sup>4</sup> baryonic elements, with a dark matter particle mass of  $m_{\text{DM}} = 6.26 \times 10^6 M_{\odot}$  and an average mass for baryonic particles of  $m_{\text{DM}} = 1.26 \times 10^6 M_{\odot}$ . In addition to these types of particles, Illustris uses  $(1,820)^3$  passive tracer particles to track the flow of the baryonic mass in stars, gas and SMBHs (see Genel et al. 2013).

The spatial resolution achieved both for the dark matter or hydrodynamics and baryonic processes is given by the softening length ( $\epsilon$ ). For dark matter particles, the softening length is kept constant to 1.4 kpc in comoving units. Below this scale, gravitational forces cannot be resolved. For baryonic particles (stars and SMBHs), the softening length equals that of dark matter for  $z \geq 1$ , and 0.71 kpc in physical units for lower redshifts (see below). Gas cells have an adaptive softening length that depends on the cell radius in the mesh, with an allowed maximum value of the softening length equal to 0.71 physical kpc. The radius of gas cells is redefined by the mesh to prevent them from exceeding a factor of two the maximum target gas mass of  $1.26 \times 10^6 M_{\odot}$ , keeping them close to this value. In addition, a regularization scheme for the mesh is applied that consists in steering the mesh towards its central regions (Springel 2010; Vogelsberger et al. 2012, 2013), which results

<sup>4</sup>Although the number of dark matter particles is kept fixed with time, the number of baryonic particles does change. In the beginning of the simulation, the number of baryonic elements (gas cells, in this case) is  $(1,820)^3$ . This number of gas cells will drop in time as stars and black holes are formed, but the total number of baryonic particles (gas cells, stellar particles, stellar wind particles and black holes) will not be conserved due to the fact that gas cells are redefined so that they do not exceed a factor of 2 the mean mass of the baryonic elements (i.e. the *target mass*).

in a better spatial resolution in these central parts. The smallest gas cells at  $z = 0$  have a typical radius of 48 pc, and the least massive cells, a mass of  $1.5 \times 10^4 M_{\odot}$ .

Since the softening length for baryonic particles is constant in comoving units and equal to that of dark matter for  $z \geq 1$  (1.4 kpc), we can calculate the value of this softening length at each redshift in physical units by multiplying it by the scale factor,  $a$ , where  $a = 1/(1+z)$ . This results in  $\epsilon_{\text{baryon}} = 0.71$  kpc for  $z = 1$ , and 0.28 kpc for  $z = 4$ . This spatial resolution in Illustris-1 is similar to that observed with HST and JWST for galaxies at those redshifts<sup>5</sup> and higher than the size of the smallest regions where we will measure SEDs on the images ( $\sim 0.18''$  a side, corresponding to 1.48 and 1.28 kpc for  $z = 1$  and 4, respectively) for all the considered redshifts. The latter condition, which is fundamental in order to obtain robust measurements of the stellar mass distribution from our 2D photometric analysis on Illustris images, is hardly fulfilled for Illustris-2 and definitely not for Illustris-3, with worse resolutions (by a factor of 2 and 4, respectively) than Illustris-1 (see Table 2.1).

When released, Illustris was one of the largest cosmological hydrodynamical simulation in terms of resolution elements (see Fig. 1 in Genel et al. 2014), being able to resolve  $L^*$  galaxies with  $\sim 10^5$  elements and with spatial resolutions down to kiloparsec scales. This, together with the improved physical implementations for the formation of stars and the evolution of baryons in general (Section 2.2.3), made the Illustris simulation become the first large-scale hydrodynamical simulation that produced a population of galaxies which successfully reproduced the basic properties of the ones observed (see Section 2.2.6 for an overview of Illustris major accomplishments in this matter). In addition, the Illustris volume is sufficiently big not to suffer major cosmic variance (Genel et al. 2014).

### 2.2.3 Galaxy formation model in Illustris

The model for galaxy formation physics implemented in Illustris-(1,2,3) is described in detail in Vogelsberger et al. (2013). This includes a set of sub-resolution models with relevant physical processes that take place in the formation of galaxies at lower scales than the resolution scale in the simulation:

- *Radiative gas cooling* (both primordial and metal-line cooling by heavy elements). Gas cooling rates are calculated with self-shielding corrections (Rahmati et al. 2013) and as a function of gas density, metallicity, temperature, the radiation field of AGNs and the uniform, redshift-dependent, ionizing UV background (Katz et al. 1996; Faucher-Giguère et al. 2009).
- *Interstellar medium model (ISM) and star formation*. Illustris has a subgrid ISM model consisting of a two-phase medium in which cold clouds lie in a tenuous hot phase. Star formation takes place in high-density hydrogen gas following the Springel & Hernquist (2003) implementation: when a gas cell reaches the hydrogen number density of  $\rho_{\text{SF}} = 0.13 \text{ cm}^{-3}$ , it stochastically produces a stellar particle on a time-scale that depends on the gas density:  $t_{\star}(\rho) = t_{\text{SF}}(\rho/\rho_{\text{SF}})^{-1/2}$ , with a star formation time-scale of  $t_{\text{SF}} = 2.2$  Gyr, and following the

---

<sup>5</sup>Assuming a common pixel scale of  $0.06''/\text{pix}$  for both HST and JWST (see Chapter 3), this corresponds to a spatial resolution of  $\sim 0.49$  kpc/pix (physical units) at  $z = 1$  and  $\sim 0.43$  kpc/pix at  $z = 4$ .

Kennicutt-Schmidt law (Kennicutt 1989). Each stellar particle in Illustris represents a single-age stellar population (SSP) born with a Chabrier (2003) initial mass function (IMF), i.e., a set of individual stars born simultaneously, where the sum of their individual masses (whose distribution is given by the IMF) equals the mass of the stellar particle at its birth time.

- *Stellar evolution and chemical enrichment.* Stellar particles acquire the gas mass from which they originated and then continuously decrease in mass as a result of their stellar evolution. This stellar evolution is tracked by modeling Type I/II supernovae (SNeI/II) and the asymptotic giant branch (AGB), taking into account stellar mass-loss processes (gas recycling) that return mass to the gas phase and enrich the surroundings of the stellar populations. The associated chemical enrichment in galaxies is traced by following the evolution of nine chemical elements (H, He, C, N, O, Ne, Mg, Si, and Fe).
- *Feedback.* Stellar feedback is implemented in the form of kinetic galactic-scale winds driven by SNe explosions (with  $1.09 \times 10^{51}$  erg each), where the metal loading of the winds can be adjusted independently from the actual mass loading. The latter is necessary to reproduce the stellar mass content of low-mass galaxies and their oxygen abundances in the gas (Zahid et al. 2014). Feedback from SMBHs is included both in quasar and radio (bubbles) mode (details in Springel et al. 2005a; Sijacki et al. 2007), depending the operation of each mode on the accretion rate. A new implementation of radiative electromagnetic AGN feedback is also included, which heats the surrounding gas and modifies its ionization state.
- *SMBH seeding and growth.* Illustris includes prescriptions for black hole seeding, accretion and merging in which black holes are represented by collisionless, massive sink particles. Following previous works (Sijacki et al. 2007; Di Matteo et al. 2005), black holes sink particles are placed with a seed mass of  $1.42 \times 10^5 M_{\odot}$  in halos more massive than  $7.1 \times 10^{10} M_{\odot}$  which do not contain a black hole particle already. These black holes particles increase their mass either through the accretion of their surrounding gas or by mergers with other black holes.

Any mismatch between the Illustris predictions and the observations (see Chapter 6) might come from limitations on the above assumptions and recipes. All the free parameters of the Illustris galaxy formation model have physical meaning and physically plausible values, but their exact values have not been observationally determined. That is the reason why the values for these free parameters (namely, those of the feedback models) have been calibrated and tuned to roughly reproduce the observed stellar mass function at  $z = 0$ , the stellar mass-halo mass relation, and the history of cosmic star formation rate density (SFRD). This calibration was performed using smaller-scale simulations of 35.5 Mpc on a side (i.e., 27 times smaller in volume than Illustris; Vogelsberger et al. 2013).

#### 2.2.4 Illustris halos and subhalos

Illustris uses a standard Friends-of-Friends (FoF) algorithm (Davis et al. 1985) to define halos which is run on the dark matter particles, identifying halos with at least 32 particles. After that, the baryonic particles are assigned to the same halo as that of their nearest dark matter particles. Halos can contain zero or more subhalos. These subhalos can be considered as galaxies in case they contain stellar particles, but subhalos with no stars are highly common at low masses. Subhalos are found via the Subfind halo finder algorithm (Springel et al. 2001; Dolag et al. 2009), which uses

an “unbinding” procedure that removes gravitationally unbound member particles from the halo. The minimum particles limit for subhalos is 20. In case a halo hosts any subhalos, these subhalos are classified into “central” (or “primary”; the most massive subhalo in the halo) and “satellite” (or “secondary”; the rest, if they exist).

The halos and subhalos found in the simulation are provided by the FoF halo catalog and the Subfind subhalo catalog, respectively. These catalogs provide different fields with information about the halos/subhalos, such as masses at several radii (total or from the different simulated components), sizes (e.g., the radius that encloses half of the mass for subhalos, or  $R_{200}$  and  $R_{500}$  for halos), positions in the simulation volume, velocities, number of particles of each type belonging to them, etc. At  $z = 0$ , there are 7,713,601 FoF-halos with at least 32 particles and 4,366,546 individual subhalos (Vogelsberger et al. 2014b). Out of these subhalos at  $z = 0$ , there are  $\sim 40,000$  galaxies with at least 500 stellar particles in them. The most massive halo found in Illustris has  $M_{200} \approx 2.4 \times 10^{14} M_{\odot}$ , which means that the volume is not big enough to produce the most massive halos found in the Universe like the Coma cluster (with  $M_{200} \approx 2.7 \times 10^{15} M_{\odot}$ ; Kubo et al. 2007). Nevertheless, there are 10 halos in Illustris with  $M_{200} > 10^{14} M_{\odot}$  and 733 “Milky Way-like” halos with  $10^{12} M_{\odot} < M_{200} < 2 \times 10^{12} M_{\odot}$  (Genel et al. 2014).

Finally, in order to reconstruct the assembly history of any given subhalo across snapshots, Illustris offers two merger trees associated to the subhalo catalogs: SUBLINK (Rodríguez-Gomez et al. 2015) and LHALOTREE (Springel et al. 2005a), where the latter is basically identical to that of the Millennium simulation. Such merger trees are extremely useful, e.g., to identify and study the properties of high-redshift progenitors of  $z = 0$  galaxies of a similar type (massive, quiescent, etc.). As we show in Chapter 5, in this thesis we will make use of the Illustris merger trees in order to track high-redshift galaxies forward in time to pinpoint their descendants at  $z = 0$ . Fig. 2.2 shows an example of a merger tree for the descendant at  $z = 0$  of the lowest-redshift galaxy considered in García-Argumánuez et al. (2023; see also Chapter 5). This progenitor galaxy (marked with a green dotted circle) has a redshift of observation of  $z = 1.04$  in the Illustris synthetic images that we will use in this work (see 2.3), and a total stellar mass of  $M_{\star} = 10^{10.72} M_{\odot}$ , while its descendant at  $z = 0$  (cyan circle) has a total stellar mass of  $M_{\star} = 10^{11.14} M_{\odot}$ .

### 2.2.5 Snapshots in Illustris

There are 136 snapshots (or instants of time) for which the output of the simulation has been saved across time.<sup>6</sup> These snapshots correspond to 136 different redshifts that span between  $z = 0$  (snapshot 135) and  $z = 47$  (snapshot 0). Snapshots are spaced according to the scale factor: snapshots at  $z > 3$  are spaced with  $\log(a) \approx 0.02$ , and with  $\log(a) \approx 0.01$  for those at  $z < 3$ . Table 2.2 shows the full snapshot list with the equivalent redshifts, scale factors and corresponding ages of the Universe. Snapshots include all the particles (and their associated fields) in the simulation volume, together with the halo and subhalo catalogs found for each snapshot. Particles in every snapshots are not organized by their spatial position in the simulation box, but they are sorted according to their membership to their halos or subhalos. Both halos/subhalos and the particles belonging to them can be downloaded. Each of these individual particles presents different information fields

<sup>6</sup>In practice, there are only 134 available snapshots in Illustris-1. This is because snapshots 53 and 55 were corrupted and are not available for downloading.

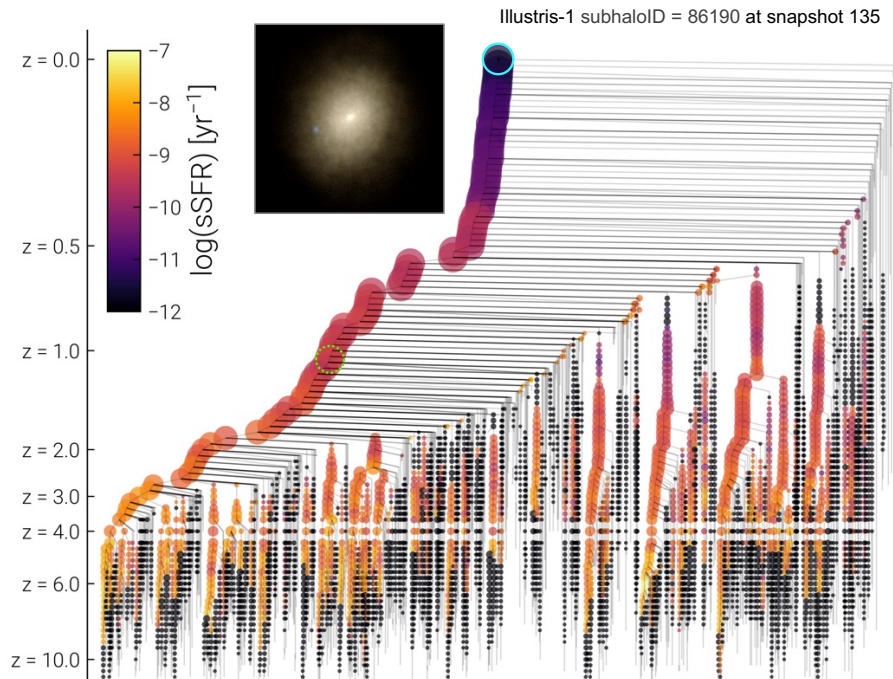


**Figure 2.2:** Example of an Illustris merger tree for  $z = 0$  descendant of a galaxy from the main high-redshift sample analyzed in García-Argumániz et al. (2023; see also Chapter 5). The descendant at  $z = 0$  is highlighted with a cyan circle, while the considered progenitor galaxy at  $z \sim 1$  is marked with a green dotted circle. Bigger circle sizes correspond to higher halo masses. The circles are color-coded by specific SFR (sSFR). We show an RGB image for the  $z = 0$  galaxy generated by Torrey et al. (2015). The two empty horizontal lines correspond to the corrupted snapshots 53 and 55.

which depend on the particle type (e.g., mass, coordinates, velocities for all particles, formation masses or formation times for the stellar particles, SFR or density for the gas cells, instantaneous mass accretion rate for black holes particles, etc.). A full listing of the available fields for each particle type can be found in Nelson et al. (2015) or on the Illustris website<sup>7</sup>.

The information provided by the stellar particles belonging to a galaxy (at a certain snapshot) can be used to build the SFH of the galaxy (or galaxy SFH) according to the simulation. This galaxy SFH, directly built from the stellar particles of the galaxy, is what we will refer to as *ground-truth* galaxy SFH. In Section 2.4, we describe how the ground-truth galaxy SFHs are built by accessing the simulated particles of galaxies located in snapshots with  $1 < z < 4$ . The aim of this work is to be able to successfully recover those ground-truth SFHs (especially their first stages) when applying 2D SPS to the synthetic images of galaxies in Illustris (described in Section 2.3), i.e., to achieve that our galaxy SFH resulting from the 2D-SPS analysis on a certain galaxy resembles as closely as possible the (initial parts of the) corresponding ground-truth SFH provided by their stellar particles.

<sup>7</sup><https://www.illustris-project.org/data/docs/specifications/>



**Table 2.2:** Illustris snapshots with redshifts, scale factors and ages of the Universe. The relevant snapshots for this thesis, with  $1 \lesssim z \lesssim 4$ , are highlighted with a gray shade.

Snapshot	$z$	Scale factor	Age [Gyr]	Snapshot	$z$	Scale factor	Age [Gyr]	Snapshot	$z$	Scale factor	Age [Gyr]
0	46.77	0.021	0.054	50	4.94	0.168	1.223	100	0.58	0.635	8.171
1	44.56	0.022	0.058	51	4.66	0.177	1.312	101	0.55	0.647	8.369
2	42.45	0.023	0.062	52	4.43	0.184	1.398	102	0.52	0.656	8.520
3	40.64	0.024	0.066	53	-	-	- <sup>a</sup>	103	0.50	0.665	8.672
4	38.71	0.025	0.071	54	4.01	0.200	1.577	104	0.48	0.675	8.827
5	36.87	0.026	0.076	55	-	-	- <sup>a</sup>	105	0.46	0.685	8.983
6	35.12	0.028	0.082	56	3.71	0.212	1.728	106	0.44	0.694	9.141
7	33.61	0.029	0.087	57	3.49	0.223	1.854	107	0.42	0.704	9.301
8	32.01	0.030	0.093	58	3.28	0.233	1.990	108	0.40	0.714	9.463
9	30.48	0.032	0.100	59	3.08	0.245	2.134	109	0.38	0.725	9.626
10	29.03	0.033	0.108	60	3.01	0.249	2.195	110	0.36	0.735	9.791
11	27.64	0.035	0.116	61	2.90	0.257	2.289	111	0.35	0.742	9.902
12	26.44	0.036	0.123	62	2.73	0.268	2.438	112	0.33	0.753	10.071
13	25.17	0.038	0.132	63	2.58	0.280	2.596	113	0.31	0.763	10.240
14	23.96	0.040	0.142	64	2.44	0.290	2.745	114	0.29	0.774	10.412
15	22.81	0.042	0.153	65	2.32	0.302	2.902	115	0.27	0.785	10.585
16	21.81	0.044	0.163	66	2.21	0.312	3.047	116	0.26	0.793	10.701
17	20.76	0.046	0.175	67	2.10	0.322	3.198	117	0.24	0.804	10.877
18	19.75	0.048	0.188	68	2.00	0.333	3.356	118	0.23	0.816	11.054
19	18.79	0.051	0.201	69	1.90	0.344	3.521	119	0.21	0.823	11.173
20	17.96	0.053	0.215	70	1.82	0.354	3.669	120	0.20	0.835	11.353
21	17.09	0.055	0.231	71	1.74	0.364	3.823	121	0.18	0.847	11.534
22	16.25	0.058	0.248	72	1.67	0.375	3.983	122	0.17	0.855	11.656
23	15.45	0.061	0.266	73	1.60	0.384	4.120	123	0.15	0.867	11.839
24	14.76	0.063	0.283	74	1.53	0.395	4.291	124	0.14	0.876	11.963
25	14.03	0.067	0.304	75	1.47	0.405	4.438	125	0.13	0.888	12.149
26	13.34	0.070	0.327	76	1.41	0.414	4.590	126	0.11	0.901	12.336
27	12.67	0.073	0.351	77	1.36	0.424	4.747	127	0.10	0.910	12.462
28	12.04	0.077	0.376	78	1.30	0.434	4.908	128	0.08	0.923	12.652
29	11.50	0.080	0.401	79	1.25	0.445	5.074	129	0.07	0.931	12.779
30	10.92	0.084	0.431	80	1.21	0.453	5.210	130	0.06	0.945	12.971
31	10.37	0.088	0.463	81	1.15	0.464	5.384	131	0.05	0.954	13.100
32	10.00	0.091	0.486	82	1.11	0.473	5.528	132	0.03	0.967	13.294
33	9.84	0.092	0.497	83	1.07	0.482	5.674	133	0.02	0.977	13.424
34	9.39	0.096	0.529	84	1.04	0.491	5.824	134	0.01	0.991	13.620
35	9.00	0.100	0.560	85	1.00	0.501	5.977	135	0.00	1.000	13.751
36	8.91	0.101	0.568	86	0.99	0.503	6.015				
37	8.45	0.106	0.610	87	0.95	0.513	6.172				
38	8.01	0.111	0.655	88	0.92	0.520	6.292				
39	7.60	0.116	0.703	89	0.89	0.530	6.455				
40	7.24	0.121	0.750	90	0.85	0.540	6.622				
41	7.01	0.125	0.782	91	0.82	0.550	6.791				
42	6.86	0.127	0.805	92	0.79	0.558	6.921				
43	6.49	0.133	0.864	93	0.76	0.569	7.096				
44	6.14	0.140	0.927	94	0.73	0.577	7.230				
45	6.01	0.143	0.954	95	0.70	0.588	7.412				
46	5.85	0.146	0.989	96	0.68	0.597	7.550				
47	5.53	0.153	1.061	97	0.64	0.608	7.737				
48	5.23	0.161	1.139	98	0.62	0.617	7.880				
49	5.00	0.167	1.205	99	0.60	0.626	8.024				

**Notes:**

<sup>a</sup> Snapshots 53 and 55 are not available because they were corrupted.

## 2.2.6 Illustris predictions and comparison with observations

Even though the physical galaxy models in Illustris were tuned to roughly match some observed global relations (see Section 2.2.3), many other additional observables are also reproduced by the simulation both in the local Universe (Vogelsberger et al. 2014a,b) or regarding the basic properties of high-redshift galaxies (Genel et al. 2014). Below, we give an overview of the most relevant accomplishments of Illustris in reproducing the structure formation and galaxy populations properties.

### 2.2.6.1 Large-scale structure and impact of baryons on dark matter

*Large-scale structure.* The distribution of dark matter of Illustris reproduces the well-known cosmic web. This is shown in the Illustris panel in Fig. 2.1 (bottom right quadrant), where the dark matter density at  $z = 0$  (shown on the left) gradually transforms into gas density (on the right), which follows the gravitational field created by dark matter at large scales. The figure is centered on the most massive cluster in Illustris ( $R_{200} = 1.26$  Mpc and  $M_{200} = 2.4 \times 10^{14} M_{\odot}$ ).

*Impact of baryons on the power spectrum and on the halo mass.* Theoretical models that connect the present-day  $P(k)$  to the initial power spectrum are usually based on dark matter-only simulations. Nevertheless, Illustris predicts a non-negligible, scale-dependent impact of the baryonic effects on the dark matter distribution on larger scales than usually assumed caused by AGN outflows and gas cooling processes (Vogelsberger et al. 2014a). Baryonic processes also affect the individual halo masses: halos with  $\sim 10^{11} M_{\odot}$  (close to the mass scale where star formation is more efficient) are  $\sim 10\%$  more massive in Illustris than in its dark matter-only analog, while the masses of less and more massive halos are reduced because of the feedback processes (up to 20 – 30% at the lowest and highest masses,  $\sim 10^{8.5}$  and  $\sim 10^{14.5} M_{\odot}$ , respectively).

*Halo mass function.* The theoretical prediction of the halo mass function is usually based on N-body simulations and usually ignores baryon effects on dark matter (e.g., Tinker et al. 2008). Nevertheless, Illustris finds the halo mass function is reduced by the baryonic component at very low and high halo masses (up to  $\sim 30\%$  at both ends), where the feedback processes are stronger.

### 2.2.6.2 Reproducing galaxy population properties

*Galaxy morphologies.* Illustris population of galaxies shows a wide range of morphologies, from elliptical galaxies to star-forming disks and irregular galaxies (Vogelsberger et al. 2014a,b; Snyder et al. 2015). The resolution in  $M_{\star} \gtrsim 10^{10-11} M_{\odot}$  galaxies (with  $\sim 10^4-10^5$  stellar particles) is enough to study galaxy morphologies or internal kinematic (Vogelsberger et al. 2014b). In addition, the morphological evolution in Illustris up to  $z = 5$  galaxies is in very good agreement with several observed trends (Genel et al. 2014). Snyder et al. (2015) present a comprehensive study of Illustris massive galaxies at  $z = 0$ , finding that while  $M_{\star} \sim 10^{11} M_{\odot}$  galaxies have comparable  $g$ -band sizes to those observed,  $M_{\star} \sim 10^{10} M_{\odot}$  galaxies present too large half-light radii (by a factor of  $\sim 2$ ).

*Galaxy luminosity and stellar mass functions.* Illustris galaxy luminosity and stellar mass functions (GLF and GSMF, respectively) agree reasonably well with observations (Vogelsberger et al. 2014b) over the probed ranges ( $M_{\star} \sim 10^9$  to  $10^{12.5} M_{\odot}$  and  $M_r \sim -15.0$  to  $-24.5$ ). However,

Illustris GLF slightly overestimates the number of bright (and massive) galaxies as a consequence of insufficient AGN feedback, and Illustris GSMF overpredicts slightly too many low mass (poorly resolved) galaxies at  $M_{\star} \lesssim 10^9 M_{\odot}$ , as well as in the most massive end ( $M_{\star} \gtrsim 10^{11-12} M_{\odot}$ ). The GSMF also agrees in general with observations for redshifts up to  $z = 7$  (Genel et al. 2014), despite the free parameters in Illustris physical model were calibrated to roughly reproduce the GSMF at only  $z = 0$ . Nevertheless, there are some tensions with observations, especially at lower redshifts where, e.g., the number of  $M_{\star} \gtrsim 10^{11} M_{\odot}$  is overestimated for  $z \lesssim 1.5$  or that Illustris overshoots the number of low-mass ( $M_{\star} \lesssim 10^{10} M_{\odot}$ ) galaxies for  $z \lesssim 2$ . The latter also happens for  $z \gtrsim 4$ , but for less massive galaxies ( $M_{\star} \lesssim 10^9 M_{\odot}$ ). This probably denotes the need for an additional suppression of SF both for the least and most massive galaxies.

*Cosmic SFRD history.* By construction, the cosmic SFRD history for Illustris (Vogelsberger et al. 2014b) is in agreement with observations up to  $z \sim 10$ , even with the lower limits beyond  $z \sim 8$  (Ellis et al. 2013a; Oesch et al. 2014). However, at  $z < 1$  the Illustris SFRD does not decrease as fast as observations and slightly overestimates the present-day SFRD by 0.15 – 0.45 dex (Genel et al. 2014) due to an insufficient AGN feedback at these recent epochs, namely the radio-mode AGN feedback in  $\sim 10^{11-12} M_{\odot}$  halos (main contributors to the SFRD at those lower redshifts).

*Baryon conversion efficiency from the gas to the stellar phase.* The baryon conversion efficiency (or SF efficiency) is very dependent on both the feedback and cooling processes implemented in the simulation, and plays an important role to reproduce the GLF and GSMF. Illustris baryon conversion efficiency at  $z = 0$  is in reasonable agreement with observations (within the  $1\sigma$  uncertainties), and reproduces the fact that the SF efficiency is maximum (reaching values of  $\sim 20 - 30\%$ ) around halo masses close to those of the Milky Way ( $M_{200} \sim 10^{12} M_{\odot}$ ), while it is significantly reduced (by several orders of magnitudes) at lower and higher masses as a consequence of the SN and AGN feedback. The evolution with redshift of the stellar to halo mass relation for  $z \lesssim 3$  agrees with the common points of observations from Moster et al. (2010) and Behroozi et al. (2013), such as that the peak of the baryon conversion efficiency moves towards higher masses as redshift increases.

*Galaxy star-forming main sequence.* Illustris reproduces the observed tight relation between the SFR and stellar mass (“star forming main sequence”, SFMS) up to  $z = 4$  for  $M_{\star} > 10^9 M_{\odot}$  galaxies (Sparre et al. 2015). This SFMS is consistent with observations for  $z = 0$  and  $z = 4$ , but presents a significant lower normalization at intermediate redshifts ( $z = 1$  and  $z = 2$ ) mainly owing to the use of too unsophisticated feedback models. Illustris also has a paucity of strong starbursts (i.e., galaxies located significantly above the SFMS) at all redshifts, probably caused by an insufficient spatial resolution in the simulation but also, by a relatively too stiff equation of state for the Illustris star formation model in the ISM. In spite of that, the scatter of the Illustris SFMS ( $\sim 0.27$  dex) is in very good agreement with that of observations (typically 0.21 – 0.39 dex; Behroozi et al. 2013).

*Satellite galaxies around massive halos.* The stellar mass content and spatial distribution of satellite galaxies in massive halos in Illustris agrees with observations (Genel et al. 2014). Illustris reproduces the monotonic increase of the baryonic conversion efficiency for satellite galaxies as halo mass increases and the galaxy number densities profiles for satellite galaxies at  $0.15 < z < 0.40$ .

*Environment and mass quenching.* In agreement with Peng et al. (2010) observations, the fraction of Illustris red galaxies is bigger for larger stellar masses and for higher galaxy overdensities

(Vogelsberger et al. 2014b) as a consequence of “mass quenching” and “environment quenching”<sup>8</sup>. Illustris also reproduces how the SFR of star-forming galaxies does not depend on the galaxy overdensity (i.e., a higher environment increases the probability of a galaxy quenching and becoming redder, but does not affect the SFR of star-forming galaxies).

*Metallicity and HI content in galaxies.* Illustris reproduces the observed relation between the metallicity in galaxies and their stellar mass (“stellar mass-metallicity relation”; Gallazzi et al. 2005; Woo et al. 2008; Kirby et al. 2013), including the flattening above  $M_{\star} \approx 10^{11} M_{\odot}$  (Vogelsberger et al. (2014a)). As in observations, Illustris also reproduces the decreasing trend for the HI to stellar mass ratio as the galaxy stellar mass increases.

### 2.3 Synthetic images in Illustris: the “mock ultra-deep fields”

The realistic galaxy morphologies observed in Illustris galaxies, together with the fact that the evolution of these galaxies is followed from relatively soon after the Big Bang, and that Illustris reproduces reasonably well the properties of galaxy populations at different redshifts, enables the construction of synthetic images that resemble those from real deep survey observations such as, e.g., the Hubble Ultra Deep Field (HUDF; Beckwith et al. 2006a, Oesch et al. 2010b, Ellis et al. 2013b, Koekemoer et al. 2013a, Illingworth et al. 2013a). In fact, Illustris was the first hydrodynamical simulation that constructed faithful deep UDF-like images<sup>9</sup> (Vogelsberger et al. 2014a), and this was possible due to the high-resolution and large volume of the simulation. Other examples of synthetic images created from the Illustris simulation are shown in, e.g., Torrey et al. (2015) for individual galaxy images or Snyder et al. (2017) for mock deep survey-like observations.

In this thesis work, we will make use of the Illustris synthetic deep survey images, also called the Illustris “mock ultra-deep fields” (Snyder et al. 2017), and downloadable via MAST<sup>10</sup>. These synthetic images resemble those of real deep galaxy surveys and are available in a broad range of broad-band filters, such as those onboard HST and JWST, among other observatories. Each of the three synthetic deep survey images, with  $2.8' \times 2.8'$  in size, corresponds to a different field, labeled as Field A, B, and C. Those fields are shown in Fig. 2.3, together with a comparison with the HST eXtreme Deep Field (XDF; Illingworth et al. 2013b). Both of them are surprisingly similar regarding the characteristics of the population of galaxies shown (e.g., galaxy colors, sizes, morphologies, etc.).

<sup>8</sup>In mass quenching, AGN feedback in massive halos heats and/or expels the available star-forming gas in the galaxy and causes the galaxy to get redder due to stellar population aging. In environment quenching, the denser environment mainly affects low massive galaxies which are deprived from their gas by ram pressure as they fall into larger halos.

<sup>9</sup>In fact, there already existed similar synthetic images generated from semianalytical models before Illustris (e.g., Kitzbichler & White 2007; Henriques et al. 2012). Nevertheless, since one of the objectives of this thesis is to analyze the spatial distribution of stellar populations (from real broadband-based observations), for the calibration of our method it is important to use synthetic images that are as close to reality as possible, especially regarding the spatial distribution of baryonic matter in galaxies. In this regard, images generated from hydrodynamical simulations (based on the stellar particles distribution in each galaxy), will be more realistic than those produced by semianalytical models (based on certain assumptions or recipes applied to the post-processing of the dark matter-only distribution).

<sup>10</sup><https://archive.stsci.edu/prepds/illustris/>

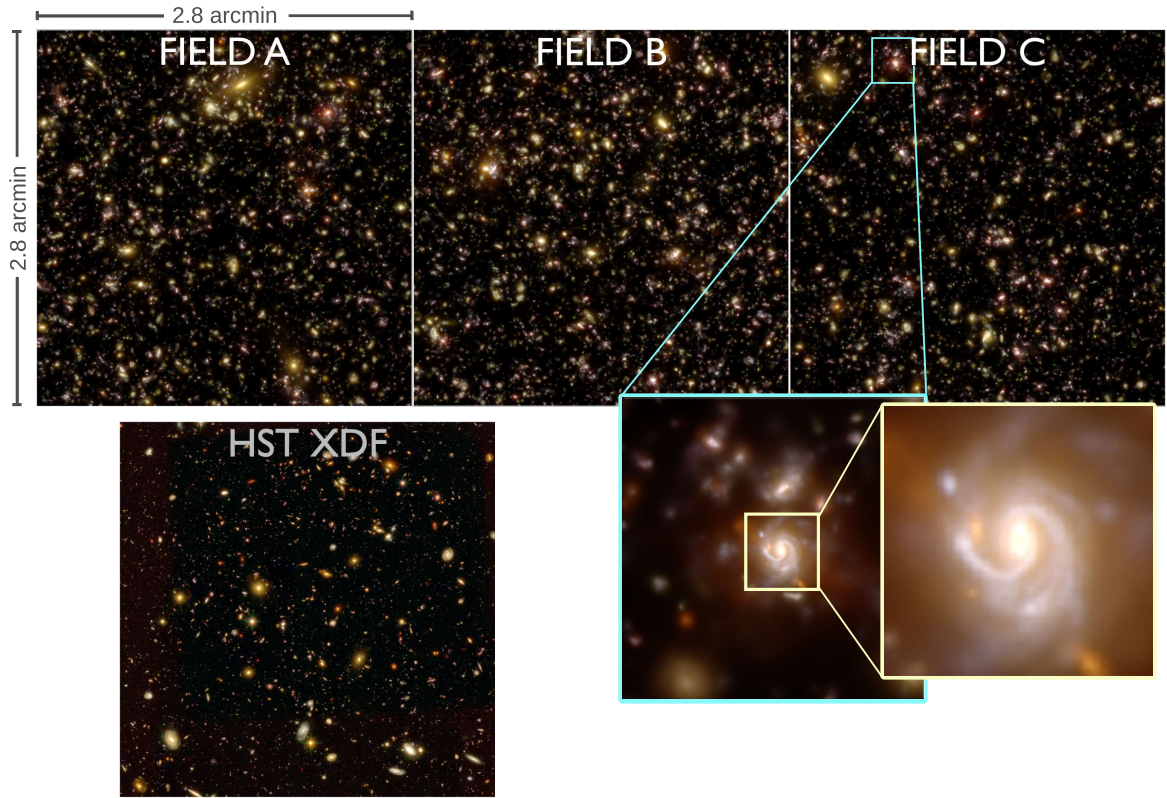


**Figure 2.3:** Illustris deep survey images (or Illustris mock ultra-deep fields) from Snyder et al. 2017 (three images on top), with a zoomed-in region in Field C (cyan and yellow squares). Each field is 2.8 arcmin a side. The HST Ultra-Deep Field is shown above as a comparison. *Credit:* Adapted from <https://archive.stsci.edu/hlsp/illustris>.

As described in Snyder et al. (2017), each of these three deep survey images has been created by applying the lightcone technique proposed in Kitzbichler & White (2007) to the periodic Illustris-1-simulation volume. This technique is based on replacing distant volume in the simulation with the output from an earlier cosmic time. It consists in first replicating the periodic cubic volume simulation until a desired comoving distance is reached and tracing a lightcone across all the simulation replications. Then, the output time of the simulation that fills the lightcone volume is varied as a function of the comoving distance, i.e., the distant volume in the lightcone is replaced with the output from an earlier cosmic time in the simulation. The three different survey images used in this work have been generated using the same lightcone geometry with three different orientations. Each of these lightcones contains unique galaxies in the simulation up to  $z \sim 18$  with no repetition, although some of these galaxies can be repeated between the three different fields.

Finally, to generate the synthetic images, the information from the simulated particles in the lightcones at each redshift (see, e.g., Torrey et al. 2015) is processed using stellar population synthesis (SPS) models and the spectral synthesis code SUNRISE (Jonsson 2006; Jonsson et al. 2010). These SPS models (described in Chapter 4) are able to assign a spectrum to each stellar particle belonging to a galaxy depending on its characteristics, in particular, its age, mass and metallicity (which are first projected to the hypothetical cameras). To generate spectra, Starburst99

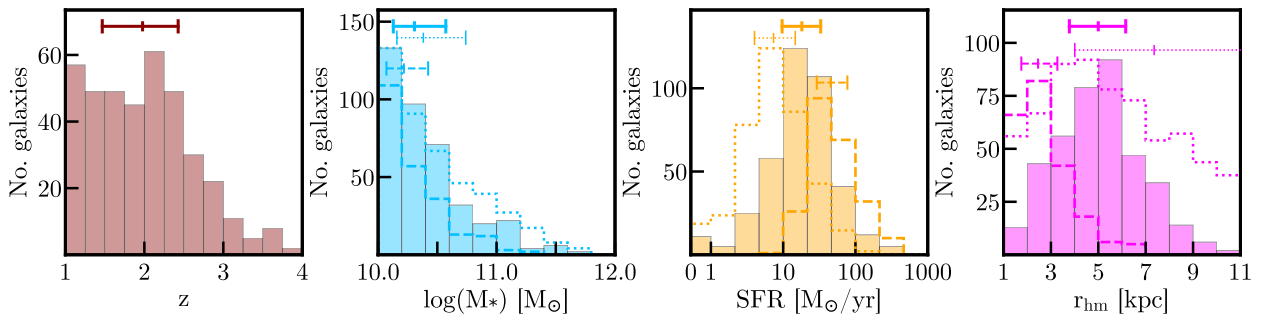


**Figure 2.4:** Distributions for redshift, stellar mass, SFR, and stellar half-mass radius for massive galaxies at  $1 < z < 4$  in the catalogs of Illustris mock-ultra deep fields (filled histograms). These catalogs only include galaxies brighter than  $g < 30.0$  mag. With unfilled histograms, we show the distributions for the 4,295 massive galaxies in the snapshot  $z = 1$  (dotted) and the 232 massive galaxies in that at  $z = 4$  (dashed) of the simulation (not necessarily appearing in the images). The histogram for  $z = 1$  has been normalized so that its maximum coincides with that of the massive,  $1 < z < 4$  galaxies in the images. Median and quartile values are shown at the top with segments.

stellar population models (Leitherer et al. 1999) were assumed, and a Kroupa (2001) IMF. Dust absorption is included in the images assuming a simple birth cloud plus diffuse dust model (Charlot & Fall 2000). This models the total effects of dust at our wavelengths of interest, without requiring expensive dust radiative transfer simulations for the entire fields. The spectrum of all stellar particles in the galaxy is then convolved with the transmission function of different broadband filters to calculate spectral energy distributions (SEDs). For the generation of these SEDs, common broadband filters from widely-used observatories are used, such as those from HST or JWST, although the latter was not even still launched at the time the images were produced.

Each of the Illustris mock ultra-deep fields has an associated catalog which includes all the galaxies in the survey image with rest-frame  $g$ -band apparent magnitude brighter than  $g < 30.0$  mag. Those catalogs will be used in this thesis to select our sample of massive,  $1 < z < 4$  galaxies in Illustris (see Chapter 5). In total, the three catalogs include 19,347 galaxies, out of which 388 are massive ( $M_{\star} \geq 10^{10} M_{\odot}$ ) galaxies lying at  $1 < z < 4$ . Fig. 2.4 shows the distribution for the redshift, total stellar mass, SFR, and stellar half-mass radius<sup>11</sup> of these massive,  $1 < z < 4$  galaxies which appear in the catalogs associated to the images (filled histograms). As a comparison, we include the distributions of all massive galaxies in the simulation (not necessarily in the synthetic images) from the snapshots corresponding to  $z = 1$  (snapshot 85; dotted) and 4 (snapshot 54; dashed), with 4,295 and 232 massive galaxies, respectively.

The advantage of using Illustris synthetic images is that we can compare our results derived from applying our 2D-SPS method on them (namely, the galaxy SFHs) with the reference or ground-truth values from the simulation (i.e., those provided by the particles information for each galaxy). This makes Illustris the ideal tool to test potential procedures to be applied in real galaxy images and it is, precisely, the purpose for what we use Illustris in this thesis (see Chapter 5). In the following section, we show how we can extract from the simulation the (ground-truth) information provided by the simulated particles in galaxies at different snapshots (see Section 2.2.5) and show an example of how we can use that data to build the ground-truth SFH for a galaxy.

<sup>11</sup>The stellar half-mass radius,  $r_{\text{hm}}$ , is the radius that contains half of the total stellar mass of the galaxy.

## 2.4 Massive galaxies at $1 < z < 4$ in Illustris: building the ground-truth galaxy SFH from their stellar particles

For this thesis work, we will focus only on Illustris massive galaxies from the snapshots with  $1 \lesssim z \lesssim 4$  (highlighted in gray in Table 2.2). At  $z \approx 1$  (snapshot 85) and  $z \approx 4$  (snapshot 54), the number of galaxies with at 500 stellar particles is 39,016 and 10,344, respectively, out of which 4,295 and 232 have a total stellar mass above  $M_{\star} \geq 10^{10} M_{\odot}$  (the stellar properties for these massive galaxies at  $z = 1$  and  $z = 4$  were shown as the unfilled histograms in Fig. 2.4). Apart from the total mass<sup>12</sup>, Illustris also provides estimates for the stellar mass (and other stellar quantities) within other radii<sup>13</sup>, such as the stellar half-mass radius (i.e., the radius enclosing half of the total stellar mass of the galaxy;  $r_{\text{hm}}$ ), or twice this radius ( $2r_{\text{hm}}$ ). For the latter radius, the number of galaxies in the simulation with stellar mass  $M_{\star} \geq 10^{10} M_{\odot}$  within  $2r_{\text{hm}}$  is 3,700 for  $z \approx 1$  (snapshot 85) and 144 for  $z \approx 4$  (snapshot 54).

Since papers often compare results based on observations with what Illustris predicts for galaxies within  $2r_{\text{hm}}$ , here we will show an example of how the ground-truth galaxy SFH can be built from the information provided by the simulated particles in the galaxy located within this radius. Consider, for instance, the Illustris galaxy located at snapshot 73 ( $z = 1.60$ ) with subhalo ID 141918 (labeled as `Illustris-1_073_0141918` in this work). According to their simulated particles at this snapshot, this galaxy has a stellar mass within  $2r_{\text{hm}}$  (and in total) of  $M_{\star} = 10^{10.76} M_{\odot}$  ( $M_{\star} \geq 10^{10.89} M_{\odot}$ ) and a star formation rate<sup>14</sup> (SFR) of  $34.0 M_{\odot}/\text{yr}$  ( $46.6, M_{\odot}/\text{yr}$ ).

To build the ground-truth SFH of this galaxy, we first load from the Illustris database all the simulated stellar particles (and gas particles) belonging to it. By accessing the positions of these particles, we discard all of them which are located at a larger radius of the galaxy center than  $2r_{\text{hm}}$ . For the remaining stellar particles (within  $2r_{\text{hm}}$ ), we load their formation times or ages (by accessing their `GFM_StellarFormationTime` field) and their initial masses at the moment of formation (with the `GFM_InitialMass` field). The formation times of the stellar particles are converted to lookback times (measured from the galaxy redshift) in order to build a histogram for these lookback times of formation ages. We assume time bins for the formation ages of 25 Myr up to a lookback time of 1 Gyr, and 250 Myr afterwards. Then, for each bin in this histogram, we load the formation masses of the stars inside the bin and sum them to have an estimate of how much stellar mass was formed per lookback time bin. We convert the latter to a SFR (in  $M_{\odot}/\text{yr}$ ) by dividing the mass formed in lookback time bin by the width of the bin. For each SFR value calculated in this way, we assign its corresponding lookback time value, which coincides with the lookback time at the center of its bin.

We modify this galaxy SFH at both ends of lookback time so that 1) the age of the SFH coincides with that of the stellar particle that first formed in the galaxy 2) and also to include the instantaneous SFR at the redshift of observation (i.e., when the lookback time equals zero). In the first case, this is done by extending (or modifying) the SFH at the furthest lookback times with

<sup>12</sup>The total mass of the galaxy is the sum of the mass of all stellar particles that belong to it.

<sup>13</sup>In those cases, the stellar mass is computed as the mass of the stellar particles which are closer to the galaxy center than the corresponding radius.

<sup>14</sup>The SFR within  $2r_{\text{hm}}$  is calculated as the sum of the `SFR` field value associated to the gas particles in the galaxy which are closer to its center than  $2r_{\text{hm}}$  (or all its particles, for the total SFR).

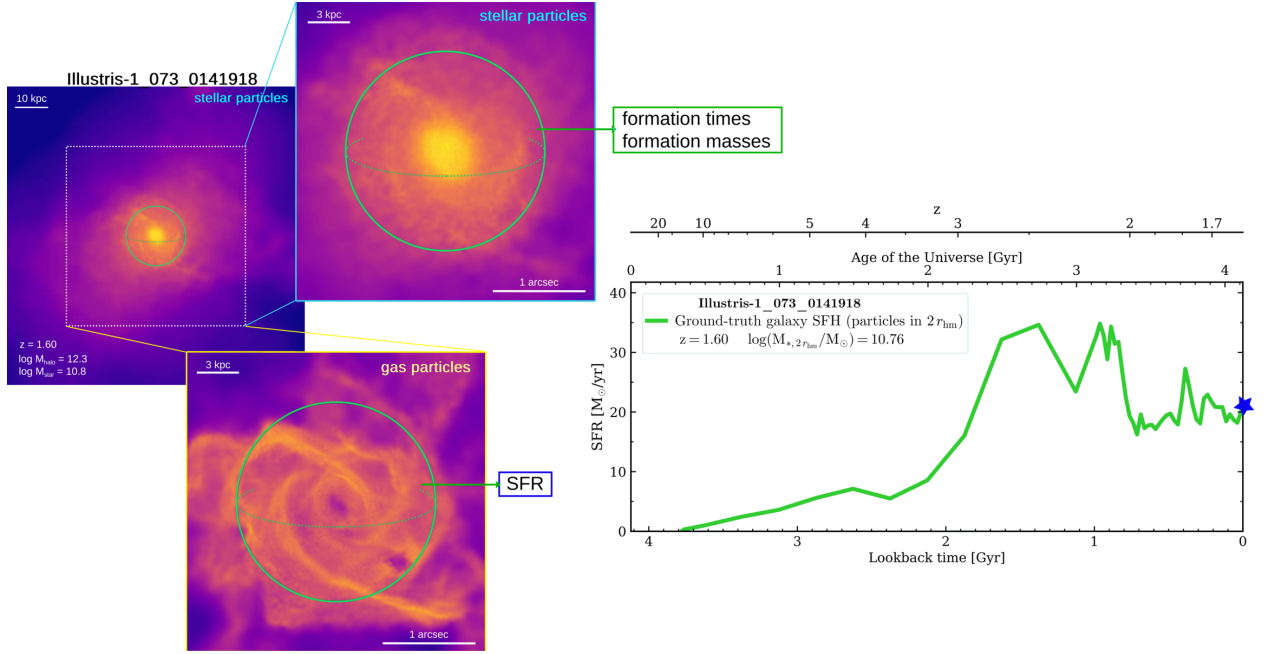


**Figure 2.5:** Ground-truth SFH for *Illustris-1\_073\_0141918* calculated from its stellar and gas particles within  $2r_{\text{hm}}$ . The left panel shows the stellar mass density distribution in this galaxy. Particles within  $2r_{\text{hm}}$  are located inside the green sphere. We show as zoomed-in panels the same stellar mass density distribution (cyan rectangle on top) and the gas mass density distribution (yellow rectangle at the bottom). For stellar particles inside  $2r_{\text{hm}}$ , we load their formation and formation times. We make a histogram of the formation times (expressed as lookback times) and sum the formation masses of the stars formed in each bin to generate the SFH. We force the SFH to have an age equal to that of the first star formed in the galaxy. The SFR at the origin of lookback time is calculated by summing the SFR values of gas particles in the green sphere (marked with a blue star in the SFH figure). Finally, we normalize the resulting SFH to recover the stellar mass of all the stellar particles inside  $2r_{\text{hm}}$ .

that corresponding to the formation of the first star and a SFR of 0. This marks the age of the galaxy. In the second case, the SFR of the galaxy at the redshift of observation is computed by considering all the gas particles in the galaxy within  $2r_{\text{hm}}$  and adding together their instantaneous SFR values (SFR field in these gas particles). This SFR value, assigned to a zero lookback time, is then added to the SFH calculated above. Finally, after the latter two steps, the galaxy SFH is normalized so that its integral over cosmic time (until the redshift of observation) recovers the stellar mass within  $2r_{\text{hm}}$ . The resulting galaxy SFH after this normalization is our ground-truth galaxy SFH (in this case, within  $2r_{\text{hm}}$ ). Fig. 2.5 shows the ground-truth galaxy SFH (in green) for *Illustris-1\_073\_0141918*, together with the stellar mass and gas mass distribution within the considered  $2r_{\text{hm}}$  (marked as a green sphere in the figure).

Although in the above example we have calculated the ground-truth galaxy SFH within  $2r_{\text{hm}}$ , the galaxy SFH can be computed from particles located within any other considered distance. In Chapter 6 we do use  $2r_{\text{hm}}$  to calculate the ground-truth SFHs for some samples of *Illustris* galaxies, but in Chapter 5, the ground-truth galaxy SFHs will be built by considering only particles within a radius equal to that of the galaxy photometric aperture on the synthetic images (to make the comparison of this ground-truth SFH with the 2D-SPS-derived SFH more fair). This will be further discussed in the corresponding chapters.



## 2.5 On the representativeness of the sample of massive galaxies at $1 < z < 4$

As commented in Chapter 1, this thesis aims at advancing in our comprehension of the early stages of formation of the most massive galaxies in the local Universe (with  $M_{\star} > 10^{11} M_{\odot}$ ) by analyzing the stellar populations of massive ( $M_{\star} > 10^{10} M_{\odot}$ ) galaxies at  $1 < z < 4$ , which are thought to be their most likely progenitors. Nevertheless, observationally it is not possible to actually know which galaxies at  $1 < z < 4$  will evolve to a very massive galaxy at  $z = 0$ . Therefore, doubts may arise as to whether our sample of massive galaxies at  $1 < z < 4$  is truly representative of the actual sample of progenitors of very massive galaxies at  $z = 0$ . Since we are interested in the early stages of the SFH, it is essential to demonstrate that by analyzing a sample of massive galaxies at  $1 < z < 4$  we are able to recover a representative SFH of the most massive galaxies in the local Universe. This will be analyzed in detail in Section 5.6, where the results of applying our 2D-SPS method to Illustris synthetic images (see Section 2.3) are discussed. However, we give here the reader a preview of how this can be done in general and how it will be carried out specifically in our case.

The advantage of using Illustris is that we can use its merger trees to follow the evolution of any of its simulated galaxies along its snapshots to the local Universe. Therefore, in Illustris we are able to distinguish whether a massive galaxy at a given redshift will evolve into a very massive galaxy at  $z = 0$ . As we will see in Chapter 5, this will allow us, starting from the galaxies that appear in the Illustris deep survey images, to construct a sample of massive galaxies at  $1 < z < 4$  that are *bona-fide* progenitors of a very massive galaxy at  $z = 0$ . Fig. 2.6 shows a schematic diagram of how the sample of Illustris massive progenitors at  $1 < z < 4$  (represented by circles with blue star inside) is built. To do this, we start from all galaxies in the Illustris deep survey images at  $1 < z < 4$  (illustrated by the region between the two horizontal gray lines on top), and select those galaxies in the images which 1) are massive, and 2) evolve into a very massive galaxy at  $z = 0$ . This will be our main  $1 < z < 4$  sample considered in Chapter 5. The  $z = 0$  descendants of galaxies in our sample are shown with an orange square with a star inside (on the  $z = 0$  horizontal dotted line at the bottom). Massive galaxies at any redshift independently of their descendants are represented with a circle, non-massive galaxies with a small black dot, and very massive galaxies at  $z = 0$  with a square. We caution the reader that the descendants at  $z = 0$  of galaxies in the images (located on the bottom  $z = 0$  horizontal line) do not appear in the Illustris images but are available in the simulation.

As shown in Fig. 2.6, the  $z = 0$  descendants of our sample of massive progenitors at  $1 < z < 4$  can have other progenitors which are not included in our sample, which may have an impact on the SFH of these  $z = 0$  descendants. The first thing to evaluate is whether the 2D-SPS-derived SFH of our sample of massive progenitors at  $1 < z < 4$  in the images (circles with blue star inside) can recover the first stages of the ground-truth SFH of their  $z = 0$  descendants (orange squares in Fig. 2.6). In addition, since these  $z = 0$  descendants are only a subset of all the  $M_{\star} > 10^{11} M_{\odot}$  galaxies at  $z = 0$  in the Illustris simulation (all squares in Fig. 2.6), we will also compare our results with those predicted by the whole population of very massive galaxies at  $z = 0$  in Illustris.

Finally, to mimic what we get in real observations, we will build a final sample composed of all massive galaxies at  $1 < z < 4$  in the images (regardless of the stellar mass of their descendants at  $z = 0$ ). This second sample would consist of all the circles in Fig. 2.6 between the  $z = 1$  and  $z = 4$

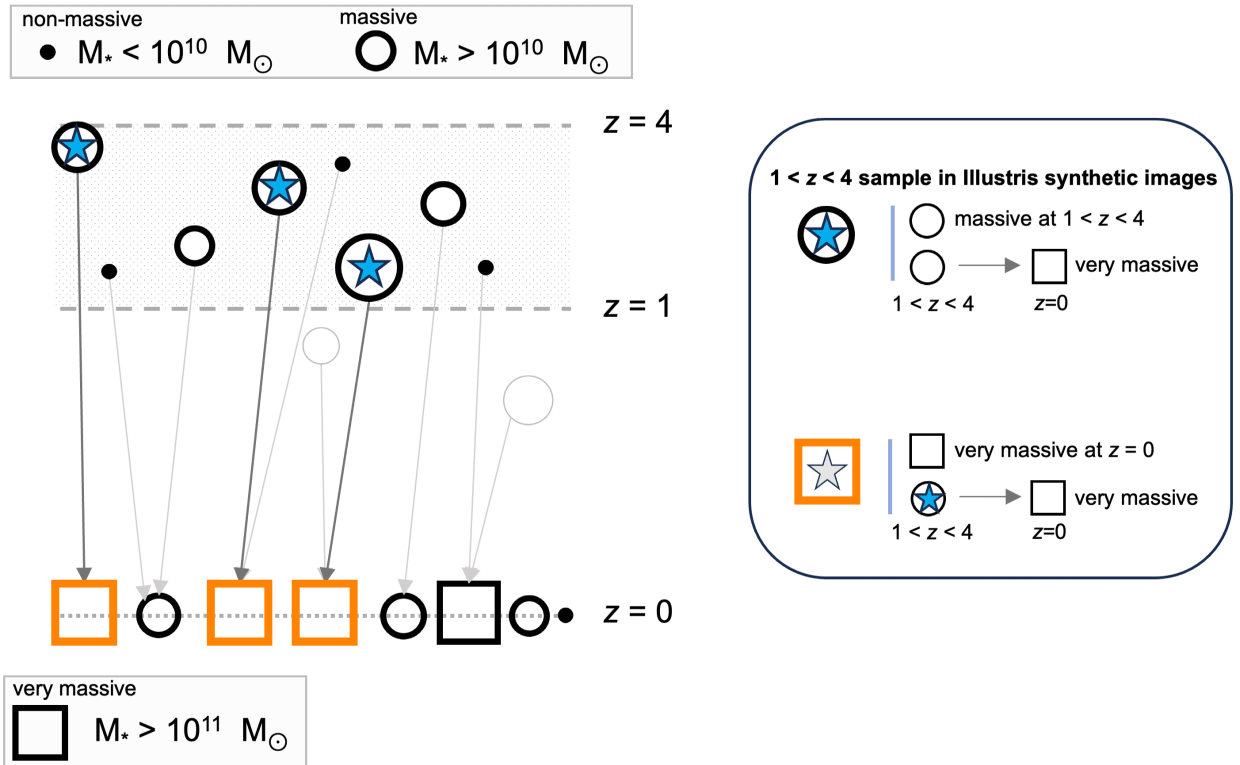


**Figure 2.6:** Schematic diagram of our sample of Illustris massive  $1 < z < 4$  progenitors to be analyzed in Chapter 5. We start from all the massive (circle) and non-massive (small black dot) galaxies in the Illustris synthetic deep survey images which are located at  $1 < z < 4$  (between the two horizontal dashed lines on the left). Using Illustris merger trees, we can follow the evolution of all the galaxies in the images at those redshifts until  $z = 0$  (bottom dotted line). Those  $z = 0$  galaxies do not appear in the images. Galaxies with  $M_* > 10^{11} M_\odot$  at  $z = 0$  are represented by a square. Our sample of massive  $1 < z < 4$  progenitors (circles with a blue star inside) is composed of massive  $1 < z < 4$  galaxies in the images which end up as a very massive galaxy at  $z = 0$ . The descendants at  $z = 0$  of this sample are shown with orange squares with a star inside. These  $z = 0$  descendants can have other progenitors different from those considered in our  $1 < z < 4$  sample. On the right, we layout the conditions fulfilled by galaxies in our sample of  $1 < z < 4$  progenitors (top) and by their  $z = 0$  descendants (bottom).

dashed lines (with and without a star inside). We will evaluate whether the (realistic) analysis of this latter sample of all  $1 < z < 4$  massive galaxies in the images can recover the SFH of very massive galaxies at  $z = 0$ . This will be done by applying our 2D-SPS method to the images of these massive  $1 < z < 4$  galaxies and directly comparing the results inferred from their SFHs with those inferred for our initial sample of massive progenitors at  $1 < z < 4$ . Since in real observations we cannot assure whether a massive galaxy at high redshift will evolve into a very massive in the nearby Universe, this analysis is important in order to prove whether the sample of all massive galaxies at  $1 < z < 4$  in the images can truly yield a representative SFH of the *bona-fide* progenitors of very massive galaxies at  $z = 0$ , which is the ultimate goal of this thesis.

## 2.6 Final considerations

As it has been shown in this chapter, the Illustris simulation constitutes a perfect scenario to test and improve our possible techniques to be applied in real galaxy observations. This is mainly due to the complete population of galaxies that Illustris is able to generate, which reproduce many of the observed relations both locally and at higher redshifts, and the available synthetic deep survey-like images it provides. As it will be shown in Chapter 5, Illustris synthetic deep survey images will be used to develop our 2D-SPS method (to be applied on real deep survey images). This will be done by comparing our 2D-SPS galaxy SFHs, derived from our 2D-SPS analysis on Illustris synthetic images, to the ground-truth galaxy SFHs built from the simulated particles belonging to each galaxy.

It is true that, as commented in Section 2.2.6, Illustris presents some tensions between its predictions and observations. These tensions suggest, mainly, the need to improve the existing physical models, but they may also be due to the lack of more sophisticated models of physical processes that are not taken into account. Certainly, cosmological simulations do not include all the physics that is potentially relevant at all times, but only a subset of this physics can be included. For example, magnetohydrodynamics, cosmic rays, dust or neutrino physics are usually neglected, and Illustris is not an exception in this sense. In addition, a fully rigorous treatment of SMBH is a pending matter not only in the Illustris simulation, but also in the rest of cosmological simulations. The growth and energy liberation of SMBHs cannot be done *ab initio* and are very coarsely parametrized (see Section 2.2.3). This is mainly due to the fact that the coupled evolution of dark matter, galaxies and SMBHs is a physical problem that links many different scales together. To simulate this in an *ab initio* is unfeasible to be done even with the best codes, since only a range of scales can be addressed and simulated at any given time.

It is worth mentioning, however, that the differences between the Illustris-simulated and the observed Universe are not a concern for us and our intended use of the simulation, which is primarily to use Illustris as a test scenario for our techniques. The only thing to keep in mind is that any scientific results we obtain from the Illustris-simulated galaxy population may not be strictly the same as those derived from real observations (e.g., the exact time values at which massive, high-redshift galaxies began to form may vary). This is applicable to Illustris or any other similar simulation. Precisely, the results we derive from applying the same techniques to HST+JWST observations (shown in Chapter 6) will aim to highlight possible discrepancies from those predicted by simulations (Illustris, in our case) and which of the known limitations listed above are most critical and also what subgrid physics should be changed and in what direction. This will contribute to improve our understanding of the currently accepted models of galaxy formation, which may need to be refined if indicated by observations.



## Observational data: the *Hubble* and *James Webb* Space Telescopes

---

*Space: the final frontier. Here we present the voyages of the Hubble and James Webb Space Telescopes. Their continuing mission: to explore strange new worlds. To seek out new life and new distant galaxy populations. To boldly probe where no one has reached before!*

— Jean-Luc Picard (modified), *Star Trek: The Next Generation*

Space telescopes offer imaging capabilities infeasible to be reached nowadays from ground-based telescopes thanks to the fact that they are diffraction-limited and that they are not subject to light absorptions from the Earth’s atmosphere. The *Hubble Space Telescope*, launched in 1990, was a revolution in its time. Its 2.4 m primary mirror unveiled a more galaxy populated Universe than we thought, giving us access from the UV to  $\sim 1.7 \mu\text{m}$  to a previously unknown population of galaxies.

With the recent launch of the *James Webb Space Telescope*, which has large 6.6 m primary mirror, we now have access to NIR and MIR wavelengths with unprecedented spatial resolution and sensitivity. The gains of *Webb* over other previous infrared space telescopes such as *Spitzer* are several: the collecting area of *Webb* is  $\sim 50$  times larger than that of *Spitzer*, allowing, e.g., a significantly higher angular resolution (on the order of 10) and sensitivity ( $>50$ ), especially at longer wavelengths (Rigby et al. 2022a). The main limitation of *Spitzer*, with a 0.85 m aperture, was resolution: its point-spread function (PSF) had a full-width high maximum (FWHM) of  $\sim 6''$  at  $24 \mu\text{m}$ . In contrast, *Webb* provides sub-arcsec resolution up to  $28 \mu\text{m}$ , in addition to other non-imaging capabilities that neither *Hubble* nor *Spitzer* have.

*Webb*’s exceptional characteristics, together with its wide spectral coverage in the infrared, not only allow us to expand the frontier of the universe we can observe, but, combined with previous *Hubble* data at shorter wavelengths, allow us to improve the determination of stellar parameters in intermediate- and high-redshift galaxies by better constraining their SEDs. The latter, due to *Webb*’s high angular resolution (similar to that of *Hubble* in the visible), is possible for both the integrated and spatially-resolved emission of galaxies (*Webb* in the NIR, like *Hubble* in the optical, has PSFs with  $\text{FWHM} \lesssim 0.2''$ ). Since the physical angular scale in  $1 < z < 4$  galaxies ranges from approximately 8 to 7 kpc/arcsec, this implies that both *Hubble* and *Webb* data can be used if we aim at studying the stellar populations of  $1 < z < 4$  galaxies in the subkiloparsec scale, providing a wider wavelength coverage if both telescopes are combined.

### 3.1 The Hubble Space Telescope

Conceived in the 1940s and initially called the *Large Space Telescope*, the *Hubble Space Telescope* was named in 1983 after the astronomer Edwin Powell Hubble (1889–1953). The project officially began in 1977 when it was approved by the United States Congress (Garner 2022a). It was a collaboration between the National Aeronautics and Space Administration (NASA) and the European Space Agency (ESA), which had joined the project in 1975 and contributed by providing the solar panels and the Faint Object Camera (FOC). Although the telescope was already assembled in 1985, its launch was delayed due to the explosion of the space shuttle *Challenger*. On 24 April 1990, it was finally launched onboard the space shuttle *Discovery* with five astronauts from the Kennedy Space Center in Cape Canaveral, Florida. It was deployed the following day, thanks to the help of the shuttle crew, who guided the telescope from the shuttle to its orbit above the Earth.

Unfortunately, soon after it was launched, it was discovered that the primary mirror of the telescope suffered from spherical aberration due to a flaw in the manufacturing of the mirror (Garner 2019). This primary mirror, which had been ground  $2.2\ \mu\text{m}$  too flat in its outer edge, made HST return images significantly less clear and sharp than expected. The good news was that HST had been designed to be periodically visited by astronauts to be repaired and upgraded. Therefore, the first space shuttle mission was programmed to compensate the optical aberration. In the meantime, since replacing the primary mirror was not feasible, corrective optics and replacement instruments were designed and constructed, and computer image reconstruction techniques were used on the observed images to partially mitigate the effects produced by the flaw.

In 1993, it took place the first space shuttle mission to HST, named Servicing Mission 1 (SM-1). During this mission, a more powerful camera with built-in corrective optics, the Wide Field and Planetary Camera 2 (WFPC2), replaced the first-generation camera, the WFPC1. For the other HST instruments onboard, the spherical aberration was corrected by installing the Corrective Optics Space Telescope Axial Replacement (COSTAR) instrument, which had several corrective mirrors that countered the aberration produced by the primary mirror and allowed HST to observe at its diffraction limit, with an angular resolution below  $0''.1$ . Fig. 3.1b shows an HST image of M100 before and after SM-1. In total, there have been five HST servicing missions, from 1993 to 2009. Fig. 3.1a shows a picture taken during the Servicing Mission 3A (SM-3A), in which HST was brought again to operation after having been in dormancy mode for approximately a month due to the failure of the fourth of its six gyroscopes. During this mission, all gyroscopes were replaced and a more powerful main computer was installed, apart from new insulation, a new transmitter, a more advanced solid-state data recorder, and some other equipment.

These space shuttle missions have been essential to keep the observatory running with state-of-art instruments for more than 30 years, and it is expected to continue operating until the late 2020s, maybe, beyond. During this time, HST has proven to be one the of most scientifically productive astronomy projects in history, with observations in almost every research area in astrophysics, covering galaxies, stars, comets, nebulae, outer planets and satellites, exoplanets, etc. Among the most famous achievements from HST observations, we can mention the measurement by SNIa of the accelerated expansion of the Universe (awarded the 2011 Nobel Prize), the confirmation of the existence of SMBHs in galaxy cores, measurements of the composition of exoplanet atmospheres, or the observation of distant galaxies in the Hubble Deep Field.

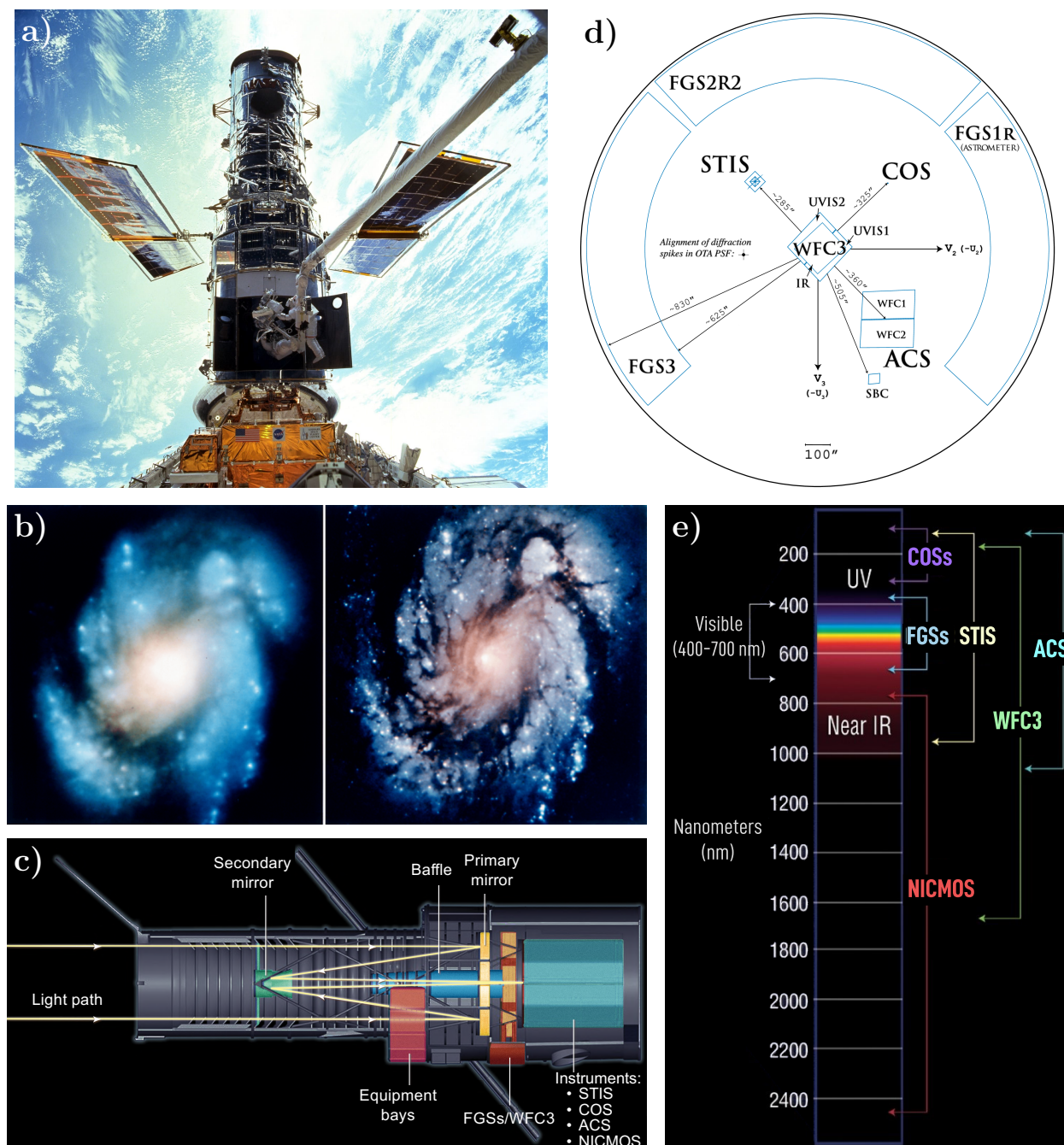


**Figure 3.1:** *Hubble* images. **a)** HST coupled to space shuttle *Discovery* during the third HST servicing mission (SM-3A) in December 1999, with two astronauts in the front of the image and the Earth in the background. **b)** Comparison between the core of M100 observed by HST before (left) and after (right) the spherical aberration was corrected during the first servicing mission in December 1993. The left image, taken with the original Wide Field and Planetary Camera 1 (WFPC-1), misses fine and faint details owing to the starlight blur produced by the optical aberration in the primary mirror. The right image was taken with the Wide Field and Planetary Camera 2 (WFPC-2), installed during the servicing mission, and shows the significant improvement produced by the corrective optics that compensated the aberration. **c)** HST cross section that shows the Cassegrain design of the telescope and the path that light follows when it enters the telescope until it reaches the instruments. **d)** HST field of view after SM4 with the instruments entrance apertures in the focal plane as they are projected on the sky. **e)** Wavelength ranges (in nm) covered by the current scientific instruments in HST. *Images credits:* ESA/Hubble & NASA.

### 3.1.1 General characteristics

HST is a Cassegrain reflector with two hyperbolic mirrors: a 2.4 m primary mirror and a smaller 30.5 cm secondary mirror. The hyperbolic shape of both mirrors makes HST a Ritchey-Chrétien variant of standard Cassegrain telescopes (with parabolic mirrors), which prevents *Hubble* from suffering comatic aberration and allows it to obtain sharper images. When the aperture door is open, light enters the telescope and is collected and reflected by the primary mirror towards the secondary mirror, suspended ahead (see Fig. 3.1c). This secondary mirror reflects the light back through a hole in the primary mirror to reach the guidance and science instruments. Both mirrors are made of glass, which is coated with aluminum in order to provide reflectivity. On top of the aluminum, a coated magnesium fluoride layer protects the mirrors from oxidation and increases their UV reflectivity (Garner 2022b).

The size of the observatory is 13.3 m  $\times$  4.2 m (approximately a school bus) and weighed  $\sim$ 10,800 kg when it was launched ( $\sim$ 12,200 kg after its last servicing mission). It is located at a circular Low Earth Orbit with an altitude of roughly 535 km and an inclination of 28.5 degrees to the equator. Traveling at a speed of  $\sim$ 27,000 km/h, it completes every orbit in approximately 95 minutes (Belleville 2022) powered by its two solar panels and the batteries that allow HST to operate even when the Earth blocks the sunlight.

*Hubble* rotates thanks to the combination of four internal reaction wheels and four magnetic torquers. The reaction wheels, located near the center of gravity of HST, are used to reorient the telescope (using Newton's third law) and point to the different targets based on the schedule provided by the Operations Control Center. The magnetic torquers can create magnetic fields which interact with that of the Earth, pushing or pulling HST towards it, and helping HST rotate. To detect the movement of the telescope, three high-precision gyroscopes (out of the six it carries) are typically used to measure its rate and direction of motion. In addition, *Hubble* has three Fine Guidance Sensors (FGSs), two of which are used for the pointing of the telescope and lock it on target (with an absolute pointing error of less than 0.''01). The third FGS can be used for astrometric measurements. Communications are received and transmitted through two high-gain antennas on HST (Garner 2022c).

*Hubble* can observe from  $\sim$ 100 nm to 2.4  $\mu$ m, but it is primarily optimized to observe in UV and optical wavelengths. In Section 3.1.2, we briefly discuss the current scientific instruments onboard HST, focusing on the instruments used for this thesis.

### 3.1.2 Scientific instruments

HST is equipped with different scientific instruments that provide both spectroscopy and high-resolution imaging from the ultraviolet to near-infrared wavelengths. Currently, the scientific instruments onboard which are still operating are the following:

- The Advanced Camera for Surveys (ACS)
- The Wide Field Camera 3 (WFC3)
- The Cosmic Origins Spectrograph (COS)



- The Space Telescope Imaging Spectrograph (STIS)
- The Near Infrared Camera and Multi-Object Spectrometer (NICMOS) – inactive since 2008
- Fine Guidance Sensors (FGSs)

ACS and WFC3 are the HST main cameras, which can be combined to provide high resolution imaging of a wide field over a wide wavelength coverage. Although both cameras are equipped with a comprehensive set of filters that span a broad range of wavelengths, ACS is usually selected for visible observations, while WFC3 usually observes UV and NIR. COS and STIS are the primary HST spectrographs. STIS is a very versatile instrument that provides high-resolution UV-to-NIR spectroscopy of spatially-resolved sources, while COS focuses on providing UV-spectroscopy of extremely deep and faint sources. In addition to COS and STIS, the NICMOS instrument, currently inactive, was another spectrograph that provided both imaging and spectroscopy in the NIR. Finally, the FGSs on HST are three interferometers that, apart from being used to help in the pointing of the telescope by locking HST on guide stars, one of the FGSs can sometimes be used for precise astrometric measurements (e.g., relative positions of stars, changes in brightness, or for resolving double-star systems). Fig. 3.1d schematically shows the location and the field of view of the scientific instruments in HST focal plane. The wavelength coverage covered by these instruments is shown in Fig. 3.1e.

For this thesis, we make use of the two main HST imaging instruments, ACS and WFC3, which provide UV-to-NIR photometric measurements in a wide range of filters. In Section 3.1.2.1, we describe the ACS instrument based on the *ACS Instrument Handbook* (Ryon 2022). WFC3 is described in Section 3.1.2.2, based on the *WFC3 Instrument Handbook* (Dressel 2022).

### 3.1.2.1 The Advanced Camera for Surveys (ACS)

The Advanced Camera for Surveys (ACS) is a third-generation HST instrument installed in 2002 (SM-3B) to replace the former most-used HST camera, WFPC2. Still today, ACS continues to be an excellent tool for high-resolution imaging in UV and optical bands.

ACS originally included three different channels of observations: the Wide Field Channel (WFC), the High Resolution Channel (HRC), and the Solar Blind Channel (SBC). These channels were primarily optimized for different tasks: WFC for wide deep field imaging (from visible to NIR), HRC for high-resolution imaging (from near-UV to NIR), and SBC for solar-blind UV imaging. In addition to imaging, ACS was designed to provide additional capabilities with the three different channels, such as grism and prism low-resolution spectroscopy (SBC and HRC), imaging polarimetry (WFC and HRC), and coronagraphy (HRC). Unfortunately, WFC and HRC suffered a malfunction in 2007. SM-4 in 2009 was able to repair the WFC, but HRC could not be restored and is no longer operating. The SBC was unaffected and continues in operation together with the WFC. Some general characteristics of the three ACS channels are shown in Table 3.1. In this thesis, we only make use of observations taken by the WFC channel, highlighted in gray in this table.

Regarding the ACS filters, they are located in three different filter wheels. Two of these wheels were shared by WFC and HRC, and the other is used by the SBC. Figure 3.2 shows the HST maximum total system throughput for several HST instruments as a function of wavelength. It can

**Table 3.1:** General characteristics of the ACS channels. Observations for this thesis have been taken by the WFC channel, highlighted in gray.

	Wide Field Channel (WFC)	High Resolution Channel (HRC; unusable since 2007)	Solar Blind Channel (SBC)
Wavelength coverage (nm)	350–1,100	170–1,100	115–170
Field of View (arcsec <sup>2</sup> )	202 × 202	29 × 26	34.6 × 30.5
Plate Scale (arcsec <sup>2</sup> /pix)	~ 0.05 × 0.05	~ 0.028 × 0.025	~ 0.034 × 0.030
Pixel Size (μm <sup>2</sup> )	15 × 15	21 × 21	25 × 25
Image format (pix <sup>2</sup> )	2 × 2,048 × 4,096	1,024 × 1,024	1,024 × 1,024

Reference: *ACS Instrument Handbook* (Ryon 2022)

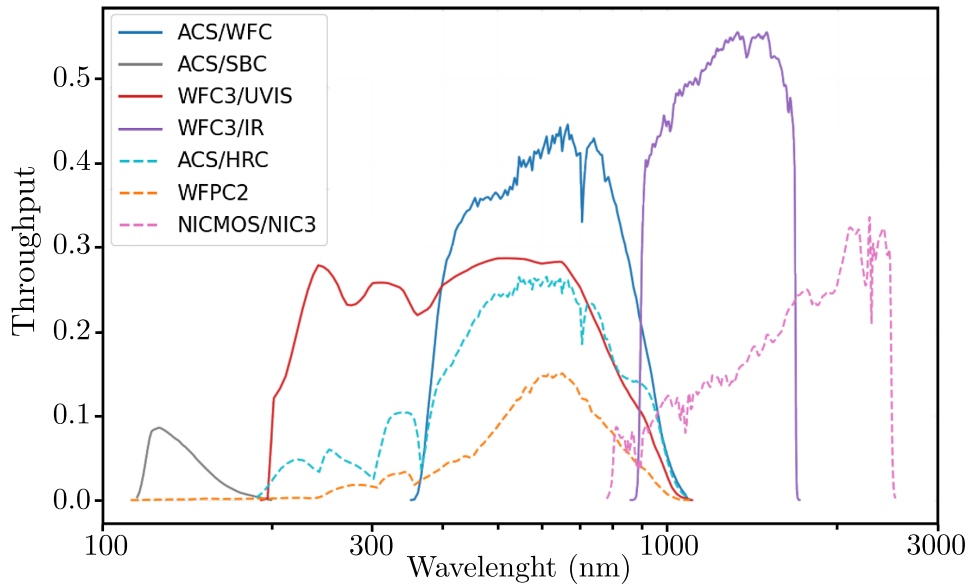


**Figure 3.2:** Modified figure from the *ACS Instrument Handbook* (Ryon 2022). HST total system throughput as a function of wavelength for several HST instruments. The lines show the maximum throughputs for each instrument at a given wavelength. Current operating instruments are shown with solid lines, and replaced (WFPC2) or inoperable (ACS/HRC, NICMOS) instruments with dashed lines.

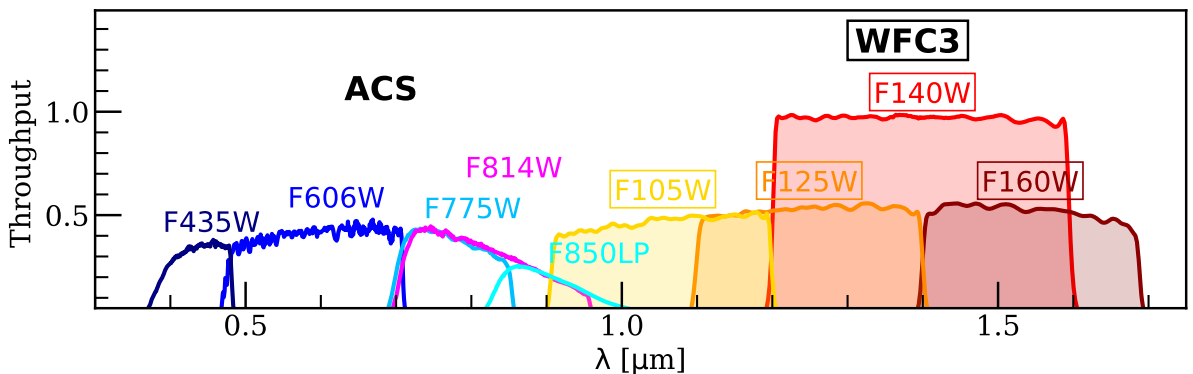


**Figure 3.3:** Throughput of ACS and WFC3 filters used in this thesis. WFC3 filters are shaded inside, and their names have been boxed.

**Table 3.2:** Broadband ACS/WFC filters used in this thesis.

Filter name	Central wavelength <sup>a</sup> (nm)	FWHM <sup>b</sup> (nm)	Description
F435W	433.0	93.7	Johnson <i>B</i>
F606W	592.2	232.2	Broad <i>V</i>
F775W	769.3	151.1	SDSS <i>i</i>
F814W	804.5	185.8	Broad <i>I</i>
F850LP	903.1	120.7	SDSS <i>z</i>

**Notes:**

<sup>a</sup> The provided central wavelengths, unless otherwise stated, correspond to the pivot wavelength:  $\lambda_{\text{pivot}} \equiv \frac{\int T(\lambda) d\lambda}{\int T(\lambda) d\lambda/\lambda^2}$ , where  $T(\lambda)$  is the filter transmission.

<sup>b</sup> The width of the filter is calculated as the difference between the two wavelengths at which the transmission of the filter is half maximum.

*References:* *ACS Instrument Handbook* (Ryon 2022) and the Spanish Virtual Observatory (SVO; <https://svo.cab.inta-csic.es/>)

be seen the significant improvement of the ACS/WFC throughput with respect to its precursor, the WFPC2. ACS/WFC also presents a higher transmission in the optical wavelengths when compared to that of the WFC3. In particular, for this thesis, we use the broadband filters from the ACS which are shown in Table 3.2. Figure 3.3 shows the transmission curves for these filters.

### 3.1.2.2 The Wide Field Camera 3 (WFC3)

The Wide Field Camera 3 was installed during Servicing Mission 4 in 2009, also with the aim to replace the WFPC2. Designed to last until the end of HST mission, WFC3 presents excellent imaging capabilities, combining a wide wavelength coverage (200 nm – 1.7  $\mu\text{m}$ ), high sensitivity, and a wide field of view. This makes WFC3 the suitable instrument for multi-wavelength surveys for which both a wide field of view and a wide spectral coverage (down to 200 nm) are required. In addition to high resolution imaging, WFC3 offers low resolution ( $R \sim 70 - 130$ ) slitless spectroscopy in three different ranges (190 – 450, 800 – 1,150, and 1,075 – 1,700 nm).

WFC3 has two independent channels which are sensitive to different wavelengths: the UVIS channel, which can observe UV and visible wavelengths (200 – 1000 nm), and the IR channel, for NIR wavelengths (800 – 1,700 nm). These channels cannot be used simultaneously, but they can be sequentially used. Fig. 3.1d schematically shows the location of the field of view of both channels in the HST focal plane. In this figure, it can be seen that the UVIS detectors consist of two  $4,096 \times 2,051$  pixel CCDs (UVIS 1 and UVIS 2), which are joined together to form a  $4,096 \times 2,051$  array with a separation of  $\sim 31$  pixels (or 1.2 arcsec) that can be filled using dithering techniques. Table 3.3 shows some general characteristics of these channels. We have highlighted in gray the IR channel, for it is the one used in this thesis.

**Table 3.3:** General characteristics of the WFC3 channels. Observations for this thesis have been taken with the IR channel, highlighted in gray.

	UVIS	IR
Wavelength coverage (nm)	200–1,000	800–1,700
Field of View (arcsec <sup>2</sup> )	162 × 162	136 × 123
Plate Scale (arcsec <sup>2</sup> /pix)	0.04 × 0.04	0.135 × 0.121
Pixel Size (μm <sup>2</sup> )	15 × 15	18 × 18
Image format (pix <sup>2</sup> )	2 × 2,051 × 4,096	1,014 × 1,014

Reference: *WFC3 Instrument Handbook* (Dressel 2022)

**Table 3.4:** Broadband WFC3 filters used in this thesis

Filter name	Central wavelength <sup>a</sup> (nm)	FWHM <sup>b</sup> (nm)	Description
F105W	1055.0	291.7	Wide <i>Y</i>
F125W	1248.6	300.5	Wide <i>J</i>
F140W	1392.3	394.1	Wide <i>JH</i> gap
F160W	1537.0	287.5	WFC3 <i>H</i>

**Notes:**

<sup>a</sup> The provided central wavelengths, unless otherwise stated, correspond to the pivot wavelength:  $\lambda_{\text{pivot}} \equiv \frac{\int T(\lambda) d\lambda}{\int T(\lambda) d\lambda/\lambda^2}$ , where  $T(\lambda)$  is the filter transmission.

<sup>b</sup> The width of the filter is calculated as the difference between the two wavelengths at which the transmission of the filter is half maximum.

References: *WFC3 Instrument Handbook* (Dressel 2022) and the Spanish Virtual Observatory (SVO; <https://svo.cab.inta-csic.es/>)

As shown in Fig. 3.2, WFC3 covers a wide spectral range due to the large number of filters with which it is equipped. Each channel provides its own set of broad-, intermediate, and narrow-band filters, together with low-dispersion grisms: 47 filters and 1 UV grism in the UVIS channel (allocated in 12 filter wheels), and 15 filters and 2 grisms in IR channel (one filter wheel). Fig. 3.3 shows the throughput of the WFC3/IR filters used throughout this thesis, and their general characteristics are shown in Table 3.4.

### 3.1.3 HST cosmological fields

Cosmological fields are observations of the sky sufficiently wide and deep to include a large number of galaxies within the field, which allows us to study their properties in a statistical way. Without a doubt, the excellent capabilities of HST for observing deep cosmological fields were clearly proven

in 1995, when HST observed an apparently empty region of  $\sim 5.3$  arcmin<sup>2</sup> in the Big Dipper with the WFPC2 (filters  $U_{300}$ ,  $B_{450}$ ,  $V_{606}$ , and  $I_{814}$ ) and for a total exposure of 10 days. The result of this was the Hubble Deep Field North (HDFN; Williams et al. 1996) or, originally, the Hubble Deep Field (HDF), which stunned the extragalactic scientific community due to the large number of galaxies it contained and the different morphologies they presented, providing a considerable amount of information regarding their evolution and first stages. Follow-up observations in different wavelengths of this region, both photometrical and spectroscopic, soon made the HDFN become one of the best observed extragalactic region in the sky, with more than 3,000 galaxies detected. In 1998, the Hubble Deep Field South (HDFS; Williams et al. 2000) was observed in the southern sky, but the impact of this field was considerably smaller mainly because it was difficult to be observed from ground-based telescopes, due to the presence of stray light from several very bright stars close to the field.

In 2003, ACS observed the Hubble Ultra Deep Field (HUDF; Beckwith et al. 2006b), which was publicly released in 2004. The HUDF contained more than 10,000 galaxies, it was twice larger ( $\sim 3'.4 \times 3'.4$ ) than the HDFN and one magnitude deeper, reaching  $m_{AB} \approx 29$  in the observed filters ( $B_{435}$ ,  $V_{606}$ ,  $i_{775}$ , and  $z_{850}$ ). In 2009, after WFC3 was installed on HST, the HUDF was observed with three WFC3 NIR filters ( $Y$ ,  $J$ , and  $H$ ), reaching  $m_{AB} \approx 28.5$  (HUDF09, Bouwens et al. 2011), which allowed the exploration of higher-redshift galaxies. In 2012, the deepest image ever taken (by then) was released: the HST eXtreme Deep Field (XDF; Illingworth et al. 2013b), a  $2'.3 \times 2'$  image centered on the HUDF and observed in nine optical and NIR filters, combining 10 years of ACS and WFC3 observations, and reaching  $m_{AB} \approx 30$ .

The scientific success from the original HDF images motivated the scientific community to conduct additional multi-wavelength surveys with *Hubble*, which were often overlapped with observations from other observatories. Examples of these first HST surveys are the Great Observatories Origins Deep Surveys (GOODS; Giavalisco et al. 2004), the Galaxy Evolution from Morphologies and SEDs (GEMS; Rix et al. 2004), or the Cosmic Evolution Survey (COSMOS; Scoville et al. 2007). In this thesis, we make use of the Cosmic Assembly Near-infrared Deep Extragalactic Legacy Survey (CANDELS; Grogin et al. 2011; Koekemoer et al. 2011), which, as described in Section 3.1.3.1, is built upon previous observations of some of the HST cosmological surveys.

### 3.1.3.1 CANDELS

The installation of the WFC3 on HST in 2009, with its excellent spatial resolution and sensitivity in the NIR wavelengths, made possible to conduct deep galaxy surveys able to observe faint and distant objects undetected until then with previous instruments. An example of one these surveys was the Cosmic Assembly Near-infrared Deep Extragalactic Legacy Survey (CANDELS; Grogin et al. 2011; Koekemoer et al. 2011), a multi-wavelength 902-orbit legacy project that was designed to study galaxy formation and evolution over  $z \sim 1.5 - 8$ , thanks to the combination of deep WFC3 and parallel ACS observations, together with ancillary data from other observatories.

The survey consists of five well-studied sky regions that cover  $\sim 800$  arcmin<sup>2</sup> ( $\sim 0.22$  deg<sup>2</sup>), a sufficiently large area to mitigate cosmic variance and to include a comprehensive sample of galaxies ( $\sim 250,000$  galaxies observed). These sky regions are: the Cosmic Evolution Survey (COSMOS; Scoville et al. 2007), the Extended Groth Strip (EGS; Davis et al. 2007), the GOODS-North and

**Table 3.5:** CANDELS fields: sky positions and references.

Field name	Right Ascension (J2000)	Declination (J2000)	Area (arcmin <sup>2</sup> )	References for original field	References for CANDELS catalogs
EGS	14 <sup>h</sup> 17 <sup>m</sup> 00 <sup>s</sup>	+52° 30' 00"	206	Davis et al. (2007)	Stefanon et al. (2017); also Santini et al. (2015)
COSMOS	10 <sup>h</sup> 00 <sup>m</sup> 28 <sup>s</sup>	+02° 12' 21"	216	Scoville et al. (2007)	Nayyeri et al. (2017)
GOODS-N	12 <sup>h</sup> 36 <sup>m</sup> 55 <sup>s</sup>	+62° 14' 11"	171	Giavalisco et al. (2004)	Barro et al. (2019)
GOODS-S	03 <sup>h</sup> 32 <sup>m</sup> 30 <sup>s</sup>	-27° 48' 20"	170	Giavalisco et al. (2004)	Guo et al. 2013; also Dahlen et al. (2013) and Santini et al. (2015)
UDS	02 <sup>h</sup> 17 <sup>m</sup> 37.5 <sup>s</sup>	-05° 12' 00"	202	Lawrence et al. (2007); Cirasuolo et al. (2007)	Galametz et al. (2013); also Santini et al. (2015)

*References:* Stefanon et al. (2017) for EGS, Nayyeri et al. (2017) for COSMOS, Barro et al. (2019) for GOODS-N, Guo et al. (2013) for GOODS-S, and Galametz et al. 2013 for UDS.

GOODS-South fields (GOODS-N and GOODS-S, respectively; Giavalisco et al. 2004), and the UKIRT Infrared Deep Sky Survey (UKIDSS) Ultra-deep Survey field (UDS; Lawrence et al. 2007; Cirasuolo et al. 2007). The reason for choosing these fields was the large amount of ancillary data they presented (covering from the near-UV to the far-IR; see Grogin et al. 2011). For instance, all of them have associated deep imaging observations by Spitzer/IRAC 3.6  $\mu\text{m}$  and 4.5  $\mu\text{m}$  in the Spitzer Extended Deep Survey (SEDS; Ashby et al. 2013). Table 3.5 shows the sky positions and areas of the five CANDELS fields.

In terms of depth, CANDELS is divided into 2 regions: CANDELS/Deep & Wide. CANDELS/Deep covers  $\sim 125$  arcmin<sup>2</sup> region within GOODS-N and GOODS-S, with a  $5\sigma$  limiting magnitude of  $H = 27.7$  mag. CANDELS/Wide includes GOODS, the Extended Groth Strip (EGS), COSMOS, and UDS, reaching a  $5\sigma$  limiting magnitude of  $H \gtrsim 27.0$  mag in the whole area. These regions, together with the Hubble Ultra Deep Fields, create the so-called "wedding-cake" approach regarding depth and field of view.

CANDELS images and the associated multi-wavelength photometric catalogs are publicly available. Catalogs are presented in different papers: Guo et al. 2013 for GOODS-S, Galametz et al. (2013) for UDS, Nayyeri et al. (2017) for COSMOS, Stefanon et al. (2017) for EGS, and Barro et al. (2019) for GOODS-N. Apart from multi-wavelength photometry, catalogs also include additional information like the stellar mass of galaxies, SFR, and photometric redshift. In the case of GOODS-S and UDS, the stellar masses for both fields are separately published in Santini et al. (2015), and the photometric redshifts for GOODS are published in Dahlen et al. (2013). For all the photometric catalogs, WFC3/F160W was chosen as the reference band and was used for source detection.

Fig. 3.4 shows the sky regions covered by the five CANDELS fields, extracted from the respective photometric catalogs, together with some existing ancillary data in the same sky region (see the corresponding photometric catalogs papers for a detailed description of all the ancillary data in each

field). In all fields, the gray shaded areas correspond to different depths of the F160W mosaic. For GOODS-N (Fig. 3.4a), the shaded zones include CANDELS/Wide and Deep. The ancillary data shown would be GOODS *HST*/ACS data (Giavalisco et al. 2004; in blue),  $K_s$  band from the Subaru MOIRCS Deep Survey (MODS; Kajisawa et al. 2009; dark red), 25 optical medium bands from the Survey for High- $z$  Absorption Red and Dead Sources (SHARDS; Pérez-González et al. 2013) at Gran Telescopio de Canarias (GTC; orange), GOODS *Spitzer*/IRAC data (Dickinson et al. 2003; gold), together with both *Spitzer*/IRAC from the *Spitzer* Extended Deep Survey (SEDS; Ashby et al. 2013) and  $K$  photometry from MegaCam at Canada–France–Hawaii Telescope (CFHT; Hsu et al. 2019) that cover the whole field.

For GOODS-S (Fig. 3.4b), the gray shaded areas include the CANDELS wide and deep region, *HST*/WFC3 Early Release Science (ERS; Windhorst et al. 2011), and HUDF09 (Bouwens et al. 2010). Ancillary data shown correspond to  $U$ -band images (Nonino et al. 2009; magenta) taken by the Visible Multi-Object Spectrograph (VIMOS) on the Very Large Telescope (VLT), GOODS *HST*/ACS (Giavalisco et al. 2004; in blue),  $K_s$ -band image taken by both the VLT/Infrared Spectrometer and Array Camera (ISAAC; Retzlaff et al. 2010; green) and the VLT/High Acuity Wide field K-band Imager (HAWK-I; Fontana et al. 2014; in yellow), and GOODS *Spitzer*/IRAC (Dickinson et al. 2003; red). The whole field is also covered by SEDS in *Spitzer*/IRAC.

For UDS (Fig. 3.4c), CANDELS WFC3 F160W data is marked as the gray hatched area inside the red solid line, and ACS data are inside the red dashed line. Additional data shown are CFHT  $u$ -band (Almaini et al., in prep.; pink), Subaru data ( $BVR_c i' z'$ ; Furusawa et al. 2008, blue), UKIRT Infrared Deep Sky Survey (UKIDSS; ( $JHK$ ; Almaini et al., in prep.; green),  $YK_s$  bands from the HAWK-I UDS and GOODS Survey (HUGS; Fontana et al. 2014; black dashed), *Spitzer*/IRAC SEDS (3.6 and 4.5  $\mu\text{m}$  orange solid), and the 4 IRAC bands from the *Spitzer* UKIDSS Ultra Deep Survey (SpUDS, PI: J. Dunlop; orange dashed).

For EGS (Fig. 3.4d), the light-blue shaded region represents the ACS F606W data from the All-Wavelength Extended Groth Strip International Survey (AEGIS; Davis et al. 2007), which overlaps the CANDELS WFC3 F160W data (dark gray inside). Additional data shown are optical broadband  $u^*$ -to- $z'$  from the CFHT Legacy Survey (CFHTLS; Gwyn 2012; blue line),  $J$ ,  $H$ , and  $K_s$  bands from the Wide-field InfraRed Camera (WIRCam) Deep Survey (WIRDS; Bielby et al. 2012; red), IRAC 3.6-to-8  $\mu\text{m}$  from the *Spitzer*-Cosmic Assembly Deep Near-infrared Extragalactic Legacy Survey (S-CANDELS; Ashby et al. 2015; 28 h in pink, 50 h in magenta), the NOAO Extremely Wide-Field Infrared Imager (NEWFIRM) Medium-Band Survey (NMBS; Whitaker et al. 2011; orange contour), and the WFC3 F140W band from 3D-HST (Skelton et al. 2014; green).

Finally, for COSMOS (Fig. 3.4e) CANDELS ACS (blue solid line) overlaps most of the WFC3 F160W footprint (gray shaded area). The ancillary data shown correspond to *Spitzer*/IRAC (3.6 and 4.5  $\mu\text{m}$  from Ashby et al. 2013, and 5.8 and 8.0  $\mu\text{m}$  from Sanders et al. 2007; red) and NEWFIRM ( $J_1 J_2 J_3 H_1 H_2 K$  bands; cyan). Other additional data that cover the whole WFC3 footprint are observations from CFHT/MegaPrime (Gwyn 2012;  $u^*$ ,  $g^*$ ,  $r^*$ ,  $i^*$ , and  $z^*$ ), from Subaru/Suprime-Cam (Taniguchi et al. 2007;  $B$ ,  $g^+$ ,  $V$ ,  $r^+$ ,  $i^+$ , and  $z^+$ ), and from the Ultra Deep Survey with the VISTA telescope (UltraVISTA; McCracken et al. 2013).

In Table 3.6 we show the *HST* WFC3 and ACS images available in each CANDELS fields, according to the photometric catalogs papers. General information such as the FWHM of the PSF and the limiting depths at  $5\sigma$  are also included in this table.

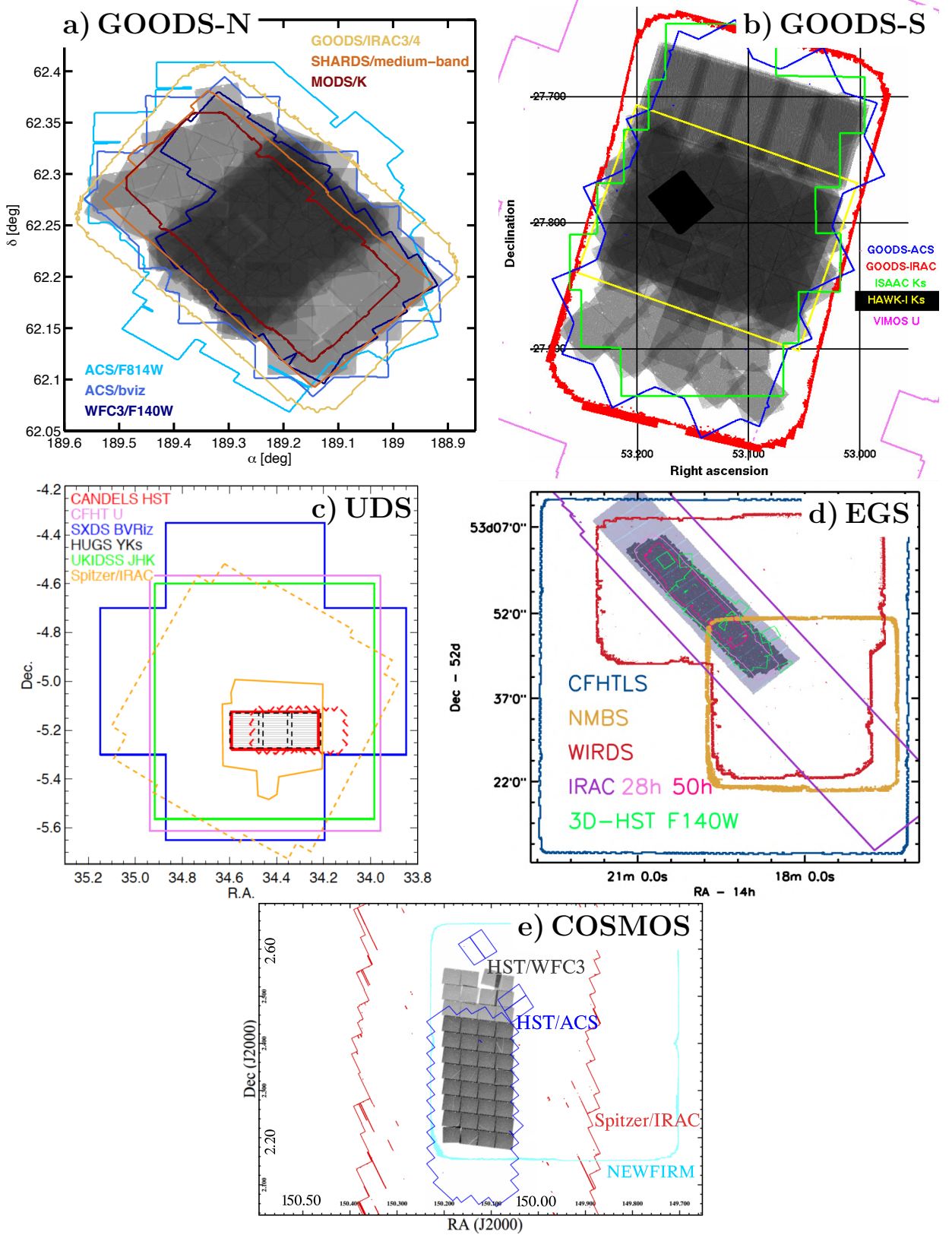


**Figure 3.4:** Sky coverage of CANDELS fields: GOODS-N (a), GOODS-S (b), UDS (c), EGS (d), and COSMOS (e). Adapted figures from Barro et al. (2019), Guo et al. (2013), Galametz et al. (2013), Stefanon et al. (2017), and Nayyeri et al. (2017), respectively. Gray shaded zones represent CANDELS WFC3 F160W mosaic, where darker zones correspond to deeper data, except for UDS, where WFC3 data are the hatched region delimited by the red solid line and, ACS, inside the dashed red line. In EGS (d), ACS data are the light blue larger shaded zone enclosing the WFC3 data in the center (dark gray). See details in main text.



**Table 3.6:** CANDELS fields: HST ACS and WFC3 images.

Field name	Filter name	Filter $\lambda_{\text{pivot}}$ (nm)	PSF FWHM (arcsec)	Depth at $5\sigma$ ( $m_{\text{AB}}$ )	References
EGS	ACS F606W	592	0.12	28.8	Koekemoer et al. (2011)
	F814W	805	0.12	28.2	...
	WFC3 F125W	1249	0.19	27.6	...
	F140W	1392	0.19	26.8	Skelton et al. (2014); Brammer et al. (2012)
	F160W	1537	0.20	27.6	Koekemoer et al. (2011)
COSMOS	ACS F606W	592	0.10	28.3	Koekemoer et al. (2011)
	F814W	805	0.10	27.72	...
	WFC3 F125W	1249	0.14	27.72	...
	F160W	1537	0.17	27.56	...
GOODS-N	ACS F435W	433	0.10	27.1	Giavalisco et al. (2004)
	F606W	592	0.10	27.7	...
	F775W	769	0.11	27.2	...
	F814W	805	0.11	28.1	Grogin et al. (2011); Koekemoer et al. (2011)
	F850LP	903	0.11	26.9	Giavalisco et al. (2004)
	WFC3 F105W	1055	0.18	26.4	Grogin et al. (2011); Koekemoer et al. (2011)
	F125W	1249	0.18	27.5	...
	F140W	1392	0.18	26.9	AGHAST survey (GO: 11600; PI: B. Weiner)
F160W	1537	0.19	27.3	Grogin et al. (2011); Koekemoer et al. (2011)	
GOODS-S	ACS F435W	433	0.08	28.95 / 30.55 <sup>b</sup>	Giavalisco et al. (2004); Bouwens et al. (2011)
	F606W	592	0.08	29.35 / 31.05 <sup>b</sup>	...
	F775W	769	0.08	28.55 / 30.85 <sup>b</sup>	...
	F814W	805	0.09	28.84	Grogin et al. (2011); Koekemoer et al. (2011)
	F850LP	903	0.09	28.55 / 30.25 <sup>b</sup>	Giavalisco et al. (2004); Bouwens et al. (2011)
	WFC3 F098M	986	0.13	28.77	Windhorst et al. (2011)
	F105W	1055	0.15	27.45 / 28.45 / 29.45 <sup>c</sup>	Grogin et al. (2011); Koekemoer et al. (2011) and Bouwens et al. (2011)
	F125W	1249	0.16	27.66 / 28.34 / 29.78 <sup>c</sup>	...
F160W	1537	0.17	27.36 / 28.16 / 29.74 <sup>c</sup>	...	
UDS	ACS F606W	592	0.10	28.49	Grogin et al. (2011); Koekemoer et al. (2011)
	F814W	805	0.10	28.53	...
	WFC3 F125W	1249	0.20	27.35	...
	F160W	1537	0.20	27.45	...

**Notes:**

<sup>a</sup> The  $5\sigma$ -depths in this table, unless otherwise specified, have been measured in  $\sim 5,000$  circular apertures, with radius equal to the FWHM of the PSF, randomly placed in regions of the image which are free of objects.

<sup>b</sup> Limiting depths in these ACS images have been measured inside an aperture with a fixed radius of  $0''.09$ . Each filter has two measurements: one for GOODS-S v2.0 images and the other one for HUDF.

<sup>c</sup> Limiting depths in these WFC3 images have been measured inside an aperture with a fixed radius of  $0''.17$ . Each filter has three measurements: for CANDELS Wide, CANDELS Deep, and HUDF09 (respectively, as they appear in the table).

*References:* Data for this table has been extracted from Stefanon et al. (2017) for EGS, Nayyeri et al. (2017) for COSMOS, Barro et al. (2019) for GOODS-N, Guo et al. (2013) for GOODS-S, and Galametz et al. (2013) for UDS.

## 3.2 The James Webb Space Telescope

JWST is currently the most powerful observatory ever built and is expected to be the premier observatory of the next decade. It is the result of an international collaboration led by NASA, ESA and the Canadian Space Agency (CSA) on which more than ~20,000 people have worked.

The history of JWST began in 1989, when it took place the first conference about the successor space telescope of *Hubble*, the then called Next Generation Space Telescope (NGST), and in which its scientific opportunities and technological requirements for the mission were discussed. The feasibility of the project was evaluated during the following years and it was officially initiated in 1996. In 2002, the NGST was renamed the *James Webb Space Telescope* (JWST, or also, *Webb*), after James E. Webb (1906-1992), the second administrator of NASA, and its construction began in 2004. The project suffered from numerous delays and multiple cost overruns, which made that final tests and the folding of the telescope were not completed until 2021 and that the launch was postponed several times.

Finally, on 25 Dec 2021, *Webb* was launched on an *Ariane 5* rocket from EAS's spaceport in French Guiana and was released to its route ~26 min after the liftoff. Unlike *Hubble* that orbited the Earth, the destination of JWST was the second Sun-Earth Lagrange point (or L2), located at ~1.5 million kilometers away from the Earth in the opposite direction of the Sun, and which makes service missions impossible. Both the launch and subsequent deployments of the telescope were successfully completed and, 29 days after launch, the telescope arrived at its desired orbit around L2 with minimal propellant costs (see Fig. 3.5a). The following 6 months of commissioning and calibration showed that the mission and science requirements were met or, even, exceeded (Rigby et al. 2022a). On 12 July 2022, the first JWST science images and spectra were publicly released (JWST Early Release Observations, ERO; Pontoppidan et al. 2022) showing the exceptional capabilities of JWST for both imaging and spectroscopy.

In July 2022, JWST began normal science operations and, in the following months, science papers quickly began to appear. Originally, there are four main themes into which JWST science goals are divided: *First Light and Reionization*, *The Assembly of Galaxies*, *The Birth of Stars and Protoplanetary Systems*, and *Planetary Systems and the Origins of Life* (Gardner et al. 2006). In this regard, JWST can, among other things, observe galaxies from the earliest phases of the Universe to nowadays, study the birth of stars and protoplanetary systems, or shed light onto the origin of life by observing exoplanets or objects within our Solar System.

Regarding the future of *Webb*, the observatory has propellant for significantly more than the initially programmed 5-10-year mission, possibly for 20-26 years. However, there are other factors that can determine its lifetime apart from propellant, such as micrometeoroid impacts or instrument failures. In May 2022, JWST was hit by a micrometeoroid that produced a significant larger damage than expected on the primary mirror. Should a similar impact be repeated ~10 times more, it would mean the end of the observatory lifetime because of the wavefront degradation. Although Cycle 2 will reduce the probability of these impacts (by limiting the pointing into the direction of these micrometeoroids), the statistics of how often these big impacts occur are still uncertain. In addition to this, science instrument and spacecraft components do not last forever and, unlike *Hubble*, *Webb* is not designed to be serviced by any space shuttle. But, although the factors that will ultimately limit the science lifetime of JWST are still known, *Webb* is expected to have a long, productive life.

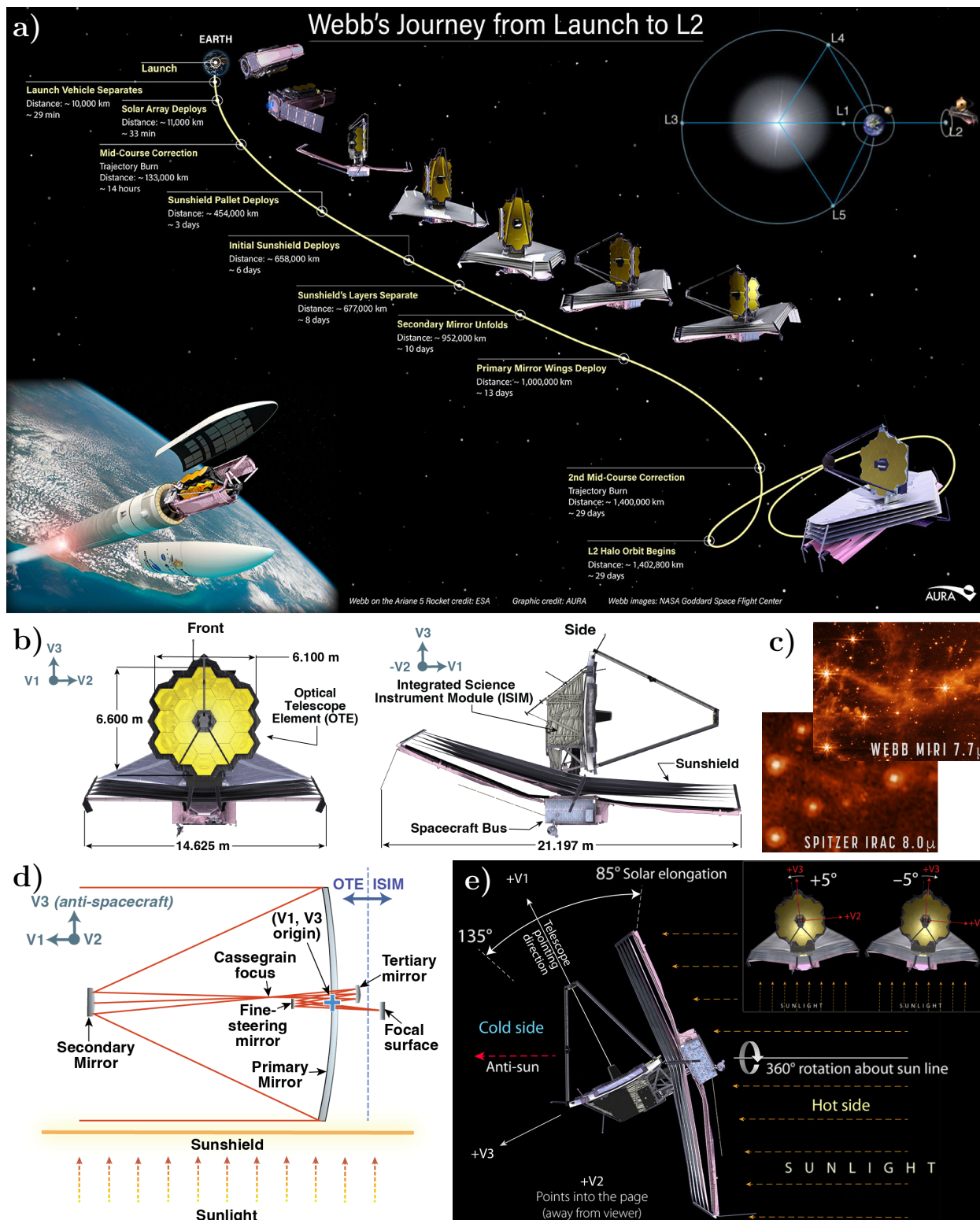


**Figure 3.5:** *Webb* images. a) JWST from launch to L2. The position of Sun-Earth L2 is shown on the top right. b) Front (left) and side (middle) view of JWST. Images show how the Optical Telescope Element (OTE) and the Integrated Science Instrument Module (ISIM) are separated from the spacecraft bus and are shaded from sunlight by the sunshield. c) Comparison between JWST image quality (with MIRI) with respect to that of *Spitzer* IRAC 8.0  $\mu$ m. d) Schematic view of the optical design of JWST, which is a three-mirror anastigmat with a primary mirror, secondary mirror, tertiary mirror, and an additional fine steering mirror. e) Angles in which JWST can rotate for observations. The inset shows the allowed rotation with respect to the axis pointing to the Sun direction. Adapted figure from STScI. Credits: AURA/S. Lifson for a), McElwain et al. (2023) for b) and d), NASA/ESA/CSA/STScI/JPL-Caltech for c), STScI for e).

### 3.2.1 JWST general characteristics

JWST is the largest, infrared-optimized space telescope ever built (Gardner et al. 2006), with a primary mirror of 6.605 m in diameter ( $25.0\text{ m}^2$  in area) and a total weight of  $\sim 6,500$  kg. Regarding its optical design, *Webb* is a three-mirror anastigmat, with a primary, secondary and tertiary mirror that correct spherical aberration, astigmatism, coma, and field curvature (Korsch 1972). In addition to these three mirrors, JWST uses an additional fine steering mirror to actively point light into the science instruments. Fig. 3.5d shows a schematic view of this optical design. As shown in Fig. 3.5b, the primary mirror is composed of 18 independent 1.32 m segments separated by 7 mm gaps and which are capable of folding up to minimize the volume of the telescope during the launch. These mirrors are semi-rigid and are controlled by six actuators each. The size of the secondary, tertiary and fine steering mirrors is  $74\text{ cm}\times 74\text{ cm}$ ,  $73\text{ cm}\times 52\text{ cm}$ , and  $17\text{ cm}\times 17\text{ cm}$ , respectively, and their surface shapes are convex, concave, and flat. All mirrors are made of beryllium, an ultra-light material, coated with a 100 nm layer of gold to increase their IR reflectivity. *Webb* has an effective focal ratio of  $f/20$  and an effective focal length of 131.4 m. At the focal plane, the field is  $\sim 18'\times 9'$ .

*Webb* orbits the Sun-Earth L2, one of the five Sun-Earth Lagrange points in which the gravitational force exerted by the Sun and Earth equals the centripetal force of JWST as it moves with the Earth (Fig. 3.5a, top right). This position enables *Webb* to keep its orbit with reduced propellant costs and, also, to keep communications with the Earth through the Deep Space Network, NASA's international array of giant antennas managed by the Jet Propulsion Laboratory. Like *Hubble*, *Webb* has reaction wheels onboard that are used to rotate the observatory for pointing with an absolute accuracy below  $0.1''$ . During observations, solar photons pressure causes the reaction wheel to accumulate momentum, which is periodically released by firing propellant through the thrusters.

The telescope can be divided into three main parts: the Optical Telescope Element (OTE), the Integrated Science Instrument Module (ISIM), the sunshield, and the spacecraft bus. The spacecraft bus is where all the necessary support functions for JWST operation are, providing electrical power (from the solar array), thermal and attitude control, communications services, and propulsion. The sunshield separates the spacecraft bus, located at the bottom of JWST, from the telescope and science instruments. This sunshield consists of five layers of  $\sim 21\text{ m}\times 14\text{ m}$  in size (around the size of a tennis court), composed of Kapton E (a polymer) with aluminum and doped-silicon coatings. While *Webb* is observing, the sunshield protects the telescope from the heat and light of, mainly, the Sun, but also from that of the Earth (and Moon). This is essential for keeping the optics and instruments cold for infrared measurements (the operating temperature range for the mirrors is  $\sim 35\text{--}55\text{ K}$ ; McElwain et al. 2023) and for limiting undesired background measurements (see Rigby et al. 2022b for a discussion of JWST backgrounds). In this regard, the shade produced by the sunshield on the telescope and science instruments limits the accessible portion of sky observed by *Webb* at each time. Fig. 3.5e shows the orientation of JWST with respect to the Sun and the allowed angles in which the telescope can rotate for pointing. *Webb* can observe  $\sim 40\%$  of the sky at each position, but as it moves around its L2 orbit, the whole sky becomes accessible in approximately 6 months time.

*Webb* is optimized to observe infrared wavelengths, presenting a broader wavelength coverage ( $\sim 600\text{ nm}$  to  $28\text{ }\mu\text{m}$ ) than that of *Hubble* and a higher sensitivity. In fact, the imaging sensitivity of *Webb* (considered as the faintest point source that it can detect in 10,000 s with  $\text{SNR} = 10$ ) is

$\sim 6$  times better than that of *Hubble* at  $1.5\ \mu\text{m}$ , and 68 better at  $3.6\ \mu\text{m}$  than that of *Spitzer*/IRAC<sup>1</sup> (Rigby et al. 2022a). Although the requirement for JWST was to be diffraction limited at  $2\ \mu\text{m}$ , during the commissioning it was found that this requirement was exceeded, being *Webb* diffraction limited at  $1.1\ \mu\text{m}$  (see Rigby et al. 2022a for more about JWST science performance, which is better than expected across the board). This implies that JWST has approximately the same angular resolution at  $2\ \mu\text{m}$  than that of *Hubble* at  $700\ \text{nm}$ . 3.5c shows the image quality improvement of JWST with respect to *Spitzer* IRAC  $8.0\ \mu\text{m}$ .

### 3.2.2 Scientific instruments

All the scientific instruments in *Webb* are located within the ISIM. There are four operating instruments onboard:

- Near-Infrared Camera (NIRCam; Rieke et al. 2003, 2005; Beichman et al. 2012)
- Near-Infrared Spectrograph (NIRSpec; Jakobsen et al. 2022)
- Near-Infrared Slitless Spectrograph/Fine Guidance Sensor (NIRISS/FGS; Doyon et al. 2012)
- Mid-Infrared Instrument (MIRI; Rieke et al. 2015; Wright et al. 2015)

All instruments except MIRI are passively cooled and operate at  $\sim 39\ \text{K}$  ( $-234\ ^\circ\text{C}$ ), which is the ideal temperature for their HgCdTe NIR detectors. MIRI observes in the mid-infrared and has a different type of detectors (arsenic doped silicon, Si:As), which need an operating temperature below  $\sim 7\ \text{K}$  ( $-266\ ^\circ\text{C}$ ) to operate properly. Since passively cooling alone is not able to reach such a temperature, MIRI uses a helium cryocooler system to cool its detectors.

The two primary cameras onboard are NIRCam and MIRI, optimized for near-infrared ( $0.6\text{--}5.0\ \mu\text{m}$ ) and mid-infrared ( $5.6\text{--}25.5\ \mu\text{m}$ ) imaging, respectively. In addition to imaging, these instruments also offer other operating modes like coronagraphy imaging or low/medium-resolution spectroscopy. NIRSpec offers four different spectroscopic modes with  $R \sim 100, \sim 1,000$ , and  $\sim 2,700$  and over the  $0.6\text{--}5.0\ \mu\text{m}$  wavelength range: multi-object spectroscopy (MOS) mode with a microshutter assembly (MSA), imaging spectroscopy with the Integral Field Unit (IFU), a fixed SLIT mode for high contrast spectroscopy of single objects, and a time-series spectroscopy mode for bright sources. NIRISS complements NIRCam and NIRSpec by providing, in the wavelength range from  $0.6$  to  $5.0\ \mu\text{m}$ , slitless spectroscopy for both wide field and single objects ( $R = 150$  and  $700$  at  $1.4\ \mu\text{m}$ , respectively), high-contrast interferometric imaging, and medium- and broad-band imaging. The FGS, which is packed with NIRISS, is a near-infrared camera ( $\sim 0.6$  to  $5.0\ \mu\text{m}$ ) that uses guide stars in the focal plane to provide data for fine pointing, and attitude determination and stabilization. In contrast to the one on HST, it is used exclusively for the latter purposes and it is not available for scientific proposals. Fig. 3.6a shows the locations of the scientific instruments on JWST focal plane and their fields of view, together with some of the operating modes offered for them.

<sup>1</sup>JWST limiting point source sensitivities, measured for  $SNR = 10$  detections in  $10,000\ \text{s}$  using  $r = 0.08''$  apertures, are  $7.9\ \text{nJy}$  ( $29.1\ \text{mag}$ ) for NIRCam/F150W ( $\lambda \sim 1.5\ \mu\text{m}$ ), and  $8.8\ \text{nJy}$  ( $29.0\ \text{mag}$ ) for NIRCam/F356W ( $\lambda \sim 3.6\ \mu\text{m}$ ).

In this thesis, we have made use of broad-band images taken with NIRC*am* imaging mode. In Section 3.2.2.1, we give an overview of this instrument based on the *JWST User Documentation* (JDOX, 2016-; updated in Dec 2022).

### 3.2.2.1 NIRC*am*

NIRC*am* is the primary near-infrared camera for *Webb* and can observe from 0.6 to 5.0  $\mu\text{m}$ . It has two different channels for imaging: the Short Wavelength channel (SW; 0.6-2.3  $\mu\text{m}$ ) and the Long Wavelength channel (LW; 2.4-5.0  $\mu\text{m}$ ). The LW channel has 2 detectors with  $2,040 \times 2,040$  pixels of  $0.063''/\text{pix}$  and with a field of view of  $129'' \times 129''$  each, while the SW has 8 detectors of  $2,040 \text{ pix} \times 2,040 \text{ pix}$  with  $0.031''/\text{pix}$  and whose fields of view,  $64'' \times 64''$  each, almost overlap that of the LW (see in Fig. 3.6b). The two NIRC*am* modules, A and B, are separated by a 42-48'' gap, provide a total field of view is  $2 \times 2.2' \times 2.2'$  ( $9.7 \text{ arcmin}^2$ ) and can be simultaneously observed in the SW and LW channels by using a dichroic. General characteristics of the SW and LW channels are summarized in Table 3.7

NIRC*am* detectors achieve a Nyquist sampling of the PSF or better (PSF FWHM  $> 2$  pix) above 2  $\mu\text{m}$  in the SW channel and 4  $\mu\text{m}$  in the LW channel. For the undersampled PSFs at lower wavelengths, the PSF sampling can be improved by using subpixel dithering techniques. According to the Cycle 1 Absolute Flux calibration program, the FWHM of the PSFs for NIRC*am* filters ranges from  $0.029''$  (or 0.94 pix) to  $0.164''$  (2.6 pix) for the shortest wavelength filter (F070W;  $\lambda = 0.704 \mu\text{m}$ ) and longest wavelength filter (F480M;  $\lambda = 4.834 \mu\text{m}$ ), respectively. Regarding the sensitivity, this is very high for the imaging mode: NIRC*am* can detect point sources of  $m_{\text{AB}} \sim 29$  ( $m_{\text{AB}} \sim 29.75$ ) with SNR = 10(5) in 10,000 s F200W (F277W) images.

NIRC*am* provides imaging in different filters: 13 filters for SW and 16 for LW. These filters are classified into narrow ( $R \sim 100$ ), medium ( $R \sim 10$ ), wide ( $R \sim 4$ ), and extra-wide ( $R \sim 1$ ). Most of these filters are located in the filter wheel, but there is an additional pupil wheel that holds 6 filters and other elements like grisms, coronagraph masks, or a clear position, among others, and which can be combined with filters from the filter wheel. In total, per each NIRC*am* module, there are 48 optical elements distributed into two filter wheels and two pupil wheels (one filter and pupil wheel per NIRC*am* channel). For this thesis, we have made use of six out of the eight NIRC*am* wide filters: F115W, F150W, and F200W in the SW channel, and F277, F356W, and F444W in the LW channel. General information for these filters is shown in Table 3.8 and total (system) throughputs are shown in Fig. 3.6c.

In this section, we have focused on the imaging mode of NIRC*am*, since it is the observing mode used in this thesis. Nevertheless, NIRC*am* provides four additional observing modes: coronagraphy imaging, wide field slitless spectroscopy (WFSS), together with time-series imaging and time-series spectroscopy. Coronagraphy imaging can be performed in different wavelengths (1.8-2.2  $\mu\text{m}$  and 2.8-5.0  $\mu\text{m}$ ) with 5 occulter masks and in a  $20'' \times 20''$  field of view (outside that of the imaging field of view; see Fig. 3.6 a,b). Wide field slitless spectroscopy can be conducted in the LW channel (2.4-5.0  $\mu\text{m}$ ,  $R \sim 1,600$  at 4  $\mu\text{m}$ , and a field of view of  $2 \times 129'' \times 129''$ ) by using two grisms with orthogonal orientations (GRISMC and GRISMR in Fig. 3.6 b). Time-series imaging is the photometric monitoring of time-variable bright sources in the whole NIRC*am* wavelength range and has the same field of view as that of the imaging mode. Grism time-series spectroscopy

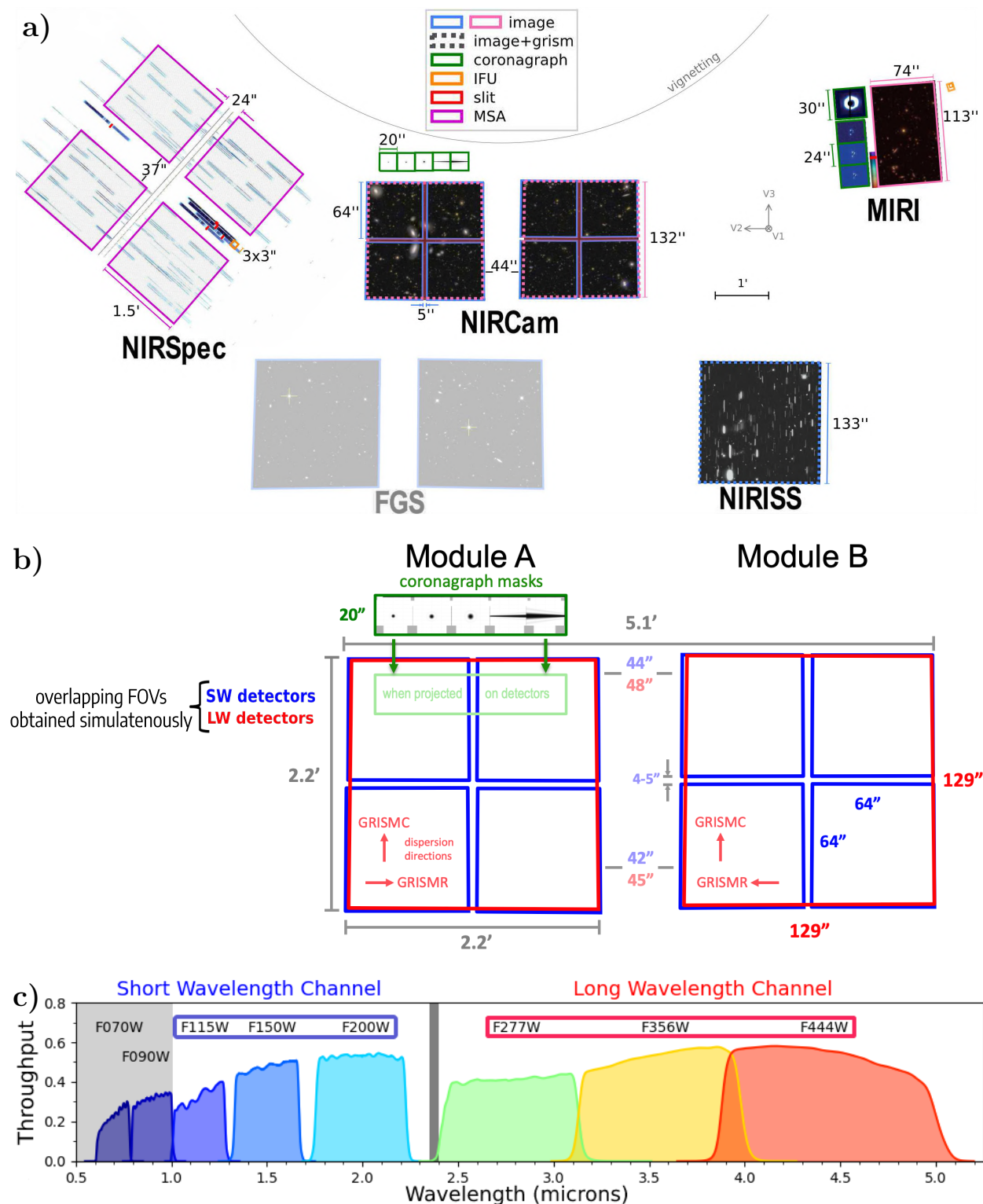


**Figure 3.6:** Scientific instruments and NIRCам images. **a)** JWST focal plane and field of view of the scientific instruments (highlighted) and the FGS. Several observing modes for the instruments are marked in different colors. **b)** NIRCам modules and field of view for both the short wavelength (SW) and long wavelength (LW) channels. Both channels can be simultaneously observed. **c)** Total system throughputs for NIRCам broadband filters. The ones used in this work have been highlighted. The dark gray bar in the middle is approximately the dichroic cutoff between the SW and LW channels. Adapted figure from STScI. Credits: STScI for all images.

**Table 3.7:** General characteristics of NIRCcam channels.

	Short Wavelength (SW) channel	Long Wavelength (LW) channel
Wavelength coverage	0.6–2.3 $\mu\text{m}$	2.4–5.0 $\mu\text{m}$
Number of detectors	8	2
Field of view (per detector)	64'' $\times$ 64''	129'' $\times$ 129''
Field of view (all detectors)	2 $\times$ 2.2' $\times$ 2.2' (with 5'' gaps)	2 $\times$ 2.2' $\times$ 2.2'
Gap between detectors	5'' and 44''	48''
Pixel Scale	0.031''/pix	0.063''/pix
Pixel Size	18 $\mu\text{m}$ $\times$ 18 $\mu\text{m}$	18 $\mu\text{m}$ $\times$ 18 $\mu\text{m}$
Image format (pix <sup>2</sup> )	8 $\times$ 2,040 pix $\times$ 2,040 pix	2 $\times$ 2,040 pix $\times$ 2,040 pix
PSF FWHM	2 pix at 2.0 $\mu\text{m}$	2 pix at 4.0 $\mu\text{m}$

Reference: *JWST User Documentation* (JDOX, 2016-; updated in Dec 2022).

**Table 3.8:** Broadband NIRCcam filters used in this thesis.

Filter name	Central wavelength <sup>a</sup> ( $\mu\text{m}$ )	FWHM <sup>b</sup> ( $\mu\text{m}$ )	Channel
F115W	1.154	0.264	SW
F150W	1.501	0.335	SW
F200W	1.989	0.469	SW
F277W	2.762	0.706	LW
F356W	3.568	0.724	LW
F444W	4.404	1.114	LW

**Notes:**

<sup>a</sup> The provided central wavelengths, unless otherwise stated, correspond to the pivot wavelength:  $\lambda_{\text{pivot}} \equiv \frac{\int T(\lambda) d\lambda}{\int T(\lambda) d\lambda/\lambda^2}$ , where  $T(\lambda)$  is the filter transmission.

<sup>b</sup> The width of the filter is calculated as the difference between the two wavelengths at which the transmission of the filter is half maximum.

References: *JWST User Documentation* (JDOX, 2016-; updated in Dec 2022) and the Spanish Virtual Observatory (SVO; <https://svo.cab.inta-csic.es/>)



is the spectroscopic monitoring of time-varying, isolated, bright sources over 2.4–5.0  $\mu\text{m}$  and with  $R \sim 1,600$  at 4  $\mu\text{m}$ . In addition, NIRCam also performs wavefront measurements which are essential to periodically align the segments of the primary mirror.

### 3.2.3 Introduction to JWST cosmological surveys

The combination of *Webb*'s large aperture, diffraction-limited images, and unprecedented IR sensitivity over a wide wavelength range makes JWST a perfect observatory for deep galaxy surveys. As discussed in Section 1.3, one of the most promising features of *Webb* is that, thanks to its exceptional capabilities, can expand the  $z \sim 10 - 11$  limit of detectable galaxies with *Hubble* (e.g. Castellano et al. 2022). This redshift limit is imposed by the red cutoff at 1.7  $\mu\text{m}$  in HST, which limits the detection of the characteristic Lyman-break signature in the galaxy SEDs of LBGs to redshifts below that limit (see Section 1.3.1). In contrast, the wide IR coverage by JWST enables it to reach higher redshifts (possibly, up to  $z \sim 15$ ).

Nevertheless, *Webb* will not only be useful for the detection of high-redshift galaxies, but it will also study intermediate-redshift galaxy populations (e.g.,  $1 < z < 4$ ) with better spatial resolution (subarcsec resolution in all bands) and IR sensitivity than ever. This will be particularly helpful to better constrain the properties of the stellar populations in galaxies, together with their photometric redshifts, which is of particular interest for this thesis. Fig. 3.7, adapted from Carnall et al. (2023), shows the improvement JWST has provided in the derivation of galaxy properties from SED-fitting techniques. This figure shows, with blue dots, previous available CANDELS photometry measurements for a galaxy from the CANDELS EGS catalog (Stefanon et al. 2017), and the best-fitting SED model in green. The posterior distributions of the galaxy redshifts and stellar masses are shown in green in the insets. According its redshift distribution, this galaxy could be located in almost anywhere at cosmic history between  $0.5 \lesssim z \lesssim 4.5$ , and this is mainly due to the enormous uncertainties in the available photometric points. Since the wavelength limit of HST in  $\sim 1.7 \mu\text{m}$ , this galaxy would only be detected in HST in very few bands, since most bands would be below the Lyman break. Beyond this limit, we rely on a combination of ground-based data in the K-band and *Spitzer*/IRAC data at longer wavelengths (5 right-most blue dots). However, there are not photometric data at  $\lambda \approx 2.0 - 3.0 \mu\text{m}$  between  $K_s$  and IRAC 3.6  $\mu\text{m}$ , which means that the Balmer break/D4000 spectral feature cannot be constrained, which also contributes to the stellar mass and redshift uncertainties. The new NIRCam available data from JWST is shown in orange, with significantly smaller photometric uncertainties. This, together with the wide wavelength coverage provided by NIRCam, enables a better SED fit that constrains the redshift and stellar mass distributions considerably better.

There are 13 JWST Director's Discretionary-Early Release Science (DD-ERS) program that were conducted in the 5 following months after the JWST commissioning. These ERS have no exclusive data access period and their data are immediately public. In this thesis, we make use of data from the Cosmic Evolution Early Release Science Survey (CEERS; PI: S. Finkelstein; Finkelstein et al., in prep.), an ERS program in the category of "Galaxies and Intergalactic Medium". Other ERS programs in the same category that probe intermediate to high-redshift galaxies are GLASS (JWST-ERS-1324; PI: T. Treu) and TEMPLATES (Targeting Extremely Magnified Panchromatic Lensed Arcs and Their Extended Star Formation; JWST-ERS-1335; PI: J. Rigby).

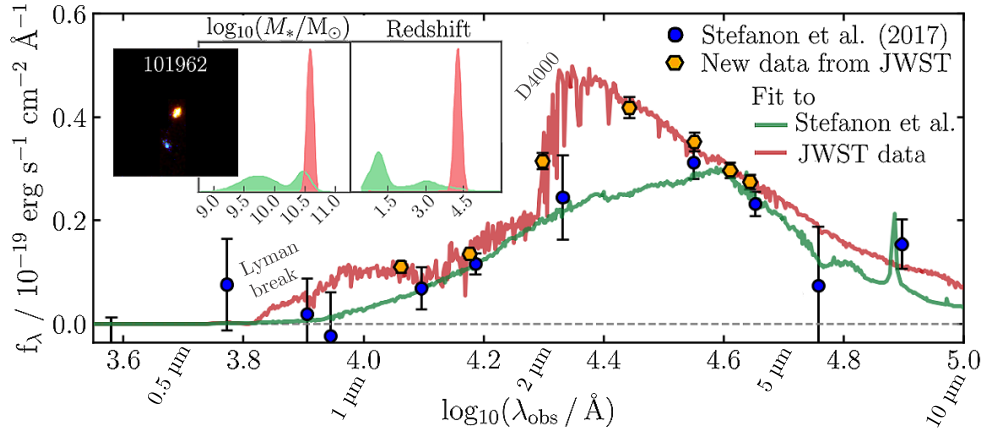


**Figure 3.7:** Comparison of the SED fit of a  $z > 4$  galaxy in the pre-JWST era (blue dots and green model) and using new JWST CEERS data (orange dots and red model). The object belongs to the CANDELS EGS photometric catalog (Stefanon et al. 2017). The blue dots correspond to CANDELS HST photometry, together with  $K_s$  band and the four *Spitzer*/IRAC bands from the photometric catalog. The orange dots correspond to new NIRCcam photometric data. The SED-fitting-derived probability distributions for stellar mass and redshift are shown as an inset (green for the CANDELS fit and red for the JWST fit). The JWST SED fit significantly better constrains the redshift and stellar mass distributions. An RGB postage stamp of the galaxy is also shown ( $5'' \times 5''$ ), created with NIRCcam F444W, F200W, and F150W images. *Credits:* Adapted figure from Carnall et al. (2023).

### 3.2.3.1 The CEERS Survey

The Cosmic Evolution Early Release Science Survey (CEERS; PI: S. Finkelstein; Finkelstein et al., in prep.) is one of 13 JWST ERS programs that covers  $100 \text{ arcmin}^2$  using imaging and spectroscopy. The primary goal of CEERS is to find galaxies at the earliest cosmic times ( $z \gtrsim 9 - 10$ ), demonstrating at the same time the efficiency of using survey parallel observations with JWST for the exploration of the high-redshift Universe. These observations include NIRCcam and MIRI imaging,  $R \sim 100$  and  $R \sim 1,000$  with NIRSpc, and  $R \sim 1,500$  slitless grism spectroscopy with NIRCcam. The main motivation for this key science goal is the poor agreement in the history of the SFRD at  $z \gtrsim 8$ , which is due to the scarce number of galaxies observed at these high redshifts in the pre-JWST era. CEERS will provide a more complete census of high-redshift galaxies, observing  $\sim 5 - 50$  galaxies at  $z > 10$  (based on predictions of previous simulations). Depending on the abundance of high-redshift galaxies observed by this survey, CEERS will be able to distinguish between different cosmological models that predict different star formation efficiencies at early epochs.

The CEERS science addresses two main JWST scientific themes: *First Light and Reionization* and *The Assembly of Galaxies*. According to the CEERS program proposal (Finkelstein et al. 2017), this will be done by: ii) discovering and constraining the abundance and physical nature of  $z > 9$  galaxies, as well as robustly estimating the stellar mass of galaxies at  $z > 4$ ; ii) by providing spectra for  $\sim 1,000$  galaxies at  $z \sim 1 - 9$ , which will enable to constrain their redshifts and physical conditions; iii) by quantitatively studying morphological features of  $z > 3$  galaxies, and iv) by measuring mid-IR emission in galaxies to look into dust-obscured star formation and SMBH growth at  $z \sim 1 - 3$ . All this will allow us to improve our knowledge about the galaxy assembly and black hole growth at  $z \sim 1 - 10$ , shedding light onto the interrelated processes that affect the evolution of galaxies (see Finkelstein et al., in prep., for a full description of CEERS science goals).

a)

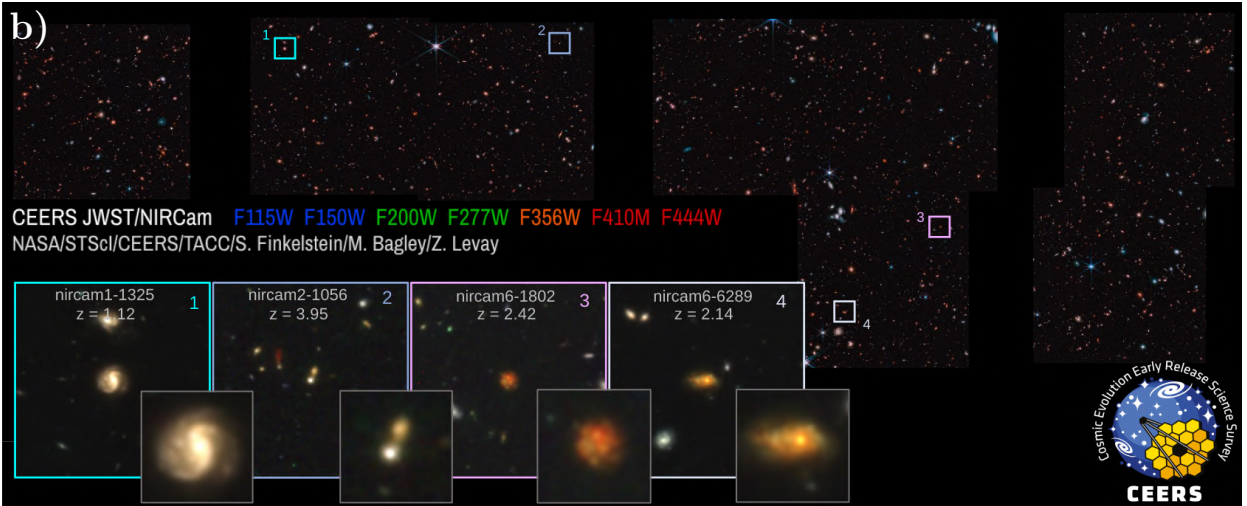
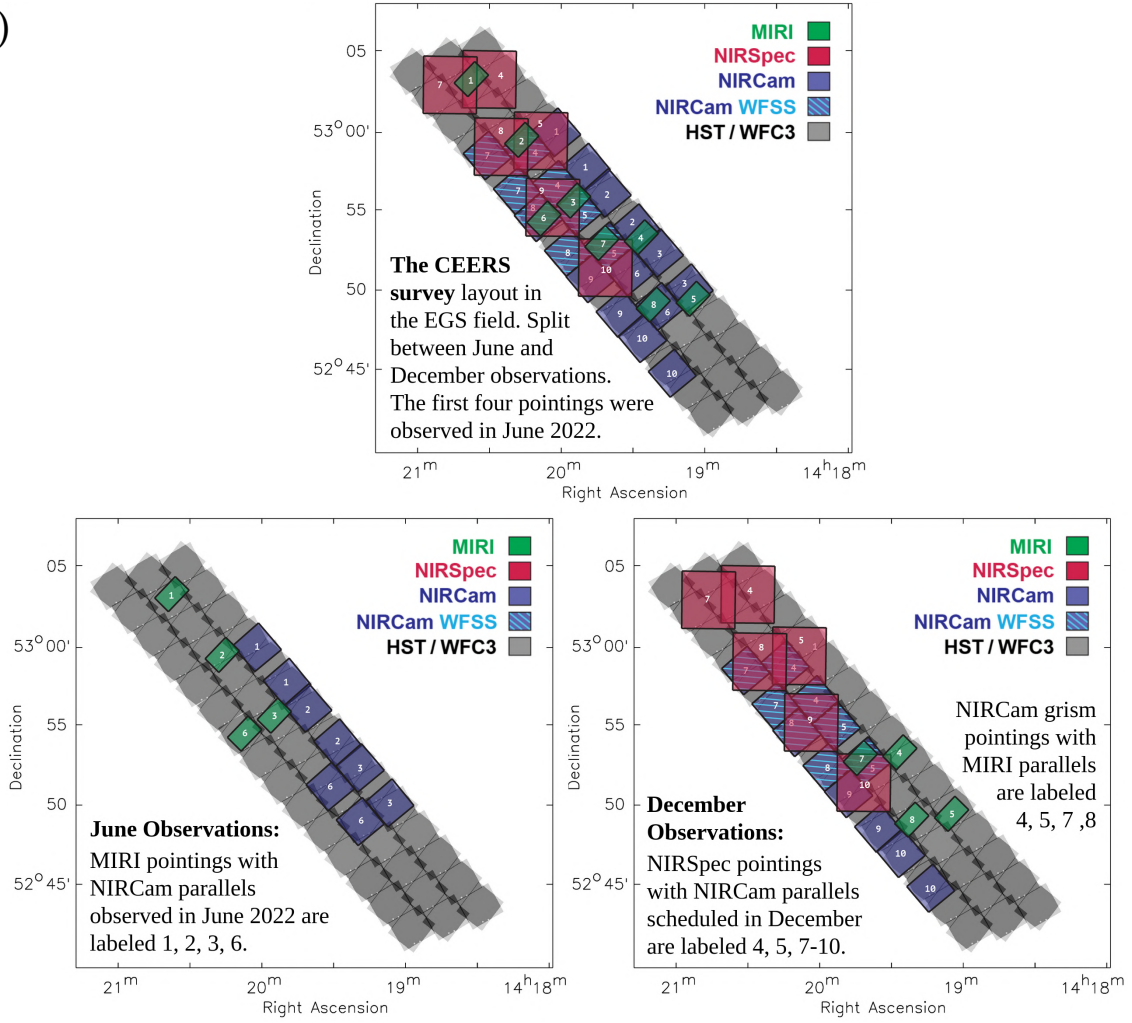


**Figure 3.8:** CEERS images. **a)** Layout of CEERS observations: whole program (top middle), June observations (bottom left), and December observations (bottom right). **b)** CEERS NIRCam Epoch 1 color mosaic. We have highlighted and zoomed-in four  $1 < z < 4$  galaxies with  $M_{\star} > 10^{10} M_{\odot}$ . Credits: D. Kocevski for a), and NASA/STScI/CEERS/TACC/S. Finkelstein/M. Bagley/R. Larson/Z. Levay for the mosaic in b).

The CEERS field covers the majority of the CANDELS/EGS field probed with HST/WFC3, for which multiple multi-wavelength data are available, including imaging and spectroscopy observations from ground-based and space telescopes (see Fig. 3.4d). CEERS observations will cover the  $\sim 1 - 20 \mu\text{m}$  wavelength range and will finally consist of 10 NIRCam pointings for imaging in the SW and LW channels, with 4 of these pointings observed in parallel with NIRSpectroscopic observations, and 6, with MIRI imaging. In addition, 4 of the 10 pointings include NIRCam wide-field slitless spectroscopy. Originally, CEERS observations were originally planned to be conducted in one observing period, either in the June or December observability window of the EGS field. Nevertheless, it was finally decided to split the observations into two epochs due to time limitations in June after the JWST commissioning. Thus, CEERS observations can be divided into: CEERS Epoch 1, taken the 21<sup>st</sup> June 2022, and CEERS Epoch 2, in Dec 2022. Fig. 3.8a shows CEERS observations layout for the complete survey (top), and separated for June (bottom left) and December (bottom right) observations. On the background of this figure, CANDELS HST/WFC3 observations are shown in gray.

The results from this thesis are based on CEERS Epoch 1 data. These consist of 4 out of the 10 NIRCam pointings, labeled as 1, 2, 3, and 6 pointings, together with 4 parallel MIRI observations (see Fig. 3.8a, bottom left). In particular, for this thesis, we make use of CEERS Epoch 1 NIRCam observations, as described in Chapter 6, which will be combined with CANDELS HST observations in the same field. CEERS Epoch 1 NIRCam observations cover an area of  $35.5 \text{ arcmin}^2$ . Fig. 3.8b shows an RGB image of the NIRCam mosaic for Epoch 1, formed from NIRCam1, NIRCam2, NIRCam3, and NIRCam6 pointings, together with a zoom-in of four  $M_\star > 10^{10} M_\odot$  galaxies at  $1 < z < 4$ . CEERS Epoch 2 was observed in December 2022 and is composed of the remaining CEERS observations: 6 NIRCam imaging pointings with parallel NIRSpectroscopic MSA observations ( $R \sim 1,000$ ), plus 4 NIRCam WFSS pointings ( $R \sim 100$ ) in parallel with MIRI imaging.

NIRCam Epoch 1 observations were conducted by simultaneous imaging of the following NIRCam SW and LW filters: F115W+F277W, F115W+F356W, F150W+F410M, and F200W+F444W. Table 3.9 shows a summary of NIRCam Epoch 1 images presented in Finkelstein et al. (2023), together with the available HST broadband images in these mosaics. The reduction and calibration of Epoch 1 NIRCam images is described in Bagley et al. (2022). Regarding Epoch 1 MIRI observations, these were obtained in parallel to NIRCam images in the following filters: F560W, F770W, F1000W, F1280W, F1500W, F1800W and F2100W (see Yang et al. 2023 for more information about these images and their reduction).

As regards this thesis, CEERS moderate depth (see Table 3.9) and relatively large area form a perfect combination to study massive galaxies at  $1 < z < 4$ , in which we are interested in this thesis. In addition to this, as part of the CEERS collaboration, we have a privileged access to CEERS data months before they are publicly released, which will facilitate our work. CEERS reduced observations (images and spectra) and other derived data products will be publicly released and available to the scientific community on its website [ceers.github.io/releases.html](https://ceers.github.io/releases.html) and, in the upcoming future, via MAST:10.17909/z7p0-8481. Among the derived data products, we can mention a robust sample of  $z > 9$  candidates and preliminary photometric catalogs for NIRCam+HST data, MIRI data, and spectroscopic catalogs.

**Table 3.9:** CEERS NIRCам Epoch 1 imaging data and HST broadband filters.

Telescope	Instrument	Filter	PSF FWHM (arcsec)	Limiting Magnitude ( $5\sigma$ )
JWST	NIRCам SW	F115W	0.066	29.2
		F150W	0.070	29.0
		F200W	0.077	29.2
	NIRCам LW	F277W	0.123	29.2
		F356W	0.142	29.2
		F410M	0.155	28.4
		F444W	0.161	28.6
HST	ACS	F606W	0.118	28.6
		F814W	0.124	28.3
	WFC3	F105W	0.235	27.1
		F125W	0.244	27.3
		F140W	0.247	26.7
		F160W	0.254	27.4

**Notes:** Values have been extracted from Finkelstein et al. (2023) and are averaged over the four Epoch 1 NIRCам fields. Limiting magnitudes are measured in  $r = 0.1''$  apertures, and corrected to total magnitudes based on the PSF flux enclosed in that aperture.

### 3.3 Final considerations

Fortunately for the scientific community (and for this thesis), not only JWST did not explode when it was launched, but it is currently running with technical imaging capabilities which are better than expected. These exceptional imaging capabilities allow JWST to extend the high-spatial resolution of HST in the optical to the NIR, reaching a resolution of  $\sim 0.16''$  at  $4.4\ \mu\text{m}$  with JWST. In addition, the CEERS survey, which overlaps the majority of the CANDELS/EGS field probed with HST, meets the scientific requirements, in terms of depth and area, to allow us to study a representative sample of massive galaxies at  $1 < z < 4$ . And these data are already available for us. The aim of the following chapter will be to present the tools to be applied on these massive galaxies in order to derive the properties of their stellar populations and, namely, their SFHs from our 2D analysis.



# Recovering Star Formation Histories: Stellar Population Synthesis in 2D

---

Stellar population synthesis (SPS) is a fundamental tool in the study of unresolved stellar populations. Since its early beginnings (e.g., Tinsley 1968; Spinrad & Taylor 1971; Faber 1972; Searle et al. 1973; Tinsley & Gunn 1976; Bruzual 1983), SPS methods have improved as we have increased our understanding of stellar physics and evolution, hand in hand with computational advances (e.g., Charlot & Bruzual 1991; Bruzual & Charlot 1993; Worthey et al. 1994; Fioc & Rocca-Volmerange 1997; Leitherer et al. 1999; Bruzual & Charlot 1993). Due to the difficulty in probing the UV and IR spectral ranges, the first synthesis models were based on optical-to-NIR SEDs, but in recent decades, significant progresses have been made in adding information from the far-ultraviolet (FUV) to the far-infrared (FIR) SEDs (see Conroy 2013 and references therein).

In this chapter, we first give a brief overview of the most extended SPS modeling technique, highlighting the main fundamental parameters that affect the SPS modeling in Section 4.1 (see Walcher et al. 2011 and Conroy 2013 and for a comprehensive review of SPS modeling). In Section 4.2, we discuss the details and assumptions made in the SPS modeling used for this work. The SPS code used in this work is presented in Section 4.3. Finally, in Section 4.4, we outline the SPS method developed and applied for each galaxy in this thesis, which makes use of the information provided by its spatially-resolved SEDs.

## 4.1 Stellar population synthesis modeling: an overview

The aim of stellar populations synthesis is to determine the characteristics of the unresolved stellar population in a galaxy from its spectrum or, in our case, from its SED. More specifically, the final goal of SPS is to recover the fundamental properties of the stellar population which is responsible for that SED, such as the galaxy Star Formation History (SFH), total stellar mass, metallicity, dust attenuation, or initial mass function (IMF), all of which leave an imprint on the SED. The most extended SPS technique is the “isochrone synthesis” (Chiosi et al. 1988; Charlot & Bruzual 1991) and, as its name indicates, it makes use of isochrones to determine the spectral evolution of stellar populations. This method, schematically shown in Fig. 4.1 from Conroy (2013), assumes that the evolution of the stellar population in a galaxy can be described by a series of Simple/Single Stellar Populations (SSPs), which consist of families of stars that are simultaneously and instantaneously born with the same metallicity,  $Z$ .

To model the evolution of the spectrum emitted by an SSP, three different ingredients are required: isochrone tables to model stellar evolution, an IMF, and a library of stellar spectra (see Section 4.1.1). Isochrones define the position in the Hertzsprung-Russell (HR) diagram of stars with a same age and metallicity. The IMF indicates how the different evolutionary stages in the isochrone are populated by stars with different initial masses. Stellar spectra libraries include (theoretical or empirical) spectra for stars of all the spectral types and for a wide range of metallicities. The spectrum emitted by each SSP is calculated by summing the spectrum of all the individual stars on each isochrone and is given by (Conroy 2013)

$$S_{\text{SSP},\lambda}(t, Z) = \int_{m_{\text{low}}}^{m_{\text{up}}} f_{\text{star},\lambda}(m, t, Z) \phi(m) dm \quad (4.1)$$

where  $S_{\text{SSP},\lambda}$  is the emitted spectrum by the time- and metallicity-dependent SSP per unit wavelength and time interval (normalized to an initial mass of  $1 M_{\odot}$ ),  $f_{\text{star},\lambda}$  is a stellar spectrum,  $\phi(m)$  is the IMF, and  $m$  is the zero-age main sequence (or initial) stellar mass.

To reproduce the spectrum of the stellar population in a galaxy we need to use what is known as a Composite Stellar Population (CSP), for which SSPs are the building blocks. To build the CSP, the SSPs spectra are combined with a parametrized evolution of the star formation rate (i.e., the star formation history, SFH),  $SFR(t)$ , and a chemical enrichment model described by  $Z(t)$ . The shape of the SFH is not known *a priori* and a parametrized functional form is usually adopted. For instance, the middle-left panels of Fig.4.1 show time-delayed exponentially declining SFHs, i.e.,  $SFR(t) \propto t \cdot e^{-t/\tau}$  for different star formation time-scales,  $\tau$ , together with the corresponding chemical enrichment.

The effects of dust on the spectrum must also be taken into account. On the one hand, dust attenuates the spectrum in the UV-to-NIR. This is usually modeled by applying a dust attenuation curve, whose shape is kept fixed, but its normalization is fitted. On the other hand, dust emits in the IR. This emission consists of the continuum (dominates at  $\lambda > 50 \mu\text{m}$  and it is produced by dust at low temperatures,  $T \sim 15 - 20 \text{ K}$ , or/and very large grains) together with several emission features (clearly visible at  $\lambda < 12 \mu\text{m}$  and mainly attributed to polycyclic aromatic hydrocarbons, PAHs). Fig.4.1 (bottom) shows the final spectrum recovered from the SPS modeling before (blue) and after (red) applying the dust model.

Thus, taking into account all the above ingredients, the spectrum emitted at a time  $t$  by a stellar population in a galaxy is given by (Conroy 2013)

$$S_{\text{CSP},\lambda}(t) = \int_0^t \left( SFR(t-t') S_{\text{SSP},\lambda}(t-t', Z) e^{-\tau_{d,\lambda}(t-t')} + k f_{\text{dust},\lambda}(t-t', Z) \right) dt' \quad (4.2)$$

where the integration variable  $t'$  is the stellar population age of each SSP, and the dust modeling is incorporated by the dust optical depth,  $\tau_{d,\lambda}(t')$ <sup>1</sup>, for dust attenuation, and by the function  $f_{\text{dust},\lambda}$  for dust emission, being  $k$  a normalization constant to balance the bolometric luminosity absorbed and reradiated by dust.

<sup>1</sup> $\tau_d$  is directly related to the attenuation  $A_{\lambda}$ :  $\tau_d = \frac{\ln 10}{2.5} A_{\lambda} = 0.921 A_{\lambda}$



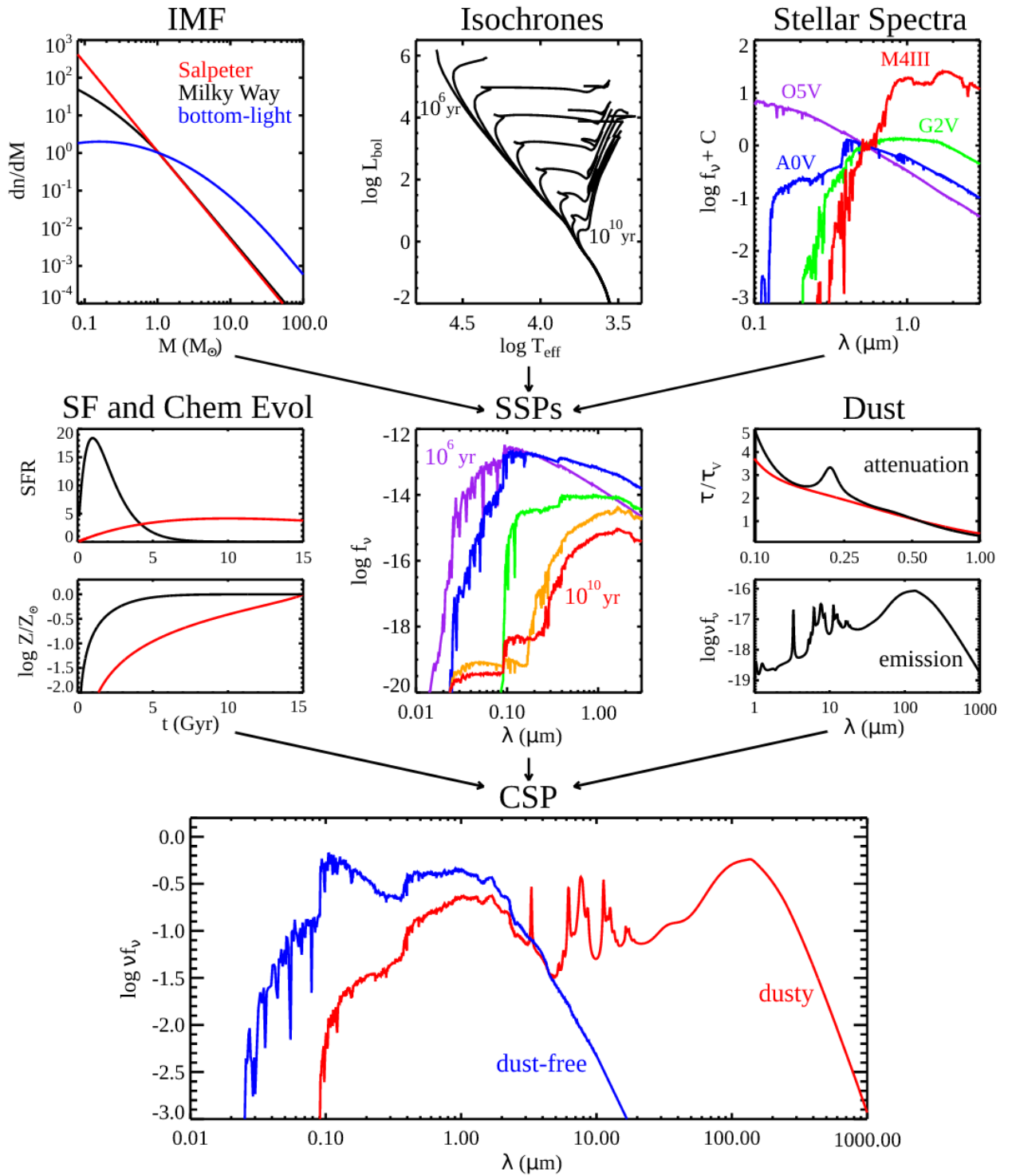


**Figure 4.1:** Schematic diagram of the SPS modeling with the isochrones technique, extracted from Conroy (2013). SSPs are built from an IMF, isochrone tables, and stellar spectra libraries. These SSPs are combined with a parametrized SFH and chemical enrichment and dust models to produce the CSP spectrum (see details in the main text). The middle-left panels show an example of SFH parametrized by a time-delayed exponential, i.e.,  $\text{SFR}(t) \propto t \cdot e^{-t/\tau}$ , for two different star formation time-scales:  $\tau = 1$  Gyr (black) and  $\tau = 10$  Gyr (red), and the corresponding assumption on the evolution of the metallicity (below). The dust attenuation panel (middle right) shows the attenuation law from Calzetti et al. (2000; red line) and the MW extinction curve (Cardelli et al. 1989; O’Donnell 1994; in black). In the bottom panel, the resulting SPS spectrum is shown before (blue) and after (red) applying the dust model. Nebular emission is not included in these models.

Finally, although not included in equation 4.2, the emission of the ionized gas, known as nebular emission, should also be considered when modeling SEDs, since it can account for  $\sim 20-60\%$  of the UV-optical broadband fluxes in some extreme cases (Anders & Fritze-v. Alvensleben 2003). Nebular emission is composed of two components: continuum emission and nebular emission lines. The continuum consists of free-free, free-bound, and two-photon emission, while nebular emission lines are mainly generated in recombination processes and forbidden and fine structure line transitions. Only a handful of the widely used SPS codes include prescriptions for nebular emission (e.g., neither Bruzual & Charlot 2003 nor Maraston 2005 include it), although they can be coupled with existing photoionization codes, such as CLOUDY (Ferland et al. 2013) or MAPPINGS-III (Groves et al. 2004) that treat the stellar and nebular energy distributions in a detailed fashion.

For the fit to photometric SEDs (the case of this thesis), the CSP spectrum is transformed into broadband colors by convolving the spectrum with the filter transmission curves for each band. These synthetic SEDs, whose shapes depend on the stellar population parameters, are compared with the observed SED using, e.g., a  $\chi^2$  technique that explores the parameter space in order to recover the best-fitting stellar parameters. One of these parameters is the stellar mass-to-luminosity ratio,  $M/L$ , which can be converted into stellar mass by multiplying this value by the observed luminosity,  $L$ .

In recent years, an alternative SPS approach that fits non-parametric SFHs has gained popularity when modeling SEDs (e.g., the *Prospector* SED fitting code; Leja et al. 2017; Johnson et al. 2021). The basis of this technique, which is computationally more expensive than traditional ones, will not be discussed here.

#### 4.1.1 Basic ingredients of SPS

As shown in equations 4.2 and 4.1, the main parameters that affect the different types of SPS models found in the literature are the following:

- *IMF*. The IMF,  $\phi(m) \equiv dN/dm$ , indicates the birth mass distribution of stars, defined such that  $\phi(m) dm$  is the number of stars born with a mass between  $m$  and  $m + dm$ , and usually normalized so that  $\int_{m_{\text{low}}}^{m_{\text{up}}} \phi(m) dm = 1 M_{\odot}$ . Since the stellar evolution is very dependent on its initial mass, the IMF crucially affects the evolutionary history and observable properties of stellar populations (e.g., the CSP spectrum or the normalization of the stellar mass-to-light ratio,  $M/L$ ). The IMF is usually assumed universal (also independent of time), although this could not be true (see, e.g., Bastian et al. 2010 or Smith 2020 reviews). Commonly adopted IMFs are the classical Salpeter (1955), with  $\phi(m) \propto m^{-2.35}$ , or those from later works from Kroupa (2001) and Chabrier (2003), both with a shallower slope at low stellar masses.
- *Isochrones*. Based on theoretical stellar evolution models, isochrones indicate the location in the HR diagram of stars that have the same age and metallicity, i.e., for a given metallicity and age, they establish the relation between  $T_{\text{eff}}$ ,  $\log g$ , and  $m$ . Among the most widely used isochrone models, we can mention Padova (Bressan et al. 1993; Bertelli et al. 1994; Girardi et al. 2000; Marigo et al. 2008), Geneva (Maeder & Meynet 1987; Schaller et al. 1992; Meynet & Maeder 2000), or BaSTI models (Pietrinferni et al. 2004; Cordier et al. 2007).

- *Stellar spectra libraries.* Once the IMF has predicted the number of stars in each position of the HR diagram, stellar spectral libraries are required to assign an SED to each star in the isochrone (depending on its metallicity). The stellar spectral libraries can be either empirical (i.e., based on observations of stars), such as the Medium resolution Isaac Newton Telescope Library of Empirical Spectra (MILES; Sánchez-Blázquez et al. 2006), or theoretical (synthetic spectra calculated using models for stellar evolution and stellar atmospheres), like that from Coelho et al. (2005).
- *SFH.* Although the SFH of a galaxy can have any arbitrary shape, simple functional forms are usually adopted to describe the SFH (e.g. instantaneous burst, constant  $SFR$ , or other more complicated forms). The most classical adopted form is a declining exponential (or  $\tau$  model) i.e.,  $SFR(t) \propto e^{-t/\tau}$  (e.g., Gavazzi et al. 2002; Savaglio et al. 2005; Whitaker et al. 2012; Pacifici et al. 2013). Rising SFHs are also popular since they seem to provide a better SED fit for  $z \gtrsim 3$  galaxies (e.g., Lee et al. 2010; Pforr et al. 2012). Commonly used functional forms for these rising SFHs can be an *inverted  $\tau$  model*, i.e.,  $SFR(t) \propto e^{+t/\tau}$  (e.g. Maraston et al. 2010; Reddy et al. 2012) or a time-delayed exponential (or *delayed  $\tau$  models*), i.e.,  $SFR(t) = t e^{-t/\tau}$  (e.g. Sandage 1986; Gavazzi et al. 2002; Wuyts et al. 2011; Alcalde Pampiega et al. 2019).
- *Dust.* As commented above, dust attenuates the spectrum in the UV-to-NIR and emits in the IR. Dust attenuation is usually modeled with typical attenuation laws (e.g. Calzetti et al. 2000), extinction curves (e.g., MW extinction curve; Cardelli et al. 1989; O’Donnell 1994) or other attenuation prescriptions like the age-dependent Charlot & Fall (2000) attenuation model. Regarding dust emission, there are sophisticated models that predict the IR emission of dust, including PAH emission features, by taking into account grain size distributions and grain optical properties (e.g., Draine & Li 2007), although simpler models based on templates with fewer parameters are often used (e.g., those from Chary & Elbaz 2001 and da Cunha et al. 2008). In practice, dust emission is usually neglected when only modeling rest-frame UV-to-optical SEDs.

In Section 4.2, we describe the details regarding the above parameters in our SPS modeling.

## 4.2 Details of the SPS model used in this work

In this thesis, we make use of both the STARBURST99 (SB99; Leitherer et al. 1999; Vázquez & Leitherer 2005; Leitherer et al. 2010) and Bruzual & Charlot (2003) (hereafter, BC03) models. As shown in Chapter 5, we use SB99 for the SPS modeling of the stellar populations in Illustris synthetic images. The reason for this was that, although the stellar evolution in Illustris is modeled with Bruzual & Charlot (2003), the synthetic images used for this thesis were generated by applying SB99 models to the Illustris simulated particles in each galaxy (see Section 2.3). Besides, we use BC03 models in the second part of this thesis, when modeling the stellar populations in real CANDELS+CEERS observations, since BC03 models are considerably more widely used than SB99 in the extragalactic community, especially when dealing with stellar ages beyond  $\sim 1$  Gyr.

In the following subsections, we describe our SPS details regarding the basic SPS ingredients described in Section 4.1.1. We point out that the descriptions below of characteristics of our SPS

modeling apply to all the photometric SEDs fitted in this work, either for integrated SEDs (i.e., from the integrated flux of the galaxy) or spatially-resolved SEDs (i.e., those from a pixel-by-pixel or a set of pixels analysis). In Section 4.4, we outline how the galaxy SFH is recovered from our SPS modeling in two dimensions (2D SPS), which will be described in detail in Chapter 5.

#### 4.2.1 IMF

BC03 models are available only for a Salpeter (1955) and a Chabrier (2003) IMF. We adopt the Chabrier (2003) IMF in BC03, parametrized as a lognormal distribution given by (Bruzual & Charlot 2003)

$$\phi(m) \propto \begin{cases} m^{-1} \cdot e^{-\frac{(\log m - \log m_c)^2}{2\sigma^2}}, & \text{for } m \leq 1 M_\odot \\ m^{-2.3}, & \text{for } m > 1 M_\odot \end{cases} \quad (4.3)$$

where  $m_c = 0.08 M_\odot$  and  $\sigma = 0.69$ .

SB99 models allow to select a customized IMF by specifying one or more IMF exponents (and the associated mass boundaries) for a power-law IMF. We select a Kroupa (2001) IMF, which is a broken power law given by

$$\phi(m) \propto m^{-\alpha} \quad (4.4)$$

with

$$\phi(m) \propto \begin{cases} \alpha = 1.3, & \text{for } m \leq 0.5 M_\odot \\ \alpha = 2.3, & \text{for } m > 0.5 M_\odot \end{cases} \quad (4.5)$$

In both cases, we use  $m_{\text{low}} = 0.1 M_\odot$  and  $m_{\text{up}} = 100 M_\odot$  as the lower and upper mass cut-offs<sup>2</sup>, respectively, where both IMFs are practically indistinguishable and the spectral properties obtained with any of them are very similar (Bruzual & Charlot 2003). Fig. 4.2 shows the comparison of both IMFs, together with the canonical Salpeter IMF:  $\phi(m) \propto m^{-2.35}$ , all normalized so that the integral under each curve between  $0.1 M_\odot$  and  $100 M_\odot$  is  $1 M_\odot$ . The major differences between Chabrier (2003) and Kroupa (2001) IMFs are below  $0.1 M_\odot$ , outside of our considered mass range.

#### 4.2.2 Isochrones

In BC03, we use the Padova 1994 library of stellar evolutionary tracks, computed by Alongi et al. (1993), Bressan et al. (1993), Fagotto et al. (1994a,b), and Girardi et al. (1996). This library includes  $Z = 0.0001, 0.0004, 0.004, 0.008, 0.02, 0.05,$  and  $0.1$  metallicities and models all phases of

<sup>2</sup>Actually, the original Kroupa (2001) IMF has two different values of  $\alpha$  for  $m \leq 0.5 M_\odot$ : 1)  $\alpha = 1.3$  for  $0.08 < m \leq 0.5 M_\odot$  and 2)  $\alpha = 1.3$  for  $0.01 < m \leq 0.08 M_\odot$ . In practice, we only consider the former since our lower mass limit ( $m_{\text{low}} = 0.1 M_\odot$ ) is above the mass value where the  $\alpha$  changes in this mass range ( $0.08 M_\odot$ ).

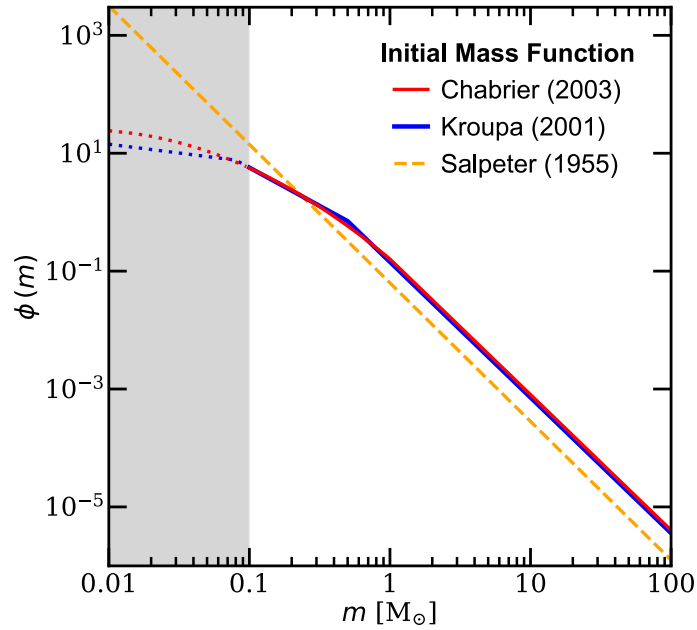


**Figure 4.2:** IMF comparison: Chabrier (2003) (red), Kroupa (2001) (blue), and the canonical Salpeter (1955) (orange dashed) IMF. All IMFs have been normalized to recover  $1 M_{\odot}$  when they are integrated from  $0.1 M_{\odot}$  to  $100 M_{\odot}$  (white area). The dotted red and blue lines (in the gray shaded area) show the values of the Chabrier (2003) and Kroupa (2001) IMFs, respectively, outside the range of initial stellar masses considered in this work.

stellar evolution from the zero-age main sequence to the beginning of the thermally pulsing asymptotic giant branch (TP-AGB) phase for low- and intermediate stellar masses or the core-carbon ignition for more massive stars. These tracks are supplemented with the TP-AGB evolutionary tracks from Vassiliadis & Wood (1993) and those from Vassiliadis & Wood (1994) for the post-AGB evolution. The reason for using Padova 1994 instead of its more recent version Padova 2000 (Girardi et al. 2000), also available in BC03, is that Bruzual & Charlot (2003) recommends the previous version, since the latter yields worst agreement with observed galaxy colors.

For SB99, we use the tracks included in the SB99 upgrade (Vázquez & Leitherer 2005), and which are presented in Girardi et al. (2002). These consist of the Padova tracks updated by Girardi et al. (2000) for low and intermediate masses ( $0.15 - 7 M_{\odot}$ ), which are combined with the original Padova 1994 tracks for the most massive stars. Like in BC03, TP-AGB stars are included following the models of Vassiliadis & Wood (1993).

### 4.2.3 Stellar spectra libraries

We use BC03 with the semi-empirical STELIB/BaSeL 3.1 stellar spectral library, which provides high-resolution spectra from  $91 \text{ \AA}$  to  $160 \mu\text{m}$  for all metallicities in the Padova stellar evolutionary tracks. This library is composed of stellar spectral from the empirical STELIB spectral library (Le Borgne et al. 2003) for  $3200 - 9500 \text{ \AA}$  ( $R = \lambda/\Delta\lambda \sim 2000$ ), and from the theoretical BaSeL 3.1 stellar spectral library (Westera et al. 2002) in the remaining wavelength range (with  $\lambda/\Delta\lambda \sim 200 - 500$ ).

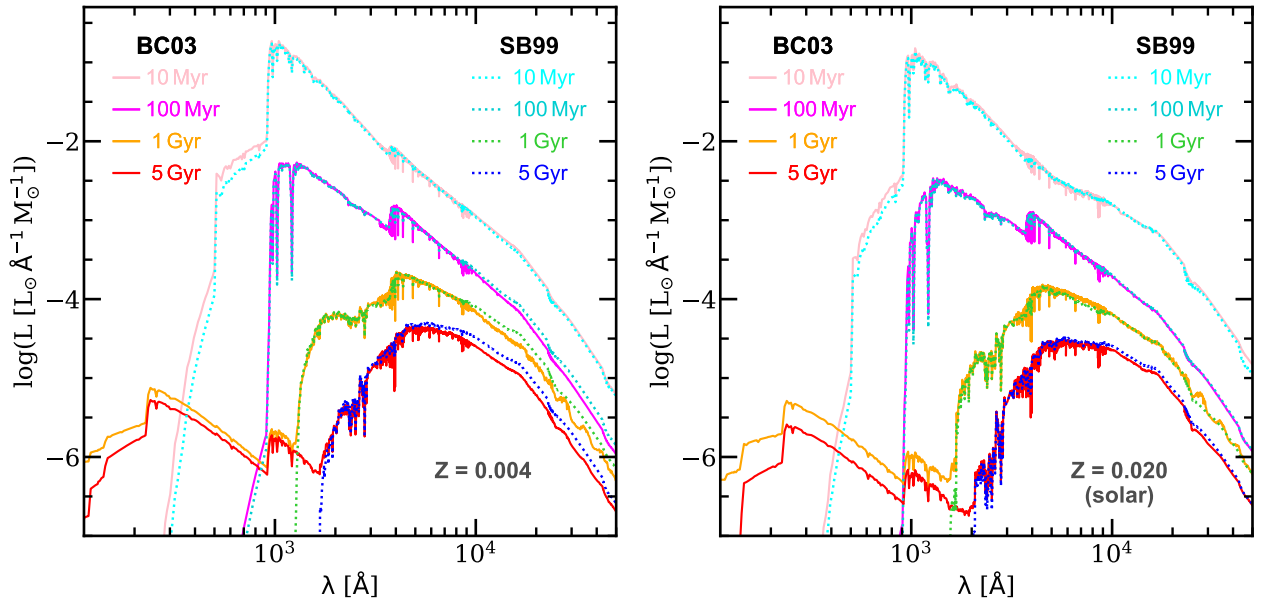


**Figure 4.3:** SEDs for SSP models in SB99 and BC03. Models have been created assuming a Salpeter IMF (0.1 to 100  $M_{\odot}$ ) for both SB99 (dotted) and BC03 (solid), for two metallicities:  $Z = 0.004$  (left panel) and  $Z = 0.020$  (solar; right). Ages of 10 Myr, 100 Myr, 1 Gyr, and 5 Gyr are shown in different colors.

Since none of these libraries provides spectra for carbon-rich TP-AGB stars, these spectra are constructed from period-averaged spectra of atmosphere models from Höfner et al. (2000) with solar metallicity. Spectra of stars in the superwind phase at the end of the TP-AGB phase are constructed from observations from Le Sidaner & Le Bertre (1996) and Le Bertre (1997).

SB99 uses a comprehensive set of spectral libraries, most of them theoretical, and each optimized for a specific spectral range. Among them, we can mention the theoretical UV spectral library of OB stars (Leitherer et al. 2010) that generates spectra between 912 and 3000  $\text{\AA}$  with a resolution of  $\Delta\lambda = 0.4 \text{\AA}$ , which was updated to include the theoretical UV emission from Wolf-Rayet stars (Leitherer et al. 2014). Also, the theoretical optical spectral library presented in Martins et al. (2005), which covers from 3000 to 7000  $\text{\AA}$  with a resolution of  $\Delta\lambda = 0.3 \text{\AA}$ . In addition, a theoretical low-resolution spectrum ( $\sim 20 \text{\AA}$ ) that covers from X-rays to radio is produced by choosing between several stellar atmosphere models. We chose the recommended Pauldrach + Hillier models (Hillier & Miller 1998; Pauldrach et al. 2001) for the generation of this spectrum.

SB99 and BC03 show very similar SEDs for the SSP models in the optical bands, being the major differences in the UV emission. In particular, the main differences arise from the different UV emission of the old stellar populations in both models. Fig. 4.3 shows the comparison of the SEDs of the SSPs in SB99 and BC03 for different ages and two different metallicities ( $0.2 Z_{\odot}$  and  $1 Z_{\odot}$ ), assuming a Salpeter IMF for both of them. This figure shows how the differences in the SEDs between BC03 and SB99 are relevant only in the UV and for the oldest ages in the figure (1 and 5 Gyr), for which BC03 predicts non-negligible UV emission compared to SB99. Nevertheless, the UV emission coming from younger stellar populations is  $\geq 2$  orders of magnitude larger than that of older populations in this wavelength range. Although the differences in the UV spectra between SB99 and BC03 could have a strong impact when modeling red and dead galaxies, the massive high-redshift galaxies considered in this work have a substantial ongoing star

formation (i.e., they host very young stellar populations), which makes that any UV emission from these younger bursts will dominate the UV spectra and will make irrelevant the UV contribution from older stellar populations in the galaxy, some of which have not even appeared at the redshifts of the sample.

#### 4.2.4 SFH

Both in the BC03 and SB99 models, we assume that the SFH of each SED can be described by a double time-delayed exponential, i.e., its SFH consists of the sum of an old and a young population, each of them described by  $SFR(t) \propto t e^{-t/\tau}$  from  $t = 0$  (onset of star formation) up to  $t_{\text{burst}}$ , where  $t_{\text{burst}}$  is the age of the burst and  $\tau$  the star formation time-scale. The burst strength,  $b$ , is defined as the fraction of the total stellar mass that is created by the most recent burst.

We remind the reader that this two population model for the SFH is assumed for all the SEDs analyzed in this thesis, either integrated or spatially-resolved SEDs (see more details in Section 4.4). Fig. 4.4a shows an example of a SFH described with this double-burst parametrization, in this case, for an integrated SED. As described in Chapter 5, simpler parametrizations of the SFH for each SED (e.g., consisting of only one burst) cannot successfully reproduce the arbitrary SFH a galaxy can have, and, mainly, they are unable to recover the first stages of the stellar mass assembly, in which we are interested.

#### 4.2.5 Dust

Regarding dust attenuation, we assume the empirical attenuation law from Calzetti et al. (2000) both for the BC03 and SB99 models. Calzetti et al. (2000) was derived from UV and optical data of local starburst galaxies by assuming a simple screen model and it is commonly adopted when fitting SEDs at high redshift. An important feature of this law is the absence of the 2175 Å UV bump. Fig. 4.1 (dust attenuation panel) shows the Calzetti et al. (2000) law in terms of the optical depth (red line) compared with the MW extinction curve (Cardelli et al. 1989; O'Donnell 1994; in black).

The Calzetti et al. (2000) attenuation law is described in terms of the reddening as

$$k_{\lambda} = \begin{cases} 2.659 (-2.156 + 1.509/\lambda - 0.198/\lambda^2 + 0.011/\lambda^3) + R_V, & \text{for } 0.12 \leq \lambda < 0.63 \mu\text{m} \\ 2.659 (-1.857 + 1.040/\lambda) + R_V, & \text{for } 0.63 \leq \lambda \leq 2.20 \mu\text{m} \end{cases} \quad (4.6)$$

where  $R_V \equiv A_V/E(B-V) = k(\lambda)$  is the total-to-selective extinction ratio in the  $V$  band, being  $E(B-V)$  the color excess.  $R_V$  is usually assumed to be 3.1 for the MW and Large Magellanic Cloud (LMC) extinction curves, but for the Calzetti law ( $R_V = 4.05 \pm 0.80$ ). The reddening curve can be expressed as the attenuation of the continuum at any wavelength,  $A_{\lambda}$ , normalized by the attenuation in  $V$ ,  $A_V$ , as follows

$$A_{\lambda}/A_V = k_{\lambda}/R_V \quad (4.7)$$

Fig. 4.4b shows the Calzetti et al. (2000) attenuation law expressed as  $A_\lambda/A_V$  as a function of wavelength for  $R_V = 3.1$  (gray solid) and  $R_V = 4.05$  (black solid). As mentioned above, we assume  $R_V = 4.05$  for this work, as suggested by Calzetti et al. (2000).

Regarding dust emission, the longest rest-frame wavelength covered by our broadband filters is  $\sim 2.5 \mu\text{m}$  (corresponding to the right end of the NIRCam/F444W filter at  $z = 1$ ). At this wavelength (and lower), dust emission is still unimportant (PAHs emission features begin to be relevant at wavelengths redder than  $\sim 3 \mu\text{m}$ ; see Section 4.1). Thus, we can neglect the contribution of dust emission in our SEDs and will not discuss its implementation in our SPS modeling.

### 4.3 Synthesizer code

We have used the `synthesizer` code (described in Pérez-González et al. 2003, 2008) to perform the SPS modeling of our UV-to-NIR SEDs. This code assumes that the stellar population responsible of each SED can be described by a composite stellar population. To perform the fitting procedure with `synthesizer`, several choices are required *a priori*:

- 1) the SPS model (SB99 or BC03, in our case)
- 2) the IMF (Kroupa 2001 or Chabrier 2003)
- 3) the SFH parametrization (double-burst time-delayed exponential)
- 4) the attenuation recipe (Calzetti et al. 2000)

Together with these input variables, the user has to define the allowed values or ranges within which each parameter is allowed to vary in the fitting procedure. For our choice of a double-burst exponentially declining SFH (see Section 4.2.4), the parameters to fit (and finally yielded) by `synthesizer` can be split into those for the old stellar population (age  $t_{\text{old}}$ , star formation time-scale  $\tau_{\text{old}}$ , metallicity  $Z_{\text{old}}$ , and attenuation  $A_{V,\text{old}}$ ) and those for the young population ( $t_{\text{young}}$ ,  $\tau_{\text{young}}$ ,  $Z_{\text{young}}$ , and  $A_{V,\text{young}}$ ). Additional parameters are the total stellar mass,  $M$ , and the burst strength,  $b$ , which measures the contribution of the young population to the total stellar mass.

To perform the fit, `synthesizer` compares the observed SED points for each filter with those predicted by the SPS models, taking into account observational photometric errors. For this, the stellar population models are first shifted to the redshift of the galaxy, and then, convolved with the corresponding filter transmission curves. In particular, the variables to fit are the colors of the SED, which are considered as statistical gaussian distributions with a standard deviation equal to the associated error (more details in Gil de Paz & Madore 2002). The best model that fits the data is determined with a minimized  $\chi^2$  estimator that measures the goodness of the fit, given by

$$\chi^2 = \frac{1}{N_{\text{filt}}} \sum_{i=1}^{N_{\text{filt}}} \frac{(F_i^{\text{model}} - F_i^{\text{SED}})^2}{(\Delta F_i^{\text{SED}})^2} \quad (4.8)$$

where  $F_i^{\text{SED}}$  is the observed flux in filter  $i$ ,  $\Delta F_i^{\text{SED}}$  is its associated uncertainty,  $F_i^{\text{model}}$  is the flux predicted by the models for that filter, and  $N_{\text{filt}}$  is the number of filters (or SED points) considered.



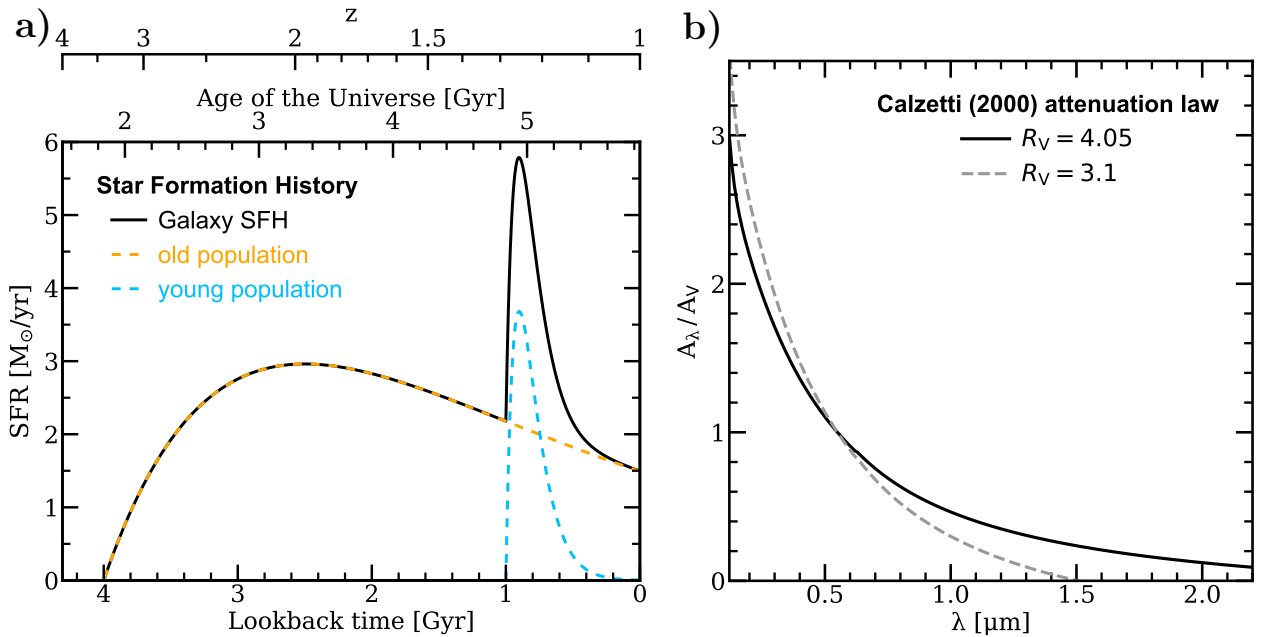


**Figure 4.4:** **a)** Double-burst SFH. The galaxy SFH (black solid) results from the combination of an old population (orange dashed) and a young population (blue dashed), each described by  $SFR(t) \propto t e^{-t/\tau}$ . The ages of the old and young population are  $t_{\text{old}} = 4$  Gyr and  $t_{\text{young}} = 1$  Gyr, respectively, and their time-scales,  $\tau_{\text{old}} = 1.5$  Gyr and  $\tau_{\text{old}} = 100$  Myr. This synthetic galaxy would be at  $z = 1$ , with a stellar mass of  $10^{10} M_{\odot}$ , where the young burst accounts for 10% of this mass. **b)** Calzetti (2000) attenuation law expressed as  $A_{\lambda}/A_V$  as a function of wavelength. Two different values for  $R_V$  have been adopted:  $R_V = 4.05$  (Calzetti law; black solid) and the typically adopted value of  $R_V = 3.1$  (gray dashed).

Since the models predict luminosities per unit of stellar mass at all wavelength, the stellar mass is calculated by scaling the luminosities predicted by the models with those observed for each band (i.e., by multiplying by a factor the luminosities predicted by the models). The final stellar mass and its uncertainty are the median stellar mass and the standard deviation of all the scaling factors for all filters.

Due to the large number of parameters and SEDs to fit, the amount of time required to probe the whole parameter space for each SED is extremely high. For this reason, we make use of the genetic algorithm (Charbonneau 1995) implemented in `synthesizer`. This algorithm samples the parameter space (or grid of solutions) in an optimized way that considerably reduces the amount of time required for the fit, being able to recover the best estimate of the parameters given by the model best fitting the data (see more details in Pérez-González et al. 2008).

`Synthesizer` provides uncertainties for the derived parameters and allows to study the existing degeneracies in the solutions of the fit. This is done using a Monte Carlo (MC) algorithm that first alters the original SED points by letting their associated fluxes randomly vary following a gaussian distribution with a standard deviation given by the (uncorrelated<sup>3</sup>) photometric uncertainties.

<sup>3</sup>To perform the different MC realizations, `synthesizer` assumes uncorrelated photometric uncertainties by default. This means the seed used to randomly vary the flux for each photometric band is different. The contrary to this would be to use the same seed to vary all photometric bands, which would lead to a shift of the whole SED upwards or downwards.

Then, the resulting modified SED is refitted and a new set of solutions for the stellar parameters are yielded by `synthesizer`. By repeating this procedure many times (typically, hundreds; 300 iterations in our case), we get an estimate of the posterior probability distributions encountered for the parameters fitted and the existing degeneracies of them.

`Synthesizer` takes into account the effects of nebular emission by adding its contribution to the stellar-only predictions of the BC03 and SB99 models. Regarding nebular continuum, this is calculated from the number of Lyman photons predicted by the evolutionary synthesis models assuming the emission and recombination coefficients given by Ferland (1980), with an electron temperature of  $T_e = 10^4$  K. For the hydrogen emission lines (Balmer, Paschen and Brackett), the relations given by Brocklehurst (1971) are used, together with the theoretical line ratios predicted by Osterbrock (1989) for a low-density gas ( $n_e = 10^2 \text{ cm}^{-3}$ ) with  $T_e = 10^4$  K in the recombination case B. The emission of the most important forbidden lines ([OII] $\lambda\lambda$ 3726, 3729 Å, [OIII] $\lambda\lambda$ 4959, 5007 Å, [NII] $\lambda\lambda$ 6548, 6583 Å, and [SII] $\lambda\lambda$ 6717, 6731 Å) is also accounted for, based on the line ratios calculated in Gallego et al. (1996) for local star-forming galaxies.

## 4.4 2D SPS

The SFH of galaxies at high redshift is traditionally inferred by performing SPS on their integrated SEDs, assuming for that a relatively simple SFH parametrization (constant, instantaneous,  $\tau$  model, time-delayed exponential, etc.). Since most of the stellar emission of a stellar population is emitted in the (rest-frame) UV-optical, the better we cover this spectral range when building the galaxy integrated SED, the more robust the stellar parameters derived from the SPS modeling will be. As described in Chapter 3, with the advent of JWST, galaxies at high redshift are now observed in the IR with a higher spatial resolution than ever, which allows us to probe many rest-frame optical morphological features previously missed by *Hubble*. Thus, when these IR data from JWST are combined with high-spatially-resolved data in the UV-optical from *Hubble*, we are able not only to extend to longer wavelength the integrated SEDs provided by HST, but also those for smaller parts of the galaxy than can now be simultaneously resolved with HST and JWST.

In this sense, what we will do in this thesis is to make use of these HST+JWST spatially-resolved SEDs to build the integrated galaxy SFH, i.e., to combine the information of the SPS in two dimensions (2D SPS) of the galaxy to build the galaxy SFH. Since the SFH of a galaxy can have very diverse shapes, its global (integrated) SFH may not always be successfully recovered when assuming a functional form to describe it. By combining the SFH from the 2D SPS, we can obtain more complex galaxy SFHs by adding together the contributions of the different SFHs derived for each one of the smaller regions considered, for which a simple functional form was assumed in their SED fit<sup>4</sup>. In addition, the smaller the region of the galaxy on which the SPS is applied, the simpler its SFH will be, in general (at least, the part of the SFH that has a noticeable impact on the SED).

---

<sup>4</sup>A simple example to understand this would be to consider a galaxy whose SFH can be described with three instantaneous burst that occur in different parts of the galaxy at different times. If we try to derive the galaxy SFH using a two population model, one of the burst in the SFH will be not reproduced. Nevertheless, if we split the galaxy into the three regions where the bursts occurred and perform SPS modeling on them, the SFH recovered for each of these regions will likely recover each one of the bursts. If the SFHs for these individual regions are then added together, the resulting SFH will probably be able to reproduce the SFH of the galaxy in a better way than when considering only integrated SED.

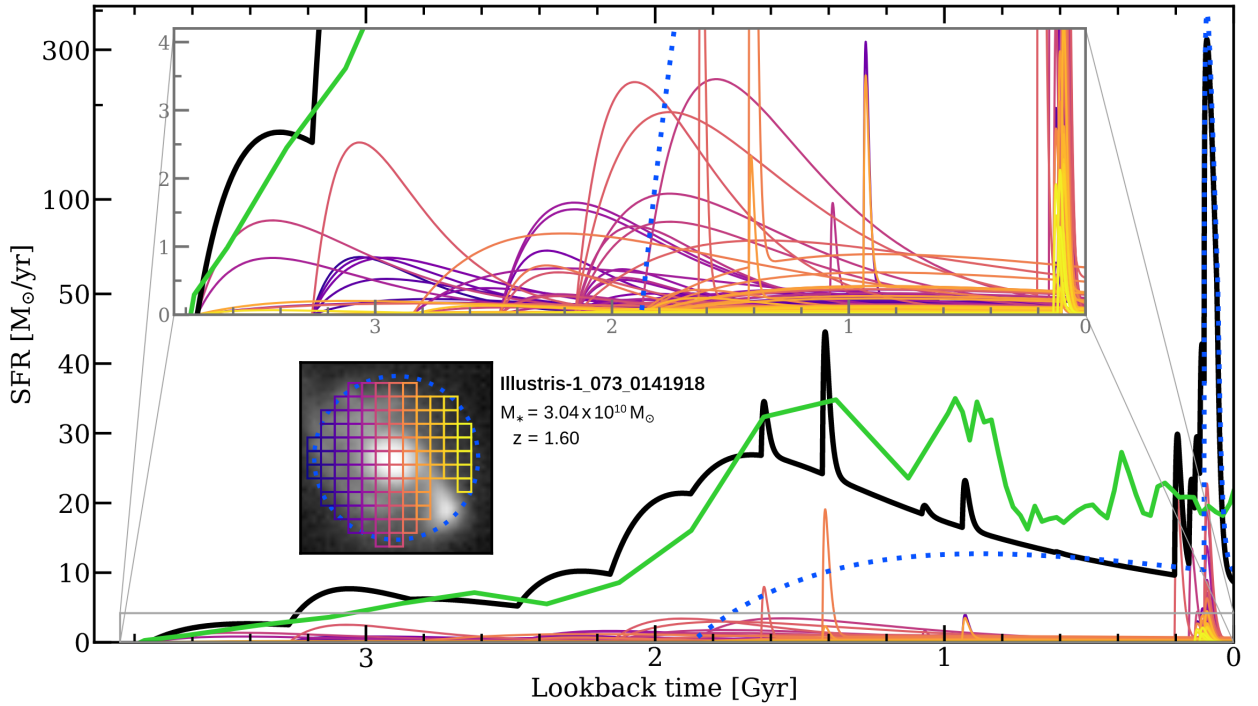


**Figure 4.5:** Example of galaxy SFH recovered from the 2D-SPS modeling for an Illustris galaxy. The black solid line shows the galaxy SFH obtained by adding together the individual SFHs of the spatially-resolved SEDs (thin colored lines), for which a two population SFH is assumed. The square inset shows an WFC3/F160W image of the galaxy. The grid shows the regions from where these 2D SEDs have been measured (same color code as used for their SFHs). The alternative galaxy SFH derived from the integrated SED, measured inside the integrated aperture, is shown in dotted blue, also assuming a two population SFH. The green solid line shows the ground-truth SFH for the galaxy, provided by the simulated particles belonging to the galaxy in Illustris. The figure shows how the galaxy SFH derived from the 2D-SPS modeling, unlike that of the integrated SED, is able to capture the shape of the true SFH, especially at higher lookback times.

Therefore, by deriving the SFH of spatially-resolved regions of the galaxy we are breaking down a complex problem (the galaxy SFH) into simpler subproblems that we can address in a more feasible and flexible way.

For this analysis, we assume that the spatially-resolved SEDs are not correlated. This will make us use spatial resolution elements (cells; see Chapters 5 and 6) that avoid spatially oversampling SEDs at individual regions. Fig. 4.5 shows an example of how the galaxy SFH is recovered from our 2D analysis on the Illustris synthetic deep survey images (see Section 2.3) for galaxy *Illustris-1\_073\_0141918*. The synthetic WFC3/F160W image of this galaxy is shown as an inset, with the different apertures considered. SEDs are first measured both in an integrated aperture (dotted blue) and for each of the cells of a grid defined inside this aperture (a different color is used for each cell). Only cells that belong to the galaxy are considered. The blue dotted SFH in the figure shows the integrated SFH derived from applying SPS to the integrated SED with the two population model described in Section 4.2.4 (i.e., a double-burst SFH). The thick black SFH is the resulting galaxy SFH recovered by considering the 2D-SPS information. This black SFH is built by adding together the individual SFHs derived for each cell in the grid after applying SPS

to them. The SFH of each grid region is shown with thin lines (same color code as the grid) and is also described by a double burst SFH (see zoomed inset on top).

As described in Section 2.4, the ground-truth galaxy SFH can be built from the information provided by the simulated particles belonging to this galaxy (green SFH). In fact, this ground-truth SFH in green is the same as that shown in Fig. 2.5, where the distributions for the stellar and gas particles belonging to the galaxy are also shown. Fig. 4.5 shows how the galaxy SFH derived from the 2D SPS (thick black) is able to better recover the true SFH of the galaxy (in green) than the integrated SFH (blue dotted). This is especially noticeable at the beginning of the ground-truth galaxy SFH (at the highest lookback times), in which we are interested in this thesis, for which the integrated SFH does a rather poor job.

In the figure above, the galaxy SFH derived from the 2D-SPS analysis (in black) has been built by only considering one of the 300 MC realizations performed by `synthesizer` for each SED (see Section 4.3). Nevertheless, when all the MC realizations are considered, different galaxy SFH can be obtained from the 2D-SPS analysis, providing a better estimation of the most probable galaxy SFH (e.g., by calculating the median galaxy SFH of all of them). In addition, the MC realizations allow us to access the information on the uncertainties and degeneracies of the parameters that we will derive from the inferred galaxy SFH.

This new 2D-SPS method of inferring the galaxy SFH is described in detail in Chapter 5 (see also García-Argumániz et al. 2023), where we discuss the calibration of this method with simulated galaxies from the Illustris simulation. As it will be discussed there, the SPS input parameters have been optimized for best recovering the earliest parts of the galaxy SFH, which provide information about the beginning of the stellar mass assembly in the galaxy. In Chapter 6 we will apply this 2D-SPS method to galaxies observed in the CEERS survey, with the aim to shed light on when real massive galaxies at  $1 < z < 4$  began to form.

# Probing the earliest phases in the formation of massive galaxies with simulated HST+JWST imaging data from Illustris

---

This chapter is largely based on García-Argumániz et al. (2023).

## 5.1 Introduction

As discussed in Chapter 1, there are still many open questions regarding when massive galaxies began to form. The way to address the latter issue in this thesis is to study the massive progenitors at high redshift of the most massive galaxies observed today and analyze their stellar populations, namely, their SFH. Our approach is to use spatially-resolved multiwavelength broad-band data from JWST, combined with already existing broad-band data from HST, to extract SEDs of progenitors of nearby massive galaxies at high redshift and apply 2D-SPS modeling on them. The determination of stellar population parameters in two dimensions, and not only for the galaxy as a whole, will help us to analyze stellar mass distributions inside galaxies and to recover realistic integrated galactic SFHs. The power of analyzing the stellar populations in 2D resides in the fact that smaller regions of a given galaxy should have its observational properties driven by a more simple SFH, which can therefore be characterized with fewer parameters compared to that required to characterize an entire galaxy (which easily could count with several, quite different stellar populations). Analyzing the stellar content of high-redshift systems in 2D will be fundamental to identify the evolutionary stages a galaxy can undergo regarding its stellar content evolution and to determine when its assembly began.

This work aims at determining the robustness of spatially-resolved SFHs for massive galaxies at  $1 < z < 4$ , derived from the 2D-SPS analysis of simulated HST+JWST broad-band photometry, to infer when these massive progenitors began their stellar mass assembly. The reason for focusing on this  $1 < z < 4$  redshift interval, for which JWST is expected to provide high-quality data, is that it includes the so-called ‘cosmic noon’, i.e., the epoch of the Universe where the cosmic star formation rate density history was maximum at  $z \sim 2$  and where a considerable fraction of the local stellar mass was formed: half of the present-day stellar mass was formed before  $z = 1.3$  (see Madau & Dickinson 2014 and references therein). The results of this work will help us identify the first progenitors of massive galaxies around cosmic noon, an epoch of the Universe of great interest for many JWST studies in the upcoming years.

In order to establish a methodology and test its performance, we use galaxy images in different bands simulated by the *Illustris* Project. One of the most appealing features of recent cosmological simulations such as *Illustris-1* (Vogelsberger et al. 2014b, Nelson et al. 2015) is that some of them provide synthetic stellar images generated for simulated galaxies at different redshifts in common broad-band filters from HST or JWST (Torrey et al. 2015) and with “realistic” morphologies (at least, relative to the morphologies provided by typical semi-analytical models). These images, when compared to the available information of the stellar particles for each galaxy in the simulation, make them the perfect benchmark to test how successful our 2D stellar population synthesis method is at recovering the early formation of massive galaxies at high redshift when upcoming JWST broad-band photometry data become available.

The present chapter is structured as follows. In Section 5.2, we give a brief overview of the *Illustris* simulation and explain how the sample of simulated galaxies has been selected from the synthetic images. In Section 5.3, we present the processing of the images and the photometric method conducted to build SEDs in 2D. Section 5.4 describes the SPS modeling of the SEDs measured in 2D and the derivation of the integrated SFHs from these 2D-SPS analysis. In Section 5.5, we evaluate the success of our method in recovering the earliest phases in the formation of each galaxy in the sample. Finally, in Sections 5.6 and 5.7, we present our results and outline our conclusions, respectively.

Throughout this chapter, we adopt the same cosmology as specified in the *Illustris-1* simulation:  $\Lambda$ CDM cosmology with  $\Omega_m = 0.2726$ ,  $\Omega_\Lambda = 0.7274$ ,  $\Omega_b = 0.0456$ , and  $h = 0.704$ . We assume a Kroupa (2001) initial mass function (IMF). All magnitudes presented in this work are calculated using the AB system (Oke & Gunn 1983).

## 5.2 Dataset

In this chapter, we present a method to study the star formation history of massive, spatially-resolved high-redshift galaxies using HST and JWST photometric data. We apply this method to a sample of galaxies simulated by the *Illustris* Project. Our aim is to assess the utility of HST plus JWST combined datasets for the analysis of the earliest evolutionary phases of nearby massive galaxies. For that purpose, our approach consists in selecting the progenitor galaxies at high redshift of nearby massive galaxies, and then analyzing their pixel-by-pixel and resulting integrated-galactic SFHs. In this Section, we describe the simulations, the sample, and the data. Since the *Illustris* Simulation has already been described in Chapter 2, here we only summarize its most relevant characteristics for this chapter.

### 5.2.1 *Illustris* Simulation and synthetic deep-survey images

As described in detail in Chapter 2, the *Illustris* Project is a set of hydrodynamical simulations of a  $(106.5 \text{ Mpc})^3$  periodic cosmological volume that trace the evolution of dark matter, gas, stars, and supermassive black holes from  $z = 127$  to  $z = 0$  (Vogelsberger et al. 2014b, Nelson et al. 2015). The *Illustris* Project comprises six different runs: *Illustris*-(1,2,3) and *Illustris*-(1,2,3)-Dark, where the former include a baryonic physical component in addition to the dark-matter content, and the

latter the dark-matter component alone (see Table 2.1). We make use of the Illustris-1 run, the one with the highest-resolution box of these six runs in terms of the number of resolution elements and their masses: it follows the evolution of  $1820^3$  dark-matter particles with a mass of  $6.26 \times 10^6 M_\odot$  each, and  $1820^3$  baryonic particles with an initial mass of  $1.26 \times 10^6 M_\odot$ . The Illustris-1 volume contains  $\sim 40,000$  galaxies at  $z = 0$  with more than 500 stellar particles – roughly equivalent to galaxy stellar masses of  $M_\star > 5 \times 10^8 M_\odot$  (Torrey et al. 2015). Out of all these galaxies at  $z = 0$  in Illustris-1, 856 galaxies have stellar masses of  $M_\star > 10^{11} M_\odot$ .

This work is based on the simulated galaxies and broad-band images from the Illustris-1 supplementary data catalogs published by Snyder et al. (2017, hereafter S+17) and available via MAST<sup>1</sup>. These catalogs correspond to three synthetic deep survey square images in three different fields, which are labeled as Field A, B, and C, each  $2.8' \times 2.8'$  in size. As described in Section 2.3, each of these three deep survey images has been created by applying the lightcone technique from Kitzbichler & White (2007) to the periodic Illustris-1 volume. As a result, each of the three lightcones created to generate the images contain unique galaxies up to  $z \sim 18$  with no repetition, although there can be repeated galaxies between the fields. To create the images in arbitrary filters from the lightcones, the physical information given by the output of the simulation at each redshift in the lightcones is processed with the spectral synthesis code SUNRISE (Jonsson 2006; Jonsson et al. 2010). This is done by assigning SEDs to the stellar particles according to their mass, age, and metallicity, and by projecting these quantities from the simulation space to pre-defined hypothetical cameras. For the creation of these images, Starburst99 stellar population models (Leitherer et al. 1999) were used, with a Kroupa (2001) initial mass function (IMF), and using a (Charlot & Fall, 2000) model to include the effect of dust absorption in the mock images.

These three synthetic deep-survey images, also called “mock ultra deep fields”, are provided down to the spatial resolution of HST and JWST, among other observatories, in a wide range of broad-band filters, imitating the conditions of real galaxy surveys (see Fig. 2.3). Publicly available catalogs associated to these images include galaxies in the survey images whose rest-frame  $g$ -band apparent magnitude is  $g < 30.0$  mag (19,347 galaxies).

### 5.2.2 Sample selection

Starting from all the galaxies included in the catalogs of the S+17 mock images, we select those at  $1 < z < 4$  which will evolve into a very massive ( $M_\star > 10^{11} M_\odot$ ) descendant at  $z = 0$ , as tracked forward in time via the Illustris merger trees (Rodríguez-Gomez et al., 2015). This means that we select  $1 < z < 4$  progenitors in the mock images of  $z = 0$  very massive galaxies in the whole Illustris-1 simulation. Among all progenitor galaxies at  $1 < z < 4$  in the images, we restrict our analysis to massive galaxy progenitors with  $M_\star > 10^{10} M_\odot$ , for which very high quality JWST data will be available in the near future. This implies that, for the same  $10^{11} M_\odot$  galaxy at  $z = 0$ , all its massive progenitors at  $1 < z < 4$  in the images are considered in our sample (e.g. two massive galaxies at  $1 < z < 4$  could merge to form a  $M_\star > 10^{11} M_\odot$  galaxy at  $z = 0$ ). Fig. 2.6 schematically shows how our sample of massive progenitors at  $1 < z < 4$  in the images has been selected.

The left panel of Fig. 5.1 shows the location in the star formation rate (SFR) vs. stellar mass plane of all the progenitor galaxies at  $1 < z < 4$  in the S+17 simulated images that have

<sup>1</sup><https://archive.stsci.edu/prepds/illustris/>

a  $M_{\star} > 10^{11} M_{\odot}$  at  $z = 0$ . These 2,994 progenitor galaxies shown in the left panel of Fig. 5.1 represent 19% of all galaxies located at  $1 < z < 4$  in the images. This is equivalent to saying that 81% of galaxies at  $1 < z < 4$  in the images do not end up as a very massive galaxy at  $z = 0$ . Out of that fraction of  $1 < z < 4$  galaxies with a very massive descendant at  $z = 0$ , our selected sample is composed of the 221 progenitor galaxies with  $M_{\star} > 10^{10} M_{\odot}$  (represented by stars in Fig. 5.1, left panel). Among them, two of them appear simultaneously in two of the three mock ultra-deep fields with different orientations, and will be considered as independent galaxies in this work regarding the photometric analysis and the derivation of the SFHs. In fact, the initial selected sample from the images is composed of 248 galaxies, but only 221 (+ 2 repetitions) are kept until the final analysis. These 248 galaxies in the initial sample of massive progenitors represent the 64% of all  $M_{\star} > 10^{10} M_{\odot}$  galaxies at  $1 < z < 4$  in the images (388 galaxies), i.e., if we were to select all massive galaxies at  $1 < z < 4$  in the images, only 64% of them would actually become a  $M_{\star} > 10^{11} M_{\odot}$  galaxy at  $z = 0$ . Interestingly, this percentage rises to 68% and 85% when the mass cutoff is set to  $10^{10.1}$  and  $10^{10.5} M_{\odot}$ , respectively. In these cases, the number of galaxies in the sample would decrease from 388 galaxies to 305 for the  $10^{10.1} M_{\odot}$  cut and to 123 for  $10^{10.5} M_{\odot}$ . In Fig. 5.1, we also show the galaxy Main Sequence for Illustris galaxies, as determined by Sparre et al. (2015).

The right panel of Fig. 5.1 shows the  $g - r$  color-stellar mass diagram for descendants at  $z = 0$  of all galaxies at  $1 < z < 4$  in the mock images of S+17. Only descendants with  $\log(M_{\star}/M_{\odot}) \geq 8.68$  are shown, for which integrated photometry data is available (5,498 galaxies). Since descendants at  $z = 0$  of galaxies in S+17 mock images have been traced via the Illustris merger tree and do not appear in these survey images, the integrated photometry magnitudes used to build this diagram have been extracted from the Torrey et al. (2015) synthetic individual galaxy images. But these mock galaxy images are only available for  $z = 0$  descendants with a minimum stellar mass of  $\log(M_{\star}/M_{\odot}) \geq 8.68$  ( $\sim 63\%$  of all the 8,768  $z = 0$  descendants of  $1 < z < 4$  galaxies in the images).

Our final 221 galaxies selected from these images evolve to 132 (unique) very massive galaxies at  $z = 0$ , which means that some galaxies in our final sample at  $1 < z < 4$  have the same descendant at  $z = 0$ . These descendants are called  $z = 0$  descendants of our main sample, hereafter, and are shown as violet stars in the right panel of Fig. 5.1. We note that 51% of all  $z = 0$   $M_{\star} > 10^{11} M_{\odot}$  with a progenitor galaxy at  $1 < z < 4$  in the images do not come from any of the galaxies in our initial sample of 248  $1 < z < 4$ ,  $M_{\star} > 10^{10} M_{\odot}$  systems. The main progenitor at  $z > 1$  in the images of those nearby massive galaxies presents a typical stellar mass  $\log(M_{\star}/M_{\odot}) = 9.12_{8.48}^{9.65}$  and a typical redshift of  $z = 2.71_{2.01}^{3.42}$  (median values and first and third quartiles).

The 221 galaxies in the sample account for 28% of the total stellar mass present in their 132  $z = 0$  descendants, where the 22 galaxies at  $3 < z < 4$  account for 8.1% of the stellar mass of their descendants, the 94 galaxies at  $2 < z < 3$  for 23%, and the 105 galaxies at  $1 < z < 2$  for 33%. These descendants are predominantly Red Sequence galaxies (RS; approximately 73%), but there are also a few galaxies in the Green Valley (GV; 14%) and in the Blue Cloud (BC; 13%). In the case of the  $M_{\star} > 10^{11} M_{\odot}$  descendants of progenitor galaxies at  $1 < z < 4$  which are not massive, their location in the diagram is similar, but with a higher fraction of them in the BC: 63% in the RS, 16% in the GV, and 21% in the BC.

The galaxies in our sample are projected into three  $2.8 \times 2.8$  arcmin<sup>2</sup> area (S+17). The typical stellar mass, star-formation rate (SFR), redshift and stellar half-mass radius (i.e., the radius enclosing half of the total stellar mass of the galaxy;  $r_{\text{hm}}$ ) of galaxies in the sample are



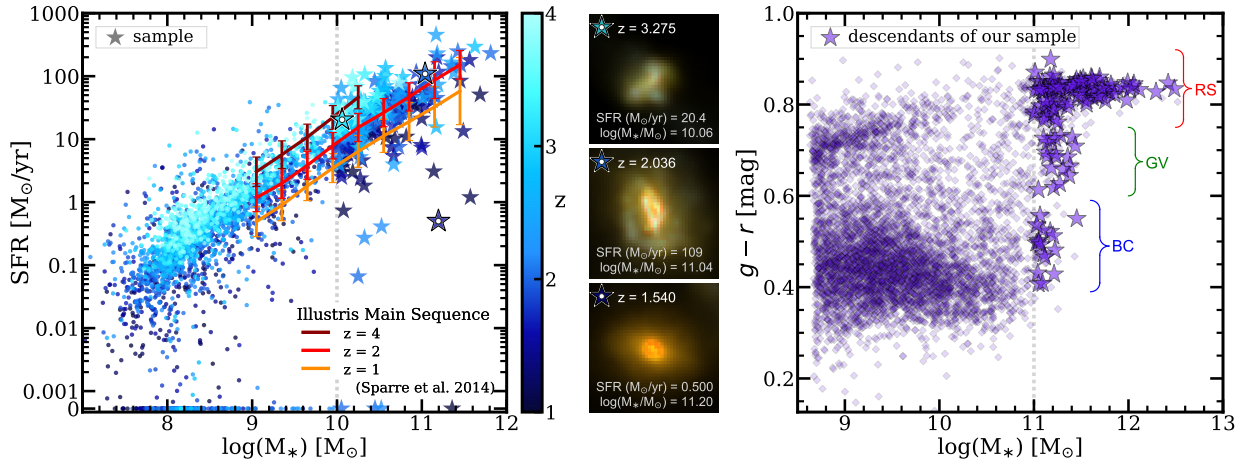


**Figure 5.1:** Left panel: Main Sequence plot for those galaxies at  $1 < z < 4$  included in the mock survey presented in S+17 which are progenitors of very massive galaxies ( $M_{\star} > 10^{11} M_{\odot}$ ) at  $z = 0$ . All progenitors are color-coded by redshift. In this chapter, we concentrate on the analysis of the most massive progenitors ( $M_{\star} > 10^{10} M_{\odot}$ ), which are plotted with star symbols. The Main Sequence found for all the Illustris simulated galaxies at different redshifts (Sparre et al. 2015) has also been plotted. Middle panel: postage stamp images for some representative examples of our galaxies (size  $2.5'' \times 2.5''$ ). These RGB images are created using ACS/F1814W, NIRCcam/F200W, and NIRCcam/F277W asinh-scaled images as B, G and R filters, respectively. The position of these galaxies in the left panel has been highlighted with a white dot inside. Right panel:  $g - r$  color vs. stellar mass diagram for descendants at  $z = 0$  of all galaxies at  $1 < z < 4$  (independently of their stellar mass) in the S+17 mock survey images. Descendants of the final sample of 221 galaxies analyzed in this chapter are plotted as stars.

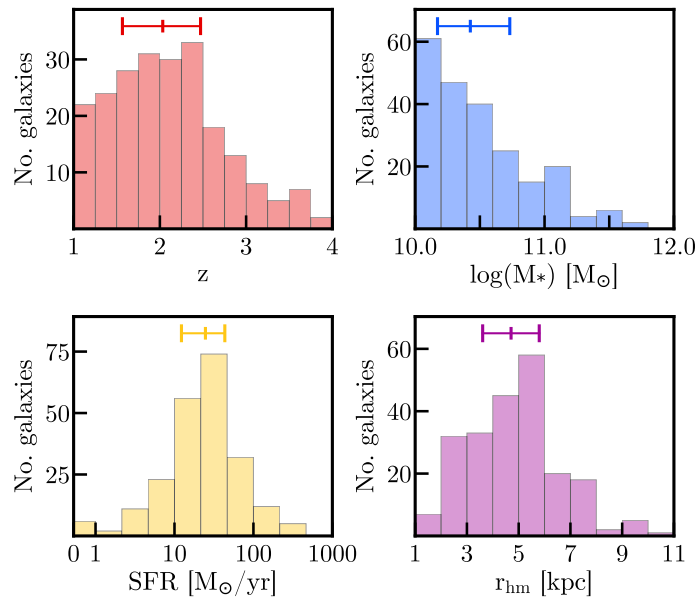


**Figure 5.2:** Histograms for our  $1 < z < 4$  sample of 221 simulated galaxies: redshift (top left panel), total stellar mass (top right), SFR (bottom left), and stellar half-mass radius (bottom right). These properties have been extracted from the Illustris-1 database. Median and quartiles are shown as segments on the top.

$\langle \log(M_\star) \rangle = 10.4_{10.1}^{10.7} M_\odot$ ,  $\langle \text{SFR} \rangle = 25_{12}^{43} M_\odot/\text{yr}$ ,  $\langle z \rangle = 2.0_{1.6}^{2.5}$ , and  $\langle r_{\text{hm}} \rangle = 4.7_{3.6}^{5.8}$  kpc (median and quartiles), respectively. Fig. 5.2 shows the histograms of these properties for our sample of 221 galaxies.

### 5.3 Photometric data from the *Illustris* simulation

In this section, we describe how the simulated deep survey images have been processed to obtain SEDs for all galaxies in our sample. We measure integrated-light photometry for each galaxy, and we also consider spatially-resolved SEDs, all constructed with data in several HST and JWST filters. Apart from simulated images, we also use redshifts and physical properties extracted from the *Illustris* database. As in the rest of the thesis, we refer to ‘ground-truth’ or ‘reference’ properties as those galaxy properties derived either from the catalogs associated to the S+17 mock images or from the *Illustris* database, in contrast to the properties obtained from SED fits to stellar population synthesis models for different regions in each galaxy, what we call 2D-SPS-derived properties.

#### 5.3.1 Photometric broad-band filters

As described in Section 5.2.1, this work uses the *Illustris*-1 “mock ultra-deep fields” from S+17, each 2.8 arcmin in size. These synthetic deep survey images are available to be used in 34 broad-band filters onboard the HST/ACS and WFC3, JWST/NIRCam and MIRI, and Roman/WFI. For this work, we consider 15 HST and JWST broad-band filters in the optical and near-infrared (see Table 5.1), which will be available for several cosmological fields covered by HST legacy projects such as the Cosmic Assembly Near-infrared Deep Extragalactic Legacy Survey fields (CANDELS; Grogin et al. 2011; Koekemoer et al. 2011), and JWST Guaranteed Time Observations (GTO), Cycle 1 Guest Observers (GO1) or Early Release Science (ERS) programs such as the MIRI Deep Survey (Norgaard-Nielsen & Perez-Gonzalez 2017), the JWST Advanced Deep Extragalactic Survey (JADES; Williams et al. 2018, Rieke et al. 2019), the Public Release IMaging for Extragalactic Research (PRIMER; Dunlop et al. 2021) or the Cosmic Evolution Early Release Science (CEERS; Finkelstein et al. 2017). The filterset covers the optical through mid-infrared observed spectral region, corresponding to rest-frame UV to near-infrared wavelengths at  $1 < z < 4$ , an adequate range to study the emission from young and old stellar populations (i.e., providing information about the SFH). The survey images released by S+17 are noise-free synthetic images with different spatial resolution depending on the instrument and telescope used (see Table 5.1) and available with or without considering the point spread function (PSF) degradation for each filter. For this work, we use as starting images those without the PSF model applied, with pixel scales provided in Table 5.1.

#### 5.3.2 Photometric measurements

We process the original idealized (without PSF and noise) images for HST and JWST filters in order to imitate CANDELS data (Grogin et al. 2011; Koekemoer et al. 2011) and the recently-begun CEERS observations (Finkelstein et al. 2017), respectively. The reason for choosing the

**Table 5.1:** Photometric broad-band images used in Chapter 5.

Instrument	Filter	$\lambda_{\text{central}}$ ( $\mu\text{m}$ )	Width ( $\mu\text{m}$ )	Pixel scale <sup>a</sup> ("'/pix)	$5\sigma$ depth <sup>b</sup> (mag)
ACS @ <i>HST</i>	F435W	0.4318	0.0993	0.03	27.3
	F606W	0.5919	0.2225	0.03	27.4
	F775W	0.7693	0.1491	0.03	26.9
	F814W	0.8057	0.2358	0.03	27.2
	F850LP	0.9036	0.2092	0.03	26.5
WFC3 @ <i>HST</i>	F105W	1.0585	0.2653	0.06	26.1 <sup>c</sup>
	F125W	1.2471	0.2867	0.06	26.1
	F140W	1.3924	0.3760	0.06	25.6
	F160W	1.5396	0.2744	0.06	26.4
NIRCam @ <i>JWST</i>	F115W	1.1512	0.2426	0.032	29.2
	F150W	1.5017	0.3309	0.032	28.9
	F200W	1.9905	0.4654	0.032	29.0
	F277W	2.7861	0.7117	0.065	29.2
	F356W	3.5594	0.8163	0.065	29.0
	F444W	4.4457	1.1197	0.065	28.6

**Notes:**

<sup>a</sup> Pixel size in original images. Final (matched) pixel size is 0.06"/pix.

<sup>b</sup> HST depths from the CANDELS/3D-HST catalogs (Skelton et al. 2014): median  $5\sigma$  depth calculated from the errors of objects in the final catalogs (apertures of 0.7") for all 5 CANDELS fields. JWST depths corresponding to the CEERS proposal: values represent the planned  $5\sigma$  point source depths per filter, assuming a total integration time of 2867 s for all NIRCam filters except for F115W (5734 s).

<sup>c</sup> This limiting magnitude is not included in the CANDELS/3D-HST catalogs from Skelton et al. 2014. We assume the same value as F125W, since the magnitudes for this band are slightly fainter/brighter than those of F105W in the CANDELS survey.

CEERS survey as a test case is that, although depths for subsequent JWST surveys are expected to be better, CEERS is expected to provide one of the first publicly available datasets for deep-field JWST observations. Cycle 1 GO / Treasury programs such as PRIMER are expected to achieve similar depths.

First, we match the pixel size of the images to that of HST/WFC3 (0.06 arcsec). Second, we convolve the image for each filter with the PSF model for the WFC3/F160W filter (FWHM  $\approx$  0.19 arcsec). Finally, we add Gaussian sky noise to the HST and JWST images to achieve the same depth as in the CANDELS and CEERS observations, respectively. We degrade HST images adding noise in order to match the median background rms noise measured around CANDELS massive galaxies ( $M_{\star} > 10^{10} M_{\odot}$ ) at  $1 < z < 4$ . For this calculation, we use actual regions covered by CANDELS/Wide, CANDELS/Deep (Grogin et al. 2011, Koekemoer et al. 2011), and the Hubble Ultra Deep field (HUDF; Beckwith et al. 2006b, Oesch et al. 2010c, Ellis et al. 2013a, Koekemoer et al. 2013b, Illingworth et al. 2013b). For JWST images, the sky noise is estimated using the official JWST exposure time calculator *Pandemia*<sup>2</sup> (Pontoppidan et al. 2016), by measuring the predicted signal-to-noise ratio (SNR) as a function of the pixels surface-brightness in CEERS observations for the selected JWST broad-band filters. The initial spatial resolution of the images for each filter (before registering) and final depths (after the noise addition) are given in Table 5.1. The limiting magnitude has been estimated (without aperture correction) from the sky rms value adopting a circular aperture with a fixed radius of 0.2'' at a  $5\sigma$  level.

We use these processed (registered, PSF-matched, and sky noise-added) deep survey images to measure photometry. To do that, we first generate a segmentation map by running *SExtractor* (Bertin & Arnouts 1996) on the WFC3/F160W image using the following parameters: we filter images with a gaussian kernel FWHM 3 pixels, set the minimum area for detections to 20 (a bit smaller than the PSF FWHM), the number of deblending sub-thresholds to the maximum (64), the contrast to  $5 \times 10^{-4}$ , and local background to a size of at least 4 times the largest galaxy in our sample. The results did not vary much when changing the relevant parameters given that we are dealing with relatively bright galaxies. In general, there is good agreement between sources detected in the segmentation map and galaxy positions given by the *Illustris* catalogs based on the original images. Then, this segmentation map is combined with the information of the sample in the *Illustris* catalogs to create circular galaxy apertures that enclose the integrated emission from all galaxies in the sample (see 5.3.2.1 below). We choose to use galaxy positions given by the *Illustris* catalogs instead of the ones provided by *SExtractor* in order to make the future comparison between our results derived from 2D-photometry and from the simulated particles in the galaxy more fair (otherwise, the centers for the galaxy photometric apertures would be shifted from the galaxy centers given by the simulated particles).

We build galaxy SEDs by measuring multi-wavelength photometry in two different ways: inside these circular galaxy apertures, which enclose the entire flux of the galaxy (hereinafter “integrated photometry”), and for small parts of the galaxy defined after creating a grid inside this circular aperture with cell size equal to 3×3 pixels, roughly the area of the FWHM of the PSF-homogenized dataset (“2D photometry”, hereafter). In both cases, the flux uncertainty is estimated as  $\sqrt{N} \times \sigma$ , where  $N$  is the number of pixels within the aperture and  $\sigma$  the rms of the sky for that filter.

---

<sup>2</sup><https://jwst.etc.stsci.edu/>. *Pandemia* Version: 1.7

### 5.3.2.1 Integrated photometry

In order to define the integrated-photometry apertures, we use both the segmentation map and information extracted from the Illustris database, in particular, the galaxy centers and stellar half-mass radii. The apertures are first defined in the segmentation map around galaxy centers with an initial radius equal to twice the stellar half-mass radius ( $r_{\text{hm}}$ ). We decided to use the  $r_{\text{hm}}$  values from the Illustris database because many of the galaxy properties provided by these simulations refer to this radius (and to  $2 \times r_{\text{hm}}$ ) and, typically, papers compare the results based on observations to what Illustris provides for  $2 \times r_{\text{hm}}$  (see, e.g., Vogelsberger et al. 2014a, Sales et al. 2015, Cook et al. 2016, Elias et al. 2018, Valentino et al. 2020). With the following procedure, we test how those apertures compare to what is directly measured in the simulated images. The initial radius is first reduced to minimize the contamination from other sources until 80% of the pixels within the aperture belong to the considered galaxy, i.e., we allow up to 20% of pixels from neighbors. If the number of sky pixels (defined as those not belonging to any source) within this new aperture is greater than 10%, we further reduce the radius to decrease that number below 10%. We refer to the final photometric aperture radius as  $r_{\text{phot}}$  hereafter. We discard galaxies (from the initial selected sample of 248 galaxies) whose final aperture radius is  $r < 0.75 \times r_{\text{hm}}$ . This showed to be effective in removing sources overblended by SExtractor and galaxies whose initial aperture (with  $r = 2 \times r_{\text{hm}}$ ) is partially beyond the edges of the simulated images. We also discard galaxies which present surface brightness values fainter than 25 mag/arcsec<sup>2</sup> in WFC3/F160W in their brightest pixel within the final aperture.

Typically, the fraction of pixels within the final integrated photometric apertures belonging to other nearby galaxies is very low, less than 1% for 75% of the sample of 221 galaxies. The maximum percentage of pixels from neighbor galaxies within the integrated apertures is  $\sim 20\%$ , but only 27 out of 221 galaxies have more than 10% of pixels belonging to other sources.

In Fig. 5.3 (top panel) we show the histogram for the final radii of the apertures as a fraction of  $2 \times r_{\text{hm}}$  for the 221 galaxies in the final sample. This means we do not have apertures in this histogram at  $r/(2 \times r_{\text{hm}}) < 0.375$ , due to the threshold imposed on the final apertures to be kept:  $r > 0.75 \times r_{\text{hm}}$ . We find the median and quartiles for  $r_{\text{phot}}/(2 \times r_{\text{hm}})$  are  $0.83_{0.66}^{1.00}$ . It can be noticed that a considerable number of galaxies presents radii very similar or equal to the (starting) aperture radius of  $2 \times r_{\text{hm}}$ :  $\sim 40\%$  and  $\sim 37\%$  of galaxies have  $r_{\text{phot}}/(2 \times r_{\text{hm}}) \geq 0.95$  and  $0.999$ , respectively. On the contrary, only  $\sim 8\%$  of galaxies have aperture radii smaller than  $r_{\text{hm}}$ . But assuming  $2 \times r_{\text{hm}}$  as the best aperture to compare our results with simulations has demonstrated not to work for a significant number of galaxies.

The stellar masses enclosed by our final apertures, a fraction of the total stellar mass of each galaxy, can be seen in the bottom panel of Fig. 5.3. As a comparison, we also show the histogram for the fraction of stellar mass enclosed by a radius of  $2 \times r_{\text{hm}}$ . For both radii, the masses have been extracted from the Illustris database, i.e., they are ground-truth masses calculated by adding up the simulated stellar particles belonging to each galaxy which are closer to the galaxy center than the radii considered. The typical percentages of the stellar masses enclosed by these two apertures are (median and quartiles)  $65_{57}^{72}\%$  for the final photometric apertures and  $75_{71}^{80}\%$  for a radius of  $2 \times r_{\text{hm}}$ . These percentages refer to total stellar masses provided by the Illustris database or using all particles (in both cases, referring to the whole dark matter halo, i.e., they include regions with very low mass surface densities, whose emission is well below our observational limits). This

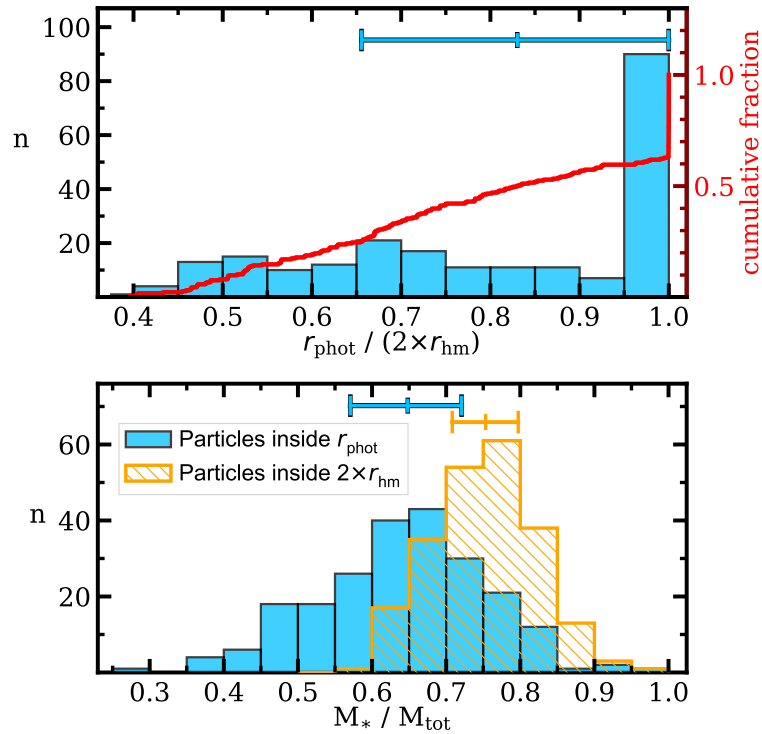


**Figure 5.3:** Top panel: histogram for the radii of the photometric apertures of the 221 galaxies in the final sample as a fraction of  $2 \times r_{\text{hm}}$  radius, the typical radius used by Illustris to compare with observations. The cumulative fraction of galaxies is shown as a red line. Bottom panel: histogram for the fraction of stellar mass enclosed by the photometric apertures (blue filled histogram) and for a radius of  $2 \times r_{\text{hm}}$  (orange hatched) with respect to the total stellar mass in the galaxy. In both cases, we neglect neighboring galaxies. These total masses have been extracted from the simulated particles belonging to each galaxy in the Illustris database. At the top of both panels, we show the median and quartiles for each histogram.

procedure aims at reproducing that to be applied to actual HST+JWST observations, so we should be able to evaluate its impact on reproducing ground-truth properties.

To measure the integrated flux for each galaxy, we only consider pixels whose center lies within the final circular aperture and which do not belong to other sources (according to the segmentation map). The fluxes of these pixels within the aperture (considered galaxy and sky pixels) are added together to build the integrated SED. In Table 5.2 we show the typical integrated magnitudes (median and quartiles) of our 221 galaxies in several filters and in different redshift bins.

### 5.3.2.2 2D photometry

Separately, we also define a grid inside the circular aperture with cell size equal to  $3 \times 3$  pixels ( $0.18'' \times 0.18''$ ) and we measure SEDs for each of these spatial resolution elements. We only consider cells inside the aperture which have at least one pixel that belongs to the galaxy we are measuring. If there are any pixels in the cells belonging to other galaxies (according to the segmentation map), the value of these pixels is replaced by sky pixels by adopting the same Gaussian sky noise distribution previously added to the images. Additionally, we only keep SEDs for our

**Table 5.2:** Integrated magnitudes of our  $1 < z < 4$  sample

Instrument	Filter	$m_{\text{AB}}$ (mag)		
		$1 < z < 2$	$2 < z < 3$	$3 < z < 4$
HST/ACS	F435W	$23.0^{23.6}_{22.1}$	$23.5^{24.6}_{22.9}$	$25.5^{26.4}_{24.9}$
HST/WFC3	F160W	$21.7^{22.4}_{21.0}$	$22.5^{23.1}_{21.9}$	$23.3^{24.1}_{23.2}$
JWST/NIRCam	F115W	$22.0^{22.6}_{21.1}$	$23.1^{23.9}_{22.5}$	$23.8^{24.3}_{23.3}$
	F200W	$21.7^{22.4}_{20.9}$	$22.5^{23.1}_{21.9}$	$23.0^{23.7}_{22.8}$
	F356W	$21.4^{22.2}_{20.7}$	$22.3^{22.8}_{21.7}$	$23.0^{23.7}_{22.8}$

**Notes:** Median values, first and third quartiles of the integrated magnitude measured in different redshift bins and for several bands.

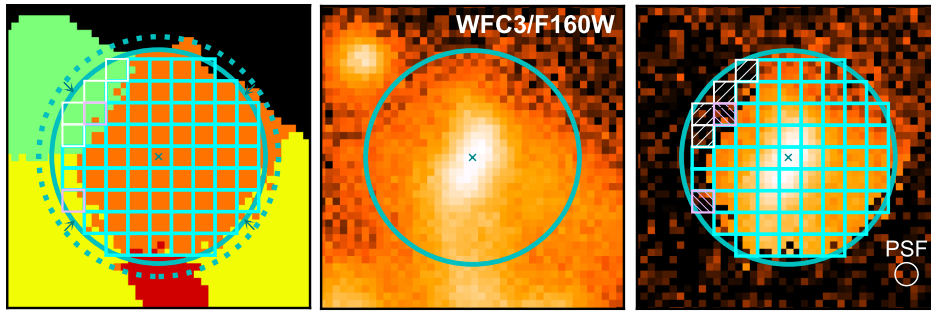
analysis from cells with a  $\text{SNR} > 3$  in at least 5 bands and with surface brightness brighter than  $25 \text{ mag/arcsec}^2$  in WFC3/F160W. Cells that do not satisfy these conditions are discarded. The reason for imposing this surface brightness limit of  $25 \text{ mag/arcsec}^2$  is to deal with the problem of the larger-than-observed galaxy sizes in Illustris galaxies with  $M_{\star} \lesssim 10^{10.7} M_{\odot}$ , which present larger half-light radii and more extended discs than real observed galaxies (Snyder et al. 2015).

Fig. 5.4 shows an example of the integrated aperture and the grid for one of the galaxies in the sample. We also include in this figure the segmentation map around this galaxy and the initial integrated aperture of  $r = 2 \times r_{\text{hm}}$  (dotted line). We show the WFC3/F160W image for this galaxy before and after replacing the values of the pixels of nearby galaxies by random values drawn from the same Gaussian sky noise distribution previously used to add the noise in this image. The initial grid covers all the region within the final integrated aperture, but we only keep cells in cyan for the stellar population analysis, as described in the previous paragraph.

The typical number of cells per galaxy decreases as we move to higher redshifts, as expected given the smaller size of high-redshift galaxies (e.g., Bouwens et al. 2004, Oesch et al. 2010a, Ono et al. 2013). Our galaxies present (median and quartiles)  $98^{136}_{69}$  cells at  $1 < z < 2$ ,  $52^{86}_{37}$  at  $2 < z < 3$ , and  $24^{29}_{21}$  at  $3 < z < 4$ . We also calculate the median SNR of the galaxy cells included in the analysis in different redshift bins, by calculating the SNR as the ratio between the measured flux and its uncertainty in these cells. Median and quartile values for ACS/F435W (WFC3/F160W) are  $31^{48}_{22}$  ( $30^{52}_{22}$ ), at  $1 < z < 2$ ,  $30^{40}_{21}$  ( $27^{38}_{22}$ ) at  $2 < z < 3$ , and  $17^{23}_{10}$  ( $24^{31}_{21}$ ) at  $3 < z < 4$ . For F115W, F200W and F356W NIRCam bands, the median SNR of the galaxy cells are:  $62^{93}_{51}$ ,  $72^{110}_{61}$  and  $92^{132}_{77}$ , respectively, at  $1 < z < 2$ ,  $43^{54}_{34}$ ,  $66^{88}_{60}$  and  $88^{110}_{77}$  at  $2 < z < 3$ , and  $53^{69}_{48}$ ,  $81^{91}_{74}$  and  $91^{108}_{80}$  at  $3 < z < 4$ .

### 5.3.3 Redshifts

Galaxy redshifts are taken from the Illustris database. Specifically, we use the ‘inferred redshift’ values in the catalogs that were used to generate the simulated images in S+17. This redshift value corresponds to the inferred cosmological redshift obtained considering the contribution of both the true cosmological redshift and the galaxy peculiar velocity. A discussion about the possible differences in the derived stellar population properties due to uncertainties in the redshifts of the



**Figure 5.4:** Postage stamp images (size  $2.5'' \times 2.5''$ ) for one of our galaxies: Illustris-1\_066\_0000006 at  $z = 2.192$  (Field A of S+17 images). This galaxy code stands for galaxy id 6 and snapshot 66 ( $z = 2.21$ ) in the Illustris-1 simulation. Left panel: Segmentation map, with colored regions delimiting the galaxy (in orange), three nearby galaxies (green, yellow, and red), and sky pixels (black). We also show the integrated photometric aperture (dark cyan solid line) and the starting aperture of  $r = 2 \times r_{\text{hm}}$  used to calculate the former (dotted line). Inside the integrated aperture, we show the grid where the 2D photometry is measured: the cells that are finally kept for the 2D-SPS analysis are shown in cyan, cells discarded for not fulfilling the SNR and surface brightness criterion as pink hatched squares, and cells discarded for not including any pixel from the considered galaxy as white hatched squares. Middle panel: WFC3/F160W image (already registered, PSF-matched, and sky noise-added) with the integrated aperture. Right panel: WFC3/F160W image where the values of the pixels from nearby galaxies have been masked by replacing them with the same Gaussian sky noise distribution previously added to the images. We also show the integrated aperture and the grid.

corresponding observed galaxies is beyond the scope of this work. Although photo- $z$  uncertainties can be substantial, it will be likely that future spectroscopic redshift samples from both JWST and the *Atacama Large Millimeter/submillimeter Array* (ALMA) will increase the fraction of galaxies with spectroscopic redshifts and, at the same time, improve the photo- $z$  accuracy at such high redshifts.

Fig. 5.5 shows the stellar mass vs. redshift plot for our galaxies. Two different values of stellar masses are shown for each galaxy: considering all particles in the galaxy or only particles inside twice the stellar half-mass radius. The median values and quartiles for these mass measurements, in  $\log(M_{\star}/M_{\odot})$ , are  $10.43_{10.17}^{10.73}$  and  $10.30_{10.05}^{10.63}$ , respectively, and  $2.03_{1.57}^{2.47}$  for the redshifts.

### 5.3.4 Ground-truth physical properties of each galaxy

We use the Illustris database to extract the information for all the simulated particles belonging to a galaxy. In particular, we extract total stellar masses and SFRs of the whole galaxy. These total stellar masses and SFRs values are the ones shown in Fig. 5.1.

We build ground-truth galaxy SFHs from the information of the individual particles that belong to each galaxy (see Section 2.4). Briefly, the SFH can be computed by first loading from the database the stellar particles in the galaxy and then making a histogram of their formation ages in lookback time. We assume time bins for the formation ages of 25 Myr up to a formation age of 1 Gyr, and 250 Myr afterwards. Subsequently, the stellar mass formed per time interval is calculated by summing the masses of the stellar particles formed in each time bin. We will also



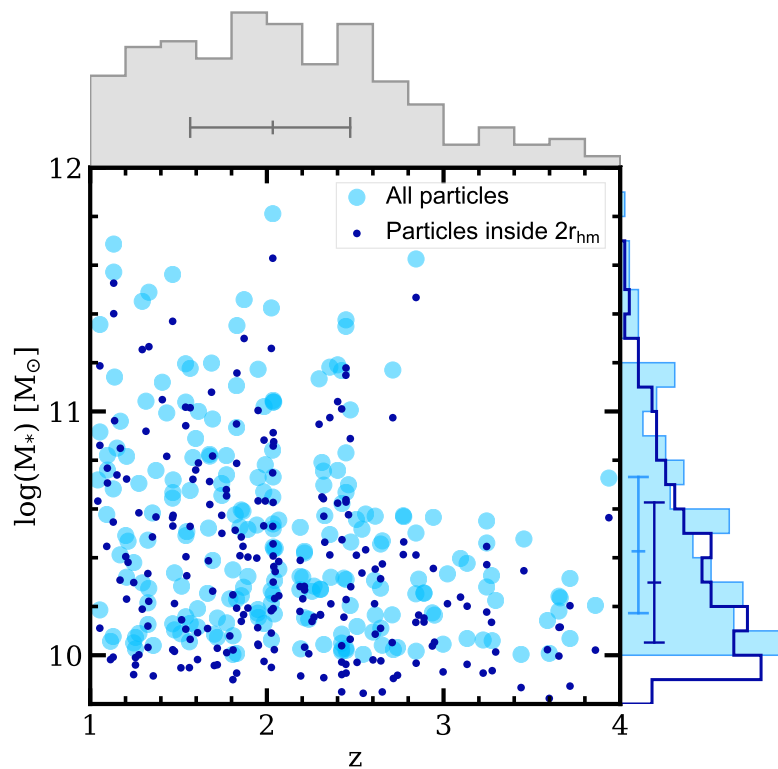


**Figure 5.5:** Stellar mass vs. redshift plot for galaxies in our sample, with values extracted from the Illustris database. We show the stellar mass when considering all the particles in the galaxy (total stellar masses) as light blue circles and the stellar mass obtained when only particles inside twice the stellar half-mass radius as small dark blue dots. Histograms of stellar masses and redshifts are shown at the top and on the right, with the median and quartiles marked.

use in the following sections an additional SFR estimation for each galaxy obtained from the SFH and calculated by loading the gas particles in the galaxy for the snapshot corresponding to the observed redshift and adding together their instantaneous SFR values. Since these ground-truth SFHs will be compared with those derived from the SED-fitting in Section 5.5, in order to make the comparison more fair, we only consider stellar and gas particles which are closer to the galaxy center than the radius of the photometric aperture. Still, our SFHs will be naturally affected by the limitation inherent to detection and photometry procedures.

## 5.4 Estimation of the SFH from 2D SED fitting

Our aim is to study the earliest formation phases of nearby massive galaxies by analyzing in detail the formation history and location of the star formation in massive galaxy progenitors at high redshift. For that purpose, our approach consists in using broad-band data covering the (observed-frame) optical-to-mid-infrared spectral range provided by HST and JWST. In this chapter, we assess the robustness of the results derived from this type of realistic but naturally simplified analysis using simulated imaging data from Illustris (see Section 5.3). As described in the previous section, we build SEDs for each source for both the integrated emission as well as in a 2D grid. In

this section, we describe the derivation of integrated SFHs for each galaxy based on SPS modeling for these SEDs. We then analyze how successfully we can recover the ground-truth SFHs when only broad-band HST and JWST photometric data is used.

#### 5.4.1 Stellar populations synthesis modeling

The integrated and grid SEDs are compared with stellar populations models of Starburst99 (Leitherer et al. 1999), assuming a Kroupa (2001) IMF and a Calzetti et al. (2000) attenuation law. To perform these fits, we use the *synthesizer* code described in Pérez-González et al. (2003, 2008). This code combines the emission of both stars and gas, compares the models with the observed data, and returns the model that best fits the data by performing a  $\chi^2$  minimization (see Section 4.3).

We assume a double-burst delayed exponential SFH, with each burst described by  $SFR(t) \propto t \cdot e^{-t/\tau}$  for  $t > 0$  up to  $t = t_{\text{burst}}$ , being  $\tau$  the star formation timescale and  $t_{\text{burst}}$  the age of the burst. The age of the burst must be understood as the time passed between the age of the Universe when the galaxy started to form stars in that burst and the time corresponding to the observed redshift. The SFH form was chosen after some testing which indicated that 2 bursts following a delayed-exponential SFH instead of other simpler parametrizations (e.g., one single exponential burst) as a more adequate parametrization to successfully reproduce the ground-truth SFHs given by *Illustris*. Several tests were performed assuming only one time-delayed exponential with different values for  $\tau$  and the minimum age of the population, but all of them resulted in the 2D-SED fits selecting too young (recent) ages for the models which were unable to recover the ground-truth galaxy SFH. We will discuss this further in Section 5.5.

The free parameters in our SED fits are the age ( $t$ ), star-formation timescale ( $\tau$ ), extinction ( $A_V$ ), and metallicity ( $Z$ ) for the two stellar populations, in addition to the burst strength ( $b$ ). This burst strength describes the fraction of the total stellar mass that has been created by the most recent burst. We consider an old burst as the one occurring first in the galaxy formation history and a young burst as the one occurring closer to the age of the Universe corresponding to the observed redshift. The stellar mass ( $M_\star$ ) is derived from the SED fits by normalizing the best-fitting model (which provides mass-to-light ratios at all wavelengths) to the observed photometry.

In order to improve the resemblance of the estimated SFHs to the ground-truth SFHs built from simulated particles in the simulation, we found that the allowed age ranges for the old and young stellar populations must depend on the galaxy redshift. In other words, the age frontier between the two stellar populations is an important parameter to set *a priori* based on the galaxy redshift. We thus tested the dependence of our results on this age separation limit ( $\text{age}_{\text{lim}}$  in Table 5.3), considering values as a function of the age of the Universe for a given redshift. The most accurate results in our analysis (considering the mass-fraction formation ages discussed in Section 5.5) are obtained when we impose an age limit between the 2 populations equal to 40% of the age of the Universe for galaxy redshifts at  $1 < z < 2$  and to 50% of the age of the Universe for  $2 < z < 4$  (i.e., 40% of the age of the Universe for the young population and 60% for the old population when  $1 < z < 2$ , and 50% of the age of the Universe for both populations when  $2 < z < 4$ ).

Similarly, we tested different values for the star formation timescales of both bursts and found the best results are obtained when setting  $200 < \tau_{\text{old}} < 1000$  Myr, and  $\tau_{\text{young}} = 10$  Myr. Table 5.3

**Table 5.3:** Free parameters and their ranges in the SED fitting for a double delayed-exponential SFH.

Parameters	Values/Range	Units	Step
$t_{\text{young}}$	0.1 - $\text{age}_{\text{lim}}^a$	Gyr	discrete <sup>b</sup>
$\tau_{\text{young}}$	10	Myr	–
$A_{V,\text{young}}$	0 - 2	mag	0.1 mag
$t_{\text{old}}$	$\text{age}_{\text{lim}} - \text{age}_{\text{Univ},z}^c$	Gyr	discrete <sup>b</sup>
$\tau_{\text{old}}$	200 - 1000	Myr	0.1 dex
$A_{V,\text{old}}$	0 - 1	mag	0.1 mag
$Z_{\text{young}} \& Z_{\text{old}}$	[0.2, 0.4, 1]	$Z/Z_{\odot}$	discrete
$b$	0.01 - 1	-	0.01

**Notes:**

<sup>a</sup> The age separation limit between the young and old populations, is measured (backwards) from the redshift of observation of the galaxy. This value depends on the redshift of the galaxy: it is set to 40% of the age of the Universe for  $1 < z < 2$  and to 50% of the age of the Universe for  $2 < z < 4$ .

<sup>b</sup> We use all the discrete values for the ages given by the SB99 models within the allowed range.

<sup>c</sup> The maximum allowed value for the age of the old population is the age of the Universe at the galaxy redshift.

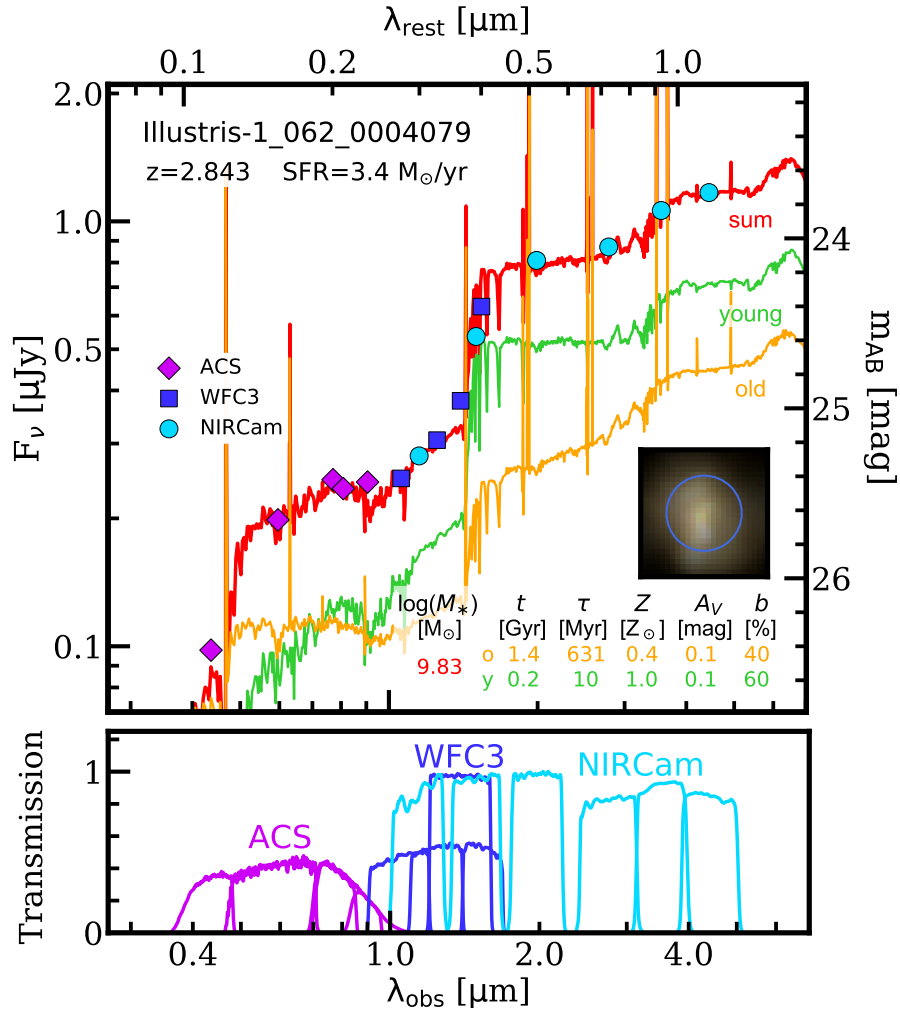
shows the ranges within which each free parameter is allowed to vary in the SED-fittings of this work.

It is impossible to present the results of the full set of tests performed to explore the parameter space here, so instead we focus on those that yield the best match and will be the most useful for upcoming JWST observations.

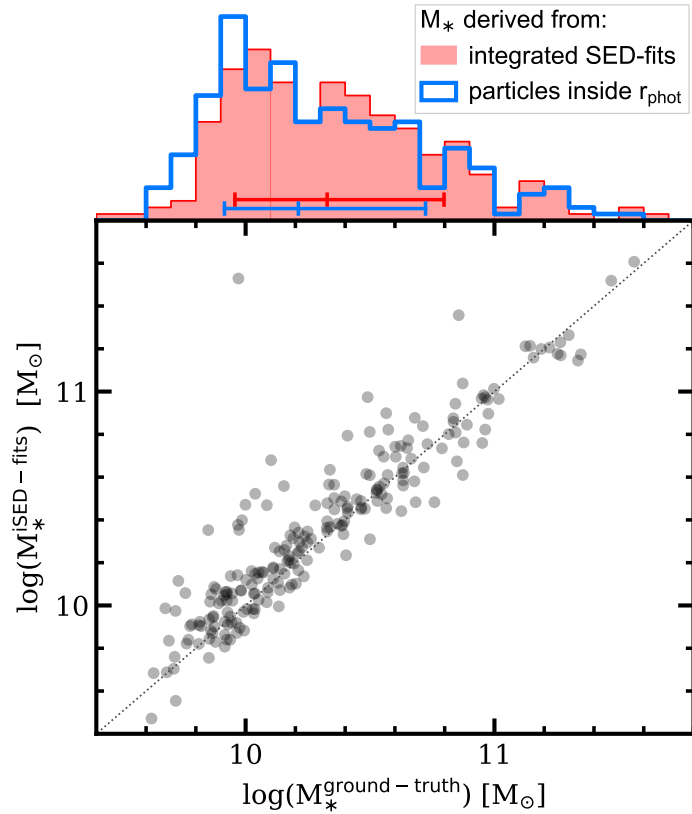
The metallicity is allowed to adopt three different values:  $Z/Z_{\odot} = 0.2, 0.4,$  and  $1$ . These values are expected for our sample according to the mass-metallicity relationship at the considered redshifts, at which this relationship shows lower metallicities than locally for a given mass (Erb et al. 2006; Maiolino et al. 2008; Mannucci et al. 2009; Zahid et al. 2011). Regarding the dust attenuation, we limit the attenuation range to values within  $0 < A_{V,\text{old}} < 1$  mag for the old population, and within  $0 < A_{V,\text{young}} < 2$  for the young population.

Fig. 5.6 shows an example of an integrated SED fit and the values of the model that best fits our data. For this particular galaxy, both the old and young stellar populations contribute at the 40%-60% level throughout the full spectral range. This analysis is performed for the 221 galaxies: both for their integrated measurements and their 2D emission (given by the cells in the grid).

To estimate uncertainties in the derived stellar population properties, Monte Carlo (MC) simulations are performed in *synthesizer* by allowing the photometric data to normally vary within their photometric uncertainty (without correlation), and then repeating the fit again for 300 resampled SEDs (more details in, e.g., Domínguez Sánchez et al., 2016). This results in 300 sets of solutions



**Figure 5.6:** Example of one integrated SED fit for one of our galaxies: Illustris-1\_062\_0004079 at  $z = 2.843$ . This galaxy code stands for galaxy id 4079 and snapshot 62 ( $z = 2.73$ ) in the Illustris-1 simulation. The best fit is shown as a red line. We also show the models corresponding to the old (green) and young (orange) stellar populations. The transmission curves of the filters have been included at the bottom of the figure. The best-fit stellar parameters for the old and young populations are also given. An RGB image (size  $1.5'' \times 1.5''$ ) with the integrated aperture is shown as an inset.



**Figure 5.7:** Stellar masses for the  $1 < z < 4$  sample derived from the integrated SED-fits vs. their ground-truth values calculated from the simulated stellar particles belonging to each galaxy (inside a sphere with the same radius as that of the integrated photometric aperture). The one-to-one relation is shown with the dotted black line. The histograms for both distributions are shown in different colors, with the median and the 68% intervals as horizontal segments.

for each SED which also provide us with information about the typical degeneracies present in these kinds of studies (e.g., age-metallicity or  $\tau$ -age degeneracy).

Fig. 5.7 shows the stellar masses for our  $1 < z < 4$  sample derived from the integrated SED-fits vs. their ground-truth values and how the one-to-one relation is recovered, with a median offset of 0.04 dex and a scatter of 0.2 dex. Each of the SPS-derived galaxy masses has been calculated as the median stellar mass provided by the integrated SED fits. The ground-truth masses have been calculated from the database by considering only the simulated particles of each galaxy closer to the galaxy center than the radius of the integrated photometric aperture. In both cases, stellar masses correspond to the current mass of stars at the redshift of observation (i.e., calculated after taking into account the time-dependent mass-loss and fraction of remnants as a function of time). The histograms for both distributions are also shown. We notice our SPS-derived stellar masses slightly overestimate the ground-truth masses, although the differences are small:  $\log(M_*/M_\odot) = 10.33_{9.96}^{10.80}$  for the integrated SED-fits vs.  $10.21_{9.92}^{10.72}$  for the stellar particles (median and 68% confidence interval).

Several effects could be responsible for the dispersion observed around the one-to-one relation between our integrated vs. ground-truth masses. One of these effects is due to the difference between the volume of the sphere used to calculate the ground-truth masses and that of the cylinder along the line of sight which would enclose all the stars contributing to photometry. This makes that, depending on the shape of the galaxy, when measuring photometry we may include the light from stellar particles in the line of sight located at large galactocentric distances (not included in spherical aperture used to calculate the ground-truth galaxy mass). In fact, this is what happens for the galaxy with an integrated mass that differs in  $\sim 1.5$  dex in Fig. 5.7, which is being outshined by an ultra-massive galaxy of  $\log(M_{\star}^{\text{ground-truth}}/M_{\odot}) = 11.47$  located at only  $0.1''$  from its center. Another effect which can cause dispersion in the recovered integrated mass is the presence of nearby neighbors and their identification in the segmentation map. Even though the light of these neighbors inside the photometric aperture is usually (but not perfectly) blocked by the segmentation map, so is the light of the considered galaxy inside this masked region. However, for the calculation of the ground-truth galaxy mass, we do take into account these stellar particles (from the considered galaxy) located in this region of the sphere.

#### 5.4.2 Estimating SFHs from HST+JWST photometry

Integrated SFHs are built for each galaxy from the 2D SED-fits, and compared with the ground-truth SFHs extracted from the *Illustris* database (see Section 5.3.4). We build 300 integrated SFHs for each galaxy using the 2D stellar population fits, which includes a MC method to estimate uncertainties and degeneracies. We first create one SFH for each resolution element in the galaxy grid. Subsequently, one global SFH is calculated by adding together all these SFHs in the grid. This procedure is then repeated 300 times, one for each of the MC particles presented in the previous section. By combining and adding the 300 SED-fits for each cell in the grid, we obtain 300 independent estimations of the integrated SFH for a given galaxy.

The resulting SFHs are smoothed using a 100 Myr square kernel. Then, we normalize these 300 galaxy SFHs with the median stellar mass of the galaxy derived from the 300 integrated SED-fits. Unless otherwise stated, these galaxy stellar masses refer to the galaxy masses at the time of observation without including remnants or yields. Finally, we calculate the median SFH of the galaxy from these 300 normalized SFHs.

In Fig. 5.8, we summarize the methodology followed for a galaxy to obtain this median 2D-SPS galaxy SFH from its 2D photometry measurements. We start from the HST+JWST data (RGB image and some individual bands shown on the figure), in our example, a galaxy presenting a red center which resembles a protobulge and what seems like a blue disk with some spiral structure. We measure integrated and 2D photometry in a grid. We show SEDs and their stellar population modeling results for some representative grid regions in the center, blue arm on the bottom left and a diffuse emission zone on the top right. We note the difference in color shown in the SEDs between the center and the disk, and how the integrated SED resembles more that of the galaxy center rather than the disk regions. In this regard, considering 2D photometry in our analysis facilitates the estimation of SFHs since small parts of a galaxy are expected to have more simple forms than the entire galaxy, whose integrated photometry is dominated by the regions with highest intensities, i.e., they outshine fainter regions located in the outskirts for this example galaxy. The individual SFHs for each grid region are added to obtain an integrated SFH. In this example,

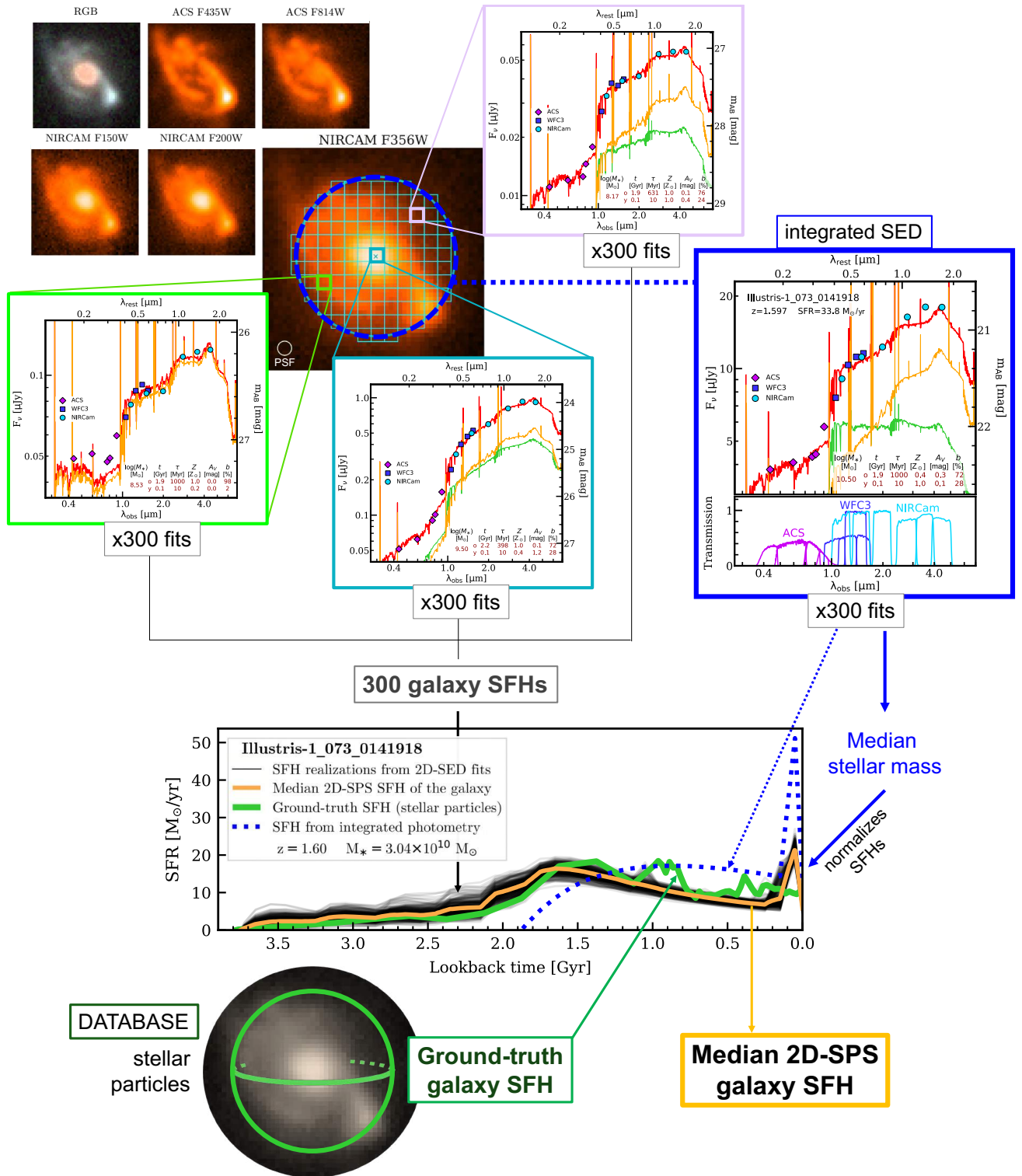


**Figure 5.8:** Schematic diagram of the methodology followed to obtain the median SFH for a galaxy from its 2D-SPS analysis. First, we show an RGB image of the galaxy and some of the HST+JWST broad-band images (in Table 5.1) processed to imitate CANDELS and CEERS observations for HST and JWST filters, respectively. We measure the 2D photometry inside a grid (in cyan) with cell size equal to the spatial resolution element, in addition to the integrated photometry (blue aperture). As an example, we show the SEDs measured for three regions of the grid: the center of the galaxy (teal cell), an arm region (light green), and a diffuse emission zone (pink). To estimate the uncertainties and degeneracies in the derived stellar populations, each SED is fitted 300 times by performing MC simulations. We add the individual SFHs inferred from all the grid regions to obtain the SFH for the whole galaxy. The black thin SFHs in the bottom subfigure show the SFHs for the whole galaxy created by accounting for the uncertainties in the SFHs of each grid region, where the median galaxy SFH from this 2D-SPS method is shown in yellow. The blue dotted SFH is the galaxy SFH inferred from the integrated photometry. The ground-truth SFH of the galaxy, given by the stellar particles belonging to the galaxy, is the green solid SFH.

we demonstrate how the derived SFHs with our method nicely reproduce the ground-truth SFH, significantly improving what can be obtained by analyzing the integrated SED. In the following section, we compare our derived SFHs from our 2D analysis of broad-band imaging data with the reference SFHs built using the simulated stellar particles in the Illustris-1 database.

## 5.5 Validation of the method

In this section, we evaluate the levels of success of our method in recovering the SFHs of massive galaxies at high redshift. In particular, in this thesis we are mainly interested in the earliest phases of massive galaxy formation. Therefore, we compare our results based on the analysis of broad-band HST and JWST images with the ground-truth provided by the Illustris database for full galaxies. We will analyze spatially-resolved stellar population properties in a future works, here we concentrate on the results about the SFHs.

### 5.5.1 Characterization of the earliest phases in the formation of massive galaxies

In order to characterize when massive galaxies start their formation, we calculate the formation times and redshifts when galaxies have formed a given (small) fraction of their total stellar mass. In particular, we discuss here the formation times when the first 5%, 10% and 25% of the stars in each galaxy and the entire sample were formed. We define  $t_k$  as the formation time (measured from the galaxy redshift) at which a galaxy formed the  $k\%$  of its total stellar mass present at the galaxy redshift. These mass-fraction formation times,  $t_k$ , can be directly computed by integrating the 2D-SED-derived galaxy SFHs over cosmic time and are similar to other parameters used in recent literature (see, e.g., Ji & Giavalisco, 2023). We remark that  $t_k$  depend on both  $t_0$  and  $\tau$ , so they might somehow alleviate possible degeneracies between ages and timescales. We also calculate mass-weighted ages,  $t_{mw}$ , from the SFHs. To test their robustness, these  $t_5$ ,  $t_{10}$ ,  $t_{25}$ , and  $t_{mw}$  extracted from the SFHs derived with our 2D-SPS method are compared with their ground-truth values, which are obtained from the SFHs of the simulation stellar particles following the same procedure and enclosed by the photometric aperture.

Fig. 5.9 shows  $t_5$ ,  $t_{10}$ ,  $t_{25}$ , and  $t_{mw}$  calculated from the SFHs derived with 2D stellar population modeling of broad-band data versus their reference values. For each galaxy, we show 300 values of these quantities (vertically spread out), which correspond to the 300 MC particles or 2D-SPS galaxy SFH as described in Section 5.4.2. The black dotted line shows the one-to-one relation between values derived from our 2D-SPS method (output) and those from the simulated particles (ground-truth). As explained in Section 5.4.1, some *a priori* parameters of our method (e.g. Table 5.3) have been optimized to reproduce this one-to-one relation for these four mass-fraction formation times. In general, we find our ages are consistent with this relation at all redshifts. As an inset in each panel, we show the histogram of relative differences between median and ground-truth values for all galaxies. We find our  $t_5$ ,  $t_{10}$ ,  $t_{25}$ , and  $t_{mw}$  values are consistent with the ground-truth values with a median (relative) offset of +71 (+4.4%), +16 (+1.8%), -2 (-0.1%), and -50 Myr (+5.2%), and a scatter (68% interval) of 0.33, 0.31, 0.27, and 0.17 Gyr, respectively. As commented in Section 5.4.1, when we consider only a single-population SFH roughly spanning the whole range of parameters ( $t$ ,  $\tau$ ,



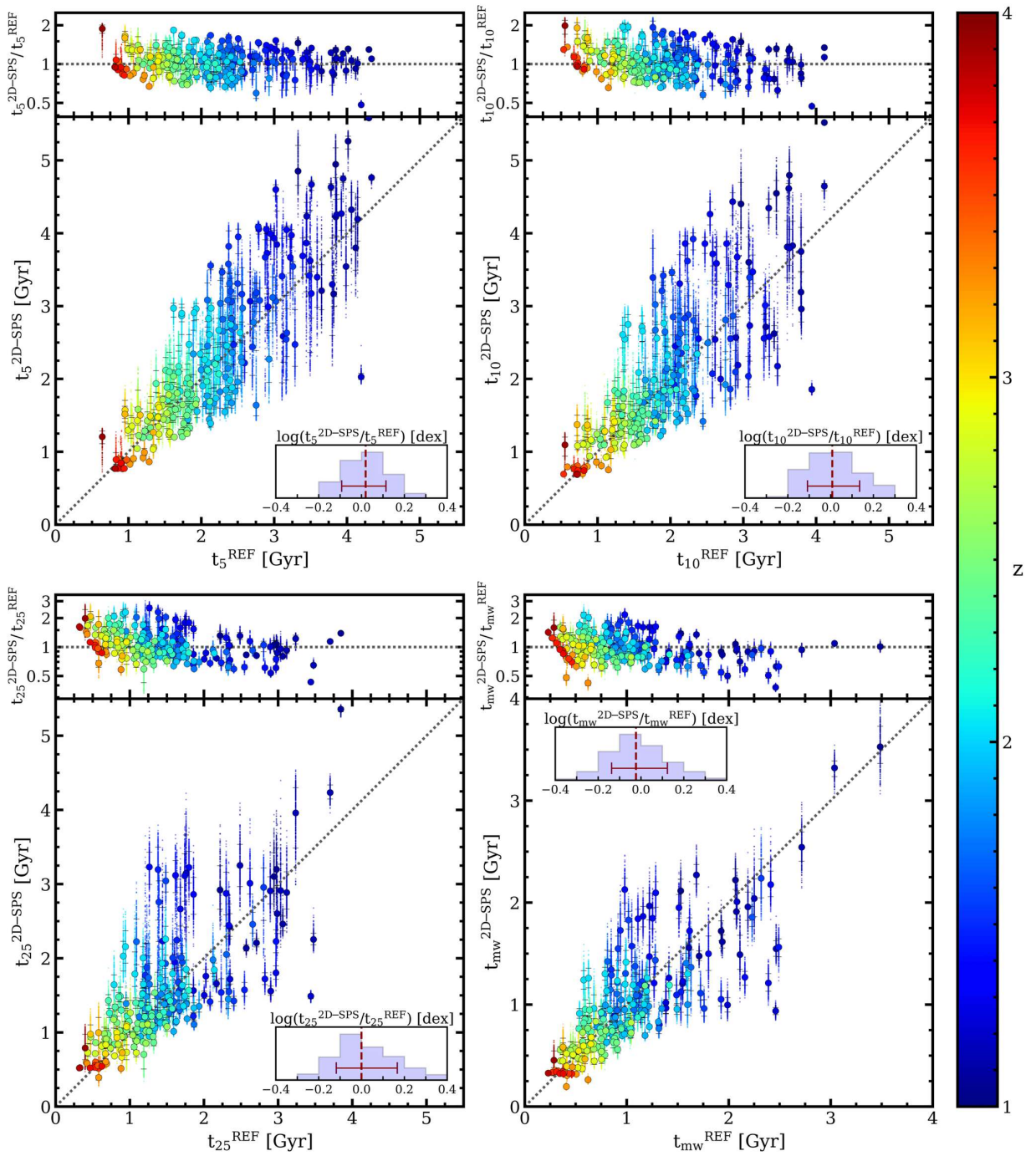


**Figure 5.9:** Comparison between the mass-fraction formation times (measured backwards from the redshift of observation of the galaxy) of our 2D-SPS method and their ground-truth values:  $t_5$  (upper-left),  $t_{10}$  (upper-right),  $t_{25}$  (lower-left) and  $t_{\text{mw}}$  (lower-right) calculated from our 2D-SPS-derived SFHs versus their reference values calculated from the SFHs built from the simulated stellar particles in galaxies. Each galaxy is represented by 300 vertically spread points, which correspond to the mass-fraction formation times of the 300 2D-SPS SFHs, built from the 300 MC particles in each resolution element in the grid. The median of these values for each galaxy is shown as bigger circles and error bars represent the standard deviation of these values (68% interval). All points are color-coded by galaxy redshift. On the top of each panel, we show the ratio between the  $t_k$  of our 2D-SPS method and their ground- $t$ -truth values as a function of the latter. As an inset, we include the offsets of the galaxies in the sample.

$A_V$ ,  $Z$ ) of the two-population fitting, too young ages are assigned in the SED-fits, which leads to an underestimation of all the ground-truth formation times. Thus, when we assume a SFH given by only one population instead of two, these median offsets are never better than -0.9, -0.8, -0.5, and -0.4 Gyr for  $t_5$ ,  $t_{10}$ ,  $t_{25}$ , and  $t_{\text{mw}}$ , respectively. In Appendix A, we show other combinations explored for the SED-fitting parameters.

We have included on the top of each panel the ratio between the  $t_k$  of our 2D-SPS method and their ground-truth values. In general, we do not see any systematic effect as a function of redshift, but we do find our  $t_{25}^{\text{2D-SPS}}$  and  $t_{\text{mw}}^{\text{2D-SPS}}$  tend to underestimate ground-truth in some galaxies as the ground-truth  $t_k$  increases:  $t_{25}$  ( $t_{\text{mw}}$ ) presents a median systematic offset of only  $\sim 5\%$  ( $-2\%$ ) with respect to ground-truth for lookback times younger than 2 (1.5) Gyr, but  $\sim -13\%$  ( $-16\%$ ) for older lookback times. We do not see this behavior in the case of  $t_5$  and  $t_{10}$ , which present a median systematic offset of less than  $\sim 6\%$  for ages younger and older than 2 Gyr. A possible interpretation for this bias in  $t_{25}$  and  $t_{\text{mw}}$  observed for some low-redshift galaxies could have its origin in the double-burst SFH model assumed for the 2D-SPS analysis. This model causes the galaxy SFH to usually rise quickly in later epochs due to the presence of the young population burst (see the median 2D-SPS galaxy SFH in Fig. 5.8). As a consequence of this late and rapid increase in the SFR, the middle of the SFH necessarily presents lower SFR in order to reproduce the given final light or mass, which would produce a bias when deriving those formation times of the galaxy that are more sensitive to this middle part of the SFH, i.e.,  $t_{25}$  and  $t_{\text{mw}}$ . Since low-redshift galaxies have a more extended and possibly more complex SFH than galaxies at high-redshift, this effect would be more noticeable in them.

Regarding the precision of our method, we find the scatter values are relatively small and similar for all  $t_k$ , but we observe the scatter tends to increase from  $t_5$  to  $t_{25}$ . Taking all this into account, we conclude that our 2D-SPS method successfully recovers  $t_5$ ,  $t_{10}$ ,  $t_{25}$  and  $t_{\text{mw}}$  for  $1 < z < 4$  massive galaxies with a  $\sim 30\%$  uncertainty and small  $\lesssim 5\%$  systematic effects.

## 5.6 Expectations for the derivation of the SFH of $z > 1$ massive galaxies with HST+JWST data

The aim of this section is to discuss when the early stages of stellar mass assembly took place in very massive galaxies. To do this, we apply stellar population synthesis in 2D on our galaxy sample at  $1 < z < 4$  and we compare the statistical results on the SFHs for the sample with the ground-truth values inferred from the simulation stellar particles. This comparison gives us information about the limitations and observational biases we will encounter when using this method on galaxy samples constructed with real data.

### 5.6.1 When did massive galaxies begin to form?

In Section 5.5, we showed that our 2D-SPS method successfully recovers  $t_5$ ,  $t_{10}$ , and  $t_{25}$  for our galaxy sample. These quantities represent the lookback times at which galaxies reach 5%, 10%, 25% of the stellar mass formed, respectively, and can be used to estimate the beginning of star formation in galaxies. To address the question of when the population of very massive galaxies began to form,

our approach consists in calculating  $t_5$ ,  $t_{10}$ , and  $t_{25}$  from a median SFH of the sample built from the 2D-SED fits. At this point, we should remind the reader that our sample consists of galaxies at  $1 < z < 4$  with  $M_\star > 10^{10} M_\odot$ , all having very massive descendants ( $M_\star > 10^{11} M_\odot$ ) at  $z = 0$ . Hence, we expect the median SFH from our 2D-SPS modeling to resemble the median SFH of very massive galaxies at  $z = 0$  over the redshift interval of our sample (where both SFHs overlap). We say *resemble* because our sample limitations might have implications on the derived SFHs, i.e., we have to consider the systematic effects introduced by not taking into account lower mass galaxies and by the relative number of galaxies selected at different redshifts in our full interval.

Since the final goal of our 2D-SPS method is to be applied on real galaxy samples at high redshift as soon as JWST data are available, we need to check first whether our results from the 2D-SED fits regarding the first episodes of stellar assembly in very massive galaxies are compatible with the ground-truth of the simulation. To address this issue, we build two additional samples of galaxies at  $z = 0$  in the simulation to be compared with our main  $1 < z < 4$  galaxy sample. For these initial three samples of galaxies, we build the typical (median) ground-truth SFH from the simulated particles in their galaxies, which will be compared with the typical SFH from the 2D-SPS analysis on the  $1 < z < 4$  studied sample of massive progenitors. The samples of galaxies in the Illustris-1 simulation considered in this section are:

- 1) Our main galaxy sample at  $1 < z < 4$  used for the 2D-SPS analysis. It consists of the 221 (out of the 248)  $M_\star > 10^{10} M_\odot$  progenitors at  $1 < z < 4$  in the S+17 images with a very massive descendant at  $z = 0$ , and which have not been discarded during the analysis procedure (see Section 5.2.2). This is the “high-redshift sample of (massive) progenitors” or “main sample”, hereafter.
- 2) The descendants at  $z = 0$  of our main  $1 < z < 4$  galaxy sample, all of them with  $M_\star > 10^{11} M_\odot$  (132 descendants). This sample is a subset of the whole population of very massive galaxies at  $z = 0$ .
- 3) The whole population of very massive galaxies ( $M_\star > 10^{11} M_\odot$ ) at  $z = 0$ . This sample is composed by 856 galaxies.

Although the main sample of this study is composed of massive progenitors of local  $M_\star > 10^{11} M_\odot$  galaxies, our selection criteria could not be applied as such to real observations where the estimation of the final mass at  $z = 0$  of observed high-redshift galaxies is not easy without additional assumptions (see also Section 2.5). To study the impact of this, we apply the same 2D-SPS method described for our main sample of  $1 < z < 4$  progenitors to the following fourth, additional sample:

- 4) All  $M_\star > 10^{10} M_\odot$  galaxies at  $1 < z < 4$  in the S+17 images, regardless of the stellar mass of their descendants at  $z = 0$ . It consists of the 350 (out of the 388) massive galaxies at  $1 < z < 4$  in the images that are not discarded when the 2D-SPS method is applied to them. This sample is a combination of our main galaxy sample of 221 massive progenitors plus other 129 massive galaxies at  $1 < z < 4$  in the images that do not reach  $M_\star > 10^{11} M_\odot$  at  $z = 0$  for any reason.

The median SFH of this sample of  $1 < z < 4$  massive galaxies built from the 2D-SPS analysis, and also the ground-truth median SFH from the simulated particles in each galaxy, will also be compared to the results of our main sample of  $1 < z < 4$  progenitors.

We remind the reader that the S+17 images only contain a limited number of galaxies from the full Illustris-1 simulation. Thus, the descendants at  $z = 0$  of the galaxies we have studied through their HST+JWST simulated imaging data are also a limited subset of all the galaxies at  $z = 0$  in the simulation (see Fig. 2.6 for a diagram of the sample of massive progenitors at  $1 < z < 4$  in the images and their  $z = 0$  descendants in Illustris). Our aim is to see if, by analyzing the SFHs for high-redshift,  $M_{\star} > 10^{10} M_{\odot}$  progenitor galaxies in the images of  $z = 0$  very massive galaxies, we can learn when the whole population of very massive galaxies began to form.

If we consider the masses of all the simulated stellar particles in galaxies, our main  $1 < z < 4$  sample of 221 galaxies accounts for only 28% of the total stellar mass present in their 132  $z = 0$  descendants, of which  $1 < z < 2$ ,  $2 < z < 3$ , and  $3 < z < 4$  galaxies in the sample would account for 33%, 23%, and 8.1% of the stellar mass in their descendants, respectively. If we also take into account the total stellar masses of less massive progenitors at  $1 < z < 4$  in the images, none of them considered by the mass cutoff, this number raises to 32% (36% for galaxies at  $1 < z < 2$ , 27% for  $2 < z < 3$ , and 11% for  $3 < z < 4$ ). This means that the remaining 68% of the stellar mass in nearby massive galaxies must be explained by either more recent *in-situ* star formation events or by subsequent mergers at  $z < 1$ . We refer the reader to Section 5.2.2 for more information about the main  $1 < z < 4$  galaxy sample and their  $z = 0$  descendants.

In Fig. 5.10 we compare the histograms for the ground-truth stellar masses of galaxies in the four samples, calculated from the simulated particles in the database. On different panels we show the histograms for the stellar masses corresponding to all particles in galaxies and to particles inside  $2 \times r_{\text{hm}}$ . In both cases, the distribution of the stellar masses for our  $1 < z < 4$  sample of massive progenitors resembles that of all massive galaxies at  $1 < z < 4$ , although the former is biased towards higher masses: the median and 68% interval are  $\log(M_{\star}/M_{\odot}) = 10.4_{10.1}^{11.0}$  vs.  $10.3_{10.1}^{10.8}$  when all particles are considered, and  $10.3_{10.0}^{10.8}$  vs.  $10.2_{10.0}^{10.6}$  for particles inside  $2 \times r_{\text{hm}}$ , respectively. Regarding the two samples of  $z = 0$  galaxies, we find that the distribution of masses for the population of very massive galaxies at  $z = 0$  and for the specific descendants are very similar:  $\log(M_{\star}/M_{\odot}) = 11.3_{11.1}^{11.7}$  vs.  $11.2_{11.1}^{11.6}$  (all particles), and  $11.1_{11.0}^{11.5}$  vs.  $11.1_{11.0}^{11.4}$  (particles inside  $2 \times r_{\text{hm}}$ ). As discussed below in this section, this difference in the median masses is a consequence of the mass-cutoff imposed for the selection of the  $1 < z < 4$  sample and will have an impact on the mass-fraction formation times of both samples. In summary, we conclude that our limited sample of progenitors would indeed provide representative results for the full population of massive galaxies at  $z = 0$ .

In Section 5.6.1.1, we calculate the median ground-truth SFH for these subsets of galaxies using only the simulated particles in them, while in subsection 5.6.1.2 we compare these results with the median SFH of our main high-redshift sample of  $M_{\star} > 10^{10} M_{\odot}$  precursors built using our 2D-SPS method. Finally, in subsection 5.6.1.3 we show the variation of the onset of star formation of massive galaxies.

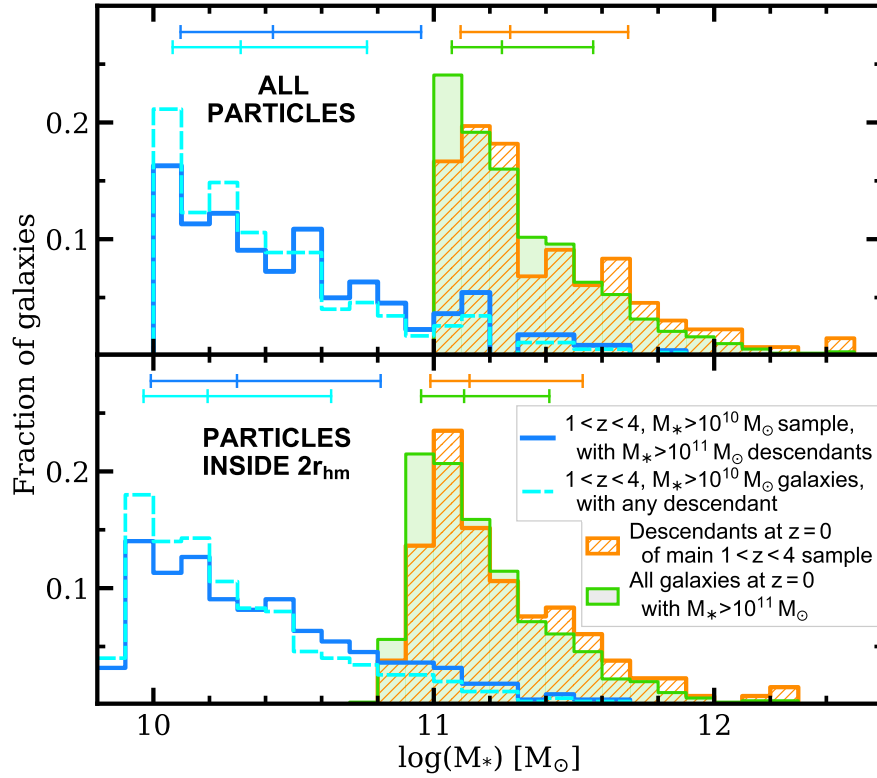


**Figure 5.10:** Ground-truth stellar mass histograms for the different samples extracted from the Illustris-1 database: when considering all particles in galaxies (top panel) or only particles inside twice the stellar half-mass radius (bottom panel). We show our main 2D-SPS sample of progenitors at  $1 < z < 4$  in blue, massive galaxies at  $1 < z < 4$  in cyan, the descendants at  $z = 0$  of our  $1 < z < 4$  progenitors in orange, and the whole population of very massive galaxies at  $z = 0$  in green. The median and the 68% intervals are shown at the top of each panel.

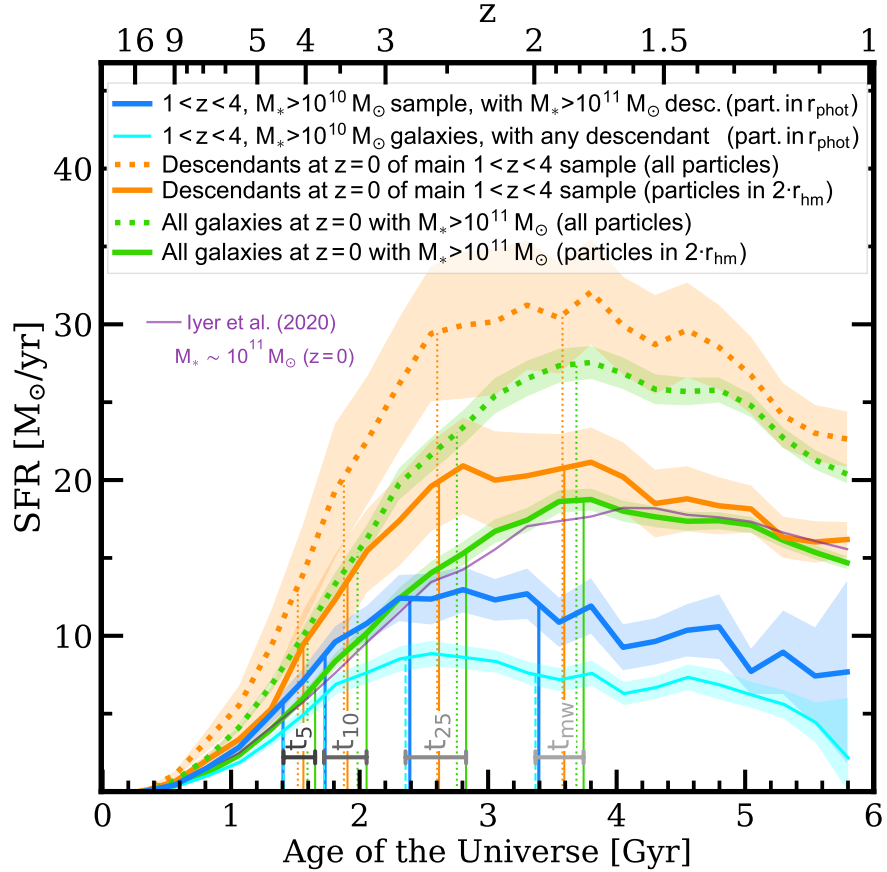
### 5.6.1.1 Ground-truth SFHs: very massive $z = 0$ galaxies in Illustris and the $1 < z < 4$ sample

Fig. 5.11 shows the sample-averaged (median) SFHs built from the Illustris simulated particles for the four different subsets of galaxies considered: the  $1 < z < 4$  main sample of  $1 < z < 4$  progenitors (blue line), massive galaxies at  $1 < z < 4$  (cyan), the descendants at  $z = 0$  of our main sample of  $1 < z < 4$  progenitors (orange lines), and all massive galaxies at  $z = 0$  in Illustris-1 (green lines). To study whether there is any aperture effect on the SFHs, the SFHs of the two subsamples of  $z = 0$  galaxies have been built by selecting simulated particles at  $z = 0$  in two different ways: either by considering all the stellar particles belonging to each galaxy (dotted lines), or only the stellar particles inside a sphere with radius  $2 \times r_{\text{hm}}$  (measured at  $z = 0$ ; solid lines). In the case of the two high-redshift samples, the radius of each sphere has been set to match the radius of the photometric aperture used for the 2D-SED fits,  $r_{\text{phot}}$ , and only particles within this radius have been considered. These typical SFHs have been smoothed using a 250 Myr square kernel. Shaded areas correspond to the uncertainty in the median SFH calculated as the 95% confidence interval:  $t_{N-1} \times \sigma / \sqrt{N}$ , where  $t$  is the  $t$  value from the  $t$ -distribution for 95% confidence,  $\sigma$  has been estimated from the dispersion

of the different SFHs, and  $N$  is the number of galaxies at each age. We only show median SFHs of the galaxies at  $z = 0$  down to  $z = 1$ , the lower limit of our main  $1 < z < 4$  sample. Additionally, we point out that the typical SFH of both samples at  $1 < z < 4$  has been calculated from different numbers of galaxies at different ages (what we would be able to perform when working with real data), in contrast to the median SFHs of the other two  $z = 0$  samples, which count with the same number of galaxies in the entire redshift range.

We remark that no normalization has been applied to the median SFHs shown in Fig. 5.11. Regarding the different absolute levels of these SFHs, these are a consequence of several factors. First, the difference in SFR values between the dotted lines with respect to the solid lines of the same color, corresponding to the  $z=0$  samples (green and orange) can be explained by the construction method of the SFH followed in each case: SFHs which have been built using all particles present generally higher SFRs than those built using only particles in  $2 \times r_{\text{hm}}$ . This is expected, since both for the population of  $z = 0$   $10^{11} M_{\odot}$  galaxies and for the  $z = 0$  descendants of the main  $1 < z < 4$  sample, the stellar mass inferred from the typical SFHs of particles within  $2 \times r_{\text{hm}}$  (i.e., the area enclosed by the SFH) is  $\sim 66\%$  of the stellar mass inferred from the typical SFH built from all the particles in galaxies. We will address the difference between the median SFH of both  $z = 0$  samples below in this section. Secondly, the average SFR values from the median SFH calculated for the  $z = 0$  samples (green and orange) is systematically higher than for the  $1 < z < 4$  samples (blue and cyan). This difference is mainly due to the fact that we calculate the SFH for each  $z = 0$  galaxy from their particles at  $z = 0$  instead of computing it after tracing and independently considering the actual precursors of the  $z = 0$  galaxy at high-redshift (unfeasible in real observations). As a consequence, the average SFR per  $z = 0$  galaxy is bigger than the average SFR per precursor, due to the lower number of galaxies considered at  $z = 0$ . In the case of the difference between the median SFH of our main  $1 < z < 4$  sample (blue) and their descendants at  $z = 0$  (solid orange for particles in  $2 \times r_{\text{hm}}$ ), there is an additional contribution based on the fact that some of the stellar mass of the  $z = 0$  descendants comes from other less massive progenitors which are not included in our main  $1 < z < 4$  sample of massive progenitors due to our mass cut-off. In addition to this, the different apertures considered for both  $1 < z < 4$  samples with respect to the other  $z = 0$  samples also plays a role in lowering the average SFR of these two high-redshift samples: the radii of the photometric apertures used to build the sphere that contains the simulated particles in these high-redshift samples are usually smaller than  $2 \times r_{\text{hm}}$  measured at the observed redshift, as explained in Section 5.3.2, and should be smaller than  $2 \times r_{\text{hm}}$  measured at  $z = 0$ . In fact, we remind the reader that the typical photometric aperture radius for our main  $1 < z < 4$  sample of progenitors is nearly 20% smaller than  $2 \times r_{\text{hm}}$  and encloses around 65% of the total stellar mass in the galaxies (see Fig. 5.3). When all massive  $1 < z < 4$  galaxies are considered, these numbers are similar: the photometric aperture has a median radius 19.8% smaller than  $2 \times r_{\text{hm}}$  and includes  $\sim 64.8\%$  of the stellar mass.

If we integrate the median SFH of both high-redshift samples over cosmic time, the difference in their SFR levels leads to our main  $1 < z < 4$  sample (in blue) recovering a stellar mass of 0.17 dex higher than for all  $1 < z < 4$  massive galaxies (cyan). This is a likely consequence of our main  $1 < z < 4$  sample containing only massive progenitors of local  $10^{11} M_{\odot}$  galaxies, and these progenitors, in order to reach such elevated stellar masses at  $z = 0$ , are expected to be more massive (in average) and have higher SFRs than ordinary massive galaxies at the sample redshift range. In fact, our main  $1 < z < 4$  progenitors sample has a median stellar mass 0.08 dex higher than all



**Figure 5.11:** Ground-truth median SFHs calculated from the simulated particles for the subsamples of galaxies: all  $M_{\star} > 10^{11} M_{\odot}$  galaxies at  $z = 0$  (green lines), all massive galaxies at  $1 < z < 4$  (cyan), our main  $1 < z < 4$  progenitors sample (blue), and the descendants at  $z = 0$  of this high-redshift sample of progenitors (orange). The results from the 2D-SPS analysis are not included in this figure. The median SFHs for the  $z = 0$  subsets have been calculated in two ways: considering all the particles in galaxies (dotted lines) or only the particles inside a sphere with radius  $2 \times r_{\text{hm}}$  to the galaxy center (solid). The median SFH of the two high-redshift samples has been built using only particles whose distance to the galaxy center is lower than the radius of the photometric aperture used for each galaxy. Shaded areas represent the uncertainty of the median. As vertical lines, we show the  $t_5$ ,  $t_{10}$ ,  $t_{25}$ , and  $t_{\text{mw}}$  calculated for each SFH shown. As a comparison, we show in purple the median SFH calculated in Iyer et al. (2020) for all galaxies at  $z = 0$  in the Illustris simulation with  $M_{\star} \sim 10^{11} M_{\odot}$ .

$1 < z < 4$  massive galaxies (for particles inside  $r_{\text{phot}}$ ) and a SFR (in  $r_{\text{phot}}$ , median and quartiles) of  $16_7^{31}$  vs.  $11_5^{23}$   $M_{\odot}/\text{yr}$  for all massive galaxies at  $1 < z < 4$ .

In Fig. 5.11, we also show with vertical lines the mass-fraction formation times  $t_5$ ,  $t_{10}$ ,  $t_{25}$ , and  $t_{\text{mw}}$  calculated by integrating each sample-averaged SFH over cosmic time. As mentioned before, we only take into account for these calculations the stellar mass formed in each SFH at ages of the Universe below that of the minimum redshift of our main  $1 < z < 4$  sample ( $z \sim 1$ ), as at lower redshifts we lack information on the photometric properties of any of the galaxies in this sample-averaged SFH. This means we only consider the  $z > 1$  part of the median SFHs for the  $z = 0$  galaxy subsets and the whole SFH for the high-redshift samples. We find the mass-fraction formation times for the SFH of the high-redshift samples (blue and cyan) are systematically shifted towards earlier times (expressed in terms of the age of the Universe; or correspond to older lookback times), than the ones for the descendants at  $z = 0$  of our main sample (orange), and these, in turn, are younger than those from the whole population of massive galaxies at  $z = 0$  (green). These  $\sim 200$ – $400$  Myr shifts ( $\sim 10\%$  in relative terms) could be explained by a progenitor bias, which appears as a consequence of the mass cutoff of  $M_{\star} > 10^{10} M_{\odot}$  imposed on our main sample selection. We first focus on the younger (or earlier) formation epochs of the descendants (orange) with respect to those of all the very massive galaxies at  $z = 0$  (green). The mass cutoff makes the sample of  $z = 0$  descendants to be biased towards larger masses and more massive galaxies tend to present older stellar population ages. In contrast, when taking into account all  $M_{\star} > 10^{11} M_{\odot}$  galaxies at  $z = 0$ , i.e., a complete sample of local massive galaxies, we obtain slightly later formation ages. In fact, as it can be seen in Fig. 5.10, the median and quartile stellar masses are  $0.1 - 0.2$  dex larger for the descendants of our sample of  $M_{\star} > 10^{10} M_{\odot}$  galaxies at  $1 < z < 4$  compared to the complete sample of  $M_{\star} > 10^{11} M_{\odot}$   $z = 0$  galaxies. In addition, our mass cut at  $1 < z < 4$  implies losing  $17\%$  of massive  $M_{\star} > 10^{11} M_{\odot}$  galaxies at  $z = 0$ .

Indeed, this progenitor bias also explains why the time-averaged SFR for  $z = 0$  descendants (orange) is higher than that for the population of very massive galaxies (green). This applies to the galaxy apertures considered in Fig. 5.11 (for which no mass-normalization has been applied). The differences increase for ages corresponding to smaller fractions of the total stellar mass. Furthermore, both for all massive galaxies at  $z = 0$  and for  $z = 0$  descendants of the main high-redshift sample, mass-fraction formation times are older (smaller values in age of the Universe) when all stellar particles are included in the SFH computation than when considering only those inside  $2 \times r_{\text{hm}}$ . This may be explained by an outward migration of stars, which would result in larger apertures adding a larger fraction of older stars in the SFH computation and, consequently, earlier formation times.

Regarding the shift to earlier formation times of the main progenitors sample (blue) with respect to the  $z = 0$  descendants (orange), possibly also due to the progenitor bias, we propose a similar explanation as the one given above. Our main sample of massive progenitors at  $1 < z < 4$  is only a biased subset (cut in mass and with a given redshift distribution) of all the progenitors that evolve to a galaxy from the whole sample of  $z = 0$  descendants. The descendants, as mentioned above, also have other progenitors that do not fulfill the mass cutoff at  $z > 1$  and which may have undergone a merger with a galaxy from our main  $1 < z < 4$  sample at a lower redshift. These minor progenitors at  $1 < z < 4$  would not be included in the SFH of the (massive) progenitors sample, and they would probably host younger stellar populations, which would explain the shift towards more recent formation times for their  $z = 0$  descendants.



Finally, we notice that the ground-truth formation times for our main  $1 < z < 4$  sample of precursors (in blue) are almost identical to the ones derived for all the  $1 < z < 4$  massive galaxies (cyan), with (relative) differences of less than 34 Myr (1.4%) in all cases. This suggests that, although our main progenitors sample accounts for approximately two thirds of all the  $M_{\star} > 10^{10} M_{\odot}$  galaxies at  $1 < z < 4$ , we can estimate the formation times of local  $M_{\star} > 10^{11} M_{\odot}$  descendants by considering all the massive galaxies at the same redshift range.

### 5.6.1.2 Recovering the SFH of massive galaxies with 2D-SPS modeling of HST+JWST data

We now calculate the median SFH of the main  $1 < z < 4$  galaxy sample obtained from the 2D-SED fits (not from the Illustris database, as done in Section 5.6.1.1). For this calculation, we take the median SFH for each galaxy in this sample constructed from the 2D-SPS analysis (see Section 5.4.2), normalize each galaxy SFH to recover the median stellar mass (without remnants or yields) given by its integrated SED-fits, and combine all these normalized galaxy SFHs to build the median (or typical) SFH for the whole sample. We remark that this implies that the SFR at a given age of the Universe involves the combination of a different number of galaxies, namely, all that lie at lower redshifts compared to the redshift corresponding to that age of the Universe.

Fig. 5.12 shows this median SFH of the main  $1 < z < 4$  progenitors sample derived from the 2D-SED fits (red solid line). We compare this SFH, which could be obtained following the same procedure on real galaxy samples when JWST (plus HST) data are available, with the ground-truth. First, we compare with the averaged SFH for the same main sample of  $1 < z < 4$  precursors but built from the simulated particles inside the radius of the photometric aperture (blue). This comparison allows to evaluate the accuracy of our method. We also compare with the SFH of  $z = 0$  descendants using the stellar particles inside  $2 \times r_{\text{hm}}$  (orange). This comparison allows us to understand the bias of a sample based on imaging data linked to selection effects. The two latter comparison SFHs are the same shown in Fig. 5.11, but normalized to recover the same stellar mass as the median 2D-SPS-derived SFH of our main  $1 < z < 4$  sample ( $10^{10.57} M_{\odot}$  at  $z = 1$ ). Note that, without normalization, the corresponding stellar masses at  $z = 1$  would be  $\log(M_{\star}/M_{\odot}) = 10.67$  for the median ground-truth SFH of this high-redshift sample and 10.91 for the median SFH of their descendants at  $z = 0$  (built from particles inside  $2 \times r_{\text{hm}}$ ). As commented in Section 5.6.1.1, the difference in the mass recovered by the SFH of our main  $1 < z < 4$  of massive progenitors and the  $z = 0$  descendants is caused by the reduction in the multiplicity of galaxies when calculating galaxy averages at  $z = 0$ , the presence of less massive galaxy branches for the  $z = 0$  descendants which are not included in our main  $1 < z < 4$  sample due to the mass cut-off, and the smaller aperture radius (in average) used to calculate the galaxy SFHs for the  $1 < z < 4$  sample. Shaded areas correspond to the uncertainty in the median SFH calculated as the 95% confidence interval. Finally, we have calculated the median SFH derived from applying the 2D-SPS analysis to all  $1 < z < 4$  massive galaxies in S+17, following the same procedure than that described for our main  $1 < z < 4$  sample of progenitors. This new median SFH, also normalized to the same mass as the others, is shown in pink. For clarity, we have not included the uncertainties of this last median SFH.

We find that the general shapes of the four SFHs shown are not very different from each other, except for the SFR increase in the last 0.5-1.0 Gyr (near  $z = 1$ ) in the SFHs built from the 2D-SPS analysis (in red and pink). The SFH of our main sample of precursors built from the 2D-SED

fits (red) follows the general trend of the SFH built from the simulated particles in the sample (blue), but for this raise, and this also happens for the 2D-SPS-derived SFH of massive galaxies at  $1 < z < 4$  (pink). The number of galaxies considered in the calculation of the SFHs for the high-redshift samples drops as the redshift decreases (as clearly seen in the increase of uncertainties). Thus, there are fewer galaxies near  $z = 1$  from which to calculate the typical SFH and, when averaging, the weight of any individual galaxy SFH is bigger. The individual galaxy SFHs built from the 2D-SPS, as explained in Section 5.4.1, are the combination of the SFH of one young and one old stellar population. This causes the galaxy SFHs built from the 2D-SED fits to normally have a peak in SFR near the redshift of the galaxy, which is not necessary present in the galaxy SFH built from the simulated particles (see, for example, the median 2D-SPS galaxy SFH shown in Fig. 5.8). At higher redshifts, these individual peaks, if present, are not reflected in the median SFHs not only because the SFH is averaged over more galaxies but also because these individual peaks in SFR are located at varying redshifts and distributed across a wide time span. On the contrary, near  $z \sim 1$ , where the number of galaxies drops, we pile up some of these peaks and this is reflected in the median SFHs from the 2D-SPS analysis.

In Fig. 5.12, we include the SFR values expected from the Illustris SFMS at  $z = 1, 2,$  and  $4$  (Sparre et al. 2015) for the stellar masses obtained by integrating our median 2D-SPS SFH of progenitors down to each of those redshifts. We remind the reader that this median 2D-SPS SFH, like other SFHs in Fig. 5.12, has been normalized to recover the median galaxy stellar mass (without including remnants or yields) of the main  $1 < z < 4$  sample of progenitors given by the integrated SED-fits. We find that our median SFR values (in red in Fig. 5.12) are consistent within the errors with those expected from the SFMS in Sparre et al., although the agreement observed for the  $z \sim 1$  SFMS value with respect to our median SFR at that redshift is probably caused by the spurious rise of the SFR in this median SFH at  $z \sim 1$  (due to the second peak of star formation in the individual galaxy SFHs). On the top panel, we show the evolution of stellar mass assembly for our main high-redshift sample, calculated both from the median SFH of the 2D-SPS analysis of these progenitors (in red) and that of their stellar particles in  $r_{\text{phot}}$  (blue).

The mass-fraction formation times for each SFH in the figure are shown as vertical lines. We remark the good agreement between the  $t_5$  and  $t_{10}$  formation times derived for our main high-redshift sample of precursors using the 2D-SED fits (red) and the simulated particles (blue), with (relative) differences of -29 (-2.1%) and -9 Myr (-0.5%) in age of the Universe, respectively, with the ground-truth values being larger. Additionally, the differences in the other two formation times, although higher, are also low: +107 (+4.5%) and +149 Myr (+4.4%) for  $t_{25}$  and  $t_{\text{mw}}$ , respectively, with larger values from the 2D-SED fits. Regarding the comparison of these formation times for the main high-redshift sample (2D-SPS and particles) with their  $z = 0$  descendants (orange), the agreement is also good, with maximum (relative) differences in age of the Universe of -188 (-12%), -184 (-9.7%), -227 (-8.7%), and -199 Myr (-5.5%) for  $t_5, t_{10}, t_{25}$  and  $t_{\text{mw}}$ , respectively, and 74 (5.5%), 59 (3.5%), 112 (4.7%), and 98 Myr (2.8%) when the main progenitors sample is compared to all massive galaxies at  $1 < z < 4$  (pink). As mentioned before, the older values of the  $t_5, t_{10}$  and  $t_{25}$  formation times for the high-redshift sample with respect to the  $z = 0$  descendants are due to the progenitor bias.

According to the 2D-SPS analysis of our main  $1 < z < 4$  sample, local  $M_\star > 10^{11} M_\odot$  galaxies would have formed 5% of their stellar mass at  $z \sim 1$  by  $z = 4.5$ , 10% of their mass by  $z = 3.7$ , and 25% by  $z = 2.7$ . These redshifts correspond to ages of the Universe of 1.4, 1.7, and 2.5 Gyr,

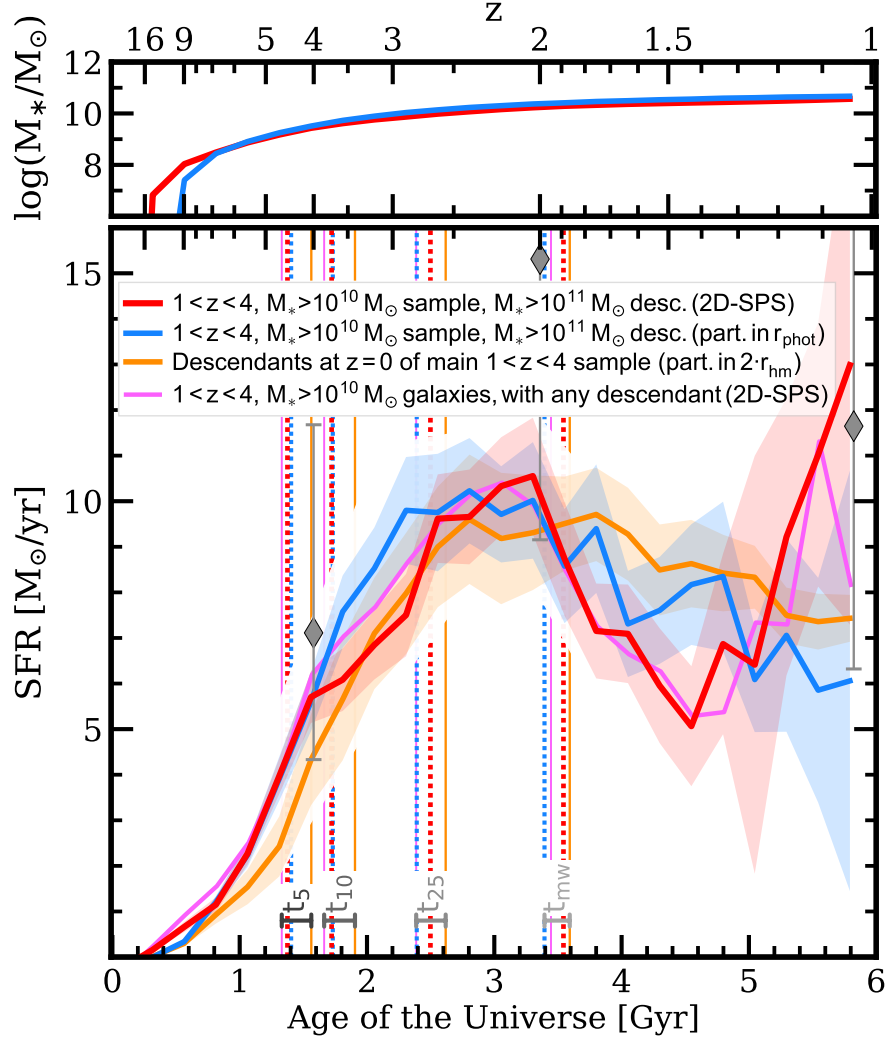


**Figure 5.12:** Comparison between the median SFH of our main  $1 < z < 4$  progenitors sample derived from the 2D-SED fits (in red) and from the simulated particles (in blue). We also include the median SFH of the descendants of this high-redshift sample at  $z = 0$  built with particles inside  $2 \cdot r_{\text{hm}}$  (in orange) and the median SFH of massive galaxies at  $1 < z < 4$  derived from applying the 2D-SPS method to this sample (pink). Shaded areas represent the uncertainty of the median. The SFHs have been normalized to recover the same stellar mass as the median 2D-SPS-derived SFH of our main  $1 < z < 4$  sample over the same redshift intervals ( $z \gtrsim 1$ ). The vertical lines depict the  $t_5$ ,  $t_{10}$ ,  $t_{25}$ , and  $t_{\text{mw}}$  mass-fraction formation times for each SFH. Gray diamonds show the Illustris SFMS level at  $z = 1, 2$ , and  $4$  (Sparre et al. 2015). On the top panel, we show the evolution of the integrated stellar mass at each redshift for our main high-redshift sample (2D-SPS and particles, same color code).

respectively. This is equivalent to saying that 5% of the stellar mass present in very massive local galaxies at  $z \sim 1$  was already assembled when the Universe was only  $\sim 10\%$  of its current age, 10% of the mass by 13% of its age, and 25% of the mass by 18% of the cosmic time.

The first star formation episodes for these galaxies are located at  $z = 16 \pm 1$  (calculated as the median redshift where the SFR starts to be larger than 0). Then it would rise up to  $z \sim 3$ . After that, it would remain approximately constant down to  $z \sim 2$ , and a slightly decreasing trend would follow. This can be clearly seen in the ground-truth SFH derived from the simulated particles in the database and agrees with the median SFHs calculated in Iyer et al. (2020) for  $10^{10.75} < M_{\star} < 10^{11.25} M_{\odot}$  galaxies at  $z = 0$  in the Illustris simulation (considering all the particles in galaxies). Nevertheless, we hardly reproduce the most recent part of the SFH from the 2D-SPS analysis, where our method begins to fail. We note that our 2D-SED fitting method was calibrated in order to successfully reproduce the first instants of the stellar mass assembly in massive galaxies, i.e.,  $t_5$ ,  $t_{10}$ ,  $t_{25}$ , along with  $t_{\text{mw}}$ . Thus, even though we successfully determine these mass-fraction formation times for the typical SFH of massive galaxies, our method fails to reproduce this SFH at higher ages of the Universe. However, the recovery of the whole SFH of massive galaxies and, consequently, their typical SFH throughout the whole redshift range, is beyond the scope of this work.

We do not find any *starburst epoch* in the typical SFH from the 2D-SPS analysis on the main  $1 < z < 4$  sample of progenitors, and the other SFHs from the simulated particles, albeit 34% (13%) of galaxies in our  $1 < z < 4$  progenitors sample reach 50 (100)  $M_{\odot}/\text{yr}$  at some time of their 2D-SPS-derived galaxy SFHs because of the young population assumptions in the SED-fits. These starburst episodes are also present in the ground-truth SFHs of this main  $1 < z < 4$  sample of progenitors with similar numbers: 31% (14%) of galaxies reach 50 (100)  $M_{\odot}/\text{yr}$  at some time of their ground-truth galaxy SFH. Starburst events, which are usually short-lived,  $\sim 100$  Myr (Tacconi et al. 2008, Wuyts et al. 2011, Espino-Briones et al. 2022), have been proven to occur during the evolution of some galaxies, as it can be inferred from the high SFR values of Main Sequence outliers or those of the population of very luminous high-redshift submillimeter galaxies, discovered by Smail et al. (1997). The reason why these brief intense star formation episodes are not present in our median SFHs is that they averaged out when we consider a whole population of galaxies, in the same way that they do not appear when calculating the cosmic star formation history (Madau & Dickinson, 2014). In addition to this, the Illustris simulation is known to have a paucity of strong starburst galaxies, i.e., a fewer fraction of galaxies that lie significantly above the SFMS when compared to observations (Sparre et al. 2015), which appears to be a consequence of the insufficient resolution of Illustris to resolve the sub-kiloparsec starbursting regions (Sparre & Springel 2016).

### 5.6.1.3 The variety of the start of SFHs in massive galaxies

Finally, we briefly concentrate on when the star formation started for the individual galaxies in the subsamples. We assume the start of the star formation for each galaxy can be given by its  $t_5$  (calculated from their individual galaxy SFH) or, even, by its  $t_1$ .

Fig. 5.13 shows the diversity in the values of  $t_5$  (left) and  $t_1$  (right) for the main sample of progenitors at  $1 < z < 4$  (2D-SPS method and ground-truth from particles in  $r_{\text{phot}}$ ), their descendants at  $z = 0$  (ground-truth from particles inside  $2 \times r_{\text{hm}}$ ), the whole population of very massive galaxies

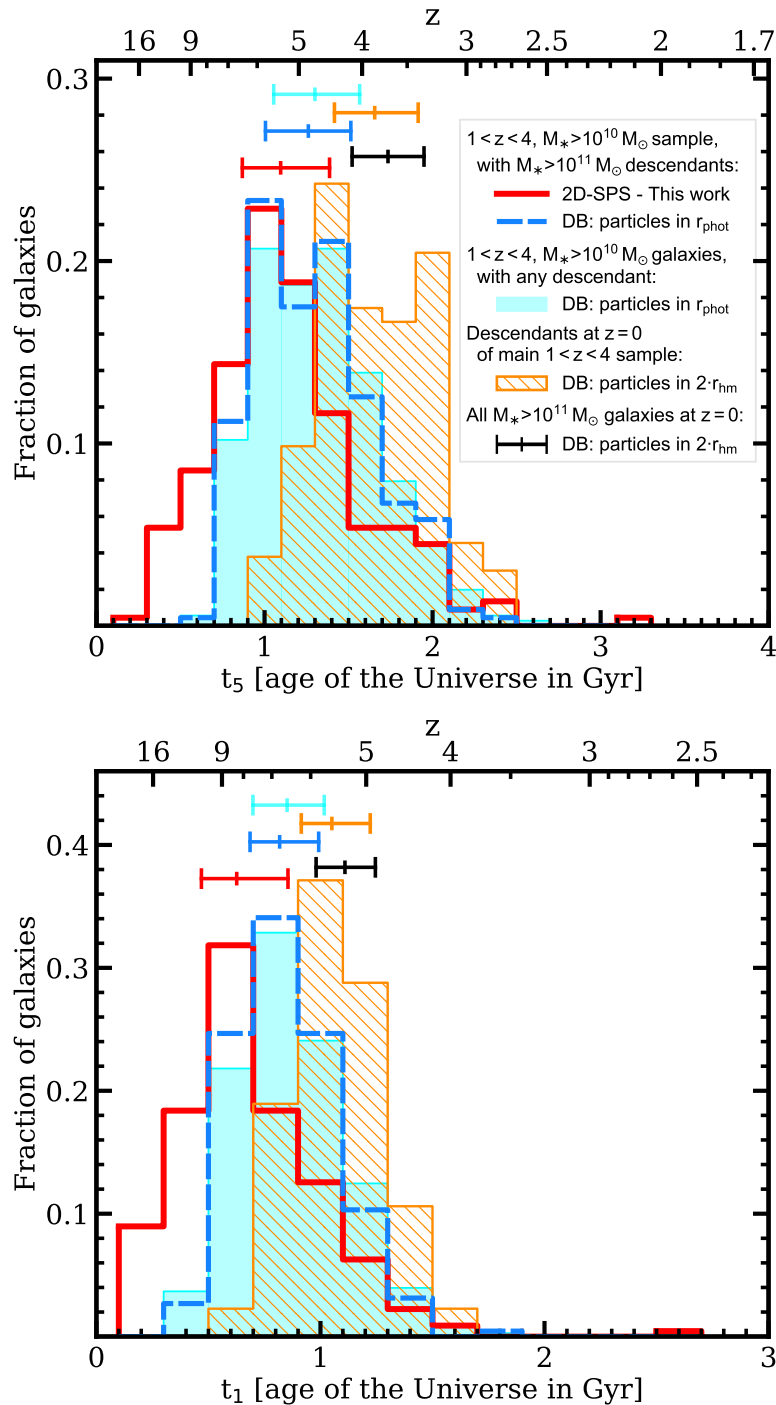


**Figure 5.13:** Histograms of  $t_5$  and  $t_1$  calculated from the SFHs of galaxies in the different samples considered. Our main  $1 < z < 4$  sample of progenitors is represented by the outlined histograms: values calculated from the 2D-SPS-derived galaxy SFHs are outlined in red, while those calculated from the ground-truth SFHs built from the database (DB) are represented with a dashed blue line. For the 2D-SPS-derived values, we only show the median  $t_5$  or  $t_1$  for each galaxy (calculated out of the 300 SFHs per galaxy). The cyan, filled histogram represents the distribution of the ground-truth  $t_5$  and  $t_1$  for massive galaxies at  $1 < z < 4$ , calculated from the ground-truth SFHs built by considering only particles inside  $r_{\text{phot}}$  in the database. The ground-truth distribution for the  $z = 0$  descendants of our main sample is shown as the orange, hatched histogram. For the whole population of very massive galaxies at  $z = 0$ , only its median and quartile values are shown (black segments). For these two  $z = 0$  samples, only particles inside  $2 \times r_{\text{hm}}$  have been considered. Median and quartiles are shown as segments on the top.

**Table 5.4:** Mass-fraction formation times and redshifts for different samples in Chapter 5.

Galaxy subset		SFHs from	$t_5$	$t_{10}$	$t_{25}$	$t_{\text{mw}}$	$z_5$	$z_{10}$	$z_{25}$	$z_{\text{mw}}$
(1)	$1 < z < 4$ , $M_\star > 10^{10} M_\odot$ sample with $M_\star > 10^{11} M_\odot$ descendants	2D-SED fits ( $r_{\text{phot}}$ )	$1.4^{1.7}_{1.1}$	$1.7^{2.1}_{1.5}$	$2.5^{3.1}_{2.2}$	$3.6^{4.1}_{3.2}$	$4.5^{5.2}_{3.8}$	$3.7^{4.2}_{3.1}$	$2.7^{2.9}_{2.2}$	$1.9^{2.1}_{1.6}$
		Particles in $r_{\text{phot}}$	1.40	1.73	2.39	3.39	4.41	3.70	2.78	1.98
(2)	Descendants at $z = 0$ of main $1 < z < 4$ sample	Particles all	1.52	1.88	2.60	3.58	4.14	3.45	2.57	1.87
		Particles in $2 \times r_{\text{hm}}$	1.56	1.91	2.62	3.59	4.04	3.41	2.56	1.86
(3)	All galaxies at $z = 0$ with $M_\star > 10^{11} M_\odot$	Particles all	1.60	1.98	2.76	3.69	3.97	3.29	2.43	1.81
		Particles in $2 \times r_{\text{hm}}$	1.66	2.05	2.83	3.74	3.85	3.19	2.37	1.78
(4)	$1 < z < 4$ , $M_\star > 10^{10} M_\odot$ galaxies with any descendant	2D-SED fits ( $r_{\text{phot}}$ )	1.33	1.66	2.39	3.45	4.61	3.83	2.79	1.95
		Particles in $r_{\text{phot}}$	1.41	1.72	2.36	3.37	4.40	3.72	2.82	1.99

**Notes:** Values have been calculated from the SFHs shown in Figs. 5.11 and 5.12. The mass-fraction formation times are measured in Gyr from Big Bang.

at  $z = 0$  (particles inside  $2 \times r_{\text{hm}}$ ), and massive galaxies at  $1 < z < 4$  (ground-truth from particles inside  $r_{\text{phot}}$ ). For clarity, in the case of the population of very massive galaxies at  $z = 0$  we do not include the histogram but only its statistical values (median and quartiles). The median values of both  $t_5$  and  $t_1$  for the main  $1 < z < 4$  progenitors sample given by the 2D-SPS (in red) are consistent with the ground-truth (in blue) for this sample (with differences of 0.26 and 0.19 Gyr, respectively), even though the histogram for our 2D-SPS method predicts that some galaxies start to form a bit earlier ( $\sim 0.2$ - $0.4$  Gyr earlier) than expected according to the database. These differences are already visible in Fig. 5.12, where the SFH corresponding to the 2D-SPS analysis (red curve) rises faster in the beginning than that of the simulated particles (in blue). Regarding the distributions of the two subsamples at  $z = 0$  (descendants of the main  $1 < z < 4$  sample in orange and the whole populations of  $M_\star > 10^{11} M_\odot$  galaxies in black), their median  $t_5$  and  $t_1$  are similar and also consistent with each other. This also happens with the ground-truth values of massive galaxies at  $1 < z < 4$  (in cyan) and our main  $1 < z < 4$  sample (in blue), and, consequently, suggests again that the whole population of massive  $1 < z < 4$  galaxies tends to reproduce the earliest formation times of actual massive progenitors (at the same high-redshift range) of  $M_\star > 10^{11} M_\odot$  galaxies at  $z = 0$ .

Fig. 5.13 can be useful if we want to know where to look for the first star formation episodes in massive galaxies. According to the ground-truth distribution of  $t_5$  and  $t_1$  for the main  $1 < z < 4$  sample of massive progenitors (in blue), 25% of these galaxies would have formed 1% (5%) of its stellar mass by  $z \sim 8$  (6), and 50% of the galaxies by  $z \sim 7$  (5).

In Table 5.4, we summarize the mass-fraction formation times (and corresponding redshifts) for all the SFHs shown in Figs. 5.11 and 5.12. We have calculated an estimation of the uncertainties for the 2D-SPS-derived values of the main sample of  $1 < z < 4$  progenitors by taking into account the (300) individual SFHs for each galaxy and by calculating the mass-fraction formation times for all of them. We estimate the uncertainty for the 2D-SPS-derived formation times as the quartile values of these distributions.

## 5.7 Summary and conclusions

We assess the power of broad-band HST+JWST imaging data for the analysis of the earliest evolutionary phases of galaxies that evolve into local massive objects ( $M_{\star} > 10^{11} M_{\odot}$ ) by analyzing the SFHs of progenitors at high redshift in deep cosmological surveys. For that purpose, we apply stellar population synthesis in 2D to a sample of 221 Illustris-1 simulated  $M_{\star} > 10^{10} M_{\odot}$  galaxies at  $1 < z < 4$  that evolve into  $M_{\star} > 10^{11} M_{\odot}$  galaxies at  $z = 0$ . We use ACS, WFC3, and NIRCcam data in the optical and near-infrared from the synthetic Illustris-1 deep survey images (S+17). We measure SEDs for galaxies in the sample from both integrated and 2D multi-wavelength photometry on these images, previously processed to mimic the depths of CANDELS imaging data from HST and ongoing CEERS observations with JWST along with the source extraction and analysis procedures to be applied to data from these surveys. From the SED modeling, we derive the SFH of each source by combining the 2D information from the fits, and compare it with the ground-truth SFH given by the simulated particles belonging to each galaxy in the Illustris-1 database. In this work, we focus on determining the capabilities of broad-band HST+JWST for determining the first episodes in the stellar mass assembly, and our main findings are the following:

(i) We evaluate the success of our 2D-SPS method in recovering the earliest phases of the stellar mass assembly by comparing the mass-fraction formation times  $t_5$ ,  $t_{10}$ , and  $t_{25}$  calculated for each galaxy from its 2D-SPS-derived galaxy SFH with those given by its ground-truth SFH. We find that our 2D-SPS method successfully recovers these quantities with a median relative offset between our values and ground-truth of +4.4%, +1.8%, and  $-0.1\%$  for  $t_5$ ,  $t_{10}$ , and  $t_{25}$ , respectively, and scatters of 0.21, 0.24, and 0.28 dex. Additionally, no systematic effects are observed as a function of galaxy redshift.

(ii) We build the median SFH of our main  $1 < z < 4$  sample of precursors from the 2D-SPS-derived individual galaxy SFHs to infer the mass-fraction formation times of the sample as a whole. Thus, local  $M_{\star} > 10^{11} M_{\odot}$  galaxies would have assembled 5% of their stellar mass present at  $z \sim 1$  by  $z = 4.5$ , 10% of their mass by  $z = 3.7$ , and 25% by  $z = 2.67$ , or equivalently, when the age of the Universe was 1.38, 1.72, and 2.50 Gyr, respectively. These ages agree with their ground-truth values derived from the typical SFH built from the simulated particles of galaxies in the sample, with relative differences of  $-2.1\%$ ,  $-0.5\%$ , and  $+4.5\%$  for  $t_5$ ,  $t_{10}$ , and  $t_{25}$ , respectively. Nevertheless, our method fails to reproduce the shape of this SFH for at  $z \lesssim 1$ , mainly because of the second star formation peaks in the 2D-SPS-derived galaxy SFHs (caused by the second burst assumed in the functional form of the SFHs) which accumulate at this redshift range.

(iii) We compare the formation times derived from the 2D-SPS analysis for this main sample of precursors with the values obtained from the ground-truth median SFH at  $z < 1$  of local  $M_{\star} > 10^{11} M_{\odot}$  galaxies and of the descendants of this high-redshift sample. The mass-fraction formation epochs from the 2D-SPS are systematically earlier than those inferred from the descendants of this sample. Besides, the latter are higher than the ones inferred from the whole population of  $M_{\star} > 10^{11} M_{\odot}$  galaxies. In both cases, these shifts in the formation redshifts, of  $\sim 200$ -400 Myr, are due to the progenitor bias. This bias arises as a consequence of the mass cut-off imposed on the high-redshift progenitor sample, aimed at reproducing the selection suffered in actual HST+JWST survey observations, and which makes this sample to contain only the most massive (and, thus, older) progenitors of local  $M_{\star} > 10^{11} M_{\odot}$  galaxies. Given the way our progenitor sample has been

selected, their descendants at  $z = 0$  also present a median stellar mass that is slightly higher than the whole population of local  $M_{\star} > 10^{11} M_{\odot}$  galaxies, which leads to mass-fraction formation times closer to the Big Bang.

(iv) With the aim of comparing our results with those that will be inferred from CEERS observations, we perform the same analysis on all the  $1 < z < 4$   $10^{10} M_{\odot}$  galaxies in the processed S+17 images. We find that the formation times derived from the median SFH of this sample are very similar to the ones inferred from our original sample of massive precursors with a local  $M_{\star} > 10^{11} M_{\odot}$  descendant (differences of  $< 1.4\%$  in all the formation times when considering the ground-truth particles and  $< 4.7\%$  from the 2D-SPS analysis). This suggests that we can consider all massive  $1 < z < 4$  galaxies observed with CEERS (+CANDELS), regardless of their actual  $z = 0$  descendant, to study the formation times of the most massive descendants at  $z = 0$ .

(v) Regarding the variety of the  $t_1$ , and  $t_5$  values, the distribution of these formation times shows that 25% of our main  $1 < z < 4$  sample of progenitors formed 1% (5%) of their stellar mass present at the redshift of observation by  $z \sim 8$  (6), and 50% of the galaxies by  $z \sim 7$  (5).

The results from this work show that our 2D-SPS method, when applied to real CANDELS + CEERS spatially-resolved broad-band observations of massive  $1 < z < 4$  galaxies, will be able to infer when the early stages of the stellar mass assembly took place in these galaxies and, from them, have an estimation of when local  $10^{11} M_{\odot}$  galaxies began to form, within the limitations and biases already discussed throughout this chapter.

We caution the reader that the numerical values of the mass-fraction formation times and other quantities shown in this work are unique to *Illustris-1*, since they are dependent on the specifications of the simulation, such as the assumed cosmology, the volume and resolution of the simulation, the physical models for galaxy formation (e.g., the star formation and feedback implementations) and on any free parameter. Thus, the values presented in this chapter for *Illustris-1* are not expected to be necessary similar to those obtained from other simulations like, for example, the *IllustrisTNG* project (Marinacci et al. 2018; Naiman et al. 2018; Nelson et al. 2018; Pillepich et al. 2018b; Springel et al. 2018), follow-up of the *Illustris* simulation which includes as main changes in the physics the incorporation of magnetohydrodynamics and updates in the feedback physics model, among others updates. This new *IllustrisTNG* series alleviates some of the tensions present between the outcome of the original *Illustris* simulations and observations (see Pillepich et al. 2018c), such as, for example, the (too) high cosmic star-formation rate density predicted by *Illustris* at  $z \leq 1$ , the excess in the stellar mass function at  $z \lesssim 1$  at the low ( $\lesssim 10^{10} M_{\odot}$ ) and the high ( $\gtrsim 10^{11.5} M_{\odot}$ ) mass end, the excessively large physical extent for  $M_{\star} \lesssim 10^{10.7} M_{\odot}$  galaxies (a factor of few larger than observed), or the overpopulation of the blue cloud and green-valley with respect to the red sequence in the galaxy color distribution (see full list in Nelson et al. 2015). An interesting matter to discuss when HST+JWST measurements are available will be to tell whether the prescriptions assumed for *Illustris-1*, *IllustrisTNG* or any other simulation are good enough to reproduce the mass-fraction formation times observed for massive high-redshift galaxies or if, on the contrary, they must be used as constraints to refine new galaxy formation models.



# Earliest phases in the formation of massive galaxies at $1 < z < 4$ from spatially-resolved Star Formation Histories

---

## 6.1 Introduction

In Chapter 5, we described and tested a method to probe the first stages of the stellar mass assembly of massive ( $M_{\star} > 10^{10} M_{\odot}$ ) galaxies at  $1 < z < 4$  using stellar population synthesis in 2D (2D SPS) with synthetic imaging data from the Illustris cosmological simulation (see also García-Argumániz et al. 2023).

The aim of this chapter, which constitutes the main objective of this thesis, is to apply the method to real data and to study the early assembly of galaxies by applying our 2D-SPS method to massive,  $1 < z < 4$  galaxies observed with NIRCcam data from JWST in the CEERS survey. These data are combined with previous spatially-resolved HST/ACS data in the optical from CANDELS of the same fields (Grogin et al. 2011; Koekemoer et al. 2011). We will present the results of the application of this method to our recently completed (CANDELS+)CEERS observations and resulting spatially-resolved SEDs, which will be published in the second paper (in prep.).

Throughout this chapter, we assume the same cosmology as specified in Planck Collaboration et al. (2020): a  $\Lambda$ CDM cosmology with  $\Omega_m = 0.3153$ ,  $\Omega_{\Lambda} = 0.6847$ , and  $H_0 = 67.36 \text{ km s}^{-1} \text{ Mpc}^{-1}$ . All magnitudes presented in this work have been calculated using the AB system (Oke & Gunn 1983).

## 6.2 Observations

In this chapter, we combine recent broad-band photometric observations from JWST in the near-infrared (NIR) taken with the Near-Infrared Camera (NIRCcam) and belonging to the CEERS survey (Section 6.2.1), with previous imaging data in the same fields from HST in the visible taken with the Advanced Camera for Surveys (ACS) and belonging to CANDELS/EGS (Section 6.2.2).

### 6.2.1 JWST imaging from CEERS

As commented in Chapter 3.2.3.1, the Cosmic Evolution Early Release Science Survey (CEERS; PI: Steven Finkelstein; Finkelstein et al., in prep.) is one of the 13 JWST Early Release Programs (ERS). The full CEERS program covers  $\sim 100 \text{ arcmin}^2$  with both imaging and spectroscopy. In this chapter, we use observations from CEERS Epoch 1, i.e., the first batch of CEERS observations taken with NIRCcam in June 2022. These consist of four NIRCcam pointings (labeled NIRCcam1, NIRCcam2, NIRCcam3, and NIRCcam6) that cover a combined area of  $35.5 \text{ arcmin}^2$  (see Fig. 3.8a, bottom left panel). In particular, we use the broad-band images taken with NIRCcam/F115W, F150W, F200W, F277W, F356W, and F444W filters. We use the public data release version 0.5 of these NIRCcam Epoch 1 images, available on <https://ceers.github.io/dr05.html>. The reduction and calibration of these images is described in Bagley et al. (2023). Briefly, they were reduced using version 1.7.2 of the JWST Calibration Pipeline with `pmmap version 0989`, taking care and removing “snowballs” and “wisps” features in the images,  $1/f$  noise, and performing a global background subtraction. The  $5\sigma$  depths for point-like sources in these NIRCcam images in circular apertures of  $0.20''$  of diameter range between  $29.0 - 29.2 \text{ mag}$ , except for the F444W filter which has  $28.6 \text{ mag}$  as limiting depth (Finkelstein et al. 2023).

### 6.2.2 HST imaging from CANDELS/EGS

CEERS area overlaps with most of the Extended Groth Strip (EGS; Davis et al. 2007) observations from the Cosmic Assembly Near-infrared Deep Extragalactic Legacy Survey (CANDELS; Grogin et al. 2011; Koekemoer et al. 2011). This allows us to complement our NIRCcam observations with the HST/ACS F606W and F814W broad-band images from CANDELS/EGS. We use the version of the ACS images provided by the CEERS team (together with the NIRCcam images in the public data release version 0.51). These consist of four ACS images per filter (one per NIRCcam pointing) which are pixel-aligned to NIRCcam Epoch 1 images and drizzled to the same pixel scale of NIRCcam images, namely  $0.03 \text{ arcsec pixel}^{-1}$ . The  $5\sigma$  depths in these images for point-like sources in  $0.2''$  apertures are  $28.6 \text{ mag}$  for F606W and  $28.3 \text{ mag}$  for F814W (Finkelstein et al. 2023). Although WFC3 data are also available for this field, we do not include them in the analysis because their images have shallower depths than the rest of considered filters ( $\sim 1 - 2 \text{ mag}$  shallower than our two ACS images and  $\sim 1 - 2.5 \text{ mag}$  shallower than our NIRCcam images) and the wavelength range probed by WFC3 filters is mostly covered by our NIRCcam filters (with considerably deeper depths and thus, smaller uncertainties for the SED fittings). Since the 2D-SPS method presented in Chapter 5 (see Section 5.5) has been validated with more filters (15) than those considered in this chapter (8), in order to check that our method is still successful at retrieving the first formation times of massive galaxies, we repeat the analysis of Section 5.5 considering only the 8 filters in this chapter (see Appendix B). In summary, we find that the median relative offsets (in absolute value) found for all the mass-fraction formation times considered are now below  $\sim 8.5\%$  when compared to ground-truth (vs.  $5.3\%$  for the 15 filters in Chapter 5), which means that we can consider that our 2D-SPS method is still sufficiently valid to infer these early formation times.

## 6.3 Selection of the preliminary sample

In this work, we are interested in probing the earliest phases in the formation of massive ( $M_{\star} > 10^{10} M_{\odot}$ ) galaxies at  $1 < z < 4$ . With this purpose, we first select an preliminary sample of  $1 < z < 4$  galaxies with estimated stellar masses of  $M_{\star} > 10^{9.5} M_{\odot}$ , on which we will perform the photometric analysis and to which we will apply SPS. Our final sample of massive,  $1 < z < 4$  galaxies will be built based upon the results of the SPS analysis (Section 6.4), by considering only galaxies in the preliminary sample with  $M_{\star} > 10^{10} M_{\odot}$  within our photometric apertures according to the SED fits and purge them afterwards. In this section we describe how the preliminary sample is built, together with the estimation of the photometric redshifts. The properties of our final sample of massive,  $1 < z < 4$  will be discussed in Section 6.5.1.

We start from the  $\sim 36,000$  galaxies in the four NIRCam Epoch 1 pointings that are detected in the version v0.51 of the CEERS photometric catalog described in Finkelstein et al. (2023). This catalog has been created with **SExtractor** (Bertin & Arnouts 1996) using as the detection image a combination of the PSF-matched F277W and F356W images. First, we search for all available spectroscopic redshifts for the sources in the catalog. Spectroscopic redshifts are extracted from the Stefanon et al. (2017) catalog, together with the new sources published in the 2021 data release of the MOSFIRE Deep Evolution Field (MOSDEF; Kriek et al. 2015; Reddy et al. 2015). We find 1024 galaxies that have available spectroscopic redshifts in the four NIRCam pointings, 97 of which with values of  $1 < z_{\text{spec}} < 4$  and associated preliminary stellar masses of  $M_{\star} > 10^{9.5} M_{\odot}$ .

### 6.3.1 Estimation of photometric redshifts and preliminary stellar masses

We estimate photometric redshifts and preliminary stellar masses for all sources in the catalog. Although the photometric analysis in this chapter is based solely on the (6) NIRCam and (2) ACS images described in Section 6.2, we use additional imaging data to estimate these photometric redshifts. More specifically, we make use of the integrated magnitudes from the photometric catalog presented in Finkelstein et al. (2023) for this calculation. The JWST images considered for this catalog consist of the NIRCam images described in Section 6.2.1 plus the additional medium-band NIRCam/F410M filter. Regarding HST, apart from the ACS images from CANDELS/EGS mentioned in 6.2.2, WFC3/F105W, F125W, F140W, and F160W images from the same survey are also considered. These images have  $5\sigma$  limiting depths of 28.4 mag for NIRCam/F410M, and 27.1, 27.3, 26.7, 27.4 mag for the WFC3 filters listed above, respectively.

We use **eazy** (Brammer et al. 2008) for the estimation of photometric redshifts and the preliminary stellar masses in the same way as described in Pérez-González et al. (2022). Briefly, we use a modified version of **eazy** that allows the template fitting algorithm to take into account ( $5\sigma$ ) upper limits provided as an input and which entail a penalty in the  $\chi^2$  estimator if exceeded by the fitting template (see also Mérida et al. 2023). For the fit, we use flat priors, no template error feature, and the v1.3 template set which includes a dusty galaxy spectrum and a spectrum with high-equivalent-width (EW) emission lines.

To assess the quality of the photometric redshifts, we compare the photometric redshift estimations from **eazy** for the 97 sources with  $1 < z_{\text{spec}} < 4$  and  $M_{\star} > 10^{9.5} M_{\odot}$  with their spectroscopic values. For this, we compute the normalized median absolute deviation ( $\sigma_{\text{NMAD}}$ ) of  $\Delta z = z_{\text{phot}} - z_{\text{spec}}$

and the number of “catastrophic outliers” (i.e.,  $\Delta z / (1 + z_{\text{spec}}) > 5\sigma_{\text{NMAD}}$ ) as defined in Brammer et al. (2008). We find a value of  $\sigma_{\text{NMAD}} = 0.033$ , with a very small fraction of outliers ( $\sim 3\%$ ), which shows the reliability of the recovery of these photometric redshifts for the range of redshifts and masses considered in this work.

### 6.3.2 Preliminary sample

To build our preliminary sample, we then select galaxies more massive than  $M_{\star} > 10^{9.5} M_{\odot}$  in the four CEERS Epoch 1 NIRCcam pointings which have  $1 < z_{\text{spec}} < 4$  (97 galaxies) or, in case no spectroscopic redshift is available, with  $1 < z_{\text{phot}} < 4$  (684 galaxies). This makes an initial sample of 781 galaxies, with a median value for the redshift of  $z = 1.75_{1.45}^{2.58}$  (median and quartiles) and a median stellar mass of  $\log(M_{\star}/M_{\odot}) = 10.0_{9.7}^{10.4}$ .

## 6.4 Methodology

In this section, we describe the methodology applied to our initial sample of  $M_{\star} > 10^{9.5} M_{\odot}$  galaxies at  $1 < z < 4$ . Our approach is to measure photometry in 2D on these galaxies with the aim to derive their galaxy SFHs from the analysis of their 2D SED fits. The results from the SPS will allow to discard galaxies in our preliminary sample with stellar masses inside the integrated photometric apertures below  $10^{10} M_{\odot}$  and build the final sample of *bona-fide* massive galaxies at  $1 < z < 4$ , on which we will concentrate to infer their early stages of stellar mass formation and assembly. We will describe how the galaxy SFHs are built for galaxies in the final sample by taking into account the results from the fits of their spatially-resolved SEDs.

### 6.4.1 Photometry: measuring integrated and 2D SEDs

Since the ACS and NIRCcam images for each of the four NIRCcam pointing are already pixel-aligned and have the same pixel scale of  $0.03 \text{ arcsec/pix}$  (Section 6.2), we start by PSF-matching these images to the NIRCcam/F444W image, with the worst PSF FWHM ( $\sim 0.16''$ ). To measure photometry, we will make use of the **SExtractor** segmentation maps provided in the Finkelstein et al. (2023) photometric catalog and, as our starting integrated apertures, we will use the associated elliptical apertures provided for each source with semi-major axes of twice the Kron radius ( $a = 2r_{\text{Kron}}$ ).

#### 6.4.1.1 Galaxy inspection and refinement of the segmentation maps

Since our goal is to measure the spatially-resolved SEDs in the preliminary sample of galaxies, the deblending of the sources in the segmentation map around should be as accurate as possible in order to reduce possible sources of error introduced by pixels that do not belong to the considered galaxy. With this in mind, and based on the lessons learned from Chapter 5, we visually inspect the segmentation maps around each galaxy in order to edit them if necessary. This is done by

comparing the segmentation map for each galaxy in the sample to an RGB image of the same region generated using the NIRCcam F115W, F200W, and F356W filters. It is worth mentioning that the segmentation maps have been generated using NIRCcam F277W+F356W as the detection image, so comparing the maps to an RGB image gives us additional information regarding galaxy colors that will be useful in locating possible flaws in the identification of sources in the original map. Among these flaws that need to be retouched, we can mention, e.g., over- and under-deblended sources, non-identified neighbors that need to be masked or neighboring galaxies whose identified region in the map needs to be extended so that it does not belong to the galaxy under consideration. In total, we edit the segmentation map for  $\sim 33\%$  of galaxies in the preliminary sample.

During this visual inspection, we discard galaxies located at the edges of the images (i.e., whose elliptical apertures with  $a = 2r_{\text{Kron}}$  are partially outside the image area in any band; 45 galaxies in total), misidentified galaxies (e.g., misidentified spurious sources that are diffraction spikes from a neighboring source or a region of a nearby galaxy; 34 galaxies) or galaxies that have a spike coming from a very bright source near them (63 galaxies). We keep the remaining 639 galaxies in the preliminary sample, for which we will measure photometry and build SEDs using the refined segmentation maps.

#### 6.4.1.2 Integrated photometry inside elliptical apertures

We will build SEDs for each source by measuring multi-wavelength photometry in two ways: inside an elliptical integrated aperture (we refer to this as “integrated photometry” that will have an “integrated SED” associated), and on a grid defined inside the integrated aperture (“2D photometry” and “2D SEDs”).

We define the integrated aperture following the same procedure as in Chapter 5 (see also García-Argumániz et al. 2023). For this, we start by placing the initial elliptical aperture of  $a = 2r_{\text{Kron}}$  on the center of each galaxy and begin reducing the aperture to minimize the contamination from other sources (according to the segmentation map). In this first step, the elliptical aperture is reduced until the number of pixels belonging to the considered galaxy is  $>80\%$  of all the pixels in the aperture that belong to any source (i.e., in this first step we do not consider pixels identified as sky in the segmentation map to calculate this percentage of galaxy pixels). After this step, if the number of sky pixels within the aperture exceeds  $10\%$  of all the pixels in the aperture, we further reduce the aperture until this limit of sky pixels is reached. In both steps, the elliptical aperture is reduced keeping its original ellipticity and position angle fixed. Hereafter, we refer to this final elliptical aperture as the photometric integrated aperture.

The median semi-major (with quartiles) of our final integrated apertures is  $0.87_{0.68}^{1.13}''$  or, in physical units,  $7.3_{5.6}^{9.7}$  kpc. When galaxies are split in different redshift bins, these values become  $0.98_{0.75}^{9.69}''$  ( $8.4_{6.5}^{10.5}$  kpc) for the 368 galaxies at  $1 < z < 2$ ,  $0.84_{0.68}^{1.04}''$  ( $7.0_{5.6}^{8.6}$  kpc) for the 145 galaxies at  $2 < z < 3$ , and  $0.67_{0.55}^{0.91}''$  ( $5.03_{4.19}^{6.95}$  kpc) for the 145 galaxies at  $2 < z < 3$ . If we compare the sizes of our final integrated apertures with those of the initial apertures, we find that the ratio between both of them is  $1.00_{0.92}^{1.00}$ . This means this reduction process leaves most of the initial integrated apertures unchanged: in only  $25\%$  of the galaxies the final integrated aperture has been reduced to  $<92\%$  of the initial size of  $2r_{\text{Kron}}$ , and only in only  $\sim 10\%$  of them to  $<75\%$  of this initial size.

We now build the integrated SED for each galaxy by measuring photometry on all the ACS and NIRC*am* images within the photometric integrated apertures. For this, we first subtract for each galaxy the median local background in each filter calculated in a  $0.1'$  region around each galaxy, computed by randomly placing 200 one-pixel apertures in this region. We estimate the background rms (or  $1\sigma$  noise) from the median absolute deviation of the flux values in these one-pixel apertures (multiplied by 1.48 to recover the standard deviation assuming a Gaussian noise distribution). After the local background is subtracted, we mask all the pixels within the integrated aperture belonging to other sources (using the edited segmentation map), and then add the flux of the remaining pixels within the aperture (i.e., those from the considered galaxy and sky pixels) to build the integrated SED of the galaxy. Photometric flux uncertainties are estimated from the local background rms as  $\sqrt{N}\sigma$ .

### 6.4.1.3 2D photometry inside a grid

To measure the 2D photometry on each source, we define a grid inside each integrated elliptical aperture with cell size of  $5 \times 5$  pixels<sup>2</sup> (i.e.,  $0.15'' \times 0.15''$ ), roughly the size of our worst PSF in FWHM. An initial grid is built by considering all cells whose center lies within the integrated photometric aperture. We only keep cells in this initial grid which contain more or the same number of pixels belonging to the galaxy under consideration than to other sources. Cells within the integrated aperture that only contain pixels identified as sky in the segmentation map (and no other pixels belonging to any source) are also kept.

Once the grid is defined, we use the segmentation map to identify those pixels in the cells belonging to neighboring galaxies. We replace the flux values of these pixels by random sky values, drawn from a Gaussian distribution with mean 0 and a standard deviation equal to the background noise  $\sigma$  previously measured for each filter around the galaxy. We build the 2D SEDs by adding the flux of all pixels inside each cell of the grid on these modified photometric images, which had been previously background subtracted. For the analysis, we only keep SEDs of those cells that have a signal-to-noise (SNR)  $> 3$  in at least 5 bands. Cells in the grid that do not satisfy this condition are discarded.

Fig. 6.1 shows a summary of the procedure described above. The first inspection the RGB image of the galaxy (first panel) shows the need for a refinement of the original segmentation map (second panel), which is edited (third panel) to include a non-identified neighboring galaxy and to extend the pixels belonging to the neighboring galaxy on top. We then reduce the initial integrated apertures following the procedure described above (fourth panel) with the information provided by the edited segmentation. Finally, we subtract the local background around the galaxy in all filters and replace the pixels belonging to other sources with random sky noise (fifth panel). The integrated SED and 2D SEDs are built by measuring photometry in the integrated aperture and in each cell of the grid, respectively (fifth panel). Fig. 6.2 shows the final (and initial) integrated aperture and final grid for some CEERS objects in our sample.

For  $\sim 5\%$  of the galaxies, instead of using the final apertures resulting from the procedure described above, we need to redefine their integrated apertures by manually editing their initial elliptical apertures (in terms of size, ellipticity and/or position angle). This is needed so that their integrated apertures better enclose the galaxy observed in their RGB images and the correspond-

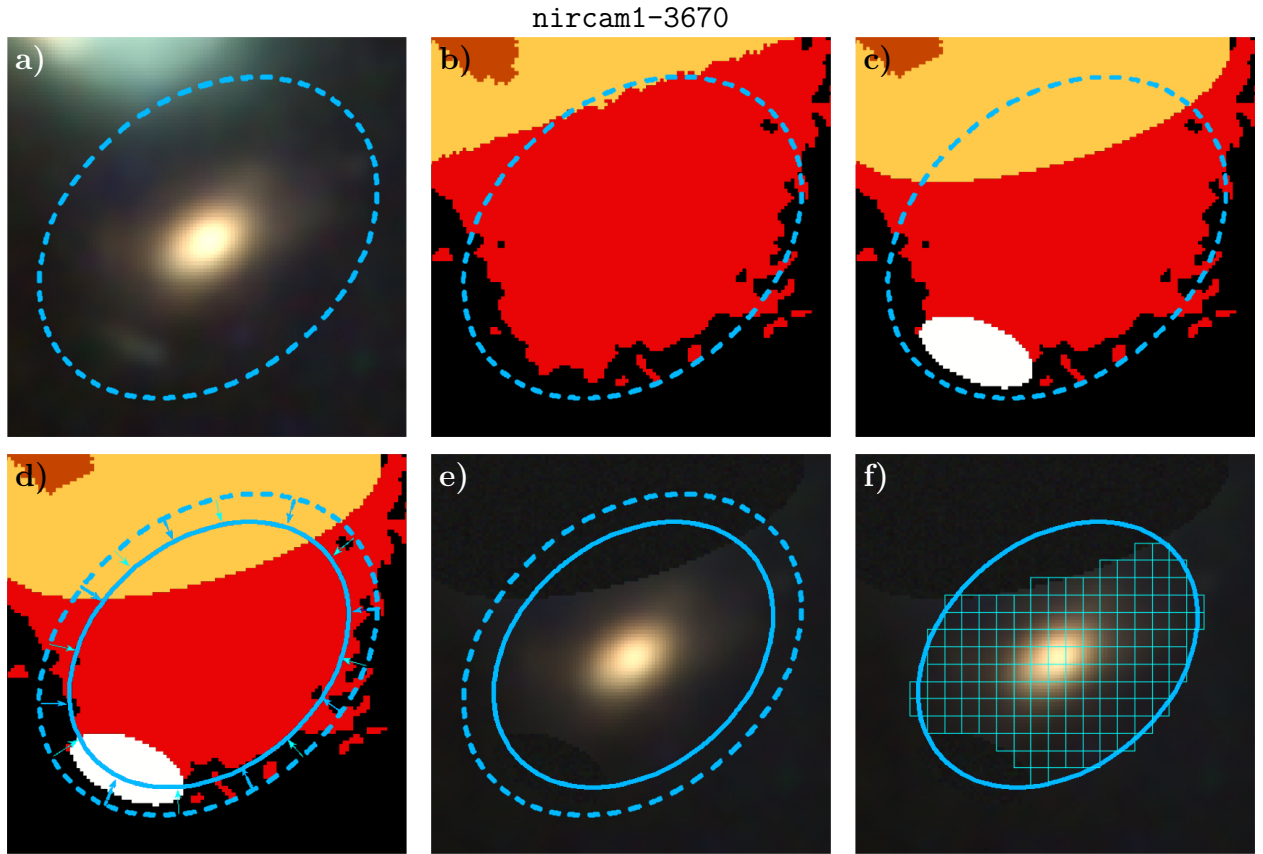


**Figure 6.1:** Postage stamp images ( $3.5'' \times 3.5''$ ) for a CEERS galaxy nircam1-3670 at  $z = 1.13$ . **a)** RGB image generated with NIRCcam filters (R:F356W, G:F200W, B:F115W) with asinh scaling, with the initial integrated aperture ( $a = 2r_{\text{Kron}}$ ; dashed red blue). **b)** Original segmentation map, where the pixels belonging to the considered galaxy are shown in red, the sky pixels in black, and pixels belonging to other galaxies, in yellow and orange. **c)** Edited segmentation map. We add a previously non-identified neighboring galaxy (in white) and we extend the pixels belonging to the neighboring galaxy on top (yellow). **d)** Reduction of the integrated aperture to minimize pixels belonging to neighbors. The new final integrated aperture is shown in solid blue. **e)** New RGB image of the galaxy in which the flux of the pixels belonging to other sources has been replaced by random sky noise. **f)** Final photometric apertures: integrated aperture for integrated photometry (blue) and grid for 2D photometry (cyan).

ing edited segmentation maps. In this small percentage of galaxies, the photometric integrated apertures will refer to their manually-edited integrated apertures (ignoring the resulting reduced apertures from the two-step procedure described above).

### 6.4.2 SPS modeling

The aim of this chapter is to infer the earliest formation phases of massive galaxies at  $1 < z < 4$ , namely, from their SFHs which are derived by applying 2D SPS. Our 2D-SPS method, summarized in this section, has been tested using simulated imaging data of galaxies from the Illustris simulation (see Chapter 5 and García-Argumánuez et al. 2023). This method, and the assumptions regarding its SPS modeling, have been optimized to recover the beginning of the SFH of massive,  $1 < z < 4$  galaxies. In this section, we discuss the details regarding the integrated and 2D SED fits. We refer the reader to Chapter 5 and García-Argumánuez et al. (2023) for more information about the choices of the SPS modeling input parameters.

We use `synthesizer` the code (described in Pérez-González et al. 2003, 2008) to perform the SPS modeling of our integrated and 2D SEDs. This code compares the observed SED points with those predicted by the SPS models for each filter, taking into account observational photometric errors and combining the emission from both stars, gas, and the effect of dust (see Section 4.3). The model that best fits the data is determined by performing a  $\chi^2$  minimization.

All integrated and 2D SEDs are compared with two stellar population models: STARBURST99 (SB99; Leitherer et al. 1999; Vázquez & Leitherer 2005; Leitherer et al. 2010) and Bruzual & Charlot (2003) (hereafter, BC03) models. We assume a Kroupa (2001) IMF for SB99 models and a Chabrier (2003) IMF for BC03. Following Chapter 5 and García-Argumánuez et al. (2023), we assume each SED to be described by a double-burst SFH, i.e., a SFH which is the sum of an old and a young population, each of them with a SFH given by  $SFR(t) \propto t e^{-t/\tau}$  for  $t > t_{\text{pop}}$ , where  $t_{\text{pop}}$  is the age of each population, and  $\tau$  is the star-formation time-scale. The time,  $t$ , in the above expression is measured in terms of the age of the universe and the age of each population,  $t_{\text{pop}}$ , is the age of the universe at which each population began to form stars. We refer to the old (young) population as the one that first (more recently) began to form stars in the galaxy SFH. The burst strength,  $b$ , indicates the contribution of stellar mass created by the most recent population (or young burst) to the total stellar mass.

The free parameters in our SED fits are, in addition to the burst strength ( $b$ ), the age ( $t$ ), star-formation timescale ( $\tau$ ), metallicity ( $Z$ ), and dust extinction ( $A_V$ ) for each one of the two stellar populations. Regarding their allowed ranges in the SED fitting, we let the age of the young population vary from 100 Myr to an specific age limit (see below), and the age of the old population within that same age limit and the age of the universe at the redshift of the galaxy. This age limit between the old and young population depends on the galaxy redshift: it is equal to 40% of the age of the universe for galaxies with  $1 < z < 2$  (i.e., 40% of the age of the universe for the young population and 60% for the old population) and equal to 50% of the age of the universe for  $2 < z < 4$  galaxies (half of the age of the universe for each population). The allowed range for the star-formation timescale is  $200 \text{ Myr} < \tau_{\text{old}} < 1 \text{ Gyr}$  for the old population, and we fix  $\tau_{\text{young}} = 10 \text{ Myr}$  for the young population. The attenuation for the old population can vary within  $0 \text{ mag} < A_{V,\text{old}} < 1 \text{ mag}$ , and  $0 \text{ mag} < A_{V,\text{young}} < 2 \text{ mag}$  for the young population. Metallicity in both populations can adopt any



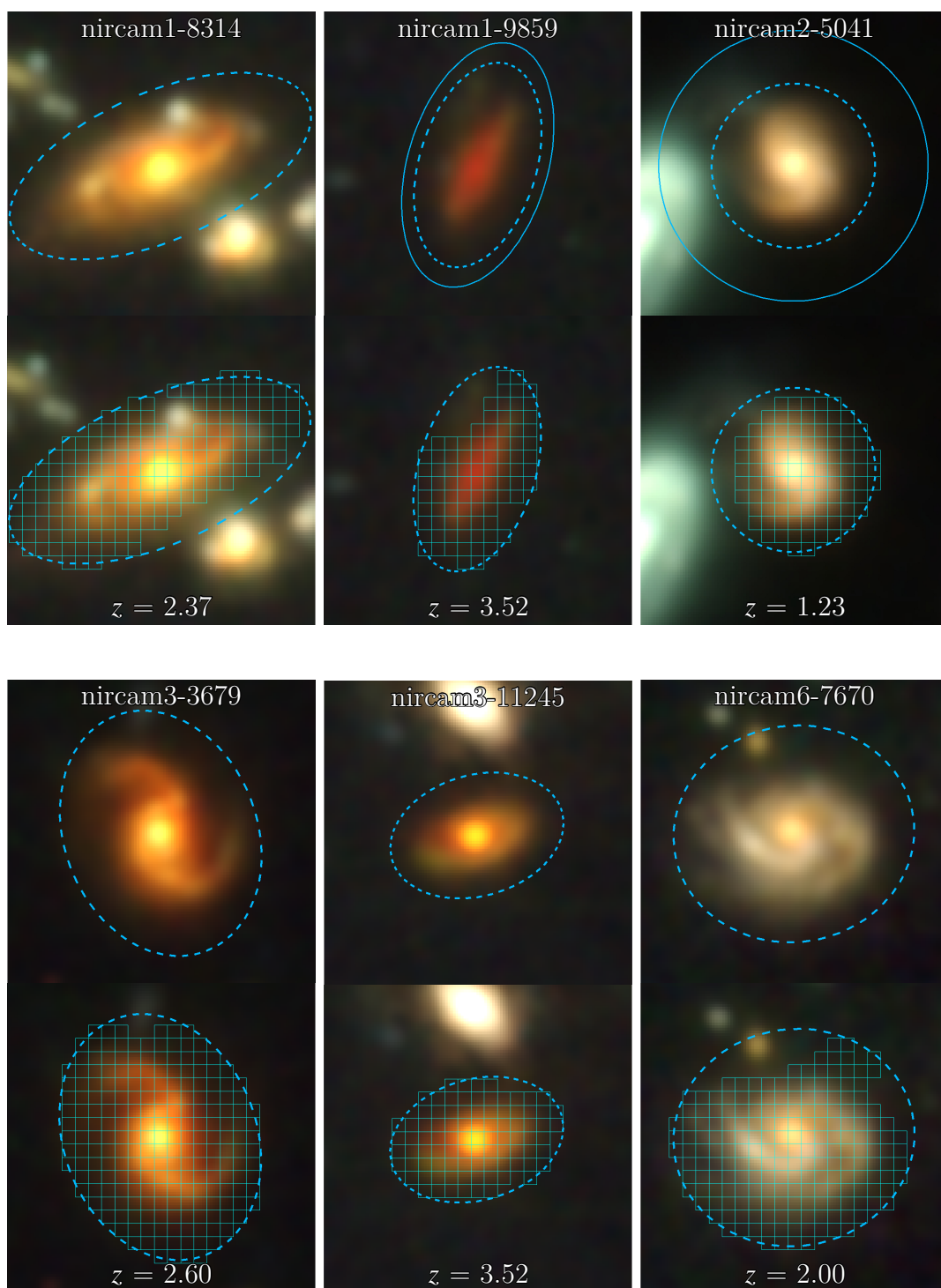


**Figure 6.2:** RGB images ( $3.5'' \times 3.5''$ ) generated with NIRCcam filters (R:F356W, G:F200W, B:F115W) and with asinh scaling for six CEERS galaxies in our final sample. *First row (of each galaxy panel):* final integrated aperture (dashed blue) and, in case this is smaller than the initial integrated aperture ( $a = 2r_{\text{Kron}}$ ), we also show the latter (solid blue). *Second row:* Final integrated aperture and final grid.

of the following three values:  $Z/Z_{\odot} = 0.2, 0.4,$  and  $1$ . As for the burst strength, we let it vary within  $0.01 < b < 1$ . The stellar mass ( $M_{\star}$ ) is calculated by normalizing the best-fitting model in the SED fit to the observed SED.

We perform Monte Carlo (MC) simulations to fit each SED 300 times by letting the photometric points of the SED randomly (and uncorrelatedly) vary within their photometric error and then refitting. This provides us with 300 sets of solutions of the derived parameters of the fit which allows us to have a better knowledge of the uncertainties and degeneracies in these parameters (see Domínguez Sánchez et al. 2016). Since we are mainly interested in inferring SFHs, this means we will be able to build 300 SFHs from each SED fit (either integrated or from each grid cell).

### 6.4.3 Massive galaxies and SFH from the 2D SED fits

First, we calculate the stellar mass for each galaxy as the median of all the masses provided by its integrated SED fits. Hereafter, we will refer to this median integrated stellar mass as the galaxy mass of the galaxy. At this step, we discard galaxies in the sample with a galaxy mass  $M_{\star} < 10^{10} M_{\odot}$ , keeping only those which are massive. This makes a final sample of 333 (386) massive galaxies in our considered redshift range when BC03 (SB99) models are used.

We build the SFH for each galaxy (or “galaxy SFH”) for these massive galaxies by combining the information provided by the 2D SED fits, using the stellar mass of the galaxy described above obtained from the integrated SED fits to normalize the SFH. First, we compute the galaxy SFH by adding all the SFHs derived for the 2D SED fits (i.e., for each cell in the grid). Then, we normalize this galaxy SFH by the galaxy stellar mass. As done in Chapter 5, instead of building just one galaxy SFH (or sum SFH), we build 300 realizations of this SFH by considering the different MC solutions obtained for each of the 2D SEDs. The final galaxy SFH is calculated as the median SFH obtained from all these galaxy SFH realizations.

Fig. 6.3 shows the galaxy SFH (solid light blue) calculated from the median of the 300 SFH realizations (thin black) obtained for `nircam2-7435` ( $z = 3.47$ ) with the SB99 models. We also show the galaxy SFH directly inferred from the integrated SED (dashed blue), which shows a considerably younger age. As a comparison, we include the galaxy SFH obtained with BC03 (dashed orange). The lower normalization of the galaxy SFH for BC03 with respect to that of SB99 is due to the difference in the median integrated mass recovered by the models:  $6.8 \times 10^{10}$  ( $4.1 \times 10^{10}$ )  $M_{\odot}$  for SB99 (BC03). In this case, the galaxy SFH for BC03 begins at an earlier cosmic time than that of SB99, although the majority of its mass is formed at later ages of the Universe compared to that of SB99 models. The integrated aperture and the 2D grid, together with the segmentation map for the galaxy, are also shown (right panels).

## 6.5 Results

In this section, we describe the final sample of CEERS massive galaxies at  $1 < z < 4$  and their galaxy SFHs, derived in Section 6.4 via 2D SPS, with the aim of addressing the question of when these galaxies began to form their stars.

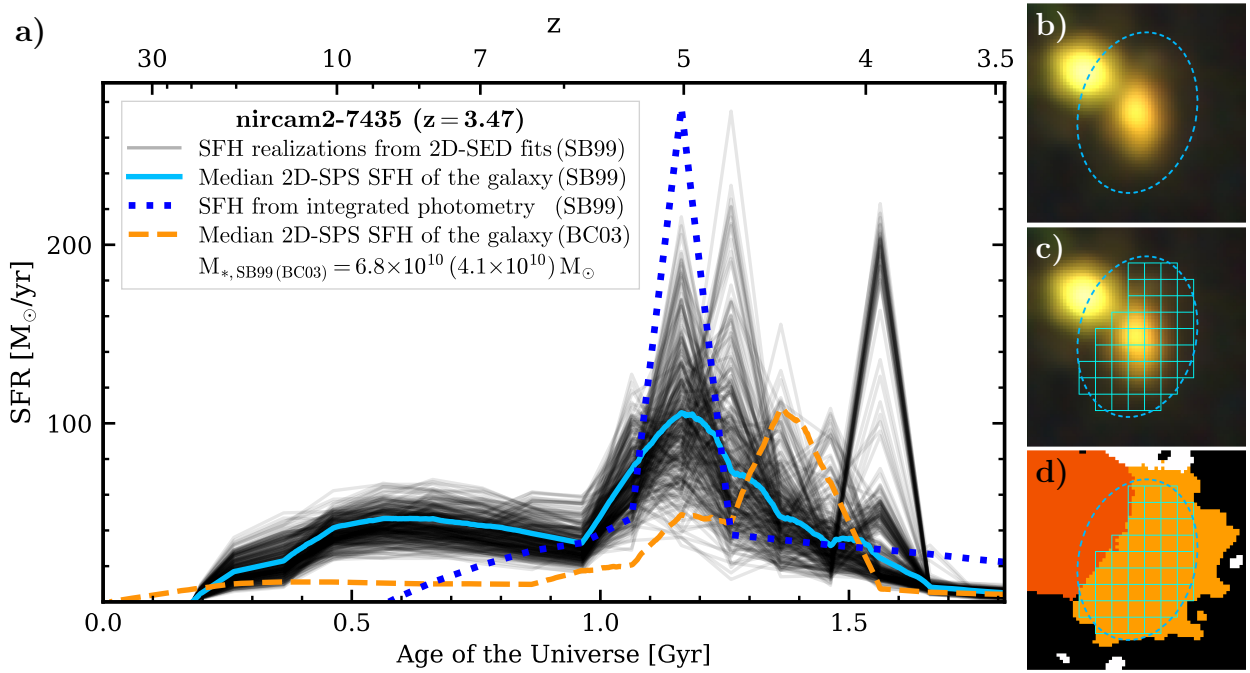


**Figure 6.3:** **a)** 2D-SPS-derived galaxy SFH for *nircam2-7435* (solid light blue), obtained as the median of the different galaxy SFH realizations (thin black) which result from the MC solutions obtained for each of the 2D SEDs and corresponding to the SB99 models. The galaxy SFH derived from the integrated SED is shown in dashed blue (also for SB99). The galaxy SFH obtained for BC03 is shown in dashed orange as a comparison. **b)** RGB image ( $2'' \times 2''$ ) of the galaxy generated with NIRC*Cam* filters (R:F356W, G:F200W, B:F115W; asinh scale) with its integrated aperture **c)** and the 2D grid. **d)** Segmentation map for the galaxy.

### 6.5.1 CEERS final sample of massive, $1 < z < 4$ galaxies: redshift and stellar mass

To build our final sample of massive galaxies at  $1 < z < 4$ , we select only those galaxies for which the stellar mass derived by the integrated SED fits with SB99 and BC03 models is simultaneously  $M_{\star} > 10^{10} M_{\odot}$  in both models. This results in a final sample of 333 galaxies, whose distributions of redshifts and stellar masses are shown in Fig. 6.4. We find that the stellar mass distributions are very similar when either SB99 (blue) or BC03 models (orange) are used: our galaxies present a median (with quartiles) redshift of  $1.72_{1.39}^{2.50}$ , and a stellar mass (in  $\log(M_{\star}/M_{\odot})$ ) of  $10.5_{10.2}^{10.7}$  ( $10.6_{10.3}^{10.8}$ ) for BC03 (SB99) models. The median difference between the stellar masses derived for each galaxy with both models is  $0.09_{0.03}^{0.15}$  dex, being slightly larger those from SB99. That is the reason why there were  $\sim 15\%$  more galaxies in the initial SB99 sample.

In Appendix C, we show flashcards for the 333 massive galaxies at  $1 < z < 4$  in our CEERS final sample. Each galaxy card includes the integrated HST+JWST photometry, some postage stamps of the galaxy (including different RGB images and the segmentation map, together with the integrated aperture and the grid), and the 2D-SPS-derived galaxy SFH for both SB99 and BC03 models. In Appendix D, we include some general characteristics for these galaxies, such as redshifts, stellar masses, and other relevant information related to their photometric apertures (see Table D.1).

We compare our sample with simulated massive galaxies at  $1 < z < 4$  from the Illustris simulation (Vogelsberger et al. 2014a,b; Genel et al. 2014) which appear in the Illustris synthetic deep survey images ( $\sim 23.5$  arcmin<sup>2</sup>; Snyder et al. 2017). Those galaxies were already analyzed in Chapter 5 (sample #4 in Section 5.6.1; see also García-Argumániz et al. 2023) following the same photometric + 2D-SPS analysis described in this chapter. For our comparison to CEERS galaxies, we impose to this sample of Illustris massive galaxies at  $1 < z < 4$  an additional stellar mass cut-off of  $10^{10} M_{\odot}$  within the photometric aperture after the SED fits (as done with CEERS galaxies here), which results in 261 Illustris galaxies (included in magenta in Fig. 6.4). The median redshift for this sample is  $z = 1.98_{1.47}^{2.40}$ , and the median galaxy stellar masses (provided by the integrated SED fits) is  $\log(M_{\star}/M_{\odot}) = 10.3_{10.1}^{10.6}$ . For these Illustris galaxies, we build the galaxy SFHs in the same way as described in Section 6.4.3 for CEERS galaxies in this chapter.

### 6.5.2 The first stages of the SFH in massive $1 < z < 4$ galaxies

As done in Chapter 5, we quantitatively characterize the first stages of the SFH by calculating the time  $t_k$ , at which a galaxy first formed small percentages ( $k\%$ ) of its stellar mass. These formation times, expressed in age of the Universe, are directly computed by integrating the galaxy SFH over cosmic time. Here, we discuss the formation times  $t_5$ ,  $t_{10}$ , and  $t_{25}$ , at which 5%, 10%, and 25% of the stellar mass was formed, respectively, focusing on  $t_5$  to determine the onset of the SFH. The reason for preferring  $t_5$  instead of  $t_0$  for establishing this beginning is that, since these  $t_k$  depend on both  $\tau$  and  $t_0$ , possible degeneracies between ages and timescales might be alleviated.

We characterize when massive galaxies start their formation in two different ways. In the first place, in Section 6.5.2.1 we analyze the onset of the star formation in CEERS massive galaxies as a whole by calculating a median SFH for the sample CEERS galaxies and determining the formation

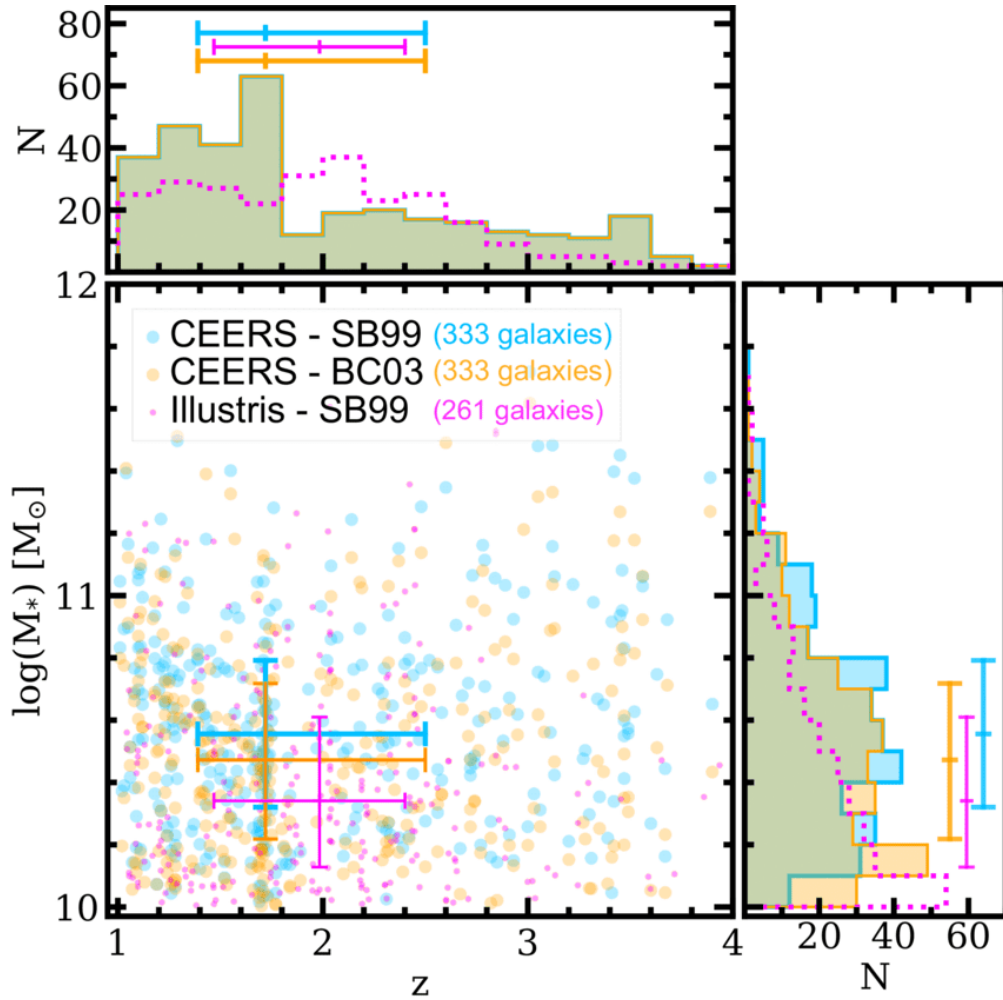


**Figure 6.4:** Stellar mass *vs.* redshift for our final CEERS sample of 333 galaxies at  $1 < z < 4$  with  $M_\star > 10^{10} M_\odot$  when SB99 (blue) and BC03 (orange) models are used. The redshift and stellar mass distributions are shown at the top and on the right, respectively, with median and quartiles marked with segments on top (and right) of the corresponding histograms. As a comparison, we include the results from applying the same photometric + 2D-SPS analysis to  $1 < z < 4$  massive galaxies from the Illustris simulation (magenta; see main text).

times  $t_5$ ,  $t_{10}$ , and  $t_{25}$  from it. Secondly, in Section 6.5.2.2 we analyze the variety of the onset of SFHs in massive galaxies directly from each individual galaxy SFH. This is done by computing the formation times  $t_k$  described above from each galaxy SFH or, alternatively to these mass-fraction formation times, by calculating the time,  $t_{10^X M_\odot}$ , at which a certain (and fixed) amount of stellar mass,  $10^X M_\odot$ , was formed according to the galaxy SFH.

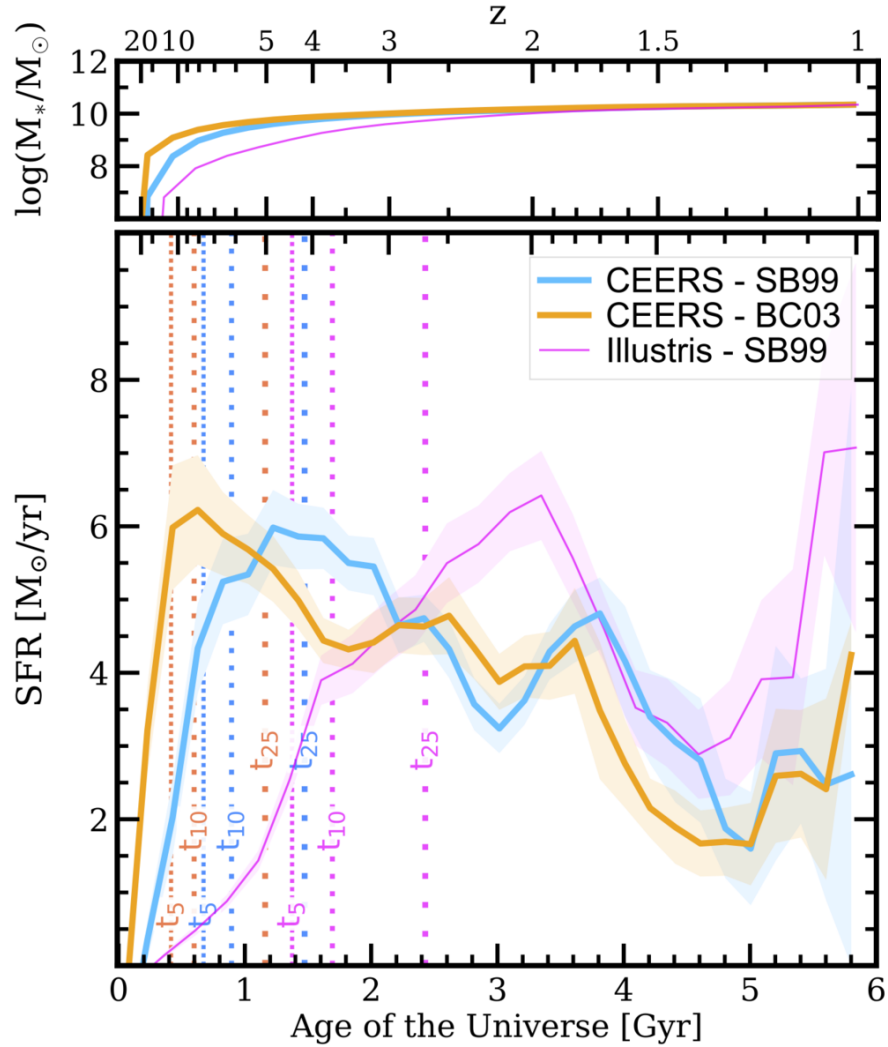
### 6.5.2.1 Results about the median SFH for CEERS galaxies

Fig. 6.5 shows the median SFH for our sample of CEERS massive galaxies at  $1 < z < 4$  when using BC03 (orange) and SB99 (blue) models. The full-sample SFH is first computed from the median of all the SFHs of the galaxies selected in the CEERS survey (see Section 6.4.3). Then, a 200 Myr smoothing square kernel is applied to the median SFH of the sample. Shaded areas show the uncertainty in the median SFH, calculated as the 95% confidence interval. When integrated across cosmic time, the median SFH for CEERS with BC03 models (in orange) yields an stellar mass of  $\log(M_\star/M_\odot) = 10.34$ . The other two SFH in Fig. 6.5 have been normalized so that they recover the same stellar mass when integrated. The original mass recovered by the median SFH for CEERS with SB99 was  $\log(M_\star/M_\odot) = 10.49$ , and 10.53 for the median SFH of Illustris massive galaxies.

We point out that, since each individual galaxy SFH spans from the age of the galaxy to the redshift of observation, each individual SFH provides no information at lower redshifts than that of the galaxy. As a consequence, the median SFH of all CEERS galaxies is calculated by considering different number of galaxies at each age of the Universe. Therefore, the shape and normalization of this median SFH depends on the redshift distribution of the sample of galaxies. However, this dependence is milder at the beginning of the median SFH (at lower ages of the Universe) since in this epoch, and in which we focus in this work, the median SFH is computed from the largest number of galaxies (virtually, with the full sample).

We find that the shape of the median SFH for CEERS is very similar when using either SB99 (blue) or BC03 (orange) models. The most striking feature of this median SFH is its steep rise in the first  $\sim 400 - 600$  Myr of the age of the Universe (beyond  $z \sim 8 - 9$ ), which is followed by a nearly constant decrease until  $z \sim 1$ . The start of the rise in the beginning of the SFH occurs  $\sim 100$  Myr earlier for BC03 than for SB99 and is slightly steeper in the case of the former (e.g., the SFH for BC03 reaches  $5 M_\odot/\text{yr}$  in after its first 300 Myr, while the SFH for SB99 needs  $\sim 600$  Myr to reach that SFR). This explains why the formation times  $t_5$ ,  $t_{10}$ , and  $t_{25}$  (vertical dotted lines) calculated for the median SFH of BC03 models are systematically shifted to earlier ages of the Universe than those of the median SFH of SB99. According to our results, the median SFH for CEERS massive galaxies at  $1 < z < 4$  would begin at  $z \sim 30$  ( $z \sim 20$ ) for BC03 (SB99). The formation times for BC03 (SB99), in age of the Universe, are  $t_5 = 0.42$  (0.67) Gyr,  $t_{10} = 0.60$  (0.89) Gyr, and  $t_{25} = 1.16$  (1.47) Gyr, which, expressed in terms of redshift of the Universe, correspond to  $z_5 = 10.9$  (7.7),  $z_{10} = 8.4$  (6.2), and  $z_{25} = 5.0$  (4.1). Table 6.1 shows the formations times and corresponding redshifts of the SFHs shown in Fig. 6.5.

The inferred formation times, especially  $t_5$  and  $t_{10}$ , denote an intense star formation at very early ages of the Universe. This early star formation is not seen in the median SFH derived for Illustris massive galaxies at  $1 < z < 4$  to which the same 2D-SPS method has been applied (in pink; see



**Figure 6.5:** Median SFH for CEERS massive galaxies at  $1 < z < 4$  for (SB99 in blue and BC03 in orange). As a comparison, we include the median SFH for massive,  $1 < z < 4$  in Illustris (pink) after applying the same photometric + 2D-SPS analysis to these galaxies (Chapter 5 and García-Argumánuez et al. 2023; see main text). All median SFHs have been normalized to recover the same mass as that of the median SFH for BC03. Shaded areas represent the uncertainty of the median. Vertical lines show the formation times  $t_5$ ,  $t_{10}$ , and  $t_{25}$  computed from these median SFHs. On top, we show the evolution of the integrated stellar mass for the median SFHs.

**Table 6.1:** Formation times and redshifts for median SFH of massive  $1 < z < 4$  galaxies in Fig. 6.5.

Galaxy sample	Redshift	SFHs from	$t_5$	$t_{10}$	$t_{25}$	$z_5$	$z_{10}$	$z_{25}$
CEERS $M_\star > 10^{10} M_\odot$ galaxies	$1 < z < 4$	2D SPS (BC03)	0.42	0.60	1.16	10.9	8.4	5.0
		(SB99)	0.67	0.89	1.47	7.7	6.2	4.1
Illustris $M_\star > 10^{10} M_\odot$ galaxies	$1 < z < 4$	2D SPS (SB99)	1.37	1.69	2.43	4.4	3.7	2.7

**Notes:** The formation times are measured in Gyr since the Big Bang.

Section 6.5.1). Instead, the median SFH for Illustris predicts a SFH that peaks considerably later ( $z \sim 2 - 3$ ) and has a less steep and delayed initial rise, with its SFH beginning at  $z \sim 15$  and needing  $\sim 600$  Myr to reach an SFR of  $1 M_\odot/\text{yr}$  ( $\lesssim 100$  Myr for both SB99 and BC03). Consequently, the inferred formation times for Illustris occur at significantly older ages of the Universe (or lower redshifts):  $t_5 = 1.37$  Gyr ( $z_5 = 4.4$ ),  $t_{10} = 1.69$  Gyr ( $z_{10} = 3.7$ ), and  $t_{25} = 2.43$  Gyr ( $z_{25} = 2.7$ ) (see Table 6.1). This later assembly of the stellar mass in Illustris can also be seen on the top panel Fig. 6.5, which shows the evolution of the integrated stellar mass at each redshift (directly computed from the median SFHs).

We remind the reader that the Illustris median SFH shown in Fig. 6.5 was already calculated in Chapter 5, with the only difference that in the latter chapter we did not remove galaxies in the sample with  $M_\star < 10^{10} M_\odot$  within the photometric aperture according to the integrated SED fits (as done here with CEERS galaxies). In fact, the Illustris median SFH shown in Fig. 6.5 is equivalent to the pink SFH in 5.12, but without purging the Illustris sample after the SPS modeling in the latter. Both SFHs are very similar, except for the final rise in the Illustris SFH of this chapter. Nevertheless, the formation times inferred from the 2D-SPS analysis in both cases are almost identical, with differences of less than  $\sim 40$  Myr in age of the Universe (0.2 in redshift) for all the considered formation times (see Table 5.4).

### 6.5.2.2 The diversity of the onset of SFH in CEERS massive galaxies

We now focus on when the star formation began in each of the individual galaxies in our CEERS sample. For this, we calculate  $t_5$  and  $t_{10}$  directly from each galaxy SFH derived from the 2D-SPS analysis and analyze their distributions. Fig. 6.5 shows the distributions for  $t_5$  (top, left panel) and  $t_{10}$  (bottom left) for BC03 and SB99 models (orange and blue, respectively), together with those inferred from the 2D-SPS-derived galaxy SFHs of our sample of Illustris massive galaxies at  $1 < z < 4$  (in pink).

Consistent with what is observed in the median SFH, CEERS massive galaxies present  $t_5$  and  $t_{10}$  distributions that peak at very early ages of the Universe in both cases, with a significant fraction of formation times at  $z \gtrsim 10$ . The median (and quartiles) for CEERS galaxies are  $t_5 = 0.46_{0.30}^{0.78}$  ( $0.65_{0.39}^{1.04}$ ) Gyr and  $t_{10} = 0.70_{0.40}^{1.12}$  ( $0.86_{0.52}^{1.37}$ ) Gyr for BC03 (SB99), or, equivalently,  $z_5 = 10.2_{6.8}^{13.8}$  ( $7.9_{5.5}^{11.5}$ ) and  $z_{10} = 7.4_{5.2}^{11.2}$  ( $6.4_{4.4}^{9.3}$ ) (see Table 6.2). In contrast, the formation times for



Illustris massive galaxies at  $1 < z < 4$  (pink) are clearly shifted towards lower redshifts, peaking at  $z \sim 5.5$  ( $z \sim 4.5$ ) for  $t_5$  ( $t_{10}$ ) and with a very scarce number of galaxies presenting values beyond  $z \sim 10$ . The median (and quartiles) for Illustris massive galaxies at  $1 < z < 4$  are  $t_5 = 1.10_{0.85}^{1.42}$  Gyr ( $z_5 = 5.2_{4.3}^{6.4}$ ) and  $t_{10} = 1.39_{1.11}^{1.83}$  Gyr ( $z_{10} = 4.3_{3.4}^{5.2}$ ) (see Table 6.1). These considerably lower-redshift formation times in Illustris are responsible for delayed beginning of the median SFH for Illustris when compared to that of CEERS galaxies (Fig. 6.5).

Following a complementary approach to understand our main result, i.e., that real galaxies started forming earlier and assembled larger amounts of stars compared to the Illustris simulation, we compare SFHs of galaxies in a narrower redshift range. To investigate this, we select all existing massive galaxies in the Illustris simulation at  $z = 4$  and calculate their  $t_5$  and  $t_{10}$  from their galaxy SFHs built from the stellar simulated particles that belong to each galaxy<sup>1</sup>. We also do the same with massive,  $z = 4$  galaxies from the TNG100 simulation (Springel et al. 2018; Naiman et al. 2018; Pillepich et al. 2018a; Nelson et al. 2018; Marinacci et al. 2018), the successor of the Illustris simulation that has the same volume and similar characteristics regarding the number and resolution of elements. This results in 144 (317) massive,  $z = 4$  galaxies in Illustris (TNG100), with a median stellar mass of  $\log(M_\star/M_\odot) = 10.23_{10.09}^{10.40}$  ( $10.22_{10.09}^{10.41}$ ), 0.24–0.34 dex less massive than that of CEERS galaxies at  $1 < z < 4$ .

Since the formation times  $t_5$  and  $t_{10}$  inferred for  $z = 4$  galaxies occur (on average) at earlier ages of the Universe than those of galaxies at lower redshifts with similar masses, the  $t_5$  and  $t_{10}$  values derived for massive,  $z = 4$  galaxies in Illustris and TNG100 can be used as a lower bound of massive galaxies at  $1 < z < 4$  in these simulations and compare it to observations. In Fig. 6.6, we show the  $t_5$  and  $t_{10}$  distributions for massive,  $z = 4$  galaxies in Illustris (black dotted) and TNG100 (dark red dashed). We find that, even after considering only  $z = 4$ , massive galaxies from these simulations do not reach the early ages of the Universe that CEERS does. In fact, the maximum formation redshifts reached by these  $z = 4$  galaxies in Illustris (and TNG100) are  $z_{5,\max} = 9.5$  (8.3), and  $z_{10,\max} = 7.9$  (7.7), with a median value (with quartiles) of  $z_5 = 7.0_{6.5}^{7.5}$  ( $6.4_{5.9}^{6.7}$ ) and  $z_{10} = 6.3_{5.8}^{6.7}$  ( $5.9_{5.5}^{6.7}$ ) (see Table 6.2).

One could argue that by setting the  $10^{10} M_\odot$  cutoff at  $z = 4$  in Illustris and TNG100, we are selecting mainly the most massive dark matter halos in the local Universe, which may have assembled later compared to less massive halos at those redshifts. To check this, the simplest way is to select also in Illustris and TNG100 the galaxies with  $M_\star \geq 10^{10} M_\odot$  at  $z = 1$ . By setting this mass cutoff at a lower redshift, we are also including galaxies formed in less massive halos in the early stages of the Universe. This makes a sample of 3700 (4350) massive,  $z = 1$  galaxies in Illustris (TNG100) with a median stellar mass of  $\log(M_\star/M_\odot) = 10.37_{10.17}^{10.70}$  ( $10.37_{10.16}^{10.60}$ ). However, the maximum redshifts reached by these  $z = 1$  galaxies in Illustris (TNG100) are  $z_{5,\max} = 9.1$  (8.9) and  $z_{10,\max} = 7.6$  (7.8), similar to the maximum values at  $z = 4$  in the simulations. The median values for these massive,  $z = 1$  galaxies in Illustris (TNG100) are  $z_5 = 3.8_{3.4}^{4.4}$  ( $3.7_{3.2}^{4.2}$ ), and  $z_{10} = 3.1_{2.8}^{3.6}$  ( $3.1_{2.7}^{3.6}$ ), well after the CEERS values (and their analogues at  $z = 4$  in the simulations). These values have not been included in Fig. 6.6, but they are included in Table 6.2.

<sup>1</sup>We select all galaxies in the Illustris simulation at  $z = 4$  which have  $M_\star \geq 10^{10} M_\odot$  within twice the stellar half-mass radius of the galaxy ( $2r_{\text{hm}}$ ). In this case, the galaxy SFH is built from the information provided by the individual stellar particles belonging to the galaxy (i.e., their formation age and stellar masses), only considering particles which are closer to the galaxy center than  $2r_{\text{hm}}$  (more details in Section 2.4, Chapter 5 and García-Argumániz et al. 2023).

**Table 6.2:** Formation times and redshifts for massive galaxies analyzed in Chapter 6.

Galaxy sample	Redshift	SFHs from	$t_5$	$t_{10}$	$z_5$	$z_{10}$	$t_{5 \times 10^8 M_\odot}$	$t_{10^9 M_\odot}$	$z_{5 \times 10^8 M_\odot}$	$z_{10^9 M_\odot}$	
CEERS $M_\star > 10^{10} M_\odot$ gals.	$1 < z < 4$	2D SPS	(BC03)	$0.46_{0.30}^{0.78}$	$0.70_{0.40}^{1.12}$	$10.2_{6.8}^{13.8}$	$7.4_{5.2}^{11.2}$	$0.32_{0.20}^{0.61}$	$0.45_{0.25}^{0.88}$	$13.1_{8.3}^{18.6}$	$10.4_{6.3}^{15.6}$
			(SB99)	$0.65_{0.39}^{1.04}$	$0.86_{0.52}^{1.37}$	$7.9_{5.5}^{11.5}$	$6.4_{4.4}^{9.3}$	$0.50_{0.27}^{0.79}$	$0.64_{0.35}^{1.05}$	$9.5_{6.8}^{14.9}$	$8.0_{5.4}^{12.6}$
Illustris $M_\star > 10^{10} M_\odot$ gals.	$1 < z < 4$	2D SPS	(SB99)	$1.10_{0.85}^{1.42}$	$1.39_{1.11}^{1.83}$	$5.2_{4.3}^{6.4}$	$4.3_{3.4}^{5.2}$	$0.94_{0.61}^{1.23}$	$1.18_{0.76}^{1.55}$	$5.9_{4.8}^{8.2}$	$4.9_{4.0}^{7.0}$
Illustris $M_\star > 10^{10} M_\odot$ gals.	$z = 4$	particles ( $2 r_{\text{hm}}$ )		$0.75_{0.69}^{0.83}$	$0.88_{0.81}^{0.96}$	$7.0_{6.5}^{7.5}$	$6.3_{5.8}^{6.7}$	$0.68_{0.60}^{0.74}$	$0.77_{0.70}^{0.87}$	$7.6_{7.2}^{8.4}$	$6.9_{6.3}^{7.5}$
	$z = 1$			$1.62_{1.38}^{1.88}$	$2.04_{1.75}^{2.35}$	$3.8_{3.4}^{4.4}$	$3.1_{2.8}^{3.6}$	$1.21_{0.93}^{1.50}$	$1.50_{1.15}^{1.88}$	$4.9_{4.1}^{6.0}$	$4.1_{3.4}^{5.1}$
TNG100 $M_\star > 10^{10} M_\odot$ gals.	$z = 4$	particles ( $2 r_{\text{hm}}$ )		$0.86_{0.81}^{0.94}$	$0.96_{0.89}^{1.04}$	$6.4_{5.9}^{6.7}$	$5.9_{5.5}^{6.2}$	$0.79_{0.71}^{0.87}$	$0.80_{0.80}^{0.97}$	$6.8_{6.3}^{7.4}$	$6.2_{5.8}^{6.7}$
	$z = 1$			$1.71_{1.43}^{1.99}$	$2.05_{1.72}^{2.39}$	$3.7_{3.2}^{4.2}$	$3.1_{2.7}^{3.6}$	$1.36_{1.07}^{1.66}$	$1.65_{1.28}^{2.04}$	$4.4_{3.7}^{5.4}$	$3.8_{3.1}^{4.6}$

**Notes:** Median and quartile values from Fig. 6.6, except for  $z = 1$  galaxies from Illustris and TNG100 (not included in Fig. 6.6). The formation times are measured in Gyr since the Big Bang.

Alternatively, to get rid of the impact of the galaxy redshift on the  $t_5$  and  $t_{10}$  calculations, we compute from each galaxy SFH the cosmic times at which the first  $5 \times 10^8 M_\odot$  and  $10^9 M_\odot$  of the stellar mass were formed ( $t_{5 \times 10^8 M_\odot}$  and  $t_{10^9 M_\odot}$ , respectively). These stellar masses correspond to the 5% and 10%, respectively, of the minimum galaxy stellar mass in our samples ( $10^{10} M_\odot$ ), which means they correspond to the assembly of fewer percentages of the mass of the rest of more massive galaxies. The distributions for  $t_{5 \times 10^8 M_\odot}$  and  $t_{10^9 M_\odot}$  are shown in the right panels of Fig. 6.6 (top-right and bottom-right, respectively).

We observe the same tendency as in  $t_5$  and  $t_{10}$ , although the distributions are now shifted towards younger ages of the Universe. The median values for CEERS galaxies with BC03 (SB99) models are  $t_{5 \times 10^8 M_\odot} = 0.20_{0.32}^{0.61}$  ( $0.50_{0.27}^{0.79}$ ) Gyr and  $t_{10^9 M_\odot} = 0.45_{0.25}^{0.88}$  ( $0.64_{0.35}^{1.05}$ ) Gyr, or, equivalently,  $z_{5 \times 10^8 M_\odot} = 13.1_{8.3}^{18.6}$  ( $9.5_{6.8}^{14.9}$ ) and  $z_{10^9 M_\odot} = 10.4_{6.3}^{15.6}$  ( $8.0_{5.4}^{12.4}$ ) (see Table 6.2). Regarding Illustris, massive galaxies at  $1 < z < 4$  (pink), although there is a small fraction of these galaxies with values above  $z = 10$  (and even 20) in both histograms, their median and quartiles are located at considerably lower redshift for both assembled masses:  $z_{5 \times 10^8 M_\odot} = 5.9_{4.8}^{8.2}$ , and  $z_{5 \times 10^8 M_\odot} = 4.9_{4.0}^{7.0}$ . This also happens for Illustris (TNG100) massive galaxies at  $z = 4$ , with  $z_{5 \times 10^8 M_\odot} = 7.6_{7.2}^{8.4}$  ( $6.8_{6.3}^{7.4}$ ) and  $z_{10^9 M_\odot} = 6.9_{6.3}^{7.5}$  ( $6.2_{5.8}^{6.7}$ ). For completeness, the median values for massive,  $z = 1$  galaxies Illustris (TNG100) are  $z_{5 \times 10^8 M_\odot} = 6.0_{4.1}^{4.9}$  ( $4.4_{3.7}^{5.4}$ ) and  $z_{10^9 M_\odot} = 4.1_{3.4}^{5.1}$  ( $3.8_{3.1}^{4.6}$ ). Again, Table 6.2 shows a summary of the median and quartile values shown in Fig. 6.6. In Appendix E, we include the individual formation times (and corresponding formation redshifts) calculated for our sample of 333 massive galaxies at  $1 < z < 4$  in CEERS (see Table E.1).

### 6.5.3 On the potential impact of Pop III stars and non-universal IMF

In the following paragraphs, we explore some potential limitations of our study. One of our major shortcomings is the fact that our estimated formation times have been obtained by considering both stellar population models and a universal IMF which are based on observations of nearby stars in the Milky Way. This kind of assumptions, although not necessarily true, are common in many literature papers when studying galaxies at high redshift, even at the highest redshifts (e.g.,

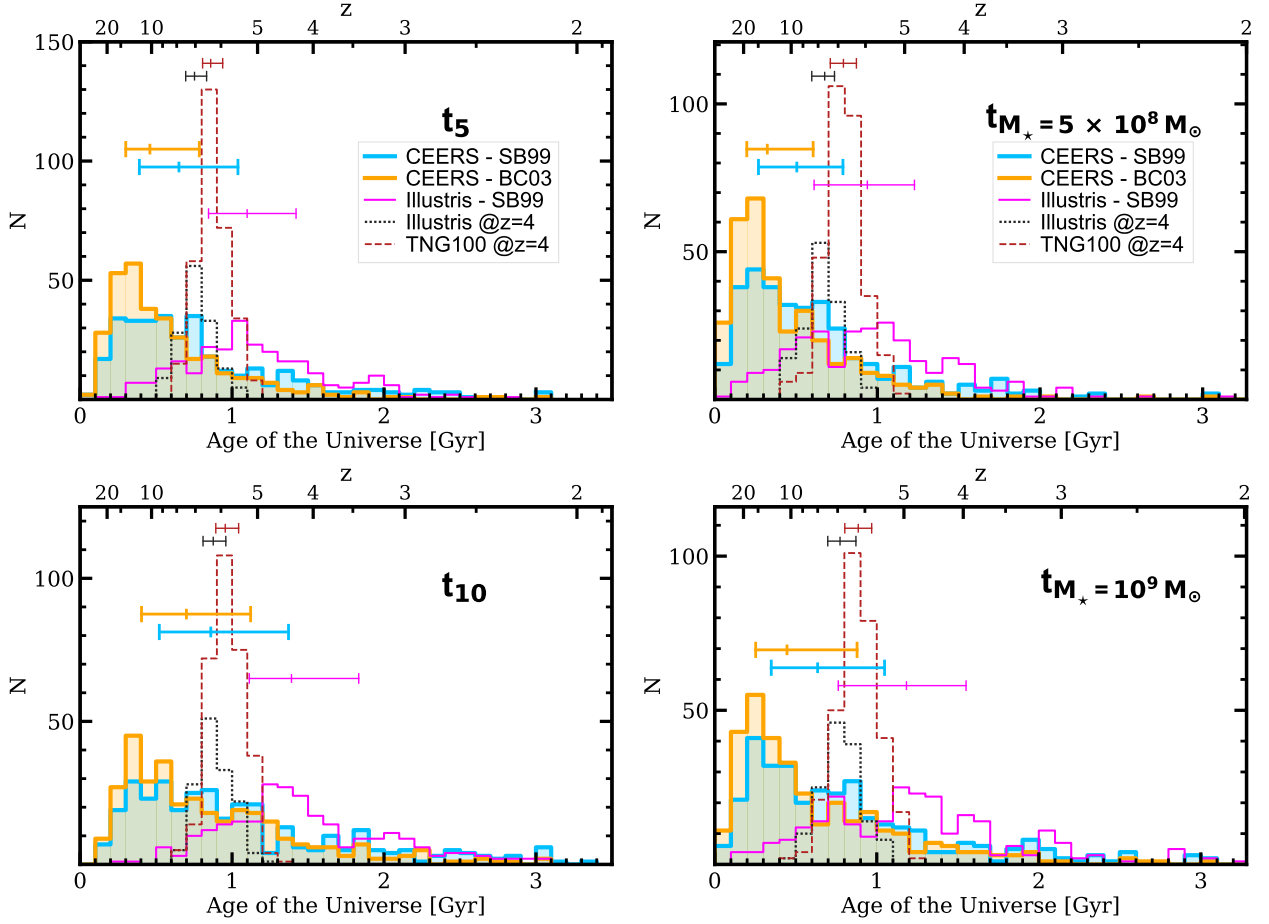


**Figure 6.6:** *Left panels:*  $t_5$  (top) and  $t_{10}$  (bottom) distributions calculated from each individual galaxy SFH in the sample. CEERS galaxies are shown in the filled histograms: BC03 in orange and SB99 in blue. Illustris massive,  $1 < z < 4$  galaxies, to which the same 2D-SPS method has been applied, are shown in pink. We include as a comparison the distributions for all Illustris and TNG100 massive galaxies at  $z = 4$ , for which the galaxies SFHs have been derived from their simulated stellar particles (instead of via 2D SPS; see main text). Median and quartiles are shown as segments at the top. *Right panels:*  $t_{5 \times 10^8 M_\odot}$  (top) and  $t_{10^9 M_\odot}$  (bottom) distributions computed from each galaxy SFH as the cosmic times at which those stellar mass were formed (same color code).

Harikane et al. 2023; Carnall et al. 2023; Pérez-González et al. 2023a; Labbé et al. 2023; Rodighiero et al. 2023; Yan et al. 2023). It is precisely at the highest redshifts where the largest differences are expected, due to the presence of Pop III stars (see Chapter 1). In fact, some recent works (e.g., Haslbauer et al. 2022; Finkelstein et al. 2023) argue that the top-heavy IMF expected for Pop III stars would explain the unexpected abundance of bright high-redshift galaxies in the early Universe ( $z > 9$ ) detected with JWST when compared to theoretical models. This top-heavy Pop III IMF, approximately flat in the logarithm of mass (Klessen & Glover 2023), would result in higher UV fluxes per unit of stellar mass and higher SFR at such high redshifts than expected for more usual IMF parametrizations (e.g., Chabrier 2003 and Kroupa 2001).

Elucidating how this would be affecting our formation times is difficult and probably beyond our reach with current data. The lifetimes of the hypothetical massive Pop III stars responsible for the large UV emission at high redshift are not long enough to have survived until the observational redshifts of this work (see Klessen & Glover 2023 for a review). Therefore, they would not have a direct impact on the SEDs we observe from our galaxies, except from minor effects associated to the uncertain early chemical enrichment produced by such stars (e.g., high N/O ratios; Cameron et al. 2023; Isobe et al. 2023). However, they do participate in the early stages of formation of massive galaxies and, in particular, represent the onset of their SFH. We can neither rule out that low-mass Pop III stars, with longer lifetimes, have survived until our observational redshifts<sup>2</sup>, but we expect that their contribution to the SEDs to be too small to be appreciable, due to their negligible contribution in stellar mass to the galaxies in which they would reside. Unfortunately, the understanding of Pop III stars is quite limited, including their IMF and their minimum and maximum masses, and is not expected to be significantly improved in the coming years (at least from direct JWST observations of these stars at high redshift; Robertson 2022; Klessen & Glover 2023). However, there is a small hope that the observation of local low-mass Pop III stars that could have survived to present day, if they exist, will shed some light on the properties of these stars.

In order to achieve more robust results on the properties of stellar populations of high-redshift galaxies, an effort is recently being made in the scientific community to use neither a single stellar population model nor a single fitting code (e.g., Finkelstein et al. 2022b; Adams et al. 2023; Donnan et al. 2023; Pérez-González et al. 2023b; Yan et al. 2023; Zavala et al. 2023). Nevertheless, the use of different IMFs (i.e., different from those usually used for low redshift), although desirable, is not yet widespread, although there are theoretical studies that argue that the IMF can evolve in time by depending on physical parameters such as the  $Z$  or the gas temperature in star-forming molecular clouds (e.g., Larson 1985; Bernardi et al. 2017). However, although our stellar models and IMF may not be as realistic as desirable to describe the evolution of stellar populations from high redshift to our observational redshift, the fact that we use stellar models and an IMF commonly used in the literature, both in works based on SED analysis and in numerical simulations, allows our results to be directly comparable with other similar works, while a detailed analysis of the possible systematic effects derived from this type of simplifications is pending.

Related to the latter point, we also point out that the latter discussion does not apply to the results derived for Illustris galaxies. The reason for this is that Illustris assumes both a universal

---

<sup>2</sup>For example, assuming non-rotating zero-metallicity stars, Pop III stars with  $1.7 M_{\odot}$  would have a lifetime of 9.06 Gyr, while those with more than  $4 M_{\odot}$  would only live less than 100 Myr (Murphy et al. 2021). According to our cosmology, the age of the Universe at the highest redshift of observation of this work ( $z = 4$ ) is 1.55 Gyr.

IMF and stellar populations models (to convert the output of the simulation into observable spectra) that do not evolve with cosmic time. In this regard, we remind the reader that the stellar particles that comprise each galaxy in Illustris do not represent individual stars, but a whole SSP consisting of stars formed with the same metallicity at the same time (see Section 2.2.3). The stellar mass of each stellar particle would be the sum of the stellar mass distribution of the SSP, for which a Chabrier (2003) is assumed.

## 6.6 Discussion and conclusions

The results presented in this chapter on the analysis of the SFH of massive galaxies at  $1 < z < 4$  in the CEERS survey highlight that CEERS galaxies started their star formation at very early ages in the Universe. According to our BC03 (SB99) results of the median SFH, CEERS galaxies would have started their formation at  $z \sim 30$  ( $\sim 20$ ) and would have formed the 5% of their stellar mass present at  $z \sim 1$  by  $z = 10.9$  (7.7), the 10% of this mass at by  $z = 8.4$  (6.2), and the 25% by  $z = 5.0$  (4.1). If we concentrate on  $t_5$  and  $t_{10}$ , these formation times are similar than the median values drawn from the distribution of the individual formation times of the CEERS galaxies. Such early star formation is still more evident in the distributions for  $t_{5 \times 10^8 M_\odot}$  and  $t_{10^9 M_\odot}$  of CEERS galaxies, on which the galaxy redshift should not affect (or affects less) the value of such formation times.

Although the formation redshifts found with the SB99 models are overall slightly lower than those of BC03 for CEERS galaxies, in both cases they are well above those found with the same 2D-SPS method for massive Illustris galaxies in the same redshift range. This is seen both in the median SFH for Illustris massive galaxies at  $1 < z < 4$  and in the distributions of the individual formation times. Even massive galaxies at  $z = 4$  from Illustris or TNG100 are not able to match such early formation times. These simulations represent the state of the art in our current (until JWST, at least) knowledge on the onset of star formation in galaxies and galaxy evolution in general. Although our 2D-SPS method may be biased to assign formation times somewhat younger than reality (up to  $\sim 8.5\%$ ; see Appendix B), such a bias would not be sufficient to explain the large number of galaxies with such high formation times nor could it account for the differences between the CEERS galaxies and the simulations.

The fact that our median SFH for CEERS galaxies begins at  $z \gtrsim 20$  implies, because of the way this median SFH is built, that more than the half of our CEERS galaxies have galaxy SFHs which begins at redshift higher than those values. This seems to contradict the currently (or, at least, before JWST) accepted scenario in which the first galaxies formed in  $\sim 10^8 M_\odot$  dark matter halos at  $z \sim 10$  (e.g., Wise & Abel 2007, 2008; Greif et al. 2008, 2010; see Section 1.1.2). Nevertheless, the considerable number of galaxies with  $M_\odot = 5 \times 10^8 M_\odot$  already at  $z = 10$  that our results predict is in agreement with the unexpected abundance of relatively bright galaxies at  $z > 10$  reported in the recent literature regarding results based on JWST cosmological surveys, some of which are unusually massive (with up to  $M_\star \sim 10^{11} M_\odot$ ; e.g., Finkelstein et al. 2022a; Labbé et al. 2023; Harikane et al. 2022; Bradley et al. 2022; Naidu et al. 2022; Castellano et al. 2022; Adams et al. 2023; Atek et al. 2023; Donnan et al. 2023; Yan et al. 2023; Pérez-González et al. 2023a). If confirmed spectroscopically, these galaxies could be responsible for beginning the reionization of the Universe at higher redshifts than previously assumed, and their abundance could be hardly explained with

the current  $\Lambda$ CDM cosmological model unless an unaccounted (probably implausibly) high star formation efficiency is assumed at high redshift (see [Boylan-Kolchin 2023](#)). According to that work, in case these extremely high efficiencies are actually reached, this would imply very steep early rising SFHs over time in massive halos, which is precisely what we observe in the median SFH of the CEERS sample. Other alternatives that have been recently proposed suggest that such early population of galaxies could be explained if the amplitudes of the primordial density fluctuations are not Gaussian (e.g., [Biagetti et al. 2023](#)) or if other scenarios, such as a more top-heavy IMF in the stellar populations at high redshift (e.g., [Harikane et al. 2023](#); [Finkelstein et al. 2013](#)), are at play. Nevertheless, due to the novelty of these results, all these possible explanations are still under debate.

Finally, regarding the comparison of our inferred formation times with those predicted by simulations, the considerably lower formation redshifts inferred for Illustris and TNG when compared to those of CEERS highlight a potential problem in the models regarding their (low) efficiency in forming stars compared with the observations in these early stages of the Universe. Assuming the  $\Lambda$ CDM is the correct cosmological model to describe our Universe, this would imply the need to modify the adopted galaxy formation models. As shown in Chapter 2, these simulations rely on simplistic subgrid models for star formation and feedback by SNe and AGNs which are tuned to reproduce  $z = 0$  galaxy populations. Nevertheless, these subgrid physics models might not be applicable as such to describe the high-redshift regime. Besides, as discussed in Section 6.5.3, the fact that both Illustris and IllustrisTNG assume a time-invariant IMF could also be playing a role. Further investigation is needed in order to disentangle the actual origin of these discrepancies, but it will likely require an improvement of the currently adopted galaxy formation (and, maybe, cosmological) models within the simulations to take into account the results from recent JWST data, such as those presented in this thesis.

# Conclusions and Future Work

---

## 7.1 General conclusions

The main objective of this thesis has been to address some of the most fundamental open issues on the formation and evolution of present-day massive galaxies (like the Milky Way and more massive). In particular, we focus on determining when these galaxies started to form their first stars or, alternatively, what were their formation redshifts. This has profound implications on key topics such as the epoch of reionization and the galaxies responsible for it, what is the balance between *in-situ* and *ex-situ* star formation in massive galaxies, to name a few.

The advent of JWST provides a unique opportunity to explore stellar populations with spatial resolution up to redshifts for which the photometric evolution of the stellar populations (even if they are as old as the Universe at the redshift of observation) is still measurable, while covering the spectral region (once combined with HST data) from the UV to the near-infrared rest-frame. For this purpose, we have taken advantage of the exceptional optical capabilities of both ACS and WFC3 with HST and the unprecedented infrared capabilities of NIRCам at JWST, and combined them in order to analyze the spatially-resolved stellar populations of massive  $1 < z < 4$  galaxies.

In order to analyze the stellar populations with spatial resolution in these galaxies we have implemented a novel method of Stellar Population Synthesis in two dimensions (2D SPS) aimed at reproducing the global star formation history (SFH) of our galaxies by fitting HST+JWST Spectral Energy Distributions (SED) in a pixel-by-pixel basis. The method was first tested on spatially-resolved SEDs composed of broad-band ACS, WFC3 and NIRCам imaging data built upon the predictions of the Illustris hydrodynamical simulations. Given the scientific interests outlined above, we select a sample of massive ( $M_{\star} > 10^{10} M_{\odot}$ ) galaxies at  $1 < z < 4$  that, according to the Illustris merger trees, would evolve into local  $M_{\star} > 10^{11} M_{\odot}$  galaxies. The results from this work are published in García-Argumánéz et al. (2023) and its main conclusions can be summarized as follows:

- Our method proves to be successful at recovering the early SFH of the  $1 < z < 4$  precursors of local massive galaxies. In order to quantify the success of the method we derive individual formation times ( $t_5$ ,  $t_{10}$ , and  $t_{25}$ , which represent the time since the Big Bang needed for a galaxy to reach 5%, 10%, and 25% of its mass at the epoch of observation) and compare them with those determined from the Illustris (ground-truth) SFHs. This comparison results in an accuracy (median-averaged over the whole sample) below 5%, with our 2D-SPS formation times happening earlier, and a galaxy-by-galaxy scatter in these formation times of 0.2 – 0.3 dex.

- Given that we aim to explore the early formation of *all* local massive galaxies, we take advantage of the availability of merger trees from Illustris to explore the impact of potential biases due to the fact that (1) the SFH of local massive galaxies includes the SFH of both massive and non-massive precursors merged below the redshift of observation and (2) a fraction of the local massive galaxies have no massive  $1 < z < 4$  precursors. Relative to the formation times determined for our massive precursors, we conclude:
  - Ground-truth formation times of the ( $z = 0$ ) descendants of our massive precursors ( $1 < z < 4$ ) are larger by up to  $\sim 200$  Myr than those inferred when only massive precursors are considered. This difference is attributed to the mass cut-off imposed on our sample of progenitors and which makes our sample to contain only the most massive (and, possibly older) progenitors.
  - Ground-truth formation times of the entire population of  $z = 0$  massive galaxies are larger by  $\sim 200$  Myr than those having a massive precursor at  $1 < z < 4$ .
- Finally, if we relax the condition of our simulated  $1 < z < 4$  galaxies leading to massive local galaxies (as it would be the case in real cosmological surveys at high redshift), our method and the Illustris ground-truth both yield similar median SFHs and formation times.

Thus, the selection of massive precursors (which is inherent to any magnitude-limited cosmological survey at high redshift) does not lead to major biases in terms of the formation epoch of very massive local galaxies.

The second and most relevant part of the research of this thesis regarding the actual SFH of local massive galaxies relies on applying our 2D-SPS methodology to real massive galaxies at  $1 < z < 4$  from JWST+ HST observations. In particular, we use imaging data from both CANDELS HST and CEERS JWST surveys. The conclusions from this work are the following:

- We find that massive galaxies at  $1 < z < 4$  detected in the CEERS NIRC*am* imaging data began to form stars at very high redshifts: the onset of star formation in the sample occurred at  $z \sim 30$  ( $z \sim 20$ ) according to the median SFHs derived from our BC03-based (SB99) 2D-SPS modeling. Besides, they formed 5% of their stellar mass at  $z \sim 1$  by  $z = 10.9$  (7.7) and 10% by  $z = 8.4$  (6.2).
- Similar results are obtained when analyzing the distributions for the formation times ( $t_5$ ,  $t_{10}$ , for 5% and 10%, respectively) of individual galaxies, with median associated redshifts  $z_5 = 10.2$  (7.9) and  $z_{10} = 7.4$  (6.4) for BC03 (SB99).
- The distributions for the time elapsed in order to form  $5 \times 10^8 M_\odot$  and  $10^9 M_\odot$  in stars,  $t_{5 \times 10^8 M_\odot}$  and  $t_{10^9 M_\odot}$ , respectively, which are parameters only mildly affected by the redshift distribution of our massive galaxies at  $1 < z < 4$ , yet show more evidence of this early star formation in galaxies, with median values of  $z_{5 \times 10^8 M_\odot} \sim 13$  (9.5) and  $z_{10^9 M_\odot} \sim 10$  (8) with BC03 (SB99).
- Such early formation times inferred for our sample of massive galaxies at  $1 < z < 4$  are not reached neither by the Illustris simulation used for the first part of this thesis, both from the ground-truth SFHs and those derived from our 2D-SPS method. Indeed, the median SFH of



Illustris massive galaxies at  $1 < z < 4$  predicts a formation redshift of  $z_5 = 4.4$ , with a less steep and postponed onset of star formation. This delayed formation of the stellar mass in Illustris (and also in the more recent TNG100) simulations is also seen in the distributions of the individual formation times of massive galaxies. Although our 2D-SPS method could be biased towards slightly earlier formation times than ground-truth (with a median offset  $\lesssim 10\%$ ), this offset cannot cope with the differences reported in this thesis.

- We thus conclude that, according to our results, either we do not yet fully understand how massive structures grow in the early Universe or how galaxy formation first occurs in them, which could be related to ingredients such as primordial gas cooling, initial mass function or subgrid physical processes in general. We note that our findings seem to be in agreement with those of recent works based on JWST cosmological surveys, which find a largely unexpected abundance of luminous galaxies at  $z \sim 10$  (and higher). Due to the novelty of these JWST results, a definitive consensus regarding the underlying cause of the unexpectedly abundant population of high-redshift galaxies has not yet been established.

These early results from the exploitation of JWST are testimony of the exciting future that lies ahead, where JWST is called to lead to a major leap in our understanding on the formation and evolution of high-redshift galaxies. *How far JWST is going to take us?* Only time will tell, hopefully soon.

## 7.2 Future work

This section presents some future research lines to be conducted taking advantage of the knowledge gained from this thesis. We have established several follow-up initiatives that will allow us to continue exploiting our data, together with other strategies that will make use of recent and upcoming JWST observations. Our primary areas of interest and future research goals are as follows:

- Our first straightforward goal is to extend our sample of  $1 < z < 4$  massive galaxies from CEERS Epoch 1 observations with analogous galaxies appearing in the CEERS Epoch 2 NIRCcam observations (taken in December 2022). This implies adding 6 new NIRCcam pointings to our previous 4 pointings, increasing our field of view by up to  $\sim 100$  arcmin<sup>2</sup>. Assuming a constant number of massive galaxies at  $1 < z < 4$  in each pointing, this will result in  $\sim 500$  additional galaxies to our previous sample of 333 considered galaxies.
- The results presented in this thesis focus on determining the first stages of formation of massive galaxies from their inferred integrated SFH. These SFHs are built from a spatially-resolved analysis, by combining the SFH of the resolution elements in the galaxy. Although not addressed in this thesis, we are also in the position to analyze the formation times of a galaxy in a spatially-resolved fashion. This can be done by calculating the formation times of each resolution element in the galaxy, with the aim to build galaxy maps for  $t_k$ . The spatial (e.g., radial) distribution of these formation times can be helpful to identify structures or regions of the galaxy that formed at different cosmic times and to establish different formation mechanisms for them. In addition, it would be interesting to compare the spatially-resolved formation times in a galaxy with those derived from their 2D-SPS-derived integrated SFH.

- Similarly, and related to the latter point, a detailed analysis of other properties of spatially-resolved stellar populations in our massive galaxies is still pending (such as stellar mass,  $Z$ ,  $A_V$ , etc.), although the necessary data for this study are already at our disposal. This would be very helpful to further investigate the different structures found in our  $t_k$  maps.
- Another pending issue is to study the impact of the photometric redshift uncertainties on our inferred formation times. Although for all the Illustris galaxies analyzed in this work we assumed spectroscopic redshifts, most of the CEERS galaxies considered in Chapter 6 do not have spectroscopic redshifts available and rely on photometric redshifts instead. These photometric redshifts have been estimated from the best-fitting photometric redshift distribution that results from fitting the integrated SEDs with `eazy`, and by subsequently considering the most probable redshift value of this distribution. A way to have an estimate of how the redshift uncertainties can impact our results could be to repeat the analysis for each galaxy multiple times by considering different redshift values for the galaxy at each time. These redshift values would be drawn from the photometric redshift distribution provided by `eazy`.
- CEERS has 6 MIRI pointings that overlap some of the NIRC*am* mosaics. With the full set of CEERS observations already completed and available to us, it would be particularly instructive to add the photometric bands provided by MIRI in the MIR to our analysis and study whether better sampling our SEDs in this part of the spectrum impacts the inferred formation times.
- Finally, the power of the 2D-SPS method developed in this thesis is that it can be applied to any cosmological field, with not necessarily the same photometric bands available. For example, the Guaranteed Time Observations (GTO) program called JWST Advanced Deep Extragalactic Survey (JADES) will survey GOODS-N and GOODS-S using up to 14 JWST imaging bands and 5 HST ACS bands (see details in Hainline et al. 2023). In addition to this, as time goes on, more and more data are becoming available from other different cosmological fields observed with JWST, which can also become potential targets on which to apply our 2D-SPS methodology.

## Other combinations of parameters explored in the SED fits

---

In Chapter 5, we only show the values or ranges of the SED-fitting parameters (see Table 5.3) that yield the best match between the mass-fraction formation times inferred from our 2D SPS-derived SFHs and those calculated from the ground-truth SFHs. Nevertheless, the choice of those best-fitting parameters was not something obvious from the beginning, but their values were found after spending a significant amount of the time of this thesis on exploring the parameter space and testing different combinations of them. For this reason, we have decided to dedicate an appendix to briefly explain how this search of the best-fitting parameters was conducted, and to show some examples of the explored combinations.

In the beginning of this thesis, we started our search by considering only a single time-delayed exponential SFH (instead of two populations). However, as commented in Section 5.5, it was obvious in all of the tests performed that such simple parametrization for the SFH clearly underestimated most of the mass-fraction formation times considered in all our redshift interval. This made us adopt the 2-burst time-delayed exponential described in Section 5.4.1. The subsequent tests with this double-burst SFH parametrization revealed that the most relevant parameters in the SED fits (for our comparison of our 2D-SPS-derived formation times with those provided by Illustris ground-truth SFHs) were the age frontier between the young and the old population ( $\text{age}_{\text{lim}}$ ) and the star formation time-scale of the young population ( $\tau_{\text{young}}$ ). A great amount of tests were then performed by varying only the values of the two latter parameters (and keeping fixed the rest of the parameters shown in Table 5.3). Among the values explored for  $\text{age}_{\text{lim}}$ , this was fixed to several percentages of the age of the Universe (from 10% to 90%). Regarding  $\tau_{\text{young}}$ , this was either kept fixed (to, among other, 10 Myr, 50 Myr, 100 Myr, or 200 Myr) or free to adopt values in different ranges (e.g., 10 – 100 Myr, 10 – 150 Myr, or 10 – 200 Myr). Those tests were made both for SB99 and for BC03 models, finding with SB99 a better agreement with ground-truth.

In this appendix, we show the different versions of Fig. 5.9 (our “method validation figure”) that were used in our search of the best SED-fitting parameters for a selected number of tests in which we explored different values of  $\text{age}_{\text{lim}}$  and  $\tau_{\text{young}}$  (Figures A.1 to A.12). Table A.1 shows the median relative offsets (with respect to ground-truth) and the scatter (calculated from the 68% interval of these offsets) for the formation times shown in each figure. We found that the combinations that best reproduced the ground-truth formation times were those with  $\text{age}_{\text{lim}}$  equal to 50% or 40%, and  $\tau_{\text{young}} = 10$  Myr (fixed). Those two combinations correspond to tests (6) and (10) in Table A.1, respectively. If we have a closer look at their method validation figures, we see that for  $\tau_{\text{young}} = 10$  Myr and  $\text{age}_{\text{lim}} = 50\%$  (Fig. A.6), our 2D-SPS method overpredicts the formation

**Table A.1:** Results for the validation of the 2D-SPS method for some other combinations of parameters explored for different values of  $\text{age}_{\text{lim}}$  and  $\tau_{\text{young}}$ . We have highlighted the best-fitting parameters presented in Chapter 5 with a gray shade.

Test	$\text{age}_{\text{lim}}$ (%)	$\tau_{\text{young}}$ (Myr)	Models	Median Relative Offset (%)					Scatter (%)					Figure
				$t_5$	$t_{10}$	$t_{25}$	$t_{\text{mw}}$	Median	$t_5$	$t_{10}$	$t_{25}$	$t_{\text{mw}}$	Median	
(1)	60	10	BC03	+18	+23	+35	+31	+27	20	27	41	39	33	Fig. A.1
(2)	60	10	SB99	+21	+28	+39	+26	+27	22	28	46	46	37	Fig. A.2
(3)	60	10 – 100	SB99	+18	+18	+17	-5.8	+17	20	26	44	28	27	Fig. A.3
(4)	60	10 – 150	SB99	+17	+18	+16	-7.8	+17	20	26	45	28	27	Fig. A.4
(5)	60	10 – 200	SB99	+17	+17	+15	-8.9	+16	20	25	45	26	26	Fig. A.5
(6)	50	10	SB99	+9.7	+12	+13	+7.3	+11	25	29	42	34	32	Fig. A.6
(7)	50	10 – 100	SB99	+8.8	+6.5	-2.7	-16	+1.9	23	26	41	25	26	Fig. A.7
(8)	50	10 – 100	BC03	+27	+29	+20	+0.9	+23	20	27	57	34	30	Fig. A.8
(9)	30	10	SB99	-28	-35	-36	-35	-35	26	22	20	17	21	Fig. A.9
(10)	40	10	SB99	-5.6	-9.6	-13	-16	-11	27	28	28	24	27	Fig. A.10
(11)	70	10	SB99	+29	+37	+59	+45	+41	20	29	51	53	40	Fig. A.11
(12)	80	10	SB99	+37	+50	+75	+62	+56	21	30	53	54	41	Fig. A.12
Final	40 for $1 < z < 2$ 50 for $2 < z < 4$	10	SB99	+4.4	+1.8	-0.13	-5.2	+0.81	25	29	35	30	30	Fig. 5.9

times inferred for the lowest-redshift galaxies (at  $1 < z < 2$ ; dark blue dots) with respect to ground-truth, while it seems to recover fairly well the one-to-one relation for the rest of the galaxies at higher redshifts (at  $2 < z < 4$ ; all other colors). If we now look at what happens in Fig. A.10 for  $\tau_{\text{young}} = 10$  Myr and  $\text{age}_{\text{lim}} = 40\%$ , we see that the one-to-one relation is generally recovered for all the formation times of  $1 < z < 2$  galaxies (dark blue dots), but our method underestimates the formation times for higher-redshift galaxies.

That was the reason that led us to adopt a combination of both tests (6) and (10) for our choice of the best-fitting parameters, with  $\text{age}_{\text{lim}}$  being 50% or 40% depending of the two latter redshift intervals. This final test has been included as a comparison in Table A.1 with a gray shade. As commented in Chapter 5 and shown in Table A.1, only when allowing the value of  $\text{age}_{\text{lim}}$  to depend on the redshift of the galaxy, we were able to obtain the minimum median relative offsets for each of the formation times (and for the median of all of them). In addition, the median scatter (30%) of our final test is comparable to that of the other tests, except for test (9) which has a smaller scatter (21%), but which yields formation times which are clearly underestimated with respect to ground-truth (with median relative offsets from -28% to -36%).

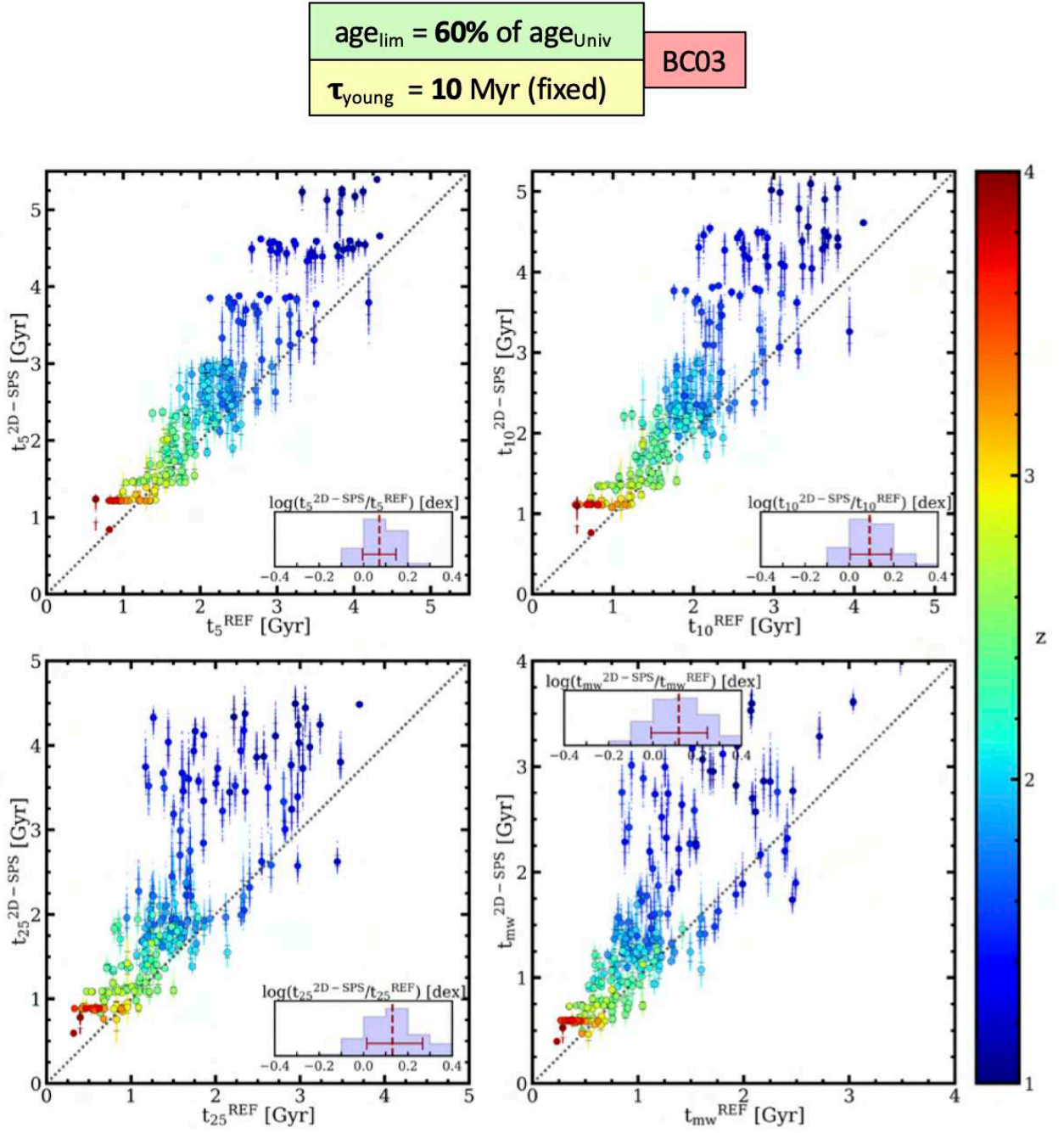


**Figure A.1:** Method validation figure for  $\text{age}_{\text{lim}} = 60\%$  of the age of the Universe, and  $\tau_{\text{young}} = 10 \text{ Myr}$ , for BC03 models.

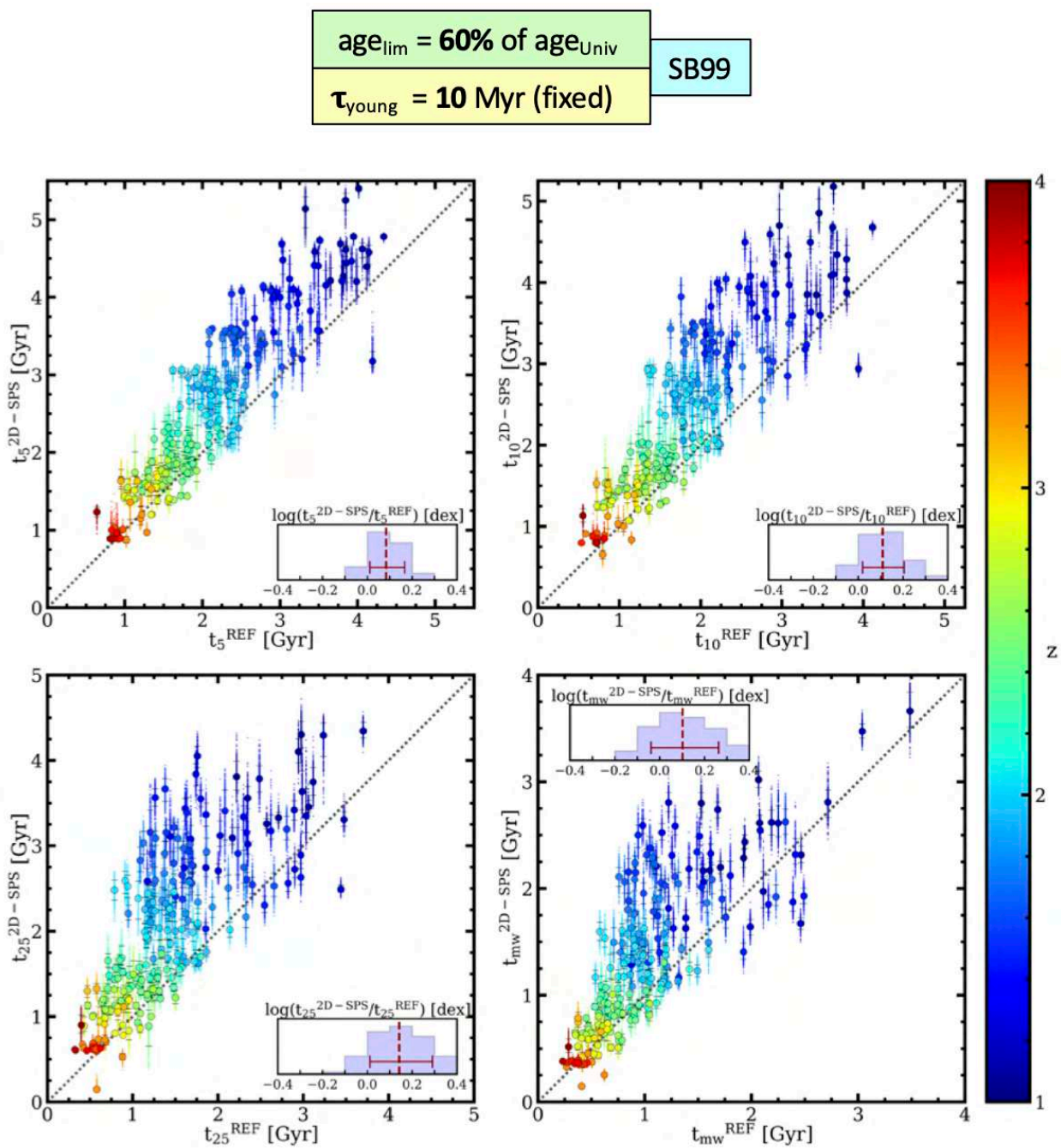


**Figure A.2:** Method validation figure for  $\text{age}_{\text{lim}} = 60\%$  of the age of the Universe, and  $\tau_{\text{young}} = 10 \text{ Myr}$ , for SB99 models.

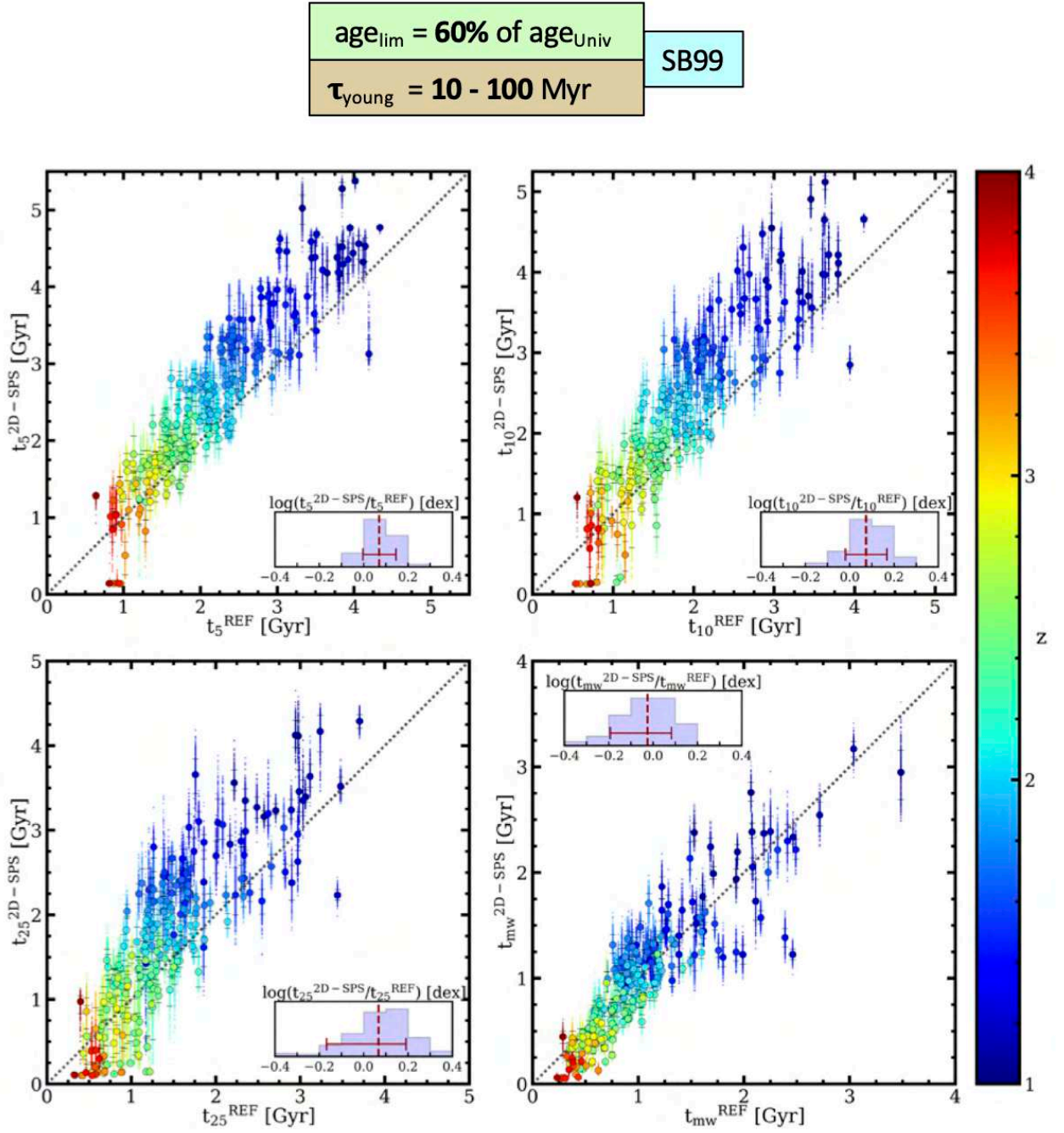


**Figure A.3:** Method validation figure for  $\text{age}_{\text{lim}} = 60\%$  of the age of the Universe, and  $\tau_{\text{young}} = 10 - 100 \text{ Myr}$ , for SB99 models.

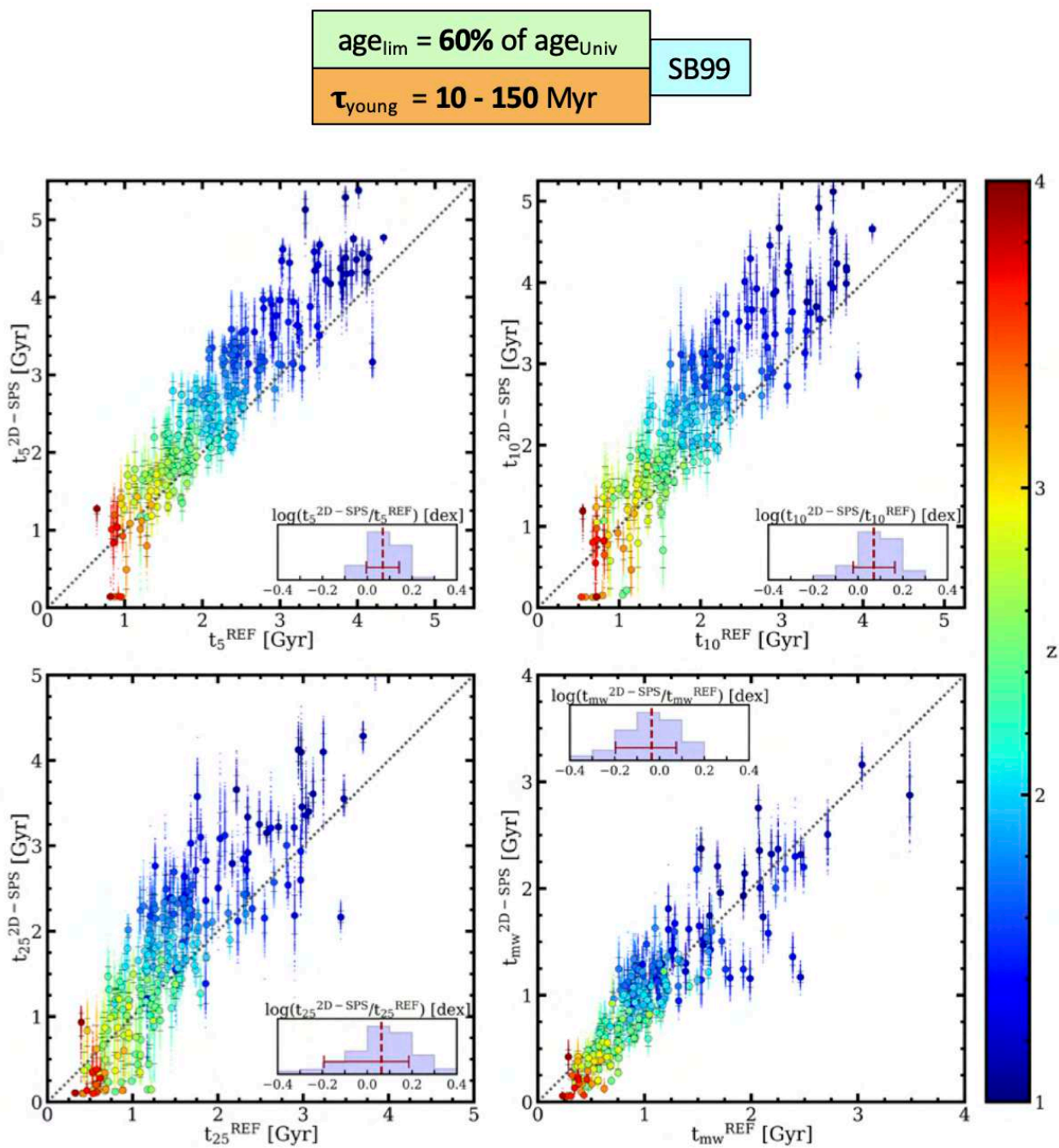


**Figure A.4:** Method validation figure for  $\text{age}_{\text{lim}} = 60\%$  of the age of the Universe, and  $\tau_{\text{young}} = 10 - 150 \text{ Myr}$ , for SB99 models.



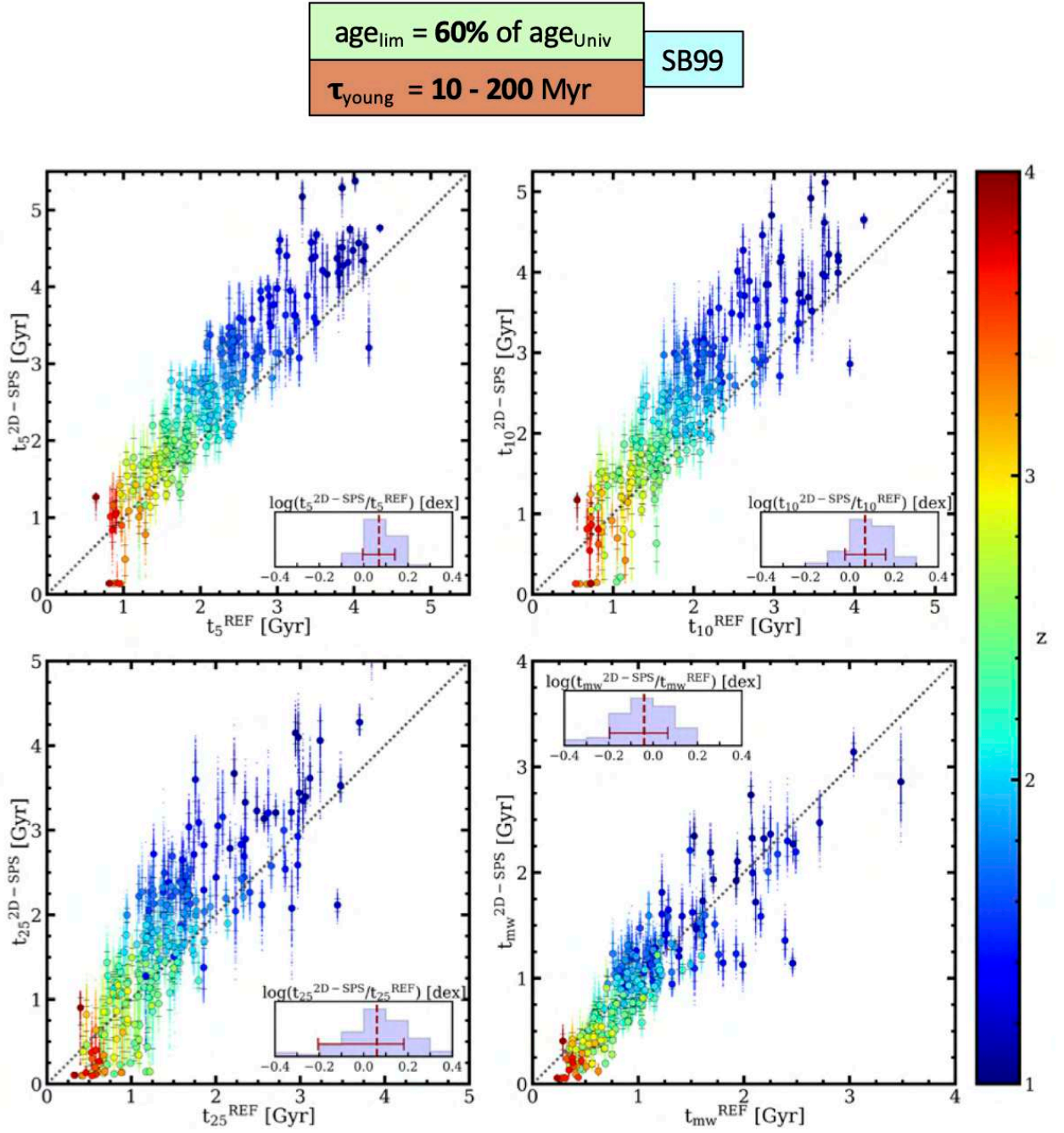


**Figure A.5:** Method validation figure for  $\text{age}_{\text{lim}} = 60\%$  of the age of the Universe, and  $\tau_{\text{young}} = 10 - 200 \text{ Myr}$ , for SB99 models.

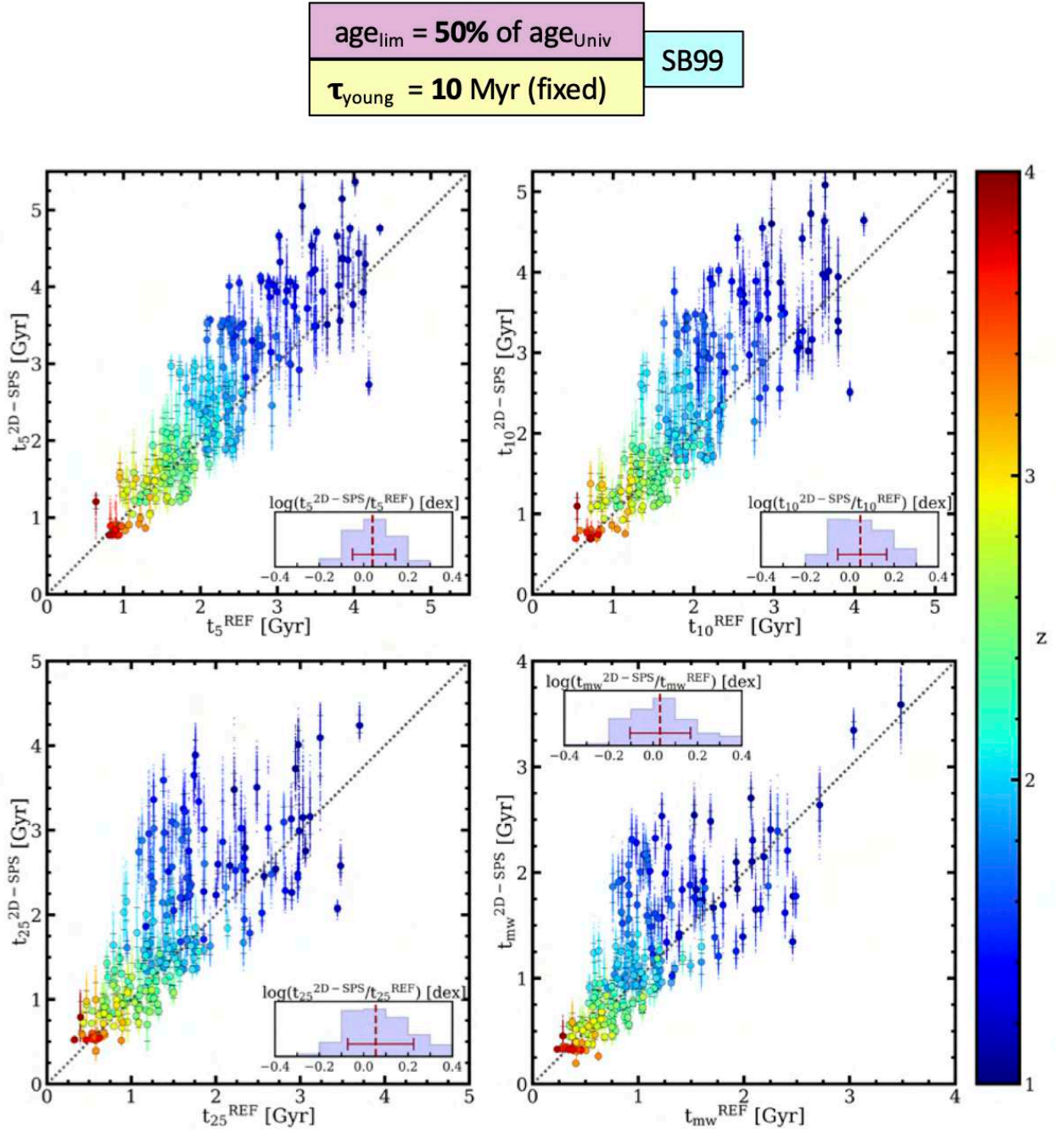


**Figure A.6:** Method validation figure for  $\text{age}_{\text{lim}} = 50\%$  of the age of the Universe, and  $\tau_{\text{young}} = 10 \text{ Myr}$ , for SB99 models.

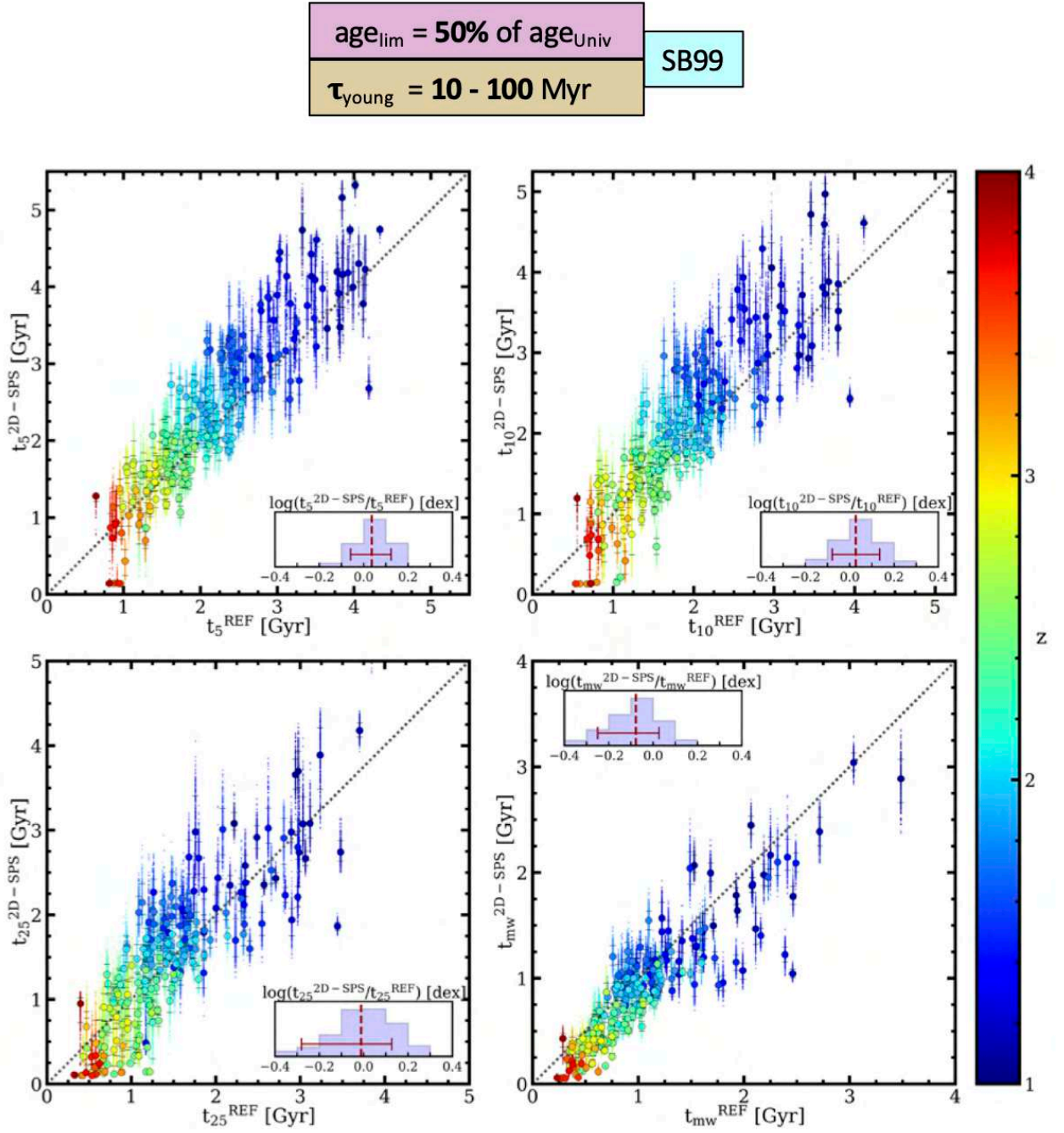


**Figure A.7:** Method validation figure for  $\text{age}_{\text{lim}} = 50\%$  of the age of the Universe, and  $\tau_{\text{young}} = 10 - 100 \text{ Myr}$ , for SB99 models.

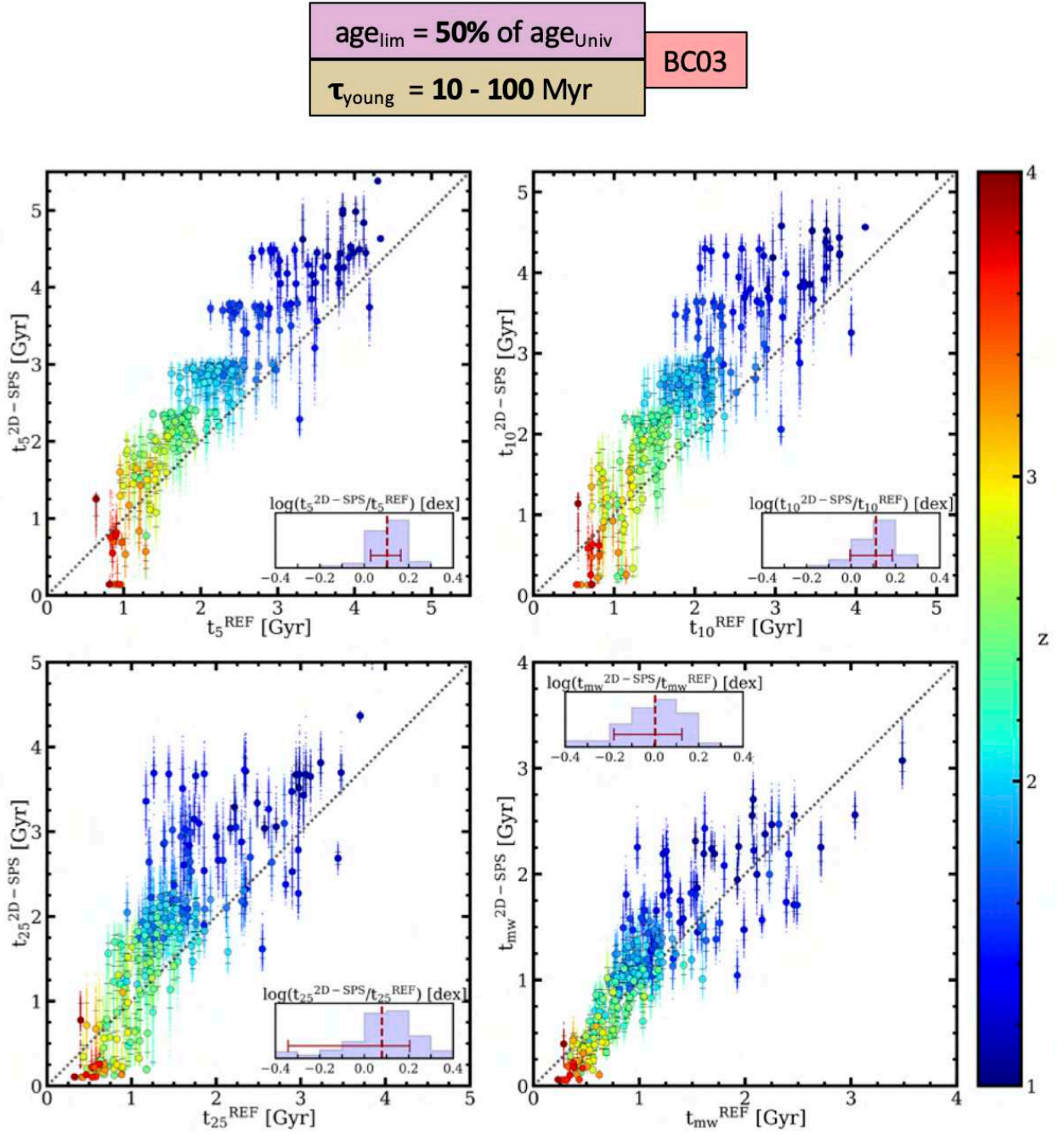


**Figure A.8:** Method validation figure for  $\text{age}_{\text{lim}} = 50\%$  of the age of the Universe, and  $\tau_{\text{young}} = 10 - 100 \text{ Myr}$ , for BC03 models.

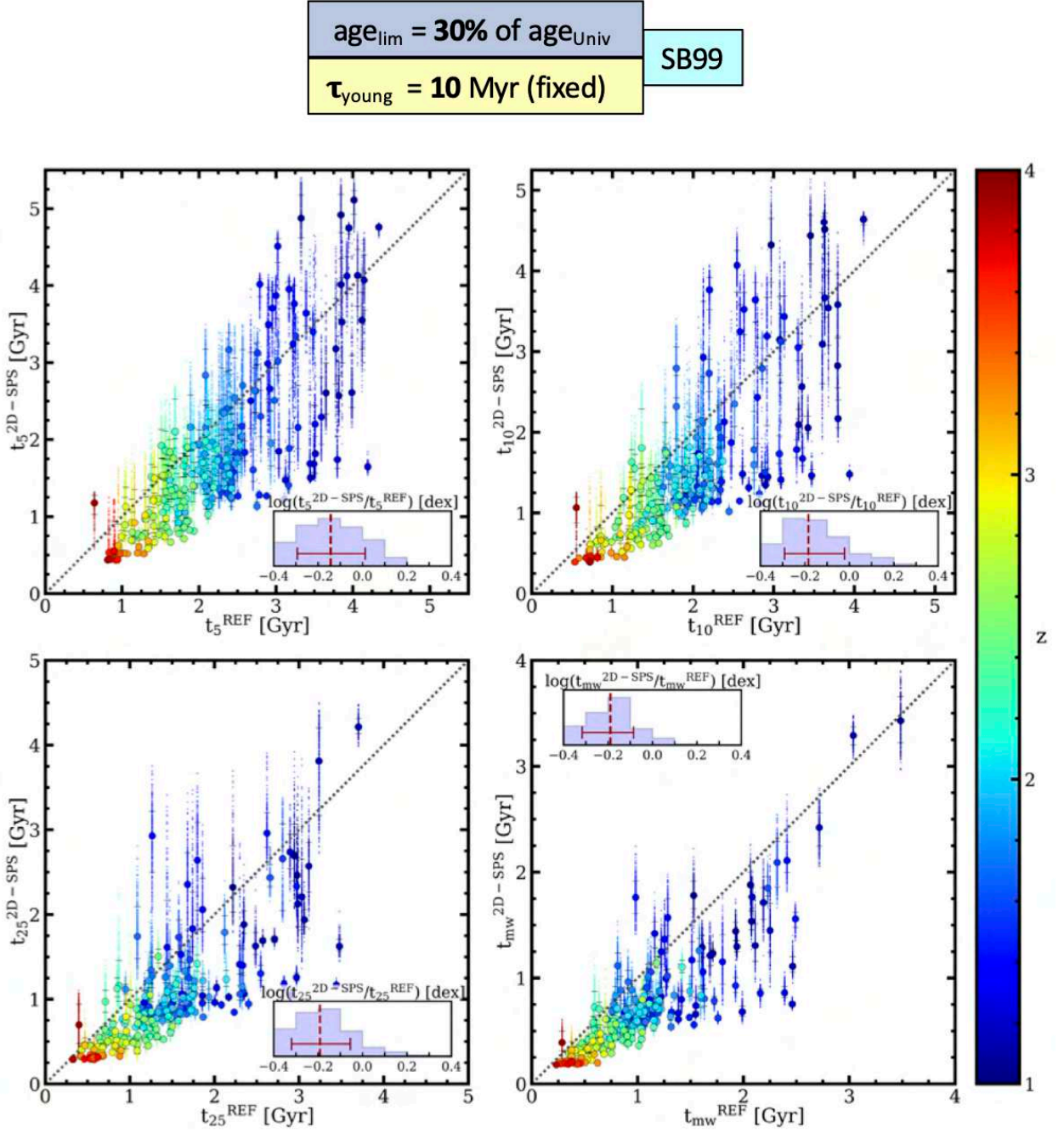


**Figure A.9:** Method validation figure for  $\text{age}_{\text{lim}} = 30\%$  of the age of the Universe, and  $\tau_{\text{young}} = 10 \text{ Myr}$ , for SB99 models.

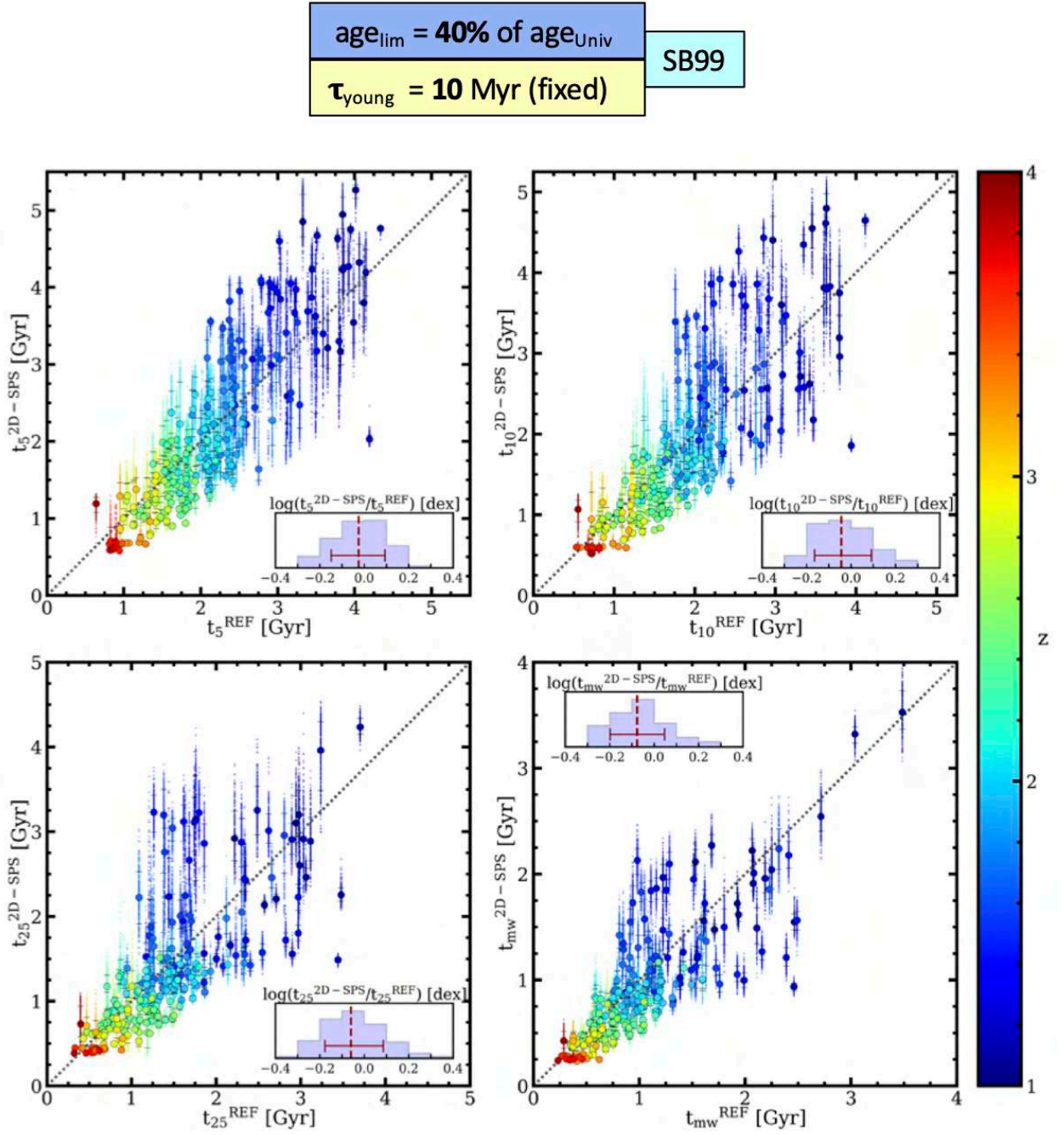


**Figure A.10:** Method validation figure for  $\text{age}_{\text{lim}} = 40\%$  of the age of the Universe, and  $\tau_{\text{young}} = 10 \text{ Myr}$ , for SB99 models.

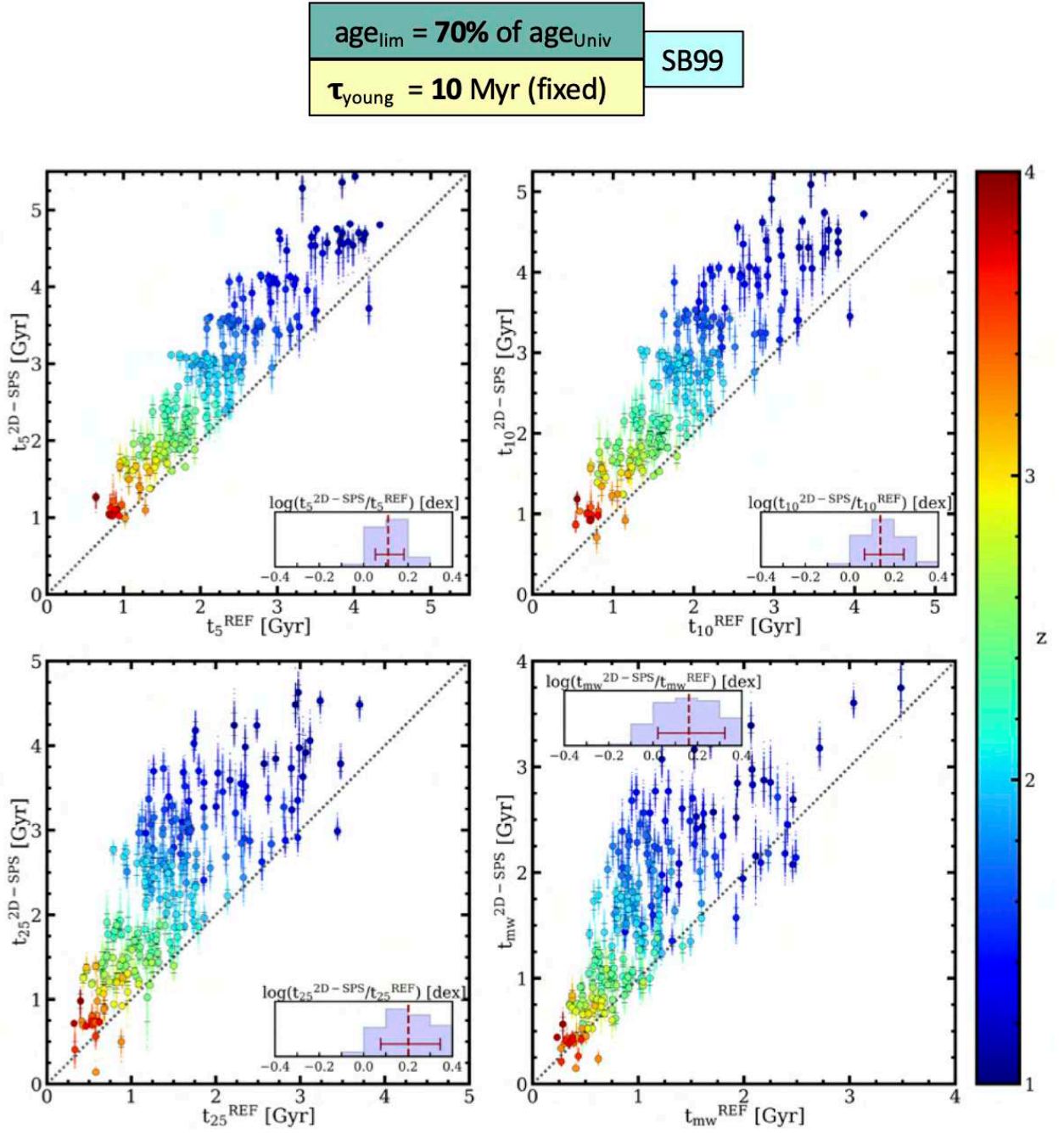


**Figure A.11:** Method validation figure for  $\text{age}_{\text{lim}} = 70\%$  of the age of the Universe, and  $\tau_{\text{young}} = 10 \text{ Myr}$ , for SB99 models.

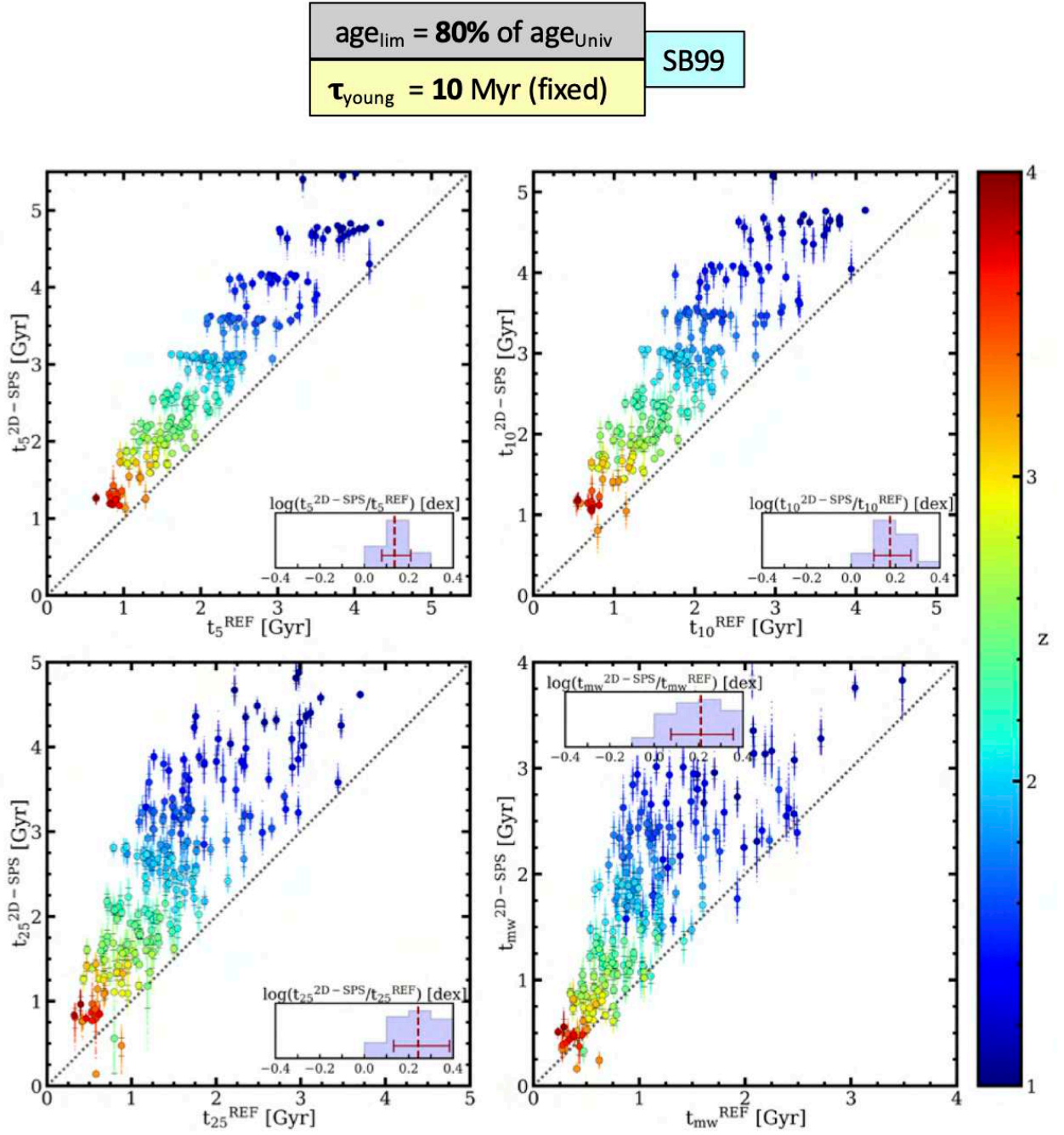


**Figure A.12:** Method validation figure for  $\text{age}_{\text{lim}} = 80\%$  of the age of the Universe, and  $\tau_{\text{young}} = 10 \text{ Myr}$ , for SB99 models.



## 2D-SPS method validation for a reduced number of filters

---

In Chapter 5, we demonstrated our 2D-SPS method could successfully recover the mass-fraction formation times  $t_5$ ,  $t_{10}$ ,  $t_{25}$ , and  $t_{\text{mw}}$  with a median systematic offset of less than  $\sim 5.5\%$  in all the four formation times (see Section 5.5 and Fig. 5.9). This analysis was performed by considering 15 filters in total (i.e., 5 ACS + 4 WFC3 + 6 NIRCcam filters), for the 2D-SPS analysis. Nevertheless, as commented in Chapter 6, the number of filters considered for this chapter is only 8 (2 ACS + 6 NIRCcam filters). For this reason, to ensure that our method is still effective in recovering the above formation times, we must repeat the method validation analysis considering only those 8 filters.

Fig. B.1 is equivalent to Fig. 5.9 and shows the formation times  $t_5$ ,  $t_{10}$ ,  $t_{25}$ , and  $t_{\text{mw}}$  derived from 2D-SPS-derived galaxy SFHs as a function of their ground-truth values, but in this case the 2D-SPS-derived galaxy SFHs have been built by fitting the SEDs to only the 8 filters in Chapter 6. *A priori*, we can see the aspect of this figure is very similar to Fig. 5.9 in the sense that our formation times seem to follow the one-to-one relation given by their ground-truth values, with no evident systematic offsets. We find that our 2D-SPS-derived  $t_5$ ,  $t_{10}$ ,  $t_{25}$ , and  $t_{\text{mw}}$ , expressed in lookback time with respect to each galaxy, for the 8 (15) filters in Chapter 6 (Chapter 5) are consistent with the ground-truth values with a median relative offset of  $+8.5\%$  ( $+4.4\%$ ),  $+8.4\%$  ( $+1.8\%$ ),  $+8.0\%$  ( $-0.1\%$ ), and  $+4.7\%$  ( $+5.2\%$ ). This means our 2D-SPS inferred formation times slightly predict earlier formation times than ground-truth, but with median relative offsets below  $\sim 8.5\%$  values for all cases. This was one of the limitations of our 2D-SPS method which already happened when using all the 15 filters, although in that case the median relative offsets were all below  $\sim 5\%$  values. Regarding the scatter (68% interval) of the individual offsets using 8 filters (15 filters), shown as an inset in each panel, these are 0.35 (0.33), 0.34 (0.31), 0.26 (0.27), and 0.17 (0.17) Gyr for  $t_5$ ,  $t_{10}$ ,  $t_{25}$ , and  $t_{\text{mw}}$ , respectively, which suggests that the previous scatter found when using the 15 filters is almost unaffected when reducing the number of filters to 8.

We can conclude that, as a consequence of using only the 8 filters in Chapter 6 for the SPS analysis, the previous limitation of our 2D-SPS method of predicting slightly earlier formation times than ground-truth is somewhat aggravated. Nevertheless, the differences with respect to the ground-truth values are still small.

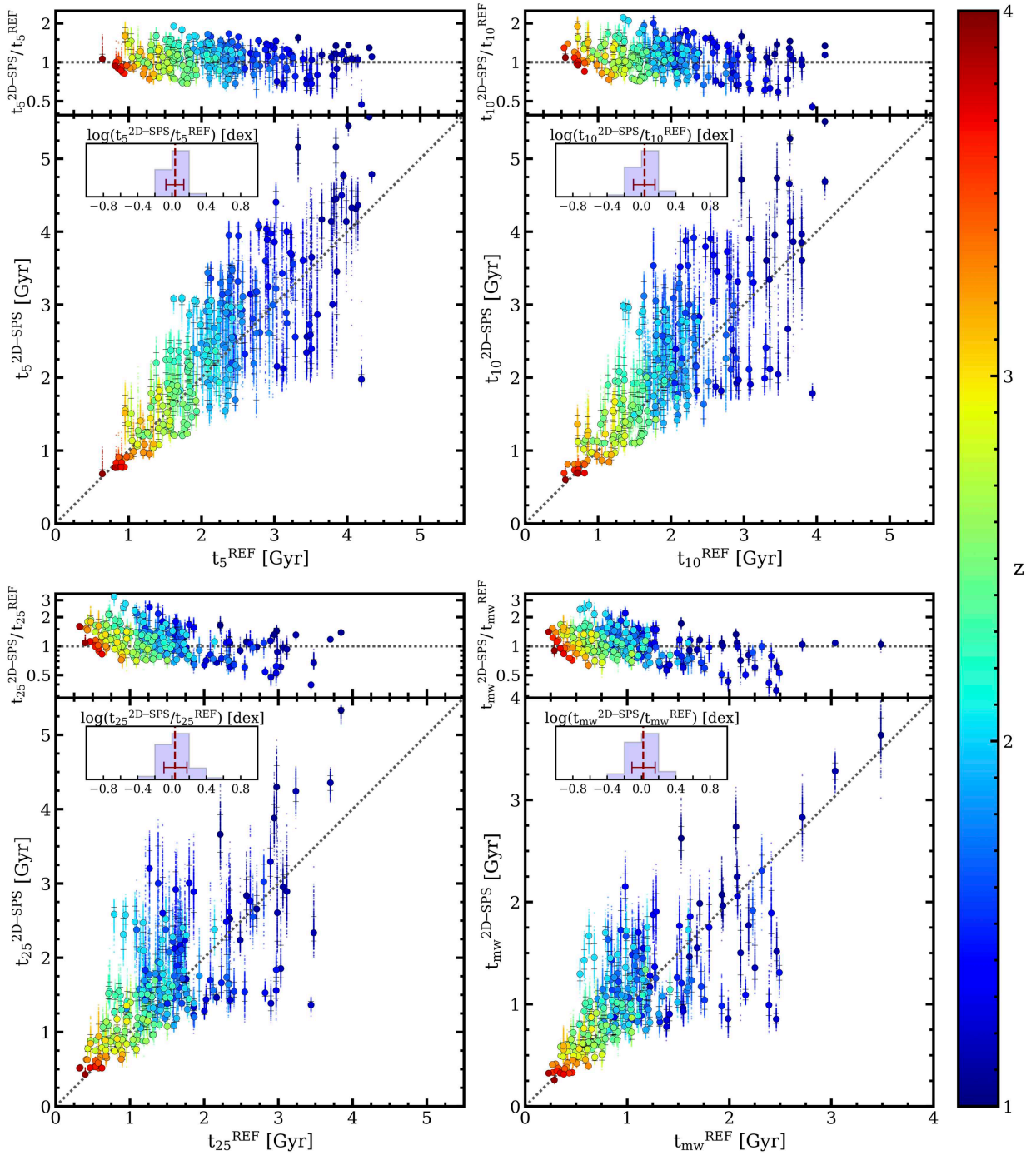


**Figure B.1:** Comparison between the mass-fraction formation times of our 2D-SPS method, considering only the 8 filters in Chapter 6, and their ground-truth values:  $t_5$  (upper-left),  $t_{10}$  (upper-right),  $t_{25}$  (lower-left) and  $t_{mw}$  (lower-right) calculated from our 2D-SPS-derived SFHs versus their reference values calculated from the SFHs built from the simulated stellar particles in galaxies. Each galaxy is represented by 300 vertically spread points, which correspond to the mass-fraction formation times of the 300 2D-SPS SFHs, built from the 300 MC particles in each resolution element in the grid. The median of these values for each galaxy is shown as bigger circles and error bars represent the standard deviation of these values (68% interval). All points are color-coded by galaxy redshift. On the top of each panel, we show the ratio between the  $t_k$  of our 2D-SPS method and their ground-truth values as a function of the latter. As an inset, we include the offsets of the galaxies in the sample.

## Flashcards of CEERS galaxies

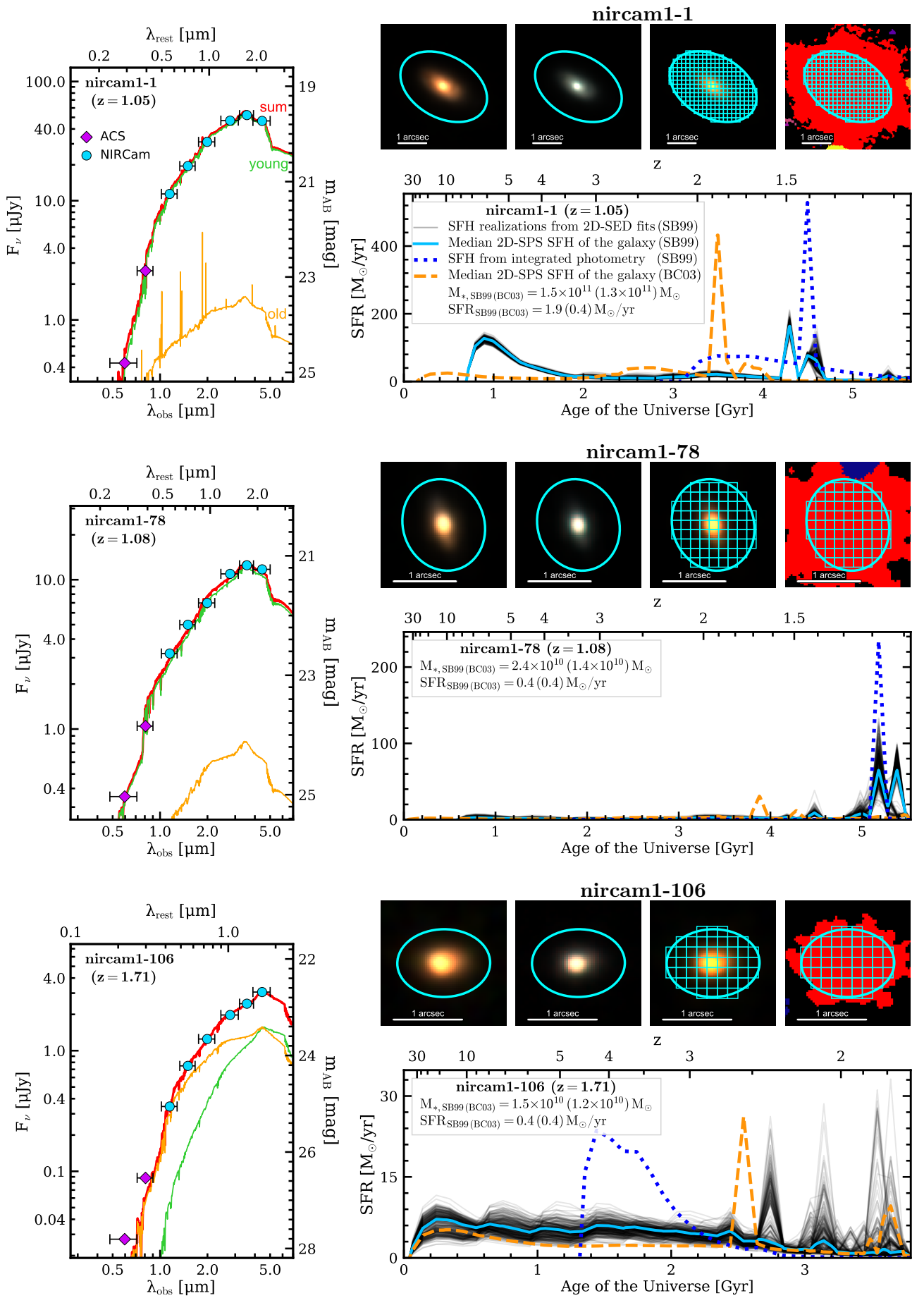
---

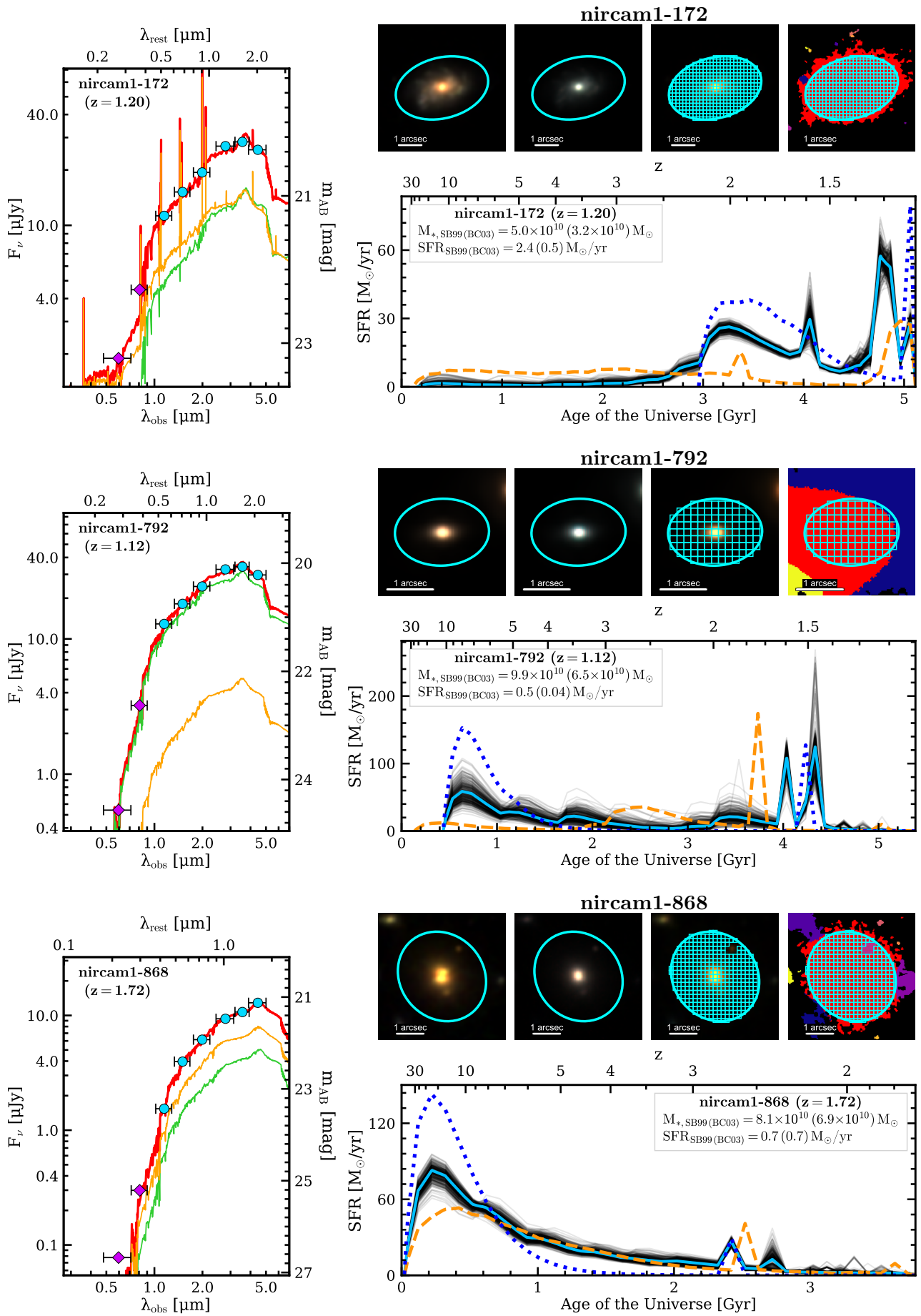
In this appendix, we include flashcards of the 333 CEERS massive galaxies at  $1 < z < 4$  considered in Chapter 6. Galaxies are first sorted by the CEERS pointing to which they belong and, within each CEERS pointing, according to their ID. We include three galaxy flashcards per page.

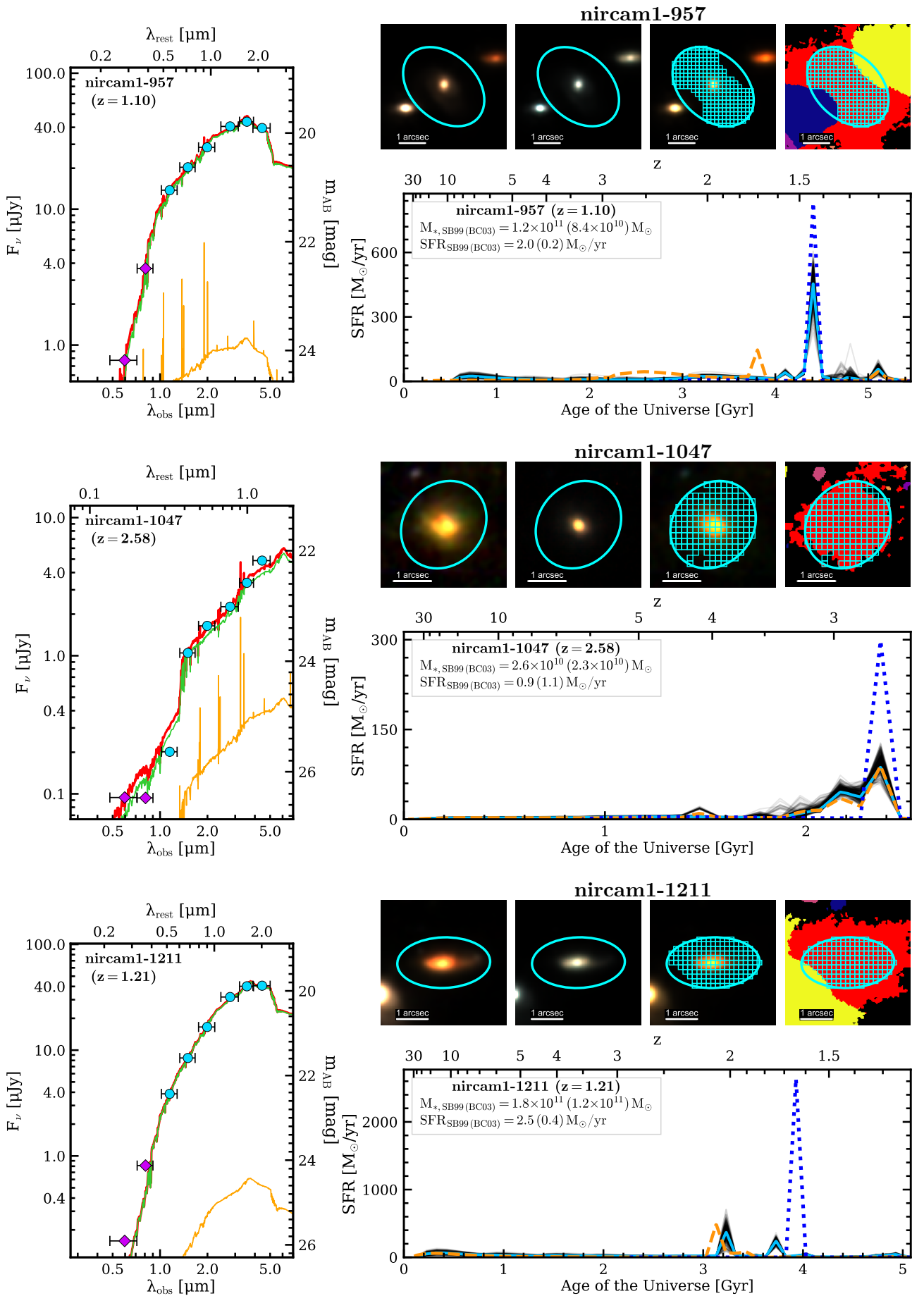
In each flashcard, the left panel shows the integrated SED measured for each galaxy as a function of both the observed wavelength (bottom x-axis) and rest-frame wavelength (top x-axis). ACS and NIRC*am* integrated fluxes are shown as purple and cyan markers, respectively. The FWHM (in wavelength) for each filter’s response curve is shown as an horizontal error bar. As an example, we show one of the model realizations (in red) that fits the integrated SED using SB99 stellar population models. This red model is the sum of the contribution of the model corresponding to the young population (in green) and the old population (orange).

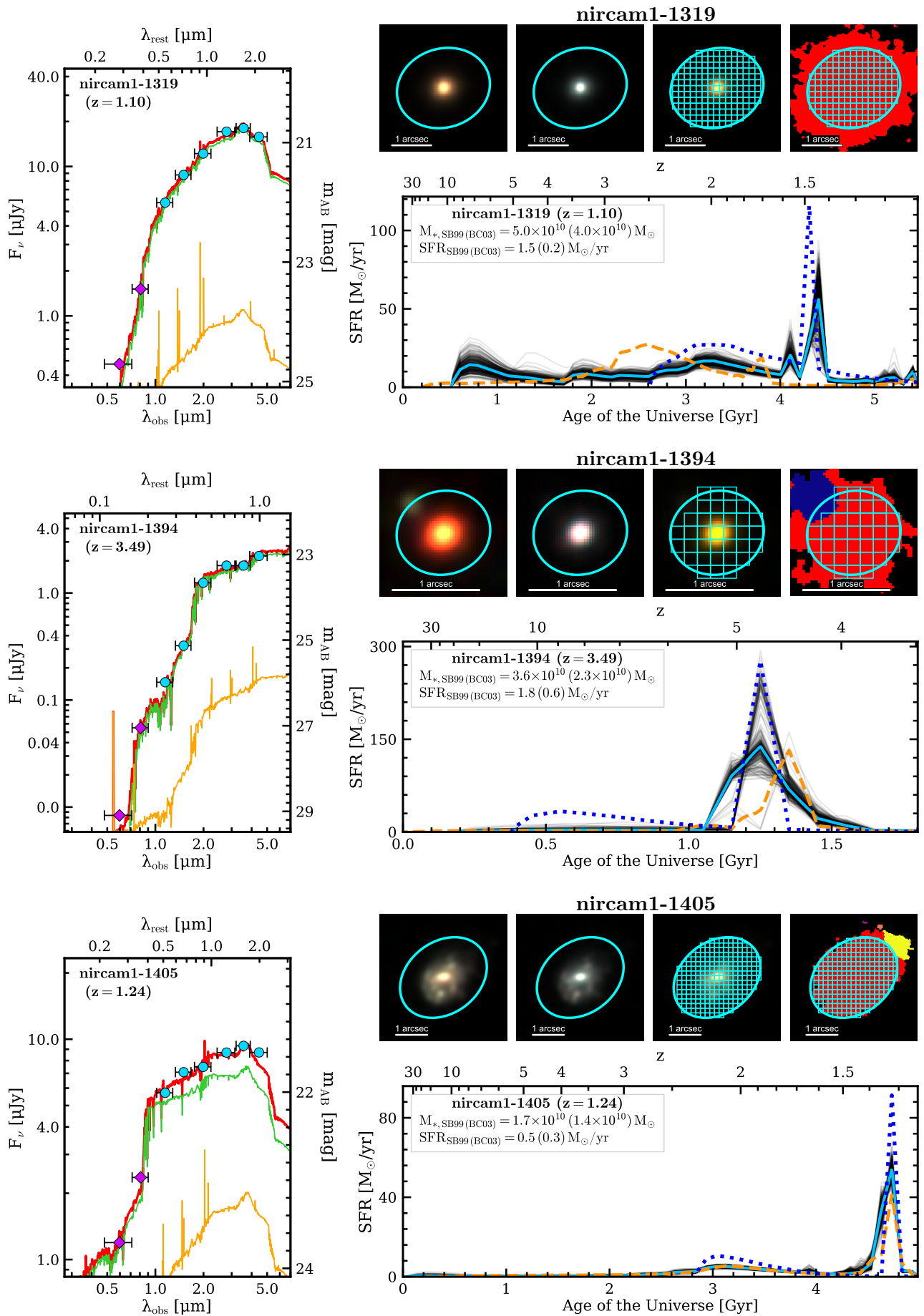
On the top right of each flashcard we show four postage stamps of the considered galaxy, in which the angular scale corresponding to 1 arcsec is marked with a white segment on the bottom left. The first three postage stamps show RGB images generated using the PSF-matched images in different NIRC*am* filters: F115W, F150W, and F200W for the first panel, F277W, F356W, and F444W for the second, and F115W, F200W, and F356W for the third. These RGB images have been produced using an asinh scale, with the minimum value set to zero in flux units, and the maximum value set to 80% of the flux (in  $\mu\text{Jy}$ ) corresponding to the brightest pixel within the integrated elliptical aperture (cyan ellipse). The fourth top-right panel shows the segmentation map. In this map, the pixels belonging to the considered galaxy are shown in red, the pixels identified as sky are in black, and those belonging to other nearby sources are shown in other different colors. In the two rightmost postage stamps, the grid is included in cyan. The size of the integrated aperture and number of cells in the grid for each galaxy are given in Appendix D (see Table D.1).

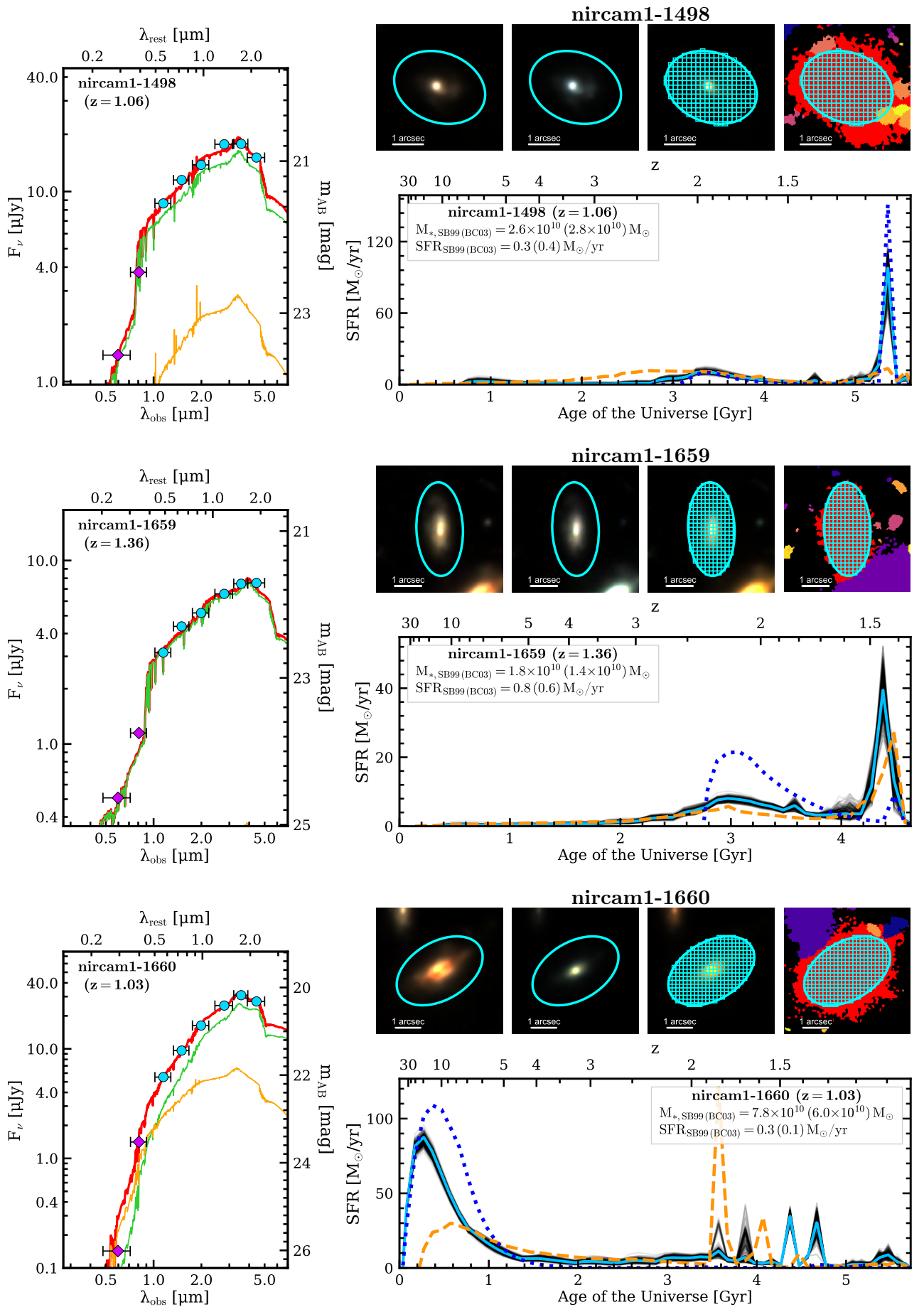
The galaxy SFH is shown in the bottom right panel, similar to that shown in Section 6.3 (see Fig. 6.3). The light blue SFH is the 2D-SPS-derived SFH obtained for the SB99 models. This SFH is computed as the median of the different SFH realizations (thin gray lines) that result from the MC solutions obtained for each of the 2D SEDs. The median SFH from all the integrated SED fits using SB99 models is shown in dotted blue. Finally, as a comparison, the 2D-SPS-derived SFH obtained for BC03 is shown in dashed orange. The stellar mass and SFR of the galaxy for both SB99 and BC03 are included in the legend of this panel. The galaxy mass is calculated as the median mass from the integrated SED fits, and is used to normalize the 2D-SPS-derived SFHs. The SFR is given by the 2D-SPS-derived SFH at the redshift of observation of the galaxy.



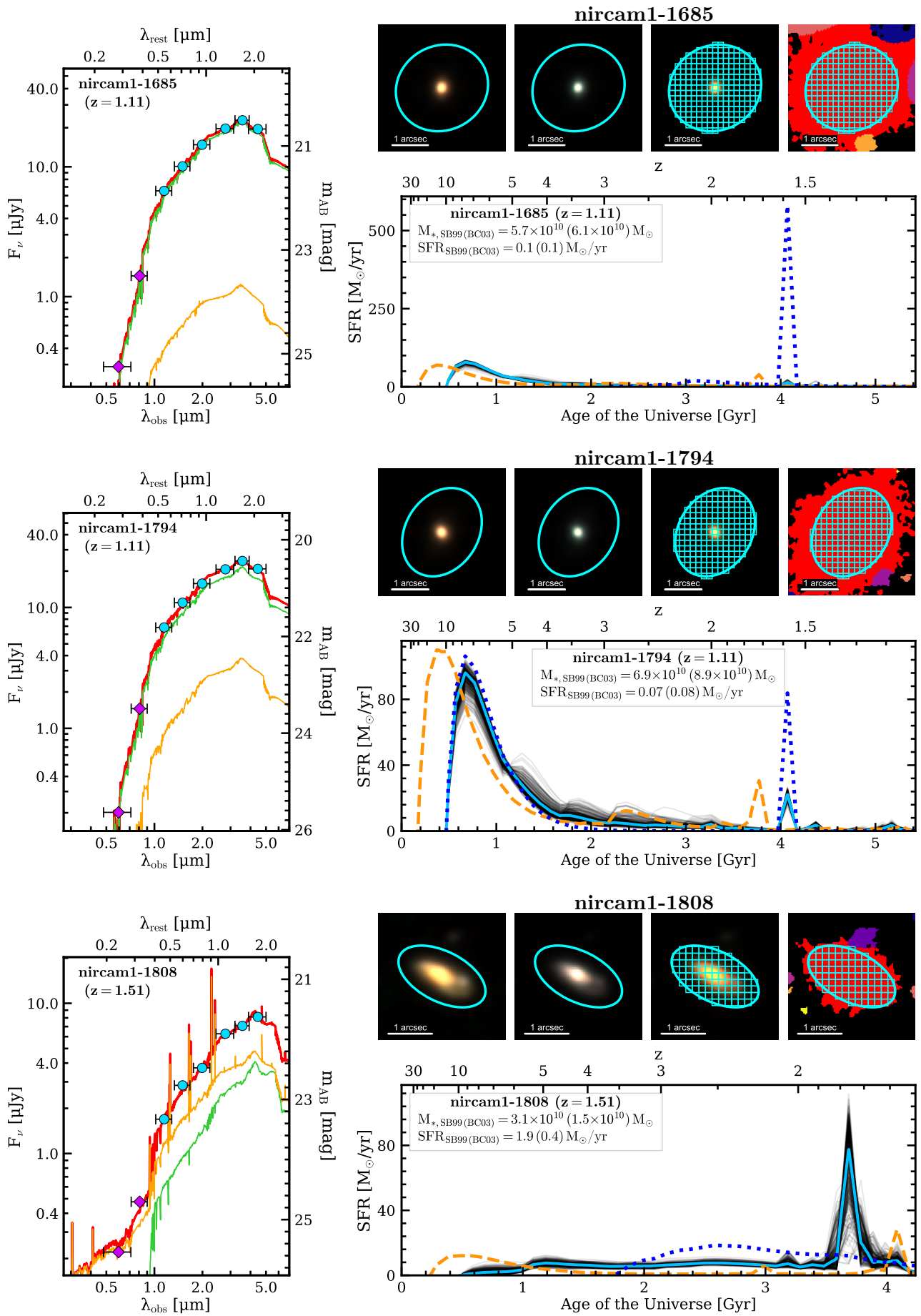


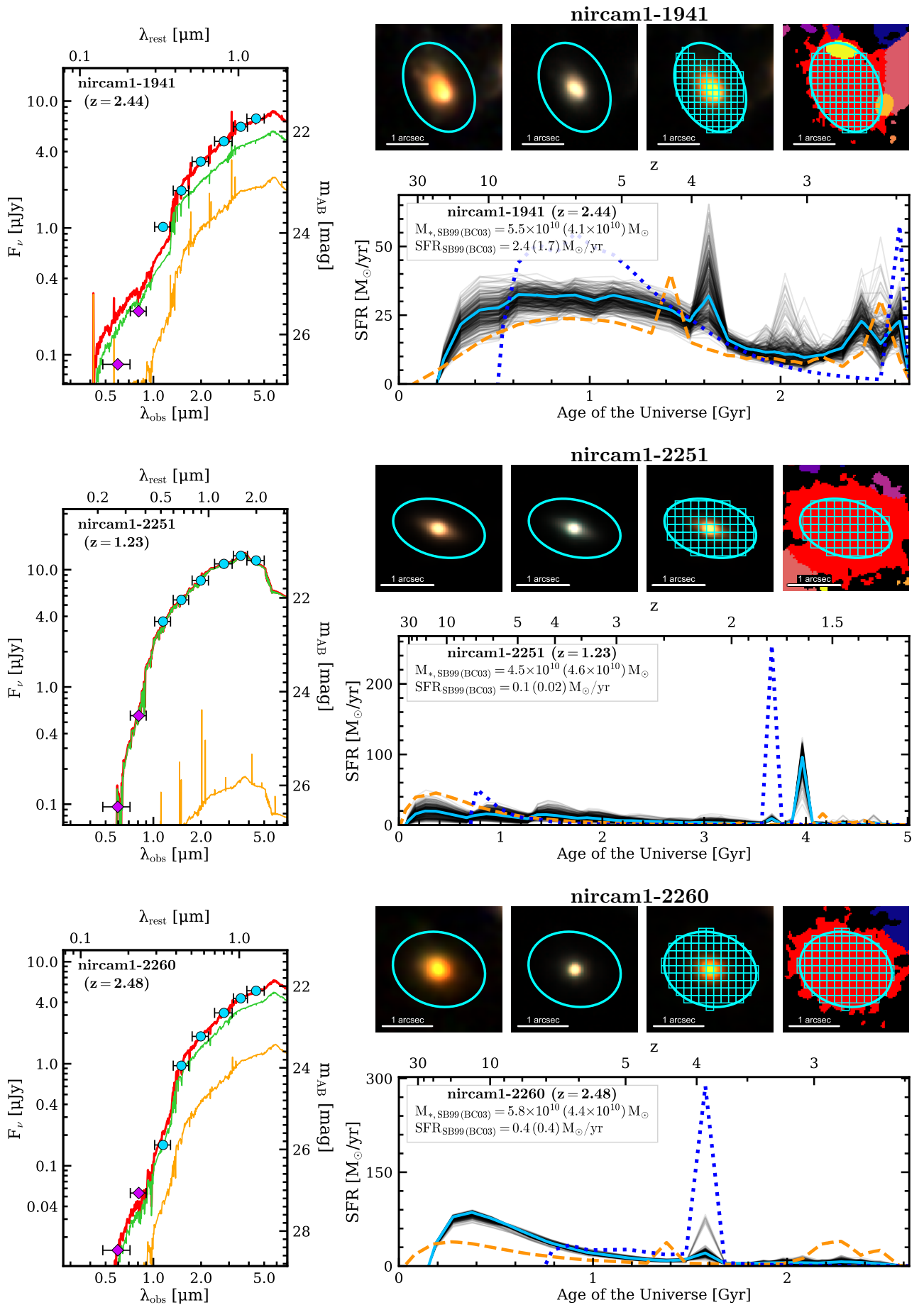


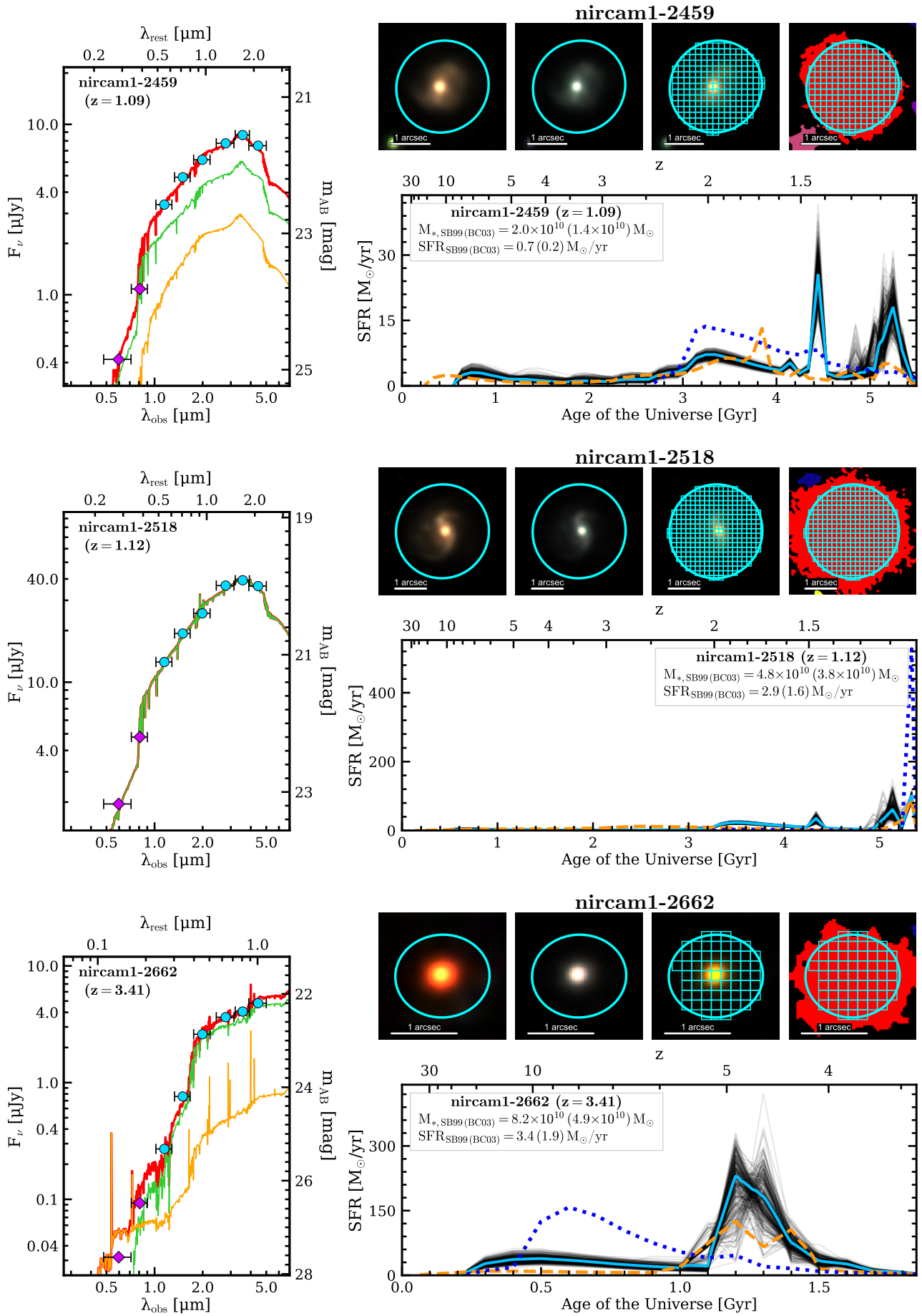


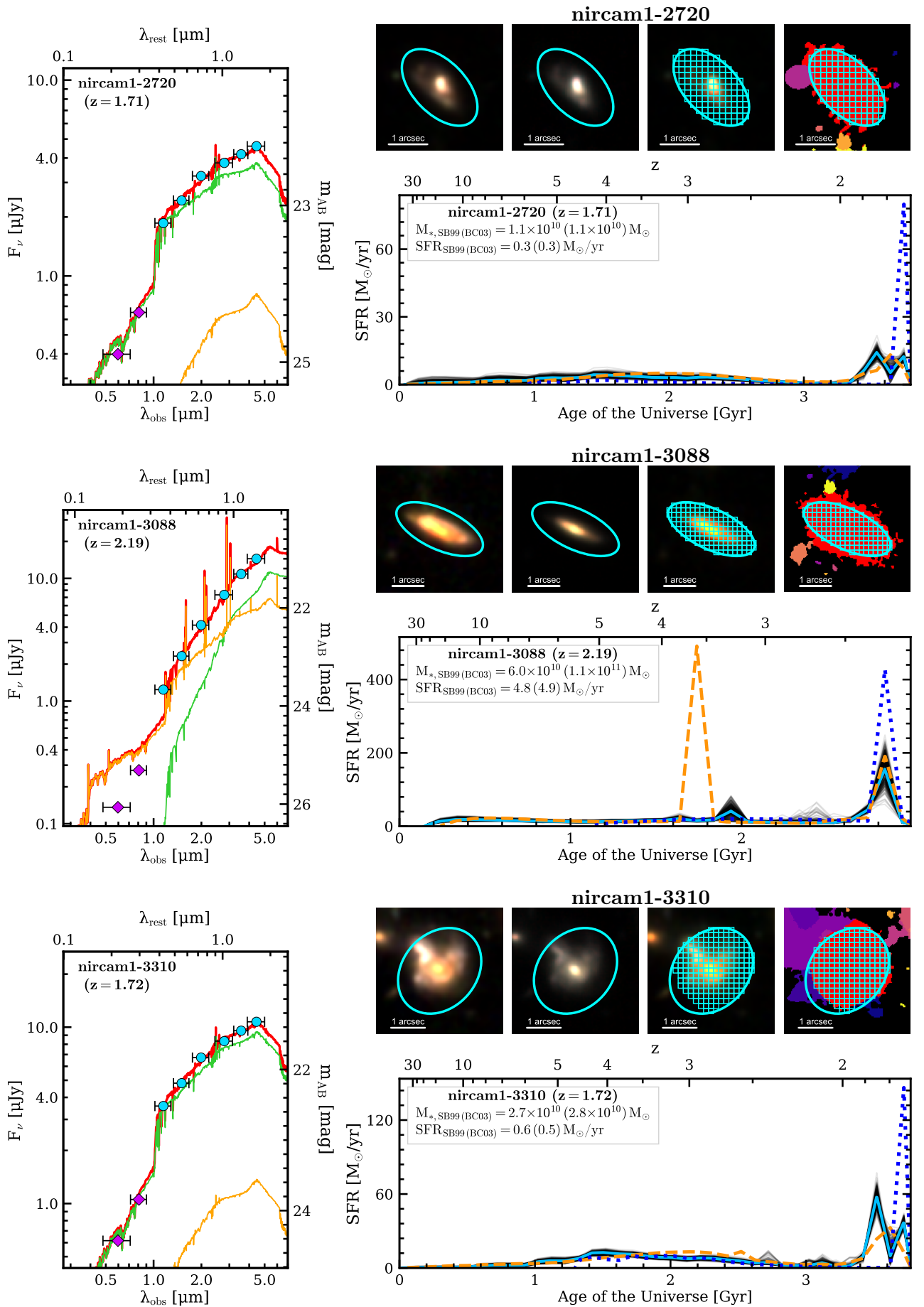


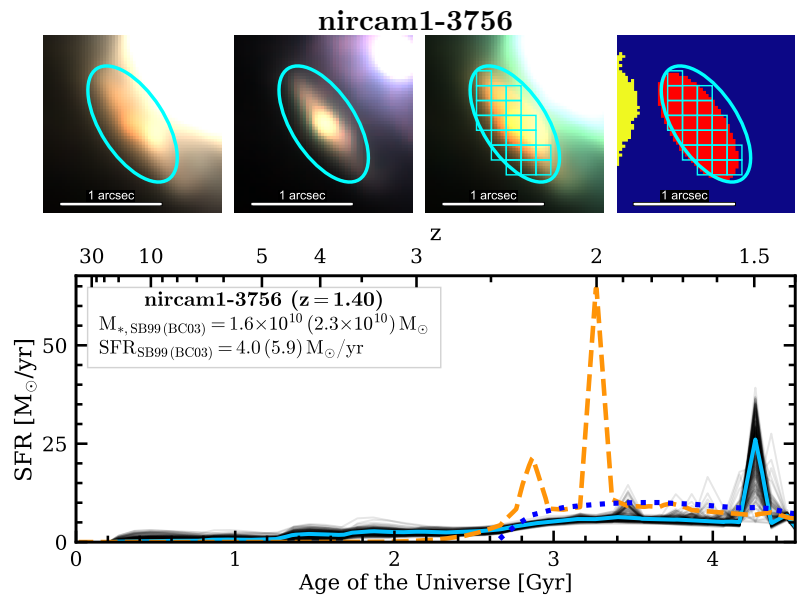
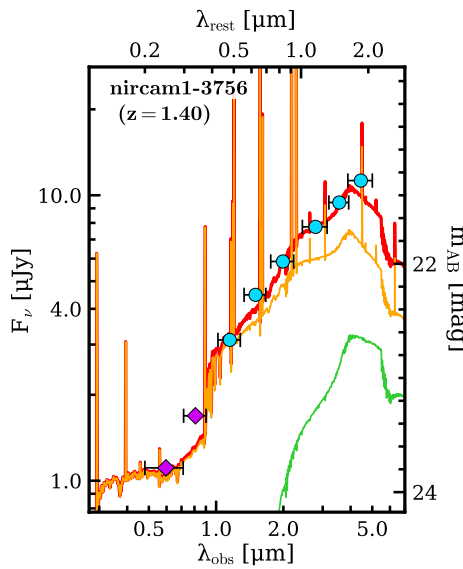
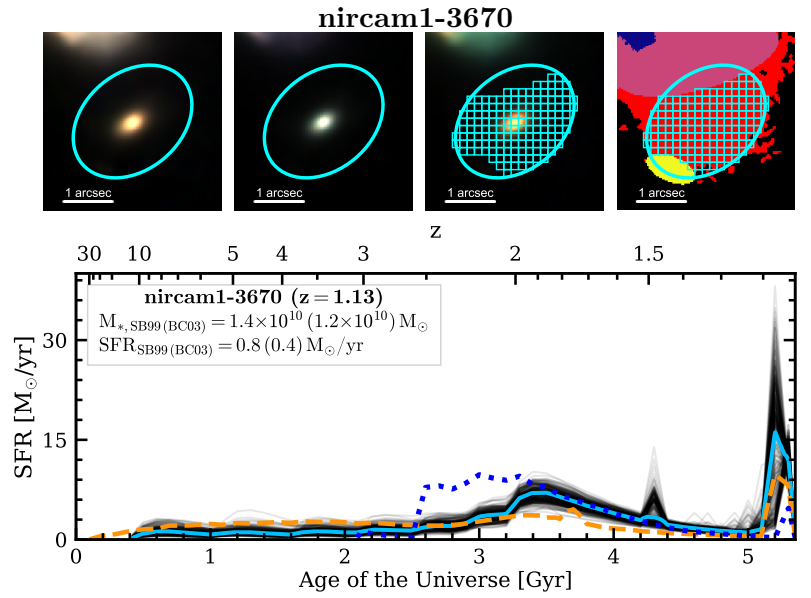
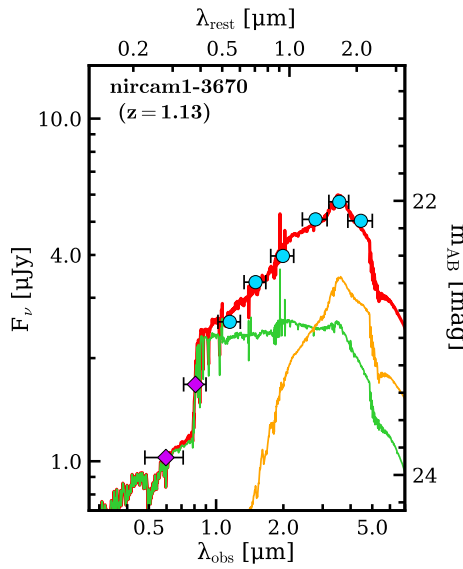
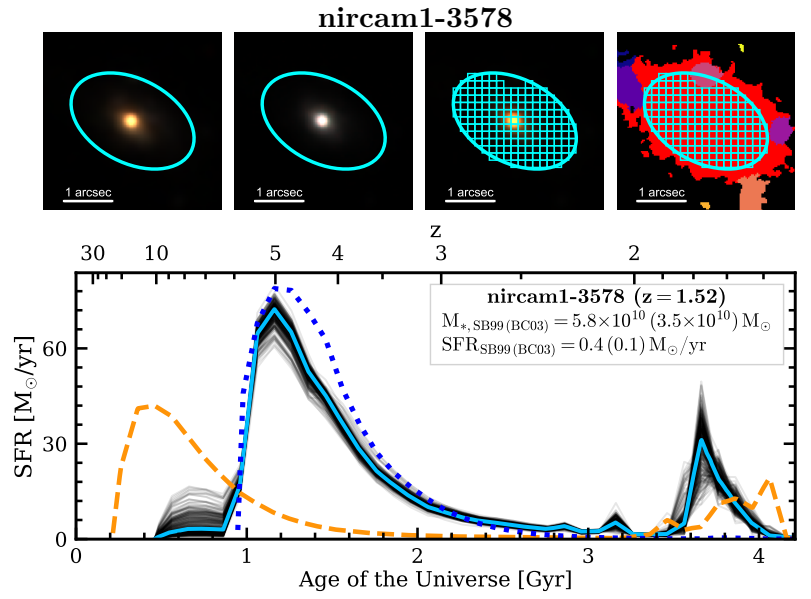
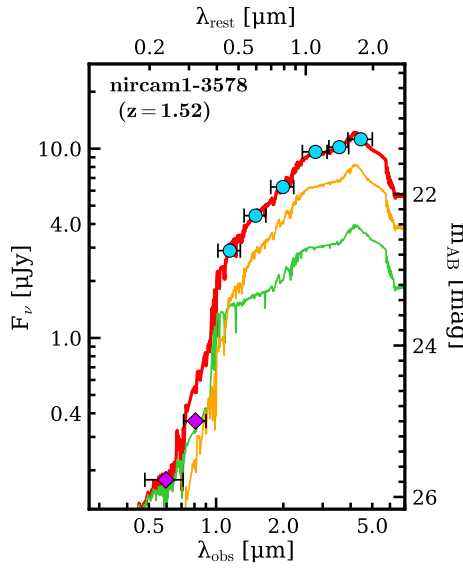


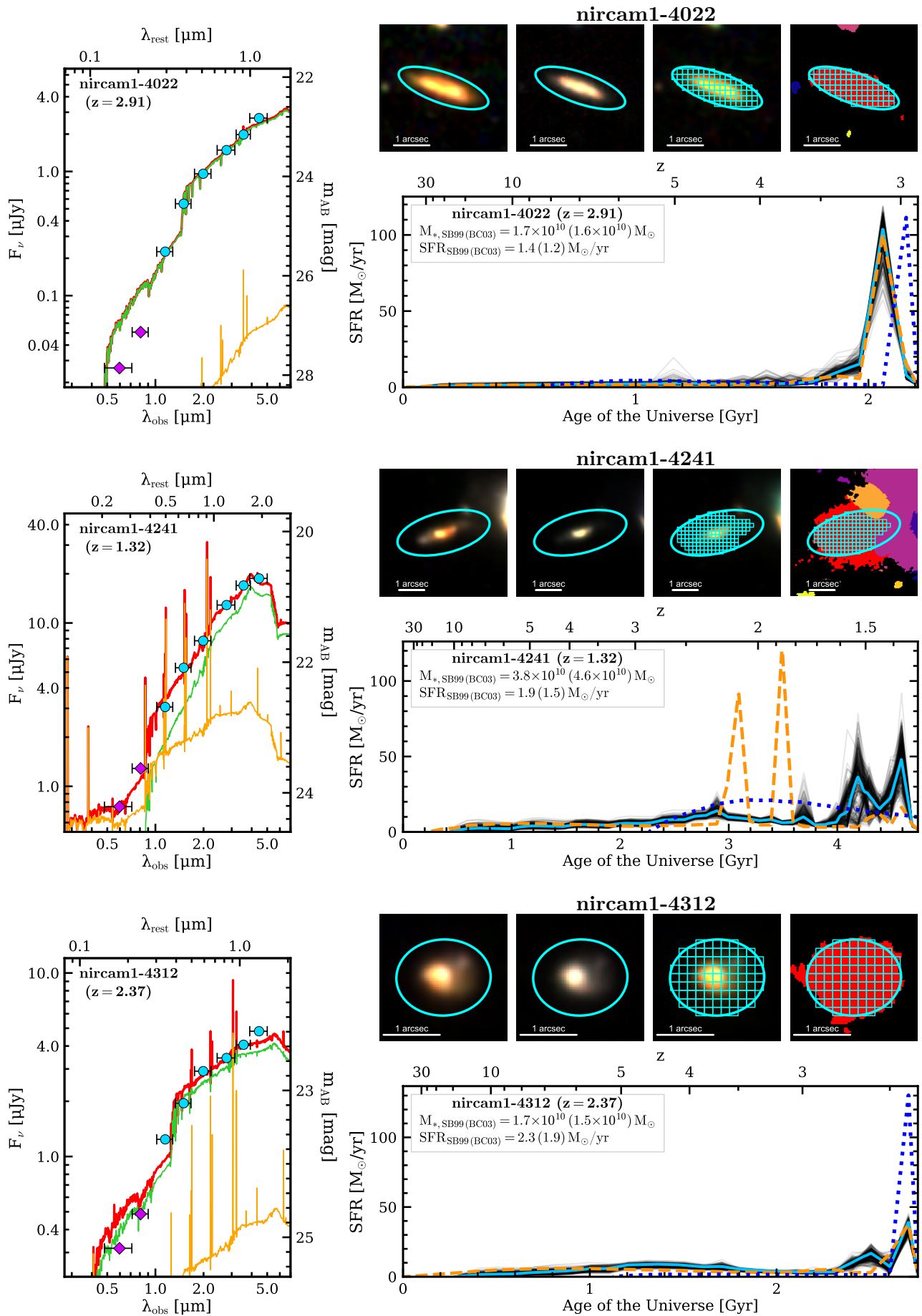


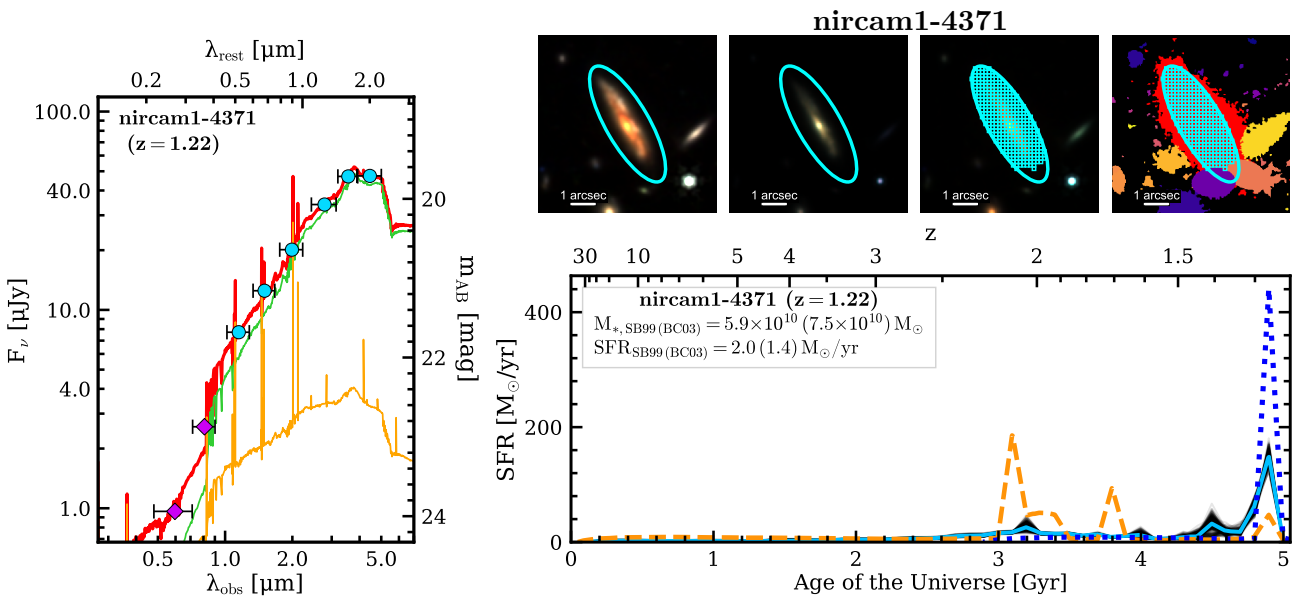
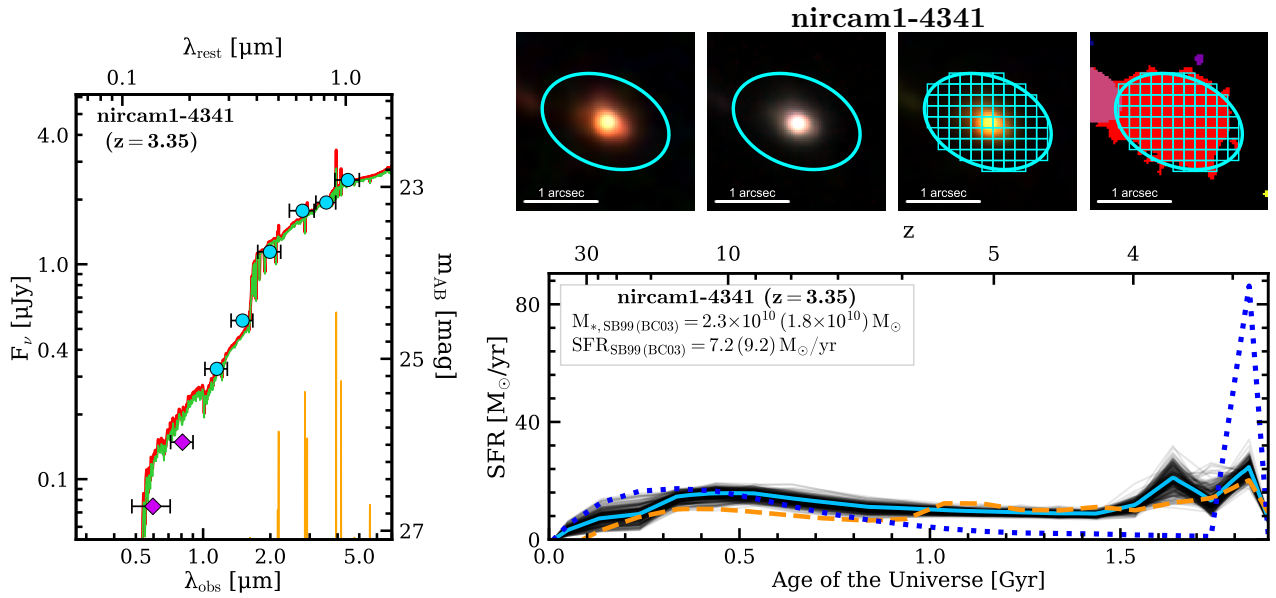
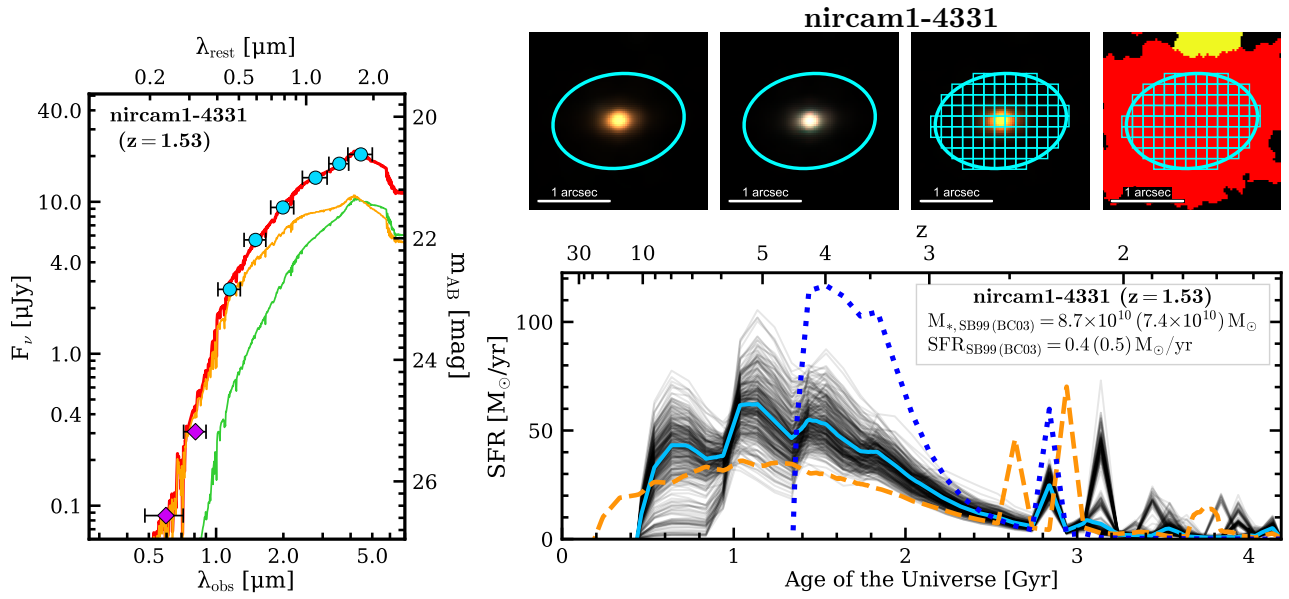


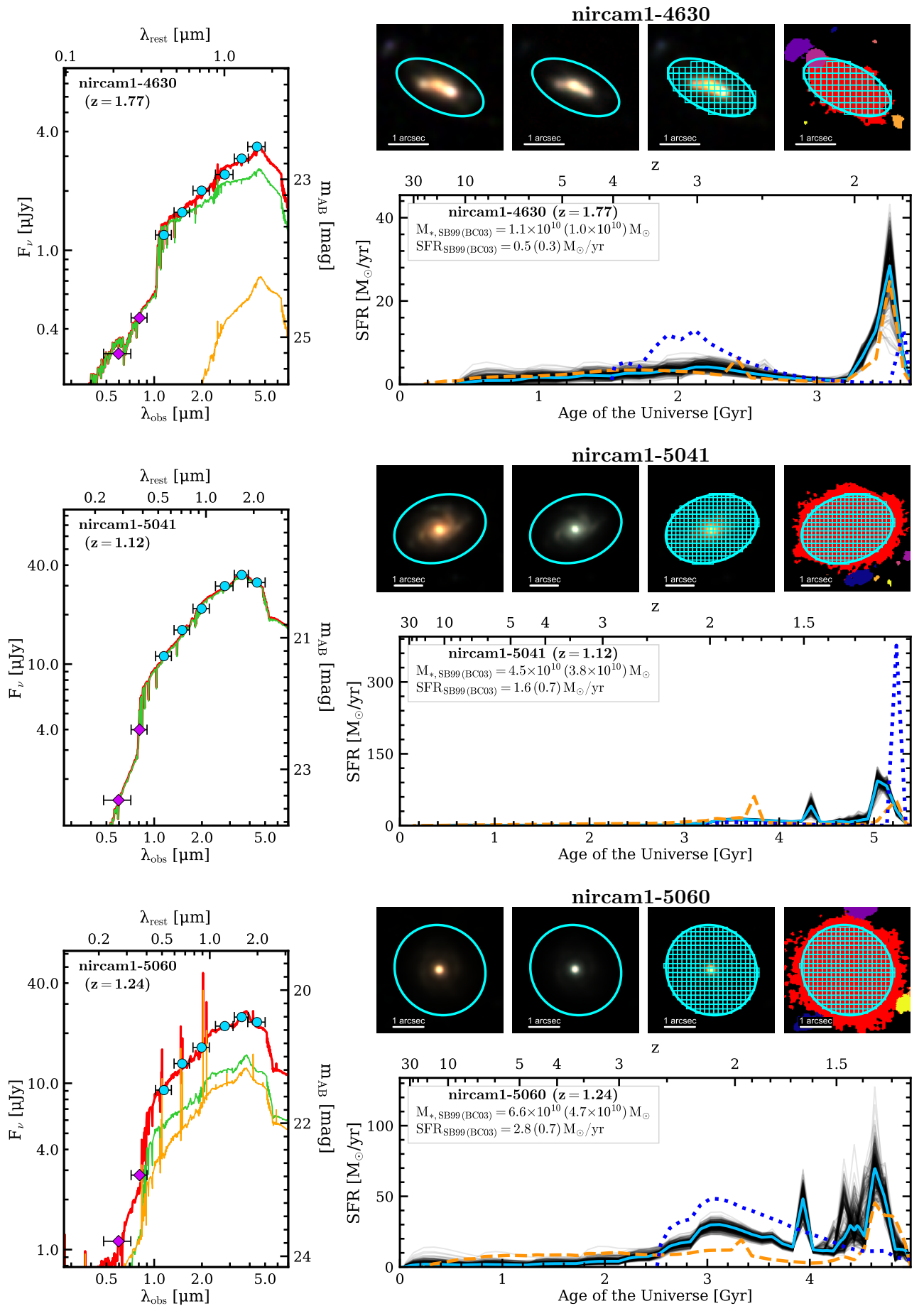




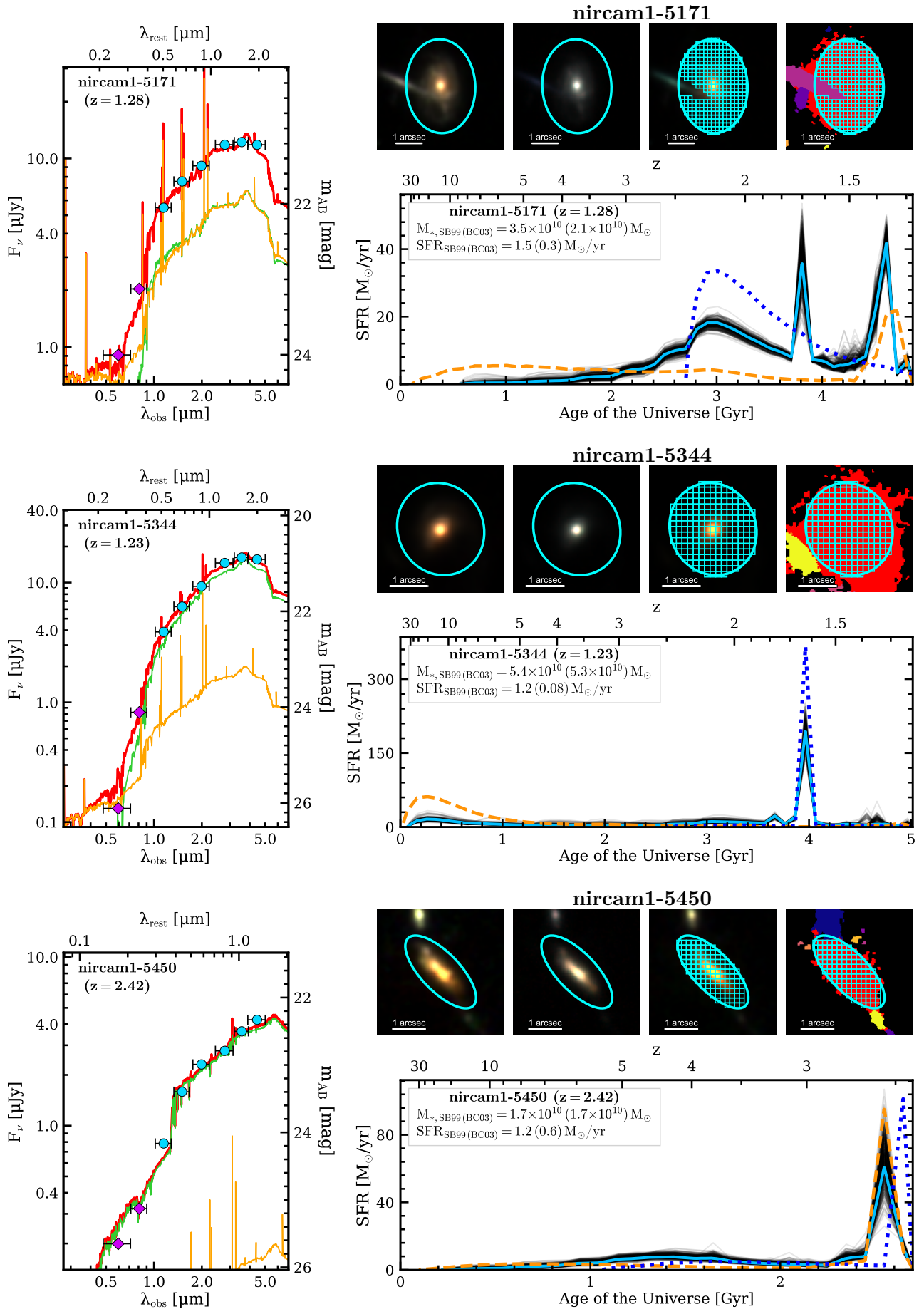


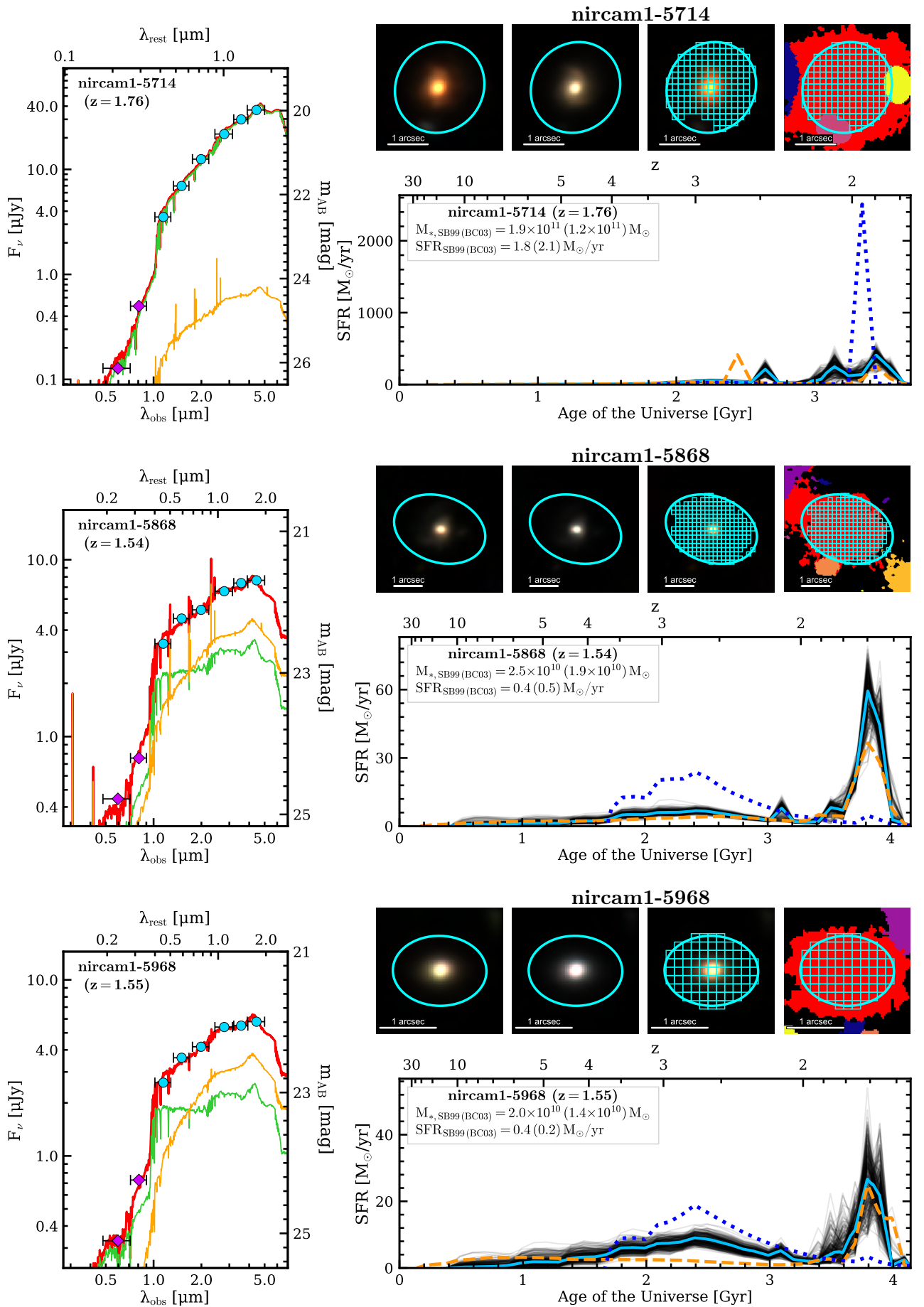


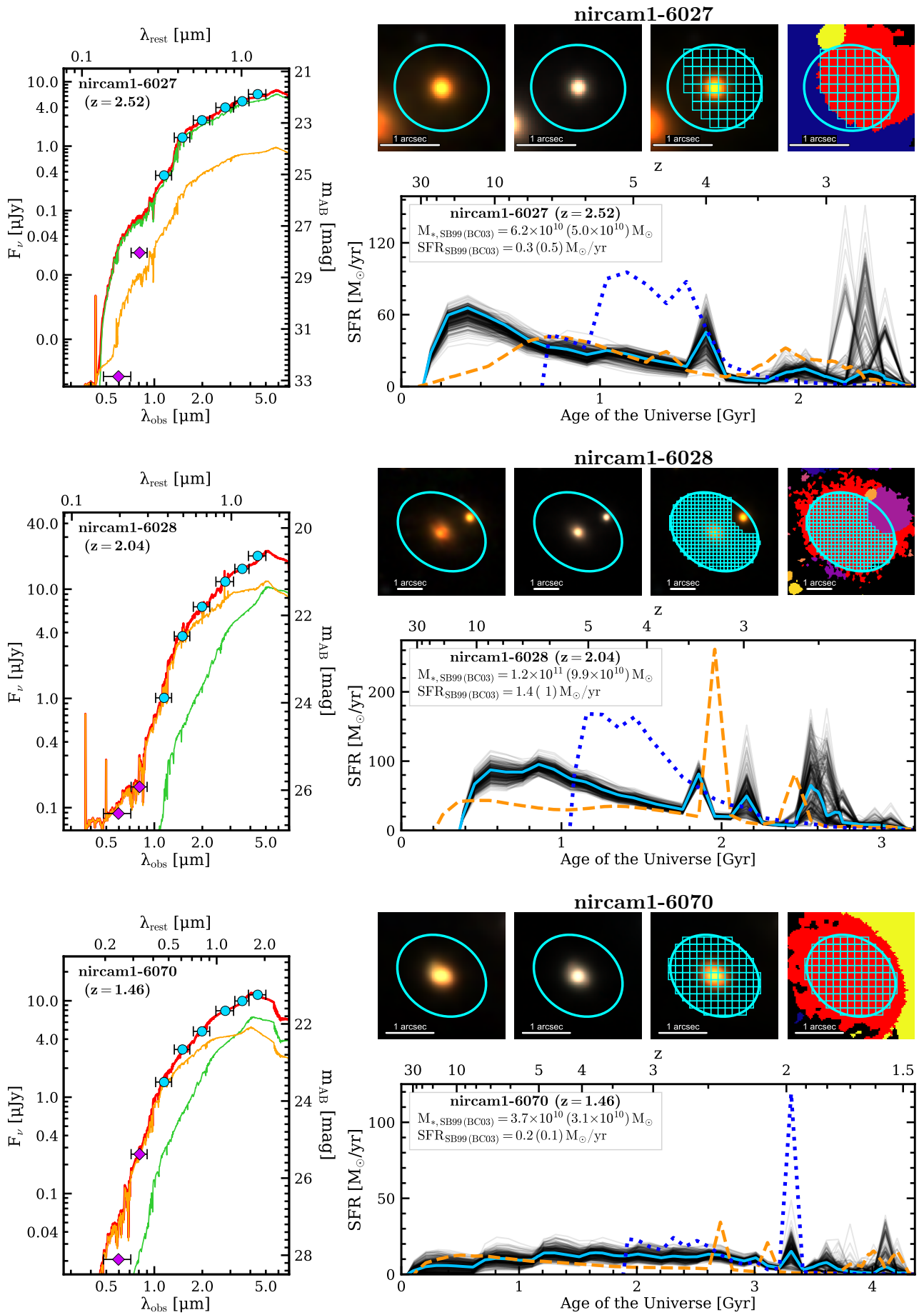


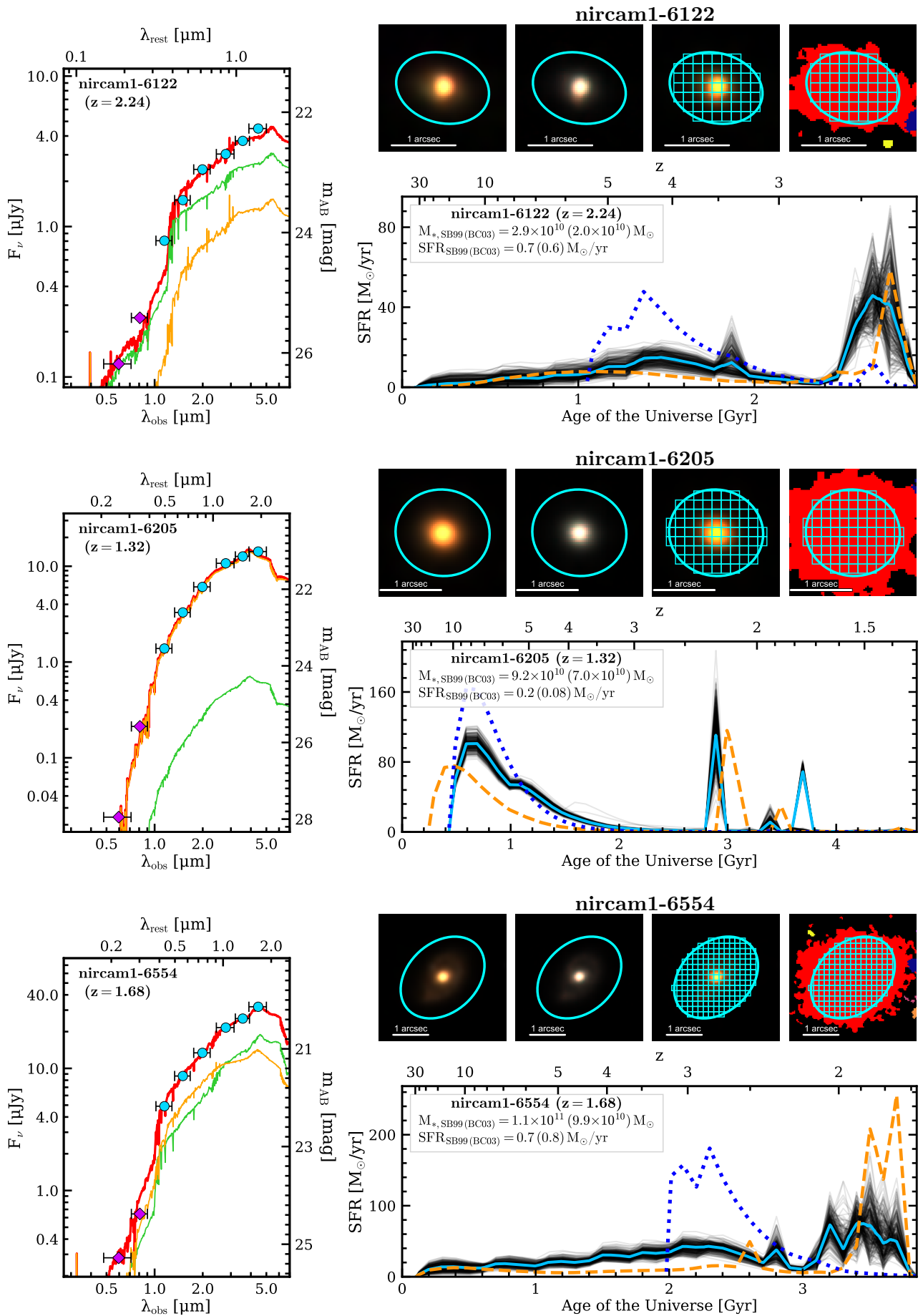


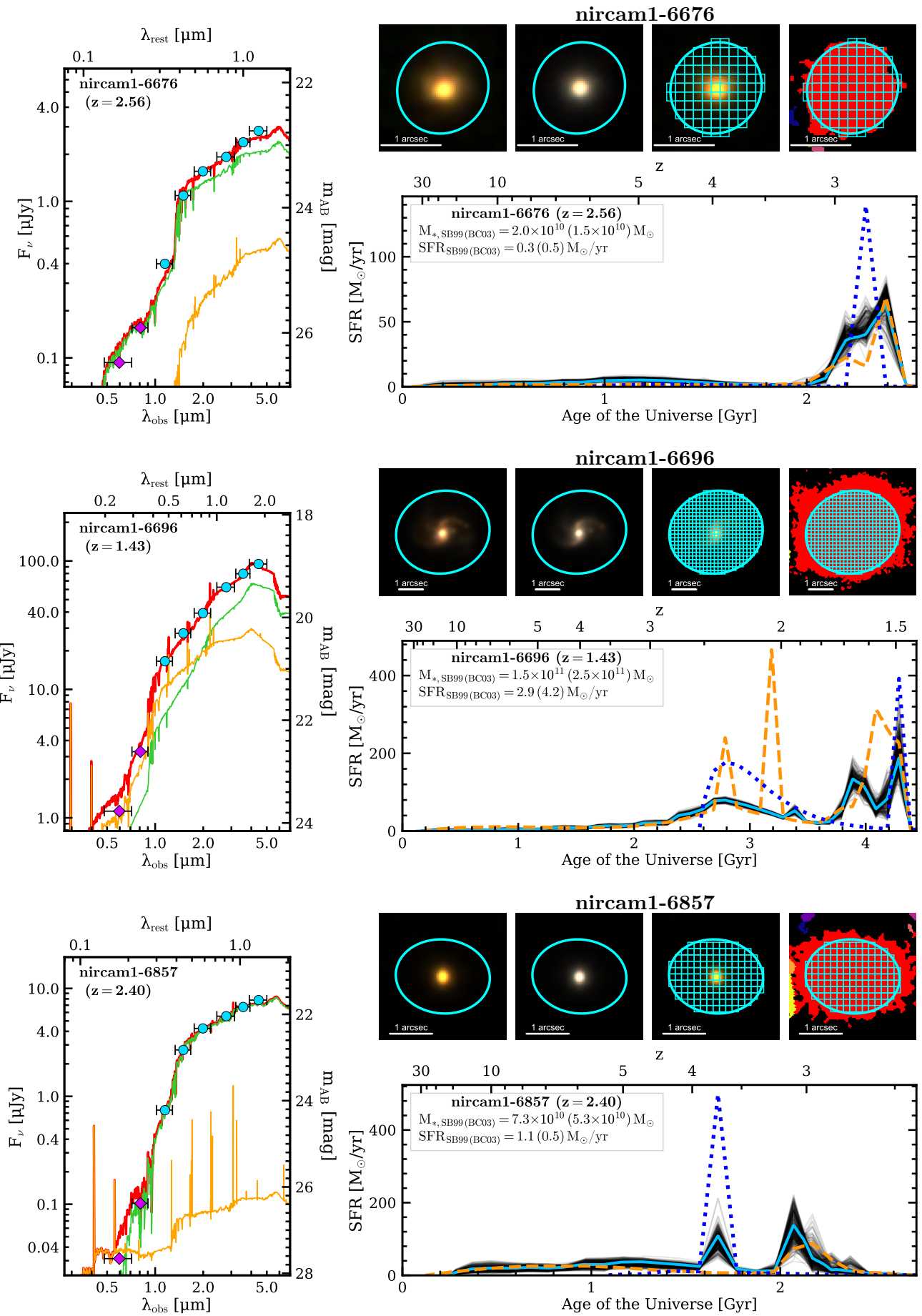


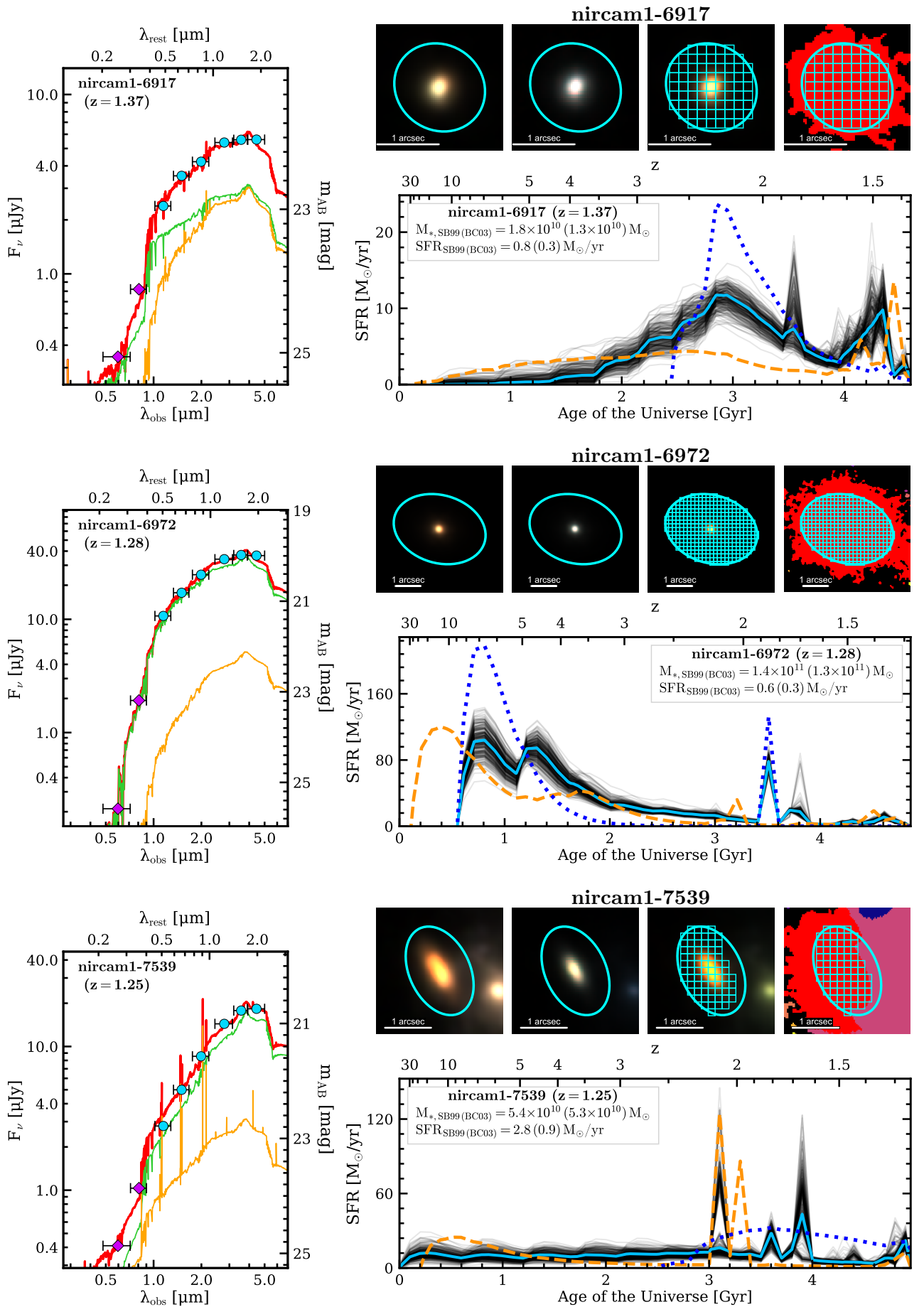


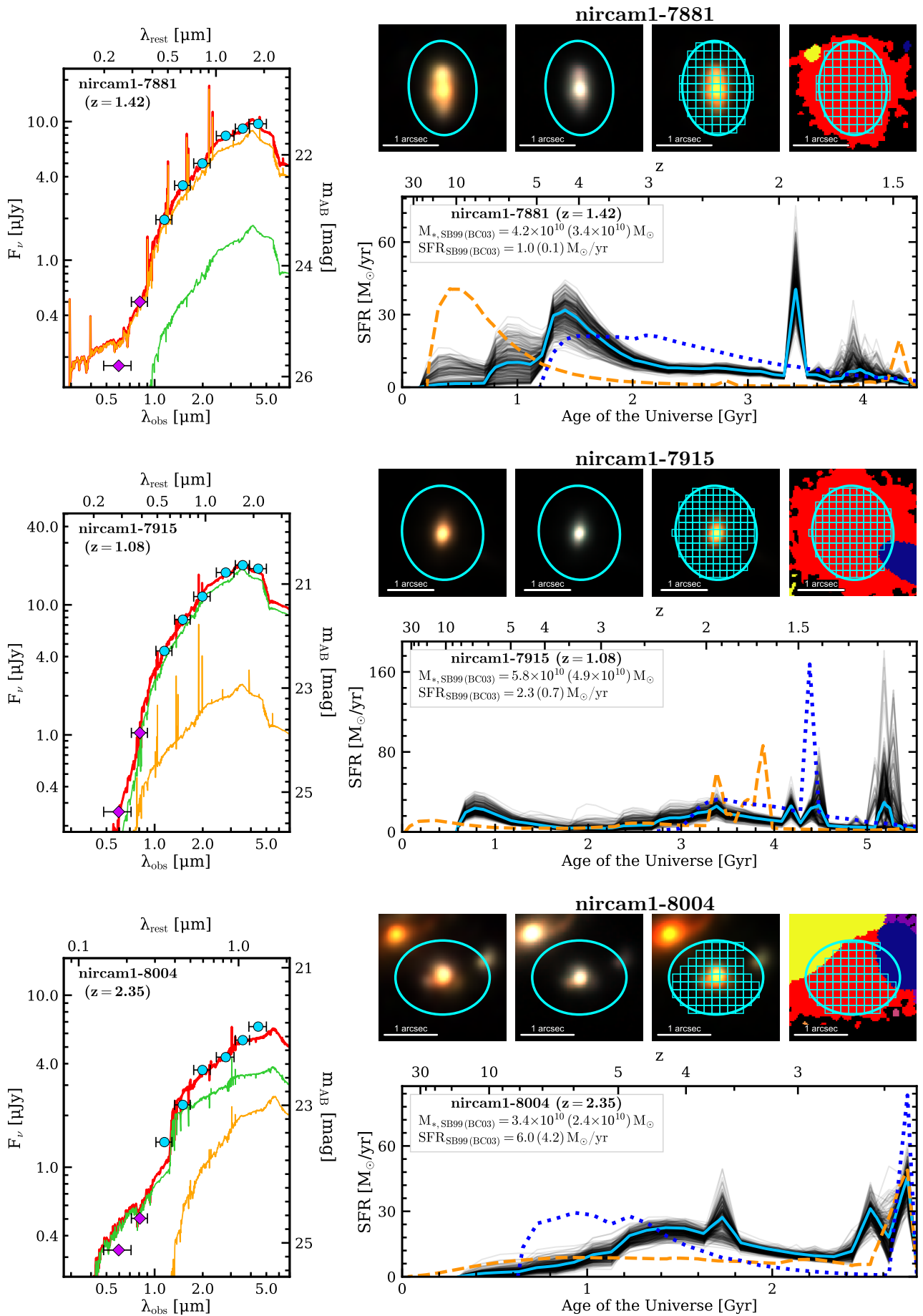


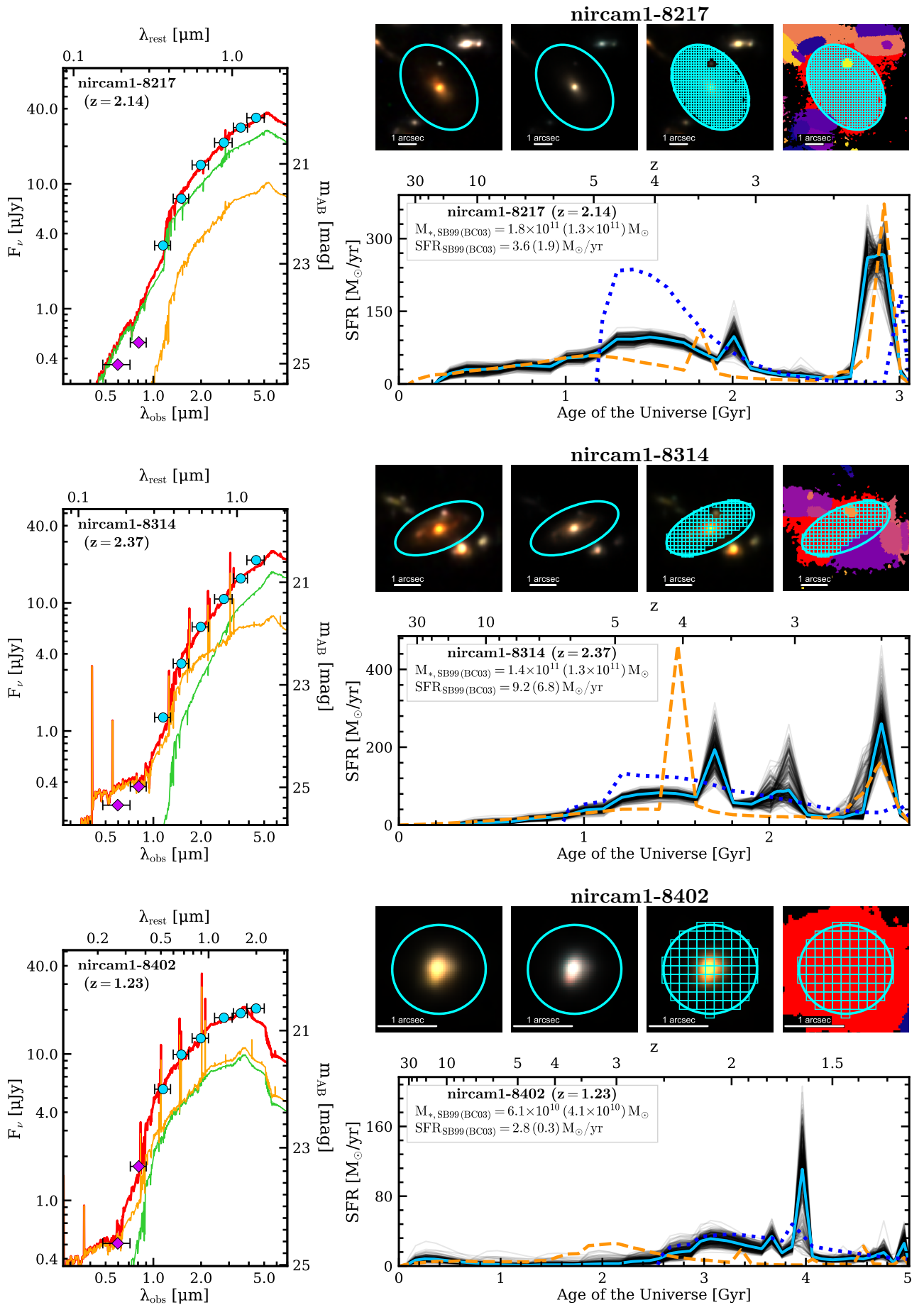




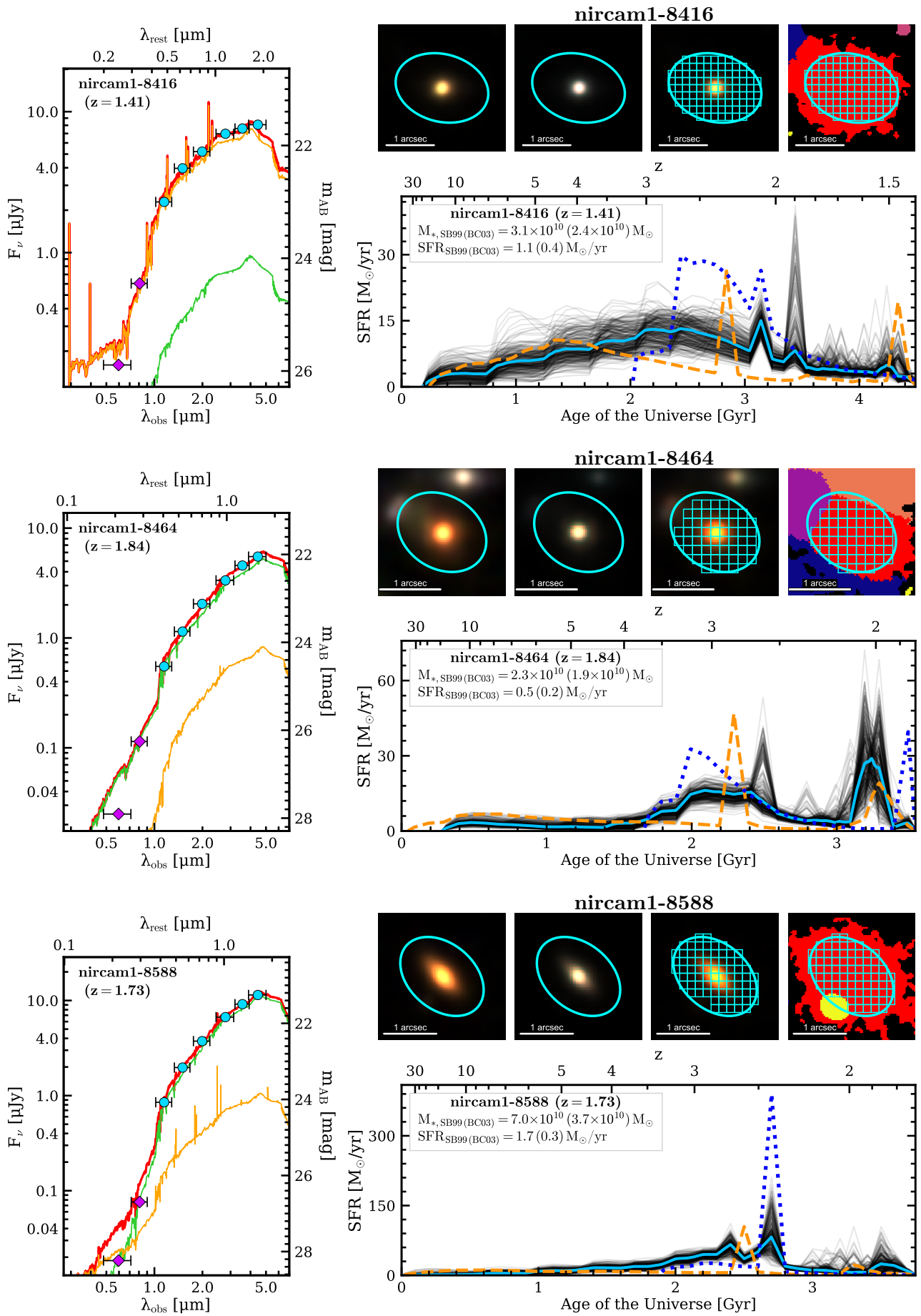


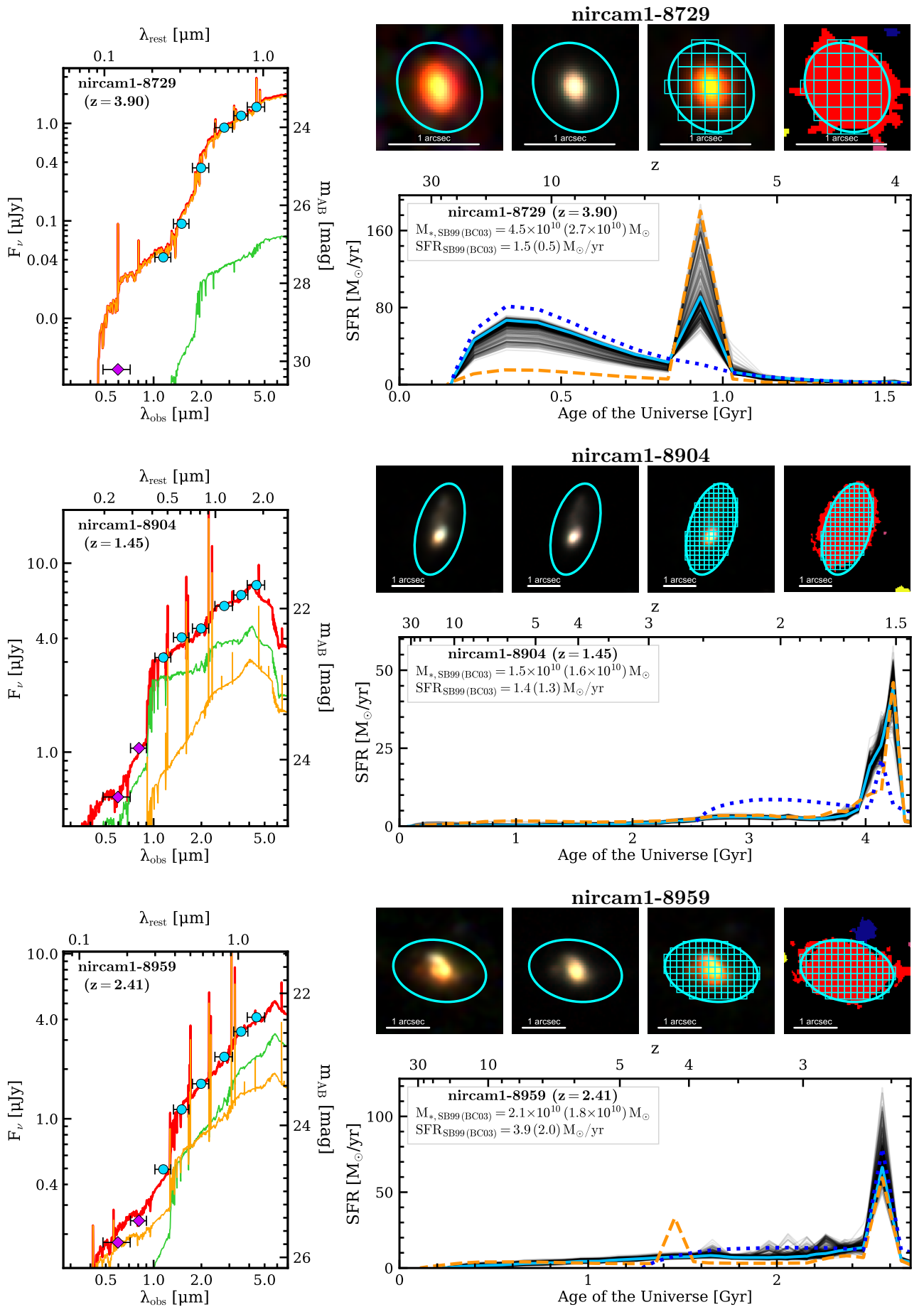


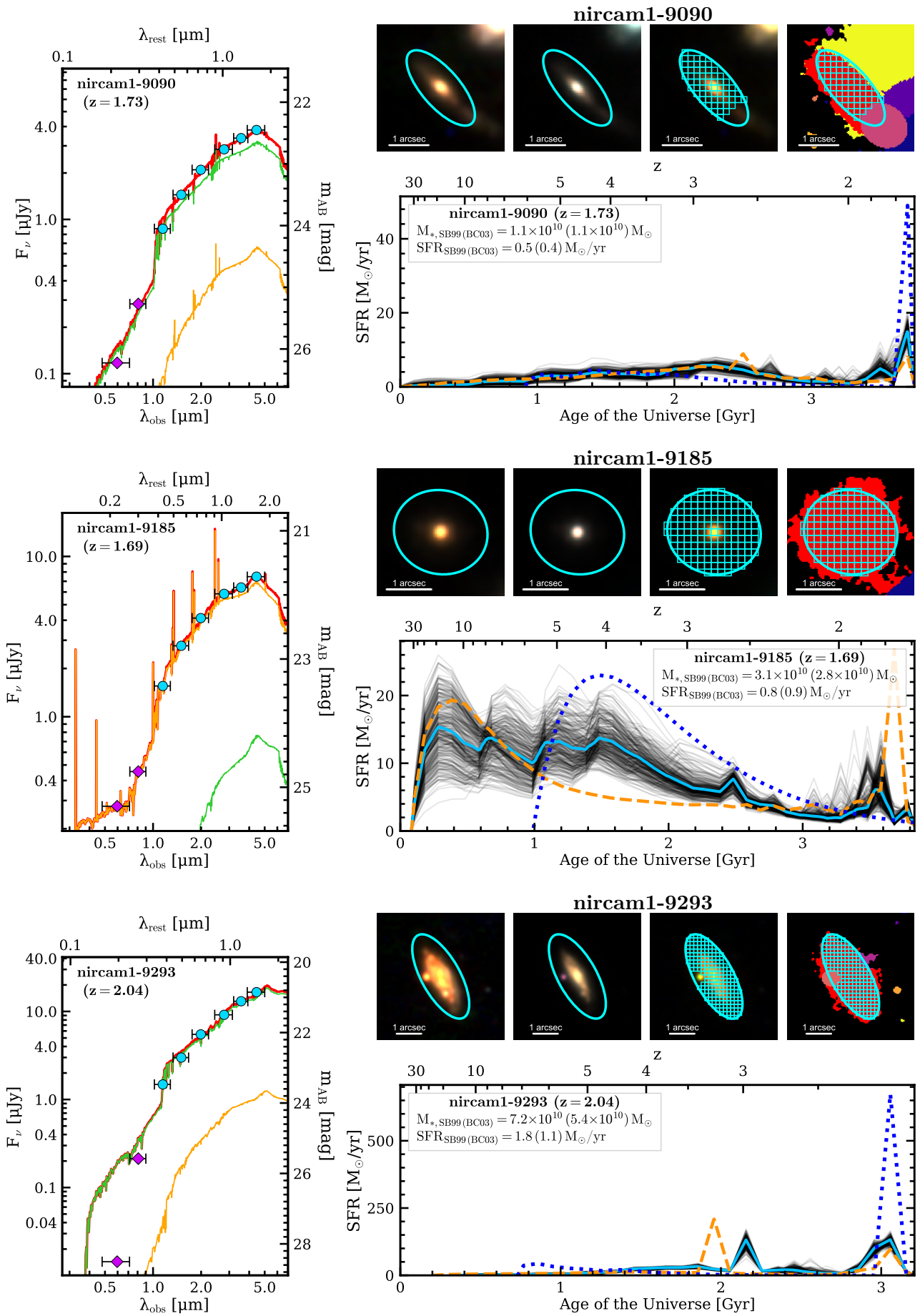


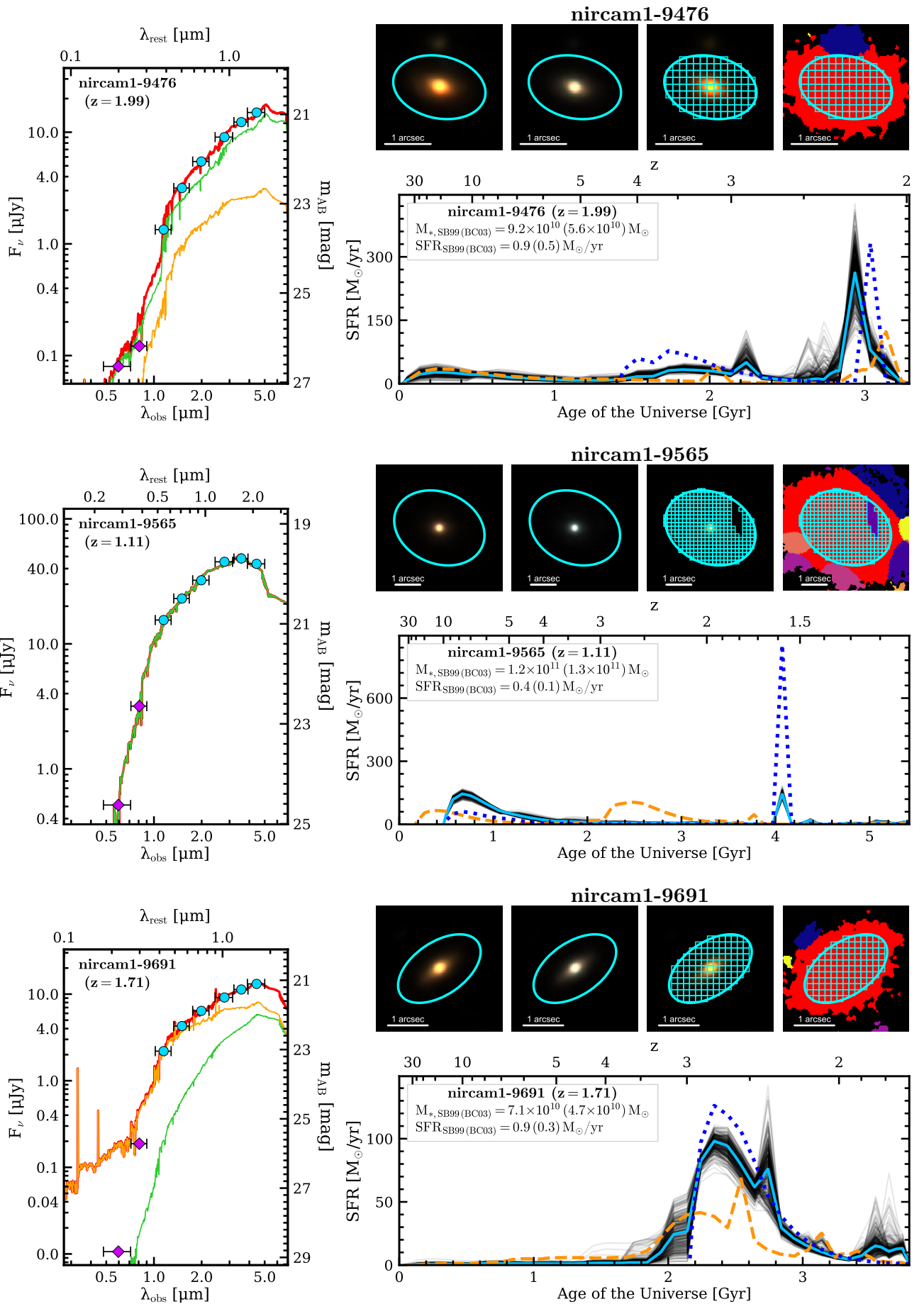


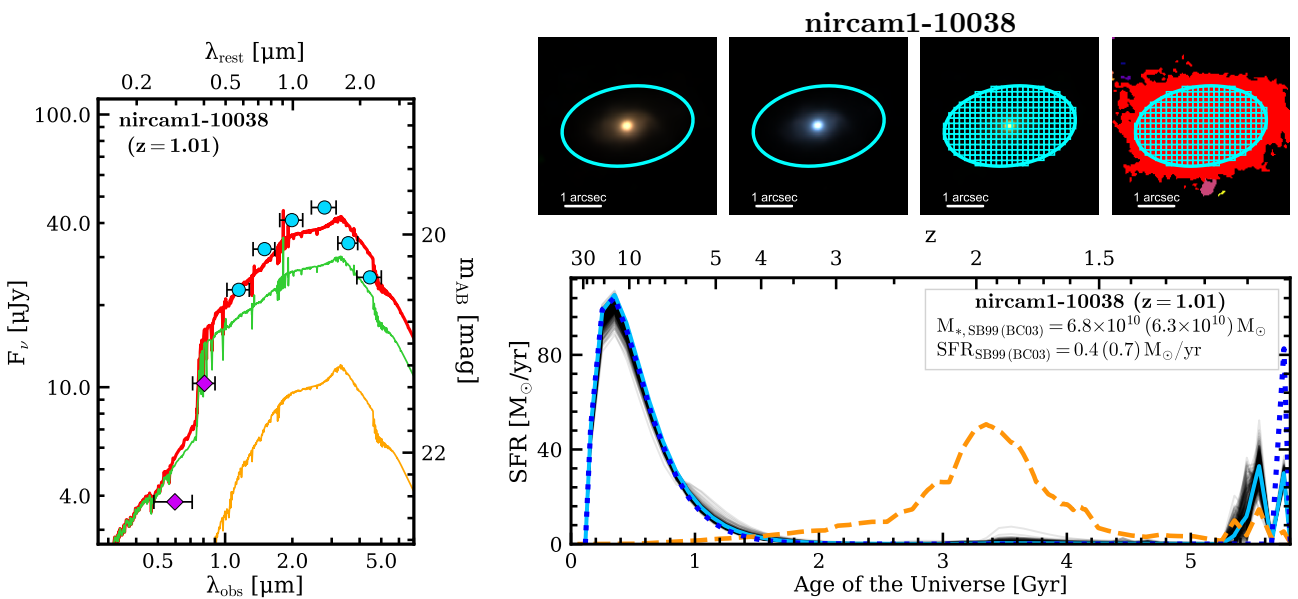
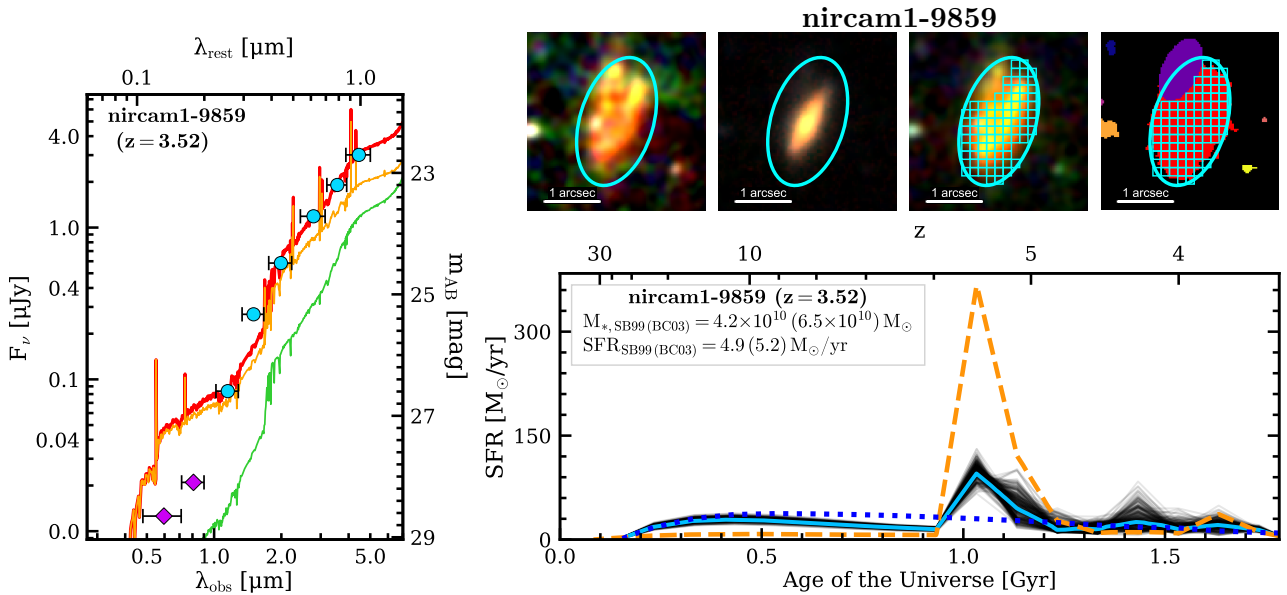
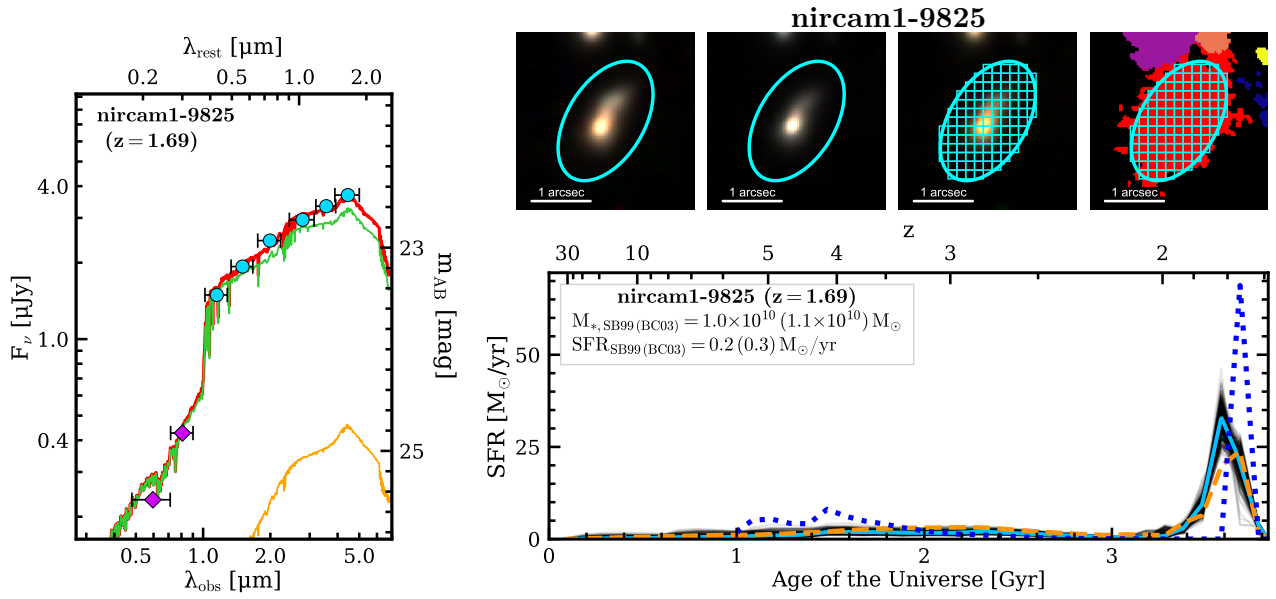


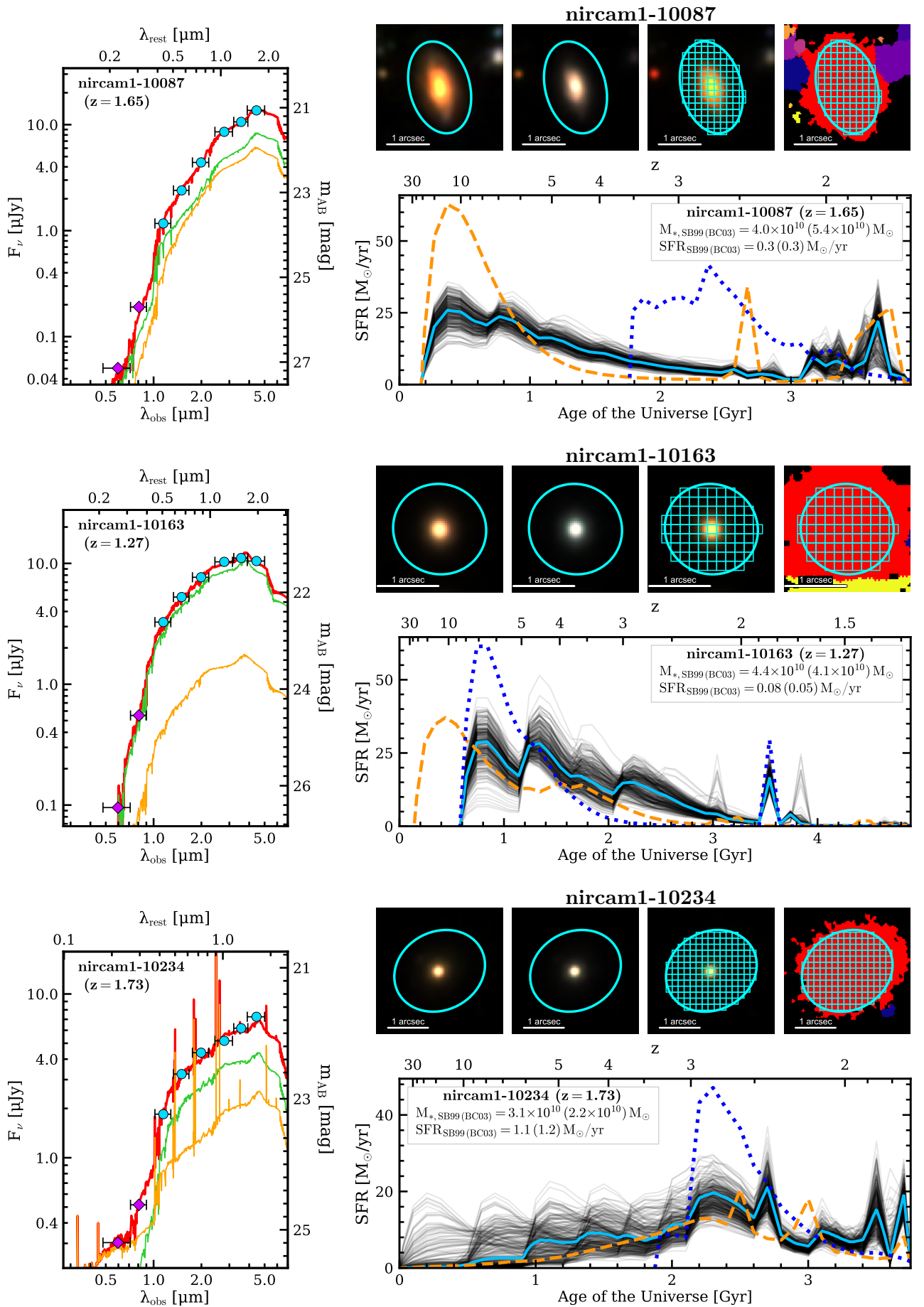


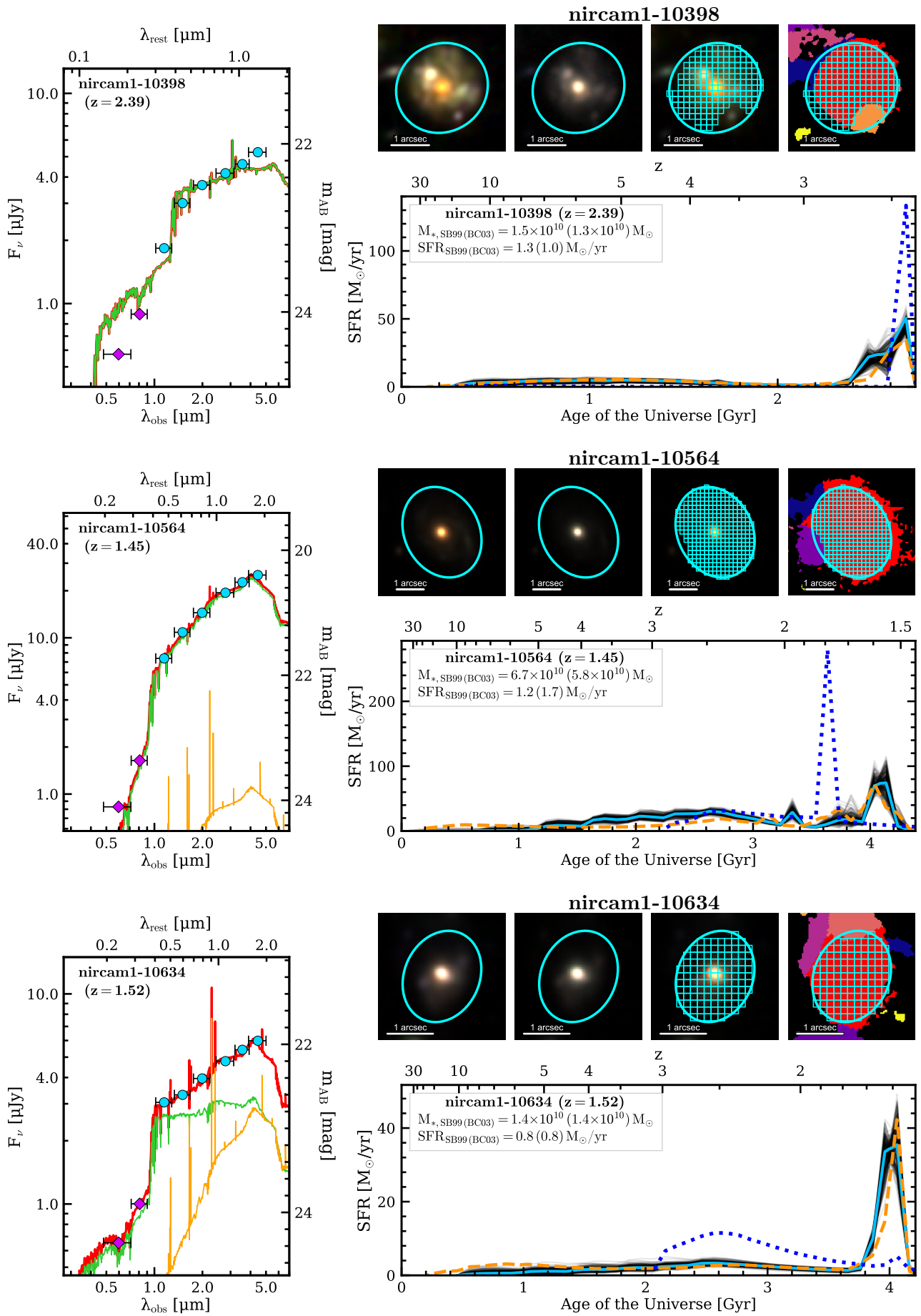


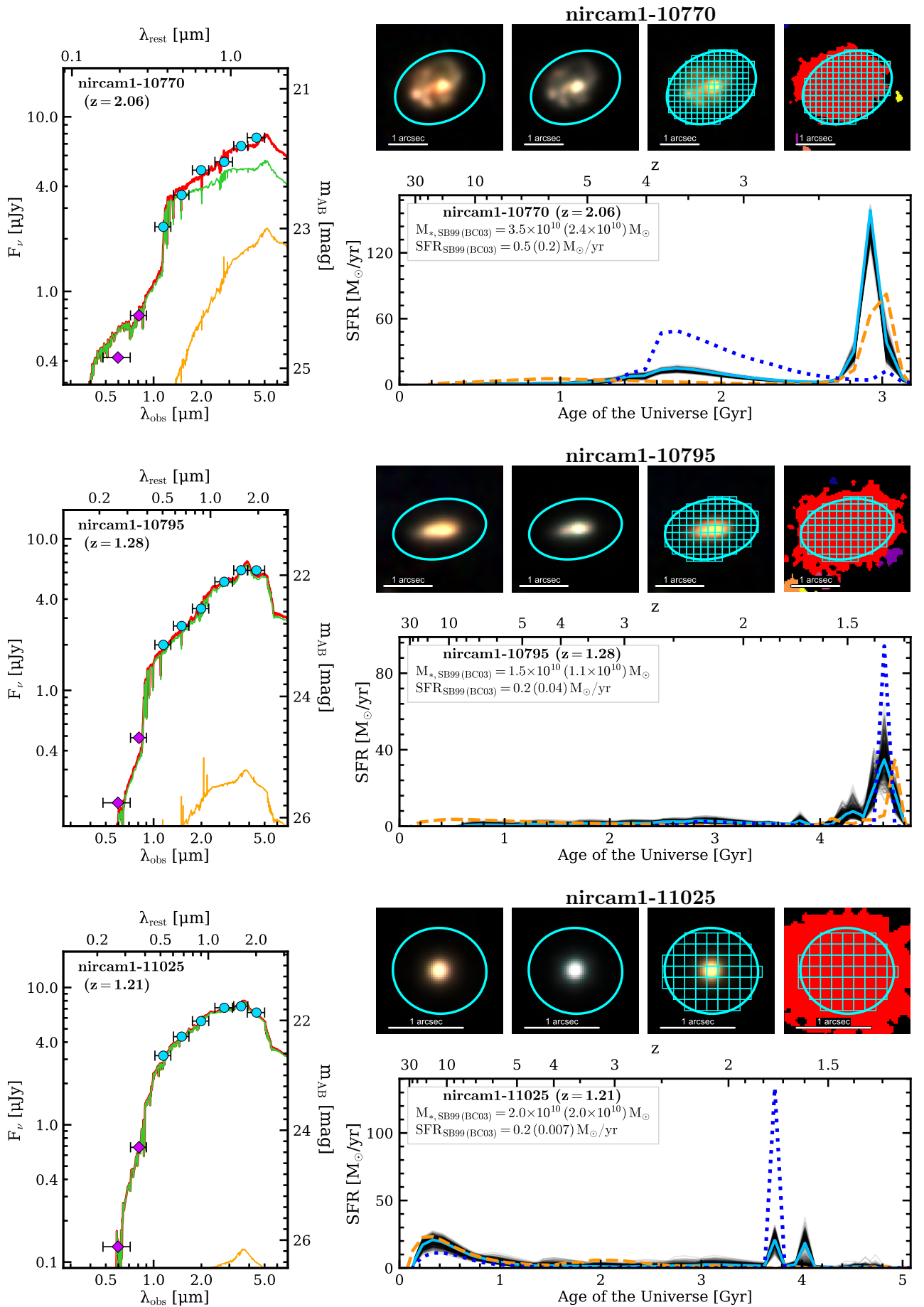




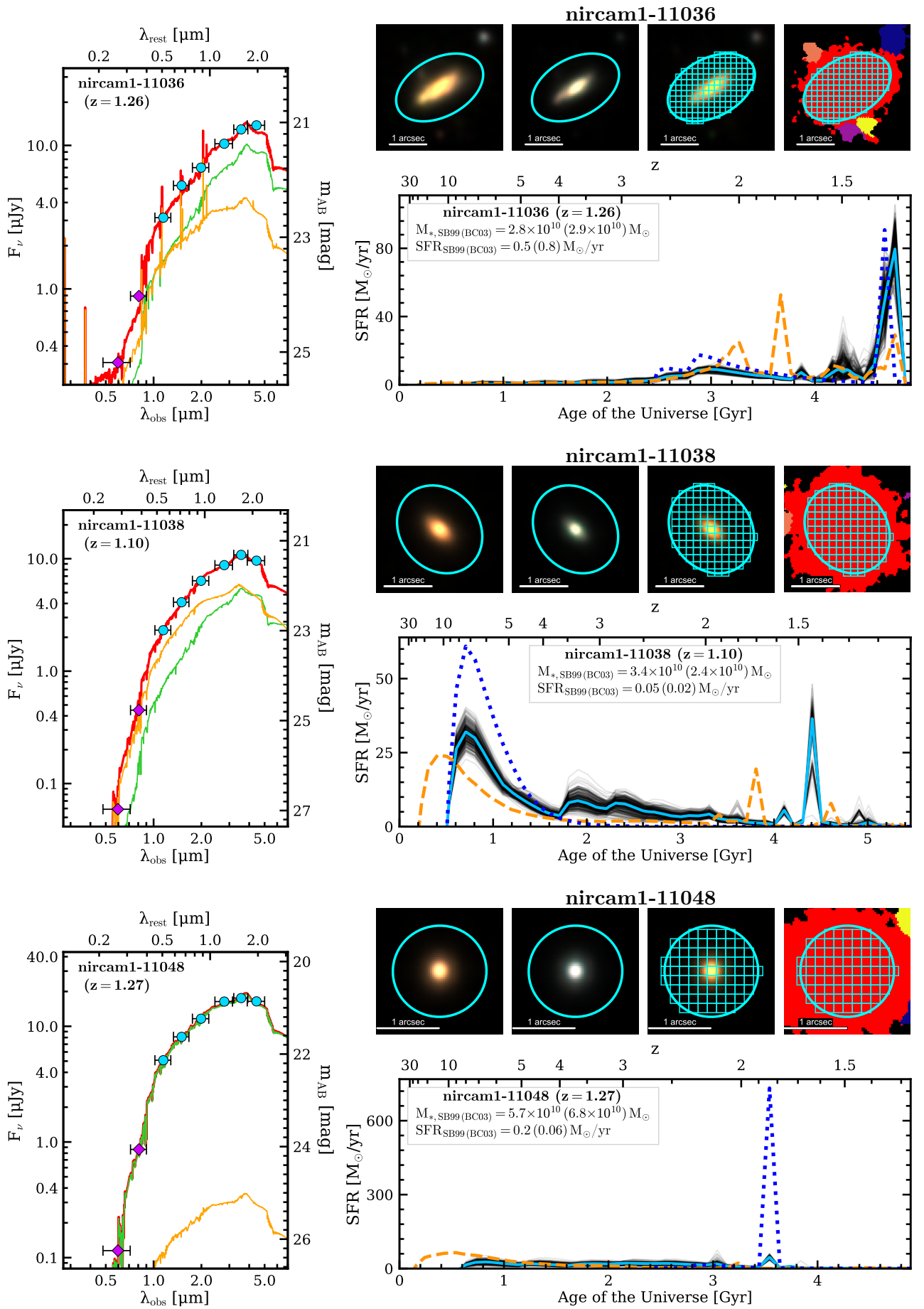


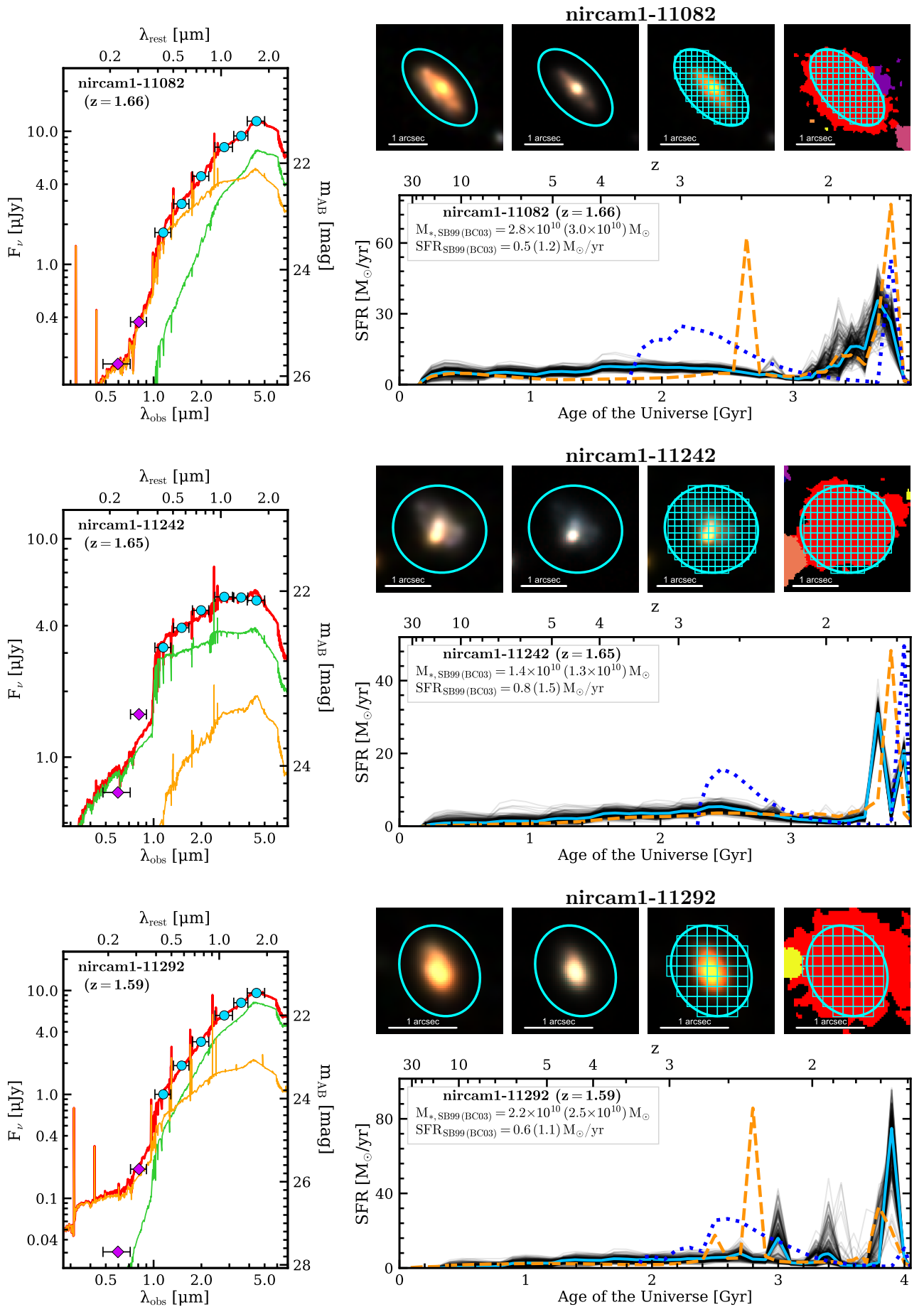


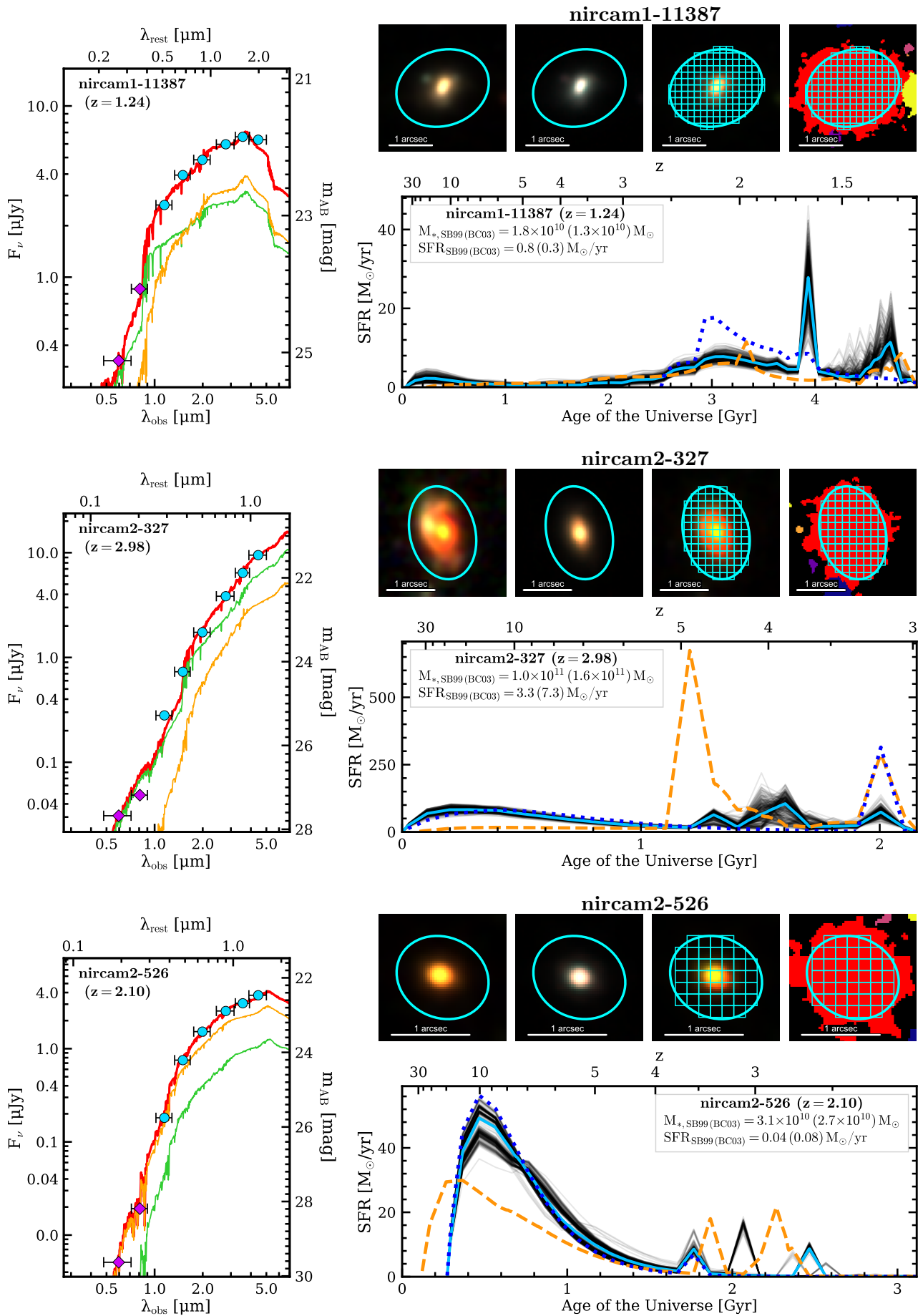


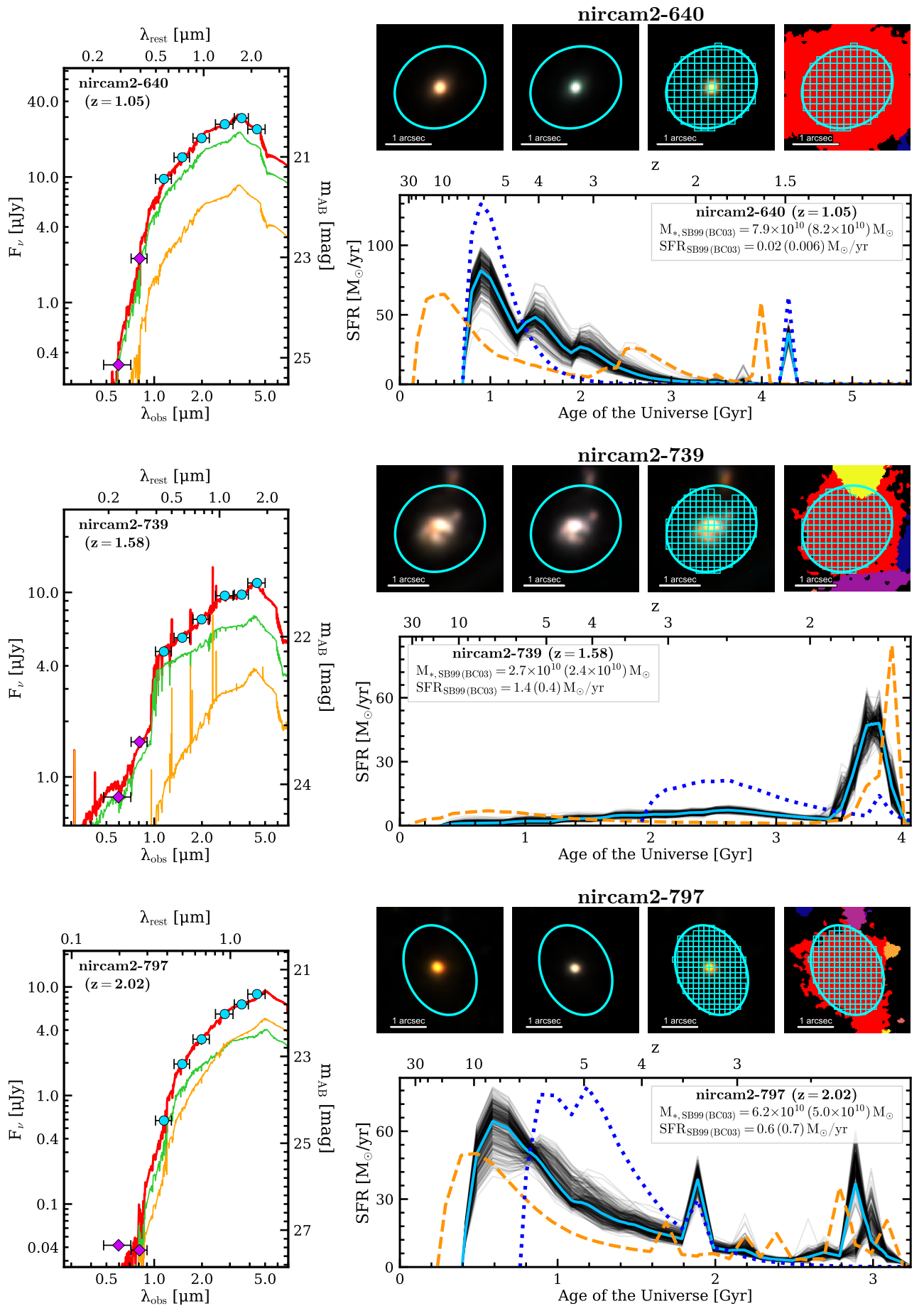


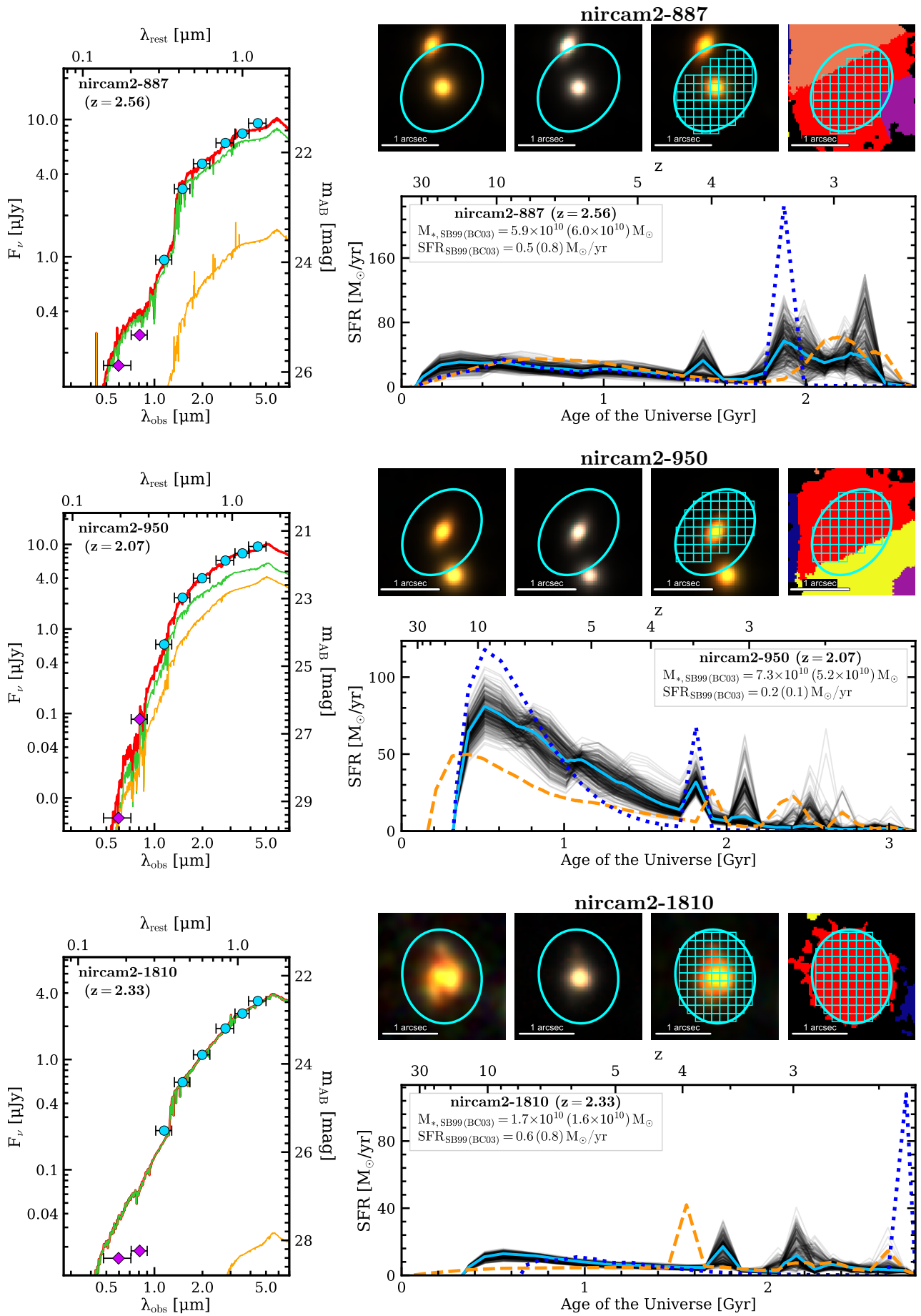


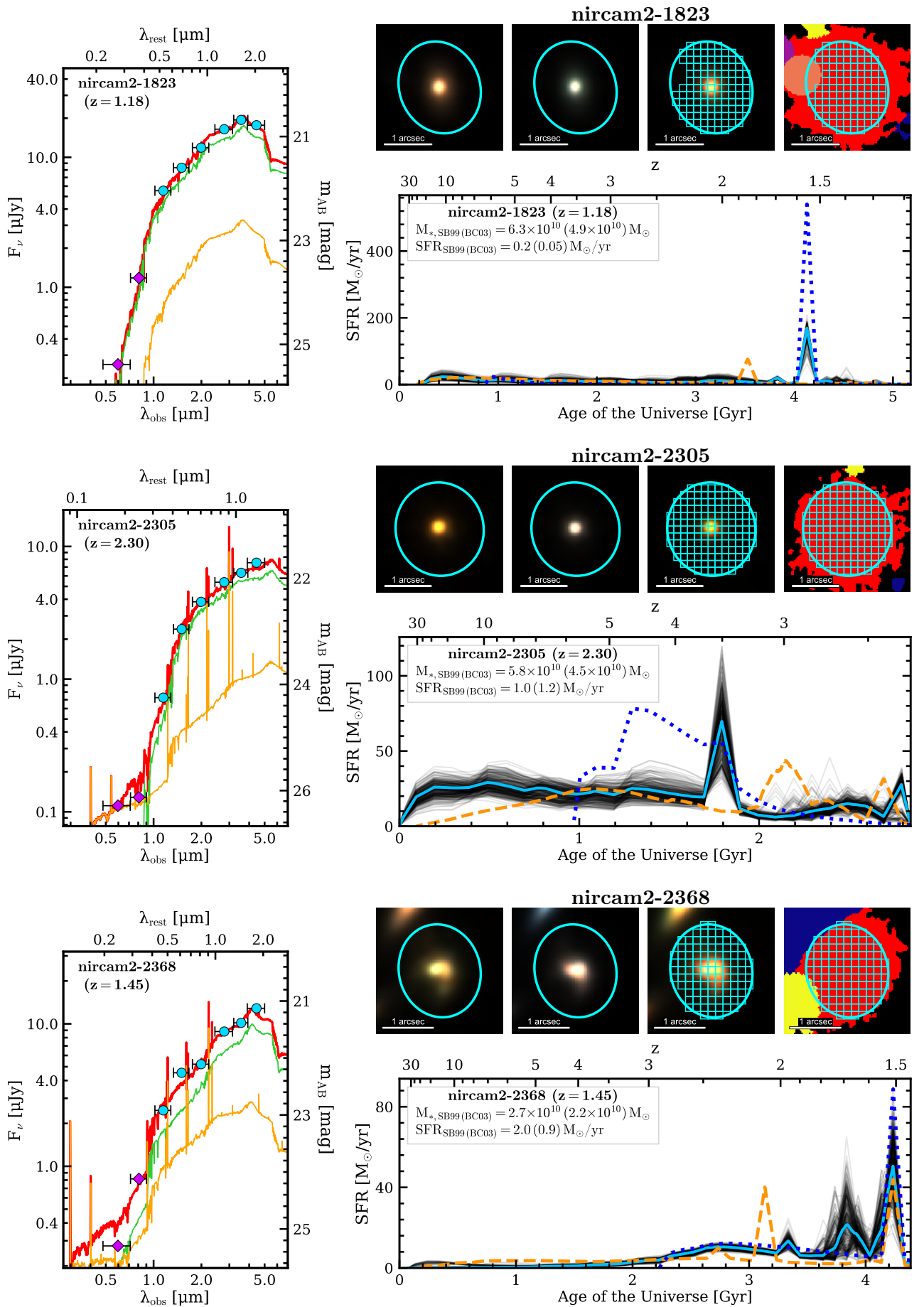


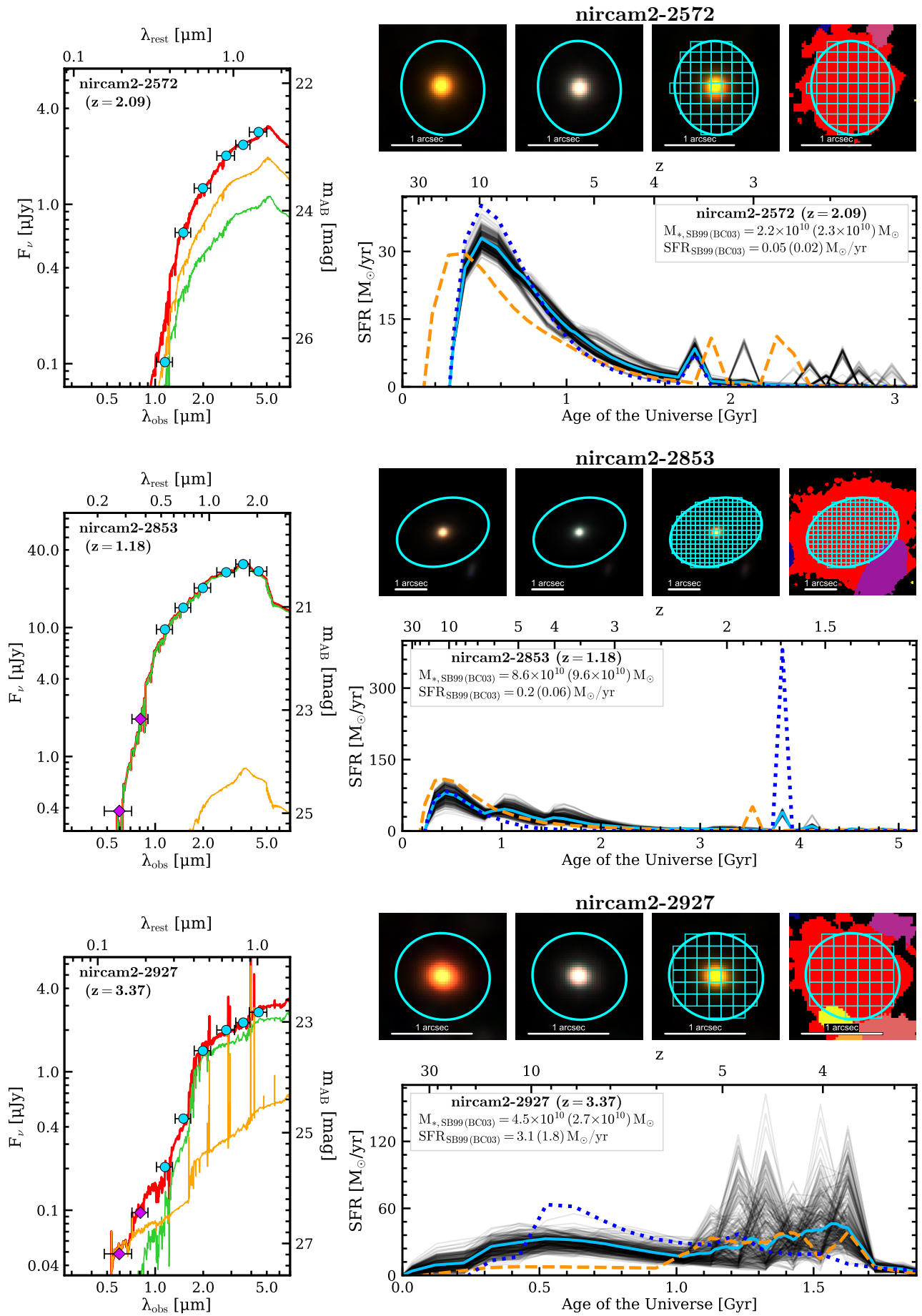


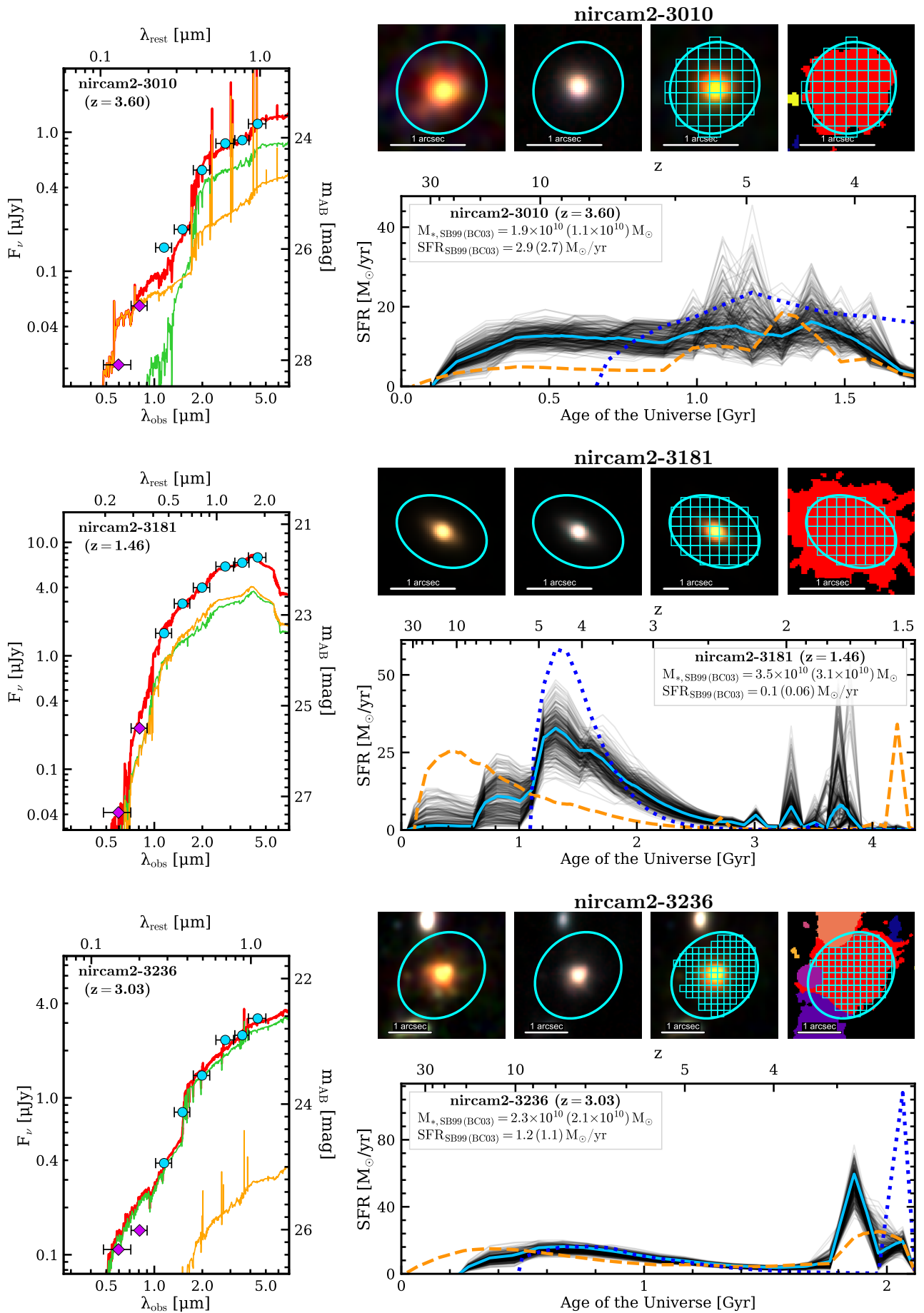




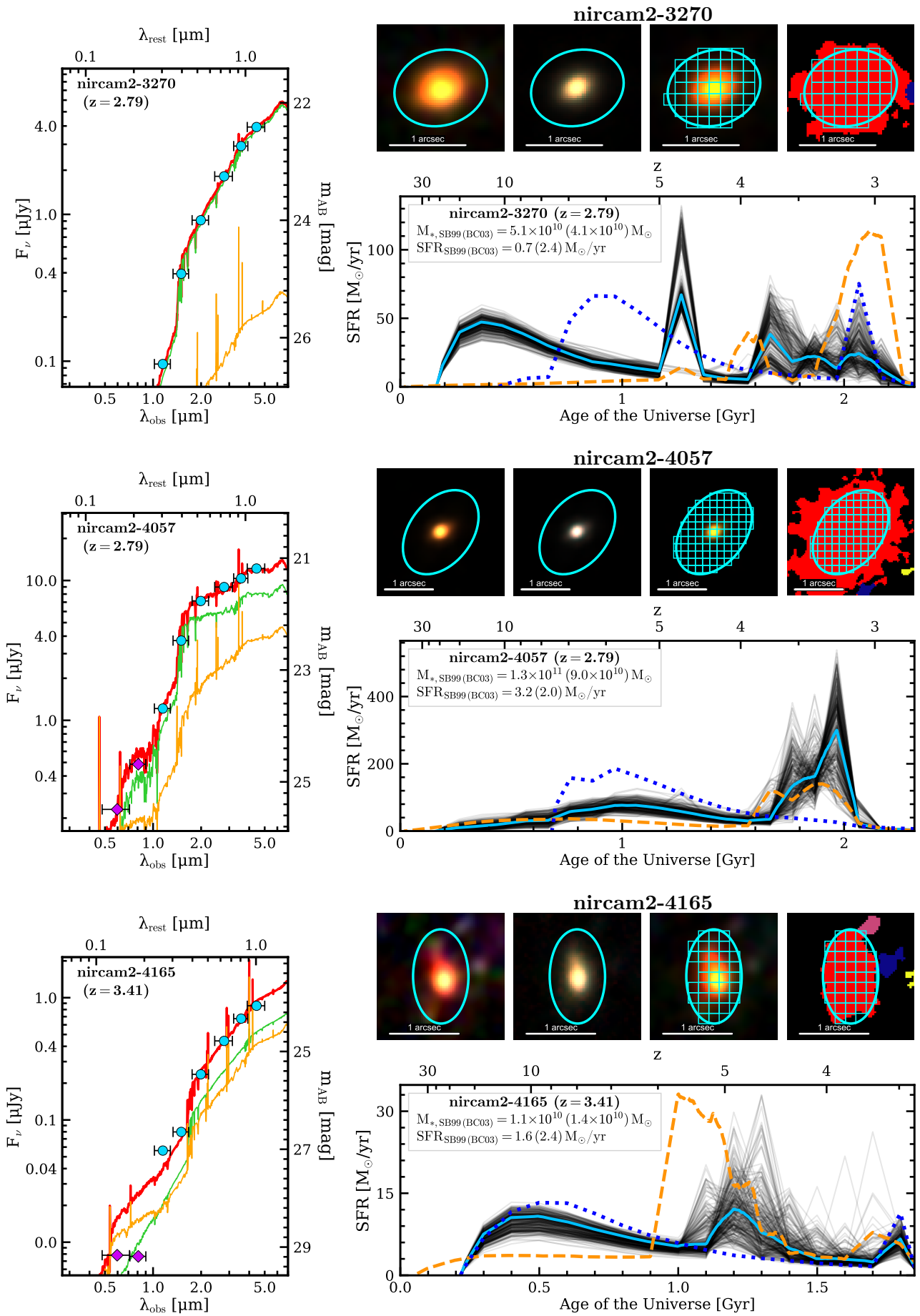


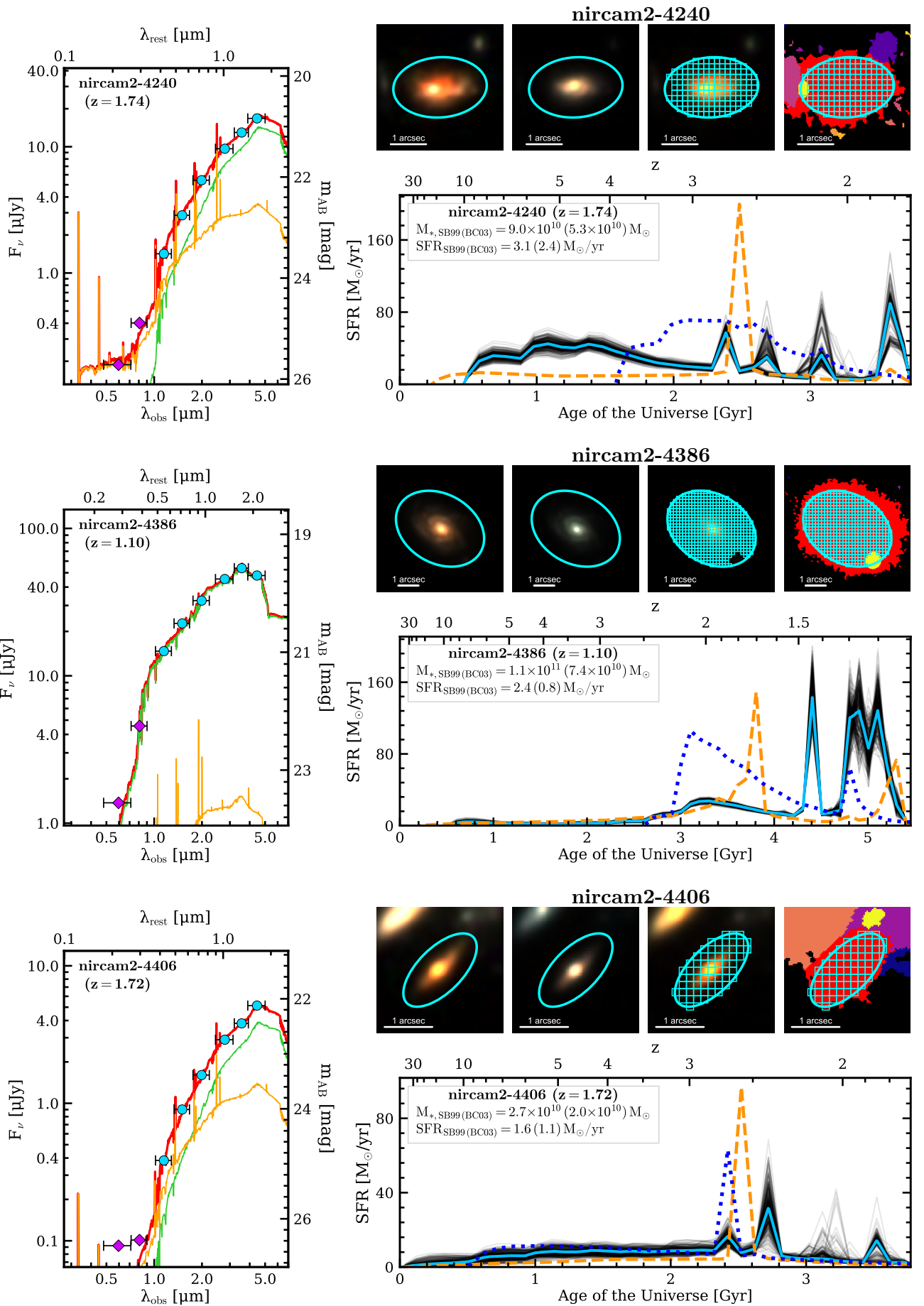


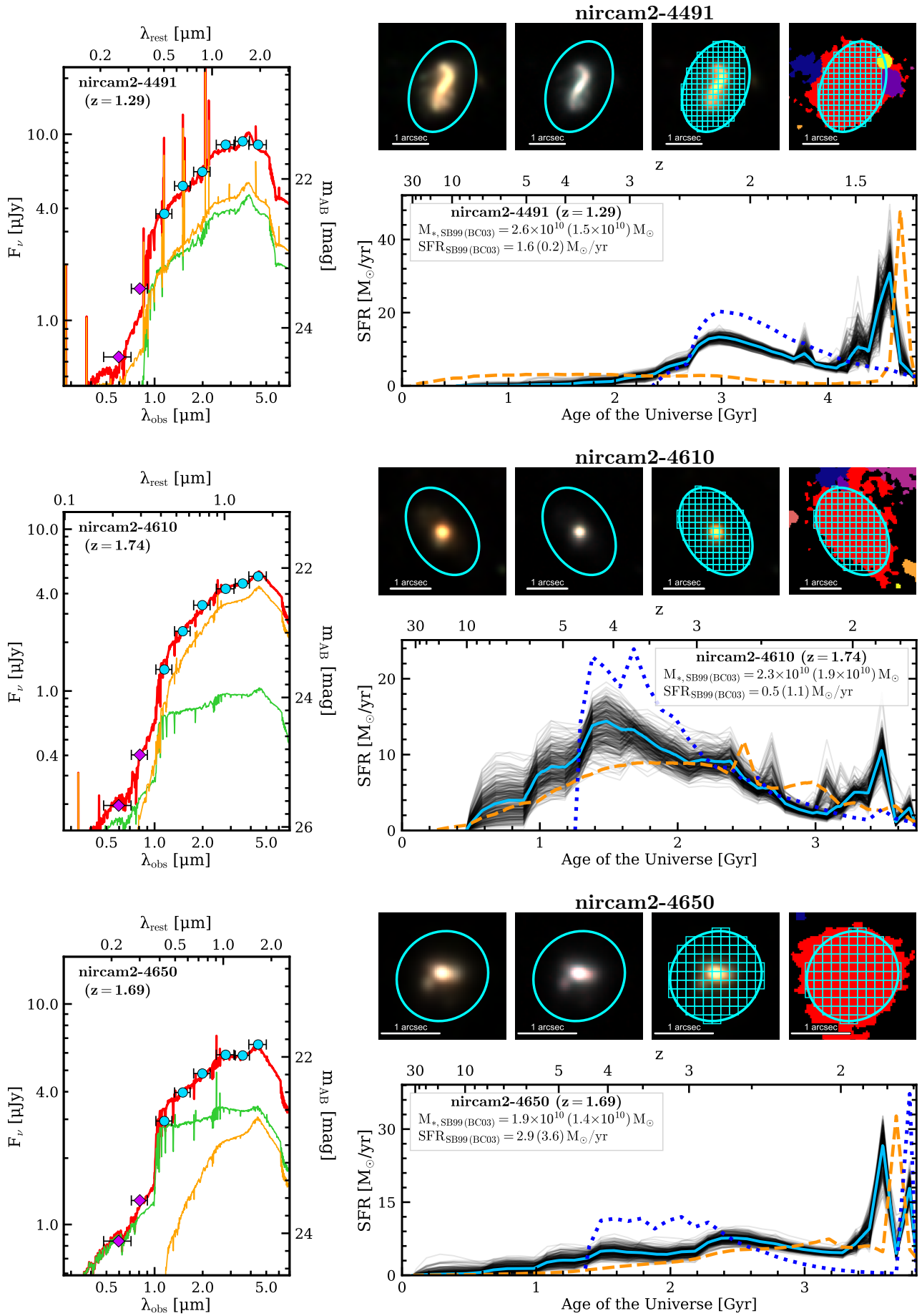


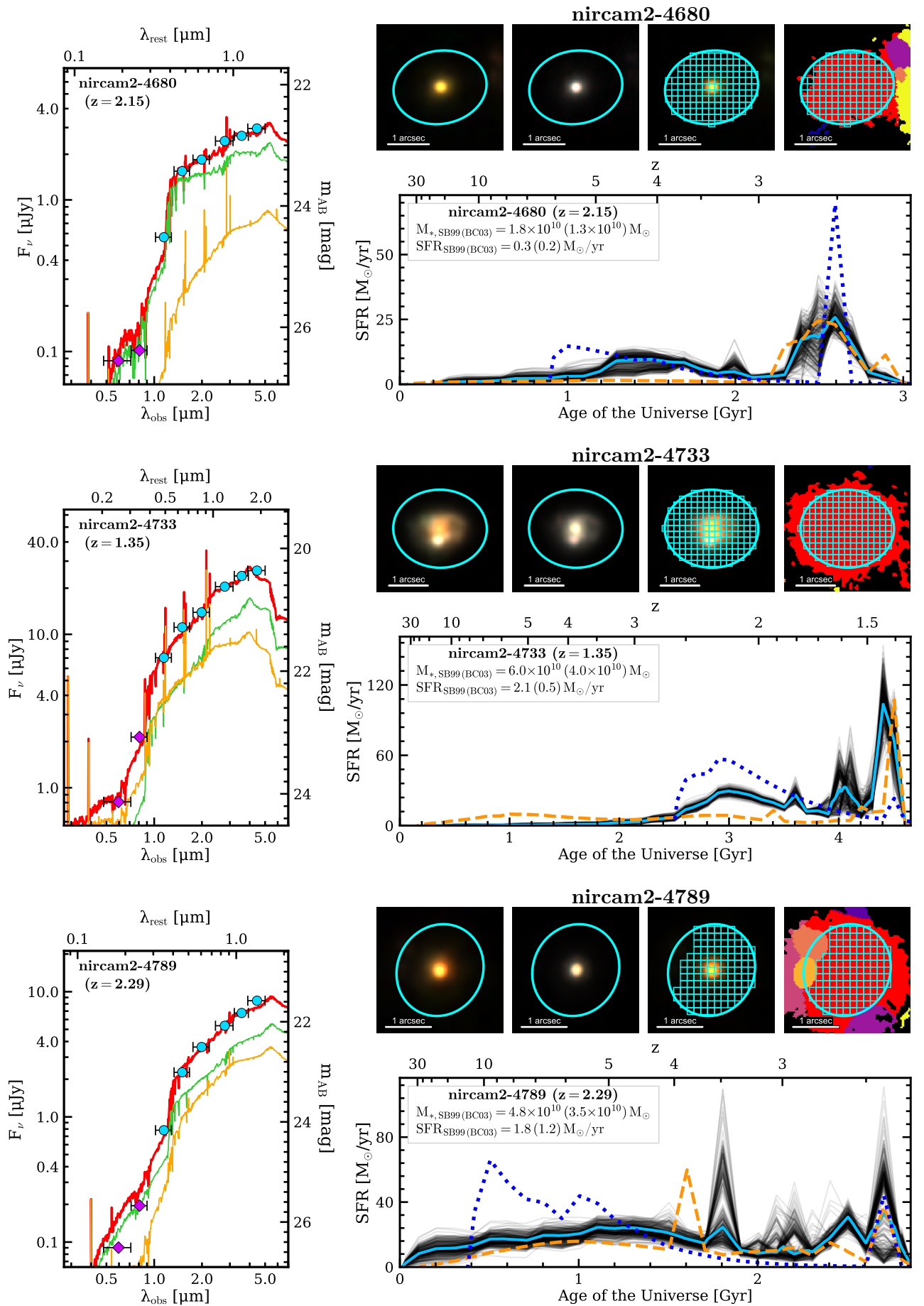


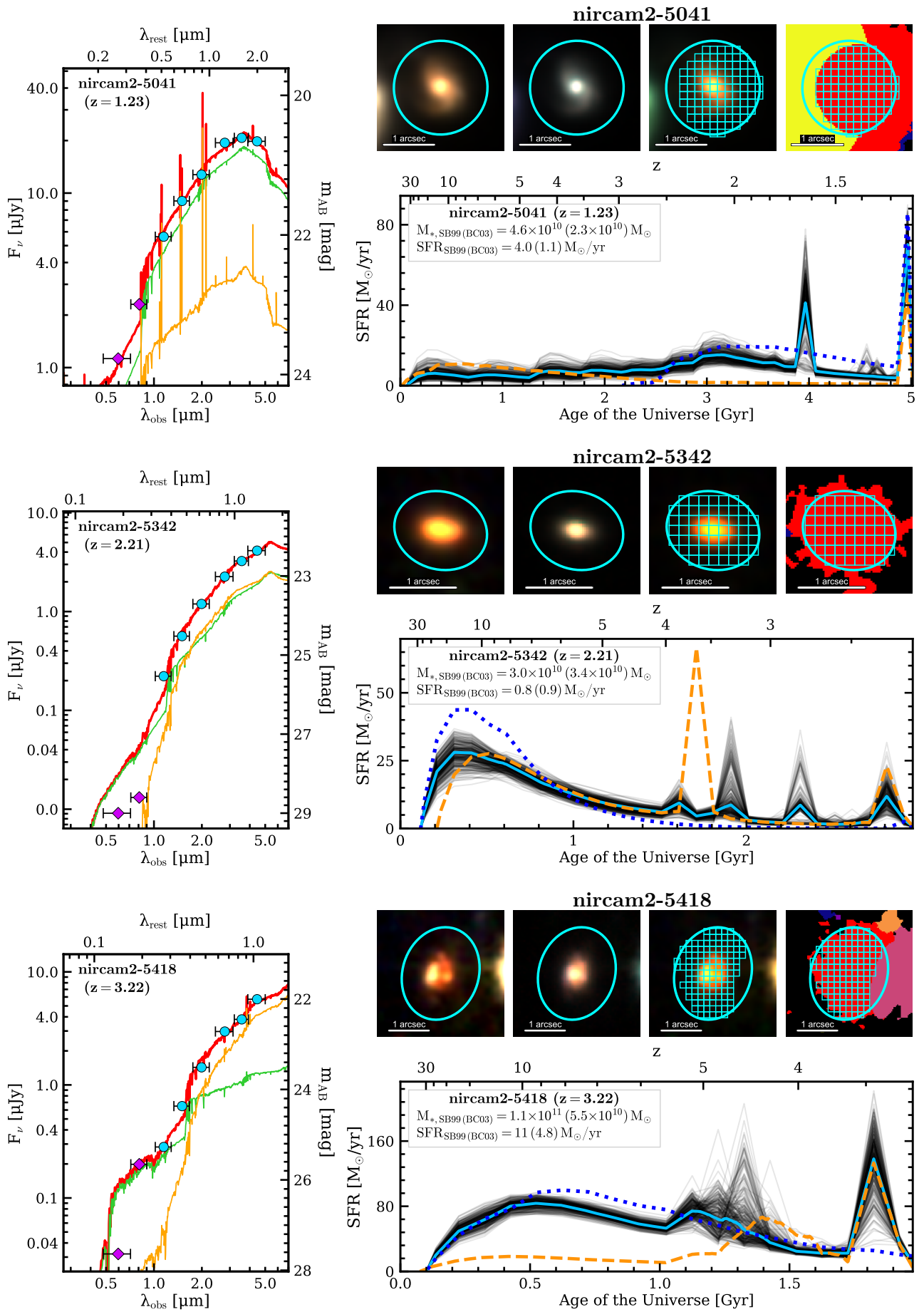


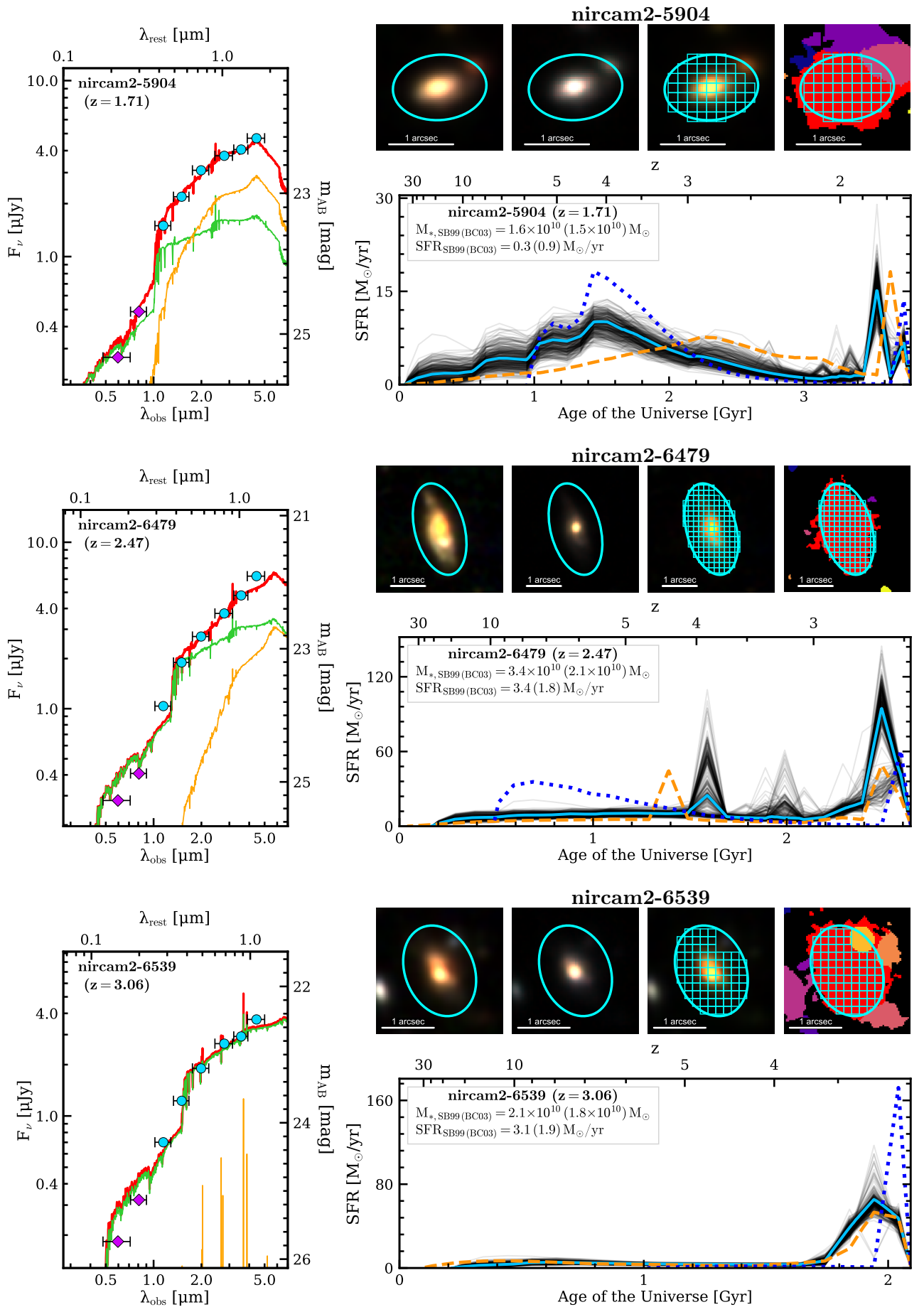


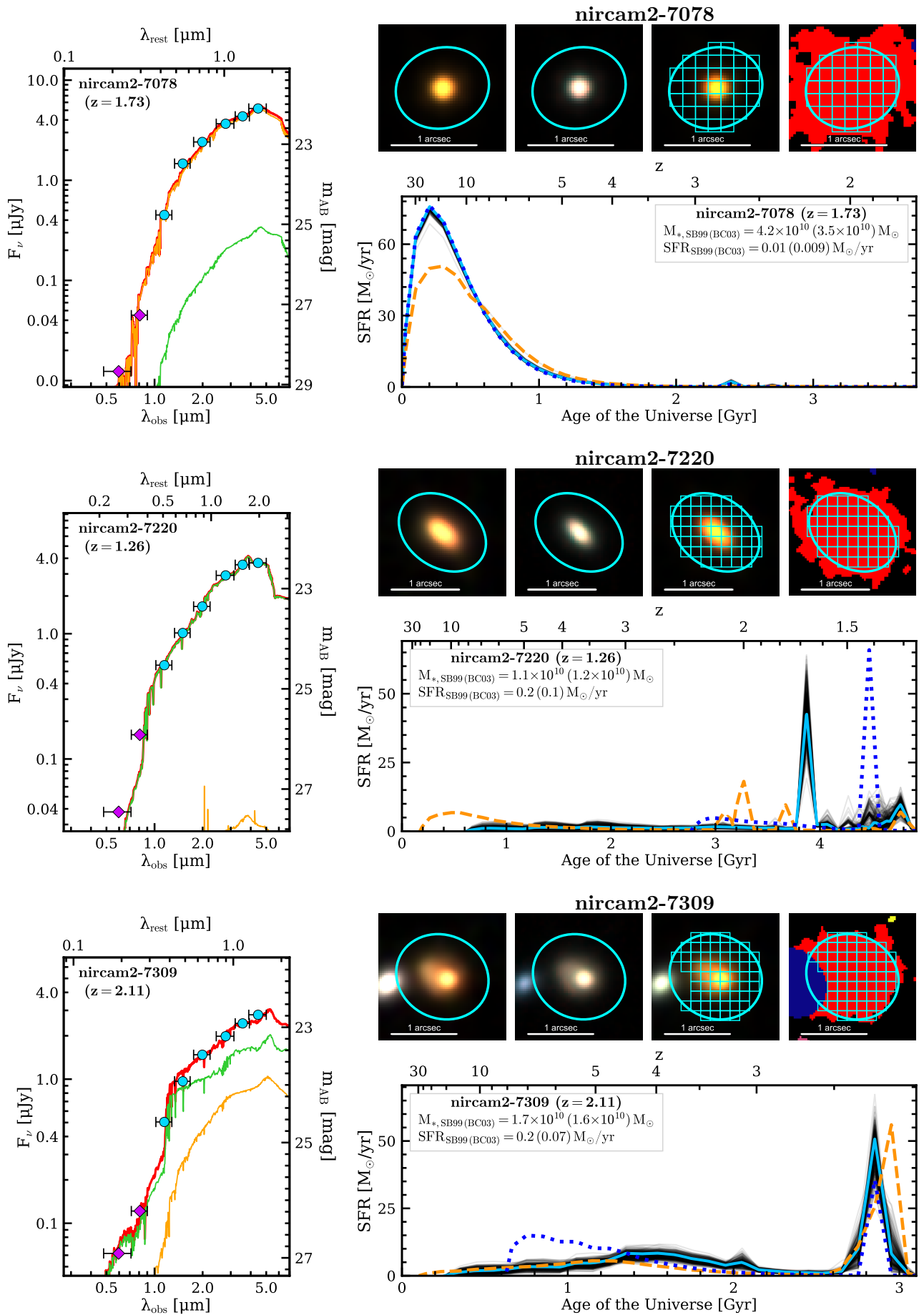


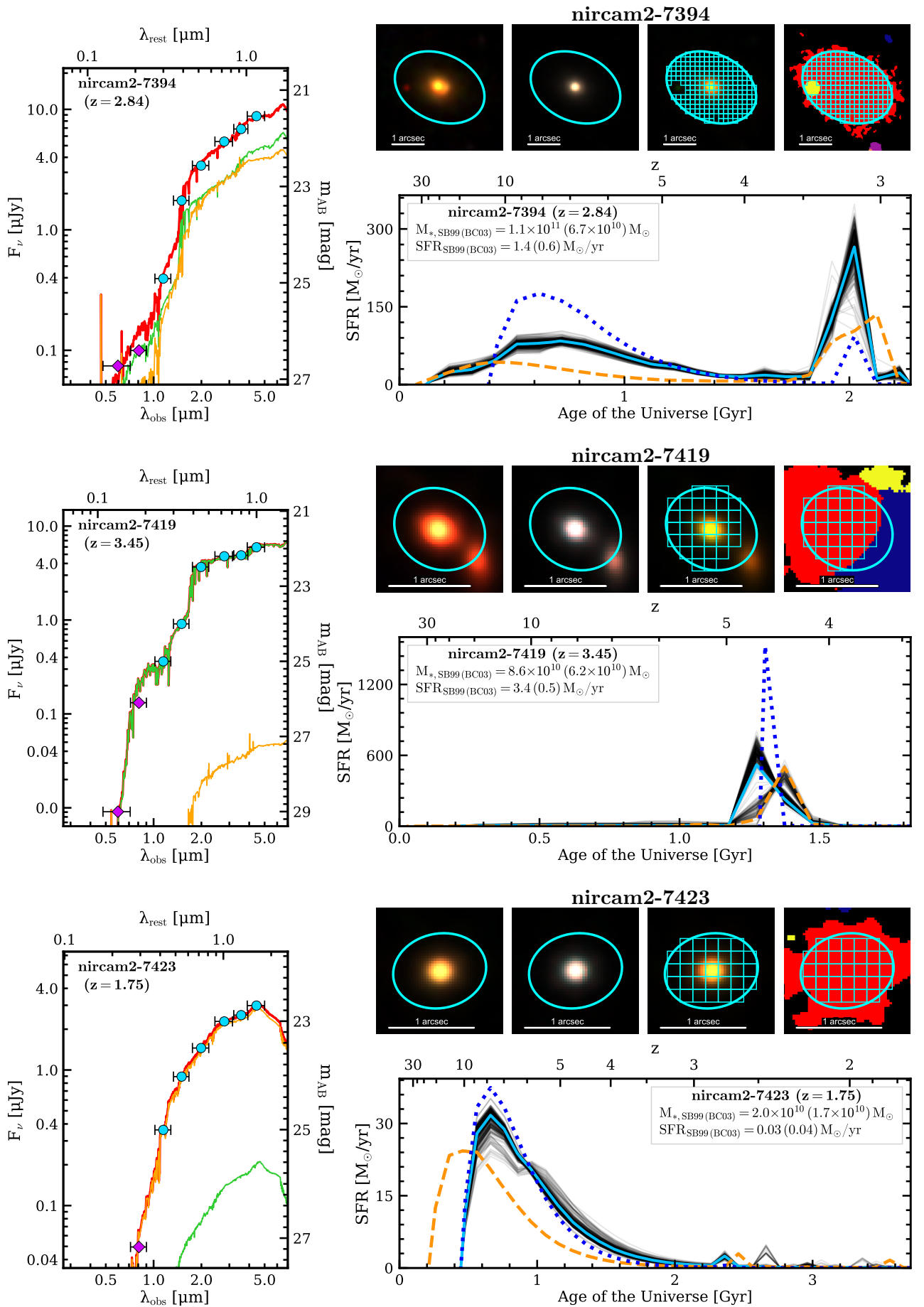




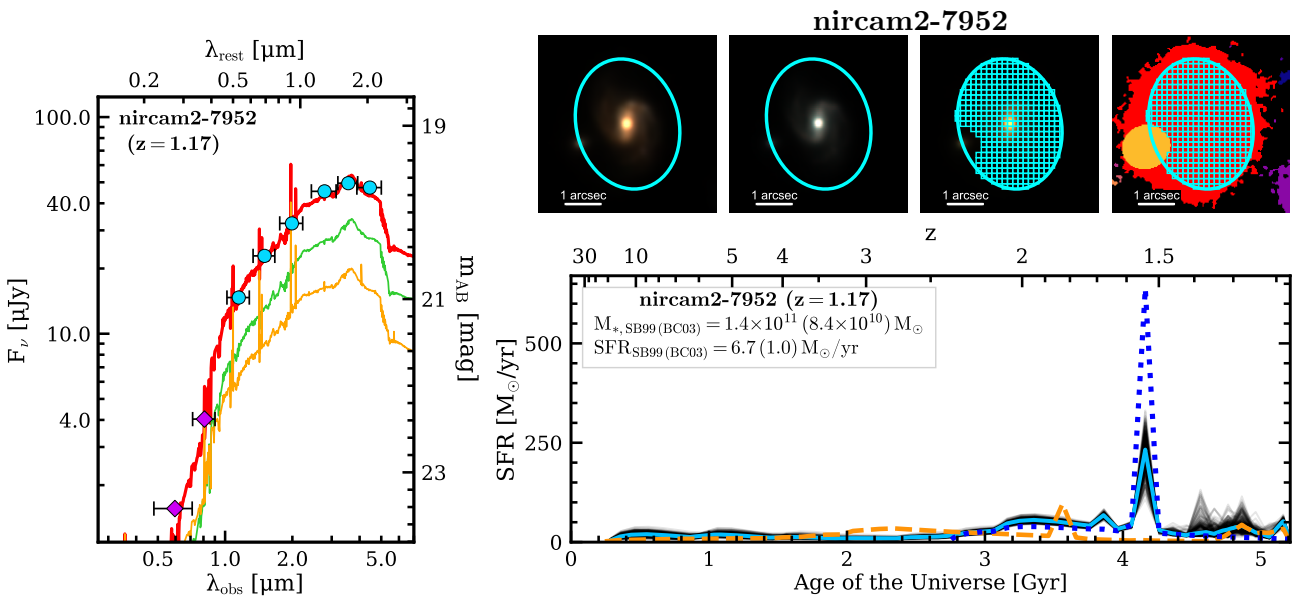
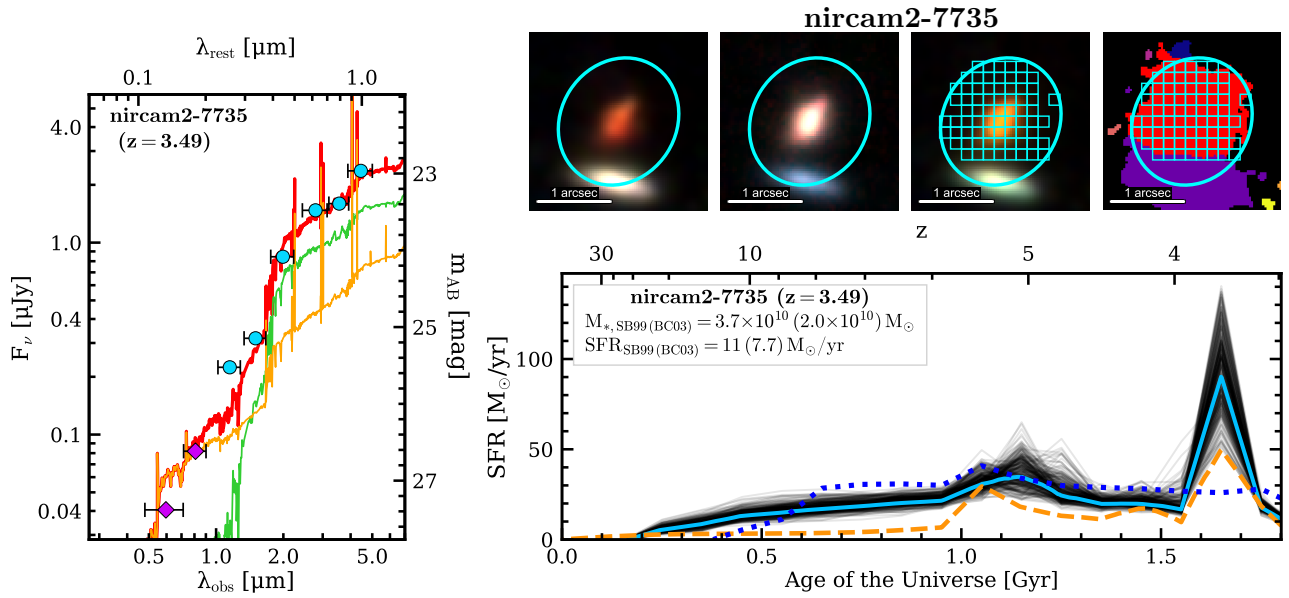
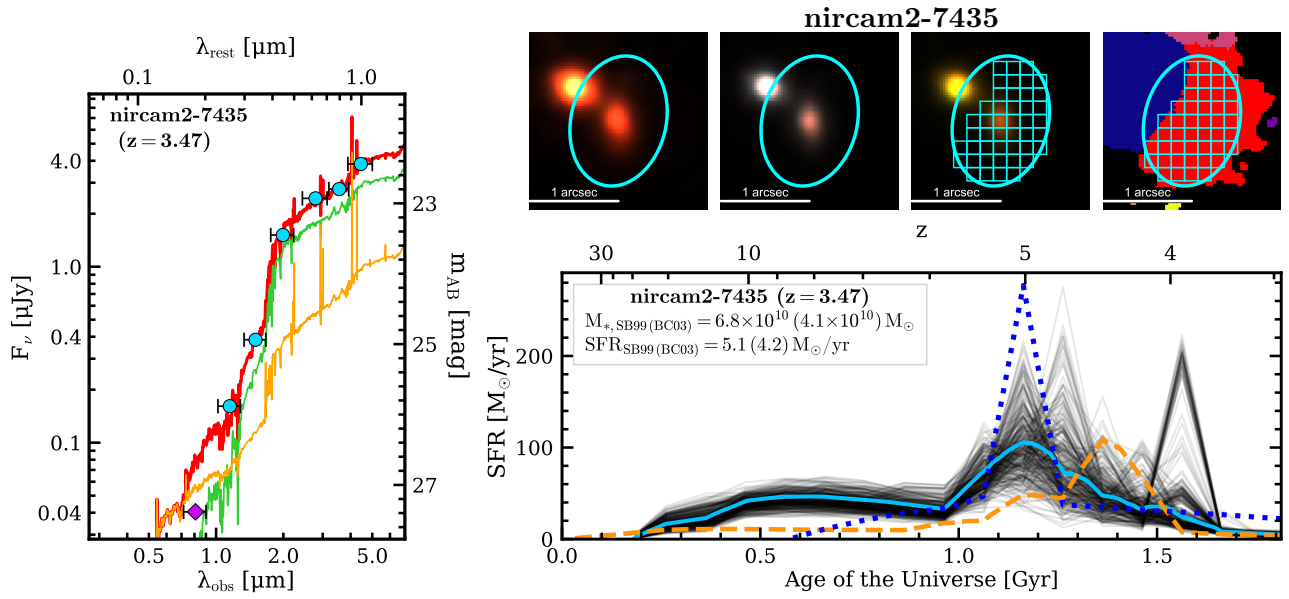


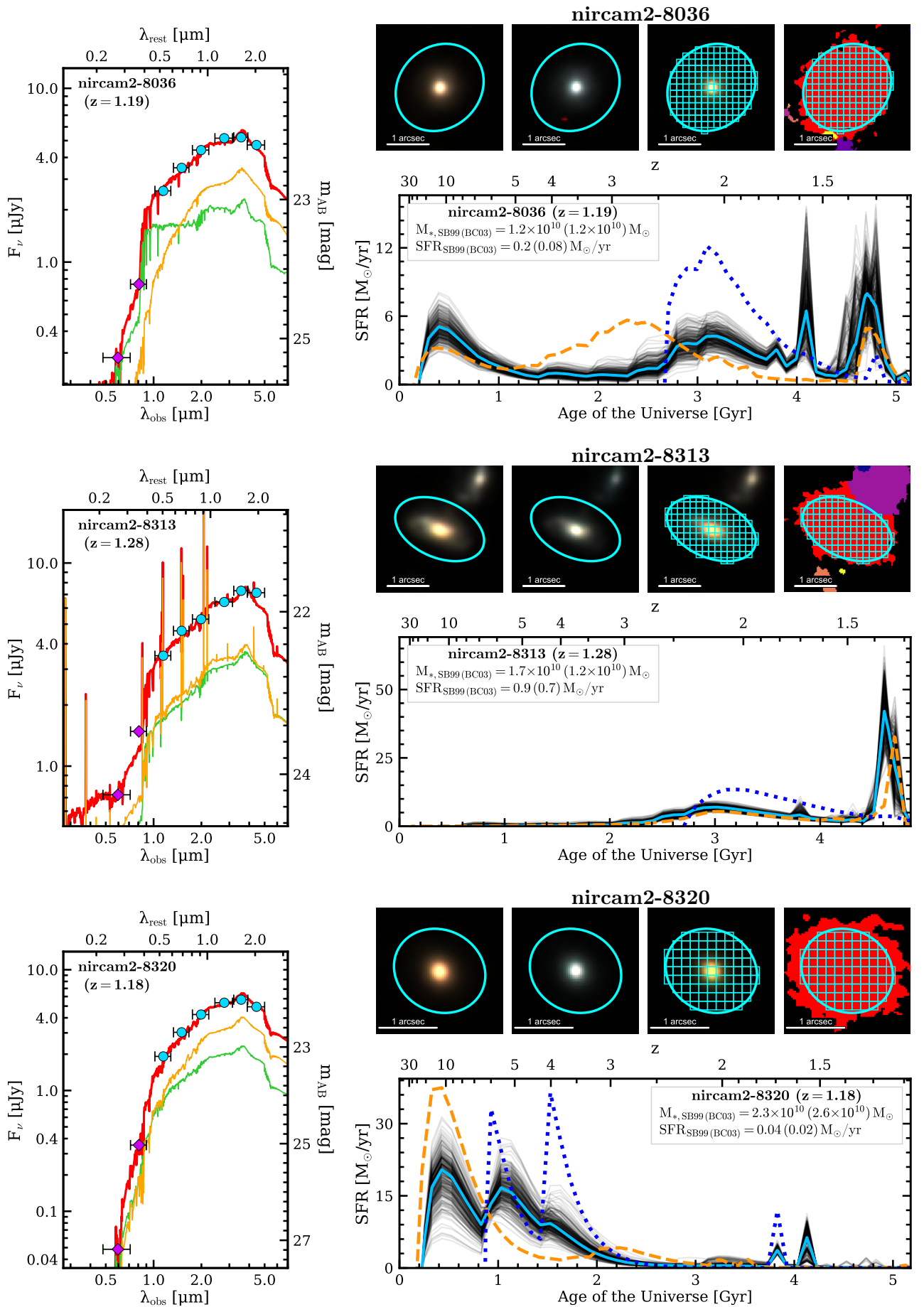


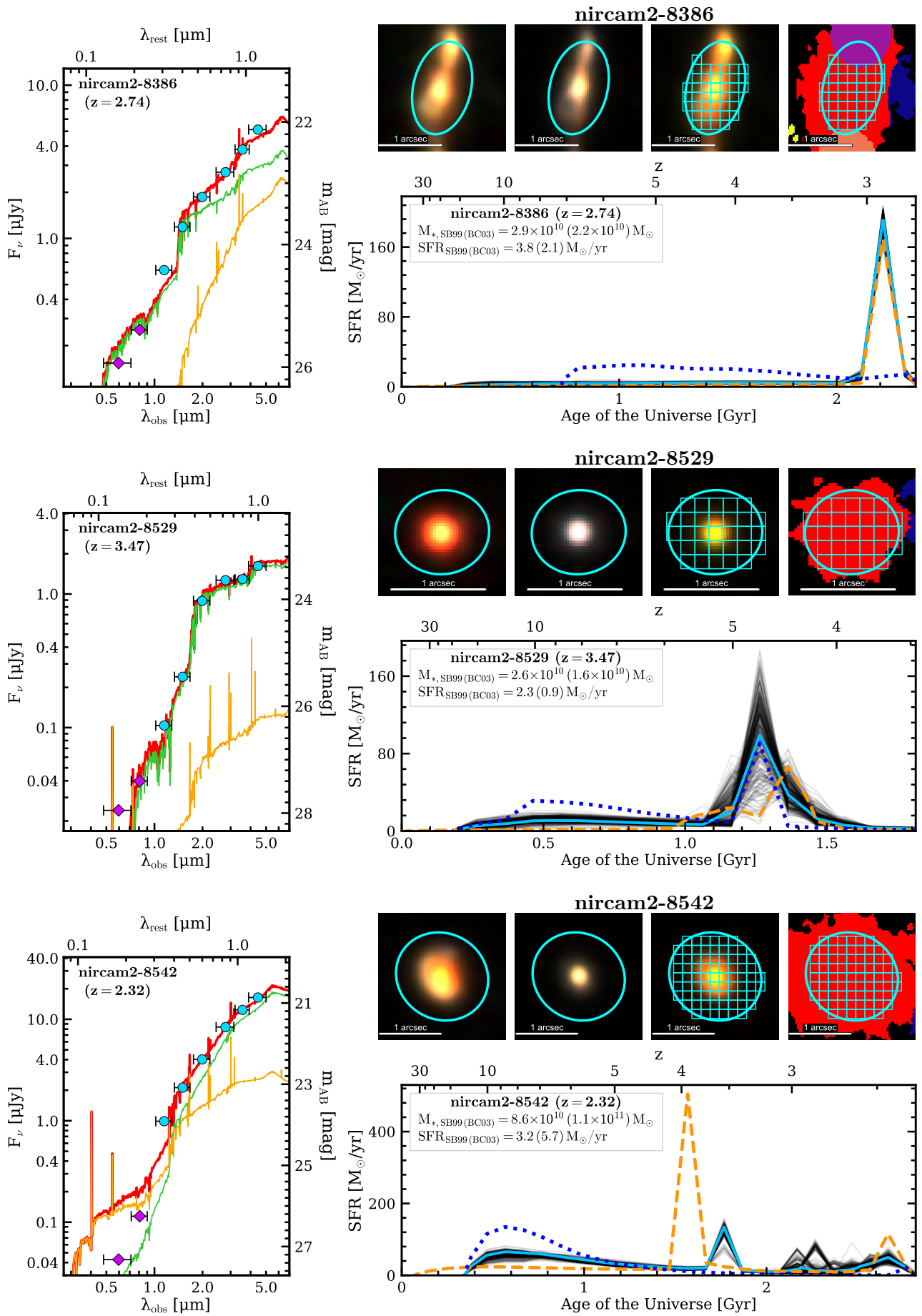


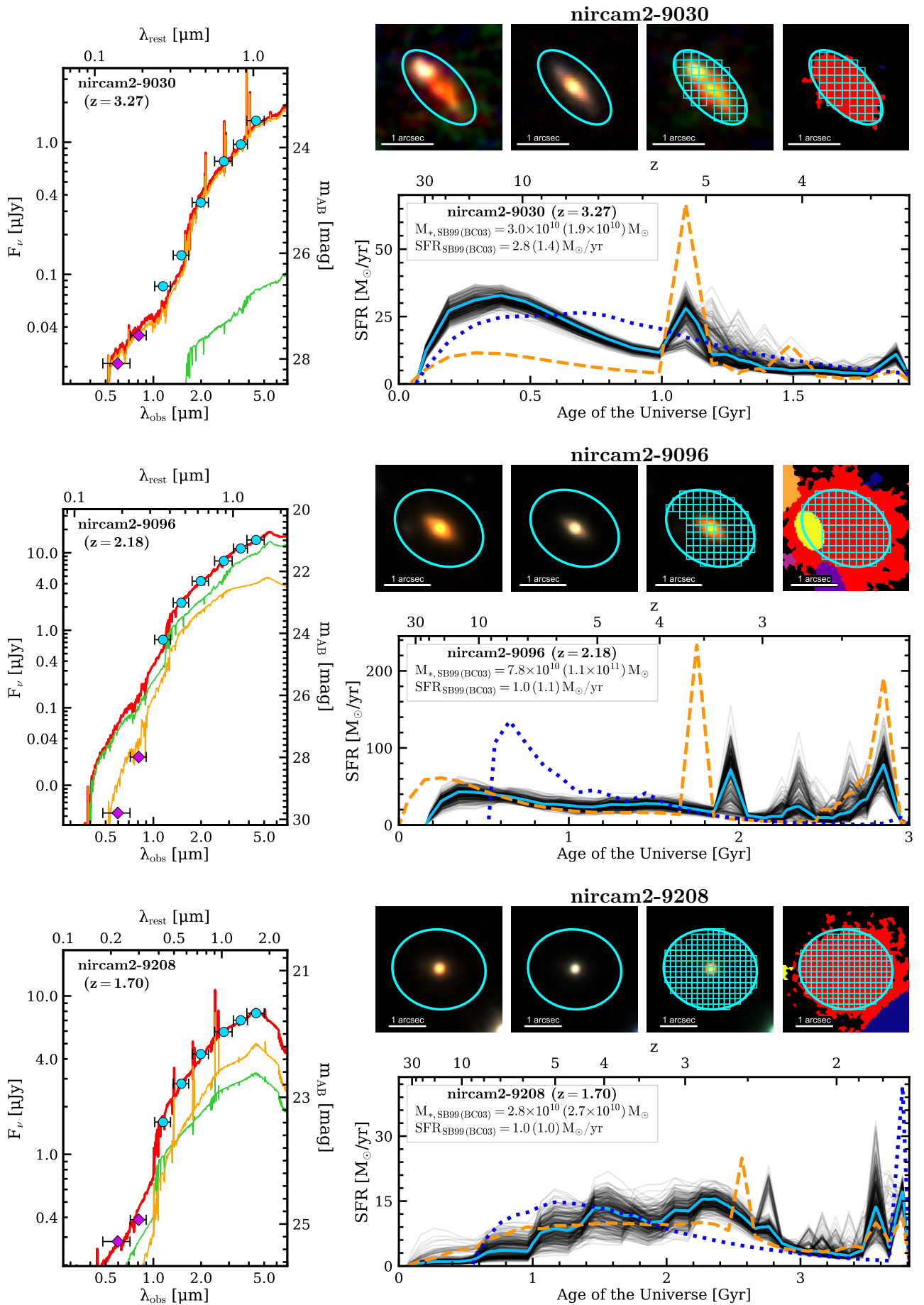


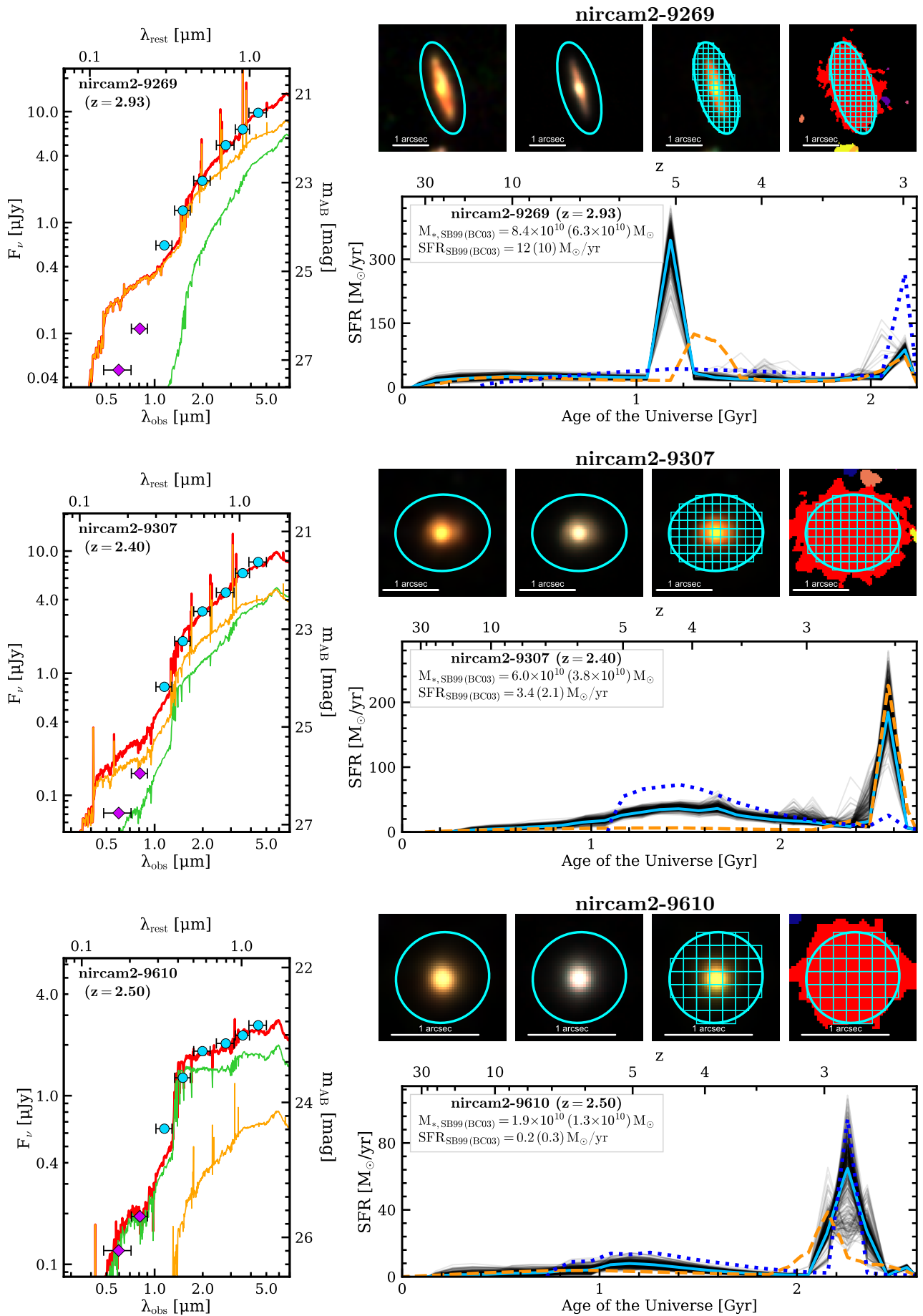


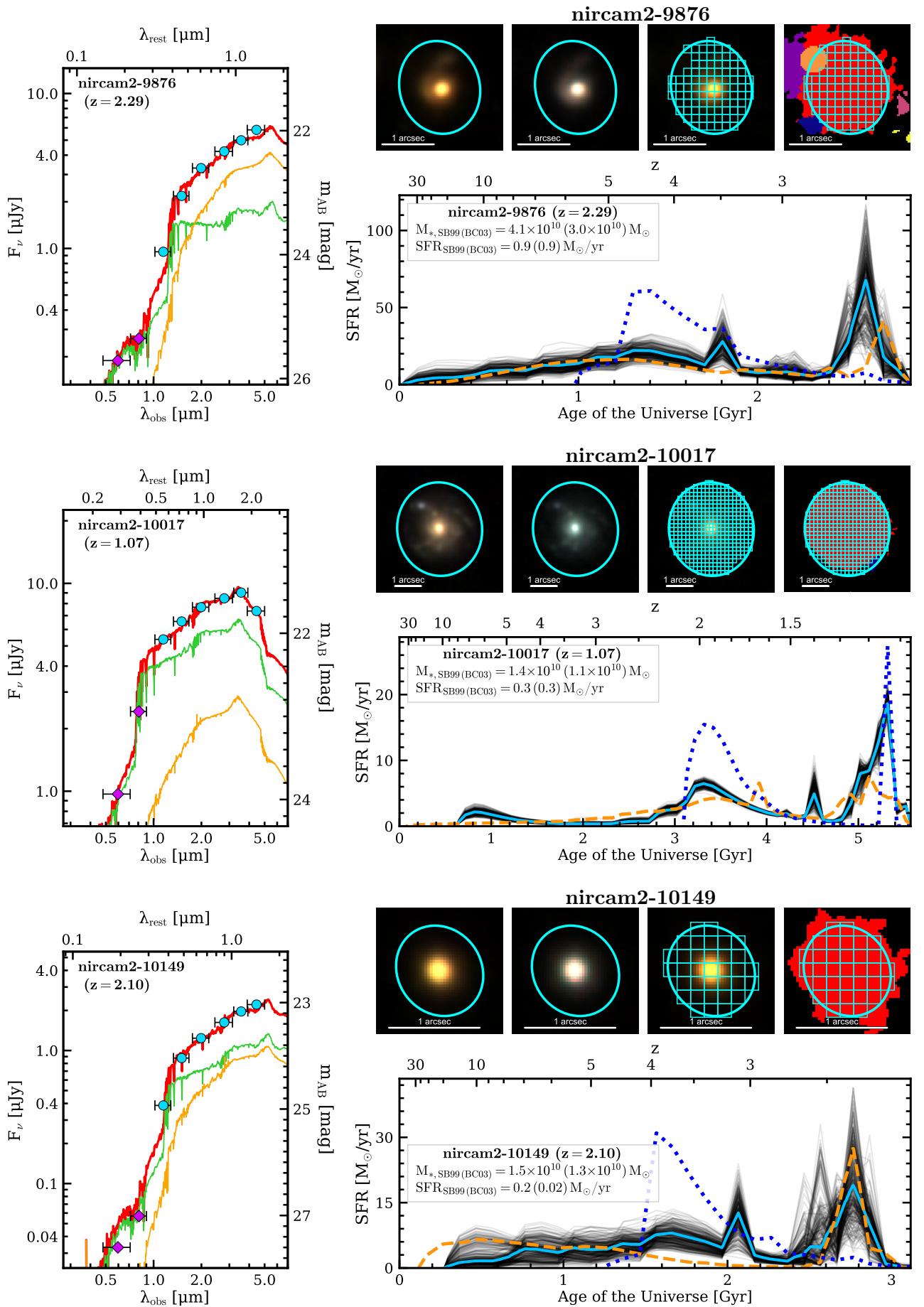


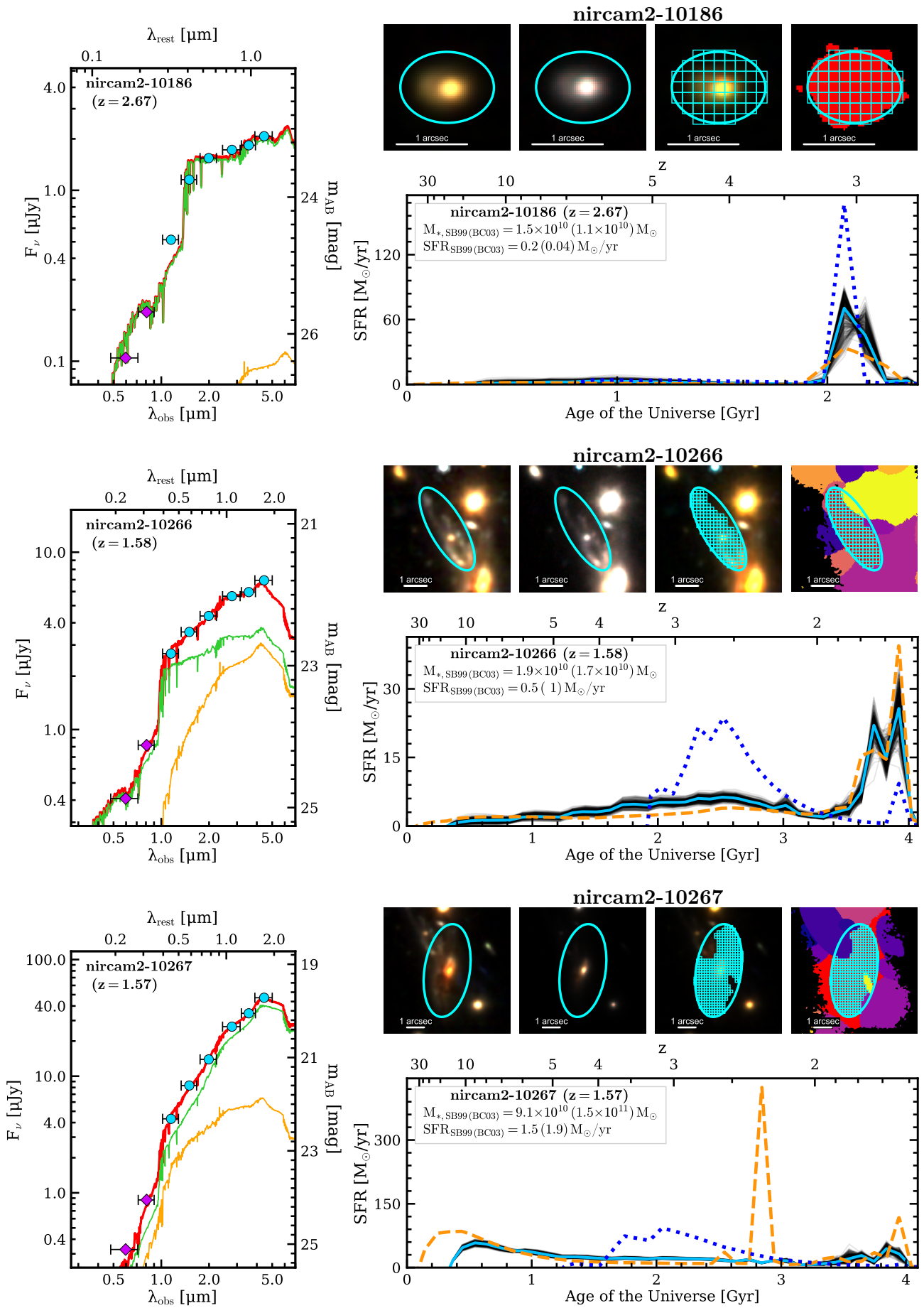


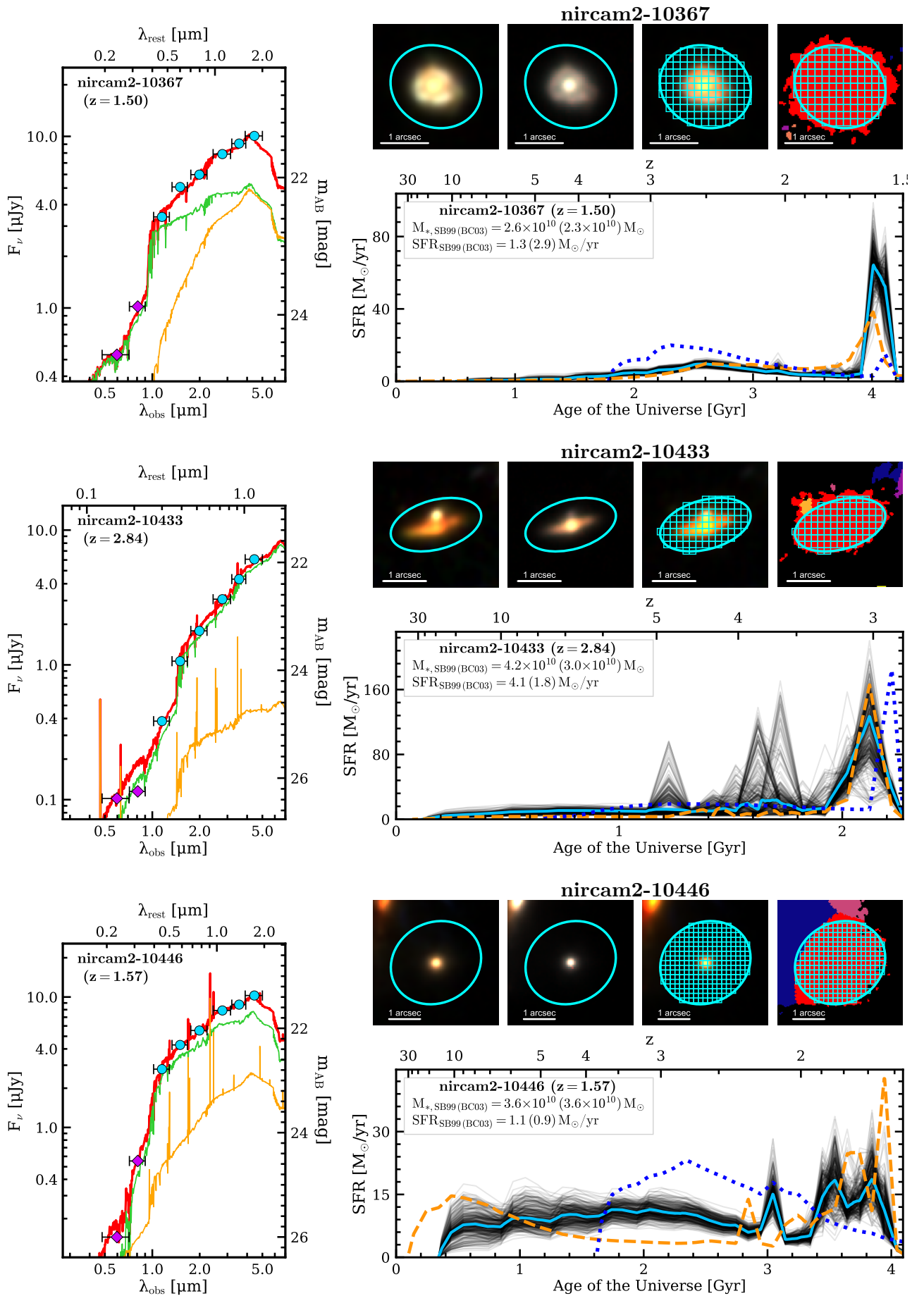




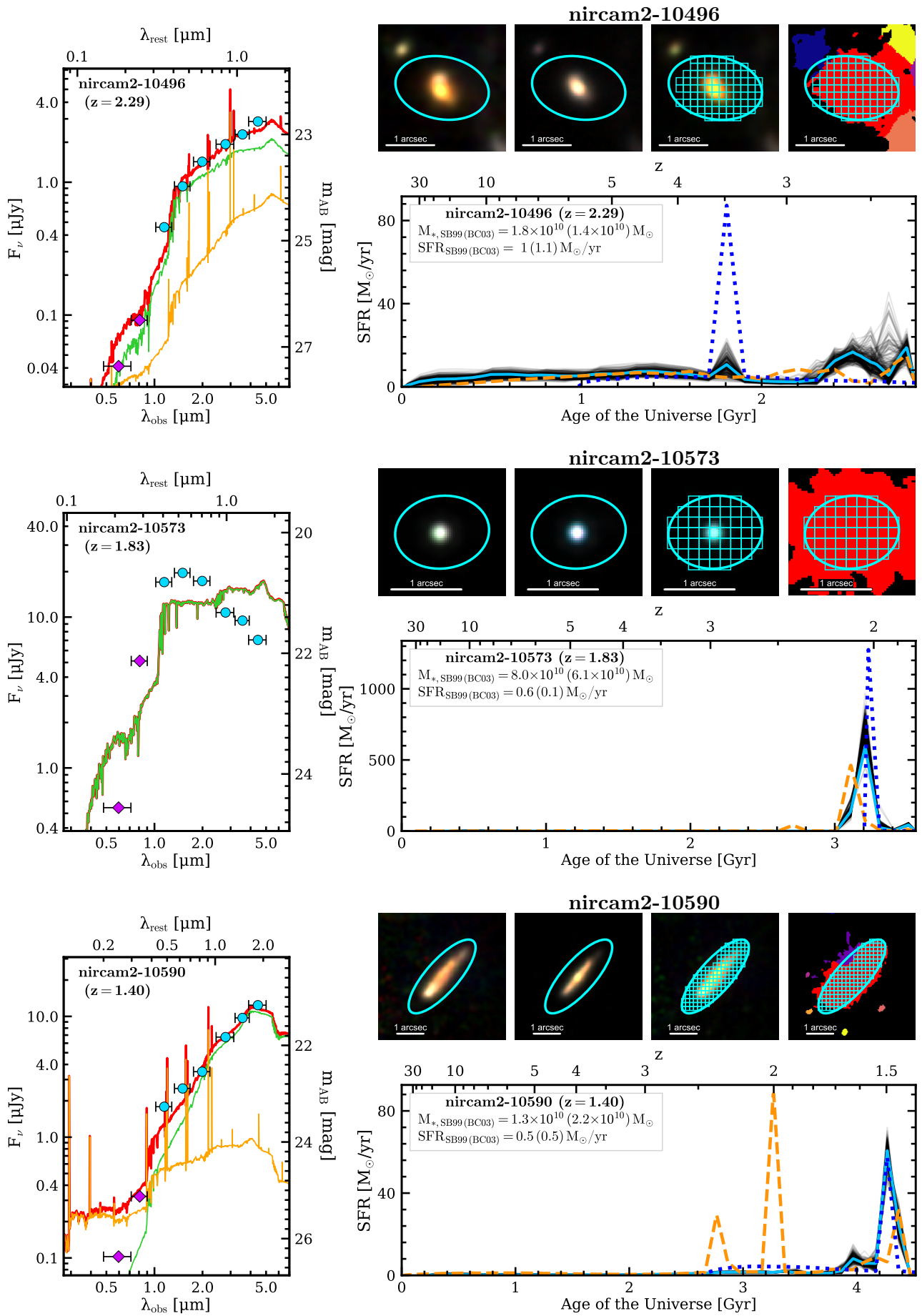


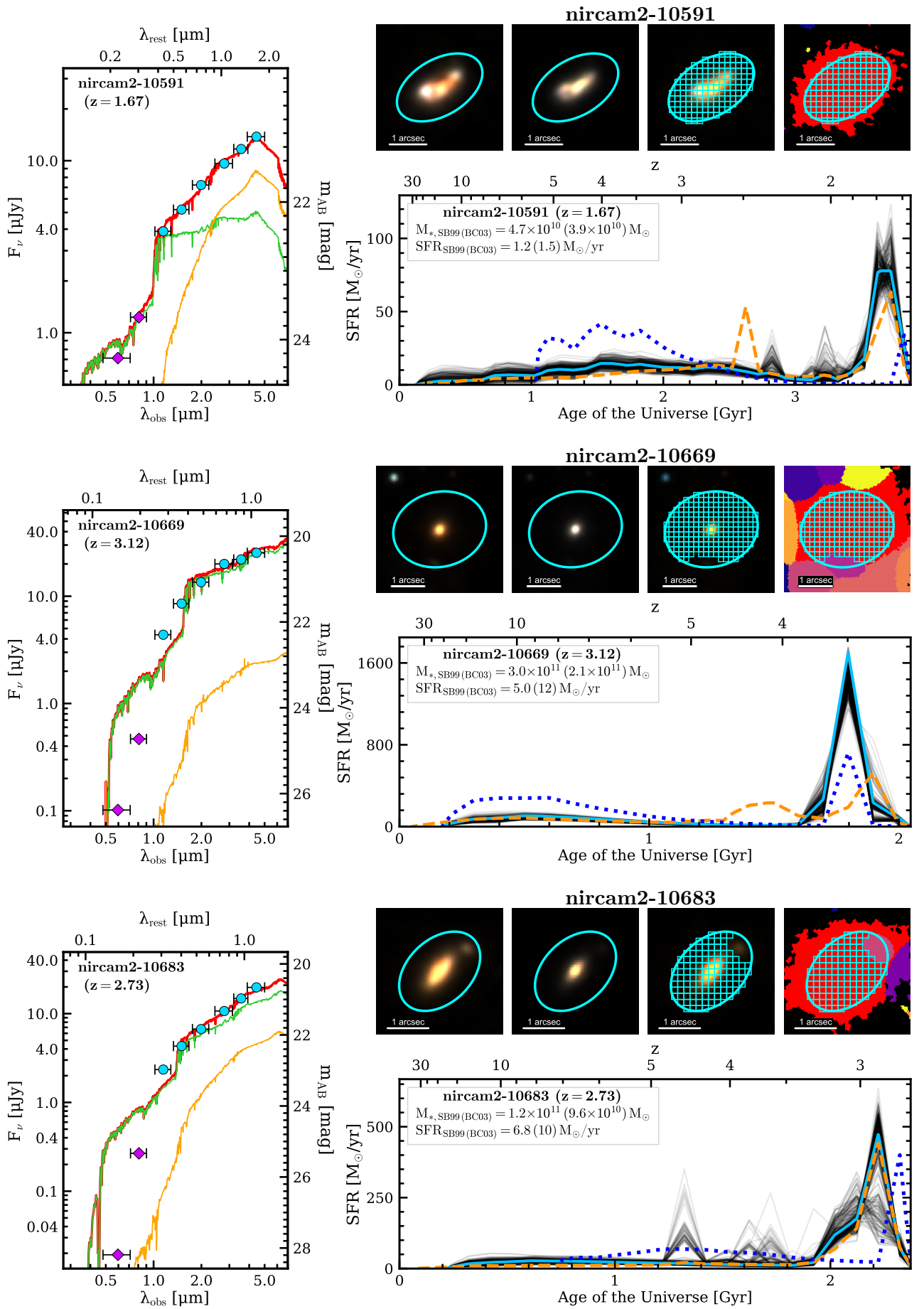


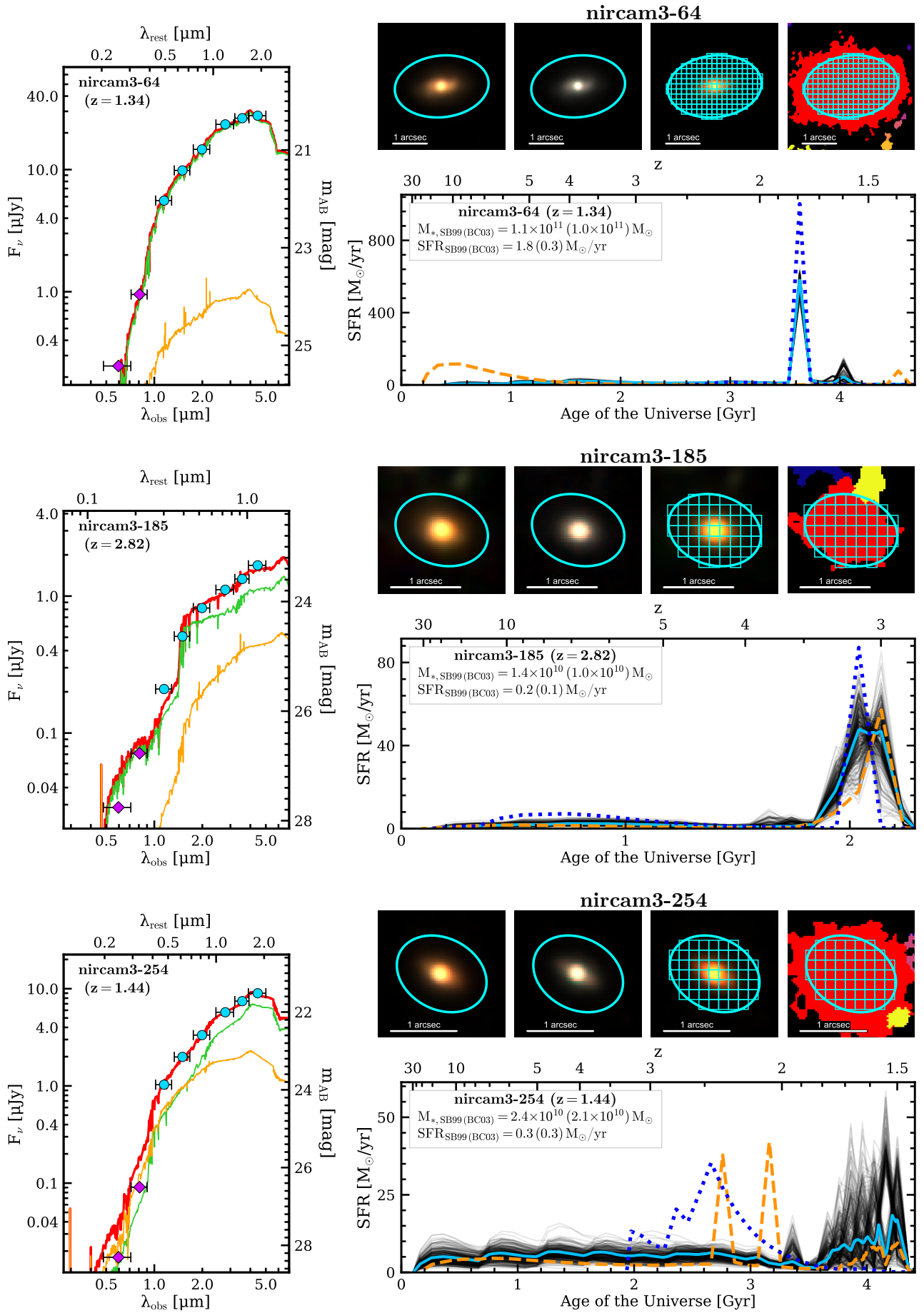


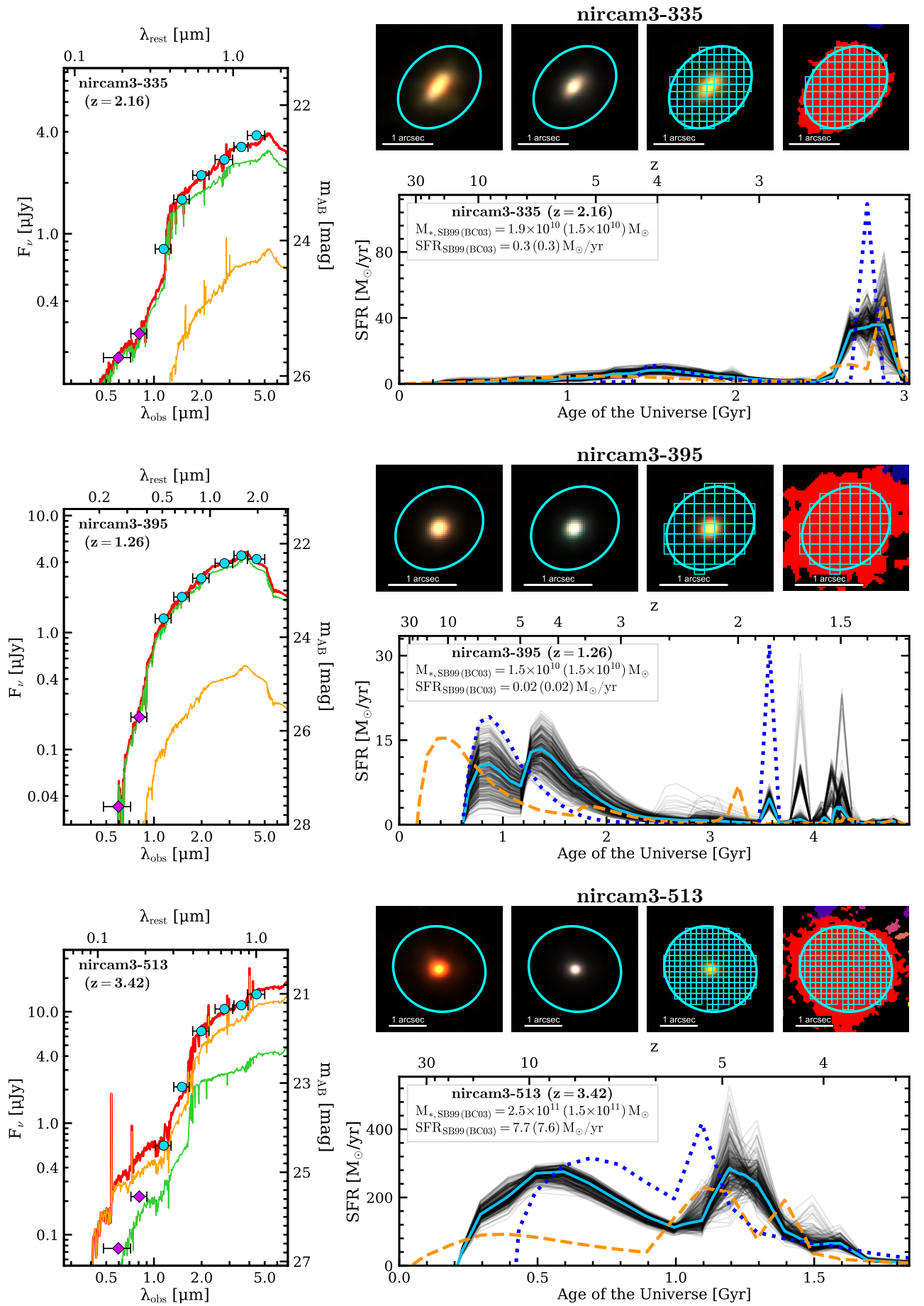


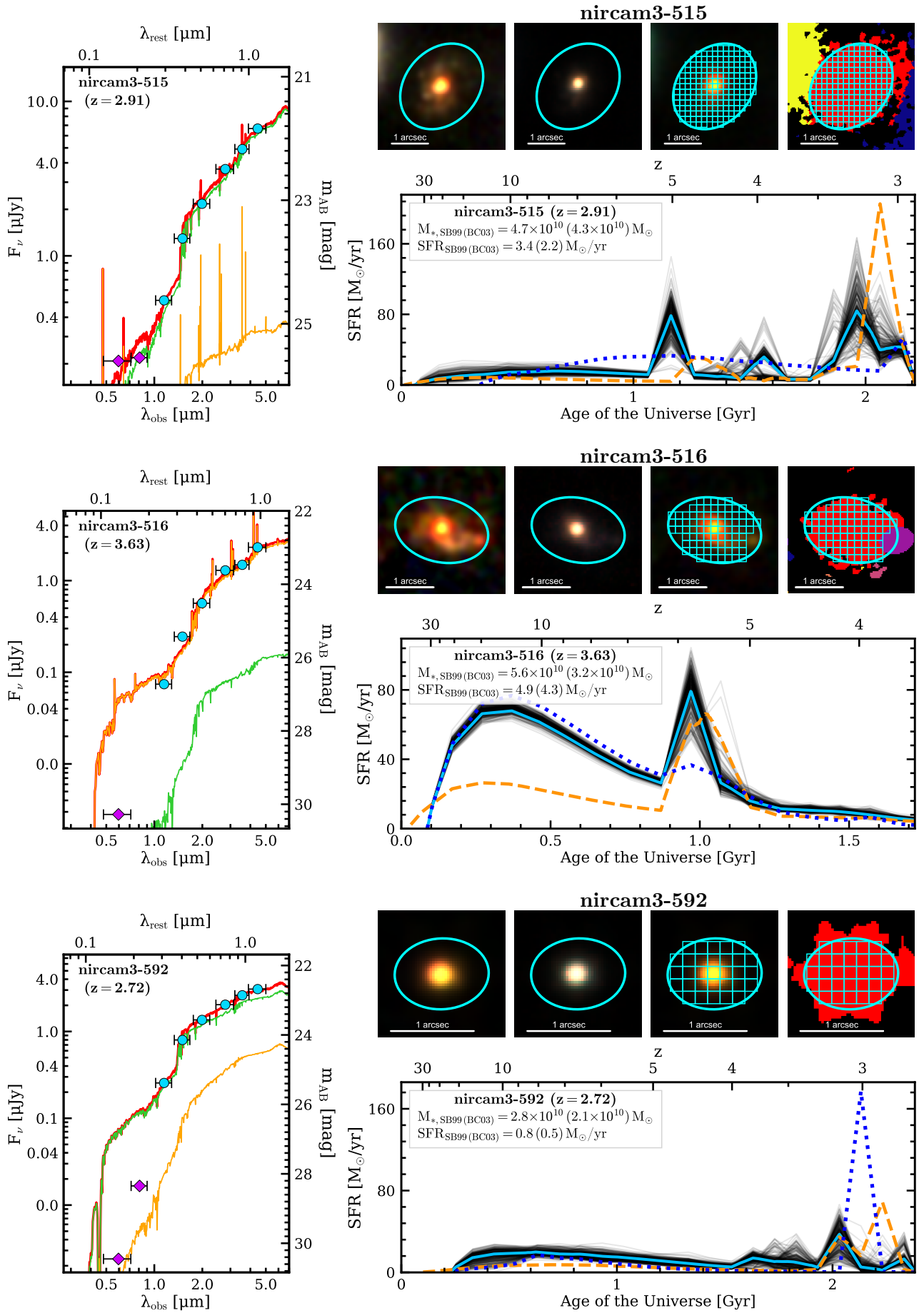


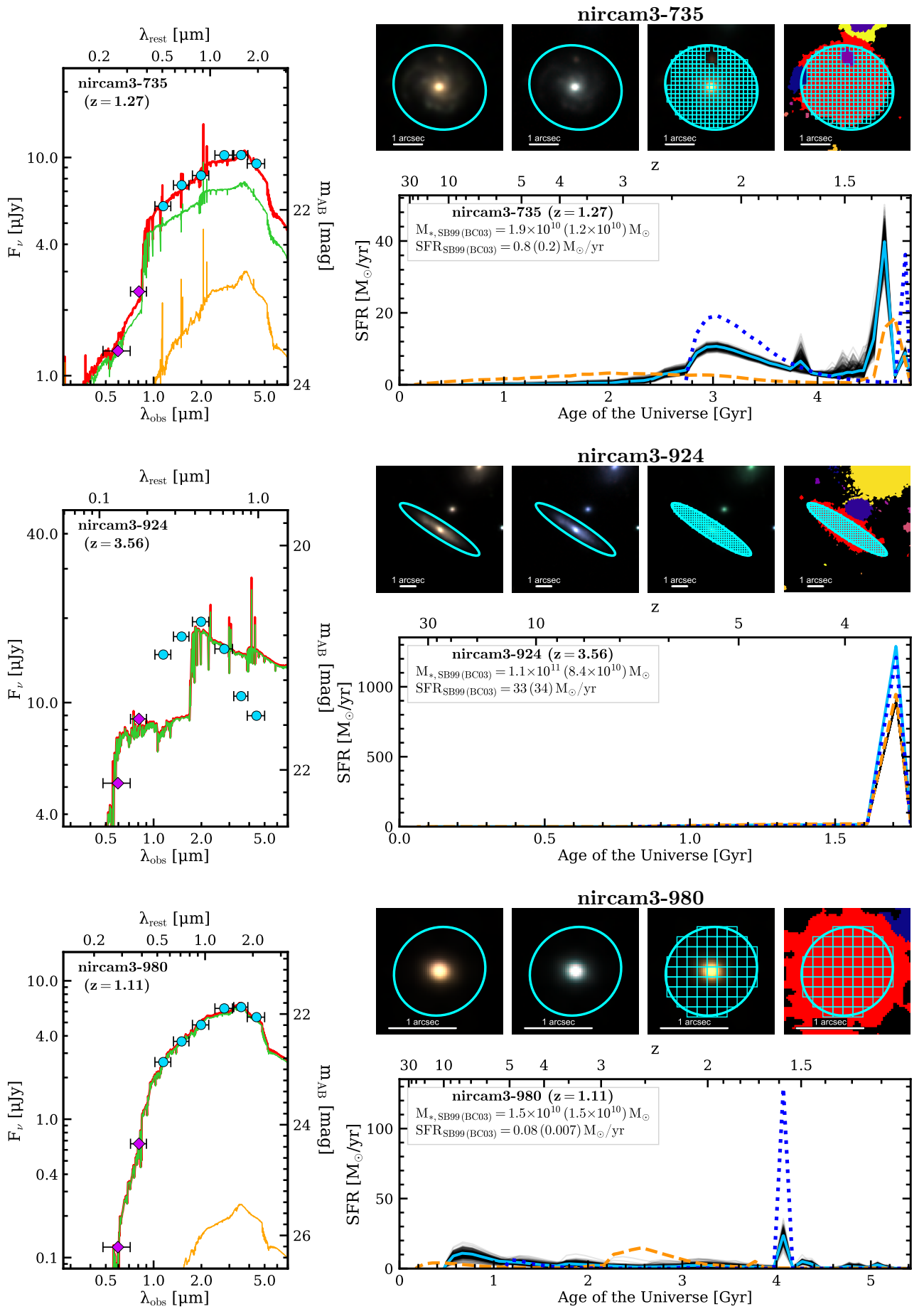


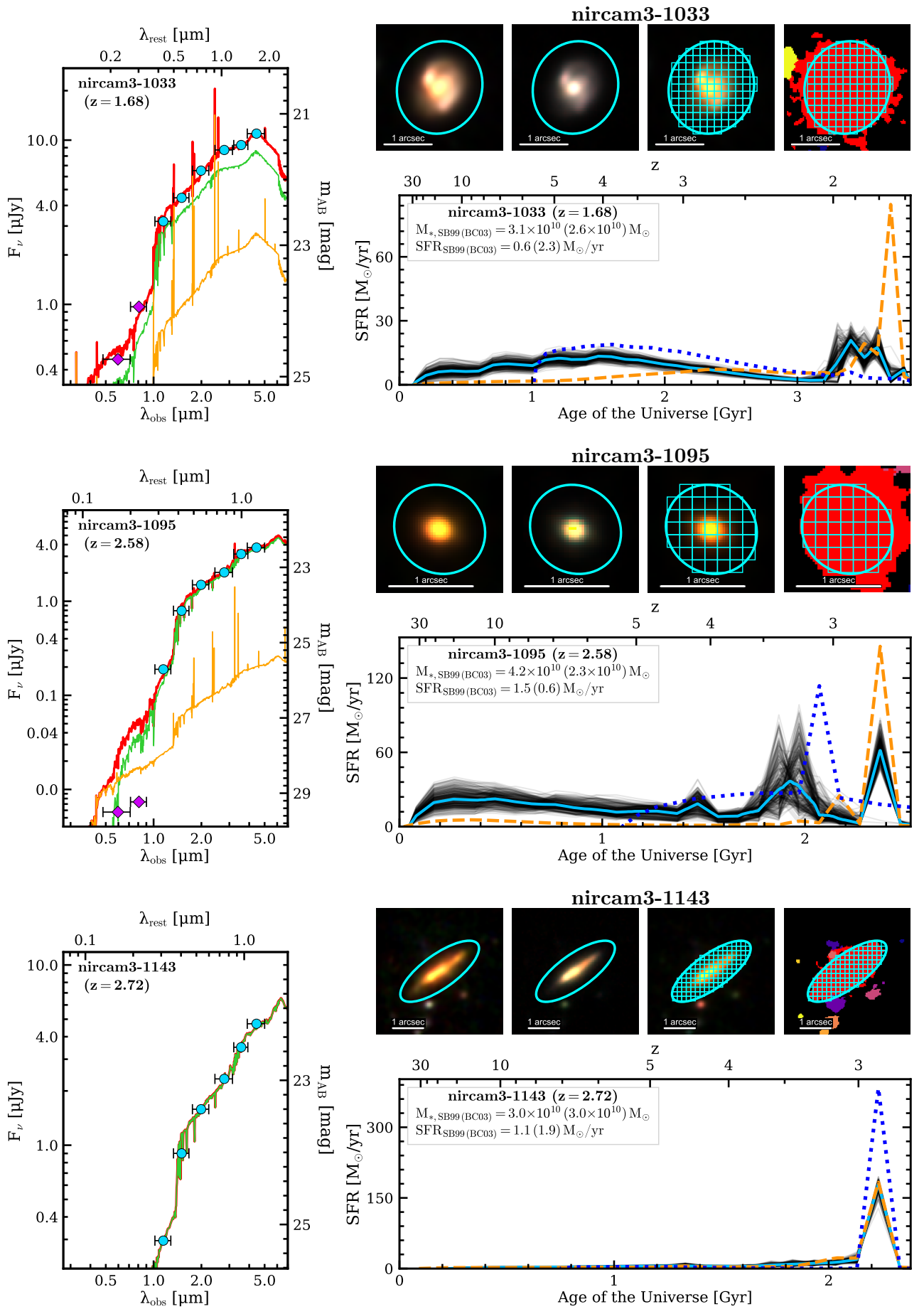


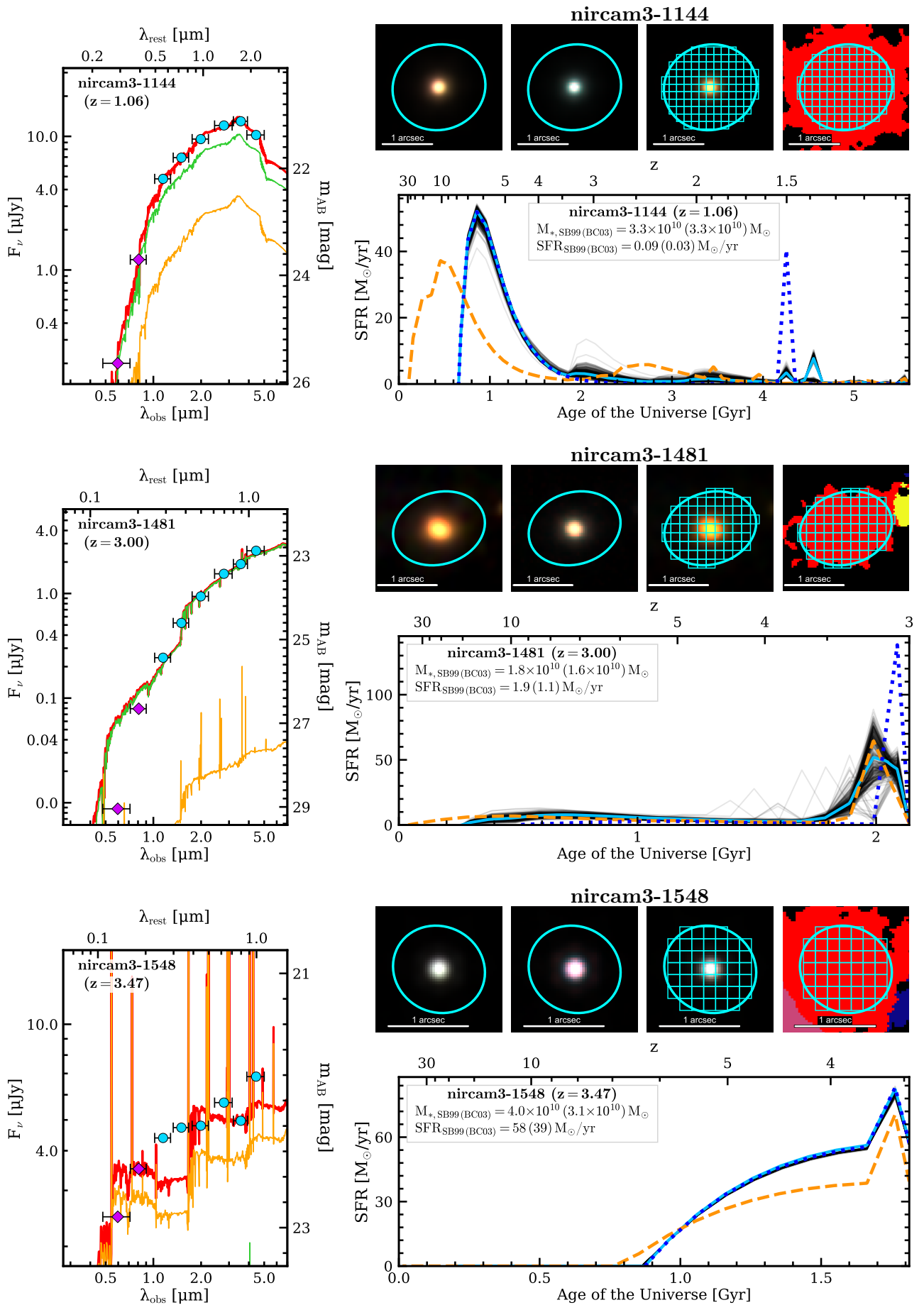




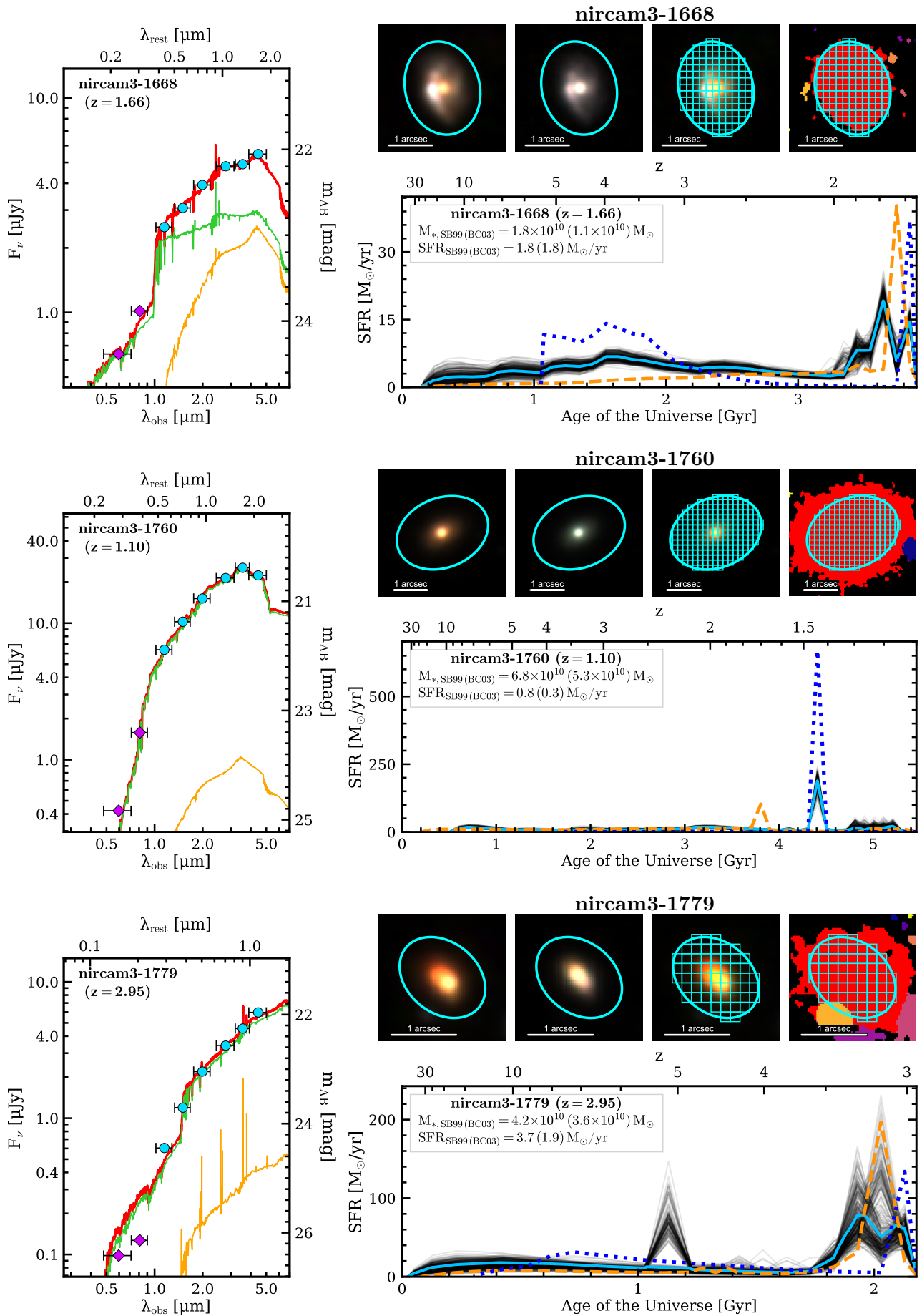


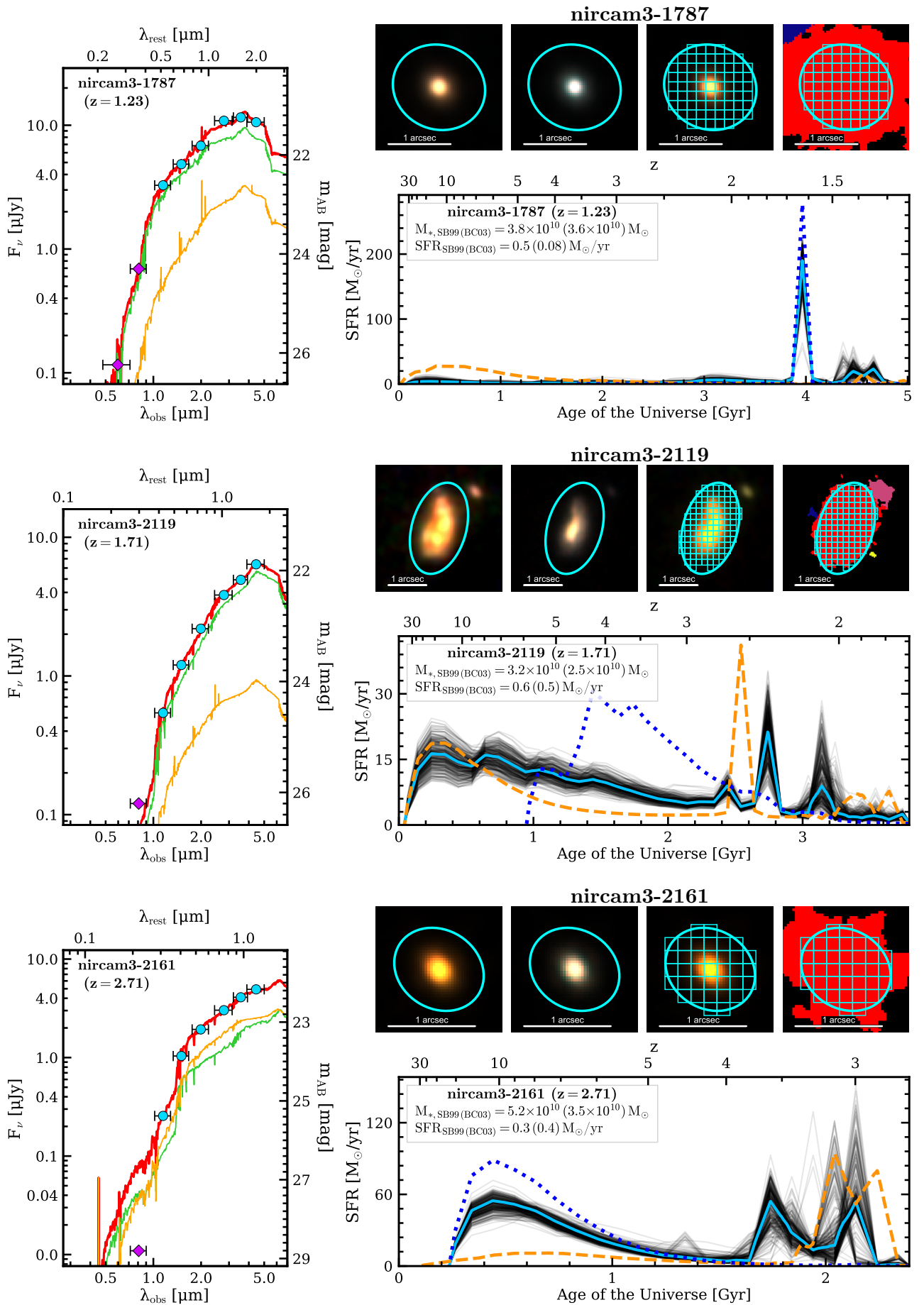


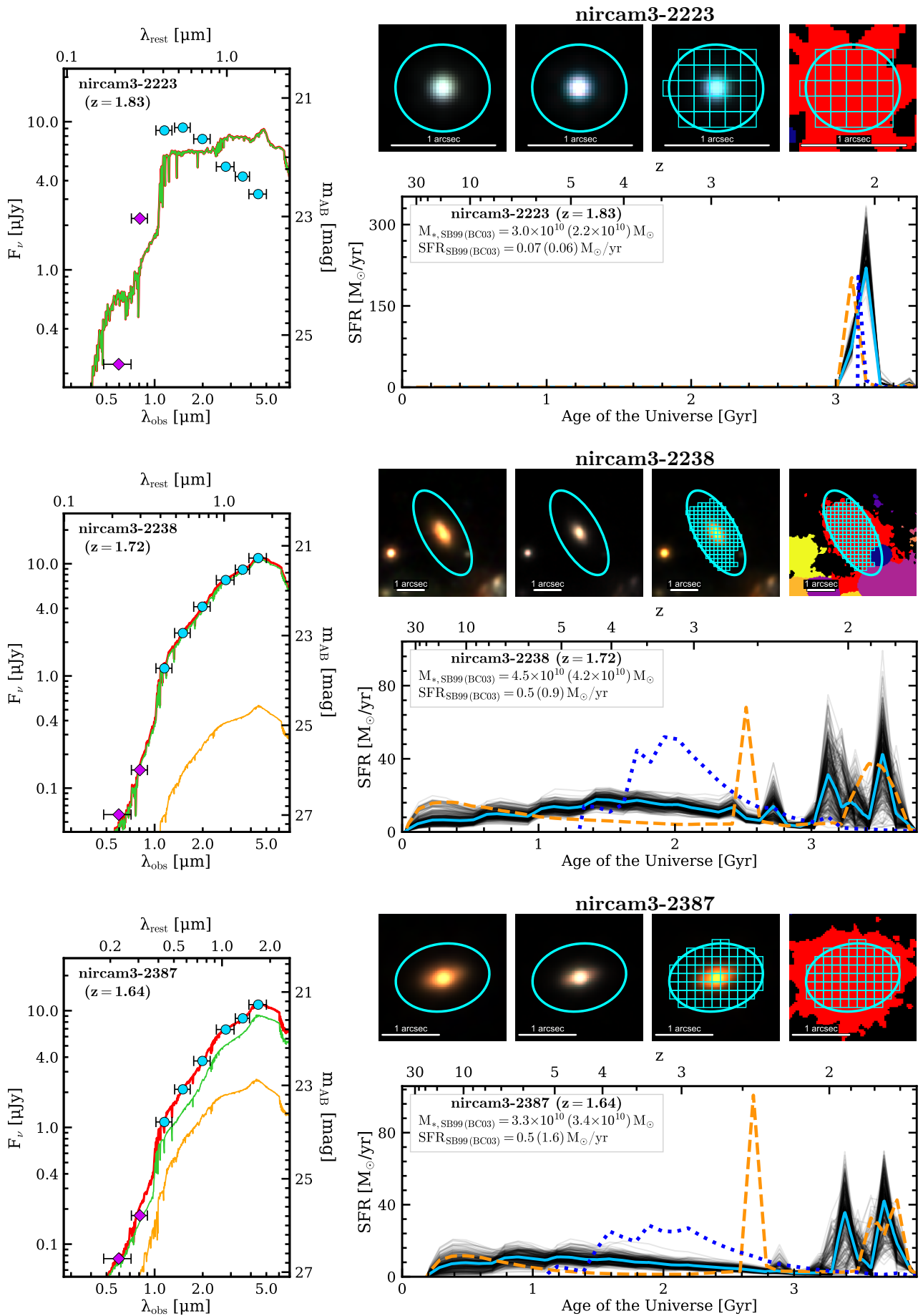


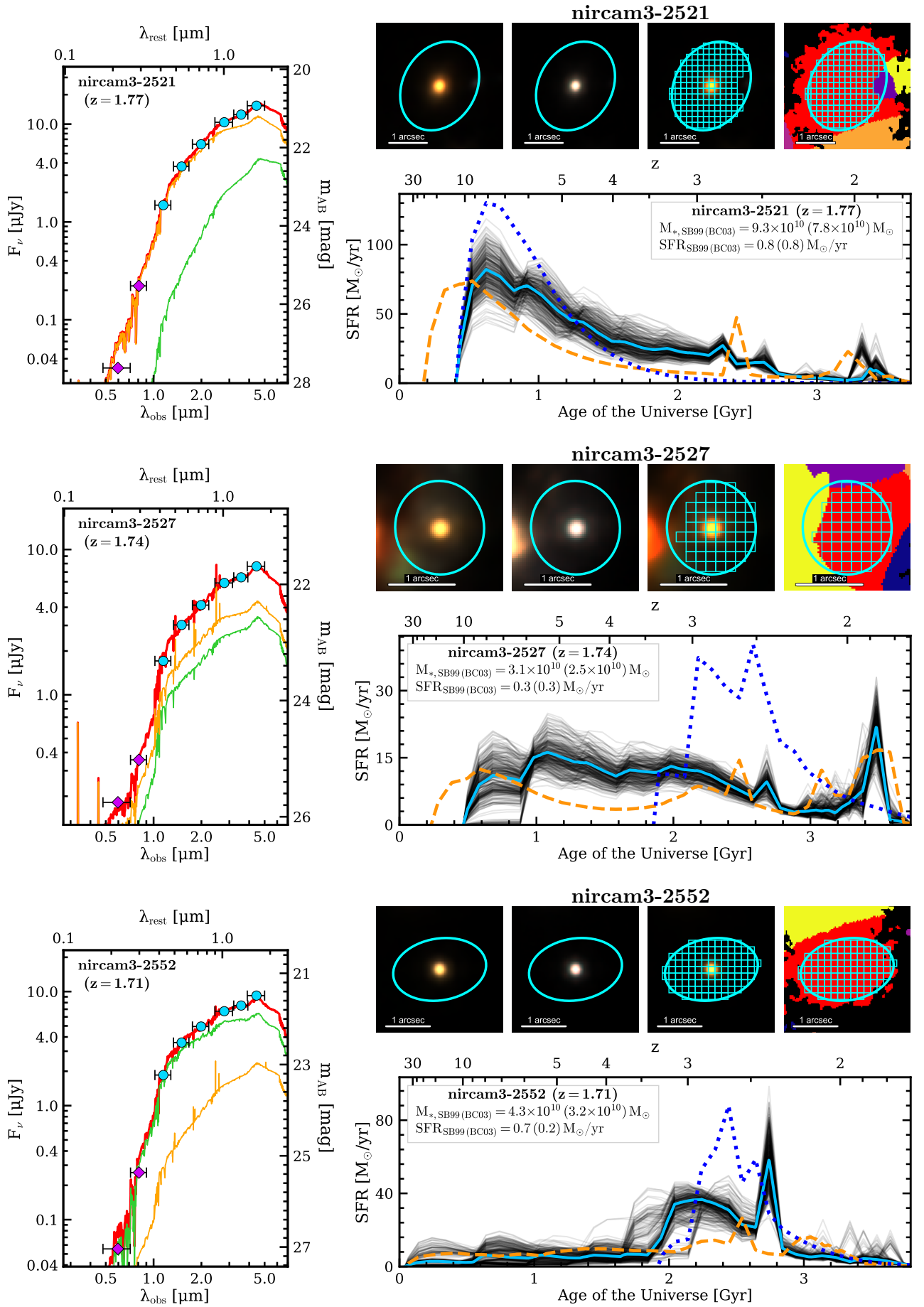


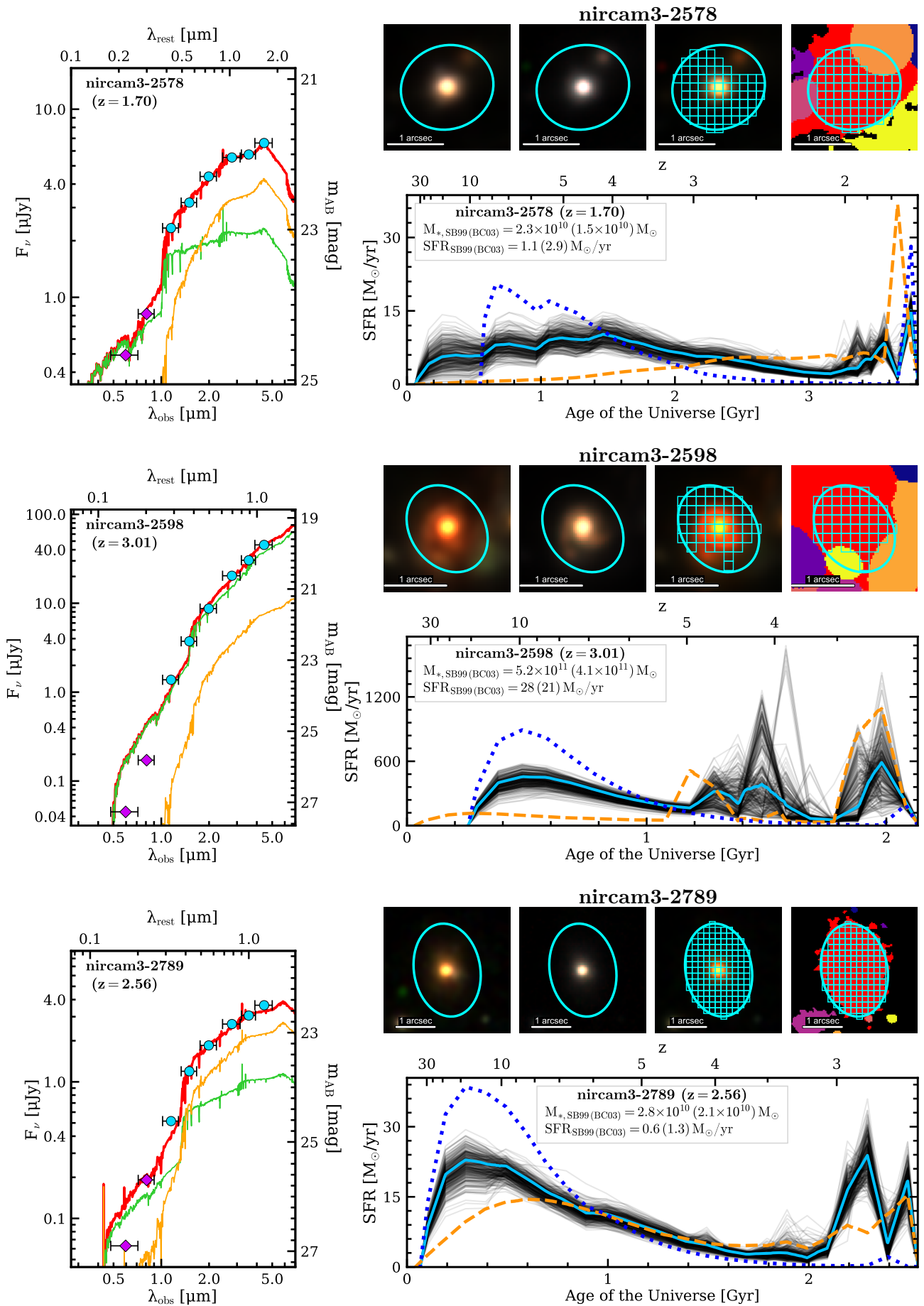


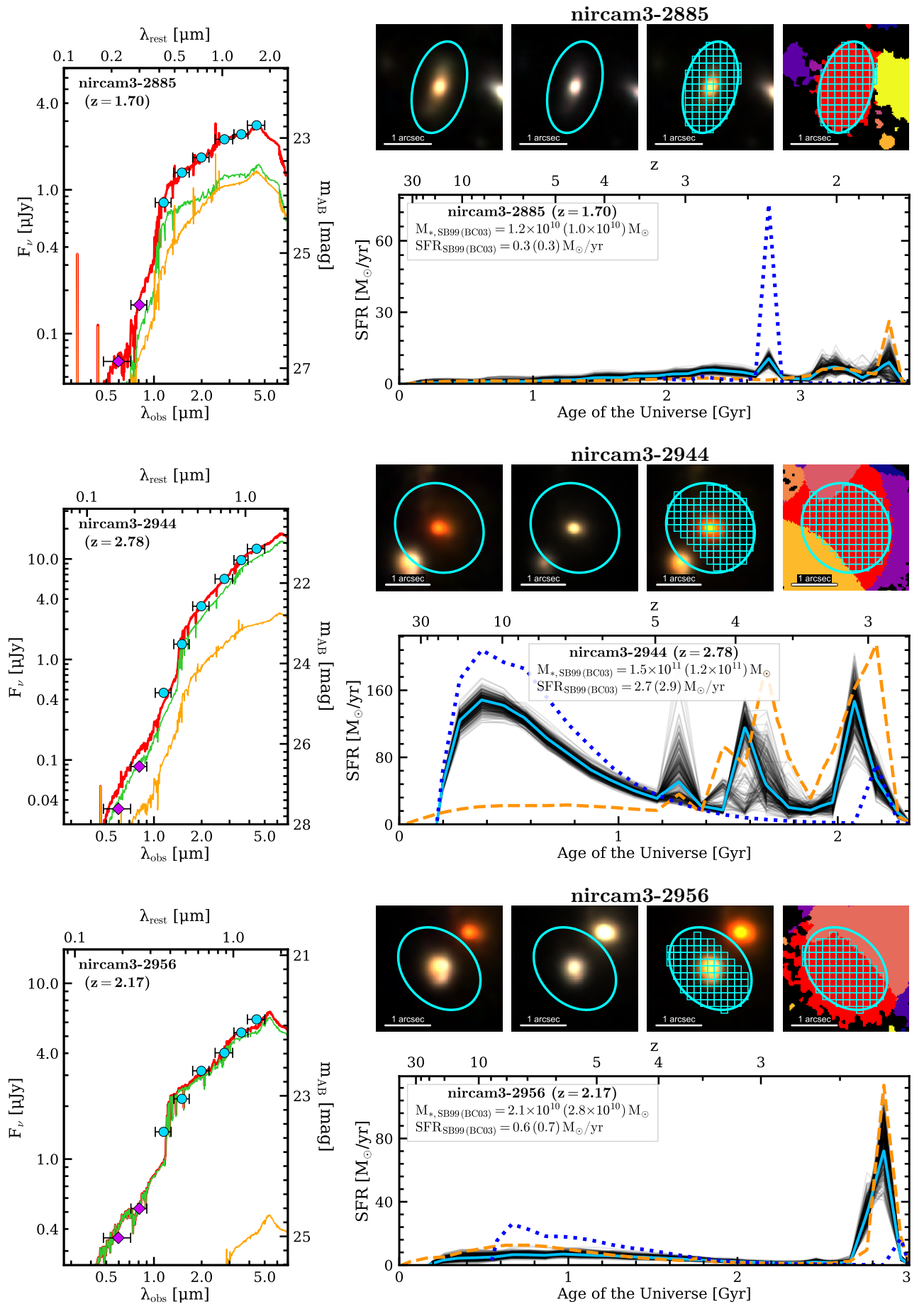


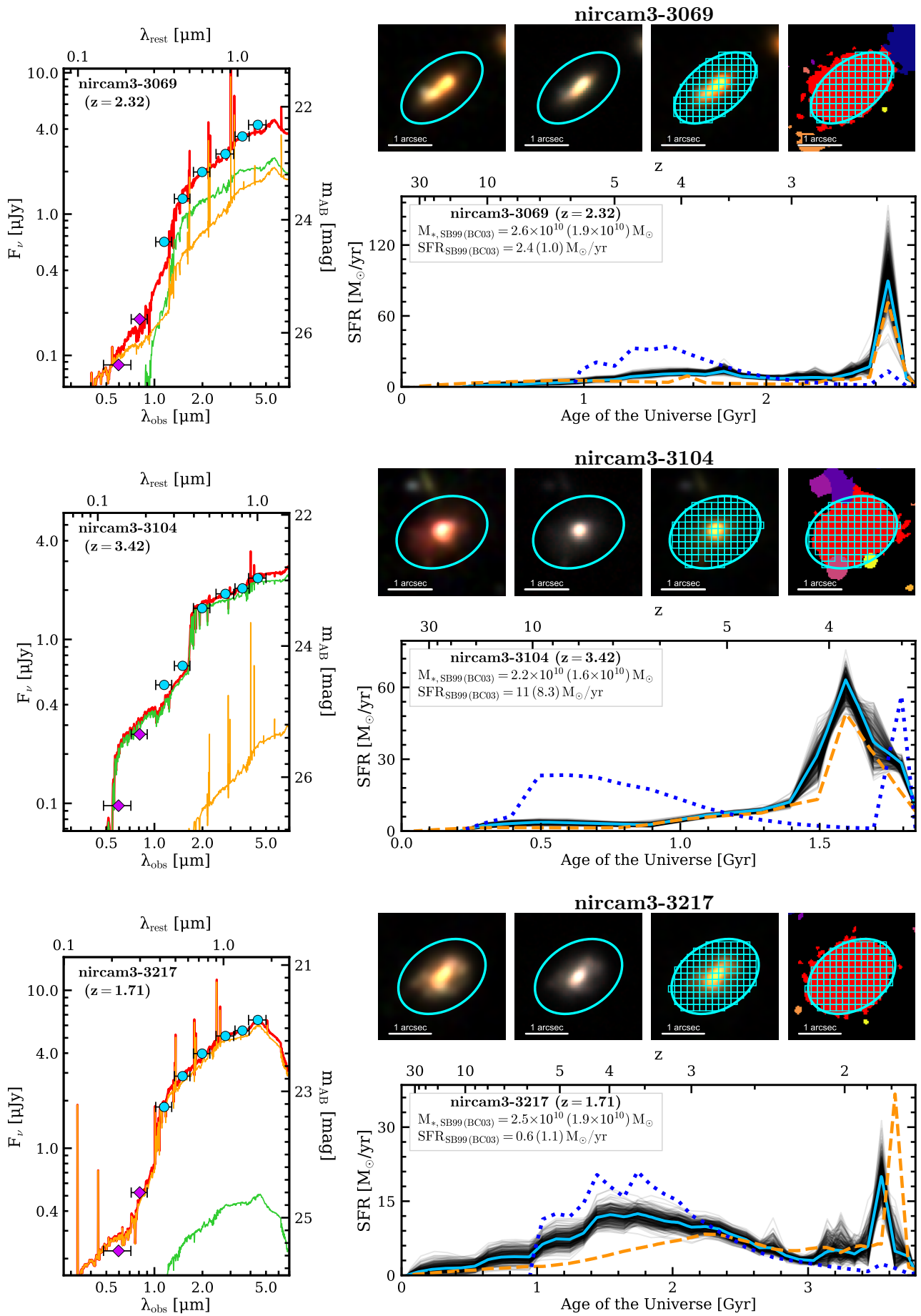


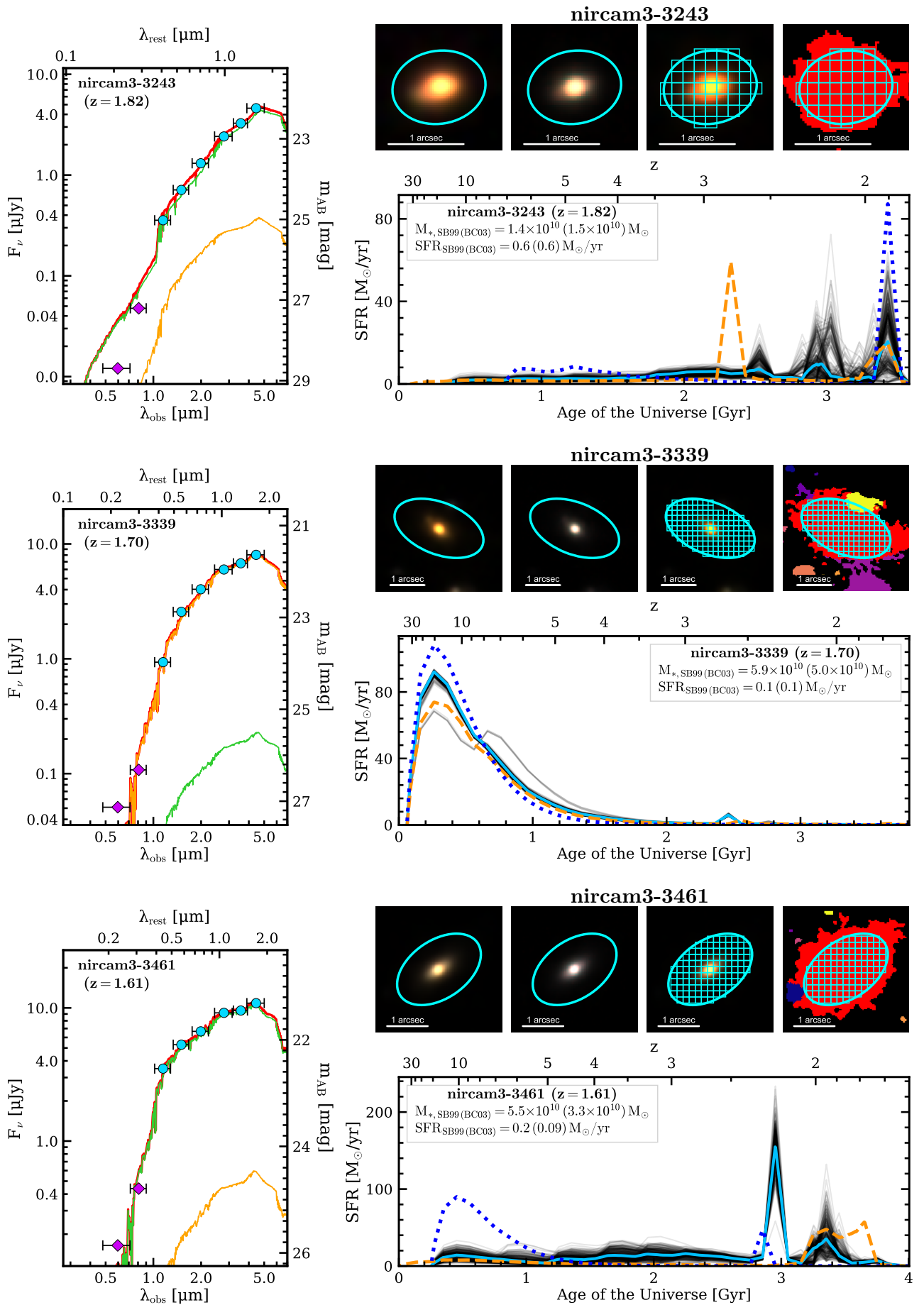




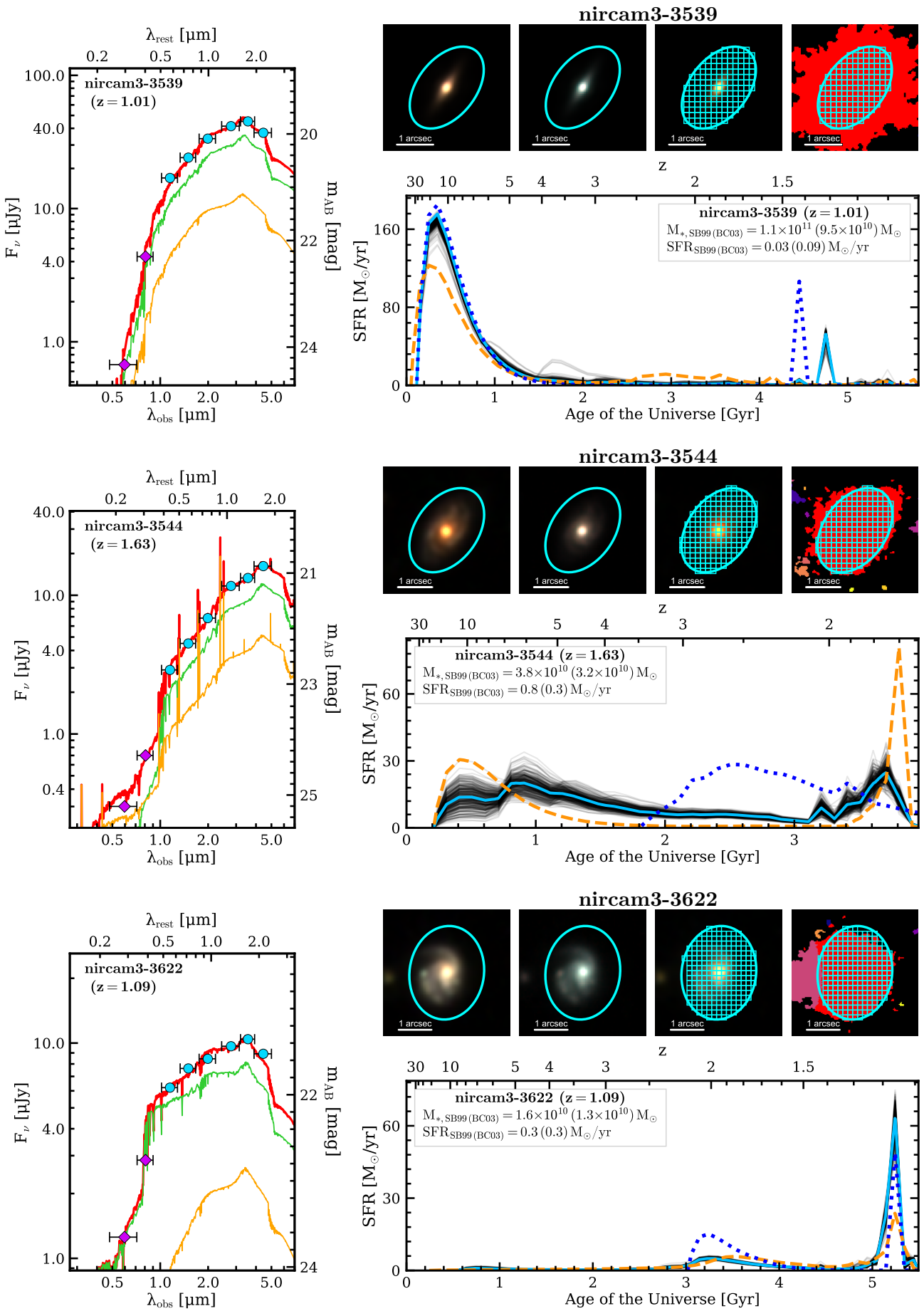


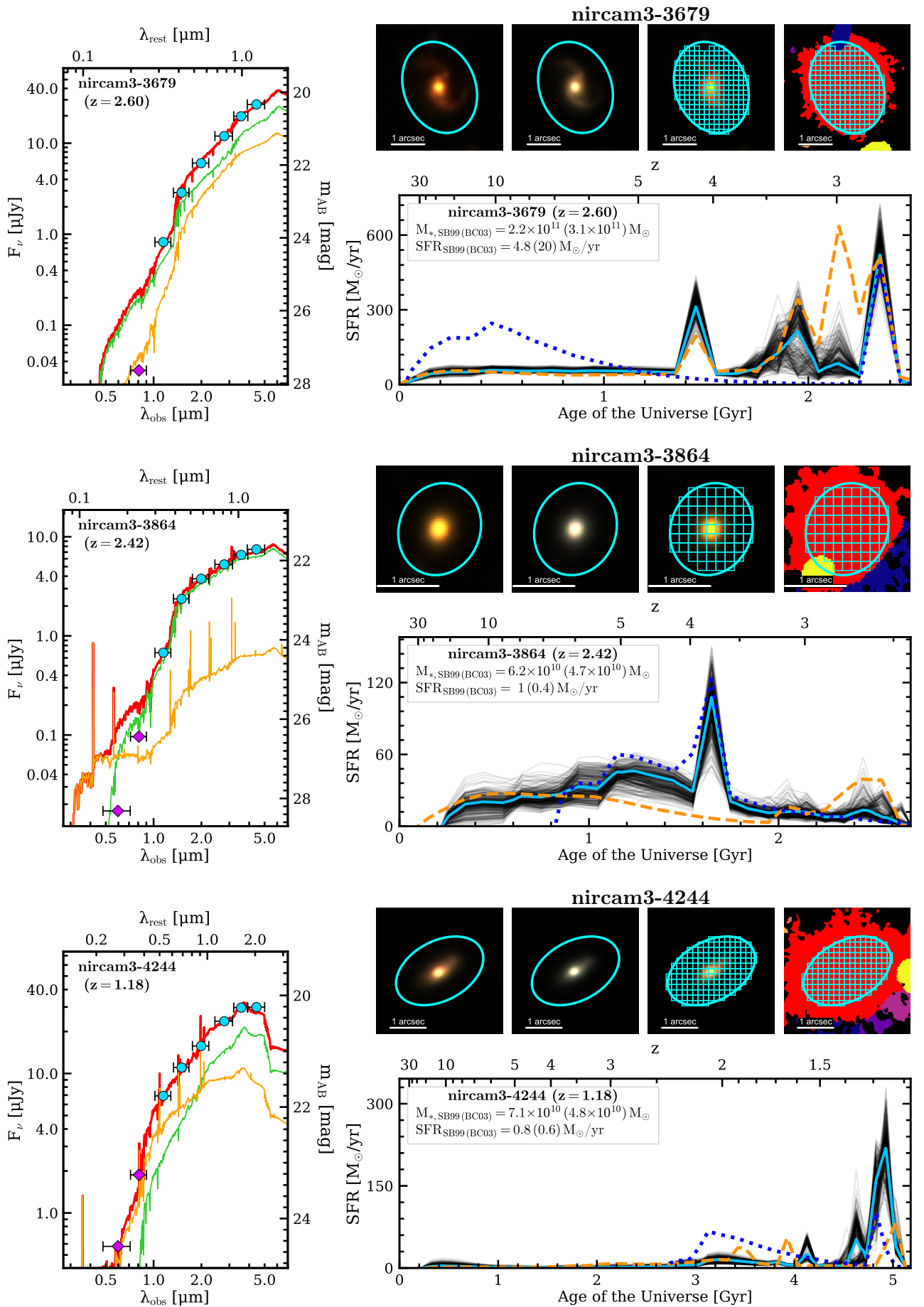


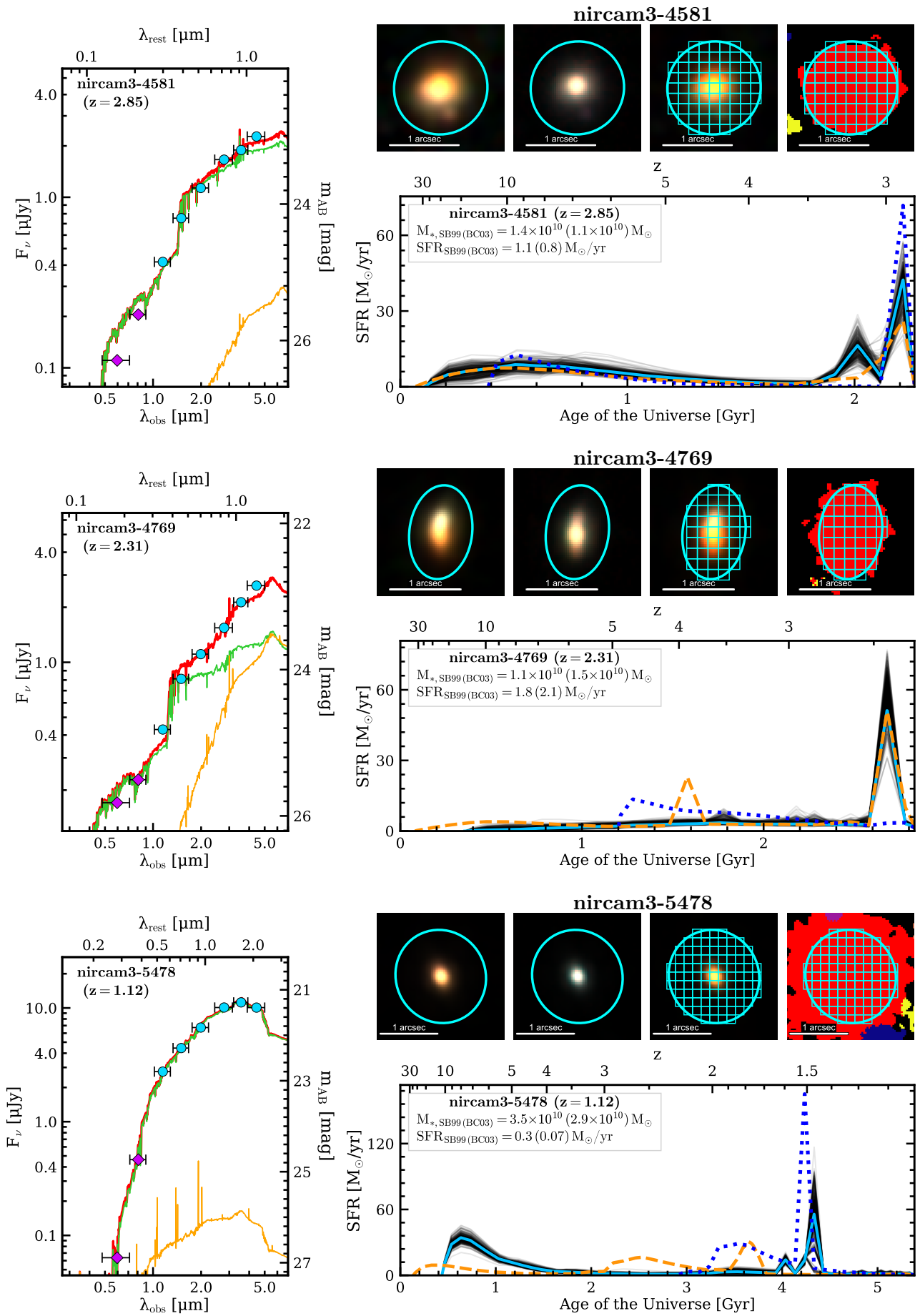


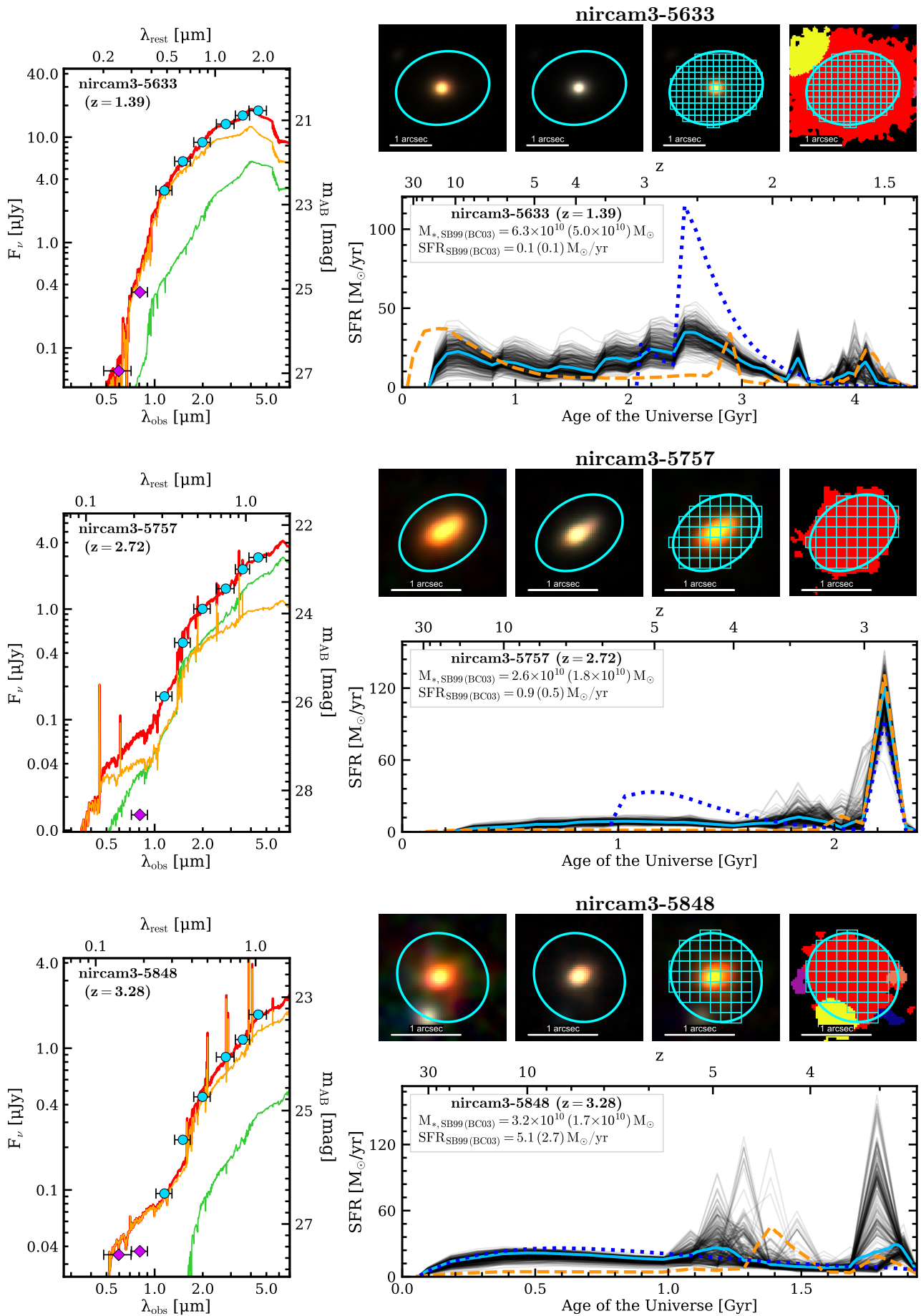


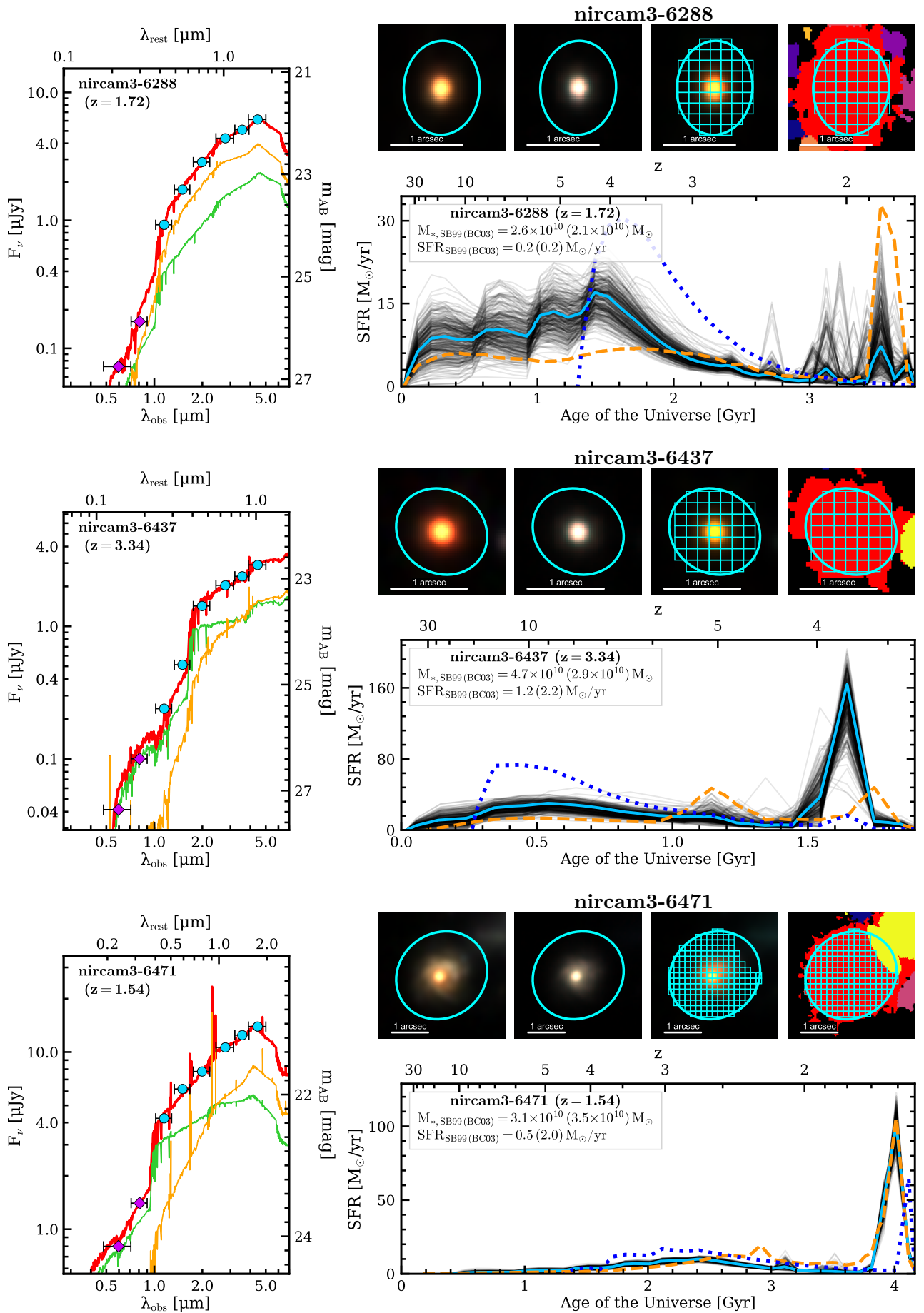


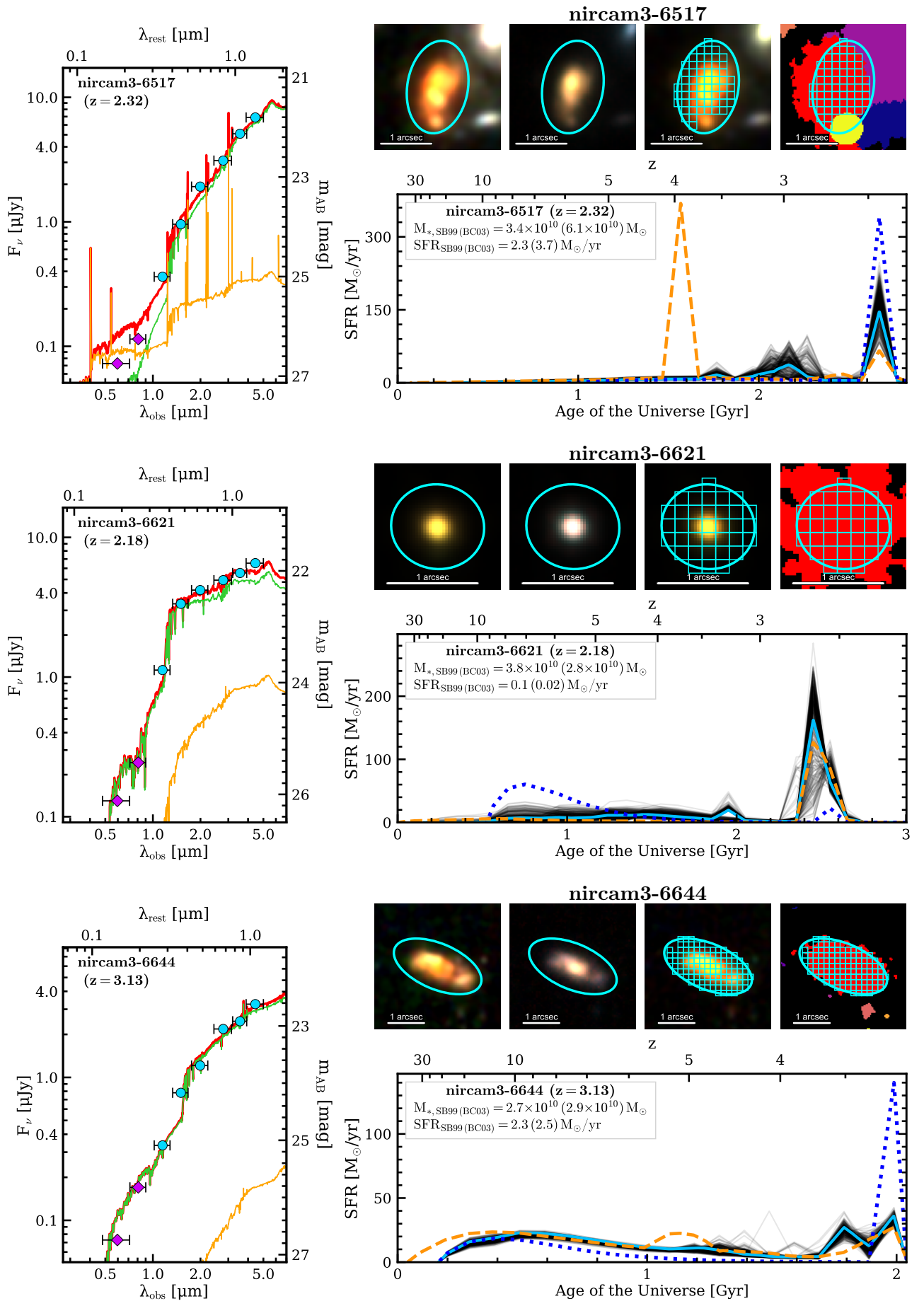


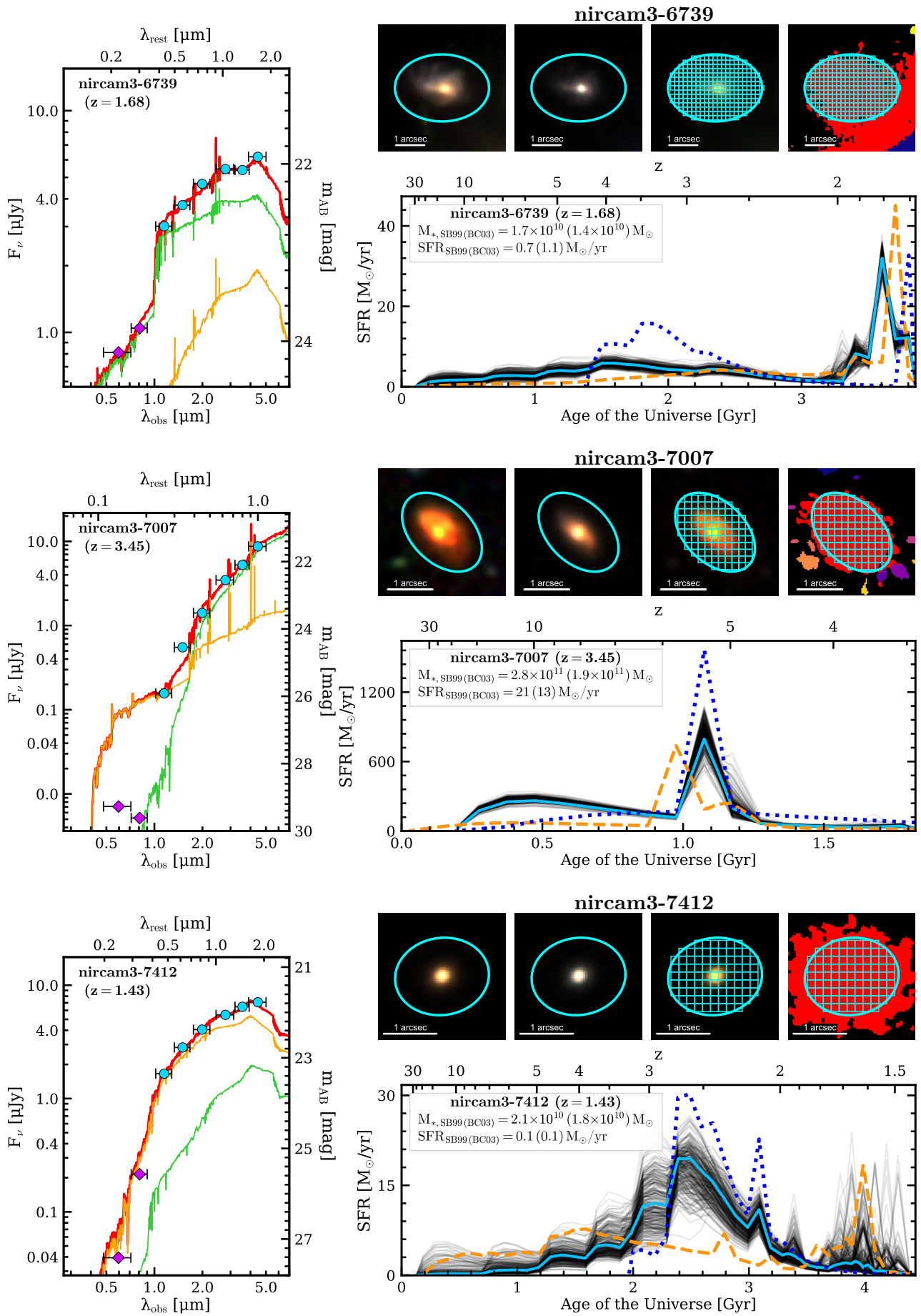


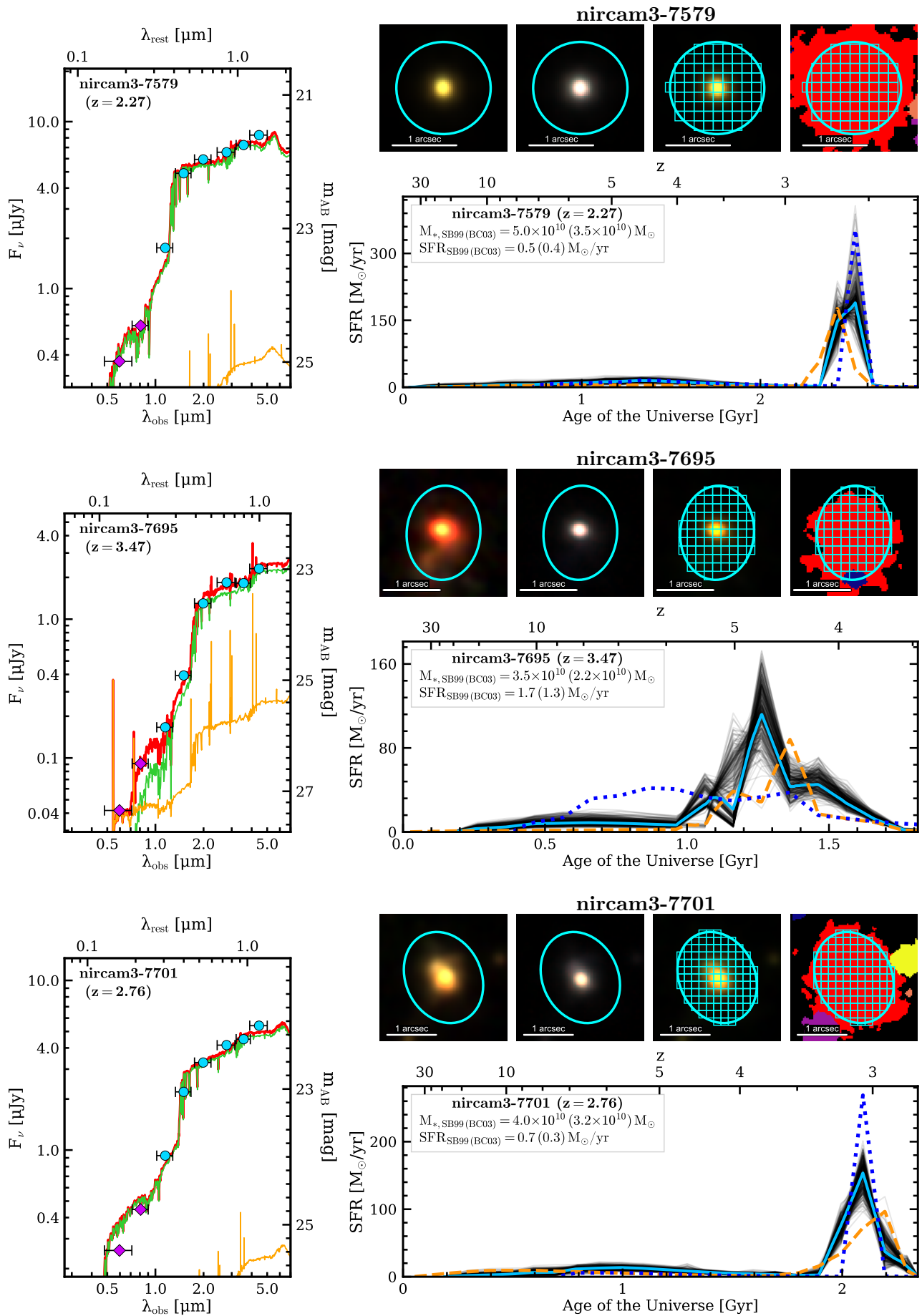




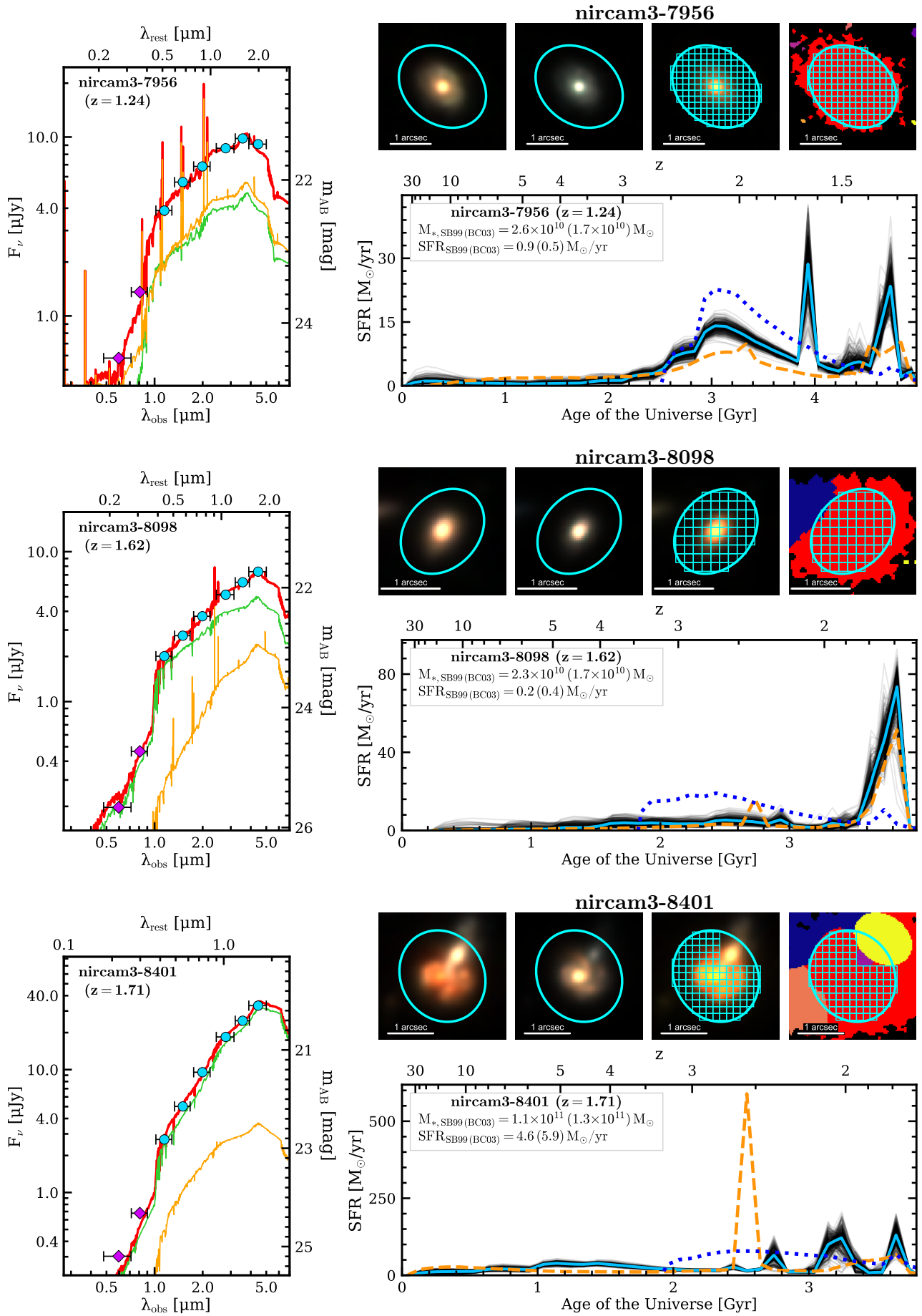


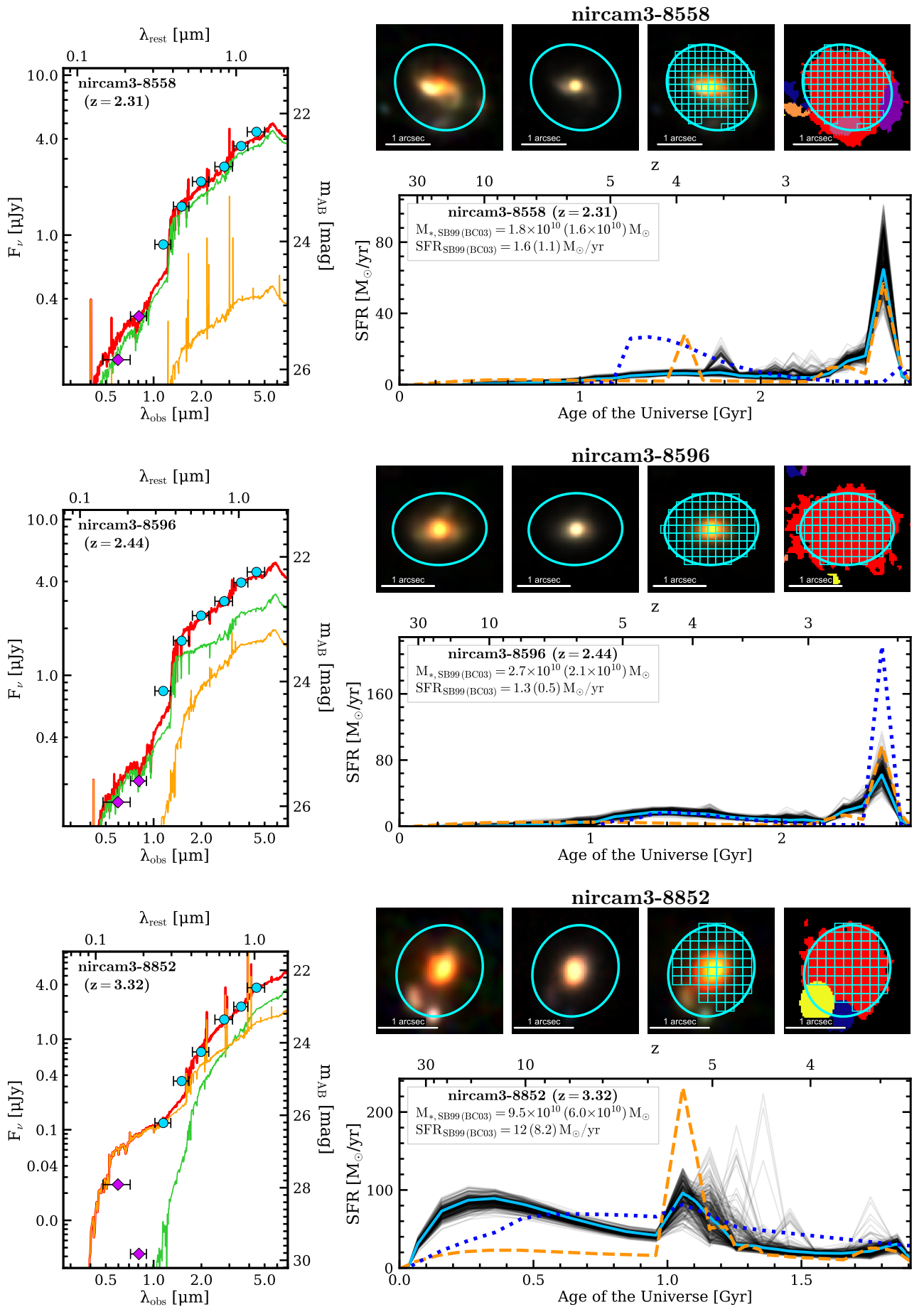


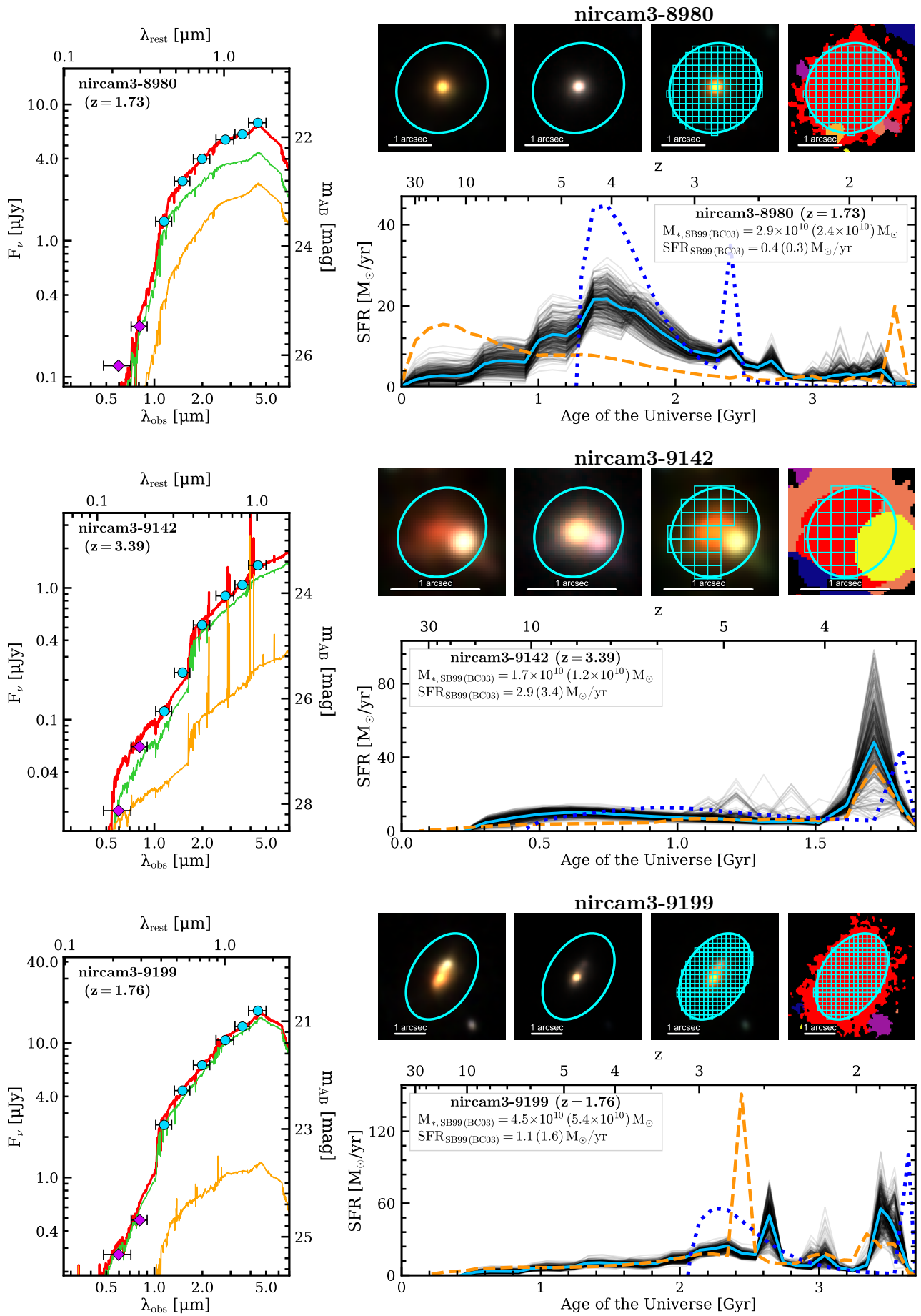


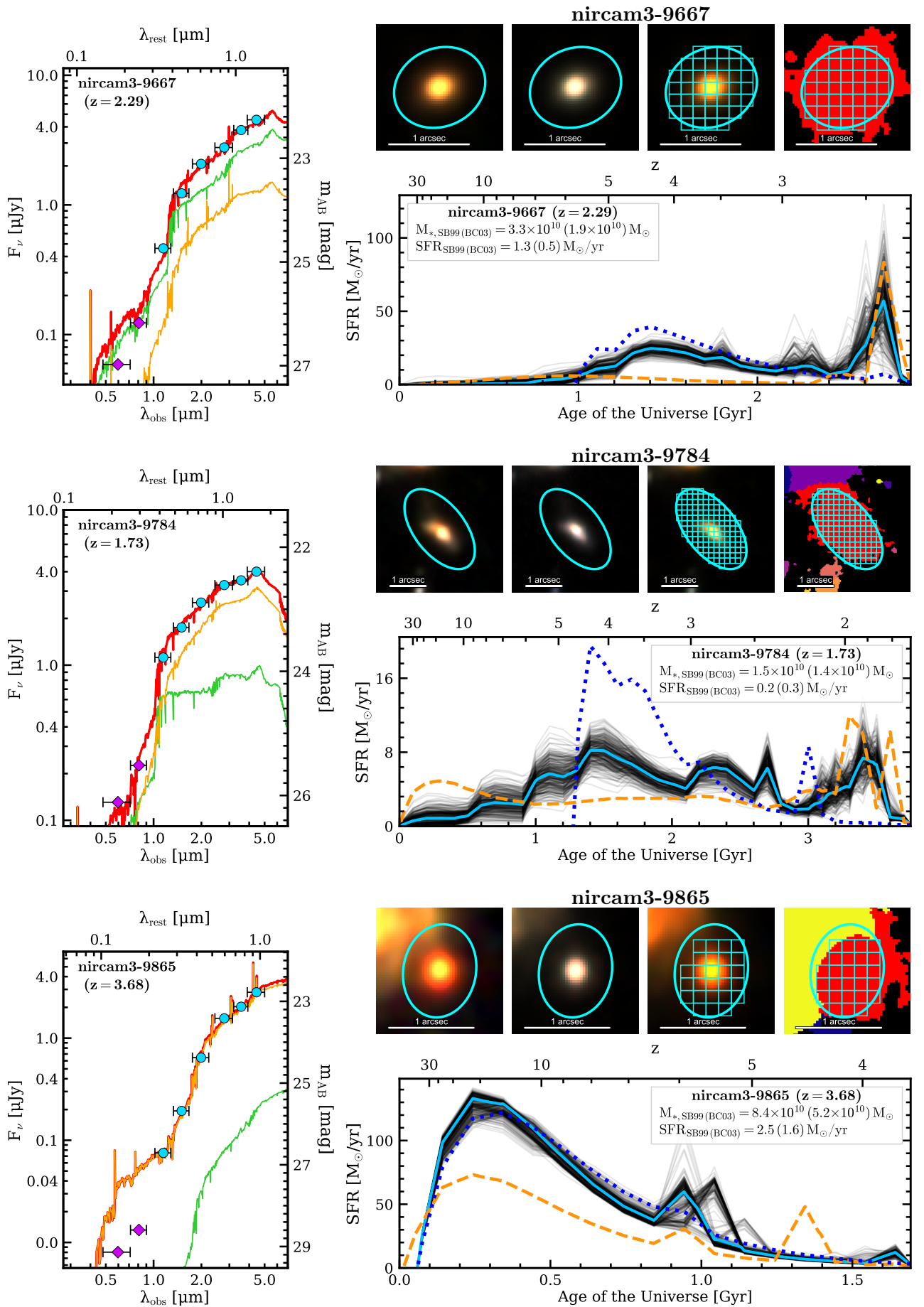


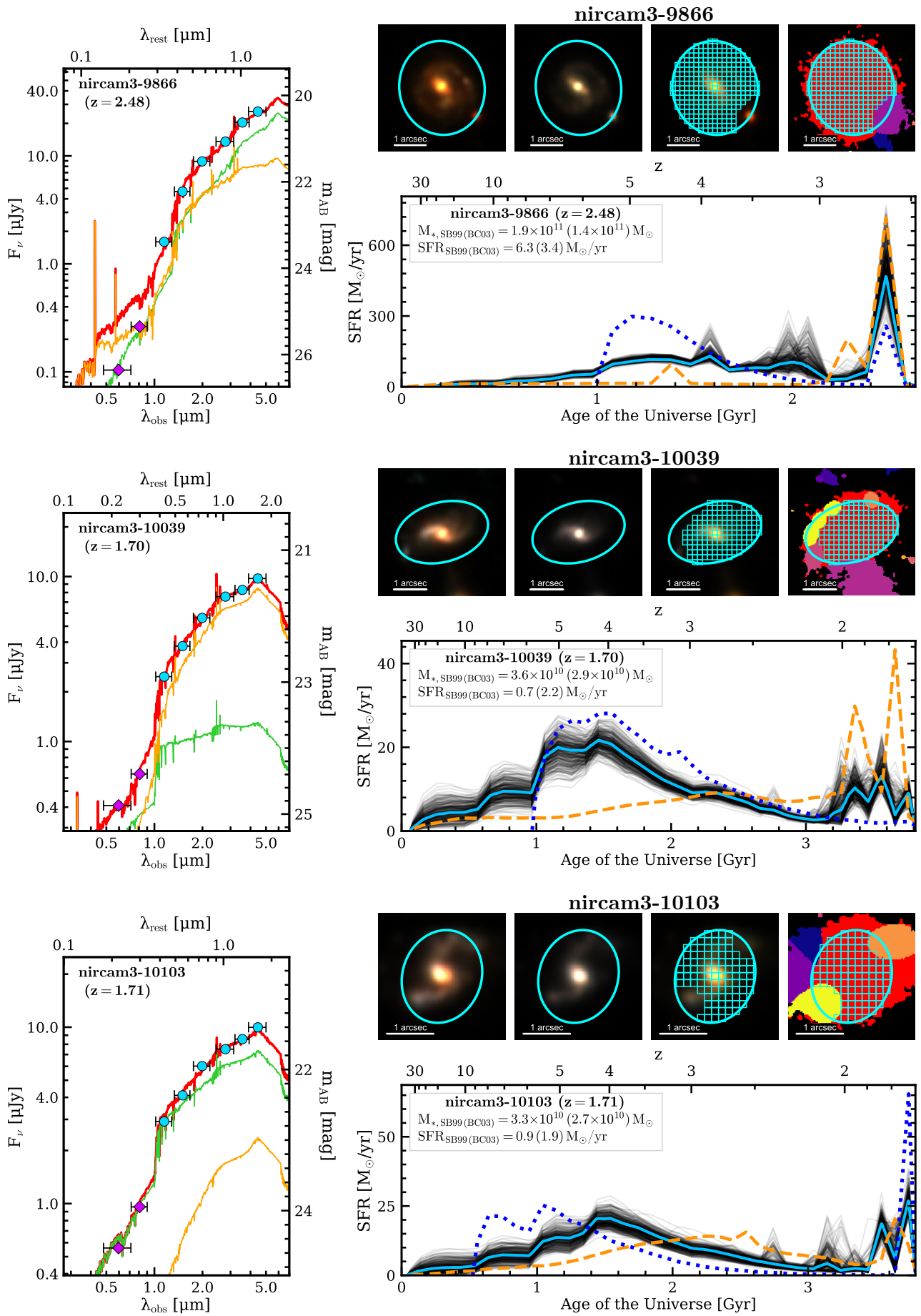


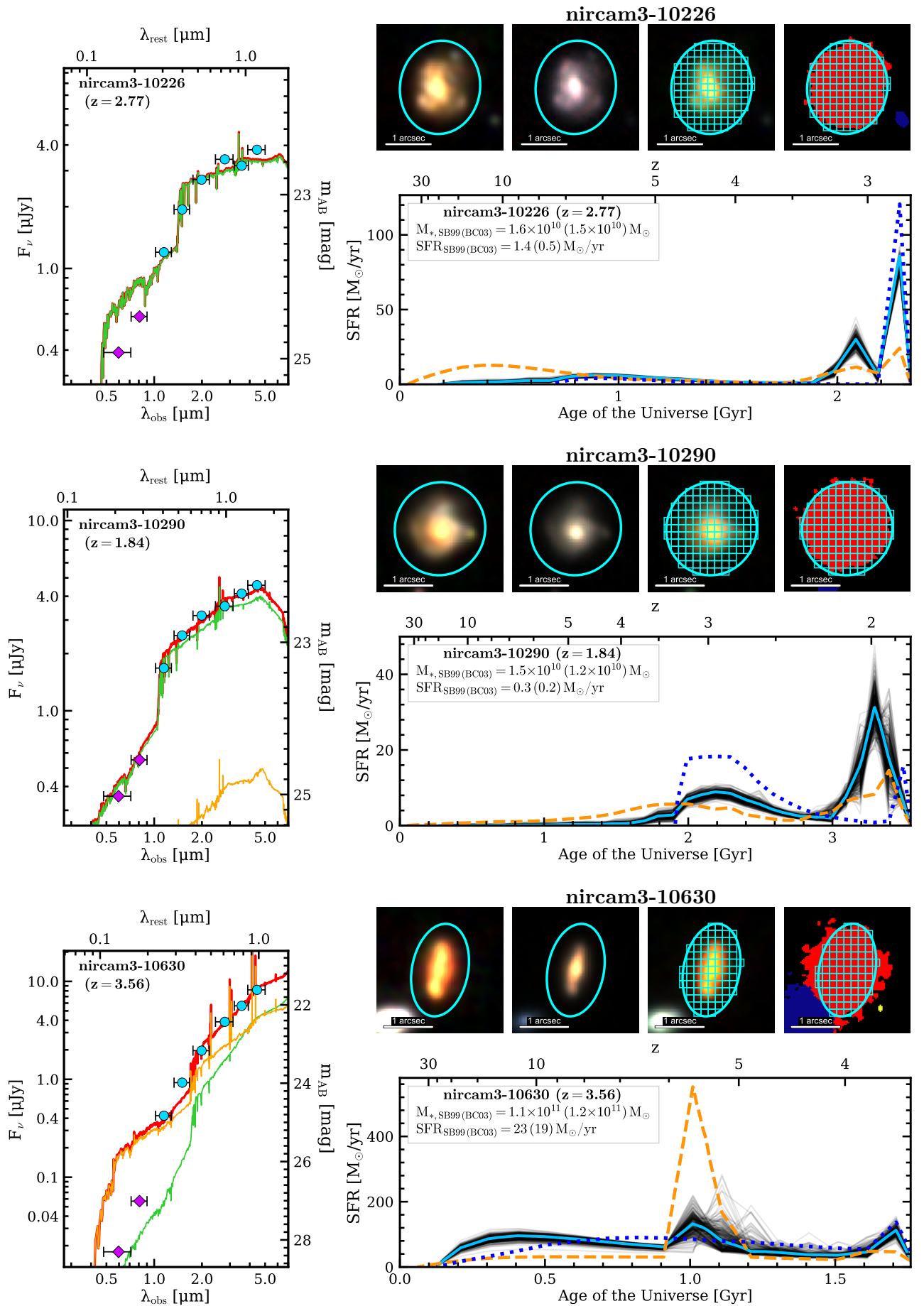


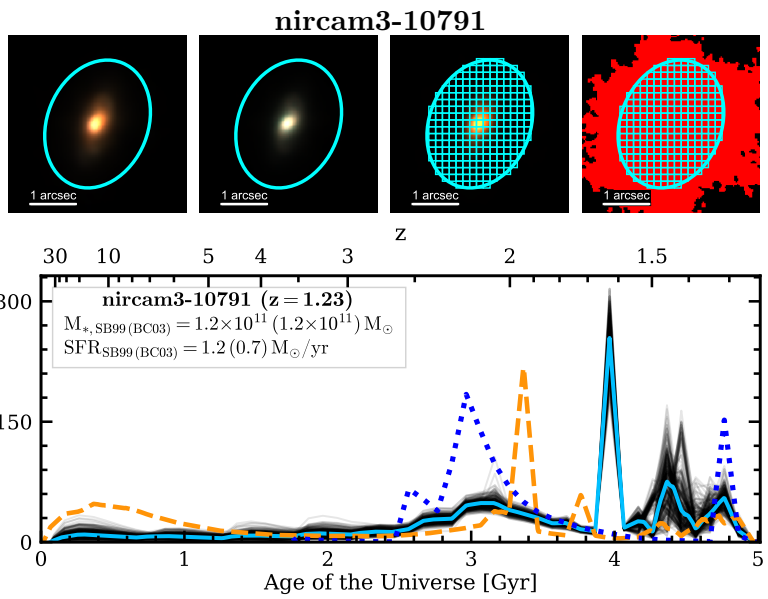
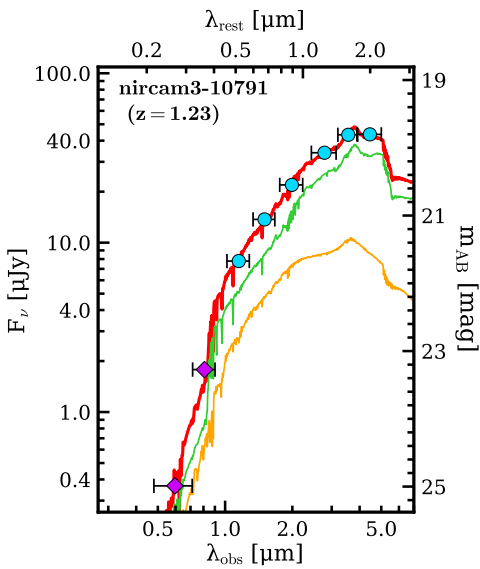
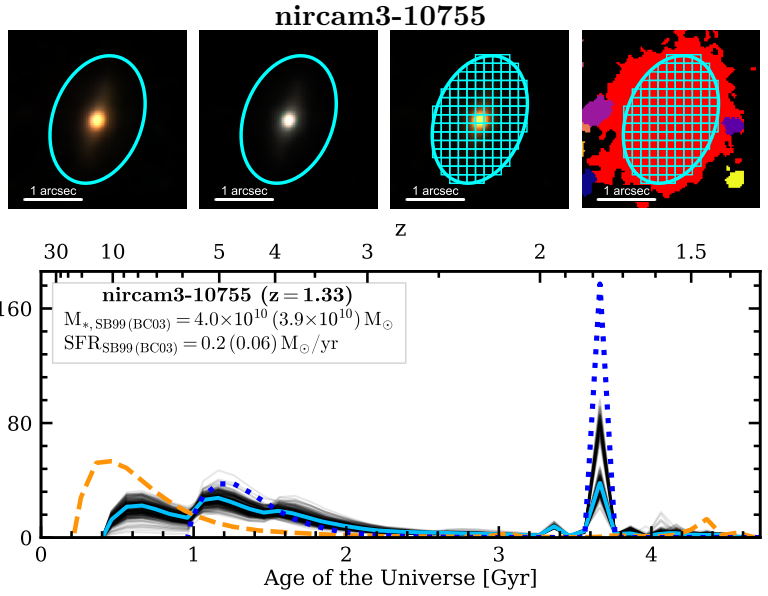
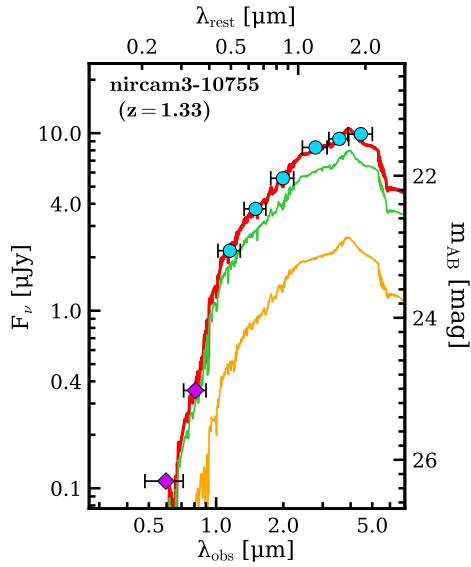
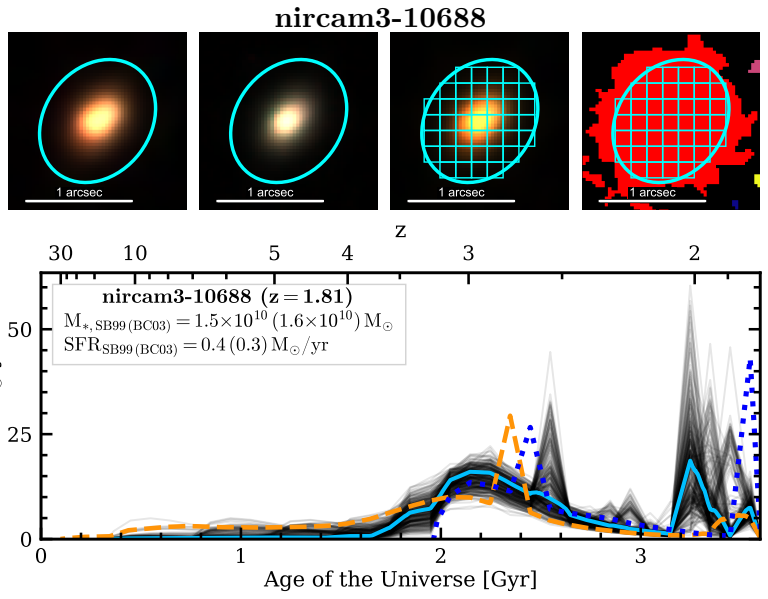
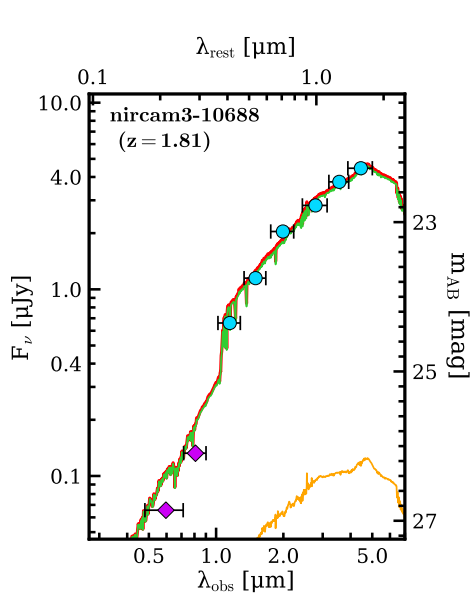


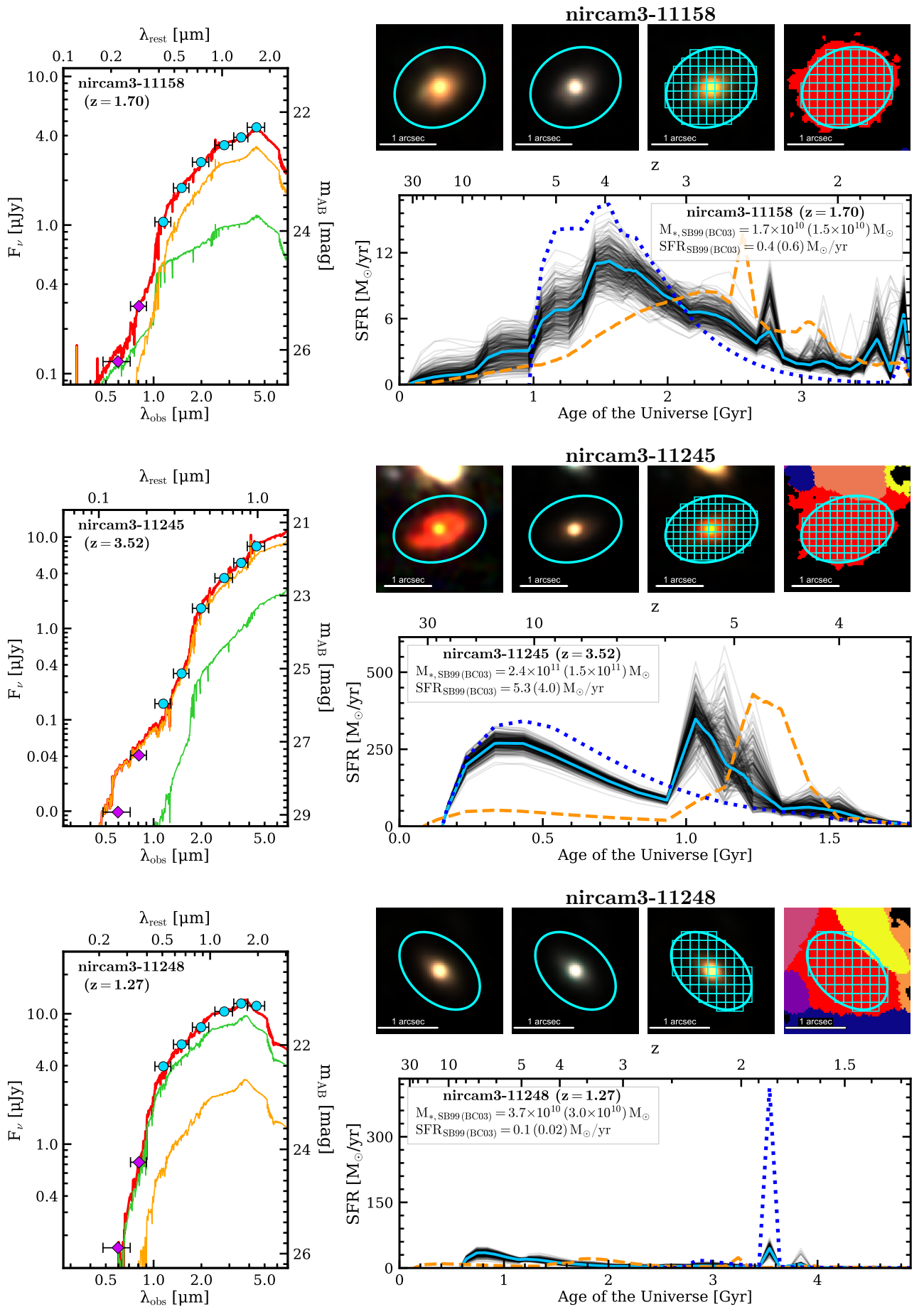




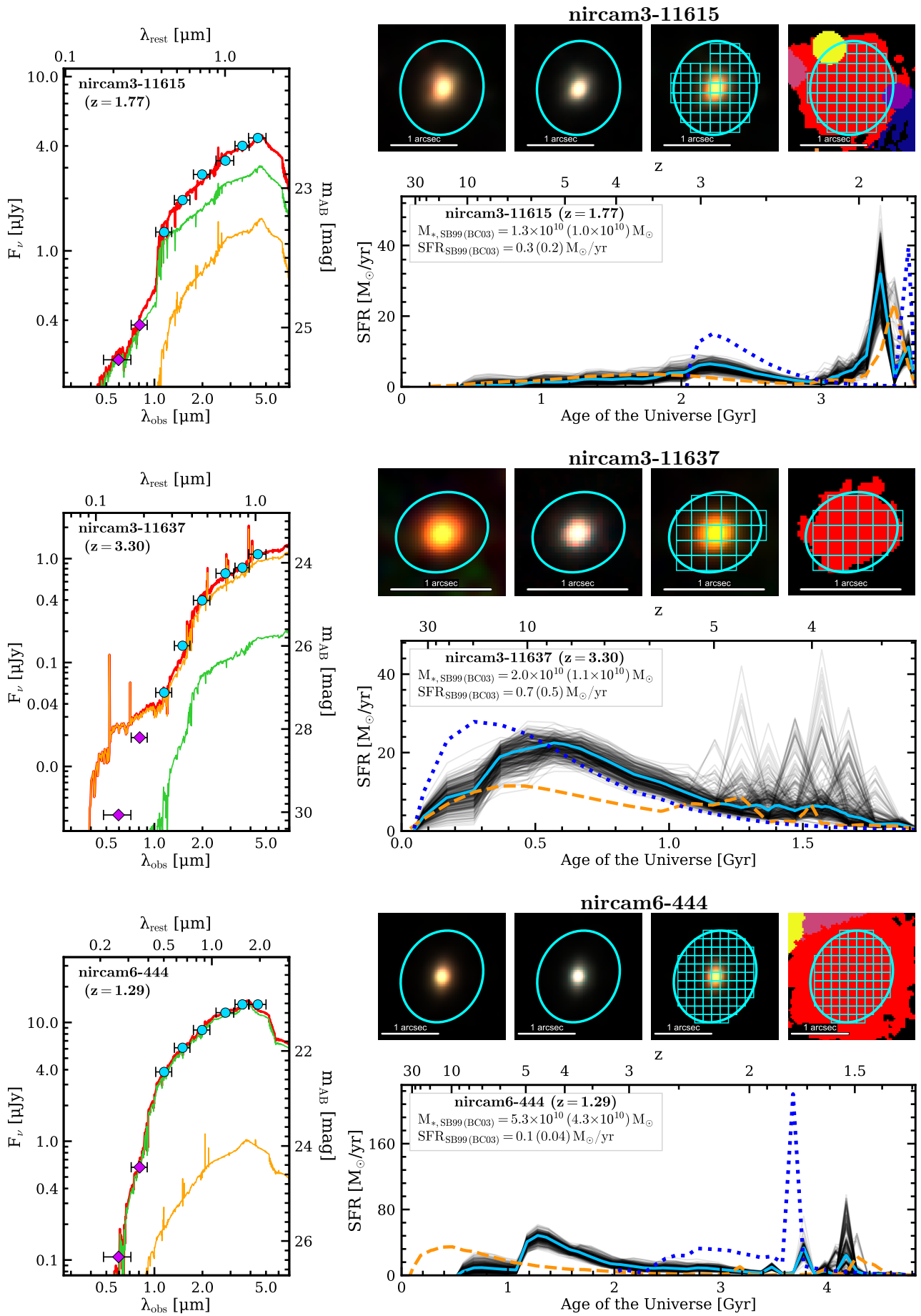


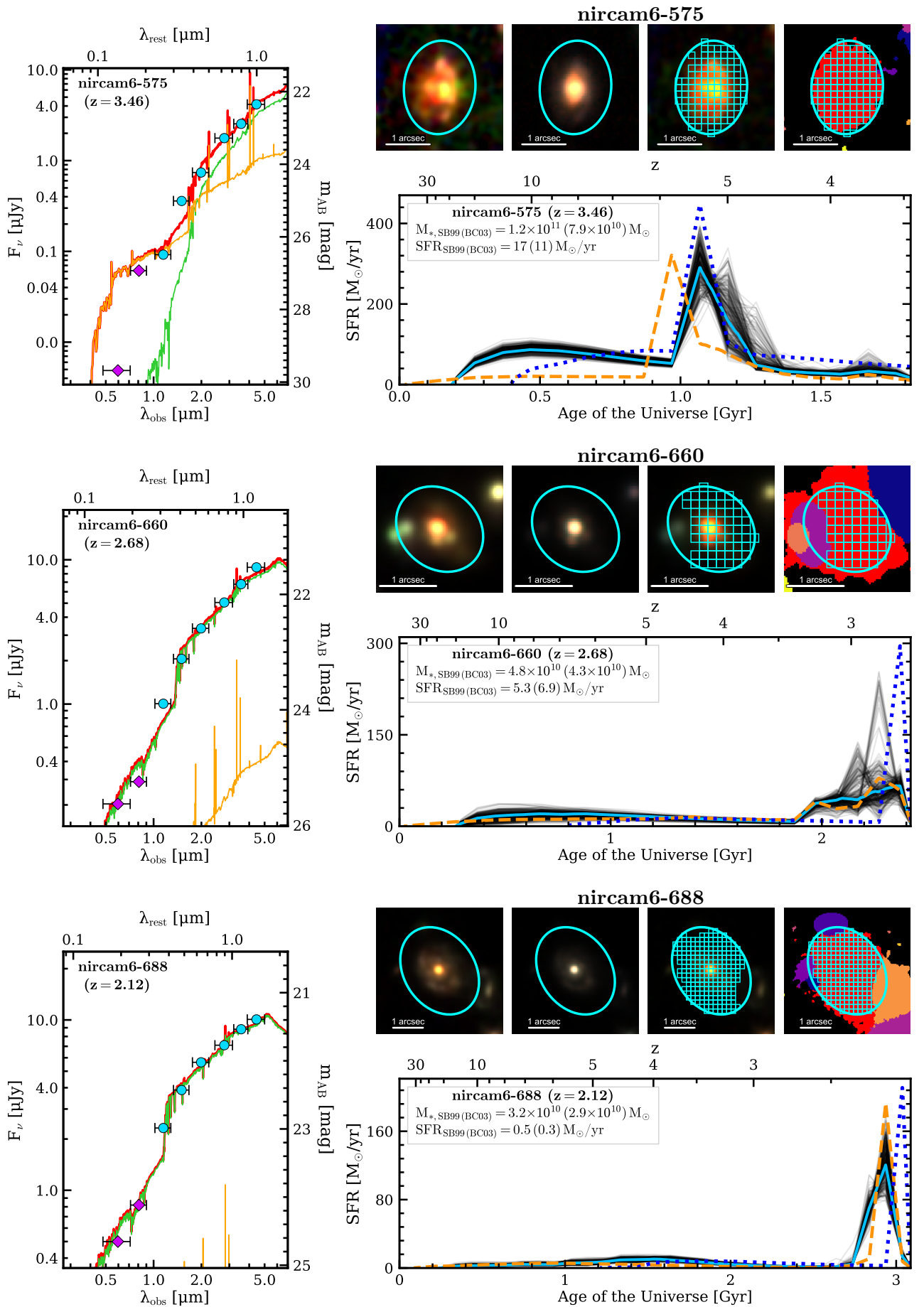


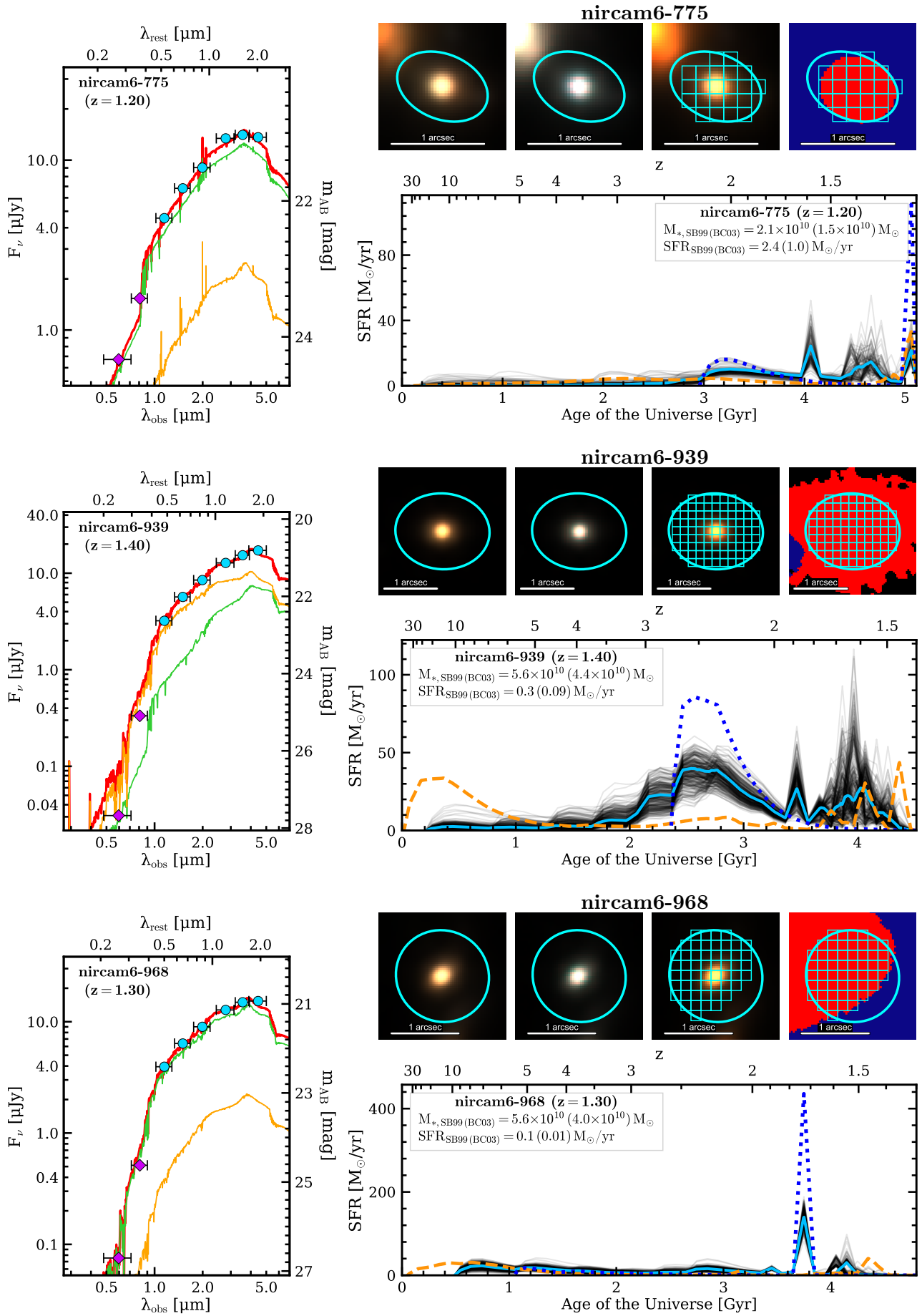


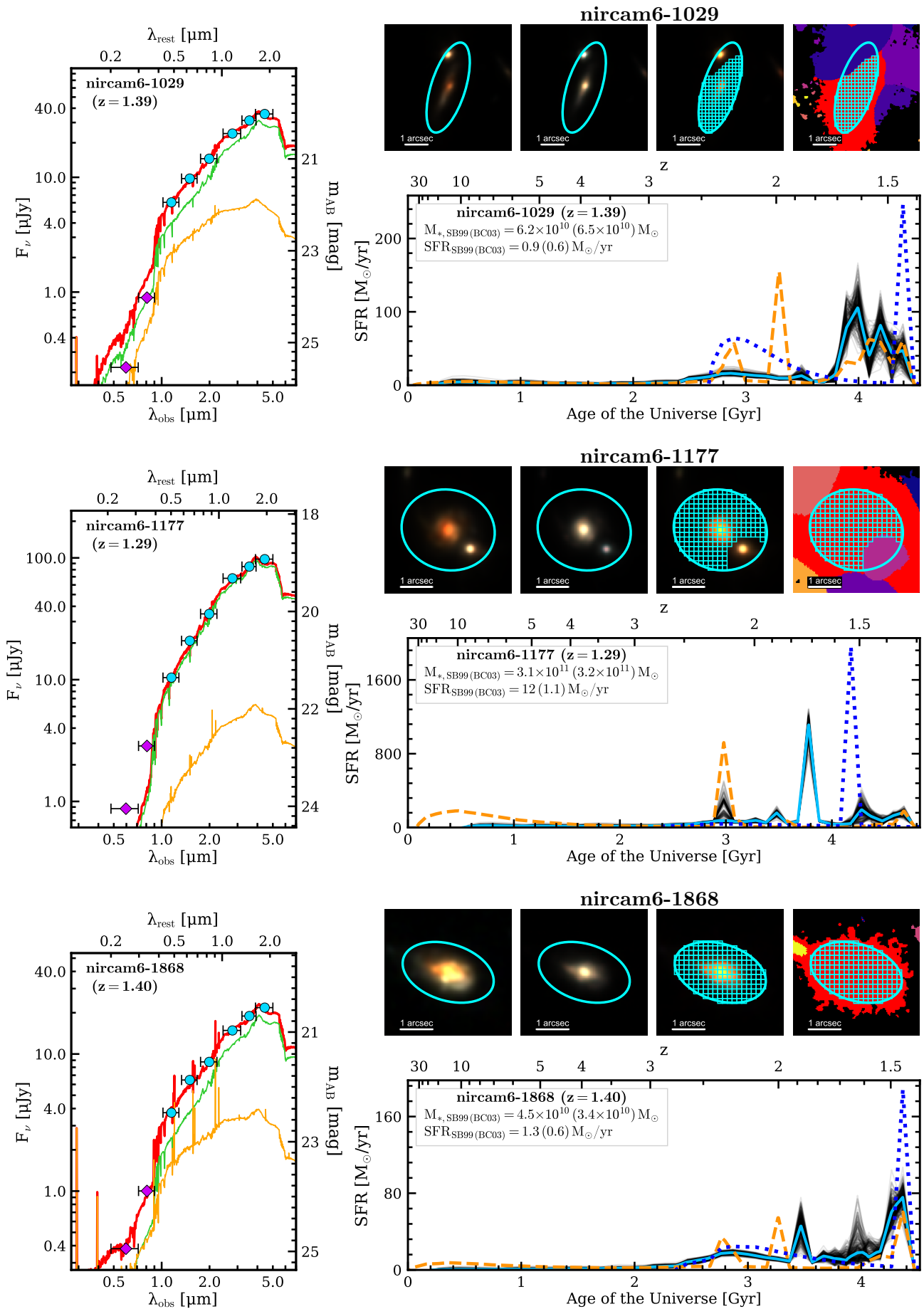


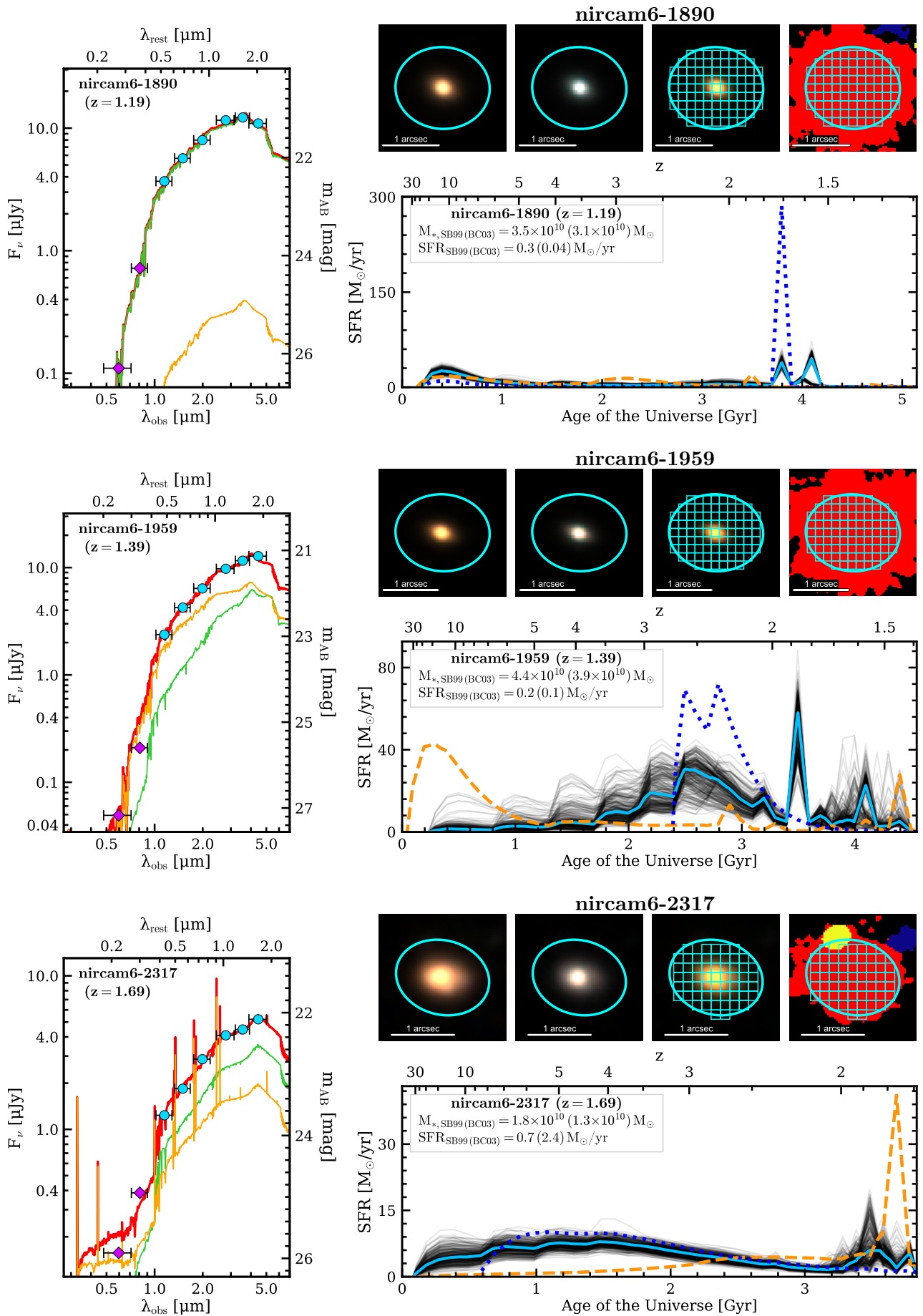


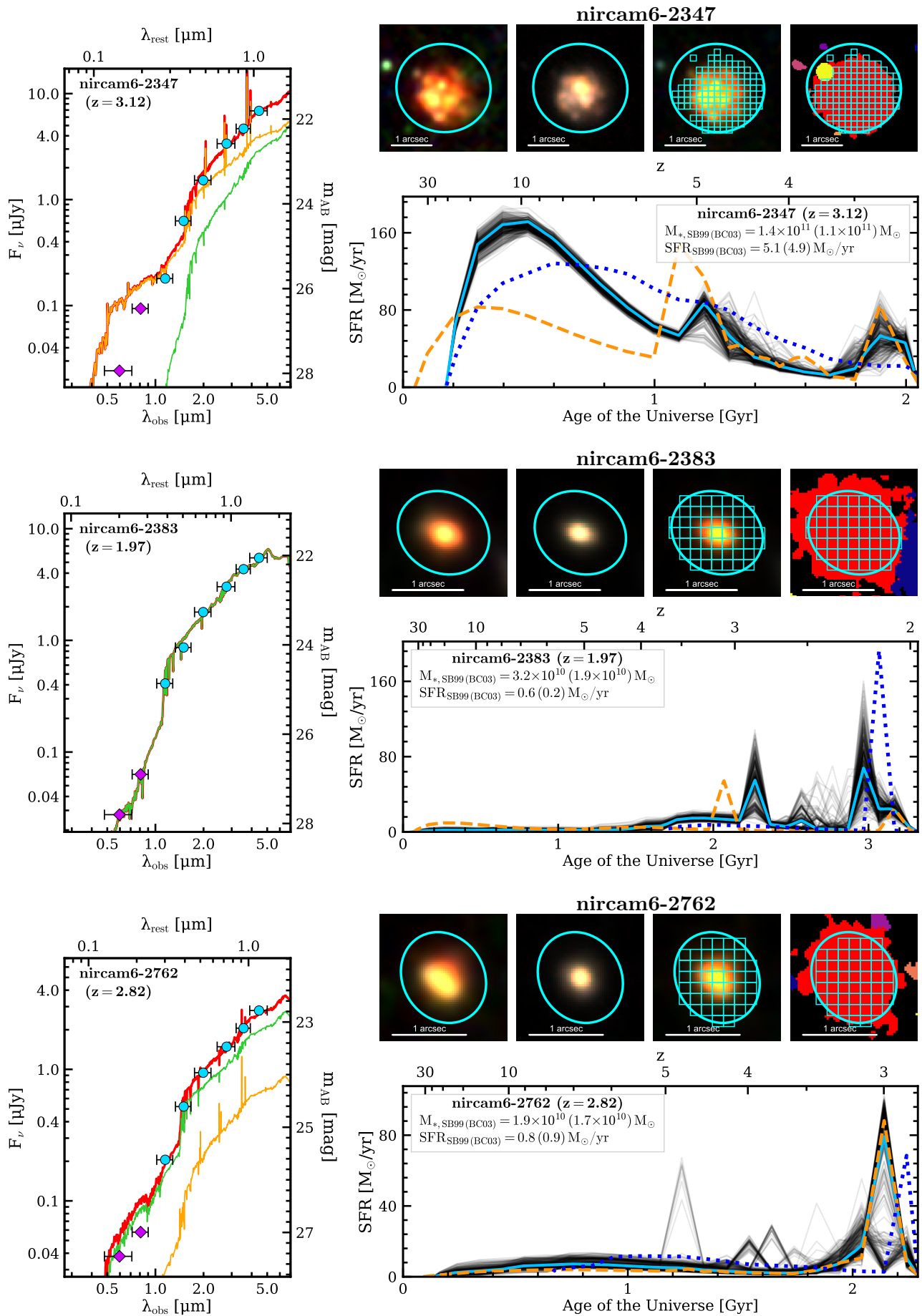


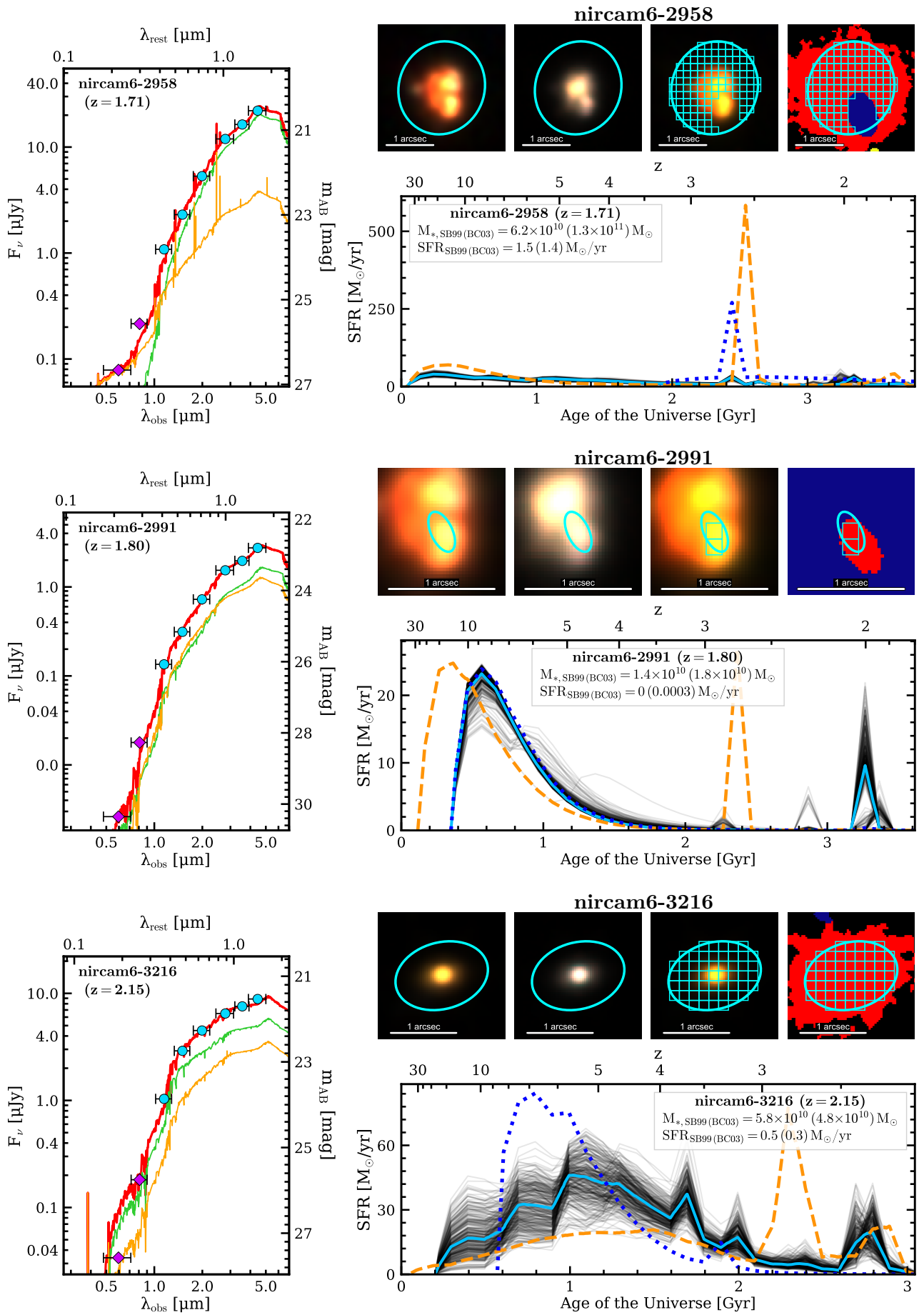


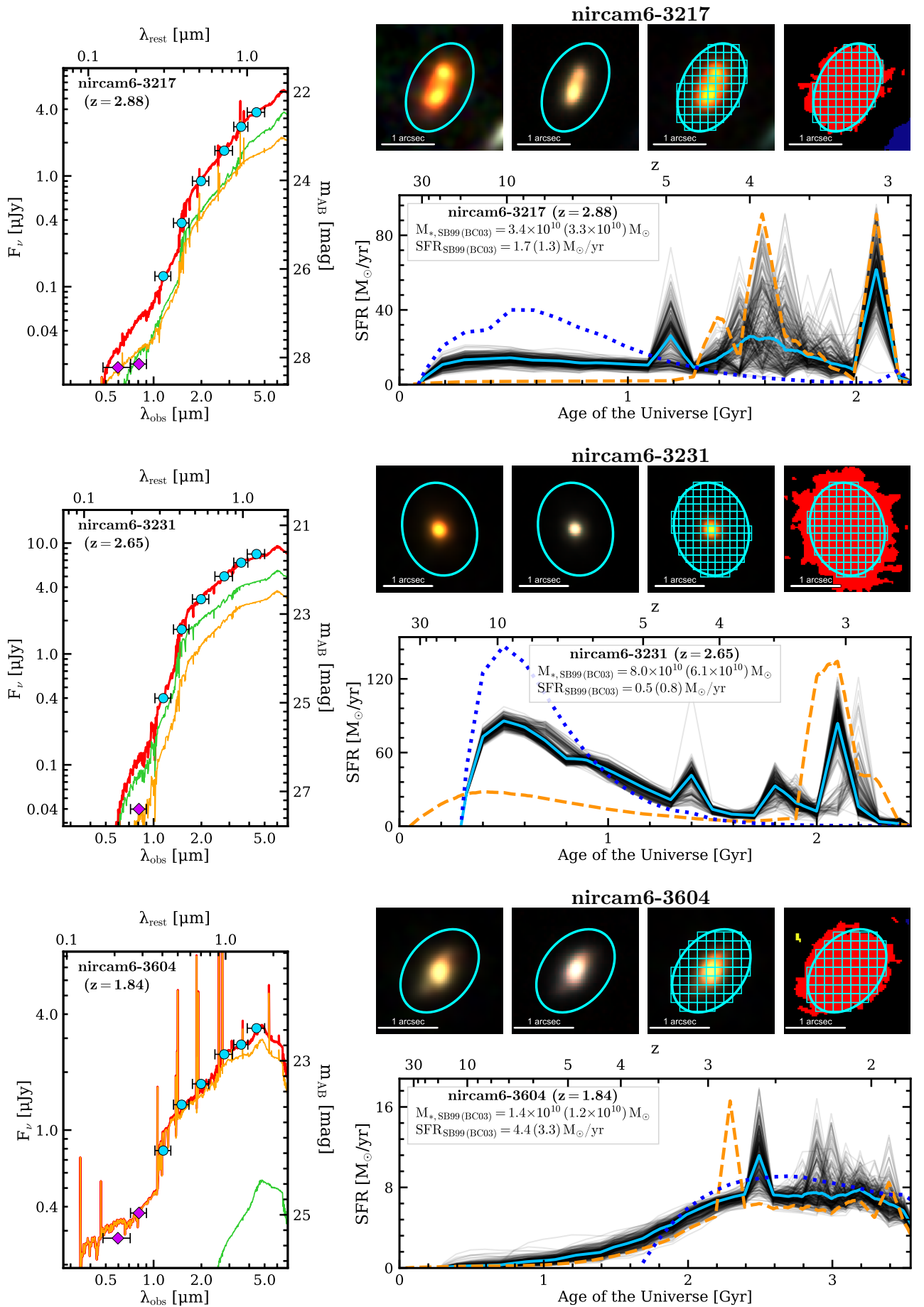




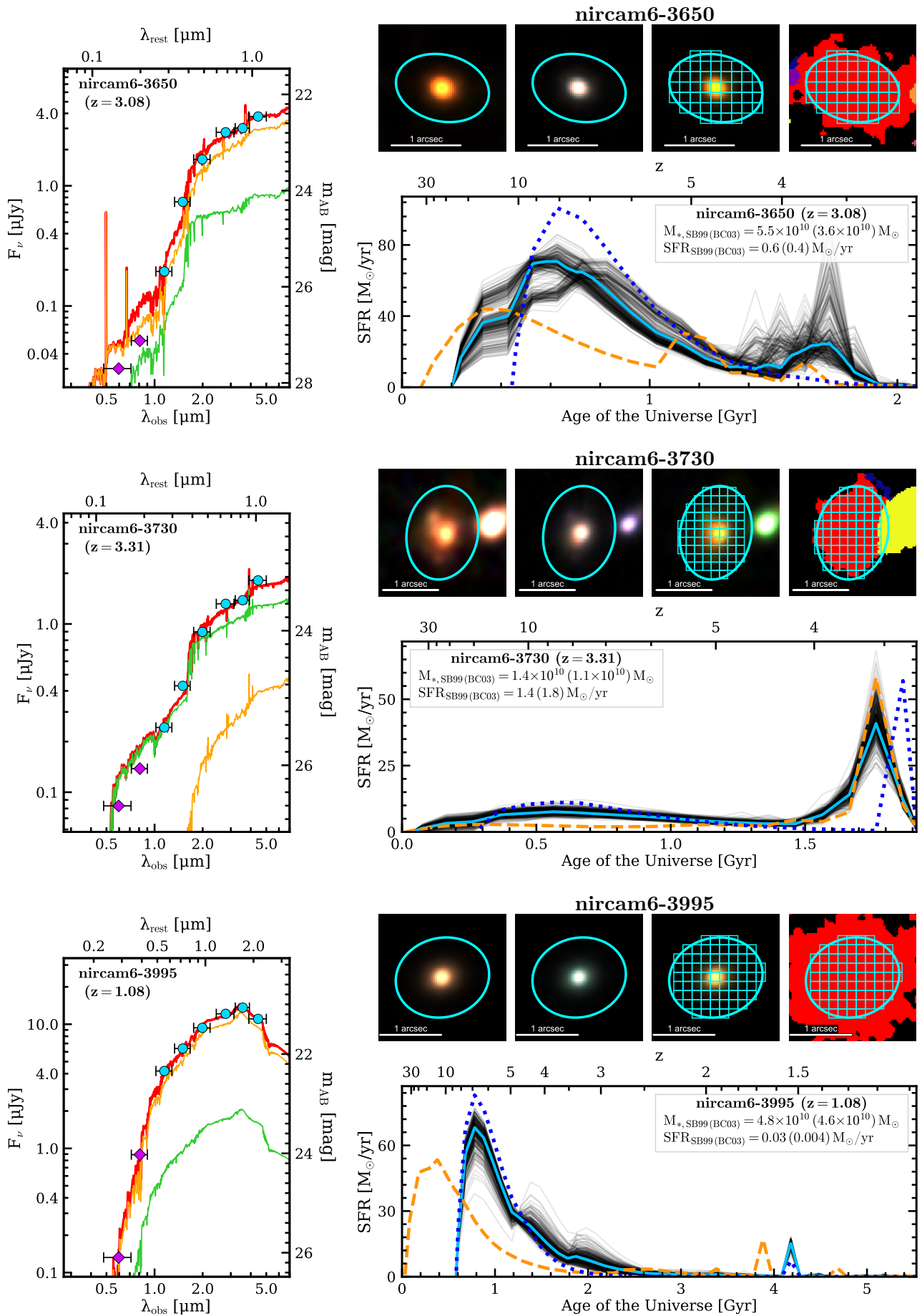


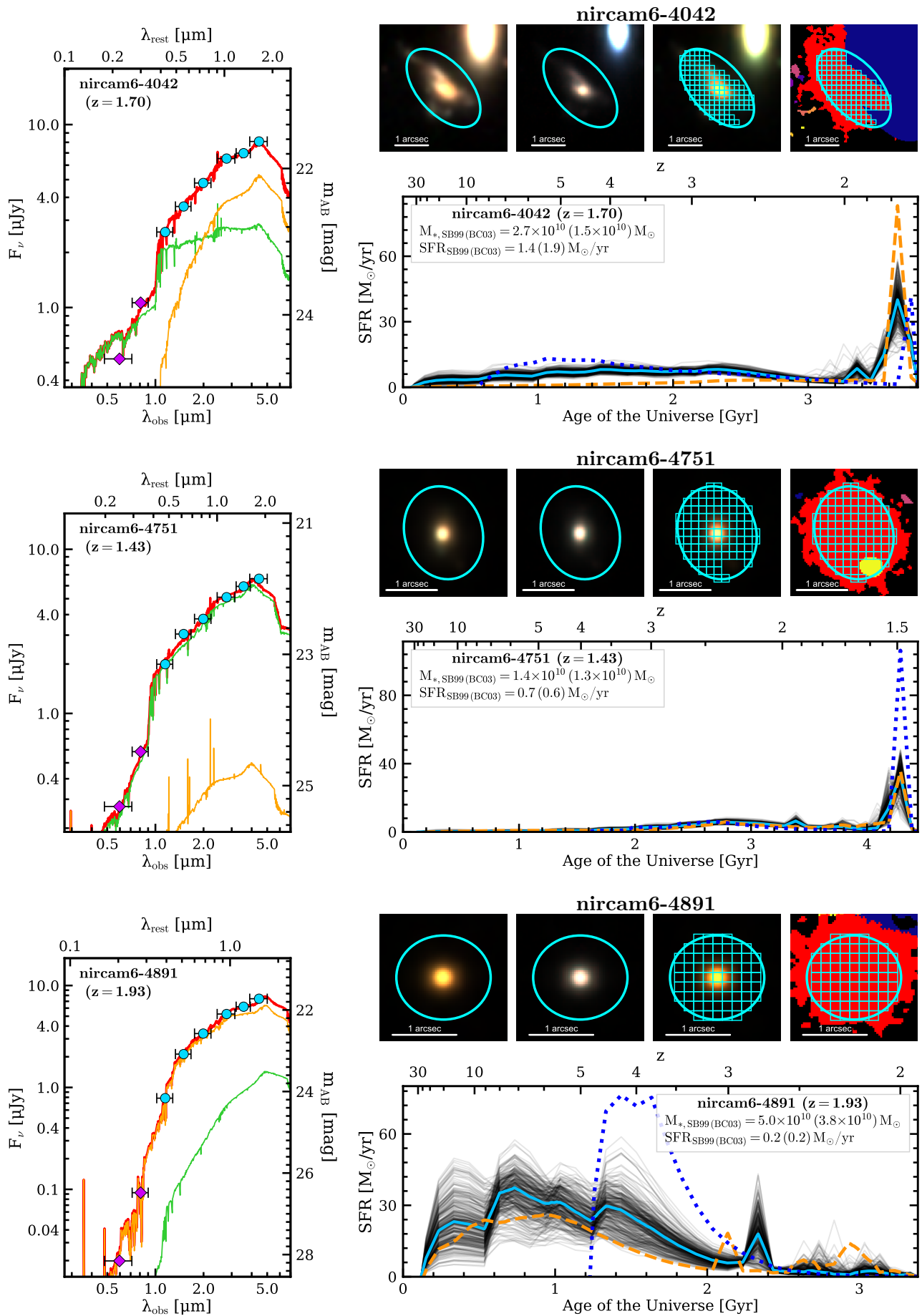


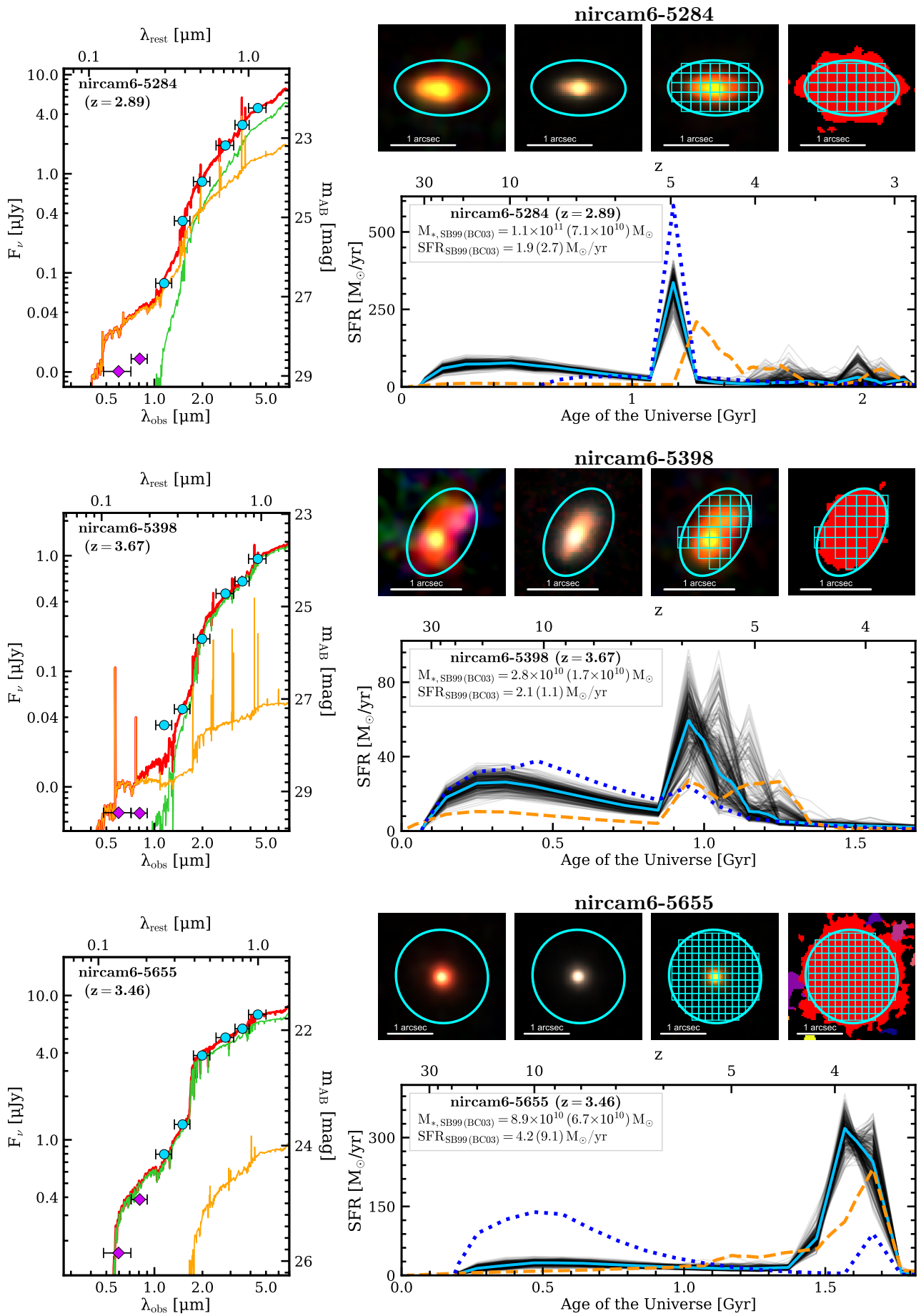


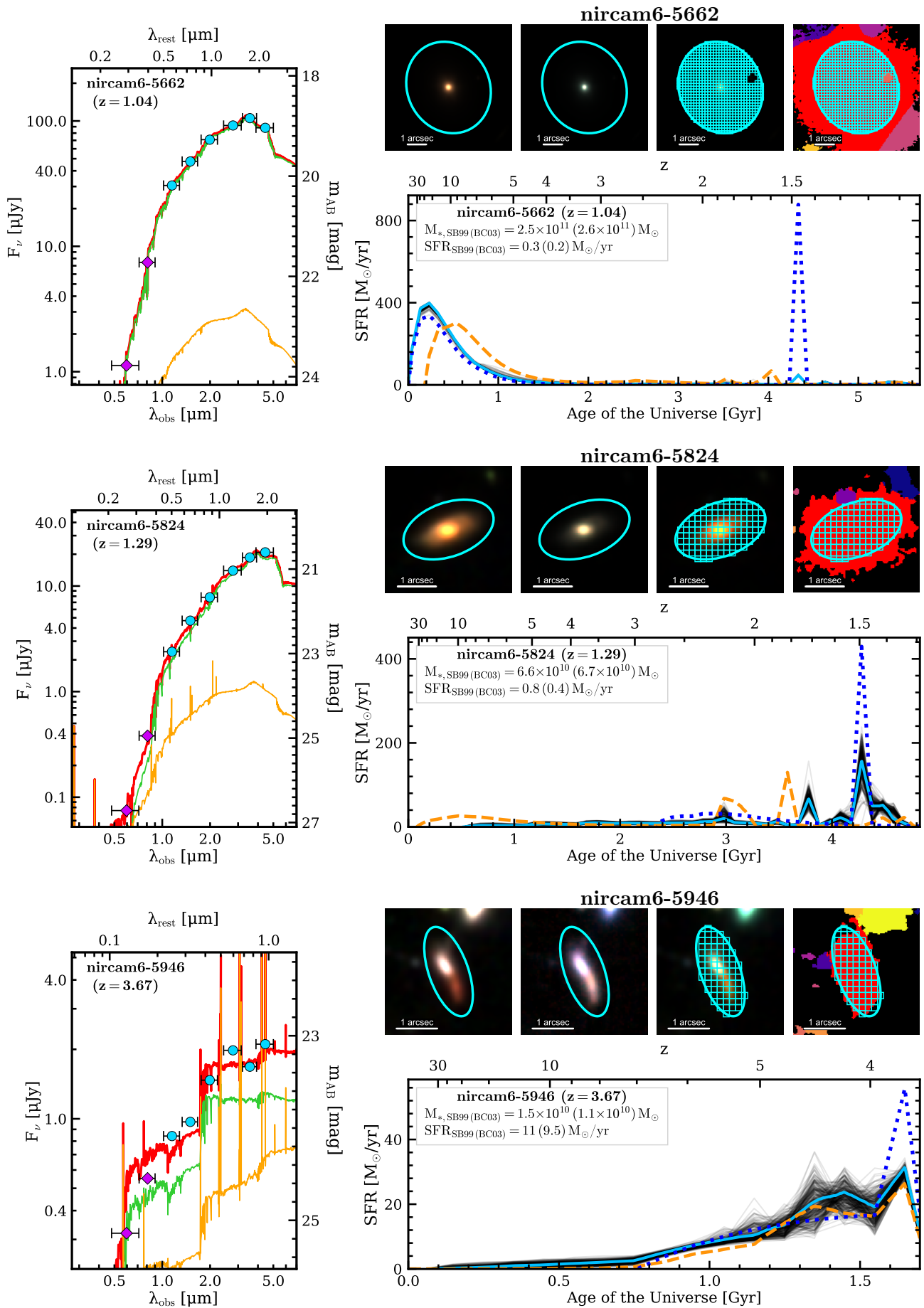


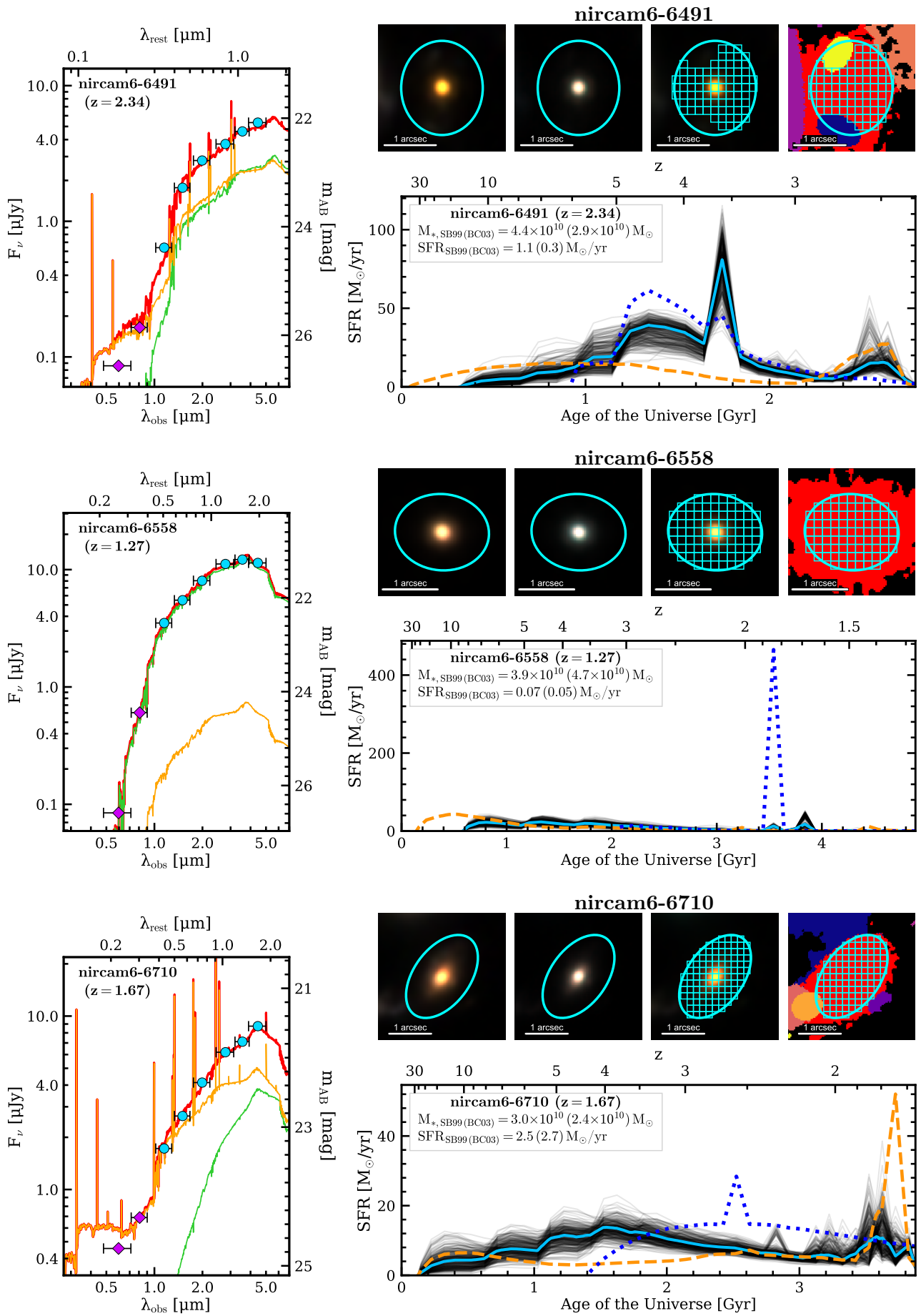


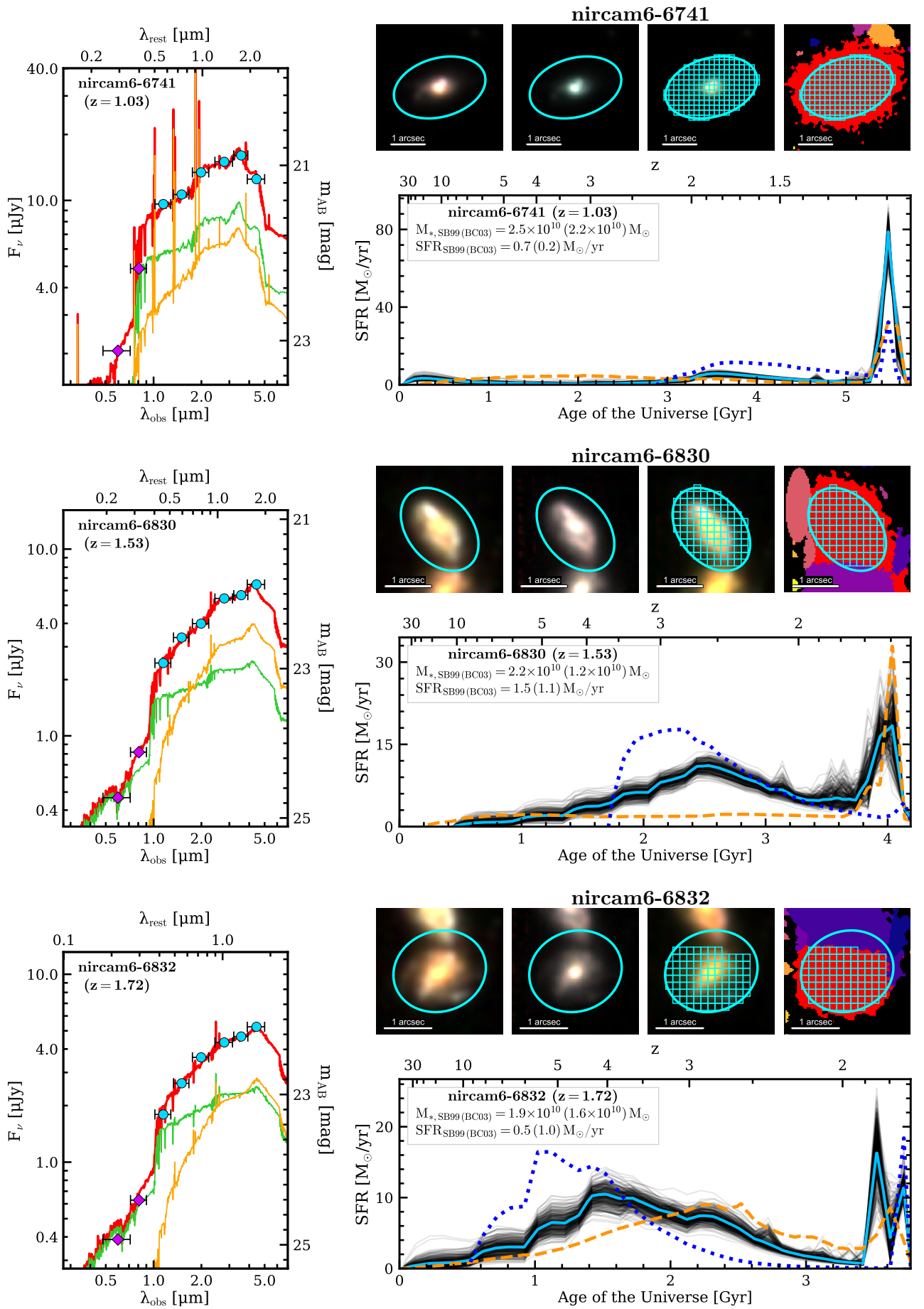


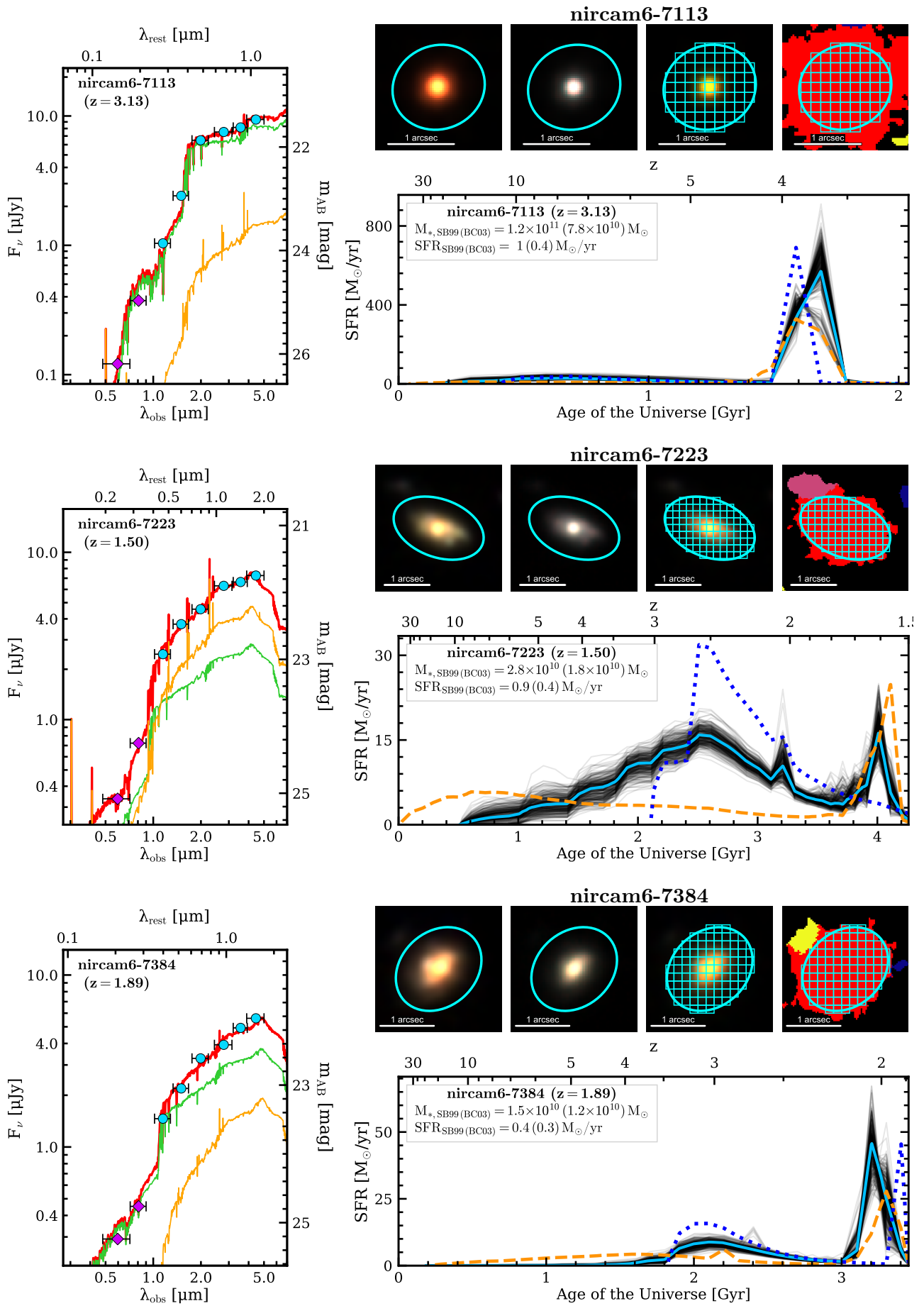


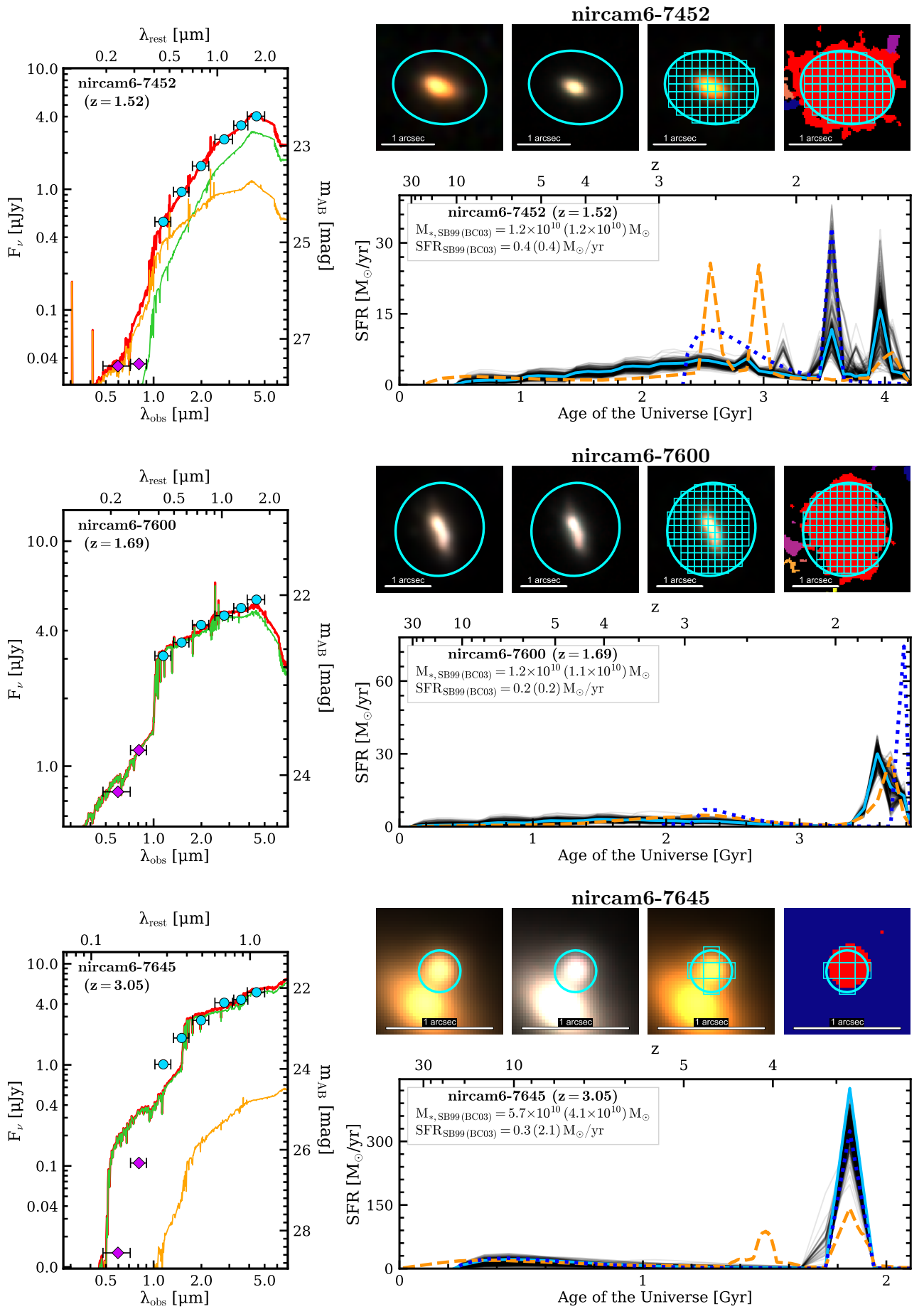




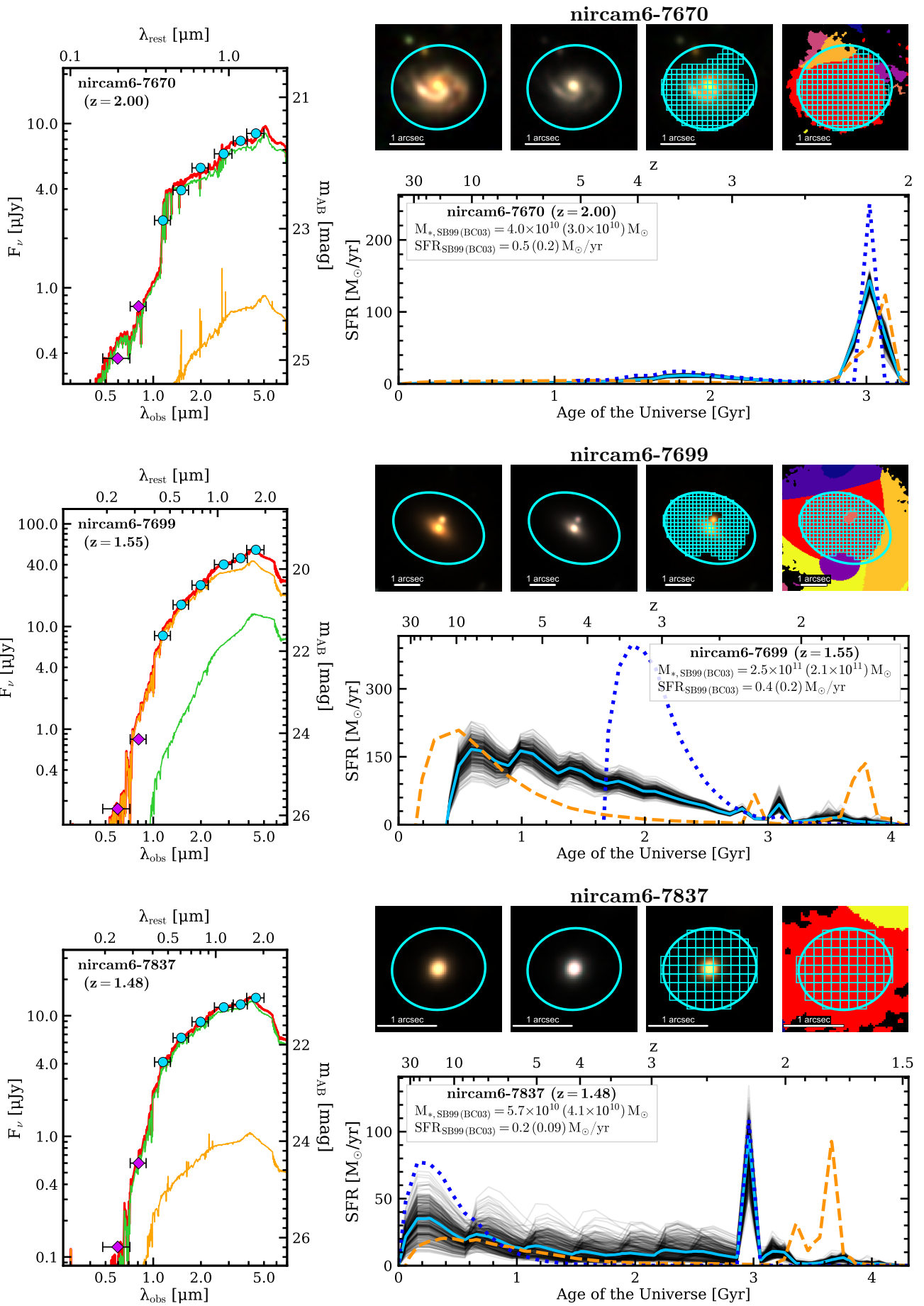


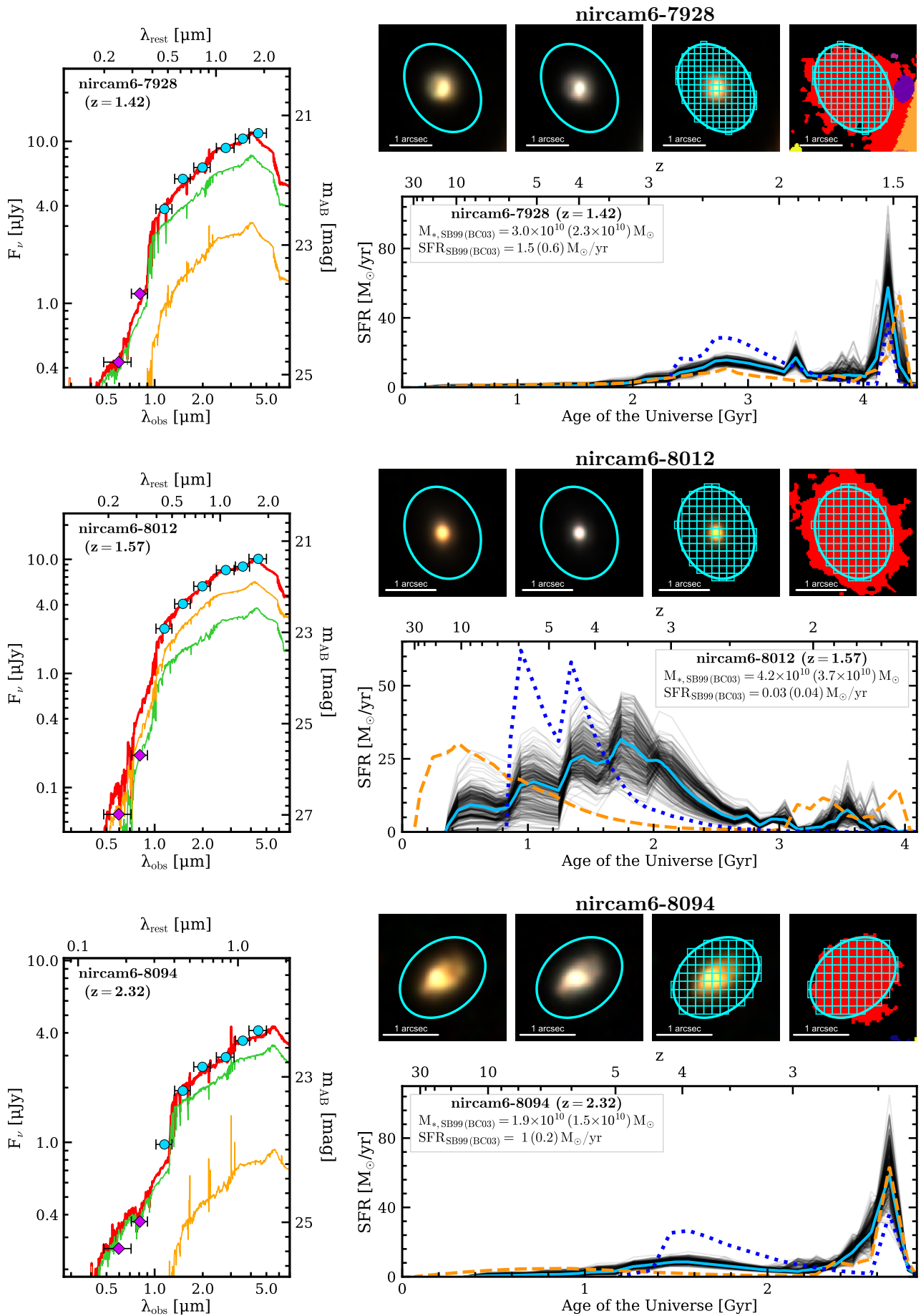


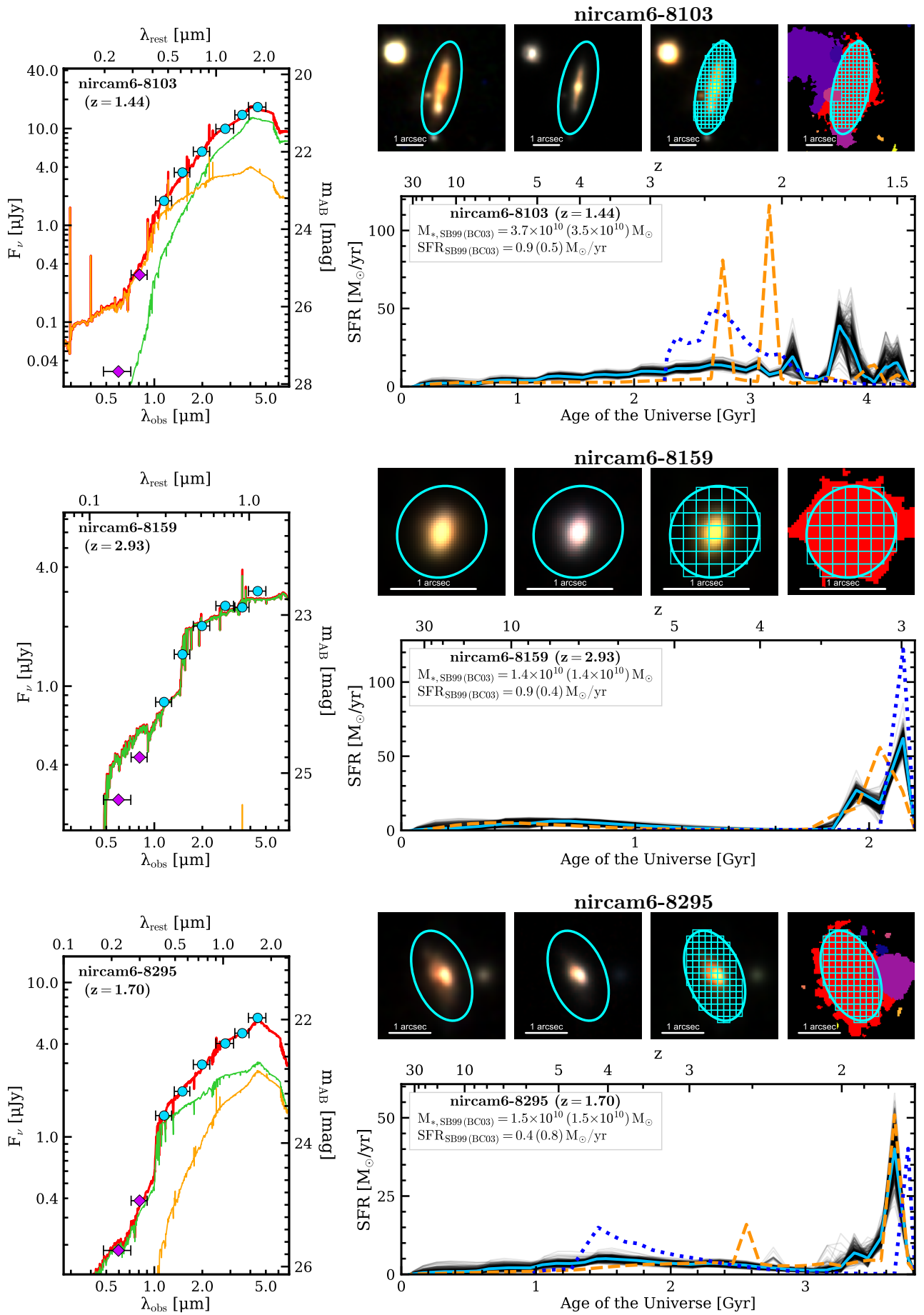


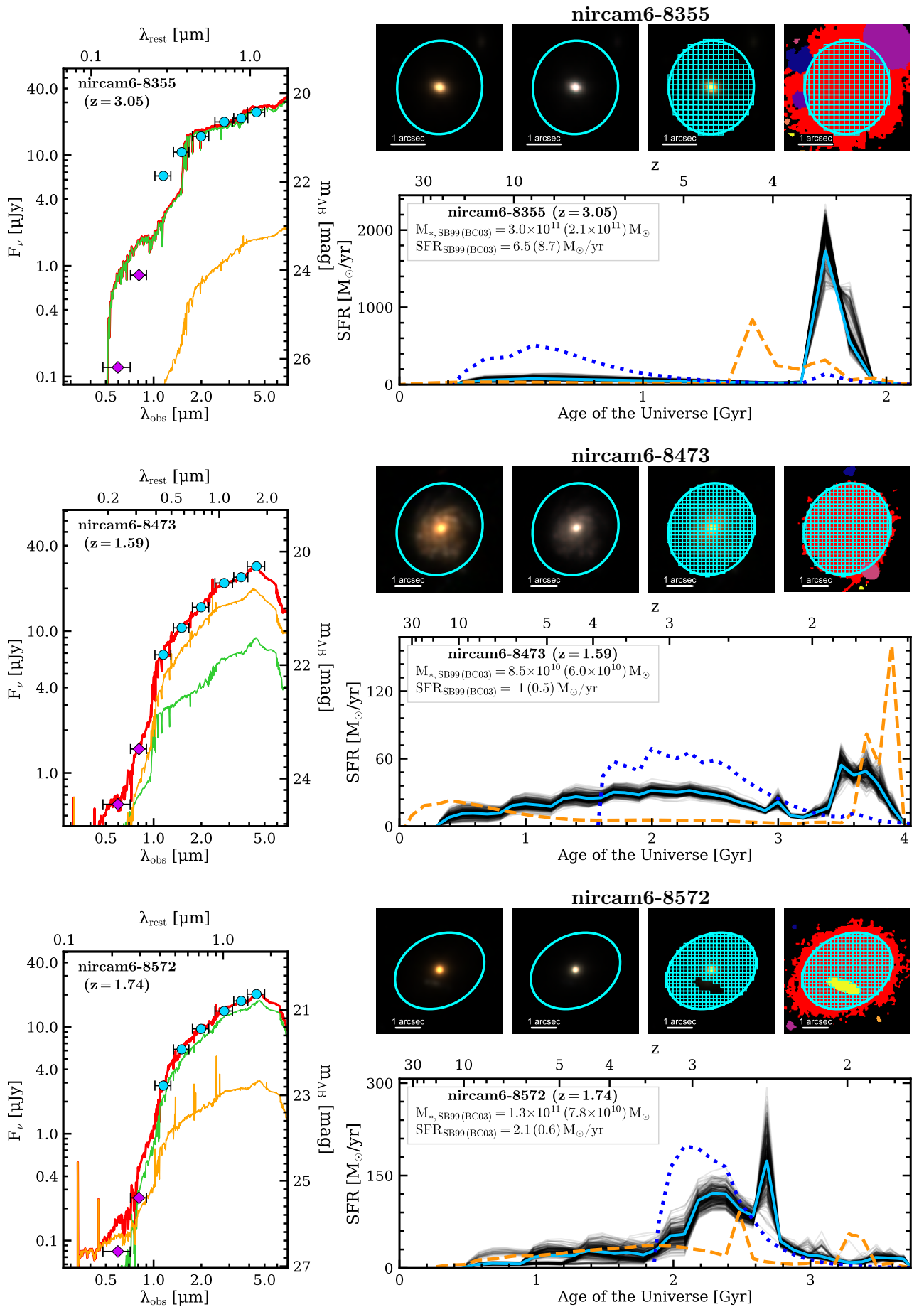


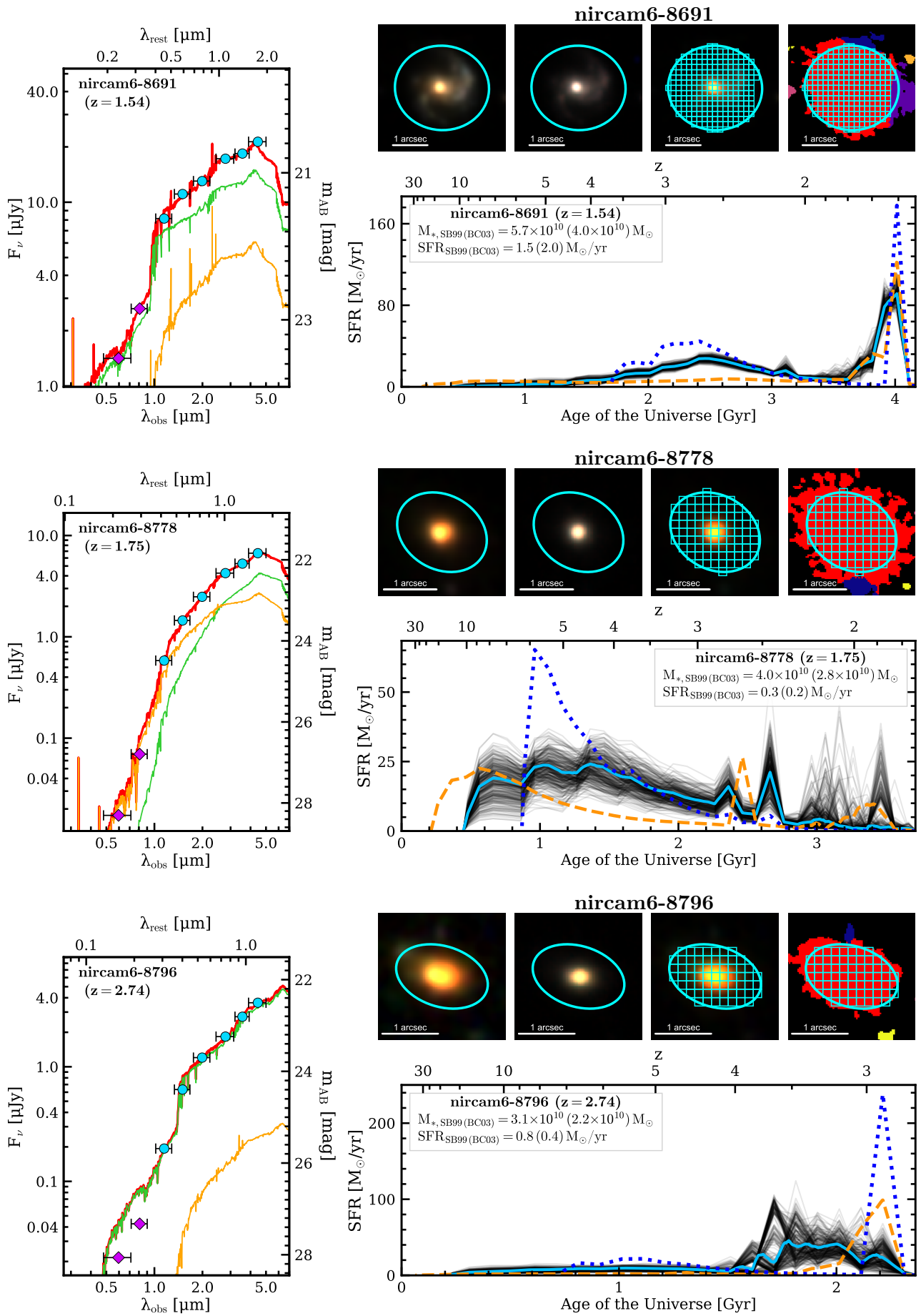


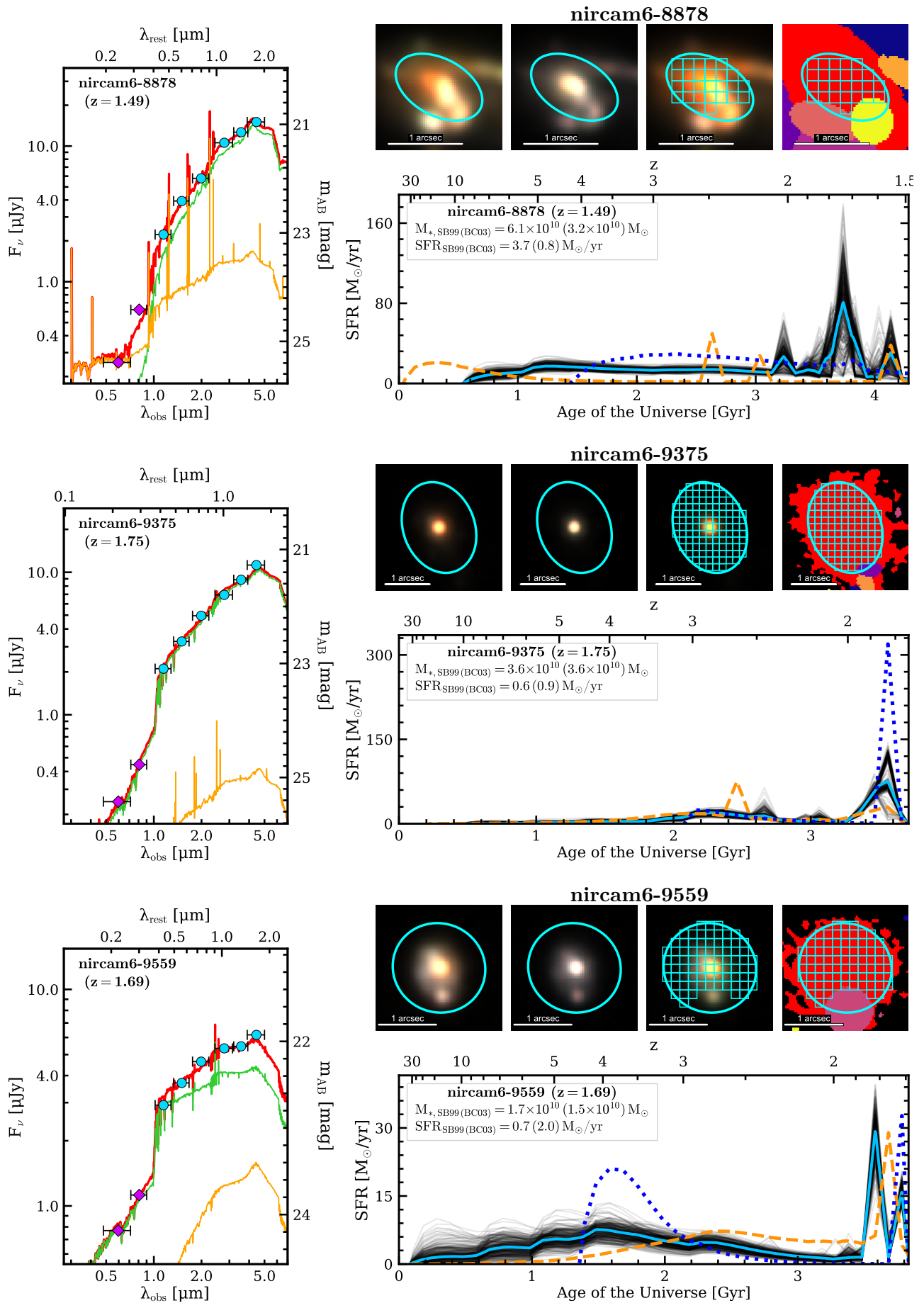


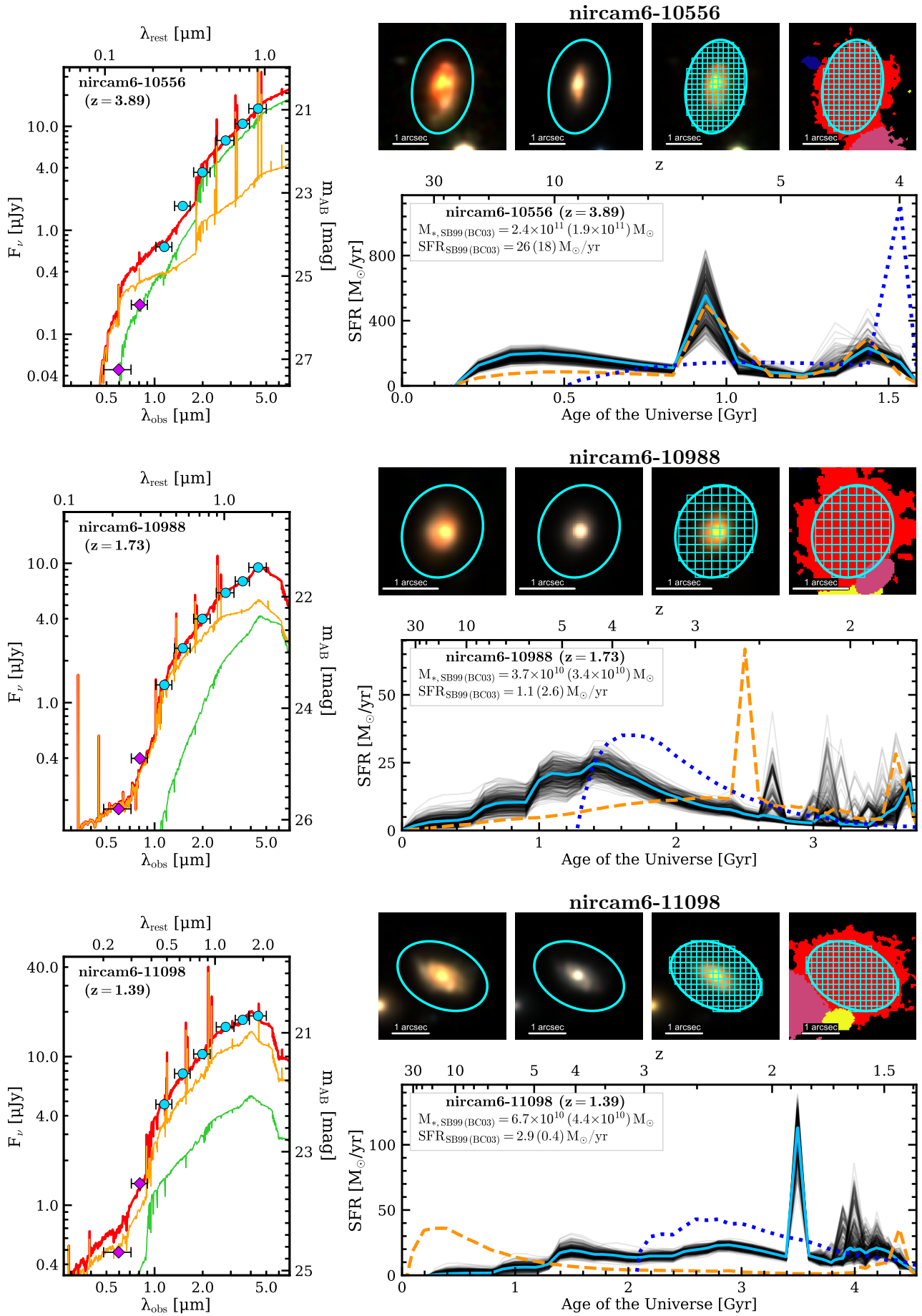


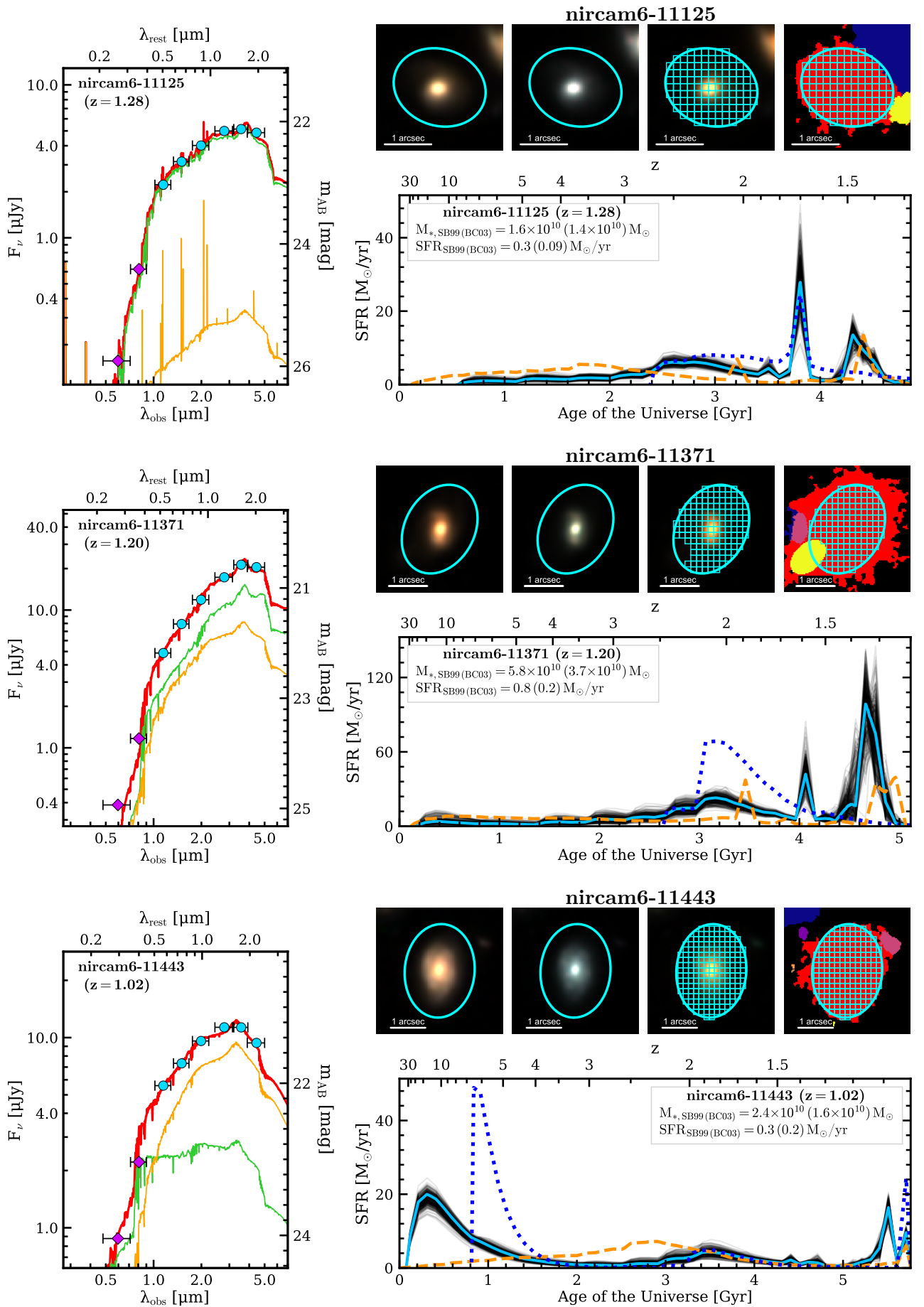




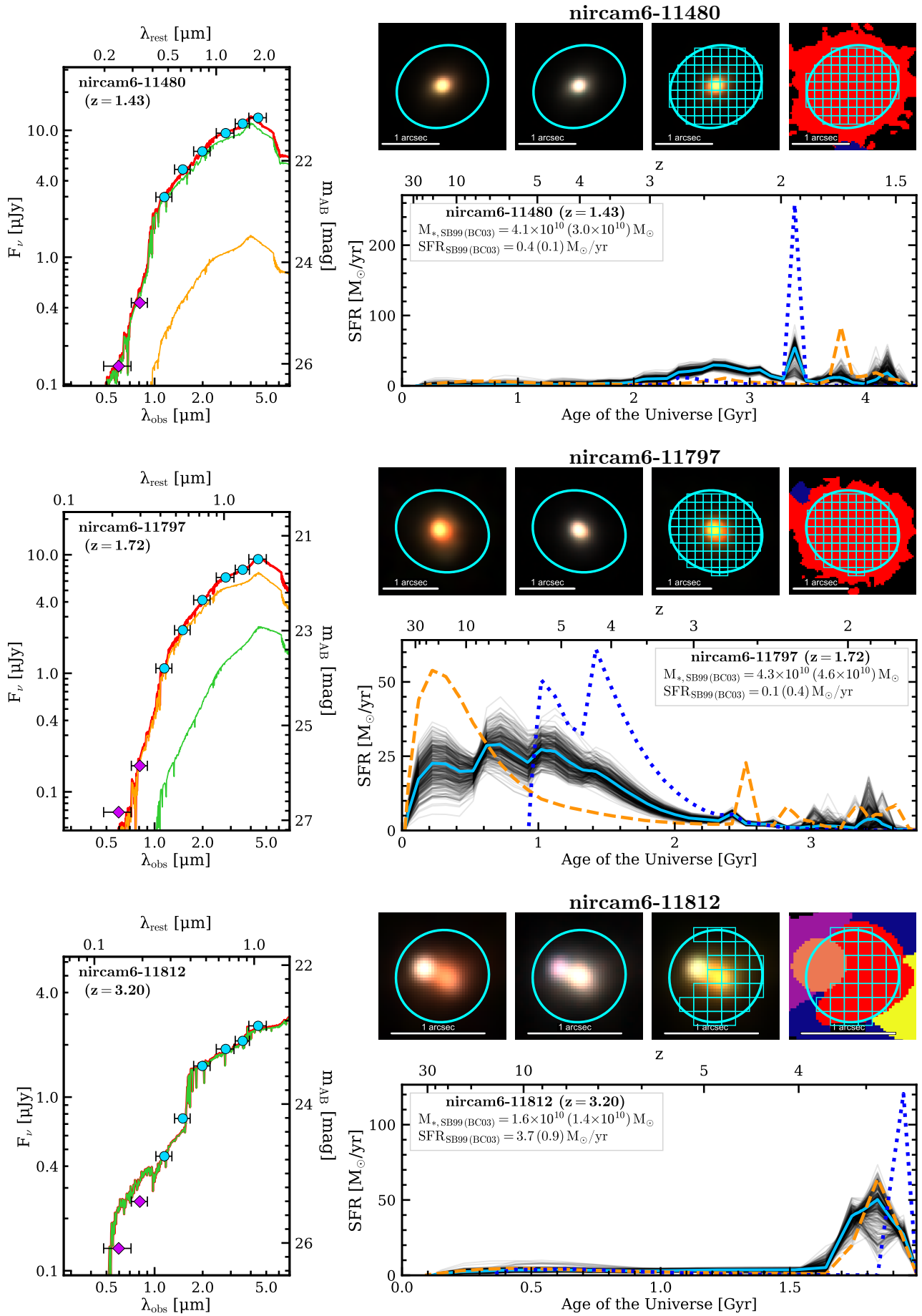












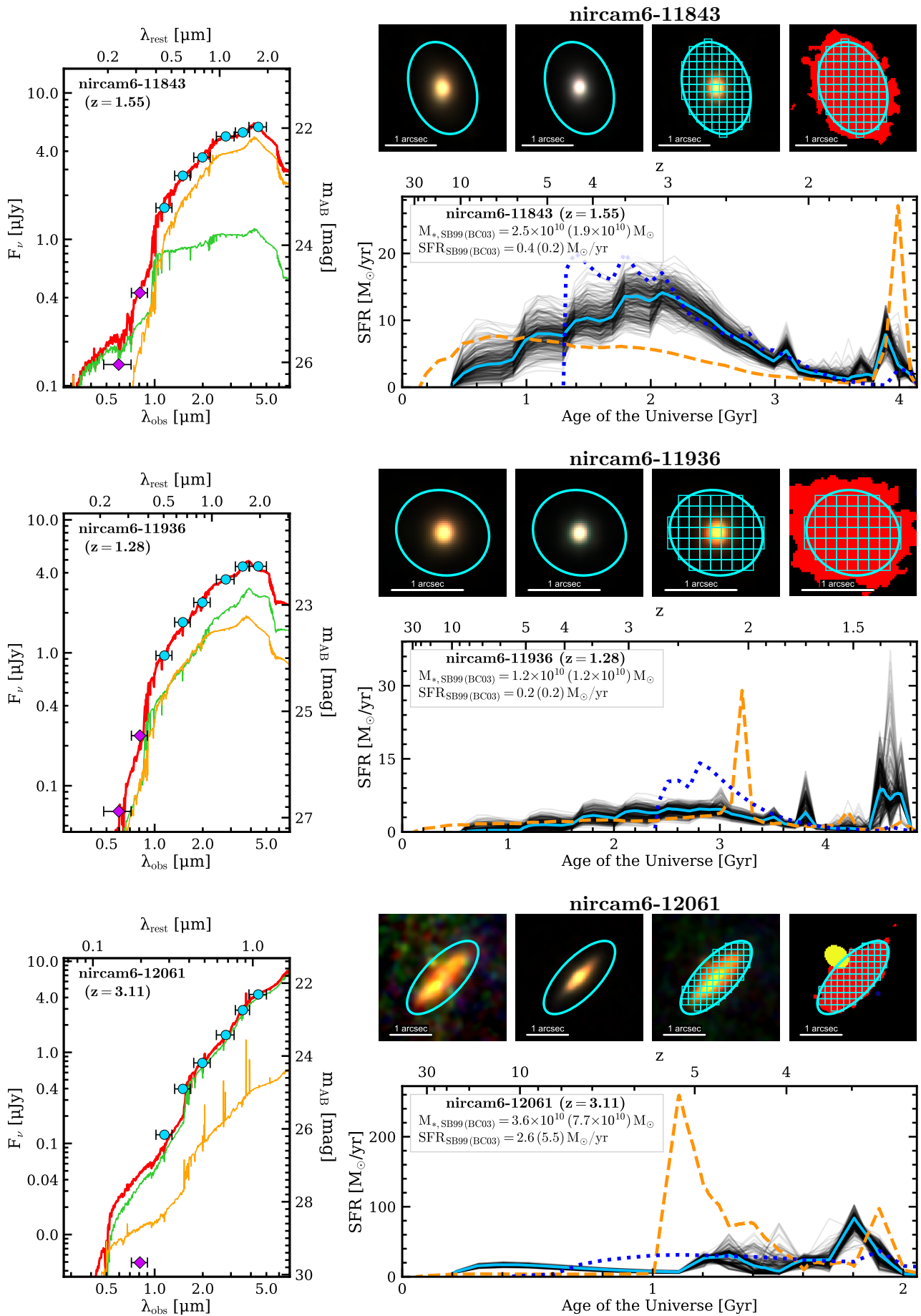


## Table of CEERS galaxies

---

Table D.1 presents some general characteristics of our sample of 333 CEERS galaxies at  $1 < z < 4$  with  $M_{\star} > 10^{10} M_{\odot}$  considered in Chapter 6. Galaxies in the table are first sorted by CEERS pointing to which they belong and, within each CEERS pointing, according to their ID.

The columns of the table are as follows:

- (1) Galaxy identifier: CEERS pointing in which the galaxy appears, followed by the galaxy ID within that pointing.
- (2) Galaxy redshift: spectroscopic redshift if available and photometric redshift otherwise.
- (3) Whether the spectroscopic redshift is available for the galaxy.
- (4-5) Galaxy sky position in equatorial coordinates for the J2000 equinox: right ascension (4) and declination (5).
- (6-7) Size of the semi-major axis of the integrated aperture which is used to measure the integrated photometry. The size of the semi-major axis of this aperture is given in arcsecs (6) and physical kiloparsecs (7).
- (8) Number of cells in the grid in which the 2D photometry is measured.
- (9-10) Galaxy stellar mass obtained from the SB99 (9) and BC03 (10) models. This mass corresponds to the median mass obtained from all the fits to the integrated SED of the galaxy and is used to normalize the 2D-SPS-derived galaxy SFH. Quartile values for this mass are included as subscripts and superscripts.

**Table D.1:** Characteristics of CEERS massive galaxies at  $1 < z < 4$  in this work (see description above).

Galaxy name	$z$	$z_{\text{spec}}?$	RA <sub>2000</sub> [deg]	Dec <sub>2000</sub> [deg]	Semi-major axis		$N_{\text{cells}}$	$M_{\text{SB99}}$ [ $M_{\odot}$ ]	$M_{\text{BC03}}$ [ $M_{\odot}$ ]
(1)	(2)	(3)	(4)	(5)	(6)	(7)	(8)	(9)	(10)
nircam1-1	1.05	Yes	214.98321556	52.95202330	1.66	13.9	261	$1.5^{+0.008}_{-0.005} \times 10^{11}$	$1.3^{+0.02}_{-0.05} \times 10^{11}$
nircam1-78	1.08	No	214.94003733	52.97350421	0.74	6.2	67	$2.4^{+0.02}_{-0.03} \times 10^{10}$	$1.4^{+0.2}_{-0.04} \times 10^{10}$
nircam1-106	1.71	No	214.94873886	52.97982488	0.68	5.9	48	$1.5^{+0.05}_{-0.07} \times 10^{10}$	$1.2^{+0.07}_{-0.07} \times 10^{10}$
nircam1-172	1.20	No	214.95119999	52.98065782	2.08	17.7	390	$5.0^{+1.8}_{-0.9} \times 10^{10}$	$3.2^{+0.2}_{-0.08} \times 10^{10}$
nircam1-792	1.12	No	214.93156438	52.96358407	1.02	8.6	99	$9.9^{+0.07}_{-0.08} \times 10^{10}$	$6.5^{+0.7}_{-0.2} \times 10^{10}$
nircam1-868	1.72	No	214.94780321	52.97494854	1.76	15.3	371	$8.1^{+0.09}_{-0.1} \times 10^{10}$	$6.9^{+0.2}_{-0.09} \times 10^{10}$
nircam1-957	1.10	No	214.93082669	52.96342130	1.81	15.2	258	$1.2^{+0.03}_{-0.02} \times 10^{11}$	$8.4^{+0.9}_{-0.6} \times 10^{10}$
nircam1-1047	2.58	No	214.97614257	52.99148810	1.23	10.1	165	$2.6^{+0.2}_{-0.04} \times 10^{10}$	$2.3^{+0.2}_{-0.008} \times 10^{10}$
nircam1-1211	1.21	No	214.92982314	52.96318555	1.50	12.8	163	$1.8^{+0.005}_{-0.2} \times 10^{11}$	$1.2^{+0.004}_{-0.002} \times 10^{11}$
nircam1-1319	1.10	Yes	214.93082530	52.96107213	1.20	10.1	163	$5.0^{+0.03}_{-0.01} \times 10^{10}$	$4.0^{+0.3}_{-0.3} \times 10^{10}$
nircam1-1394	3.49	No	214.95787657	52.98030101	0.54	4.1	35	$3.6^{+0.03}_{-0.03} \times 10^{10}$	$2.3^{+0.05}_{-0.01} \times 10^{10}$
nircam1-1405	1.24	Yes	214.99677903	53.00740099	1.52	13.0	238	$1.7^{+0.03}_{-0.2} \times 10^{10}$	$1.4^{+0.03}_{-0.03} \times 10^{10}$
nircam1-1498	1.06	Yes	214.95230344	52.97640961	1.55	13.0	246	$2.6^{+0.1}_{-0.02} \times 10^{10}$	$2.8^{+0.5}_{-0.7} \times 10^{10}$
nircam1-1659	1.36	Yes	214.98641199	52.99872645	1.77	15.3	209	$1.8^{+0.2}_{-0.2} \times 10^{10}$	$1.4^{+0.1}_{-0.05} \times 10^{10}$
nircam1-1660	1.03	No	214.98683863	52.99796261	1.88	15.6	308	$7.8^{+0.1}_{-0.6} \times 10^{10}$	$6.0^{+0.05}_{-0.05} \times 10^{10}$
nircam1-1685	1.11	No	214.97854928	52.99247250	1.32	11.1	221	$5.7^{+0.4}_{-0.05} \times 10^{10}$	$6.1^{+0.2}_{-0.2} \times 10^{10}$
nircam1-1794	1.11	No	214.97423175	52.99168337	1.28	10.8	176	$6.9^{+0.1}_{-0.2} \times 10^{10}$	$8.9^{+0.2}_{-0.1} \times 10^{10}$
nircam1-1808	1.51	No	214.94814139	52.97118671	1.08	9.4	85	$3.1^{+0.1}_{-0.08} \times 10^{10}$	$1.5^{+0.07}_{-0.05} \times 10^{10}$
nircam1-1941	2.44	No	214.99662652	53.00452190	1.15	9.5	115	$5.5^{+0.9}_{-0.8} \times 10^{10}$	$4.1^{+0.3}_{-0.4} \times 10^{10}$
nircam1-2251	1.23	No	214.98175159	52.99318283	0.89	7.7	67	$4.5^{+0.3}_{-0.3} \times 10^{10}$	$4.6^{+0.2}_{-0.2} \times 10^{10}$
nircam1-2260	2.48	No	214.98272687	52.99335774	0.94	7.8	98	$5.8^{+0.3}_{-0.2} \times 10^{10}$	$4.4^{+0.03}_{-0.03} \times 10^{10}$
nircam1-2459	1.09	No	214.98950203	52.99753657	1.23	10.3	196	$2.0^{+0.08}_{-0.3} \times 10^{10}$	$1.4^{+0.1}_{-0.1} \times 10^{10}$
nircam1-2518	1.12	Yes	214.95385063	52.97550767	1.51	12.8	312	$4.8^{+0.1}_{-0.05} \times 10^{10}$	$3.8^{+0.1}_{-0.1} \times 10^{10}$
nircam1-2662	3.41	No	214.98181750	52.99123408	0.72	5.5	61	$8.2^{+0.08}_{-0.2} \times 10^{10}$	$4.9^{+0.1}_{-0.09} \times 10^{10}$
nircam1-2720	1.71	No	215.01407868	53.01481065	1.21	10.5	118	$1.1^{+0.07}_{-0.1} \times 10^{10}$	$1.1^{+0.1}_{-0.08} \times 10^{10}$
nircam1-3088	2.19	No	215.01489826	53.01422108	1.50	12.7	136	$6.0^{+0.5}_{-0.09} \times 10^{10}$	$1.1^{+0.02}_{-0.04} \times 10^{11}$
nircam1-3310	1.72	No	215.01354005	53.00990883	1.39	12.0	189	$2.7^{+0.09}_{-0.2} \times 10^{10}$	$2.8^{+0.4}_{-0.2} \times 10^{10}$
nircam1-3578	1.52	No	214.96411221	52.97426866	1.37	11.9	160	$5.8^{+0.2}_{-0.2} \times 10^{10}$	$3.5^{+0.4}_{-0.4} \times 10^{10}$
nircam1-3670	1.13	No	214.98944847	52.98984775	1.35	11.4	148	$1.4^{+0.1}_{-0.1} \times 10^{10}$	$1.2^{+0.1}_{-0.08} \times 10^{10}$
nircam1-3756	1.40	No	214.98913972	52.99062529	0.67	5.8	21	$1.6^{+0.2}_{-0.1} \times 10^{10}$	$2.3^{+0.2}_{-0.4} \times 10^{10}$
nircam1-4022	2.91	No	214.94697119	52.96026370	1.32	10.5	73	$1.7^{+0.02}_{-0.009} \times 10^{10}$	$1.6^{+0.02}_{-0.02} \times 10^{10}$
nircam1-4241	1.32	No	214.99002592	52.99115385	1.86	16.0	155	$3.8^{+0.2}_{-0.2} \times 10^{10}$	$4.6^{+1.5}_{-0.1} \times 10^{10}$
nircam1-4312	2.37	Yes	214.93685058	52.95172863	0.84	7.0	80	$1.7^{+0.3}_{-0.03} \times 10^{10}$	$1.5^{+0.08}_{-0.04} \times 10^{10}$
nircam1-4331	1.53	No	215.02021003	53.01022970	0.93	8.1	90	$8.7^{+0.2}_{-0.3} \times 10^{10}$	$7.4^{+0.5}_{-0.4} \times 10^{10}$
nircam1-4341	3.35	No	215.00714599	53.00124264	0.90	6.9	77	$2.3^{+0.3}_{-0.3} \times 10^{10}$	$1.8^{+0.2}_{-0.08} \times 10^{10}$
nircam1-4371	1.22	No	214.99264985	52.99180764	2.86	24.5	341	$5.9^{+0.2}_{-0.2} \times 10^{10}$	$7.5^{+7.3}_{-0.07} \times 10^{10}$
nircam1-4630	1.77	No	215.00925650	53.00125743	1.19	10.3	93	$1.1^{+0.05}_{-0.1} \times 10^{10}$	$1.0^{+0.1}_{-0.07} \times 10^{10}$
nircam1-5041	1.12	Yes	214.99115164	52.98610157	1.69	14.2	279	$4.5^{+1.8}_{-0.04} \times 10^{10}$	$3.8^{+0.2}_{-0.1} \times 10^{10}$
nircam1-5060	1.24	Yes	215.00665160	52.99616489	1.55	13.3	306	$6.6^{+0.2}_{-0.2} \times 10^{10}$	$4.7^{+0.7}_{-0.4} \times 10^{10}$
nircam1-5171	1.28	No	214.93620761	52.94830038	1.83	15.7	314	$3.5^{+0.1}_{-0.2} \times 10^{10}$	$2.1^{+0.2}_{-0.2} \times 10^{10}$
nircam1-5344	1.23	No	214.96436608	52.96710175	1.25	10.7	200	$5.4^{+0.03}_{-0.02} \times 10^{10}$	$5.3^{+0.5}_{-0.4} \times 10^{10}$
nircam1-5450	2.42	No	215.02614794	53.00863204	1.46	12.2	116	$1.7^{+0.02}_{-0.01} \times 10^{10}$	$1.7^{+0.3}_{-0.07} \times 10^{10}$

(Continued on next page)

Table D.1: (Continued)

Galaxy name	$z$	$z_{\text{spec}}?$	RA <sub>2000</sub> [deg]	Dec <sub>2000</sub> [deg]	Semi-major axis		$N_{\text{cells}}$	M <sub>SB99</sub> [M <sub>⊙</sub> ]	M <sub>BC03</sub> [M <sub>⊙</sub> ]
(1)	(2)	(3)	(4)	(5)	(6)	(7)	(8)	(9)	(10)
nircam1-5714	1.76	No	215.02828906	53.00920605	1.18	10.3	165	$1.9^{+0.002}_{-0.1} \times 10^{11}$	$1.2^{+0.007}_{-0.02} \times 10^{11}$
nircam1-5868	1.54	Yes	215.01118565	52.99391255	1.68	14.7	240	$2.5^{+0.1}_{-0.09} \times 10^{10}$	$1.9^{+0.2}_{-0.2} \times 10^{10}$
nircam1-5968	1.55	No	214.97370815	52.96950823	0.84	7.3	74	$2.0^{+0.1}_{-0.08} \times 10^{10}$	$1.4^{+0.2}_{-0.07} \times 10^{10}$
nircam1-6027	2.52	No	214.94159023	52.94627766	0.81	6.7	66	$6.2^{+0.2}_{-0.08} \times 10^{10}$	$5.0^{+0.3}_{-0.2} \times 10^{10}$
nircam1-6028	2.04	No	214.94214802	52.94641413	1.95	16.7	358	$1.2^{+0.08}_{-0.08} \times 10^{11}$	$9.9^{+0.5}_{-0.5} \times 10^{10}$
nircam1-6070	1.46	No	215.01353362	52.99602772	1.00	8.6	112	$3.7^{+0.2}_{-0.1} \times 10^{10}$	$3.1^{+0.2}_{-0.06} \times 10^{10}$
nircam1-6122	2.24	Yes	214.97749522	52.97162650	0.74	6.2	55	$2.9^{+0.2}_{-0.1} \times 10^{10}$	$2.0^{+0.1}_{-0.06} \times 10^{10}$
nircam1-6205	1.32	No	214.95313048	52.95377059	0.77	6.7	77	$9.2^{+0.06}_{-0.08} \times 10^{10}$	$7.0^{+0.06}_{-0.1} \times 10^{10}$
nircam1-6554	1.68	No	214.96627688	52.96134308	1.34	11.7	185	$1.1^{+0.07}_{-0.1} \times 10^{11}$	$9.9^{+0.03}_{-0.02} \times 10^{10}$
nircam1-6676	2.56	No	215.01853044	52.99800743	0.79	6.5	83	$2.0^{+0.04}_{-0.008} \times 10^{10}$	$1.5^{+0.02}_{-0.03} \times 10^{10}$
nircam1-6696	1.43	No	215.01105937	52.99255913	1.95	16.9	461	$1.5^{+0.1}_{-0.05} \times 10^{11}$	$2.5^{+0.1}_{-0.5} \times 10^{11}$
nircam1-6857	2.40	No	215.01989869	52.99855777	1.12	9.3	135	$7.3^{+0.05}_{-0.6} \times 10^{10}$	$5.3^{+0.2}_{-0.2} \times 10^{10}$
nircam1-6917	1.37	No	214.95901164	52.95474389	0.76	6.6	71	$1.8^{+0.09}_{-0.1} \times 10^{10}$	$1.3^{+0.06}_{-0.08} \times 10^{10}$
nircam1-6972	1.28	Yes	214.95534821	52.95128913	1.87	16.1	354	$1.4^{+0.03}_{-0.03} \times 10^{11}$	$1.3^{+0.07}_{-0.08} \times 10^{11}$
nircam1-7539	1.25	No	214.95706858	52.94944155	1.02	8.7	75	$5.4^{+1.5}_{-3} \times 10^{10}$	$5.3^{+0.4}_{-0.2} \times 10^{10}$
nircam1-7881	1.42	No	214.94986835	52.94355795	0.86	7.5	75	$4.2^{+0.2}_{-0.2} \times 10^{10}$	$3.4^{+0.4}_{-0.4} \times 10^{10}$
nircam1-7915	1.08	No	214.97695194	52.96232643	1.03	8.7	120	$5.8^{+0.03}_{-0.06} \times 10^{10}$	$4.9^{+0.3}_{-0.3} \times 10^{10}$
nircam1-8004	2.35	Yes	214.97098414	52.95733745	0.90	7.5	73	$3.4^{+0.4}_{-0.4} \times 10^{10}$	$2.4^{+0.4}_{-0.2} \times 10^{10}$
nircam1-8217	2.14	No	215.00791709	52.98072325	2.76	23.5	692	$1.8^{+0.1}_{-0.09} \times 10^{11}$	$1.3^{+0.09}_{-0.1} \times 10^{11}$
nircam1-8314	2.37	Yes	214.97095742	52.95767415	1.83	15.3	178	$1.4^{+0.7}_{-0.3} \times 10^{11}$	$1.3^{+0.4}_{-0.2} \times 10^{11}$
nircam1-8402	1.23	Yes	214.95436623	52.94411414	0.81	6.9	88	$6.1^{+0.1}_{-0.2} \times 10^{10}$	$4.1^{+0.3}_{-0.3} \times 10^{10}$
nircam1-8416	1.41	No	214.95401916	52.94341522	0.99	8.6	96	$3.1^{+0.1}_{-0.1} \times 10^{10}$	$2.4^{+0.1}_{-0.1} \times 10^{10}$
nircam1-8464	1.84	No	215.00949770	52.98055850	0.78	6.7	56	$2.3^{+0.2}_{-0.2} \times 10^{10}$	$1.9^{+0.07}_{-0.06} \times 10^{10}$
nircam1-8588	1.73	No	215.00308430	52.97792460	0.90	7.8	76	$7.0^{+1.0}_{-0.4} \times 10^{10}$	$3.7^{+1.1}_{-0.1} \times 10^{10}$
nircam1-8729	3.90	No	215.03905173	53.00277846	0.52	3.8	31	$4.5^{+0.02}_{-0.03} \times 10^{10}$	$2.7^{+0.03}_{-0.1} \times 10^{10}$
nircam1-8904	1.45	No	215.00581678	52.97808877	1.47	12.8	144	$1.5^{+0.1}_{-0.06} \times 10^{10}$	$1.6^{+0.3}_{-0.2} \times 10^{10}$
nircam1-8959	2.41	No	215.01166331	52.98204542	1.10	9.2	108	$2.1^{+0.09}_{-0.08} \times 10^{10}$	$1.8^{+0.03}_{-0.04} \times 10^{10}$
nircam1-9090	1.73	No	215.00808663	52.98196550	1.20	10.4	63	$1.1^{+0.09}_{-0.07} \times 10^{10}$	$1.1^{+0.2}_{-0.1} \times 10^{10}$
nircam1-9185	1.69	No	214.95259082	52.93912216	1.05	9.1	137	$3.1^{+0.09}_{-0.1} \times 10^{10}$	$2.8^{+0.1}_{-0.1} \times 10^{10}$
nircam1-9293	2.04	No	215.04123117	53.00102285	1.92	16.4	195	$7.2^{+0.1}_{-0.08} \times 10^{10}$	$5.4^{+0.3}_{-0.2} \times 10^{10}$
nircam1-9476	1.99	No	215.01016118	52.97839966	1.02	8.8	97	$9.2^{+0.1}_{-0.4} \times 10^{10}$	$5.6^{+0.1}_{-0.1} \times 10^{10}$
nircam1-9565	1.11	No	214.98433623	52.96131846	1.86	15.7	341	$1.2^{+0.01}_{-0.01} \times 10^{11}$	$1.3^{+0.01}_{-0.01} \times 10^{11}$
nircam1-9691	1.71	No	215.02855779	52.99047437	1.17	10.2	107	$7.1^{+0.9}_{-0.3} \times 10^{10}$	$4.7^{+0.3}_{-0.4} \times 10^{10}$
nircam1-9825	1.69	No	215.02974416	52.99091638	1.12	9.8	103	$1.0^{+0.05}_{-0.02} \times 10^{10}$	$1.1^{+0.1}_{-0.1} \times 10^{10}$
nircam1-9859	3.52	No	214.97748276	52.95349135	1.20	8.9	87	$4.2^{+0.3}_{-0.09} \times 10^{10}$	$6.5^{+0.1}_{-0.1} \times 10^{10}$
nircam1-10038	1.01	Yes	215.02490555	52.98689335	1.87	15.5	296	$6.8^{+0.4}_{-0.8} \times 10^{10}$	$6.3^{+0.2}_{-0.3} \times 10^{10}$
nircam1-10087	1.65	No	214.98274720	52.95566706	1.11	9.7	110	$4.0^{+0.6}_{-0.3} \times 10^{10}$	$5.4^{+0.4}_{-0.2} \times 10^{10}$
nircam1-10163	1.27	No	214.96596497	52.94365385	0.77	6.6	78	$4.4^{+0.4}_{-0.6} \times 10^{10}$	$4.1^{+0.3}_{-0.3} \times 10^{10}$
nircam1-10234	1.73	No	215.04548942	52.99954523	1.17	10.2	159	$3.1^{+0.2}_{-0.3} \times 10^{10}$	$2.2^{+0.1}_{-0.1} \times 10^{10}$
nircam1-10398	2.39	Yes	214.96612575	52.94277829	1.25	10.4	164	$1.5^{+0.02}_{-0.01} \times 10^{10}$	$1.3^{+0.009}_{-0.005} \times 10^{10}$
nircam1-10564	1.45	No	215.01930089	52.98055823	1.72	15.0	320	$6.7^{+0.7}_{-0.4} \times 10^{10}$	$5.8^{+0.3}_{-0.2} \times 10^{10}$
nircam1-10634	1.52	No	215.01399066	52.97504813	1.03	9.0	114	$1.4^{+0.1}_{-0.06} \times 10^{10}$	$1.4^{+0.2}_{-0.1} \times 10^{10}$

(Continued on next page)

Table D.1: (Continued)

Galaxy name	$z$	$z_{\text{spec}}?$	RA <sub>2000</sub> [deg]	Dec <sub>2000</sub> [deg]	Semi-major axis		$N_{\text{cells}}$	M <sub>SB99</sub> [M <sub>☉</sub> ]	M <sub>BC03</sub> [M <sub>☉</sub> ]
(1)	(2)	(3)	(4)	(5)	(6)	(7)	(8)	(9)	(10)
nircam1-10770	2.06	No	215.03903446	52.99254487	1.23	10.5	150	$3.5^{+0.1}_{-0.2} \times 10^{10}$	$2.4^{+0.2}_{-0.03} \times 10^{10}$
nircam1-10795	1.28	No	215.02854906	52.98513613	0.98	8.4	88	$1.5^{+0.03}_{-0.01} \times 10^{10}$	$1.1^{+0.5}_{-0.1} \times 10^{10}$
nircam1-11025	1.21	No	214.97322597	52.94472259	0.63	5.4	49	$2.0^{+0.02}_{-0.01} \times 10^{10}$	$2.0^{+0.04}_{-0.009} \times 10^{10}$
nircam1-11036	1.26	Yes	215.04084421	52.99210950	1.27	10.9	141	$2.8^{+0.2}_{-0.1} \times 10^{10}$	$2.9^{+0.2}_{-0.1} \times 10^{10}$
nircam1-11038	1.10	No	215.04530052	52.99538146	0.99	8.3	114	$3.4^{+0.1}_{-0.4} \times 10^{10}$	$2.4^{+0.3}_{-0.3} \times 10^{10}$
nircam1-11048	1.27	No	214.98123276	52.94998185	0.76	6.5	76	$5.7^{+0.9}_{-0.03} \times 10^{10}$	$6.8^{+0.2}_{-0.2} \times 10^{10}$
nircam1-11082	1.66	Yes	214.97575421	52.94622220	1.24	10.8	116	$2.8^{+0.4}_{-0.1} \times 10^{10}$	$3.0^{+0.02}_{-0.06} \times 10^{10}$
nircam1-11242	1.65	No	214.97184638	52.94256186	1.04	9.1	141	$1.4^{+0.1}_{-0.04} \times 10^{10}$	$1.3^{+0.09}_{-0.07} \times 10^{10}$
nircam1-11292	1.59	No	215.03896341	52.98979201	0.69	6.0	57	$2.2^{+1.0}_{-0.1} \times 10^{10}$	$2.5^{+0.01}_{-0.004} \times 10^{10}$
nircam1-11387	1.24	Yes	215.04930137	52.99654317	1.11	9.5	136	$1.8^{+0.1}_{-0.1} \times 10^{10}$	$1.3^{+0.05}_{-0.08} \times 10^{10}$
nircam2-327	2.98	No	214.82930754	52.89392460	0.99	7.8	95	$1.0^{+0.05}_{-0.06} \times 10^{11}$	$1.6^{+0.06}_{-0.09} \times 10^{11}$
nircam2-526	2.10	No	214.82800412	52.89410944	0.61	5.2	42	$3.1^{+0.01}_{-0.03} \times 10^{10}$	$2.7^{+0.1}_{-0.1} \times 10^{10}$
nircam2-640	1.05	Yes	214.90651421	52.94605104	1.04	8.7	127	$7.9^{+0.4}_{-0.3} \times 10^{10}$	$8.2^{+0.4}_{-0.2} \times 10^{10}$
nircam2-739	1.58	Yes	214.84634409	52.90510117	1.17	10.2	159	$2.7^{+0.2}_{-0.2} \times 10^{10}$	$2.4^{+0.2}_{-0.5} \times 10^{10}$
nircam2-797	2.02	No	214.83050576	52.89349776	1.34	11.5	174	$6.2^{+0.6}_{-0.2} \times 10^{10}$	$5.0^{+0.05}_{-0.02} \times 10^{10}$
nircam2-887	2.56	No	214.85925960	52.91154006	0.84	6.9	63	$5.9^{+0.7}_{-0.1} \times 10^{10}$	$6.0^{+0.6}_{-0.5} \times 10^{10}$
nircam2-950	2.07	No	214.85905617	52.91171387	0.82	7.0	55	$7.3^{+0.03}_{-0.04} \times 10^{10}$	$5.2^{+0.8}_{-0.3} \times 10^{10}$
nircam2-1810	2.33	No	214.85208320	52.90975654	0.87	7.3	86	$1.7^{+0.02}_{-0.03} \times 10^{10}$	$1.6^{+0.6}_{-0.3} \times 10^{10}$
nircam2-1823	1.18	Yes	214.91309409	52.94551238	1.00	8.5	111	$6.3^{+0.1}_{-0.2} \times 10^{10}$	$4.9^{+0.4}_{-0.4} \times 10^{10}$
nircam2-2305	2.30	No	214.83749946	52.88945839	1.02	8.6	139	$5.8^{+0.3}_{-0.2} \times 10^{10}$	$4.5^{+0.3}_{-0.3} \times 10^{10}$
nircam2-2368	1.45	No	214.84322710	52.89394828	0.94	8.1	103	$2.7^{+0.5}_{-0.3} \times 10^{10}$	$2.2^{+0.2}_{-0.1} \times 10^{10}$
nircam2-2572	2.09	No	214.83816115	52.88885774	0.68	5.8	54	$2.2^{+0.009}_{-0.02} \times 10^{10}$	$2.3^{+0.005}_{-0.01} \times 10^{10}$
nircam2-2853	1.18	No	214.91329877	52.94074239	1.51	12.9	221	$8.6^{+0.1}_{-0.07} \times 10^{10}$	$9.6^{+0.6}_{-0.6} \times 10^{10}$
nircam2-2927	3.37	No	214.90484984	52.93535040	0.59	4.5	43	$4.5^{+0.2}_{-0.2} \times 10^{10}$	$2.7^{+0.06}_{-0.04} \times 10^{10}$
nircam2-3010	3.60	No	214.87519058	52.91347925	0.63	4.7	51	$1.9^{+0.06}_{-0.05} \times 10^{10}$	$1.1^{+0.03}_{-0.02} \times 10^{10}$
nircam2-3181	1.46	No	214.86603202	52.90607534	0.73	6.4	53	$3.5^{+0.05}_{-0.06} \times 10^{10}$	$3.1^{+0.2}_{-0.2} \times 10^{10}$
nircam2-3236	3.03	No	214.87711333	52.91280748	1.12	8.8	112	$2.3^{+0.3}_{-0.06} \times 10^{10}$	$2.1^{+0.3}_{-0.06} \times 10^{10}$
nircam2-3270	2.79	No	214.90403458	52.93270355	0.62	5.0	43	$5.1^{+0.5}_{-0.2} \times 10^{10}$	$4.1^{+0.02}_{-0.1} \times 10^{10}$
nircam2-4057	2.79	No	214.91105833	52.93312137	0.98	7.9	88	$1.3^{+0.02}_{-0.03} \times 10^{11}$	$9.0^{+0.5}_{-0.3} \times 10^{10}$
nircam2-4165	3.41	No	214.91838652	52.93789103	0.69	5.2	35	$1.1^{+0.3}_{-0.06} \times 10^{10}$	$1.4^{+0.04}_{-0.06} \times 10^{10}$
nircam2-4240	1.74	No	214.86468324	52.89908392	1.32	11.5	151	$9.0^{+0.6}_{-2} \times 10^{10}$	$5.3^{+1.6}_{-0.1} \times 10^{10}$
nircam2-4386	1.10	Yes	214.92110802	52.93793175	2.30	19.3	533	$1.1^{+0.04}_{-0.01} \times 10^{11}$	$7.4^{+2.9}_{-0.4} \times 10^{10}$
nircam2-4406	1.72	No	214.85846242	52.89259307	0.98	8.5	65	$2.7^{+0.2}_{-0.1} \times 10^{10}$	$2.0^{+0.08}_{-0.1} \times 10^{10}$
nircam2-4491	1.29	No	214.88055315	52.90914280	1.33	11.5	155	$2.6^{+0.1}_{-0.08} \times 10^{10}$	$1.5^{+0.2}_{-0.1} \times 10^{10}$
nircam2-4610	1.74	No	214.85813594	52.89115753	1.17	10.2	122	$2.3^{+0.2}_{-0.2} \times 10^{10}$	$1.9^{+0.07}_{-0.06} \times 10^{10}$
nircam2-4650	1.69	No	214.86637529	52.89834988	0.81	7.1	86	$1.9^{+0.1}_{-0.2} \times 10^{10}$	$1.4^{+0.06}_{-0.07} \times 10^{10}$
nircam2-4680	2.15	No	214.87662944	52.90501172	1.14	9.7	135	$1.8^{+0.05}_{-0.04} \times 10^{10}$	$1.3^{+0.04}_{-0.03} \times 10^{10}$
nircam2-4733	1.35	Yes	214.90873387	52.92785571	1.20	10.4	168	$6.0^{+0.4}_{-0.4} \times 10^{10}$	$4.0^{+0.5}_{-0.2} \times 10^{10}$
nircam2-4789	2.29	Yes	214.87590835	52.90459869	1.04	8.7	118	$4.8^{+0.09}_{-0.3} \times 10^{10}$	$3.5^{+0.1}_{-0.1} \times 10^{10}$
nircam2-5041	1.23	No	214.88361806	52.90994213	0.93	8.0	99	$4.6^{+1.5}_{-1} \times 10^{10}$	$2.3^{+0.2}_{-0.08} \times 10^{10}$
nircam2-5342	2.21	No	214.93696020	52.94546289	0.71	6.0	55	$3.0^{+0.2}_{-0.1} \times 10^{10}$	$3.4^{+0.1}_{-0.2} \times 10^{10}$
nircam2-5418	3.22	Yes	214.90496617	52.92240942	1.18	9.1	122	$1.1^{+0.04}_{-0.05} \times 10^{11}$	$5.5^{+0.3}_{-1} \times 10^{10}$

(Continued on next page)

Table D.1: (Continued)

Galaxy name	$z$	$z_{\text{spec}}?$	RA <sub>2000</sub> [deg]	Dec <sub>2000</sub> [deg]	Semi-major axis		$N_{\text{cells}}$	M <sub>SB99</sub> [M <sub>⊙</sub> ]	M <sub>BC03</sub> [M <sub>⊙</sub> ]
(1)	(2)	(3)	(4)	(5)	[arcsec]	[kpc]	(8)	(9)	(10)
nircam2-5904	1.71	No	214.85613887	52.88510518	0.73	6.3	48	$1.6^{+0.1}_{-0.1} \times 10^{10}$	$1.5^{+0.1}_{-0.1} \times 10^{10}$
nircam2-6479	2.47	No	214.85393805	52.88056064	1.36	11.3	136	$3.4^{+1.2}_{-0.5} \times 10^{10}$	$2.1^{+0.4}_{-0.05} \times 10^{10}$
nircam2-6539	3.06	Yes	214.93147784	52.93552773	0.91	7.1	75	$2.1^{+0.5}_{-0.01} \times 10^{10}$	$1.8^{+0.06}_{-0.02} \times 10^{10}$
nircam2-7078	1.73	No	214.88153732	52.89728689	0.55	4.8	37	$4.2^{+0.003}_{-0.01} \times 10^{10}$	$3.5^{+0.002}_{-0.002} \times 10^{10}$
nircam2-7220	1.26	No	214.88839527	52.90143406	0.70	6.0	50	$1.1^{+0.005}_{-0.001} \times 10^{10}$	$1.2^{+0.2}_{-0.1} \times 10^{10}$
nircam2-7309	2.11	No	214.94515346	52.94108039	0.72	6.2	59	$1.7^{+0.2}_{-0.05} \times 10^{10}$	$1.6^{+0.2}_{-0.2} \times 10^{10}$
nircam2-7394	2.84	No	214.86017128	52.88239635	1.48	11.9	207	$1.1^{+0.04}_{-0.03} \times 10^{11}$	$6.7^{+0.1}_{-0.04} \times 10^{10}$
nircam2-7419	3.45	No	214.86605229	52.88425171	0.58	4.4	33	$8.6^{+0.04}_{+0} \times 10^{10}$	$6.2^{+0}_{+0} \times 10^{10}$
nircam2-7423	1.75	No	214.89454935	52.90469884	0.55	4.8	31	$2.0^{+0.008}_{-0.02} \times 10^{10}$	$1.7^{+0.04}_{-0.02} \times 10^{10}$
nircam2-7435	3.47	No	214.86604381	52.88408282	0.75	5.6	45	$6.8^{+0.1}_{-0.09} \times 10^{10}$	$4.1^{+0.06}_{-0.08} \times 10^{10}$
nircam2-7735	3.49	No	214.86704322	52.88327368	0.90	6.8	72	$3.7^{+0.2}_{-0.4} \times 10^{10}$	$2.0^{+0.3}_{-0.1} \times 10^{10}$
nircam2-7952	1.17	Yes	214.87426920	52.88693657	1.89	16.1	365	$1.4^{+0.05}_{-0.03} \times 10^{11}$	$8.4^{+0.8}_{-0.6} \times 10^{10}$
nircam2-8036	1.19	No	214.87263244	52.88550454	1.13	9.6	152	$1.2^{+0.2}_{-0.03} \times 10^{10}$	$1.2^{+0.1}_{-0.07} \times 10^{10}$
nircam2-8313	1.28	No	214.93751082	52.93015741	1.13	9.7	110	$1.7^{+0.07}_{-0.1} \times 10^{10}$	$1.2^{+0.06}_{-0.1} \times 10^{10}$
nircam2-8320	1.18	No	214.87732642	52.88763336	0.81	6.9	79	$2.3^{+0.1}_{-0.2} \times 10^{10}$	$2.6^{+0.004}_{-0.004} \times 10^{10}$
nircam2-8386	2.74	No	214.88830761	52.89492719	0.76	6.1	41	$2.9^{+0.2}_{-0.08} \times 10^{10}$	$2.2^{+0.1}_{-0.1} \times 10^{10}$
nircam2-8529	3.47	No	214.87909817	52.88805928	0.50	3.8	30	$2.6^{+0.04}_{-0.03} \times 10^{10}$	$1.6^{+0.03}_{-0.01} \times 10^{10}$
nircam2-8542	2.32	No	214.95011265	52.93819648	0.77	6.5	75	$8.6^{+0.2}_{-0.1} \times 10^{10}$	$1.1^{+0.3}_{-0.02} \times 10^{11}$
nircam2-9030	3.27	No	214.92575919	52.91852424	0.92	7.1	49	$3.0^{+0.07}_{-0.1} \times 10^{10}$	$1.9^{+0.06}_{-0.2} \times 10^{10}$
nircam2-9096	2.18	No	214.92004560	52.91356745	1.03	8.7	100	$7.8^{+2.3}_{-0.4} \times 10^{10}$	$1.1^{+0.03}_{-0.3} \times 10^{11}$
nircam2-9208	1.70	No	214.95259324	52.93912123	1.30	11.3	196	$2.8^{+0.4}_{-0.3} \times 10^{10}$	$2.7^{+0.4}_{-0.4} \times 10^{10}$
nircam2-9269	2.93	No	214.87874101	52.88356208	1.34	10.7	100	$8.4^{+7.2}_{-0.4} \times 10^{10}$	$6.3^{+0.2}_{-0.06} \times 10^{10}$
nircam2-9307	2.40	No	214.93952957	52.92660526	0.86	7.1	83	$6.0^{+0.5}_{-0.4} \times 10^{10}$	$3.8^{+0.2}_{-0.7} \times 10^{10}$
nircam2-9610	2.50	No	214.87827289	52.88183168	0.54	4.5	39	$1.9^{+0.1}_{-0.1} \times 10^{10}$	$1.3^{+0.02}_{-0.02} \times 10^{10}$
nircam2-9876	2.29	Yes	214.90477374	52.89959323	0.91	7.7	92	$4.1^{+0.2}_{-0.3} \times 10^{10}$	$3.0^{+0.2}_{-0.2} \times 10^{10}$
nircam2-10017	1.07	No	214.94312334	52.92532528	1.80	15.0	396	$1.4^{+0.04}_{-0.03} \times 10^{10}$	$1.1^{+0.04}_{-0.05} \times 10^{10}$
nircam2-10149	2.10	No	214.95007167	52.92991472	0.52	4.4	34	$1.5^{+0.03}_{-0.03} \times 10^{10}$	$1.3^{+0.1}_{-0.1} \times 10^{10}$
nircam2-10186	2.67	No	214.88108076	52.88082333	0.66	5.4	49	$1.5^{+0.04}_{-0.02} \times 10^{10}$	$1.1^{+0.02}_{-0.07} \times 10^{10}$
nircam2-10266	1.58	No	214.87773497	52.87714980	2.08	18.1	175	$1.9^{+0.06}_{-0.09} \times 10^{10}$	$1.7^{+0.2}_{-0.2} \times 10^{10}$
nircam2-10267	1.57	No	214.87811459	52.87650884	2.72	23.7	401	$9.1^{+3.9}_{-0.8} \times 10^{10}$	$1.5^{+0.02}_{-0.02} \times 10^{11}$
nircam2-10367	1.50	Yes	214.93631335	52.91857836	0.98	8.5	117	$2.6^{+0.2}_{-0.3} \times 10^{10}$	$2.3^{+0.1}_{-0.07} \times 10^{10}$
nircam2-10433	2.84	No	214.90242866	52.89423963	1.08	8.7	85	$4.2^{+0.1}_{-0.1} \times 10^{10}$	$3.0^{+0.7}_{-0.01} \times 10^{10}$
nircam2-10446	1.57	No	214.87828463	52.87577860	1.49	13.0	258	$3.6^{+0.1}_{-0.08} \times 10^{10}$	$3.6^{+0.3}_{-0.3} \times 10^{10}$
nircam2-10496	2.29	No	214.87738725	52.87816610	0.98	8.3	85	$1.8^{+0.1}_{-0.06} \times 10^{10}$	$1.4^{+0.1}_{-0.09} \times 10^{10}$
nircam2-10573	1.83	No	214.94797942	52.92576763	0.67	5.8	50	$8.0^{+0.07}_{+0} \times 10^{10}$	$6.1^{+0.04}_{+0} \times 10^{10}$
nircam2-10590	1.40	Yes	214.94016590	52.92061841	1.79	15.5	143	$1.3^{+0.04}_{-0.02} \times 10^{10}$	$2.2^{+0.008}_{-0.004} \times 10^{10}$
nircam2-10591	1.67	Yes	214.95894371	52.93444233	1.27	11.0	136	$4.7^{+0.6}_{-0.6} \times 10^{10}$	$3.9^{+0.5}_{-1} \times 10^{10}$
nircam2-10669	3.12	No	214.87687445	52.87721998	1.42	11.1	213	$3.0^{+0.1}_{-0.2} \times 10^{11}$	$2.1^{+0.05}_{-0.06} \times 10^{11}$
nircam2-10683	2.73	No	214.94564437	52.92424343	1.15	9.3	114	$1.2^{+0.04}_{-0.04} \times 10^{11}$	$9.6^{+0.5}_{-0.6} \times 10^{10}$
nircam3-64	1.34	No	214.74080166	52.83467533	1.39	12.0	180	$1.1^{+0.003}_{-0.002} \times 10^{11}$	$1.0^{+0.1}_{-0.1} \times 10^{11}$
nircam3-185	2.82	No	214.74564897	52.83663176	0.68	5.4	47	$1.4^{+0.08}_{-0.02} \times 10^{10}$	$1.0^{+0.04}_{-0.01} \times 10^{10}$
nircam3-254	1.44	No	214.80003574	52.87594194	0.72	6.2	53	$2.4^{+0.06}_{-0.08} \times 10^{10}$	$2.1^{+0.01}_{-0.003} \times 10^{10}$

(Continued on next page)

Table D.1: (Continued)

Galaxy name	$z$	$z_{\text{spec}}?$	RA <sub>2000</sub> [deg]	Dec <sub>2000</sub> [deg]	Semi-major axis		$N_{\text{cells}}$	$M_{\text{SB99}}$ [ $M_{\odot}$ ]	$M_{\text{BC03}}$ [ $M_{\odot}$ ]
(1)	(2)	(3)	(4)	(5)	(6)	(7)	(8)	(9)	(10)
nircam3-335	2.16	No	214.74420717	52.83544843	0.95	8.0	93	$1.9^{+0.1}_{-0.05} \times 10^{10}$	$1.5^{+0.2}_{-0.08} \times 10^{10}$
nircam3-395	1.26	No	214.79580339	52.87166230	0.69	6.0	57	$1.5^{+0.04}_{-0.02} \times 10^{10}$	$1.5^{+0.1}_{-0.2} \times 10^{10}$
nircam3-513	3.42	No	214.76062446	52.84531499	1.29	9.7	201	$2.5^{+0.09}_{-0.1} \times 10^{11}$	$1.5^{+0.02}_{-0.02} \times 10^{11}$
nircam3-515	2.91	No	214.79377446	52.86896322	1.30	10.3	177	$4.7^{+0.2}_{-0.2} \times 10^{10}$	$4.3^{+0.03}_{-0.03} \times 10^{10}$
nircam3-516	3.63	No	214.76340141	52.84779563	0.99	7.3	84	$5.6^{+0.1}_{-0.2} \times 10^{10}$	$3.2^{+0.04}_{-0.05} \times 10^{10}$
nircam3-592	2.72	No	214.81036349	52.88317959	0.57	4.6	31	$2.8^{+0.03}_{-0.3} \times 10^{10}$	$2.1^{+0.02}_{-0.02} \times 10^{10}$
nircam3-735	1.27	No	214.76872496	52.84869203	1.66	14.2	304	$1.9^{+0.2}_{-0.05} \times 10^{10}$	$1.2^{+0.07}_{-0.05} \times 10^{10}$
nircam3-924	3.56	No	214.79665315	52.86955279	3.08	23.0	240	$1.1^{+0.005}_{+0} \times 10^{11}$	$8.4^{+0.02}_{-0.01} \times 10^{10}$
nircam3-980	1.11	No	214.74198255	52.83032302	0.70	5.9	64	$1.5^{+0.01}_{-0.02} \times 10^{10}$	$1.5^{+0.03}_{-0.02} \times 10^{10}$
nircam3-1033	1.68	No	214.74078117	52.82926986	0.99	8.6	122	$3.1^{+0.4}_{-0.3} \times 10^{10}$	$2.6^{+0.3}_{-0.2} \times 10^{10}$
nircam3-1095	2.58	No	214.82802143	52.89410982	0.56	4.6	41	$4.2^{+0.02}_{-0.1} \times 10^{10}$	$2.3^{+0.3}_{-0.03} \times 10^{10}$
nircam3-1143	2.72	No	214.81988023	52.88486911	1.54	12.5	115	$3.0^{+0.05}_{-0.03} \times 10^{10}$	$3.0^{+0.08}_{-0.04} \times 10^{10}$
nircam3-1144	1.06	No	214.82476904	52.88821225	0.94	7.9	114	$3.3^{+0.04}_{-0.06} \times 10^{10}$	$3.3^{+0.005}_{-0.2} \times 10^{10}$
nircam3-1481	3.00	No	214.76316919	52.84287430	0.79	6.3	69	$1.8^{+0.3}_{-0.05} \times 10^{10}$	$1.6^{+0.07}_{-0.06} \times 10^{10}$
nircam3-1548	3.47	Yes	214.75524370	52.83678948	0.59	4.4	44	$4.0^{+0.04}_{-0.02} \times 10^{10}$	$3.1^{+0.03}_{-0.02} \times 10^{10}$
nircam3-1668	1.66	No	214.76432567	52.84323037	1.09	9.4	129	$1.8^{+0.1}_{-0.3} \times 10^{10}$	$1.1^{+0.04}_{-0.04} \times 10^{10}$
nircam3-1760	1.10	Yes	214.82244814	52.88349661	1.41	11.8	205	$6.8^{+0.07}_{-0.06} \times 10^{10}$	$5.3^{+0.4}_{-0.2} \times 10^{10}$
nircam3-1779	2.95	No	214.77240019	52.84804407	0.73	5.8	56	$4.2^{+0.1}_{-0.1} \times 10^{10}$	$3.6^{+0.07}_{-0.08} \times 10^{10}$
nircam3-1787	1.23	No	214.76331363	52.84098645	0.75	6.4	69	$3.8^{+0.03}_{-0.01} \times 10^{10}$	$3.6^{+0.5}_{-0.5} \times 10^{10}$
nircam3-2119	1.71	No	214.76935395	52.84404602	1.23	10.7	117	$3.2^{+0.2}_{-0.4} \times 10^{10}$	$2.5^{+0.1}_{-0.1} \times 10^{10}$
nircam3-2161	2.71	No	214.82472625	52.88359245	0.54	4.4	36	$5.2^{+0.2}_{-0.1} \times 10^{10}$	$3.5^{+0.01}_{-0.008} \times 10^{10}$
nircam3-2223	1.83	No	214.80732674	52.87114049	0.45	3.9	26	$3.0^{+0.02}_{+0} \times 10^{10}$	$2.2^{+0.01}_{+0} \times 10^{10}$
nircam3-2238	1.72	No	214.75018765	52.83084761	1.78	15.4	152	$4.5^{+0.7}_{-0.4} \times 10^{10}$	$4.2^{+0.04}_{-0.05} \times 10^{10}$
nircam3-2387	1.64	No	214.76195760	52.83771710	0.83	7.3	71	$3.3^{+0.3}_{-0.5} \times 10^{10}$	$3.4^{+0.3}_{-0.1} \times 10^{10}$
nircam3-2521	1.77	No	214.74890056	52.82996380	1.24	10.8	159	$9.3^{+0.3}_{-0.9} \times 10^{10}$	$7.8^{+0.2}_{-0.2} \times 10^{10}$
nircam3-2527	1.74	No	214.75073696	52.82985729	0.71	6.2	54	$3.1^{+0.05}_{-0.08} \times 10^{10}$	$2.5^{+0.2}_{-0.1} \times 10^{10}$
nircam3-2552	1.71	No	214.74943762	52.82947943	1.07	9.3	104	$4.3^{+0.1}_{-0.9} \times 10^{10}$	$3.2^{+0.2}_{-0.1} \times 10^{10}$
nircam3-2578	1.70	No	214.75254237	52.83105745	0.85	7.4	72	$2.3^{+0.2}_{-0.2} \times 10^{10}$	$1.5^{+0.1}_{-0.06} \times 10^{10}$
nircam3-2598	3.01	No	214.75113049	52.83007884	0.76	6.0	52	$5.2^{+0.1}_{-0.1} \times 10^{11}$	$4.1^{+0.03}_{-0.03} \times 10^{11}$
nircam3-2789	2.56	No	214.77808248	52.84755691	1.22	10.0	142	$2.8^{+0.1}_{-0.1} \times 10^{10}$	$2.1^{+0.2}_{-0.1} \times 10^{10}$
nircam3-2885	1.70	No	214.75629852	52.83184792	1.01	8.8	78	$1.2^{+0.009}_{-0.1} \times 10^{10}$	$1.0^{+0.08}_{-0.07} \times 10^{10}$
nircam3-2944	2.78	No	214.81194898	52.87090005	1.07	8.6	117	$1.5^{+0.08}_{-0.06} \times 10^{11}$	$1.2^{+0.04}_{-0.05} \times 10^{11}$
nircam3-2956	2.17	Yes	214.81242858	52.87089931	1.04	8.8	90	$2.1^{+0.08}_{-0.1} \times 10^{10}$	$2.8^{+0.5}_{-0.5} \times 10^{10}$
nircam3-3069	2.32	No	214.83651309	52.88797625	1.10	9.2	94	$2.6^{+0.2}_{-0.1} \times 10^{10}$	$1.9^{+0.1}_{-0.08} \times 10^{10}$
nircam3-3104	3.42	No	214.82580314	52.88008725	1.08	8.2	105	$2.2^{+0.05}_{-0.02} \times 10^{10}$	$1.6^{+0.02}_{-0.01} \times 10^{10}$
nircam3-3217	1.71	No	214.74877180	52.82503854	1.13	9.8	119	$2.5^{+0.2}_{-0.2} \times 10^{10}$	$1.9^{+0.1}_{-0.2} \times 10^{10}$
nircam3-3243	1.82	No	214.77552077	52.84408293	0.62	5.4	43	$1.4^{+0.1}_{-0.2} \times 10^{10}$	$1.5^{+0.5}_{-0.04} \times 10^{10}$
nircam3-3339	1.70	No	214.76419696	52.83533990	1.37	11.9	141	$5.9^{+0}_{-0.004} \times 10^{10}$	$5.0^{+0.005}_{-0.01} \times 10^{10}$
nircam3-3461	1.61	No	214.77188523	52.84268569	1.15	10.0	109	$5.5^{+0.03}_{-0.1} \times 10^{10}$	$3.3^{+0.07}_{-0.1} \times 10^{10}$
nircam3-3539	1.01	Yes	214.83097324	52.88168808	1.29	10.7	145	$1.1^{+0.04}_{-0.05} \times 10^{11}$	$9.5^{+2.1}_{-0.2} \times 10^{10}$
nircam3-3544	1.63	Yes	214.77804805	52.84429968	1.36	11.9	174	$3.8^{+0.2}_{-0.2} \times 10^{10}$	$3.2^{+0.04}_{-0.2} \times 10^{10}$
nircam3-3622	1.09	No	214.83582410	52.88556261	1.43	12.0	216	$1.6^{+0.05}_{-0.02} \times 10^{10}$	$1.3^{+0.05}_{-0.04} \times 10^{10}$

(Continued on next page)



Table D.1: (Continued)

Galaxy name	$z$	$z_{\text{spec}}?$	RA <sub>2000</sub> [deg]	Dec <sub>2000</sub> [deg]	Semi-major axis		$N_{\text{cells}}$	M <sub>SB99</sub> [M <sub>⊙</sub> ]	M <sub>BC03</sub> [M <sub>⊙</sub> ]
(1)	(2)	(3)	(4)	(5)	[arcsec]	[kpc]	(8)	(9)	(10)
nircam3-3679	2.60	No	214.81946888	52.87287895	1.43	11.8	215	$2.2^{+0.3}_{-0.1} \times 10^{11}$	$3.1^{+0.03}_{-0.09} \times 10^{11}$
nircam3-3864	2.42	No	214.83817447	52.88738449	0.76	6.4	66	$6.2^{+0.5}_{-0.2} \times 10^{10}$	$4.7^{+0.3}_{-0.3} \times 10^{10}$
nircam3-4244	1.18	Yes	214.82961246	52.87776893	1.32	11.2	159	$7.1^{+0.03}_{-0.3} \times 10^{10}$	$4.8^{+0.6}_{-0.2} \times 10^{10}$
nircam3-4581	2.85	No	214.80535506	52.85932281	0.68	5.5	67	$1.4^{+0.1}_{-0.2} \times 10^{10}$	$1.1^{+0.02}_{-0.02} \times 10^{10}$
nircam3-4769	2.31	No	214.81149286	52.86267503	0.66	5.6	41	$1.1^{+0.1}_{-0.09} \times 10^{10}$	$1.5^{+0.2}_{-0.3} \times 10^{10}$
nircam3-5478	1.12	No	214.78532914	52.84023969	0.82	7.0	92	$3.5^{+0.01}_{-0.009} \times 10^{10}$	$2.9^{+0.08}_{-0.08} \times 10^{10}$
nircam3-5633	1.39	No	214.83773024	52.87705702	1.15	10.0	142	$6.3^{+0.2}_{-0.2} \times 10^{10}$	$5.0^{+0.1}_{-0.2} \times 10^{10}$
nircam3-5757	2.72	No	214.83571036	52.87530890	0.68	5.5	47	$2.6^{+0.1}_{-0.09} \times 10^{10}$	$1.8^{+0.002}_{-0.002} \times 10^{10}$
nircam3-5848	3.28	No	214.81315640	52.85891774	0.68	5.2	52	$3.2^{+0.2}_{-0.2} \times 10^{10}$	$1.7^{+0.1}_{-0.3} \times 10^{10}$
nircam3-6288	1.72	No	214.78223969	52.83491277	0.66	5.7	51	$2.6^{+0.3}_{-0.1} \times 10^{10}$	$2.1^{+0.2}_{-0.2} \times 10^{10}$
nircam3-6437	3.34	No	214.83685708	52.87344970	0.61	4.7	44	$4.7^{+0.2}_{-0.2} \times 10^{10}$	$2.9^{+0.09}_{-0.1} \times 10^{10}$
nircam3-6471	1.54	Yes	214.84318223	52.87671526	1.29	11.2	189	$3.1^{+0.4}_{-0.5} \times 10^{10}$	$3.5^{+0.4}_{-0.4} \times 10^{10}$
nircam3-6517	2.32	Yes	214.83404417	52.87010221	0.93	7.8	61	$3.4^{+0.06}_{-0.03} \times 10^{10}$	$6.1^{+0.1}_{-0.2} \times 10^{10}$
nircam3-6621	2.18	No	214.78571042	52.83607275	0.52	4.4	35	$3.8^{+0.03}_{-0.03} \times 10^{10}$	$2.8^{+0.04}_{-0.02} \times 10^{10}$
nircam3-6644	3.13	No	214.79593389	52.84319598	1.30	10.1	110	$2.7^{+0.06}_{-0.07} \times 10^{10}$	$2.9^{+0.2}_{-0.3} \times 10^{10}$
nircam3-6739	1.68	No	214.78266657	52.83259120	1.66	14.4	271	$1.7^{+0.05}_{-0.08} \times 10^{10}$	$1.4^{+0.09}_{-0.07} \times 10^{10}$
nircam3-7007	3.45	No	214.79149194	52.83803597	1.04	7.9	95	$2.8^{+0.1}_{-0.2} \times 10^{11}$	$1.9^{+0.05}_{-0.03} \times 10^{11}$
nircam3-7412	1.43	No	214.84763250	52.87610052	0.89	7.7	86	$2.1^{+0.1}_{-0.08} \times 10^{10}$	$1.8^{+0.04}_{-0.03} \times 10^{10}$
nircam3-7579	2.27	Yes	214.77684315	52.82587999	0.74	6.2	71	$5.0^{+0.1}_{-0.08} \times 10^{10}$	$3.5^{+0.1}_{-0.1} \times 10^{10}$
nircam3-7695	3.47	No	214.76722738	52.81771171	0.84	6.3	75	$3.5^{+0.04}_{-0.04} \times 10^{10}$	$2.2^{+0.03}_{-0.07} \times 10^{10}$
nircam3-7701	2.76	No	214.80105351	52.84164136	0.96	7.8	107	$4.0^{+0.01}_{-0.02} \times 10^{10}$	$3.2^{+0.1}_{-0.2} \times 10^{10}$
nircam3-7956	1.24	No	214.82413599	52.85699419	1.17	10.0	150	$2.6^{+0.1}_{-0.3} \times 10^{10}$	$1.7^{+0.1}_{-0.07} \times 10^{10}$
nircam3-8098	1.62	No	214.84732408	52.87320953	0.81	7.0	66	$2.3^{+0.3}_{-0.2} \times 10^{10}$	$1.7^{+0.06}_{-0.1} \times 10^{10}$
nircam3-8401	1.71	No	214.79301829	52.83249678	1.04	9.1	112	$1.1^{+0.09}_{-0.4} \times 10^{11}$	$1.3^{+0.06}_{-0.07} \times 10^{11}$
nircam3-8558	2.31	Yes	214.85091117	52.87345377	1.07	9.0	121	$1.8^{+0.05}_{-0.08} \times 10^{10}$	$1.6^{+0.08}_{-0.1} \times 10^{10}$
nircam3-8596	2.44	No	214.84941093	52.87304314	0.90	7.4	86	$2.7^{+0.5}_{-0.06} \times 10^{10}$	$2.1^{+0.04}_{-0.02} \times 10^{10}$
nircam3-8852	3.32	No	214.78568917	52.82581880	0.80	6.1	65	$9.5^{+0.3}_{-0.3} \times 10^{10}$	$6.0^{+0.2}_{-0.1} \times 10^{10}$
nircam3-8980	1.73	No	214.79485889	52.83152414	1.11	9.6	155	$2.9^{+0.05}_{-0.03} \times 10^{10}$	$2.4^{+0.2}_{-0.1} \times 10^{10}$
nircam3-9142	3.39	No	214.85825942	52.87609018	0.53	4.0	25	$1.7^{+0.2}_{-0.2} \times 10^{10}$	$1.2^{+0.05}_{-0.05} \times 10^{10}$
nircam3-9199	1.76	No	214.78196558	52.82095742	1.58	13.7	225	$4.5^{+0.4}_{-0.1} \times 10^{10}$	$5.4^{+1.4}_{-0.3} \times 10^{10}$
nircam3-9667	2.29	Yes	214.83911979	52.86007024	0.59	4.9	41	$3.3^{+0.3}_{-0.2} \times 10^{10}$	$1.9^{+0.1}_{-0.05} \times 10^{10}$
nircam3-9784	1.73	No	214.80112587	52.83110479	1.32	11.4	126	$1.5^{+0.06}_{-0.05} \times 10^{10}$	$1.4^{+0.2}_{-0.08} \times 10^{10}$
nircam3-9865	3.68	No	214.85057925	52.86601995	0.55	4.1	26	$8.4^{+0.1}_{-0.1} \times 10^{10}$	$5.2^{+0.05}_{-0.05} \times 10^{10}$
nircam3-9866	2.48	No	214.85058830	52.86641404	1.51	12.5	271	$1.9^{+0.1}_{-0.09} \times 10^{11}$	$1.4^{+0.07}_{-0.04} \times 10^{11}$
nircam3-10039	1.70	No	214.80059393	52.83162516	1.43	12.4	144	$3.6^{+0.3}_{-0.3} \times 10^{10}$	$2.9^{+0.2}_{-0.2} \times 10^{10}$
nircam3-10103	1.71	No	214.79958394	52.82898913	1.01	8.8	97	$3.3^{+0.3}_{-0.4} \times 10^{10}$	$2.7^{+0.5}_{-0.3} \times 10^{10}$
nircam3-10226	2.77	No	214.77737193	52.81260531	1.05	8.5	127	$1.6^{+0.01}_{-0.01} \times 10^{10}$	$1.5^{+0.02}_{-0.03} \times 10^{10}$
nircam3-10290	1.84	No	214.85386020	52.86680097	0.97	8.4	127	$1.5^{+0.1}_{-0.1} \times 10^{10}$	$1.2^{+0.09}_{-0.08} \times 10^{10}$
nircam3-10630	3.56	No	214.80029871	52.82706344	0.98	7.3	79	$1.1^{+0.09}_{-0.04} \times 10^{11}$	$1.2^{+0.4}_{-0.3} \times 10^{11}$
nircam3-10688	1.81	No	214.82944473	52.84760732	0.63	5.4	41	$1.5^{+1.5}_{-0.3} \times 10^{10}$	$1.6^{+0.06}_{-0.03} \times 10^{10}$
nircam3-10755	1.33	No	214.78611520	52.81594121	1.15	10.0	127	$4.0^{+0.04}_{-0.03} \times 10^{10}$	$3.9^{+0.2}_{-0.2} \times 10^{10}$
nircam3-10791	1.23	No	214.83391039	52.84955038	1.45	12.4	226	$1.2^{+0.07}_{-0.09} \times 10^{11}$	$1.2^{+0.02}_{-0.4} \times 10^{11}$

(Continued on next page)

Table D.1: (Continued)

Galaxy name	$z$	$z_{\text{spec}}?$	RA <sub>2000</sub> [deg]	Dec <sub>2000</sub> [deg]	Semi-major axis		$N_{\text{cells}}$	M <sub>SB99</sub> [M <sub>☉</sub> ]	M <sub>BC03</sub> [M <sub>☉</sub> ]
(1)	(2)	(3)	(4)	(5)	[arcsec]	[kpc]	(8)	(9)	(10)
nircam3-11158	1.70	No	214.81173070	52.83275015	0.85	7.4	80	$1.7^{+0.1}_{-0.1} \times 10^{10}$	$1.5^{+0.08}_{-0.08} \times 10^{10}$
nircam3-11245	3.52	No	214.85390175	52.86135518	1.00	7.5	89	$2.4^{+0.009}_{-0.04} \times 10^{11}$	$1.5^{+0.01}_{-0.03} \times 10^{11}$
nircam3-11248	1.27	No	214.85338584	52.86164262	0.79	6.8	58	$3.7^{+0.02}_{-0.01} \times 10^{10}$	$3.0^{+0.08}_{-0.06} \times 10^{10}$
nircam3-11615	1.77	No	214.86408634	52.86794846	0.72	6.2	58	$1.3^{+0.1}_{-0.06} \times 10^{10}$	$1.0^{+0.09}_{-0.03} \times 10^{10}$
nircam3-11637	3.30	No	214.79996984	52.82209160	0.47	3.6	24	$2.0^{+0.01}_{-0.04} \times 10^{10}$	$1.1^{+0.02}_{-0.01} \times 10^{10}$
nircam6-444	1.29	No	214.84496799	52.84928779	0.84	7.2	81	$5.3^{+0.4}_{-0.05} \times 10^{10}$	$4.3^{+0.2}_{-0.2} \times 10^{10}$
nircam6-575	3.46	No	214.85982010	52.86065583	1.08	8.1	108	$1.2^{+0.04}_{-0.04} \times 10^{11}$	$7.9^{+0.2}_{-0.2} \times 10^{10}$
nircam6-660	2.68	No	214.80457131	52.81976629	0.83	6.7	61	$4.8^{+0.1}_{-0.06} \times 10^{10}$	$4.3^{+0.2}_{-0.07} \times 10^{10}$
nircam6-688	2.12	No	214.84461133	52.85011675	1.57	13.4	221	$3.2^{+0.07}_{-0.04} \times 10^{10}$	$2.9^{+0.06}_{-0.04} \times 10^{10}$
nircam6-775	1.20	No	214.81232459	52.82476213	0.51	4.3	22	$2.1^{+0.1}_{-0.05} \times 10^{10}$	$1.5^{+0.3}_{-0.07} \times 10^{10}$
nircam6-939	1.40	No	214.88093781	52.87360026	0.89	7.7	86	$5.6^{+0.2}_{-0.2} \times 10^{10}$	$4.4^{+0.07}_{-0.06} \times 10^{10}$
nircam6-968	1.30	No	214.87025675	52.86508183	0.70	6.1	53	$5.6^{+0.1}_{-0.1} \times 10^{10}$	$4.0^{+0.2}_{-0.2} \times 10^{10}$
nircam6-1029	1.39	No	214.87076745	52.86482345	2.10	18.2	179	$6.2^{+1.3}_{-0.2} \times 10^{10}$	$6.5^{+0.03}_{-0.1} \times 10^{10}$
nircam6-1177	1.29	No	214.81232300	52.82501783	1.48	12.8	218	$3.1^{+0.01}_{-0.01} \times 10^{11}$	$3.2^{+0.03}_{-0.04} \times 10^{11}$
nircam6-1868	1.40	Yes	214.86109429	52.85466711	1.46	12.7	183	$4.5^{+0.3}_{-0.2} \times 10^{10}$	$3.4^{+0.03}_{-0.01} \times 10^{10}$
nircam6-1890	1.19	No	214.82329166	52.82763015	0.84	7.2	87	$3.5^{+0.04}_{-0.02} \times 10^{10}$	$3.1^{+0.5}_{-0.3} \times 10^{10}$
nircam6-1959	1.39	No	214.88510978	52.87122517	0.87	7.5	85	$4.4^{+0.2}_{-0.2} \times 10^{10}$	$3.9^{+0.07}_{-0.07} \times 10^{10}$
nircam6-2317	1.69	No	214.82912182	52.83016913	0.76	6.6	57	$1.8^{+0.2}_{-0.1} \times 10^{10}$	$1.3^{+0.08}_{-0.05} \times 10^{10}$
nircam6-2347	3.12	No	214.85540774	52.84880879	1.18	9.2	133	$1.4^{+0.06}_{-0.2} \times 10^{11}$	$1.1^{+0.04}_{-0.05} \times 10^{11}$
nircam6-2383	1.97	No	214.85080041	52.84544039	0.67	5.7	51	$3.2^{+0.07}_{-0.2} \times 10^{10}$	$1.9^{+0.04}_{-0.01} \times 10^{10}$
nircam6-2762	2.82	No	214.83488277	52.83239077	0.64	5.1	45	$1.9^{+0.2}_{-0.08} \times 10^{10}$	$1.7^{+0.01}_{-0.009} \times 10^{10}$
nircam6-2958	1.71	No	214.82268344	52.82268850	1.00	8.7	109	$6.2^{+0.2}_{-0.04} \times 10^{10}$	$1.3^{+0.004}_{-0.01} \times 10^{11}$
nircam6-2991	1.80	Yes	214.82273417	52.82260294	0.20	1.8	2	$1.4^{+0.1}_{-0.2} \times 10^{10}$	$1.8^{+0.04}_{-0.05} \times 10^{10}$
nircam6-3216	2.15	No	214.81131879	52.81356818	0.72	6.1	52	$5.8^{+0.1}_{-0.1} \times 10^{10}$	$4.8^{+0.4}_{-0.3} \times 10^{10}$
nircam6-3217	2.88	No	214.87694152	52.86038916	0.90	7.2	72	$3.4^{+0.2}_{-0.2} \times 10^{10}$	$3.3^{+0.02}_{-0.02} \times 10^{10}$
nircam6-3231	2.65	No	214.86648013	52.85269687	0.96	7.9	103	$8.0^{+0.4}_{-0.4} \times 10^{10}$	$6.1^{+0.4}_{-0.1} \times 10^{10}$
nircam6-3604	1.84	No	214.83728353	52.83038716	0.80	6.9	64	$1.4^{+0.06}_{-0.09} \times 10^{10}$	$1.2^{+0.07}_{-0.1} \times 10^{10}$
nircam6-3650	3.08	No	214.82773594	52.82376795	0.68	5.3	47	$5.5^{+0.08}_{-0.07} \times 10^{10}$	$3.6^{+0.06}_{-0.04} \times 10^{10}$
nircam6-3730	3.31	No	214.86940649	52.85253584	0.85	6.5	71	$1.4^{+0.08}_{-0.03} \times 10^{10}$	$1.1^{+0.02}_{-0.01} \times 10^{10}$
nircam6-3995	1.08	No	214.88298264	52.86166618	0.77	6.5	70	$4.8^{+0.3}_{-0.1} \times 10^{10}$	$4.6^{+0.01}_{-0.06} \times 10^{10}$
nircam6-4042	1.70	No	214.83586087	52.82573098	1.43	12.4	128	$2.7^{+0.4}_{-0.5} \times 10^{10}$	$1.5^{+0.1}_{-0.09} \times 10^{10}$
nircam6-4751	1.43	No	214.86638951	52.84567402	0.93	8.1	95	$1.4^{+0.1}_{-0.07} \times 10^{10}$	$1.3^{+0.09}_{-0.05} \times 10^{10}$
nircam6-4891	1.93	No	214.82116115	52.81247671	0.74	6.4	68	$5.0^{+0.2}_{-0.07} \times 10^{10}$	$3.8^{+0.2}_{-0.6} \times 10^{10}$
nircam6-5284	2.89	No	214.84034065	52.82495510	0.73	5.9	40	$1.1^{+0.02}_{-0.07} \times 10^{11}$	$7.1^{+0.4}_{-2} \times 10^{10}$
nircam6-5398	3.67	No	214.87066962	52.84610637	0.67	4.9	29	$2.8^{+0.05}_{-0.08} \times 10^{10}$	$1.7^{+0.03}_{-0.03} \times 10^{10}$
nircam6-5655	3.46	No	214.87123380	52.84506790	1.06	7.9	144	$8.9^{+0.2}_{-0.4} \times 10^{10}$	$6.7^{+0.2}_{-0.5} \times 10^{10}$
nircam6-5662	1.04	No	214.88619519	52.85712320	2.52	21.0	769	$2.5^{+0.1}_{-0.06} \times 10^{11}$	$2.6^{+0.08}_{-0.08} \times 10^{11}$
nircam6-5824	1.29	No	214.86897154	52.84275338	1.22	10.5	118	$6.6^{+0.2}_{-0.1} \times 10^{10}$	$6.7^{+0.2}_{-2} \times 10^{10}$
nircam6-5946	3.67	No	214.81265674	52.80517326	1.15	8.5	76	$1.5^{+0.008}_{-0.008} \times 10^{10}$	$1.1^{+0.05}_{-0.02} \times 10^{10}$
nircam6-6491	2.34	Yes	214.87240920	52.84244733	0.91	7.7	80	$4.4^{+0.2}_{-0.2} \times 10^{10}$	$2.9^{+0.2}_{-0.2} \times 10^{10}$
nircam6-6558	1.27	No	214.83287382	52.81429157	0.85	7.3	84	$3.9^{+0.2}_{-0.02} \times 10^{10}$	$4.7^{+0.2}_{-0.2} \times 10^{10}$
nircam6-6710	1.67	Yes	214.81554711	52.80001477	1.12	9.7	103	$3.0^{+0.3}_{-0.4} \times 10^{10}$	$2.4^{+0.3}_{-0.2} \times 10^{10}$

(Continued on next page)

Table D.1: (Continued)

Galaxy name	$z$	$z_{\text{spec}}?$	RA <sub>2000</sub> [deg]	Dec <sub>2000</sub> [deg]	Semi-major axis		$N_{\text{cells}}$	$M_{\text{SB99}}$ [ $M_{\odot}$ ]	$M_{\text{BC03}}$ [ $M_{\odot}$ ]
(1)	(2)	(3)	(4)	(5)	[arcsec]	[kpc]	(8)	(9)	(10)
nircam6-6741	1.03	No	214.89942466	52.86030461	1.40	11.6	174	$2.5^{+0.1}_{-0.04} \times 10^{10}$	$2.2^{+0.3}_{-0.3} \times 10^{10}$
nircam6-6830	1.53	Yes	214.85085129	52.82586813	1.04	9.0	98	$2.2^{+0.1}_{-0.2} \times 10^{10}$	$1.2^{+0.05}_{-0.02} \times 10^{10}$
nircam6-6832	1.72	No	214.85126530	52.82560650	1.00	8.7	93	$1.9^{+0.1}_{-0.1} \times 10^{10}$	$1.6^{+0.2}_{-0.1} \times 10^{10}$
nircam6-7113	3.13	No	214.89561652	52.85649304	0.71	5.5	65	$1.2^{+0.01}_{-0.01} \times 10^{11}$	$7.8^{+0.03}_{-0.007} \times 10^{10}$
nircam6-7223	1.50	No	214.81780708	52.80111690	1.03	9.0	92	$2.8^{+0.1}_{-0.09} \times 10^{10}$	$1.8^{+0.2}_{-0.2} \times 10^{10}$
nircam6-7384	1.89	No	214.90188439	52.85985089	0.87	7.5	86	$1.5^{+0.04}_{-0.02} \times 10^{10}$	$1.2^{+0.07}_{-0.03} \times 10^{10}$
nircam6-7452	1.52	No	214.86821835	52.83549506	0.90	7.8	85	$1.2^{+0.01}_{-0.05} \times 10^{10}$	$1.2^{+0.02}_{-0.2} \times 10^{10}$
nircam6-7600	1.69	No	214.88018496	52.84331802	1.03	9.0	129	$1.2^{+0.02}_{-0.007} \times 10^{10}$	$1.1^{+0.07}_{-0.06} \times 10^{10}$
nircam6-7645	3.05	No	214.82909042	52.80846397	0.20	1.6	5	$5.7^{+0.09}_{-0.04} \times 10^{10}$	$4.1^{+0.1}_{-0.1} \times 10^{10}$
nircam6-7670	2.00	No	214.88127734	52.84377593	1.37	11.8	197	$4.0^{+0.3}_{-0.2} \times 10^{10}$	$3.0^{+0.1}_{-0.2} \times 10^{10}$
nircam6-7699	1.55	No	214.82924776	52.80843600	1.89	16.5	305	$2.5^{+0.09}_{-0.1} \times 10^{11}$	$2.1^{+0.05}_{-0.07} \times 10^{11}$
nircam6-7837	1.48	No	214.82950647	52.80554676	0.80	7.0	79	$5.7^{+0.08}_{-0.2} \times 10^{10}$	$4.1^{+0.06}_{-0.06} \times 10^{10}$
nircam6-7928	1.42	No	214.87462407	52.83793640	1.14	9.9	130	$3.0^{+0.2}_{-0.1} \times 10^{10}$	$2.3^{+0.3}_{-0.1} \times 10^{10}$
nircam6-8012	1.57	No	214.82507189	52.80209427	0.95	8.3	99	$4.2^{+0.3}_{-0.2} \times 10^{10}$	$3.7^{+0.2}_{-0.2} \times 10^{10}$
nircam6-8094	2.32	No	214.87317757	52.83632713	0.86	7.3	77	$1.9^{+0.3}_{-0.09} \times 10^{10}$	$1.5^{+0.06}_{-0.1} \times 10^{10}$
nircam6-8103	1.44	No	214.87455928	52.83731456	1.85	16.0	168	$3.7^{+0.2}_{-1} \times 10^{10}$	$3.5^{+0.04}_{-0.02} \times 10^{10}$
nircam6-8159	2.93	No	214.81809995	52.79687080	0.55	4.4	40	$1.4^{+0.008}_{-0.004} \times 10^{10}$	$1.4^{+0.02}_{-0.04} \times 10^{10}$
nircam6-8295	1.70	No	214.84961067	52.81844090	1.14	9.9	101	$1.5^{+0.8}_{-0.2} \times 10^{10}$	$1.5^{+0.3}_{-0.2} \times 10^{10}$
nircam6-8355	3.05	No	214.83257820	52.80542414	1.40	11.0	243	$3.0^{+0.02}_{-0.03} \times 10^{11}$	$2.1^{+0.03}_{-0.03} \times 10^{11}$
nircam6-8473	1.59	Yes	214.82138084	52.79782889	1.83	16.0	416	$8.5^{+0.7}_{-0.6} \times 10^{10}$	$6.0^{+0.06}_{-0.06} \times 10^{10}$
nircam6-8572	1.74	No	214.90642983	52.85720090	1.91	16.6	365	$1.3^{+0.05}_{-0.03} \times 10^{11}$	$7.8^{+1.0}_{-0.8} \times 10^{10}$
nircam6-8691	1.54	Yes	214.83206252	52.80398896	1.36	11.8	223	$5.7^{+0.4}_{-0.5} \times 10^{10}$	$4.0^{+0.2}_{-0.1} \times 10^{10}$
nircam6-8778	1.75	No	214.84479784	52.81284317	0.89	7.7	87	$4.0^{+0.3}_{-0.3} \times 10^{10}$	$2.8^{+0.3}_{-0.3} \times 10^{10}$
nircam6-8796	2.74	No	214.89670579	52.84979078	0.84	6.8	63	$3.1^{+0.3}_{-0.03} \times 10^{10}$	$2.2^{+0.008}_{-0.005} \times 10^{10}$
nircam6-8878	1.49	No	214.84145045	52.81096964	0.63	5.5	26	$6.1^{+0.1}_{-0.1} \times 10^{10}$	$3.2^{+0.4}_{-0.3} \times 10^{10}$
nircam6-9375	1.75	No	214.88583115	52.83973754	1.05	9.1	114	$3.6^{+0.009}_{-0.01} \times 10^{10}$	$3.6^{+0.5}_{-0.5} \times 10^{10}$
nircam6-9559	1.69	No	214.84546341	52.81043802	0.82	7.1	78	$1.7^{+0.04}_{-0.1} \times 10^{10}$	$1.5^{+0.2}_{-0.1} \times 10^{10}$
nircam6-10556	3.89	No	214.85021575	52.80899032	1.36	9.8	156	$2.4^{+0.09}_{-0.1} \times 10^{11}$	$1.9^{+0.1}_{-0.09} \times 10^{11}$
nircam6-10988	1.73	No	214.86350399	52.81561097	0.86	7.5	82	$3.7^{+0.5}_{-0.2} \times 10^{10}$	$3.4^{+0.1}_{-0.2} \times 10^{10}$
nircam6-11098	1.39	No	214.85631023	52.81067658	1.30	11.2	158	$6.7^{+0.4}_{-0.3} \times 10^{10}$	$4.4^{+0.9}_{-0.5} \times 10^{10}$
nircam6-11125	1.28	No	214.85709917	52.81090024	1.01	8.6	115	$1.6^{+0.05}_{-0.02} \times 10^{10}$	$1.4^{+0.1}_{-0.1} \times 10^{10}$
nircam6-11371	1.20	No	214.88286592	52.83598877	1.22	10.4	143	$5.8^{+0.2}_{-0.2} \times 10^{10}$	$3.7^{+0.2}_{-0.08} \times 10^{10}$
nircam6-11443	1.02	Yes	214.83792989	52.79605613	1.35	11.2	187	$2.4^{+0.5}_{-0.5} \times 10^{10}$	$1.6^{+0.2}_{-0.2} \times 10^{10}$
nircam6-11480	1.43	No	214.90607441	52.84439819	0.84	7.3	81	$4.1^{+0.04}_{-0.06} \times 10^{10}$	$3.0^{+0.03}_{-0.03} \times 10^{10}$
nircam6-11797	1.72	No	214.84889352	52.80241390	0.86	7.5	86	$4.3^{+0.2}_{-0.07} \times 10^{10}$	$4.6^{+0.4}_{-0.3} \times 10^{10}$
nircam6-11812	3.20	No	214.88707207	52.82938978	0.51	3.9	27	$1.6^{+0.02}_{-0.01} \times 10^{10}$	$1.4^{+0.01}_{-0.02} \times 10^{10}$
nircam6-11843	1.55	No	214.83238927	52.79032232	0.94	8.1	84	$2.5^{+0.2}_{-0.2} \times 10^{10}$	$1.9^{+0.1}_{-0.1} \times 10^{10}$
nircam6-11936	1.28	No	214.90643357	52.84263784	0.66	5.7	53	$1.2^{+0.07}_{-0.06} \times 10^{10}$	$1.2^{+0.06}_{-0.2} \times 10^{10}$
nircam6-12061	3.11	No	214.90114482	52.83810191	1.15	8.9	68	$3.6^{+0.2}_{-0.1} \times 10^{10}$	$7.7^{+0.07}_{-0.2} \times 10^{10}$



## Table with formation times for CEERS galaxies

---

Table E.1 presents the formation times inferred for our sample of 333 CEERS galaxies at  $1 < z < 4$  with  $M_{\star} > 10^{10} M_{\odot}$  considered in Chapter 6. The formation times for each galaxy, expressed in ages of the Universe and in their corresponding redshifts, have been calculated from the 2D-SPS-derived SFH (shown in Appendix C). Formation times and redshifts are given for both the galaxy SFH built from SB99 and BC03 models. Galaxies in the table are first sorted by CEERS pointing to which they belong and, within each CEERS pointing, according to their ID.

Table E.1: Formation times inferred for CEERS massive galaxies at  $1 < z < 4$  analyzed in Chapter 6.

Galaxy name	$t_5^{SB99(BC03)}$ [Gyr]	$t_{10}^{SB99(BC03)}$ [Gyr]	$t_{5 \times 10^8 M_\odot}^{SB99(BC03)}$ [Gyr]	$t_{10^9 M_\odot}^{SB99(BC03)}$ [Gyr]	$z_5^{SB99(BC03)}$	$z_{10}^{SB99(BC03)}$	$z_{5 \times 10^8 M_\odot}^{SB99(BC03)}$	$z_{10^9 M_\odot}^{SB99(BC03)}$
nircam1-1	0.81 <sup>+0.81</sup> <sub>-0.81</sub> (0.50 <sup>+0.52</sup> <sub>-0.47</sub> )	0.87 <sup>+0.88</sup> <sub>-0.87</sub> (0.83 <sup>+0.89</sup> <sub>-0.77</sub> )	0.76 <sup>+0.76</sup> <sub>-0.76</sub> (0.24 <sup>+0.25</sup> <sub>-0.24</sub> )	0.80 <sup>+0.80</sup> <sub>-0.80</sub> (0.30 <sup>+0.31</sup> <sub>-0.30</sub> )	6.76 <sup>+6.7</sup> <sub>-6.7</sub> (9.6 <sup>+9.9</sup> <sub>-9.3</sub> )	6.36 <sup>+6.3</sup> <sub>-6.3</sub> (6.56 <sup>+6.9</sup> <sub>-6.2</sub> )	7.0 <sup>+7.0</sup> <sub>-7.0</sub> (16.1 <sup>+16.3</sup> <sub>-15.8</sub> )	6.76 <sup>+6.7</sup> <sub>-6.7</sub> (13.7 <sup>+14.0</sup> <sub>-13.4</sub> )
nircam1-78	1.16 <sup>+1.00</sup> <sub>-1.00</sub> (0.50 <sup>+0.56</sup> <sub>-0.44</sub> )	2.12 <sup>+2.81</sup> <sub>-1.62</sub> (1.24 <sup>+1.63</sup> <sub>-0.98</sub> )	1.14 <sup>+1.30</sup> <sub>-0.99</sub> (0.42 <sup>+0.40</sup> <sub>-0.32</sub> )	2.07 <sup>+2.55</sup> <sub>-1.64</sub> (0.89 <sup>+1.10</sup> <sub>-0.74</sub> )	5.05 <sup>+7.7</sup> <sub>-4.4</sub> (9.5 <sup>+8.8</sup> <sub>-8.8</sub> )	3.02 <sup>+3.3</sup> <sub>-2.3</sub> (4.8 <sup>+5.8</sup> <sub>-3.3</sub> )	5.1 <sup>+5.4</sup> <sub>-4.6</sub> (10.9 <sup>+11.7</sup> <sub>-10.5</sub> )	3.1 <sup>+3.8</sup> <sub>-2.6</sub> (6.2 <sup>+7.2</sup> <sub>-5.2</sub> )
nircam1-106	0.22 <sup>+0.26</sup> <sub>-0.20</sub> (0.23 <sup>+0.25</sup> <sub>-0.21</sub> )	0.34 <sup>+0.43</sup> <sub>-0.30</sub> (0.36 <sup>+0.40</sup> <sub>-0.33</sub> )	0.26 <sup>+0.32</sup> <sub>-0.23</sub> (0.30 <sup>+0.32</sup> <sub>-0.26</sub> )	0.41 <sup>+0.55</sup> <sub>-0.36</sub> (0.49 <sup>+0.55</sup> <sub>-0.42</sub> )	17.0 <sup>+18.5</sup> <sub>-15.1</sub> (16.7 <sup>+17.5</sup> <sub>-15.6</sub> )	12.6 <sup>+13.8</sup> <sub>-10.7</sub> (12.2 <sup>+13.0</sup> <sub>-11.3</sub> )	15.4 <sup>+16.6</sup> <sub>-13.3</sub> (14.0 <sup>+15.2</sup> <sub>-13.1</sub> )	11.1 <sup>+12.1</sup> <sub>-9.0</sub> (9.7 <sup>+10.8</sup> <sub>-8.9</sub> )
nircam1-172	2.29 <sup>+2.47</sup> <sub>-1.97</sub> (0.46 <sup>+0.58</sup> <sub>-0.38</sub> )	2.83 <sup>+2.91</sup> <sub>-2.75</sub> (0.68 <sup>+0.82</sup> <sub>-0.56</sub> )	0.75 <sup>+0.90</sup> <sub>-0.61</sub> (0.27 <sup>+0.33</sup> <sub>-0.23</sub> )	1.58 <sup>+1.85</sup> <sub>-1.20</sub> (0.36 <sup>+0.45</sup> <sub>-0.30</sub> )	2.83 <sup>+2.8</sup> <sub>-2.6</sub> (10.2 <sup>+11.7</sup> <sub>-8.8</sub> )	2.32 <sup>+2.4</sup> <sub>-2.2</sub> (7.6 <sup>+8.8</sup> <sub>-6.6</sub> )	7.1 <sup>+7.2</sup> <sub>-6.1</sub> (14.9 <sup>+16.9</sup> <sub>-13.0</sub> )	3.9 <sup>+3.9</sup> <sub>-3.4</sub> (12.1 <sup>+14.0</sup> <sub>-10.3</sub> )
nircam1-792	0.58 <sup>+0.60</sup> <sub>-0.57</sub> (0.49 <sup>+0.52</sup> <sub>-0.44</sub> )	0.68 <sup>+0.71</sup> <sub>-0.65</sub> (0.87 <sup>+1.05</sup> <sub>-0.72</sub> )	0.55 <sup>+0.56</sup> <sub>-0.54</sub> (0.23 <sup>+0.24</sup> <sub>-0.22</sub> )	0.61 <sup>+0.63</sup> <sub>-0.59</sub> (0.28 <sup>+0.30</sup> <sub>-0.27</sub> )	8.5 <sup>+8.7</sup> <sub>-8.4</sub> (9.8 <sup>+9.3</sup> <sub>-9.3</sub> )	7.6 <sup>+7.9</sup> <sub>-6.4</sub> (6.3 <sup>+7.3</sup> <sub>-5.4</sub> )	9.0 <sup>+9.1</sup> <sub>-8.8</sub> (16.5 <sup>+17.2</sup> <sub>-14.0</sub> )	8.3 <sup>+8.5</sup> <sub>-8.1</sub> (14.4 <sup>+15.0</sup> <sub>-14.0</sub> )
nircam1-868	0.13 <sup>+0.13</sup> <sub>-0.12</sub> (0.16 <sup>+0.16</sup> <sub>-0.15</sub> )	0.18 <sup>+0.19</sup> <sub>-0.17</sub> (0.24 <sup>+0.25</sup> <sub>-0.23</sub> )	0.06 <sup>+0.06</sup> <sub>-0.06</sub> (0.07 <sup>+0.07</sup> <sub>-0.07</sub> )	0.08 <sup>+0.08</sup> <sub>-0.08</sub> (0.09 <sup>+0.10</sup> <sub>-0.09</sub> )	25.4 <sup>+25.8</sup> <sub>-23.0</sub> (21.9 <sup>+22.4</sup> <sub>-21.4</sub> )	19.8 <sup>+20.2</sup> <sub>-15.9</sub> (16.4 <sup>+16.8</sup> <sub>-15.9</sub> )	42.9 <sup>+43.4</sup> <sub>-42.4</sub> (39.1 <sup>+39.7</sup> <sub>-38.4</sub> )	35.3 <sup>+36.0</sup> <sub>-34.7</sub> (31.2 <sup>+30.4</sup> <sub>-30.4</sub> )
nircam1-957	0.83 <sup>+0.87</sup> <sub>-0.79</sub> (1.18 <sup>+1.45</sup> <sub>-0.94</sub> )	1.19 <sup>+1.38</sup> <sub>-1.06</sub> (1.87 <sup>+2.05</sup> <sub>-1.64</sub> )	0.67 <sup>+0.69</sup> <sub>-0.65</sub> (0.40 <sup>+0.42</sup> <sub>-0.39</sub> )	0.77 <sup>+0.80</sup> <sub>-0.74</sub> (0.52 <sup>+0.55</sup> <sub>-0.50</sub> )	6.6 <sup>+6.8</sup> <sub>-6.3</sub> (5.0 <sup>+5.9</sup> <sub>-4.2</sub> )	4.9 <sup>+5.4</sup> <sub>-4.4</sub> (3.4 <sup>+3.8</sup> <sub>-3.1</sub> )	7.7 <sup>+7.8</sup> <sub>-6.7</sub> (11.2 <sup>+11.5</sup> <sub>-10.9</sub> )	6.9 <sup>+7.1</sup> <sub>-6.7</sub> (9.2 <sup>+9.6</sup> <sub>-8.9</sub> )
nircam1-1047	0.68 <sup>+0.74</sup> <sub>-0.61</sub> (0.56 <sup>+0.49</sup> <sub>-0.49</sub> )	1.10 <sup>+1.16</sup> <sub>-1.02</sub> (1.04 <sup>+1.18</sup> <sub>-0.92</sub> )	0.41 <sup>+0.46</sup> <sub>-0.37</sub> (0.44 <sup>+0.50</sup> <sub>-0.38</sub> )	0.68 <sup>+0.75</sup> <sub>-0.62</sub> (0.78 <sup>+0.89</sup> <sub>-0.67</sub> )	7.6 <sup>+8.3</sup> <sub>-7.1</sub> (8.8 <sup>+9.7</sup> <sub>-8.9</sub> )	5.2 <sup>+5.5</sup> <sub>-4.5</sub> (5.5 <sup>+6.0</sup> <sub>-5.0</sub> )	11.1 <sup>+11.9</sup> <sub>-10.2</sub> (10.4 <sup>+11.6</sup> <sub>-9.5</sub> )	7.6 <sup>+7.7</sup> <sub>-6.2</sub> (9.7 <sup>+10.8</sup> <sub>-9.6</sub> )
nircam1-1211	0.33 <sup>+0.36</sup> <sub>-0.30</sub> (0.24 <sup>+0.24</sup> <sub>-0.23</sub> )	0.47 <sup>+0.53</sup> <sub>-0.42</sub> (0.33 <sup>+0.35</sup> <sub>-0.33</sub> )	0.24 <sup>+0.26</sup> <sub>-0.23</sub> (0.13 <sup>+0.13</sup> <sub>-0.13</sub> )	0.30 <sup>+0.34</sup> <sub>-0.28</sub> (0.16 <sup>+0.16</sup> <sub>-0.15</sub> )	13.0 <sup>+13.7</sup> <sub>-12.2</sub> (16.4 <sup>+16.6</sup> <sub>-16.1</sub> )	10.9 <sup>+10.9</sup> <sub>-9.1</sub> (12.8 <sup>+13.0</sup> <sub>-12.5</sub> )	16.1 <sup>+16.6</sup> <sub>-15.3</sub> (24.3 <sup>+24.5</sup> <sub>-24.2</sub> )	13.7 <sup>+14.4</sup> <sub>-12.7</sub> (22.0 <sup>+22.2</sup> <sub>-21.7</sub> )
nircam1-1319	0.75 <sup>+0.80</sup> <sub>-0.71</sub> (1.04 <sup>+1.21</sup> <sub>-0.90</sub> )	0.95 <sup>+1.08</sup> <sub>-0.86</sub> (1.58 <sup>+1.80</sup> <sub>-1.36</sub> )	0.77 <sup>+0.83</sup> <sub>-0.73</sub> (0.52 <sup>+0.55</sup> <sub>-0.49</sub> )	1.01 <sup>+1.19</sup> <sub>-0.89</sub> (0.77 <sup>+0.83</sup> <sub>-0.67</sub> )	7.0 <sup>+7.3</sup> <sub>-6.7</sub> (5.5 <sup>+6.1</sup> <sub>-4.9</sub> )	5.9 <sup>+6.3</sup> <sub>-5.3</sub> (3.9 <sup>+4.4</sup> <sub>-3.5</sub> )	6.9 <sup>+7.2</sup> <sub>-6.5</sub> (9.3 <sup>+9.7</sup> <sub>-8.9</sub> )	5.6 <sup>+6.2</sup> <sub>-4.9</sub> (6.9 <sup>+7.7</sup> <sub>-6.6</sub> )
nircam1-1394	0.80 <sup>+0.91</sup> <sub>-0.72</sub> (0.69 <sup>+0.96</sup> <sub>-0.36</sub> )	1.07 <sup>+1.08</sup> <sub>-1.06</sub> (1.01 <sup>+1.09</sup> <sub>-0.82</sub> )	0.53 <sup>+0.59</sup> <sub>-0.48</sub> (0.50 <sup>+0.77</sup> <sub>-0.25</sub> )	0.75 <sup>+0.85</sup> <sub>-0.69</sub> (0.94 <sup>+1.02</sup> <sub>-0.42</sub> )	6.7 <sup>+7.3</sup> <sub>-6.1</sub> (7.5 <sup>+7.2</sup> <sub>-5.9</sub> )	5.3 <sup>+5.4</sup> <sub>-5.3</sub> (5.6 <sup>+6.6</sup> <sub>-5.3</sub> )	9.2 <sup>+9.8</sup> <sub>-8.4</sub> (9.5 <sup>+15.6</sup> <sub>-6.9</sub> )	7.0 <sup>+7.5</sup> <sub>-6.4</sub> (6.0 <sup>+10.8</sup> <sub>-5.6</sub> )
nircam1-1405	2.23 <sup>+2.96</sup> <sub>-1.99</sub> (1.57 <sup>+1.74</sup> <sub>-1.37</sub> )	2.78 <sup>+2.85</sup> <sub>-2.69</sub> (2.29 <sup>+2.48</sup> <sub>-2.08</sub> )	1.75 <sup>+2.04</sup> <sub>-1.33</sub> (1.36 <sup>+1.15</sup> <sub>-1.17</sub> )	2.54 <sup>+2.64</sup> <sub>-2.37</sub> (1.95 <sup>+1.74</sup> <sub>-1.74</sub> )	2.9 <sup>+3.2</sup> <sub>-2.7</sub> (3.9 <sup>+4.4</sup> <sub>-3.6</sub> )	2.4 <sup>+2.4</sup> <sub>-2.3</sub> (2.8 <sup>+3.1</sup> <sub>-2.6</sub> )	3.6 <sup>+4.5</sup> <sub>-3.1</sub> (4.4 <sup>+5.0</sup> <sub>-4.0</sub> )	2.6 <sup>+2.7</sup> <sub>-2.5</sub> (3.3 <sup>+3.6</sup> <sub>-3.0</sub> )
nircam1-1498	1.32 <sup>+1.65</sup> <sub>-1.14</sub> (1.34 <sup>+1.51</sup> <sub>-1.15</sub> )	2.80 <sup>+2.92</sup> <sub>-2.50</sub> (1.82 <sup>+2.00</sup> <sub>-1.58</sub> )	0.99 <sup>+1.04</sup> <sub>-0.92</sub> (0.89 <sup>+1.01</sup> <sub>-0.75</sub> )	1.38 <sup>+1.80</sup> <sub>-1.16</sub> (1.26 <sup>+1.42</sup> <sub>-1.07</sub> )	4.5 <sup>+5.1</sup> <sub>-3.8</sub> (4.5 <sup>+5.1</sup> <sub>-4.0</sub> )	2.3 <sup>+2.6</sup> <sub>-2.2</sub> (3.5 <sup>+3.9</sup> <sub>-3.2</sub> )	5.7 <sup>+6.0</sup> <sub>-5.5</sub> (6.2 <sup>+7.1</sup> <sub>-5.6</sub> )	4.4 <sup>+5.0</sup> <sub>-3.5</sub> (4.7 <sup>+5.4</sup> <sub>-4.3</sub> )
nircam1-1659	1.91 <sup>+1.99</sup> <sub>-1.81</sub> (1.28 <sup>+1.44</sup> <sub>-1.12</sub> )	2.41 <sup>+2.46</sup> <sub>-2.35</sub> (1.88 <sup>+2.04</sup> <sub>-1.66</sub> )	1.52 <sup>+1.61</sup> <sub>-1.42</sub> (1.07 <sup>+1.22</sup> <sub>-0.94</sub> )	2.07 <sup>+2.15</sup> <sub>-1.99</sub> (1.56 <sup>+1.74</sup> <sub>-1.38</sub> )	3.3 <sup>+3.5</sup> <sub>-3.2</sub> (4.6 <sup>+5.2</sup> <sub>-4.2</sub> )	2.7 <sup>+2.8</sup> <sub>-2.6</sub> (3.4 <sup>+3.7</sup> <sub>-3.1</sub> )	4.0 <sup>+4.3</sup> <sub>-3.9</sub> (5.3 <sup>+6.0</sup> <sub>-4.8</sub> )	3.1 <sup>+3.2</sup> <sub>-3.0</sub> (3.9 <sup>+4.4</sup> <sub>-3.6</sub> )
nircam1-1660	0.13 <sup>+0.13</sup> <sub>-0.13</sub> (0.41 <sup>+0.41</sup> <sub>-0.40</sub> )	0.19 <sup>+0.19</sup> <sub>-0.19</sub> (0.52 <sup>+0.53</sup> <sub>-0.51</sub> )	0.09 <sup>+0.09</sup> <sub>-0.09</sub> (0.29 <sup>+0.30</sup> <sub>-0.29</sub> )	0.12 <sup>+0.12</sup> <sub>-0.11</sub> (0.33 <sup>+0.34</sup> <sub>-0.33</sub> )	24.8 <sup>+25.0</sup> <sub>-24.6</sub> (11.1 <sup>+11.3</sup> <sub>-11.0</sub> )	19.2 <sup>+19.3</sup> <sub>-19.0</sub> (9.3 <sup>+9.5</sup> <sub>-9.1</sub> )	31.9 <sup>+32.0</sup> <sub>-31.7</sub> (14.0 <sup>+14.1</sup> <sub>-13.9</sub> )	27.0 <sup>+27.2</sup> <sub>-26.7</sub> (12.8 <sup>+13.0</sup> <sub>-12.7</sub> )
nircam1-1685	0.55 <sup>+0.55</sup> <sub>-0.55</sub> (0.27 <sup>+0.28</sup> <sub>-0.26</sub> )	0.60 <sup>+0.60</sup> <sub>-0.60</sub> (0.32 <sup>+0.33</sup> <sub>-0.31</sub> )	0.51 <sup>+0.51</sup> <sub>-0.51</sub> (0.21 <sup>+0.21</sup> <sub>-0.20</sub> )	0.53 <sup>+0.53</sup> <sub>-0.53</sub> (0.22 <sup>+0.22</sup> <sub>-0.22</sub> )	8.8 <sup>+8.8</sup> <sub>-8.8</sub> (14.9 <sup>+15.1</sup> <sub>-14.7</sub> )	8.3 <sup>+8.3</sup> <sub>-8.3</sub> (13.2 <sup>+13.4</sup> <sub>-12.6</sub> )	9.4 <sup>+9.4</sup> <sub>-9.4</sub> (18.1 <sup>+18.1</sup> <sub>-18.0</sub> )	9.2 <sup>+9.2</sup> <sub>-9.2</sub> (17.2 <sup>+17.3</sup> <sub>-17.0</sub> )
nircam1-1794	0.56 <sup>+0.56</sup> <sub>-0.56</sub> (0.26 <sup>+0.27</sup> <sub>-0.26</sub> )	0.60 <sup>+0.61</sup> <sub>-0.60</sub> (0.31 <sup>+0.32</sup> <sub>-0.30</sub> )	0.50 <sup>+0.51</sup> <sub>-0.50</sub> (0.20 <sup>+0.20</sup> <sub>-0.20</sub> )	0.52 <sup>+0.52</sup> <sub>-0.52</sub> (0.21 <sup>+0.21</sup> <sub>-0.21</sub> )	8.8 <sup>+8.8</sup> <sub>-8.8</sub> (15.2 <sup>+15.4</sup> <sub>-15.0</sub> )	8.3 <sup>+8.3</sup> <sub>-8.3</sub> (13.5 <sup>+13.7</sup> <sub>-13.3</sub> )	9.5 <sup>+9.5</sup> <sub>-9.5</sub> (18.4 <sup>+18.4</sup> <sub>-18.3</sub> )	9.3 <sup>+9.3</sup> <sub>-9.3</sub> (17.7 <sup>+17.8</sup> <sub>-17.6</sub> )
nircam1-1808	1.10 <sup>+1.15</sup> <sub>-1.04</sub> (0.35 <sup>+0.37</sup> <sub>-0.35</sub> )	1.31 <sup>+1.37</sup> <sub>-1.26</sub> (0.43 <sup>+0.45</sup> <sub>-0.41</sub> )	0.92 <sup>+1.00</sup> <sub>-0.81</sub> (0.31 <sup>+0.32</sup> <sub>-0.31</sub> )	1.09 <sup>+1.14</sup> <sub>-1.01</sub> (0.36 <sup>+0.37</sup> <sub>-0.35</sub> )	5.2 <sup>+5.5</sup> <sub>-5.2</sub> (12.3 <sup>+12.5</sup> <sub>-11.9</sub> )	4.6 <sup>+4.7</sup> <sub>-4.4</sub> (10.7 <sup>+11.0</sup> <sub>-10.4</sub> )	6.0 <sup>+6.7</sup> <sub>-5.6</sub> (13.4 <sup>+13.6</sup> <sub>-12.5</sub> )	5.3 <sup>+5.6</sup> <sub>-5.1</sub> (12.2 <sup>+12.5</sup> <sub>-11.9</sub> )
nircam1-1941	0.38 <sup>+0.37</sup> <sub>-0.37</sub> (0.39 <sup>+0.42</sup> <sub>-0.35</sub> )	0.48 <sup>+0.51</sup> <sub>-0.46</sub> (0.52 <sup>+0.55</sup> <sub>-0.48</sub> )	0.27 <sup>+0.27</sup> <sub>-0.26</sub> (0.24 <sup>+0.26</sup> <sub>-0.21</sub> )	0.31 <sup>+0.32</sup> <sub>-0.30</sub> (0.30 <sup>+0.33</sup> <sub>-0.27</sub> )	11.7 <sup>+12.0</sup> <sub>-11.4</sub> (11.6 <sup>+12.4</sup> <sub>-10.8</sub> )	9.8 <sup>+9.4</sup> <sub>-9.4</sub> (16.4 <sup>+16.8</sup> <sub>-15.5</sub> )	15.1 <sup>+15.3</sup> <sub>-14.9</sub> (16.4 <sup>+17.6</sup> <sub>-15.9</sub> )	13.6 <sup>+13.9</sup> <sub>-13.3</sub> (13.9 <sup>+15.0</sup> <sub>-12.9</sub> )
nircam1-2251	0.25 <sup>+0.30</sup> <sub>-0.22</sub> (0.13 <sup>+0.14</sup> <sub>-0.15</sub> )	0.37 <sup>+0.49</sup> <sub>-0.31</sub> (0.19 <sup>+0.21</sup> <sub>-0.18</sub> )	0.19 <sup>+0.22</sup> <sub>-0.17</sub> (0.07 <sup>+0.08</sup> <sub>-0.07</sub> )	0.26 <sup>+0.32</sup> <sub>-0.22</sub> (0.09 <sup>+0.10</sup> <sub>-0.09</sub> )	15.9 <sup>+17.4</sup> <sub>-13.7</sub> (25.4 <sup>+26.7</sup> <sub>-23.9</sub> )	12.0 <sup>+13.4</sup> <sub>-9.7</sub> (18.8 <sup>+19.8</sup> <sub>-17.7</sub> )	19.3 <sup>+20.6</sup> <sub>-17.2</sub> (37.3 <sup>+38.5</sup> <sub>-36.1</sub> )	15.4 <sup>+17.1</sup> <sub>-13.2</sub> (30.8 <sup>+32.2</sup> <sub>-29.3</sub> )
nircam1-2260	0.23 <sup>+0.23</sup> <sub>-0.23</sub> (0.15 <sup>+0.14</sup> <sub>-0.14</sub> )	0.28 <sup>+0.28</sup> <sub>-0.28</sub> (0.21 <sup>+0.22</sup> <sub>-0.21</sub> )	0.19 <sup>+0.19</sup> <sub>-0.19</sub> (0.09 <sup>+0.09</sup> <sub>-0.09</sub> )	0.21 <sup>+0.21</sup> <sub>-0.21</sub> (0.19 <sup>+0.12</sup> <sub>-0.11</sub> )	16.7 <sup>+16.8</sup> <sub>-16.6</sub> (22.9 <sup>+23.7</sup> <sub>-22.1</sub> )	14.5 <sup>+14.6</sup> <sub>-14.4</sub> (17.5 <sup>+17.9</sup> <sub>-17.0</sub> )	18.9 <sup>+18.9</sup> <sub>-17.9</sub> (32.3 <sup>+32.9</sup> <sub>-31.6</sub> )	17.9 <sup>+17.9</sup> <sub>-17.9</sub> (26.9 <sup>+27.7</sup> <sub>-26.2</sub> )
nircam1-2459	0.96 <sup>+1.03</sup> <sub>-0.91</sub> (0.61 <sup>+0.63</sup> <sub>-0.59</sub> )	1.57 <sup>+1.91</sup> <sub>-1.40</sub> (1.10 <sup>+1.23</sup> <sub>-0.98</sub> )	1.05 <sup>+1.07</sup> <sub>-0.97</sub> (0.58 <sup>+0.56</sup> <sub>-0.56</sub> )	1.97 <sup>+2.32</sup> <sub>-1.67</sub> (0.96 <sup>+1.03</sup> <sub>-0.87</sub> )	5.9 <sup>+5.9</sup> <sub>-5.5</sub> (8.2 <sup>+8.4</sup> <sub>-8.1</sub> )	3.9 <sup>+4.3</sup> <sub>-3.3</sub> (5.2 <sup>+5.7</sup> <sub>-4.8</sub> )	5.4 <sup>+5.8</sup> <sub>-5.4</sub> (8.6 <sup>+8.8</sup> <sub>-8.4</sub> )	3.2 <sup>+3.7</sup> <sub>-2.8</sub> (5.8 <sup>+6.3</sup> <sub>-5.5</sub> )
nircam1-2518	1.71 <sup>+2.24</sup> <sub>-1.24</sub> (0.90 <sup>+1.05</sup> <sub>-0.76</sub> )	3.08 <sup>+3.24</sup> <sub>-2.83</sub> (1.34 <sup>+1.56</sup> <sub>-1.15</sub> )	0.82 <sup>+1.01</sup> <sub>-0.71</sub> (0.56 <sup>+0.66</sup> <sub>-0.47</sub> )	1.25 <sup>+1.67</sup> <sub>-0.96</sub> (0.78 <sup>+0.89</sup> <sub>-0.63</sub> )	3.7 <sup>+4.8</sup> <sub>-3.2</sub> (6.1 <sup>+7.0</sup> <sub>-5.4</sub> )	2.1 <sup>+2.0</sup> <sub>-2.0</sub> (4.5 <sup>+5.1</sup> <sub>-3.9</sub> )	6.6 <sup>+7.4</sup> <sub>-5.4</sub> (8.8 <sup>+9.1</sup> <sub>-7.8</sub> )	4.7 <sup>+5.9</sup> <sub>-3.7</sub> (6.8 <sup>+8.1</sup> <sub>-6.2</sub> )
nircam1-2662	0.39 <sup>+0.41</sup> <sub>-0.37</sub> (0.41 <sup>+0.51</sup> <sub>-0.34</sub> )	0.50 <sup>+0.53</sup> <sub>-0.47</sub> (0.71 <sup>+0.91</sup> <sub>-0.56</sub> )	0.28 <sup>+0.28</sup> <sub>-0.27</sub> (0.23 <sup>+0.20</sup> <sub>-0.20</sub> )	0.31 <sup>+0.32</sup> <sub>-0.31</sub> (0.33 <sup>+0.38</sup> <sub>-0.27</sub> )	11.5 <sup>+11.8</sup> <sub>-11.1</sub> (11.0 <sup>+12.6</sup> <sub>-9.4</sub> )	9.5 <sup>+9.9</sup> <sub>-9.1</sub> (7.4 <sup>+8.8</sup> <sub>-6.1</sub> )	14.7 <sup>+14.9</sup> <sub>-14.4</sub> (16.7 <sup>+18.6</sup> <sub>-14.9</sub> )	13.5 <sup>+13.6</sup> <sub>-13.2</sub> (13.0 <sup>+15.0</sup> <sub>-11.6</sub> )
nircam1-2720	0.63 <sup>+0.76</sup> <sub>-0.48</sub> (0.80 <sup>+0.93</sup> <sub>-0.66</sub> )	0.89 <sup>+1.04</sup> <sub>-0.75</sub> (1.11 <sup>+1.25</sup> <sub>-0.98</sub> )	0.62 <sup>+0.66</sup> <sub>-0.46</sub> (0.82 <sup>+0.94</sup> <sub>-0.69</sub> )	0.87 <sup>+1.05</sup> <sub>-0.73</sub> (1.10 <sup>+1.30</sup> <sub>-1.01</sub> )	8.0 <sup>+9.0</sup> <sub>-7.7</sub> (6.7 <sup>+7.8</sup> <sub>-6.0</sub> )	6.2 <sup>+7.1</sup> <sub>-5.5</sub> (5.2 <sup>+5.8</sup> <sub>-4.7</sub> )	8.2 <sup>+10.2</sup> <sub>-7.0</sub> (6.6 <sup>+7.5</sup> <sub>-5.9</sub> )	6.3 <sup>+7.2</sup> <sub>-5.5</sub> (5.0 <sup>+5.6</sup> <sub>-4.6</sub> )
nircam1-3088	0.37 <sup>+0.39</sup> <sub>-0.35</sub> (0.56 <sup>+0.59</sup> <sub>-0.33</sub> )	0.54 <sup>+0.58</sup> <sub>-0.50</sub> (0.81 <sup>+0.87</sup> <sub>-0.77</sub> )	0.23 <sup>+0.24</sup> <sub>-0.23</sub> (0.36 <sup>+0.35</sup> <sub>-0.35</sub> )	0.28 <sup>+0.29</sup> <sub>-0.27</sub> (0.42 <sup>+0.41</sup> <sub>-0.41</sub> )	11.9 <sup>+12.3</sup> <sub>-11.4</sub> (8.8 <sup>+9.1</sup> <sub>-8.5</sub> )	9.1 <sup>+9.5</sup> <sub>-8.6</sub> (6.6 <sup>+6.9</sup> <sub>-6.3</sub> )	16.5 <sup>+16.9</sup> <sub>-16.1</sub> (12.2 <sup>+12.4</sup> <sub>-11.9</sub> )	14.7 <sup>+15.0</sup> <sub>-14.2</sub> (10.8 <sup>+11.1</sup> <sub>-10.5</sub> )
nircam1-3310	1.01 <sup>+1.05</sup> <sub>-0.95</sub> (0.80 <sup>+0.90</sup> <sub>-0.71</sub> )	1.25 <sup>+1.32</sup> <sub>-1.20</sub> (1.18 <sup>+1.26</sup> <sub>-1.05</sub> )	0.74 <sup>+0.81</sup> <sub>-0.68</sub> (0.51 <sup>+0.60</sup> <sub>-0.44</sub> )	0.98 <sup>+1.04</sup> <sub>-0.92</sub> (0.73 <sup>+0.83</sup> <sub>-0.65</sub> )	5.6 <sup>+5.9</sup> <sub>-5.4</sub> (6.7 <sup>+7.4</sup> <sub>-6.1</sub> )	4.7 <sup>+4.9</sup> <sub>-4.5</sub> (5.0 <sup>+5.4</sup> <sub>-4.7</sub> )	7.1 <sup>+7.6</sup> <sub>-6.7</sub> (9.4 <sup>+10.5</sup> <sub>-8.4</sub> )	5.7 <sup>+6.1</sup> <sub>-5.5</sub> (7.2 <sup>+7.9</sup> <sub>-6.5</sub> )
nircam1-3578	0.95 <sup>+0.99</sup> <sub>-0.93</sub> (0.30 <sup>+0.30</sup> <sub>-0.30</sub> )	1.05 <sup>+1.07</sup> <sub>-1.03</sub> (0.35 <sup>+0.36</sup> <sub>-0.35</sub> )	0.73 <sup>+0.84</sup> <sub>-0.63</sub> (0.25 <sup>+0.25</sup> <sub>-0.25</sub> )	0.89 <sup>+0.93</sup> <sub>-0.74</sub> (0.27 <sup>+0.27</sup> <sub>-0.27</sub> )	5.7 <sup>+6.0</sup> <sub>-5.7</sub> (13.9 <sup>+13.9</sup> <sub>-13.8</sub> )	5.4 <sup>+5.5</sup> <sub>-5.4</sub> (12.3 <sup>+12.4</sup> <sub>-12.2&lt;/</sub>		

Table E.1: (Continued)

Galaxy name	$t_5^{SB99(BC03)}$ [Gyr]	$t_{10}^{SB99(BC03)}$ [Gyr]	$t_{5 \times 10^8 M_\odot}^{SB99(BC03)}$ [Gyr]	$t_{10^9 M_\odot}^{SB99(BC03)}$ [Gyr]	$z_5^{SB99(BC03)}$	$z_{10}^{SB99(BC03)}$	$z_{5 \times 10^8 M_\odot}^{SB99(BC03)}$	$z_{10^9 M_\odot}^{SB99(BC03)}$
nircam1-3756	1.42 <sup>+1.61</sup> <sub>-1.21</sub> (2.70 <sup>+2.73</sup> <sub>-2.66</sub> )	1.81 <sup>+1.93</sup> <sub>-1.64</sub> (2.81 <sup>+2.83</sup> <sub>-2.78</sub> )	1.35 <sup>+1.53</sup> <sub>-1.02</sub> (2.68 <sup>+2.71</sup> <sub>-2.62</sub> )	1.65 <sup>+1.81</sup> <sub>-1.48</sub> (2.79 <sup>+2.81</sup> <sub>-2.75</sub> )	4.34 <sup>+9.0</sup> <sub>-2.4</sub> (2.42 <sup>+5.5</sup> <sub>-2.4</sub> )	3.53 <sup>+8.8</sup> <sub>-2.3</sub> (2.32 <sup>+3.3</sup> <sub>-2.3</sub> )	4.45 <sup>+5.5</sup> <sub>-4.0</sub> (2.42 <sup>+5.5</sup> <sub>-4.0</sub> )	3.84 <sup>+1.2</sup> <sub>-3.5</sub> (2.32 <sup>+4.4</sup> <sub>-2.3</sub> )
nircam1-4022	0.72 <sup>+0.81</sup> <sub>-0.61</sub> (0.66 <sup>+0.74</sup> <sub>-0.56</sub> )	1.10 <sup>+1.21</sup> <sub>-0.96</sub> (1.17 <sup>+1.27</sup> <sub>-0.96</sub> )	0.50 <sup>+0.57</sup> <sub>-0.40</sub> (0.55 <sup>+0.61</sup> <sub>-0.40</sub> )	0.75 <sup>+0.85</sup> <sub>-0.66</sub> (0.93 <sup>+1.06</sup> <sub>-0.83</sub> )	7.38 <sup>+3.7</sup> <sub>-7.2</sub> (7.72 <sup>+8.8</sup> <sub>-8.3</sub> )	5.25 <sup>+7.7</sup> <sub>-4.7</sub> (5.05 <sup>+5.7</sup> <sub>-4.7</sub> )	9.61 <sup>+10.8</sup> <sub>-10.8</sub> (8.9 <sup>+8.8</sup> <sub>-8.3</sub> )	7.17 <sup>+8.6</sup> <sub>-5.1</sub> (6.05 <sup>+6.4</sup> <sub>-5.4</sub> )
nircam1-4241	1.22 <sup>+1.34</sup> <sub>-1.08</sub> (0.89 <sup>+1.01</sup> <sub>-0.79</sub> )	1.68 <sup>+1.78</sup> <sub>-1.51</sub> (1.28 <sup>+1.49</sup> <sub>-1.14</sub> )	0.86 <sup>+1.01</sup> <sub>-0.75</sub> (0.61 <sup>+0.69</sup> <sub>-0.51</sub> )	1.15 <sup>+1.28</sup> <sub>-1.01</sub> (0.79 <sup>+0.89</sup> <sub>-0.67</sub> )	4.83 <sup>+5.3</sup> <sub>-4.5</sub> (6.25 <sup>+6.8</sup> <sub>-5.6</sub> )	3.74 <sup>+4.0</sup> <sub>-3.5</sub> (4.65 <sup>+4.1</sup> <sub>-4.1</sub> )	6.47 <sup>+7.1</sup> <sub>-5.6</sub> (8.37 <sup>+7.9</sup> <sub>-7.9</sub> )	5.13 <sup>+5.6</sup> <sub>-4.6</sub> (6.87 <sup>+6.2</sup> <sub>-6.2</sub> )
nircam1-4312	0.74 <sup>+0.81</sup> <sub>-0.65</sub> (0.40 <sup>+0.47</sup> <sub>-0.35</sub> )	0.95 <sup>+1.01</sup> <sub>-0.86</sub> (0.56 <sup>+0.63</sup> <sub>-0.44</sub> )	0.66 <sup>+0.74</sup> <sub>-0.58</sub> (0.41 <sup>+0.46</sup> <sub>-0.34</sub> )	0.84 <sup>+0.92</sup> <sub>-0.75</sub> (0.56 <sup>+0.63</sup> <sub>-0.50</sub> )	7.27 <sup>+9.4</sup> <sub>-6.6</sub> (11.1 <sup>+12.4</sup> <sub>-10.1</sub> )	5.96 <sup>+6.3</sup> <sub>-5.6</sub> (8.79 <sup>+8.0</sup> <sub>-8.0</sub> )	7.88 <sup>+8.6</sup> <sub>-7.1</sub> (11.1 <sup>+12.5</sup> <sub>-10.2</sub> )	6.57 <sup>+7.1</sup> <sub>-6.0</sub> (8.89 <sup>+8.6</sup> <sub>-8.0</sub> )
nircam1-4331	0.61 <sup>+0.65</sup> <sub>-0.58</sub> (0.44 <sup>+0.50</sup> <sub>-0.39</sub> )	0.71 <sup>+0.78</sup> <sub>-0.68</sub> (0.60 <sup>+0.67</sup> <sub>-0.53</sub> )	0.50 <sup>+0.52</sup> <sub>-0.49</sub> (0.27 <sup>+0.29</sup> <sub>-0.26</sub> )	0.54 <sup>+0.56</sup> <sub>-0.52</sub> (0.33 <sup>+0.36</sup> <sub>-0.30</sub> )	8.37 <sup>+9.4</sup> <sub>-9.6</sub> (10.4 <sup>+11.4</sup> <sub>-11.4</sub> )	7.37 <sup>+6.8</sup> <sub>-6.8</sub> (8.39 <sup>+7.2</sup> <sub>-7.2</sub> )	9.69 <sup>+10.2</sup> <sub>-9.4</sub> (14.8 <sup>+15.3</sup> <sub>-14.0</sub> )	9.09 <sup>+10.2</sup> <sub>-8.8</sub> (13.0 <sup>+13.8</sup> <sub>-12.1</sub> )
nircam1-4341	0.21 <sup>+0.24</sup> <sub>-0.19</sub> (0.27 <sup>+0.28</sup> <sub>-0.26</sub> )	0.32 <sup>+0.35</sup> <sub>-0.29</sub> (0.36 <sup>+0.38</sup> <sub>-0.35</sub> )	0.13 <sup>+0.14</sup> <sub>-0.11</sub> (0.23 <sup>+0.24</sup> <sub>-0.22</sub> )	0.19 <sup>+0.22</sup> <sub>-0.17</sub> (0.30 <sup>+0.31</sup> <sub>-0.28</sub> )	17.7 <sup>+19.4</sup> <sub>-16.1</sub> (15.0 <sup>+15.4</sup> <sub>-14.5</sub> )	13.3 <sup>+14.3</sup> <sub>-12.5</sub> (12.0 <sup>+12.4</sup> <sub>-11.7</sub> )	25.3 <sup>+28.1</sup> <sub>-23.2</sub> (16.7 <sup>+17.5</sup> <sub>-16.0</sub> )	19.1 <sup>+21.0</sup> <sub>-17.4</sub> (13.9 <sup>+14.4</sup> <sub>-13.4</sub> )
nircam1-4371	1.52 <sup>+1.66</sup> <sub>-1.41</sub> (0.59 <sup>+0.68</sup> <sub>-0.53</sub> )	2.31 <sup>+2.38</sup> <sub>-2.19</sub> (1.02 <sup>+1.15</sup> <sub>-0.91</sub> )	0.46 <sup>+0.51</sup> <sub>-0.41</sub> (0.21 <sup>+0.24</sup> <sub>-0.19</sub> )	0.81 <sup>+0.93</sup> <sub>-0.70</sub> (0.31 <sup>+0.36</sup> <sub>-0.27</sub> )	4.03 <sup>+3.8</sup> <sub>-3.8</sub> (8.5 <sup>+9.2</sup> <sub>-7.6</sub> )	2.82 <sup>+2.7</sup> <sub>-2.7</sub> (5.6 <sup>+6.1</sup> <sub>-6.2</sub> )	10.2 <sup>+11.0</sup> <sub>-10.2</sub> (17.7 <sup>+19.3</sup> <sub>-16.2</sub> )	6.77 <sup>+7.4</sup> <sub>-6.0</sub> (13.6 <sup>+15.0</sup> <sub>-12.2</sub> )
nircam1-4630	1.00 <sup>+1.17</sup> <sub>-0.84</sub> (0.68 <sup>+0.79</sup> <sub>-0.57</sub> )	1.32 <sup>+1.47</sup> <sub>-1.13</sub> (0.92 <sup>+1.09</sup> <sub>-0.79</sub> )	1.10 <sup>+1.28</sup> <sub>-0.93</sub> (0.74 <sup>+0.87</sup> <sub>-0.62</sub> )	1.46 <sup>+1.61</sup> <sub>-1.25</sub> (1.04 <sup>+1.22</sup> <sub>-0.90</sub> )	5.66 <sup>+5.0</sup> <sub>-5.0</sub> (7.6 <sup>+8.7</sup> <sub>-6.8</sub> )	4.51 <sup>+4.2</sup> <sub>-4.1</sub> (6.0 <sup>+6.8</sup> <sub>-5.8</sub> )	5.26 <sup>+6.0</sup> <sub>-4.7</sub> (7.1 <sup>+8.1</sup> <sub>-6.3</sub> )	4.24 <sup>+4.7</sup> <sub>-3.8</sub> (5.5 <sup>+6.2</sup> <sub>-4.8</sub> )
nircam1-5041	3.06 <sup>+3.13</sup> <sub>-2.98</sub> (1.35 <sup>+1.47</sup> <sub>-1.20</sub> )	3.40 <sup>+3.43</sup> <sub>-3.37</sub> (1.95 <sup>+2.11</sup> <sub>-1.82</sub> )	1.54 <sup>+1.81</sup> <sub>-1.30</sub> (0.63 <sup>+0.55</sup> <sub>-0.43</sub> )	2.40 <sup>+2.60</sup> <sub>-2.19</sub> (0.80 <sup>+0.98</sup> <sub>-0.75</sub> )	2.12 <sup>+2.1</sup> <sub>-2.1</sub> (4.4 <sup>+4.1</sup> <sub>-4.1</sub> )	1.91 <sup>+1.9</sup> <sub>-1.9</sub> (3.3 <sup>+3.5</sup> <sub>-3.0</sub> )	4.04 <sup>+6.5</sup> <sub>-3.5</sub> (8.0 <sup>+8.9</sup> <sub>-7.3</sub> )	2.72 <sup>+2.9</sup> <sub>-2.5</sub> (6.3 <sup>+6.7</sup> <sub>-5.1</sub> )
nircam1-5060	1.74 <sup>+2.01</sup> <sub>-1.43</sub> (0.79 <sup>+0.89</sup> <sub>-0.69</sub> )	2.42 <sup>+2.56</sup> <sub>-2.27</sub> (1.10 <sup>+1.25</sup> <sub>-0.97</sub> )	0.55 <sup>+0.83</sup> <sub>-0.37</sub> (0.49 <sup>+0.55</sup> <sub>-0.43</sub> )	1.02 <sup>+1.39</sup> <sub>-0.68</sub> (0.61 <sup>+0.69</sup> <sub>-0.54</sub> )	3.64 <sup>+4.2</sup> <sub>-3.2</sub> (6.8 <sup>+7.5</sup> <sub>-6.2</sub> )	2.72 <sup>+2.8</sup> <sub>-2.5</sub> (5.2 <sup>+5.8</sup> <sub>-4.8</sub> )	8.91 <sup>+11.9</sup> <sub>-6.5</sub> (9.8 <sup>+10.6</sup> <sub>-8.9</sub> )	5.67 <sup>+6.9</sup> <sub>-4.3</sub> (8.2 <sup>+9.1</sup> <sub>-7.5</sub> )
nircam1-5171	2.09 <sup>+2.19</sup> <sub>-1.95</sub> (0.52 <sup>+0.59</sup> <sub>-0.45</sub> )	2.45 <sup>+2.51</sup> <sub>-2.36</sub> (0.73 <sup>+0.82</sup> <sub>-0.65</sub> )	1.69 <sup>+1.79</sup> <sub>-1.51</sub> (0.36 <sup>+0.42</sup> <sub>-0.32</sub> )	2.01 <sup>+2.14</sup> <sub>-1.87</sub> (0.49 <sup>+0.56</sup> <sub>-0.43</sub> )	3.13 <sup>+3.3</sup> <sub>-3.2</sub> (9.3 <sup>+10.3</sup> <sub>-10.8</sub> )	2.72 <sup>+2.7</sup> <sub>-2.6</sub> (7.2 <sup>+7.8</sup> <sub>-6.6</sub> )	3.74 <sup>+4.0</sup> <sub>-3.5</sub> (12.0 <sup>+13.3</sup> <sub>-10.8</sub> )	3.23 <sup>+3.4</sup> <sub>-3.0</sub> (9.7 <sup>+10.7</sup> <sub>-8.8</sub> )
nircam1-5344	0.30 <sup>+0.33</sup> <sub>-0.28</sub> (0.11 <sup>+0.11</sup> <sub>-0.10</sub> )	0.50 <sup>+0.57</sup> <sub>-0.45</sub> (0.16 <sup>+0.16</sup> <sub>-0.16</sub> )	0.26 <sup>+0.25</sup> <sub>-0.25</sub> (0.05 <sup>+0.05</sup> <sub>-0.05</sub> )	0.39 <sup>+0.44</sup> <sub>-0.37</sub> (0.07 <sup>+0.07</sup> <sub>-0.07</sub> )	13.7 <sup>+14.4</sup> <sub>-13.0</sub> (28.6 <sup>+29.1</sup> <sub>-27.9</sub> )	9.51 <sup>+10.2</sup> <sub>-8.7</sub> (21.1 <sup>+21.6</sup> <sub>-20.6</sub> )	15.4 <sup>+15.9</sup> <sub>-14.6</sub> (49.7 <sup>+50.9</sup> <sub>-48.2</sub> )	11.4 <sup>+11.9</sup> <sub>-10.5</sub> (37.8 <sup>+38.3</sup> <sub>-37.3</sub> )
nircam1-5450	0.84 <sup>+0.90</sup> <sub>-0.78</sub> (0.52 <sup>+0.57</sup> <sub>-0.48</sub> )	1.06 <sup>+1.11</sup> <sub>-1.01</sub> (0.75 <sup>+0.82</sup> <sub>-0.70</sub> )	0.75 <sup>+0.81</sup> <sub>-0.68</sub> (0.45 <sup>+0.49</sup> <sub>-0.41</sub> )	0.95 <sup>+1.01</sup> <sub>-0.89</sub> (0.63 <sup>+0.69</sup> <sub>-0.57</sub> )	6.4 <sup>+6.8</sup> <sub>-6.1</sub> (9.3 <sup>+9.8</sup> <sub>-8.7</sub> )	5.45 <sup>+5.6</sup> <sub>-5.2</sub> (7.0 <sup>+7.5</sup> <sub>-6.6</sub> )	7.17 <sup>+7.6</sup> <sub>-6.1</sub> (10.4 <sup>+11.0</sup> <sub>-9.7</sub> )	5.96 <sup>+6.2</sup> <sub>-5.6</sub> (8.1 <sup>+8.6</sup> <sub>-7.6</sub> )
nircam1-5714	1.94 <sup>+1.99</sup> <sub>-1.87</sub> (1.70 <sup>+1.77</sup> <sub>-1.62</sub> )	2.20 <sup>+2.24</sup> <sub>-2.16</sub> (2.01 <sup>+2.05</sup> <sub>-1.95</sub> )	0.83 <sup>+0.96</sup> <sub>-0.72</sub> (0.66 <sup>+0.70</sup> <sub>-0.60</sub> )	1.06 <sup>+1.18</sup> <sub>-0.94</sub> (0.99 <sup>+1.13</sup> <sub>-0.88</sub> )	3.33 <sup>+3.4</sup> <sub>-3.2</sub> (3.7 <sup>+3.8</sup> <sub>-3.5</sub> )	2.93 <sup>+3.0</sup> <sub>-3.2</sub> (3.2 <sup>+3.1</sup> <sub>-3.1</sub> )	6.57 <sup>+7.3</sup> <sub>-5.9</sub> (7.8 <sup>+8.3</sup> <sub>-7.1</sub> )	5.45 <sup>+5.9</sup> <sub>-5.0</sub> (5.7 <sup>+6.3</sup> <sub>-5.1</sub> )
nircam1-5868	1.46 <sup>+1.57</sup> <sub>-1.30</sub> (0.91 <sup>+1.04</sup> <sub>-0.78</sub> )	1.85 <sup>+1.92</sup> <sub>-1.73</sub> (1.34 <sup>+1.41</sup> <sub>-1.16</sub> )	1.14 <sup>+1.29</sup> <sub>-1.02</sub> (0.72 <sup>+0.80</sup> <sub>-0.64</sub> )	1.53 <sup>+1.65</sup> <sub>-1.39</sub> (1.03 <sup>+1.18</sup> <sub>-0.88</sub> )	4.24 <sup>+4.6</sup> <sub>-4.1</sub> (6.1 <sup>+6.8</sup> <sub>-5.5</sub> )	3.43 <sup>+3.6</sup> <sub>-3.3</sub> (4.5 <sup>+4.0</sup> <sub>-4.0</sub> )	5.15 <sup>+5.6</sup> <sub>-4.6</sub> (7.3 <sup>+8.0</sup> <sub>-6.7</sub> )	4.04 <sup>+4.4</sup> <sub>-3.8</sub> (5.5 <sup>+6.2</sup> <sub>-5.0</sub> )
nircam1-5968	1.32 <sup>+1.49</sup> <sub>-1.14</sub> (0.59 <sup>+0.70</sup> <sub>-0.50</sub> )	1.63 <sup>+1.77</sup> <sub>-1.44</sub> (0.83 <sup>+0.95</sup> <sub>-0.70</sub> )	1.15 <sup>+1.34</sup> <sub>-1.00</sub> (0.54 <sup>+0.64</sup> <sub>-0.45</sub> )	1.42 <sup>+1.59</sup> <sub>-1.22</sub> (0.73 <sup>+0.86</sup> <sub>-0.61</sub> )	4.51 <sup>+4.5</sup> <sub>-4.1</sub> (8.4 <sup>+7.4</sup> <sub>-7.4</sub> )	3.83 <sup>+3.5</sup> <sub>-3.5</sub> (6.5 <sup>+5.9</sup> <sub>-5.9</sub> )	5.15 <sup>+5.7</sup> <sub>-4.5</sub> (9.0 <sup>+10.4</sup> <sub>-8.0</sub> )	4.33 <sup>+4.8</sup> <sub>-3.9</sub> (7.2 <sup>+8.3</sup> <sub>-6.4</sub> )
nircam1-6027	0.21 <sup>+0.21</sup> <sub>-0.20</sub> (0.42 <sup>+0.46</sup> <sub>-0.38</sub> )	0.27 <sup>+0.28</sup> <sub>-0.26</sub> (0.54 <sup>+0.57</sup> <sub>-0.50</sub> )	0.16 <sup>+0.16</sup> <sub>-0.16</sub> (0.26 <sup>+0.30</sup> <sub>-0.23</sub> )	0.18 <sup>+0.18</sup> <sub>-0.18</sub> (0.34 <sup>+0.38</sup> <sub>-0.30</sub> )	17.8 <sup>+18.1</sup> <sub>-17.5</sub> (10.9 <sup>+11.7</sup> <sub>-10.2</sub> )	15.0 <sup>+15.2</sup> <sub>-14.6</sub> (9.0 <sup>+9.9</sup> <sub>-8.7</sub> )	21.7 <sup>+21.8</sup> <sub>-21.6</sub> (15.3 <sup>+16.5</sup> <sub>-13.9</sub> )	19.8 <sup>+19.9</sup> <sub>-19.6</sub> (12.7 <sup>+13.9</sup> <sub>-11.7</sub> )
nircam1-6028	0.50 <sup>+0.50</sup> <sub>-0.49</sub> (0.39 <sup>+0.39</sup> <sub>-0.38</sub> )	0.58 <sup>+0.57</sup> <sub>-0.57</sub> (0.50 <sup>+0.51</sup> <sub>-0.46</sub> )	0.41 <sup>+0.41</sup> <sub>-0.40</sub> (0.27 <sup>+0.27</sup> <sub>-0.26</sub> )	0.43 <sup>+0.44</sup> <sub>-0.43</sub> (0.29 <sup>+0.30</sup> <sub>-0.29</sub> )	9.69 <sup>+9.7</sup> <sub>-9.5</sub> (11.5 <sup>+11.4</sup> <sub>-11.4</sub> )	8.68 <sup>+8.5</sup> <sub>-8.5</sub> (9.5 <sup>+9.4</sup> <sub>-9.4</sub> )	11.1 <sup>+11.2</sup> <sub>-11.1</sub> (15.0 <sup>+15.1</sup> <sub>-15.0</sub> )	10.7 <sup>+10.7</sup> <sub>-10.6</sub> (14.1 <sup>+14.2</sup> <sub>-14.0</sub> )
nircam1-6070	0.46 <sup>+0.64</sup> <sub>-0.34</sub> (0.33 <sup>+0.37</sup> <sub>-0.31</sub> )	0.74 <sup>+0.89</sup> <sub>-0.57</sub> (0.47 <sup>+0.52</sup> <sub>-0.44</sub> )	0.26 <sup>+0.38</sup> <sub>-0.20</sub> (0.22 <sup>+0.24</sup> <sub>-0.21</sub> )	0.39 <sup>+0.63</sup> <sub>-0.29</sub> (0.28 <sup>+0.37</sup> <sub>-0.27</sub> )	10.2 <sup>+12.8</sup> <sub>-7.5</sub> (12.8 <sup>+13.4</sup> <sub>-11.9</sub> )	7.18 <sup>+7.2</sup> <sub>-6.2</sub> (9.9 <sup>+10.6</sup> <sub>-9.3</sub> )	15.3 <sup>+18.2</sup> <sub>-11.7</sub> (17.0 <sup>+17.6</sup> <sub>-16.2</sub> )	11.5 <sup>+14.1</sup> <sub>-8.1</sub> (14.4 <sup>+15.1</sup> <sub>-13.4</sub> )
nircam1-6122	0.65 <sup>+0.79</sup> <sub>-0.51</sub> (0.63 <sup>+0.71</sup> <sub>-0.56</sub> )	0.91 <sup>+1.05</sup> <sub>-0.79</sub> (0.80 <sup>+0.88</sup> <sub>-0.71</sub> )	0.53 <sup>+0.65</sup> <sub>-0.37</sub> (0.58 <sup>+0.64</sup> <sub>-0.50</sub> )	0.71 <sup>+0.87</sup> <sub>-0.57</sub> (0.71 <sup>+0.80</sup> <sub>-0.63</sub> )	7.99 <sup>+4.4</sup> <sub>-6.8</sub> (8.0 <sup>+8.8</sup> <sub>-7.4</sub> )	6.15 <sup>+6.8</sup> <sub>-5.4</sub> (6.7 <sup>+7.3</sup> <sub>-6.2</sub> )	9.21 <sup>+11.8</sup> <sub>-7.9</sub> (8.6 <sup>+9.6</sup> <sub>-7.9</sub> )	7.48 <sup>+7.7</sup> <sub>-6.3</sub> (7.4 <sup>+8.1</sup> <sub>-6.7</sub> )
nircam1-6205	0.52 <sup>+0.53</sup> <sub>-0.52</sub> (0.34 <sup>+0.34</sup> <sub>-0.33</sub> )	0.58 <sup>+0.59</sup> <sub>-0.57</sub> (0.40 <sup>+0.40</sup> <sub>-0.39</sub> )	0.47 <sup>+0.47</sup> <sub>-0.47</sub> (0.29 <sup>+0.29</sup> <sub>-0.29</sub> )	0.50 <sup>+0.50</sup> <sub>-0.49</sub> (0.31 <sup>+0.31</sup> <sub>-0.31</sub> )	9.29 <sup>+3.3</sup> <sub>-9.2</sub> (12.7 <sup>+12.9</sup> <sub>-12.6</sub> )	8.68 <sup>+8.6</sup> <sub>-8.5</sub> (11.3 <sup>+11.2</sup> <sub>-11.2</sub> )	10.0 <sup>+10.1</sup> <sub>-10.0</sub> (14.1 <sup>+14.1</sup> <sub>-14.0</sub> )	9.69 <sup>+9.7</sup> <sub>-9.6</sub> (13.4 <sup>+13.5</sup> <sub>-13.4</sub> )
nircam1-6554	0.58 <sup>+0.70</sup> <sub>-0.49</sub> (0.58 <sup>+0.63</sup> <sub>-0.54</sub> )	0.93 <sup>+1.02</sup> <sub>-0.82</sub> (1.22 <sup>+1.04</sup> <sub>-1.04</sub> )	0.21 <sup>+0.24</sup> <sub>-0.19</sub> (0.21 <sup>+0.21</sup> <sub>-0.20</sub> )	0.27 <sup>+0.32</sup> <sub>-0.20</sub> (0.27 <sup>+0.32</sup> <sub>-0.29</sub> )	8.57 <sup>+7.7</sup> <sub>-7.4</sub> (8.6 <sup>+9.1</sup> <sub>-8.1</sub> )	6.05 <sup>+6.6</sup> <sub>-5.6</sub> (4.8 <sup>+4.5</sup> <sub>-4.5</sub> )	17.6 <sup>+18.9</sup> <sub>-16.3</sub> (17.7 <sup>+18.1</sup> <sub>-17.2</sub> )	14.9 <sup>+16.2</sup> <sub>-13.3</sub> (15.0 <sup>+15.6</sup> <sub>-14.3</sub> )
nircam1-6676	0.69 <sup>+0.76</sup> <sub>-0.61</sub> (0.67 <sup>+0.77</sup> <sub>-0.60</sub> )	0.97 <sup>+1.02</sup> <sub>-0.91</sub> (1.10 <sup>+1.22</sup> <sub>-0.99</sub> )	0.55 <sup>+0.63</sup> <sub>-0.48</sub> (0.63 <sup>+0.71</sup> <sub>-0.55</sub> )	0.78 <sup>+0.85</sup> <sub>-0.71</sub> (1.00 <sup>+1.11</sup> <sub>-0.88</sub> )	7.58 <sup>+7.2</sup> <sub>-7.0</sub> (7.7 <sup>+8.3</sup> <sub>-6.9</sub> )	5.86 <sup>+5.1</sup> <sub>-5.6</sub> (5.2 <sup>+5.7</sup> <sub>-4.8</sub> )	8.99 <sup>+8.1</sup> <sub>-8.1</sub> (8.1 <sup>+8.9</sup> <sub>-7.3</sub> )	6.97 <sup>+6.4</sup> <sub>-6.4</sub> (5.7 <sup>+6.3</sup> <sub>-5.2</sub> )
nircam1-6696	1.70 <sup>+1.75</sup> <sub>-1.63</sub> (1.56 <sup>+1.66</sup> <sub>-1.47</sub> )	2.18 <sup>+2.22</sup> <sub>-2.14</sub> (2.41 <sup>+2.45</sup> <sub>-2.37</sub> )	0.46 <sup>+0.58</sup> <sub>-0.39</sub> (0.37 <sup>+0.35</sup> <sub>-0.35</sub> )	0.72 <sup>+0.84</sup> <sub>-0.58</sub> (0.47 <sup>+0.51</sup> <sub>-0.45</sub> )	3.73 <sup>+3.6</sup> <sub>-3.7</sub> (4.0 <sup>+4.1</sup> <sub>-4.1</sub> )	2.93 <sup>+2.9</sup> <sub>-2.9</sub> (2.7 <sup>+2.7</sup> <sub>-2.6</sub> )	10.1 <sup>+11.4</sup> <sub>-10.5</sub> (11.9 <sup>+12.3</sup> <sub>-11.3</sub> )	7.38 <sup>+8.6</sup> <sub>-6.5</sub> (9.9 <sup>+10.3</sup> <sub>-9.4</sub> )
nircam1-6857	0.50 <sup>+0.56</sup> <sub>-0.45</sub> (0.41 <sup>+0.37</sup> <sub>-0.37</sub> )	0.69 <sup>+0.77</sup> <sub>-0.60</sub> (0.55 <sup>+0.60</sup> <sub>-0.50</sub> )	0.35 <sup>+0.38</sup> <sub>-0.33</sub> (0.27 <sup>+0.29</sup> <sub>-0.24</sub> )	0.41 <sup>+0.45</sup> <sub>-0.38</sub> (0.34 <sup>+0.37</sup> <sub>-0.30</sub> )	9.68 <sup>+8.3</sup> <sub>-11.1</sub> (11.1 <sup>+11.9</sup> <sub>-10.3</sub> )	7.58 <sup>+6.9</sup> <sub>-7.5</sub> (9.0 <sup>+9.6</sup> <sub>-8.4</sub> )	12.4 <sup>+12.9</sup> <sub>-11.8</sub> (14.8 <sup>+16.1</sup> <sub>-14.0</sub> )	11.0 <sup>+11.6</sup> <sub>-10.3</sub> (12.7 <sup>+13.7</sup> <sub>-11.9</sub> )
nircam1-6917	1.88 <sup>+1.99</sup> <sub>-1.67</sub> (0.79 <sup>+0.83</sup> <sub>-0.61</sub> )	2.16 <sup>+2.24</sup> <sub>-2.02</sub> (1.06 <sup>+1.23</sup> <sub>-0.87</sub> )	1.75 <sup>+1.89</sup> <sub>-1.52</sub> (0.75 <sup>+0.97</sup> <sub>-0.57</sub> )	2.00 <sup>+2.11</sup> <sub>-1.86</sub> (1.00 <sup>+1.18</sup> <sub>-0.81</sub> )	3.43 <sup>+3.2</sup> <sub>-3.2</sub> (6.8 <sup>+6.0</sup> <sub>-6.0</sub> )	3.02 <sup>+2.9</sup> <sub>-2.9</sub> (5.4 <sup>+4.8</sup> <sub>-4.8</sub> )	3.63 <sup>+3.3</sup> <sub>-3.0</sub> (7.1 <sup>+7.1</sup> <sub>-6.1</sub> )	3.23 <sup>+3.0</sup> <sub>-3.0</sub> (5.7 <sup>+5.0</sup> <sub>-5.0</sub> )
nircam1-6972	0.67 <sup>+0.68</sup> <sub>-0.67</sub> (0.22 <sup>+0.23</sup> <sub>-0.22</sub> )	0.75 <sup>+0.74</sup> <sub>-0.74</sub> (0.29 <sup>+0.30</sup> <sub>-0.28</sub> )	0.60 <sup>+0.60</sup> <sub>-0.59</sub> (0.14 <sup>+0.14</sup> <sub>-0.14</sub> )	0.62 <sup>+0.63</sup> <sub>-0.62</sub> (0.15 <sup>+0.15</sup> <sub>-0.14</sub> )	7.77 <sup>+7.7</sup> <sub>-7.0</sub> (17.0 <sup>+17.3</sup> <sub>-16.6</sub> )	7.17 <sup>+7.2</sup> <sub>-7.0</sub> (14.2 <sup>+14.7</sup> <sub>-13.7</sub> )	8.48 <sup>+8.4</sup> <sub>-8.3</sub> (23.9 <sup>+24.9</sup> <sub>-23.7</sub> )	8.18 <sup>+8.2</sup> <sub>-8.1</sub> (22.9 <sup>+23.0</sup> <sub>-22.6</sub> )
nircam1-7539	0.35 <sup>+0.37</sup> <sub>-0.21</sub> (0.39 <sup>+0.42</sup> <sub>-0.36</sub> )	0.60 <sup>+0.64</sup> <sub>-0.48</sub> (0.51 <sup>+0.55</sup> <sub>-0.45</sub> )	0.21 <sup>+0.24</sup> <sub>-0.19</sub> (0.30 <sup>+0.31</sup> <sub>-0.28</sub> )	0.35 <sup>+0.42</sup> <sub>-0.30</sub> (0.34 <sup>+0.37</sup> <sub>-0.32</sub> )	13.3 <sup>+15.0</sup> <sub>-12.0</sub> (11.5 <sup>+12.2</sup> <sub>-10.9</sub> )	8.39 <sup>+9.4</sup> <sub>-8.3</sub> (9.5 <sup>+10.3</sup> <sub>-8.9</sub> )	17.6<	

Table E.1: (Continued)

Galaxy name	$t_5^{\text{SB99(BC03)}}$ [Gyr]	$t_{10}^{\text{SB99(BC03)}}$ [Gyr]	$t_{5 \times 10^8 \text{ M}_\odot}^{\text{SB99(BC03)}}$ [Gyr]	$t_{10^9 \text{ M}_\odot}^{\text{SB99(BC03)}}$ [Gyr]	$z_5^{\text{SB99(BC03)}}$	$z_{10}^{\text{SB99(BC03)}}$	$z_{5 \times 10^8 \text{ M}_\odot}^{\text{SB99(BC03)}}$	$z_{10^9 \text{ M}_\odot}^{\text{SB99(BC03)}}$
nircam1-7915	0.78 <sup>0.80</sup> <sub>0.75</sub> (0.33 <sup>0.35</sup> <sub>0.30</sub> )	0.92 <sup>0.95</sup> <sub>0.87</sub> (0.59 <sup>0.66</sup> <sub>0.52</sub> )	0.73 <sup>0.74</sup> <sub>0.71</sub> (0.18 <sup>0.19</sup> <sub>0.17</sub> )	0.82 <sup>0.85</sup> <sub>0.79</sub> (0.26 <sup>0.28</sup> <sub>0.25</sub> )	6.97 <sup>0</sup> <sub>6.7</sub> (12.9 <sup>13.7</sup> <sub>12.3</sub> )	6.06 <sup>3</sup> <sub>5.8</sub> (8.59 <sup>2</sup> <sub>7.8</sub> )	7.7 <sup>4</sup> <sub>7.1</sub> (20.0 <sup>21.0</sup> <sub>19.2</sub> )	6.66 <sup>8</sup> <sub>6.4</sub> (15.2 <sup>15.9</sup> <sub>14.4</sub> )
nircam1-8004	0.91 <sup>0.97</sup> <sub>0.83</sub> (0.47 <sup>0.54</sup> <sub>0.42</sub> )	1.10 <sup>1.16</sup> <sub>1.04</sub> (0.65 <sup>0.73</sup> <sub>0.58</sub> )	0.70 <sup>0.76</sup> <sub>0.67</sub> (0.39 <sup>0.45</sup> <sub>0.34</sub> )	0.85 <sup>0.90</sup> <sub>0.77</sub> (0.53 <sup>0.46</sup> <sub>0.46</sub> )	6.16 <sup>5</sup> <sub>5.8</sub> (10.0 <sup>10.9</sup> <sub>9.6</sub> )	5.35 <sup>5</sup> <sub>5.0</sub> (7.97 <sup>2</sup> <sub>7.2</sub> )	7.57 <sup>1</sup> <sub>7.0</sub> (11.4 <sup>10.4</sup> <sub>10.4</sub> )	6.46 <sup>9</sup> <sub>6.0</sub> (9.1 <sup>8.4</sup> <sub>8.4</sub> )
nircam1-8217	0.57 <sup>0.62</sup> <sub>0.54</sub> (0.43 <sup>0.46</sup> <sub>0.40</sub> )	0.82 <sup>0.87</sup> <sub>0.78</sub> (0.65 <sup>0.67</sup> <sub>0.61</sub> )	0.27 <sup>0.27</sup> <sub>0.26</sub> (0.12 <sup>0.13</sup> <sub>0.12</sub> )	0.30 <sup>0.31</sup> <sub>0.29</sub> (0.16 <sup>0.15</sup> <sub>0.15</sub> )	8.9 <sup>0</sup> <sub>8.1</sub> (10.7 <sup>11.2</sup> <sub>10.2</sub> )	6.6 <sup>9</sup> <sub>6.3</sub> (7.97 <sup>2</sup> <sub>7.7</sub> )	15.1 <sup>15.2</sup> <sub>14.8</sub> (25.7 <sup>26.4</sup> <sub>24.9</sub> )	13.8 <sup>14.1</sup> <sub>13.4</sub> (21.9 <sup>22.9</sup> <sub>20.8</sub> )
nircam1-8314	0.91 <sup>0.95</sup> <sub>0.86</sub> (0.76 <sup>0.80</sup> <sub>0.72</sub> )	1.11 <sup>1.14</sup> <sub>1.07</sub> (1.01 <sup>1.05</sup> <sub>0.98</sub> )	0.47 <sup>0.51</sup> <sub>0.43</sub> (0.33 <sup>0.36</sup> <sub>0.31</sub> )	0.58 <sup>0.63</sup> <sub>0.52</sub> (0.45 <sup>0.48</sup> <sub>0.42</sub> )	6.15 <sup>3</sup> <sub>6.1</sub> (7.0 <sup>7.3</sup> <sub>6.7</sub> )	5.25 <sup>4</sup> <sub>5.1</sub> (5.65 <sup>7</sup> <sub>5.4</sub> )	9.9 <sup>10.6</sup> <sub>9.4</sub> (12.8 <sup>13.6</sup> <sub>12.1</sub> )	8.5 <sup>9.3</sup> <sub>8.0</sub> (10.4 <sup>10.9</sup> <sub>9.9</sub> )
nircam1-8402	0.54 <sup>0.67</sup> <sub>0.46</sub> (0.53 <sup>0.76</sup> <sub>0.36</sub> )	1.93 <sup>2.27</sup> <sub>1.49</sub> (0.85 <sup>1.22</sup> <sub>0.62</sub> )	0.34 <sup>0.37</sup> <sub>0.30</sub> (0.26 <sup>0.32</sup> <sub>0.17</sub> )	0.61 <sup>0.76</sup> <sub>0.49</sub> (0.40 <sup>0.54</sup> <sub>0.26</sub> )	9.0 <sup>10.2</sup> <sub>10.7</sub> (9.2 <sup>12.1</sup> <sub>12.1</sub> )	3.3 <sup>2.8</sup> <sub>4.1</sub> (6.4 <sup>8.2</sup> <sub>13.3</sub> )	12.7 <sup>13.8</sup> <sub>11.8</sub> (15.4 <sup>20.5</sup> <sub>13.3</sub> )	8.3 <sup>9.6</sup> <sub>7.0</sub> (11.2 <sup>15.2</sup> <sub>9.0</sub> )
nircam1-8416	0.79 <sup>0.94</sup> <sub>0.65</sub> (0.60 <sup>0.68</sup> <sub>0.54</sub> )	1.07 <sup>1.25</sup> <sub>0.96</sub> (0.81 <sup>0.92</sup> <sub>0.72</sub> )	0.58 <sup>0.75</sup> <sub>0.48</sub> (0.49 <sup>0.54</sup> <sub>0.44</sub> )	0.85 <sup>1.00</sup> <sub>0.70</sub> (0.62 <sup>0.70</sup> <sub>0.56</sub> )	6.8 <sup>7.8</sup> <sub>6.0</sub> (8.3 <sup>7.6</sup> <sub>7.6</sub> )	5.3 <sup>5.8</sup> <sub>4.7</sub> (6.7 <sup>6.2</sup> <sub>6.2</sub> )	8.6 <sup>9.9</sup> <sub>7.0</sub> (9.8 <sup>10.5</sup> <sub>9.0</sub> )	6.4 <sup>7.4</sup> <sub>5.7</sub> (8.1 <sup>8.8</sup> <sub>7.4</sub> )
nircam1-8464	0.72 <sup>0.82</sup> <sub>0.65</sub> (0.36 <sup>0.41</sup> <sub>0.31</sub> )	1.32 <sup>1.56</sup> <sub>1.04</sub> (0.52 <sup>0.57</sup> <sub>0.46</sub> )	0.62 <sup>0.70</sup> <sub>0.57</sub> (0.29 <sup>0.33</sup> <sub>0.24</sub> )	1.05 <sup>1.29</sup> <sub>0.86</sub> (0.41 <sup>0.46</sup> <sub>0.36</sub> )	7.3 <sup>7.9</sup> <sub>6.6</sub> (12.1 <sup>13.4</sup> <sub>11.0</sub> )	4.5 <sup>5.5</sup> <sub>4.0</sub> (9.3 <sup>10.1</sup> <sub>12.9</sub> )	8.1 <sup>8.6</sup> <sub>7.4</sub> (14.1 <sup>16.1</sup> <sub>10.2</sub> )	5.4 <sup>6.4</sup> <sub>4.6</sub> (11.0 <sup>12.0</sup> <sub>10.2</sub> )
nircam1-8588	1.08 <sup>1.18</sup> <sub>0.94</sub> (0.31 <sup>0.39</sup> <sub>0.24</sub> )	1.37 <sup>1.47</sup> <sub>1.27</sub> (0.49 <sup>0.58</sup> <sub>0.40</sub> )	0.95 <sup>1.05</sup> <sub>0.76</sub> (0.20 <sup>0.26</sup> <sub>0.14</sub> )	1.18 <sup>1.29</sup> <sub>1.06</sub> (0.30 <sup>0.38</sup> <sub>0.22</sub> )	5.3 <sup>5.9</sup> <sub>5.0</sub> (13.5 <sup>16.2</sup> <sub>11.1</sub> )	4.4 <sup>4.7</sup> <sub>4.1</sub> (9.7 <sup>11.3</sup> <sub>18.6</sub> )	5.9 <sup>7.0</sup> <sub>5.4</sub> (18.7 <sup>23.5</sup> <sub>15.3</sub> )	5.0 <sup>5.4</sup> <sub>4.6</sub> (13.8 <sup>17.0</sup> <sub>11.7</sub> )
nircam1-8729	0.24 <sup>0.24</sup> <sub>0.24</sub> (0.29 <sup>0.32</sup> <sub>0.26</sub> )	0.28 <sup>0.28</sup> <sub>0.28</sub> (0.39 <sup>0.34</sup> <sub>0.34</sub> )	0.20 <sup>0.20</sup> <sub>0.20</sub> (0.24 <sup>0.25</sup> <sub>0.23</sub> )	0.22 <sup>0.23</sup> <sub>0.22</sub> (0.29 <sup>0.30</sup> <sub>0.27</sub> )	16.2 <sup>16.3</sup> <sub>16.0</sub> (14.0 <sup>15.1</sup> <sub>13.2</sub> )	14.5 <sup>14.7</sup> <sub>14.3</sub> (11.5 <sup>12.8</sup> <sub>10.6</sub> )	18.7 <sup>18.9</sup> <sub>18.5</sub> (16.2 <sup>15.8</sup> <sub>15.8</sub> )	17.1 <sup>17.4</sup> <sub>16.8</sub> (14.2 <sup>14.8</sup> <sub>13.7</sub> )
nircam1-8904	2.06 <sup>2.19</sup> <sub>1.90</sub> (0.94 <sup>1.06</sup> <sub>0.81</sub> )	2.55 <sup>2.63</sup> <sub>2.47</sub> (1.40 <sup>1.62</sup> <sub>1.18</sub> )	1.81 <sup>1.98</sup> <sub>1.60</sub> (0.82 <sup>0.94</sup> <sub>0.71</sub> )	2.31 <sup>2.41</sup> <sub>2.18</sub> (1.18 <sup>1.36</sup> <sub>0.99</sub> )	3.1 <sup>3.3</sup> <sub>3.1</sub> (5.9 <sup>6.7</sup> <sub>5.4</sub> )	2.5 <sup>2.6</sup> <sub>2.5</sub> (4.3 <sup>5.0</sup> <sub>3.8</sub> )	3.5 <sup>3.9</sup> <sub>3.2</sub> (6.6 <sup>7.3</sup> <sub>5.9</sub> )	2.8 <sup>2.9</sup> <sub>2.7</sub> (5.0 <sup>5.7</sup> <sub>4.4</sub> )
nircam1-8959	0.78 <sup>0.84</sup> <sub>0.73</sub> (0.48 <sup>0.54</sup> <sub>0.41</sub> )	1.04 <sup>1.11</sup> <sub>0.93</sub> (0.70 <sup>0.82</sup> <sub>0.60</sub> )	0.65 <sup>0.69</sup> <sub>0.60</sub> (0.40 <sup>0.44</sup> <sub>0.35</sub> )	0.84 <sup>0.90</sup> <sub>0.79</sub> (0.53 <sup>0.63</sup> <sub>0.47</sub> )	6.8 <sup>7.2</sup> <sub>6.4</sub> (9.9 <sup>11.0</sup> <sub>9.1</sub> )	5.5 <sup>5.7</sup> <sub>4.8</sub> (7.4 <sup>8.4</sup> <sub>10.4</sub> )	7.9 <sup>8.4</sup> <sub>7.5</sub> (11.3 <sup>12.4</sup> <sub>10.4</sub> )	6.5 <sup>6.8</sup> <sub>6.1</sub> (8.9 <sup>10.0</sup> <sub>8.0</sub> )
nircam1-9090	0.70 <sup>0.64</sup> <sub>0.60</sub> (0.59 <sup>0.75</sup> <sub>0.46</sub> )	1.05 <sup>1.14</sup> <sub>0.92</sub> (0.85 <sup>1.03</sup> <sub>0.75</sub> )	0.85 <sup>0.98</sup> <sub>0.71</sub> (0.67 <sup>0.84</sup> <sub>0.54</sub> )	1.13 <sup>1.24</sup> <sub>1.01</sub> (0.99 <sup>1.17</sup> <sub>0.85</sub> )	7.0 <sup>8.0</sup> <sub>7.6</sub> (8.5 <sup>10.1</sup> <sub>8.7</sub> )	5.4 <sup>6.1</sup> <sub>4.1</sub> (6.4 <sup>7.3</sup> <sub>6.4</sub> )	6.4 <sup>7.4</sup> <sub>4.7</sub> (7.7 <sup>9.0</sup> <sub>6.4</sub> )	5.1 <sup>5.6</sup> <sub>4.7</sub> (5.7 <sup>6.4</sup> <sub>5.0</sub> )
nircam1-9185	0.25 <sup>0.28</sup> <sub>0.23</sub> (0.22 <sup>0.24</sup> <sub>0.21</sub> )	0.35 <sup>0.41</sup> <sub>0.32</sub> (0.30 <sup>0.34</sup> <sub>0.29</sub> )	0.18 <sup>0.19</sup> <sub>0.16</sub> (0.16 <sup>0.17</sup> <sub>0.15</sub> )	0.22 <sup>0.25</sup> <sub>0.21</sub> (0.20 <sup>0.22</sup> <sub>0.20</sub> )	15.8 <sup>16.7</sup> <sub>14.5</sub> (17.2 <sup>17.8</sup> <sub>16.2</sub> )	12.3 <sup>13.2</sup> <sub>11.1</sub> (13.8 <sup>14.3</sup> <sub>12.7</sub> )	20.1 <sup>21.4</sup> <sub>19.0</sub> (21.5 <sup>22.2</sup> <sub>20.3</sub> )	17.0 <sup>18.0</sup> <sub>15.8</sub> (18.2 <sup>18.7</sup> <sub>17.2</sub> )
nircam1-9293	1.23 <sup>1.27</sup> <sub>1.18</sub> (0.79 <sup>0.84</sup> <sub>0.74</sub> )	1.46 <sup>1.48</sup> <sub>1.43</sub> (1.15 <sup>1.19</sup> <sub>1.11</sub> )	0.65 <sup>0.71</sup> <sub>0.60</sub> (0.41 <sup>0.44</sup> <sub>0.39</sub> )	0.84 <sup>0.91</sup> <sub>0.77</sub> (0.53 <sup>0.58</sup> <sub>0.50</sub> )	4.8 <sup>5.0</sup> <sub>4.5</sub> (6.8 <sup>7.1</sup> <sub>6.5</sub> )	4.2 <sup>4.2</sup> <sub>4.1</sub> (5.1 <sup>5.2</sup> <sub>4.9</sub> )	7.9 <sup>8.3</sup> <sub>7.4</sub> (11.1 <sup>11.5</sup> <sub>10.5</sub> )	6.5 <sup>6.9</sup> <sub>6.1</sub> (9.1 <sup>9.5</sup> <sub>8.6</sub> )
nircam1-9476	0.26 <sup>0.30</sup> <sub>0.24</sub> (0.18 <sup>0.17</sup> <sub>0.14</sub> )	0.45 <sup>0.54</sup> <sub>0.40</sub> (0.26 <sup>0.25</sup> <sub>0.25</sub> )	0.09 <sup>0.10</sup> <sub>0.08</sub> (0.08 <sup>0.08</sup> <sub>0.08</sub> )	0.14 <sup>0.15</sup> <sub>0.12</sub> (0.11 <sup>0.11</sup> <sub>0.10</sub> )	15.2 <sup>16.4</sup> <sub>13.7</sub> (20.1 <sup>20.6</sup> <sub>19.3</sub> )	10.3 <sup>10.3</sup> <sub>9.0</sub> (15.1 <sup>15.6</sup> <sub>14.4</sub> )	32.1 <sup>34.1</sup> <sub>29.8</sub> (34.3 <sup>35.0</sup> <sub>33.3</sub> )	24.1 <sup>26.2</sup> <sub>22.6</sub> (28.3 <sup>29.2</sup> <sub>27.1</sub> )
nircam1-9565	0.57 <sup>0.57</sup> <sub>0.56</sub> (0.33 <sup>0.32</sup> <sub>0.32</sub> )	0.61 <sup>0.62</sup> <sub>0.61</sub> (0.43 <sup>0.45</sup> <sub>0.41</sub> )	0.51 <sup>0.51</sup> <sub>0.51</sub> (0.20 <sup>0.20</sup> <sub>0.20</sub> )	0.53 <sup>0.53</sup> <sub>0.53</sub> (0.22 <sup>0.22</sup> <sub>0.22</sub> )	8.7 <sup>8.8</sup> <sub>8.7</sub> (13.1 <sup>13.3</sup> <sub>12.7</sub> )	8.2 <sup>8.2</sup> <sub>8.2</sub> (10.8 <sup>11.1</sup> <sub>10.4</sub> )	9.9 <sup>9.4</sup> <sub>9.4</sub> (18.2 <sup>18.1</sup> <sub>17.2</sub> )	9.2 <sup>9.2</sup> <sub>9.1</sub> (17.3 <sup>17.2</sup> <sub>17.2</sub> )
nircam1-9691	1.98 <sup>2.02</sup> <sub>1.94</sub> (1.05 <sup>1.23</sup> <sub>0.93</sub> )	2.14 <sup>2.17</sup> <sub>2.08</sub> (1.45 <sup>1.60</sup> <sub>1.30</sub> )	1.11 <sup>1.32</sup> <sub>0.91</sub> (0.67 <sup>0.76</sup> <sub>0.58</sub> )	1.78 <sup>1.90</sup> <sub>1.62</sub> (0.89 <sup>1.03</sup> <sub>0.77</sub> )	3.2 <sup>3.3</sup> <sub>3.2</sub> (5.5 <sup>6.0</sup> <sub>4.8</sub> )	3.0 <sup>3.1</sup> <sub>3.0</sub> (4.2 <sup>4.6</sup> <sub>3.9</sub> )	5.2 <sup>6.1</sup> <sub>4.8</sub> (7.7 <sup>8.6</sup> <sub>7.0</sub> )	3.5 <sup>3.8</sup> <sub>3.3</sub> (6.2 <sup>6.9</sup> <sub>5.5</sub> )
nircam1-9825	1.18 <sup>1.35</sup> <sub>0.99</sub> (0.97 <sup>1.16</sup> <sub>0.79</sub> )	1.55 <sup>1.67</sup> <sub>1.39</sub> (1.38 <sup>1.52</sup> <sub>1.18</sub> )	1.23 <sup>1.40</sup> <sub>1.04</sub> (1.03 <sup>1.23</sup> <sub>0.84</sub> )	1.59 <sup>1.74</sup> <sub>1.44</sub> (1.45 <sup>1.60</sup> <sub>1.26</sub> )	5.0 <sup>5.7</sup> <sub>4.5</sub> (5.8 <sup>6.8</sup> <sub>5.0</sub> )	4.0 <sup>4.3</sup> <sub>3.7</sub> (4.4 <sup>5.0</sup> <sub>4.0</sub> )	4.8 <sup>5.5</sup> <sub>4.3</sub> (5.5 <sup>6.5</sup> <sub>4.8</sub> )	3.9 <sup>4.2</sup> <sub>3.6</sub> (4.2 <sup>4.7</sup> <sub>3.9</sub> )
nircam1-9859	0.29 <sup>0.30</sup> <sub>0.28</sub> (0.61 <sup>0.67</sup> <sub>0.54</sub> )	0.37 <sup>0.39</sup> <sub>0.37</sub> (0.94 <sup>0.93</sup> <sub>0.93</sub> )	0.23 <sup>0.24</sup> <sub>0.23</sub> (0.31 <sup>0.33</sup> <sub>0.29</sub> )	0.27 <sup>0.28</sup> <sub>0.27</sub> (0.44 <sup>0.47</sup> <sub>0.41</sub> )	14.2 <sup>14.4</sup> <sub>13.9</sub> (8.3 <sup>7.0</sup> <sub>8.3</sub> )	11.8 <sup>12.0</sup> <sub>11.5</sub> (5.9 <sup>6.0</sup> <sub>5.9</sub> )	16.5 <sup>16.6</sup> <sub>16.3</sub> (13.6 <sup>12.9</sup> <sub>12.9</sub> )	14.8 <sup>15.0</sup> <sub>14.5</sub> (10.5 <sup>11.1</sup> <sub>10.0</sub> )
nircam1-10038	0.19 <sup>0.19</sup> <sub>0.19</sub> (1.85 <sup>2.05</sup> <sub>1.59</sub> )	0.24 <sup>0.24</sup> <sub>0.24</sub> (2.29 <sup>2.47</sup> <sub>2.10</sub> )	0.13 <sup>0.13</sup> <sub>0.13</sub> (1.11 <sup>1.31</sup> <sub>0.91</sub> )	0.15 <sup>0.15</sup> <sub>0.15</sub> (1.35 <sup>1.58</sup> <sub>1.14</sub> )	19.0 <sup>19.1</sup> <sub>18.9</sub> (3.4 <sup>3.9</sup> <sub>3.1</sub> )	16.3 <sup>16.4</sup> <sub>16.2</sub> (2.8 <sup>3.0</sup> <sub>2.6</sub> )	24.3 <sup>24.4</sup> <sub>24.2</sub> (5.2 <sup>6.1</sup> <sub>4.6</sub> )	22.3 <sup>22.5</sup> <sub>22.1</sub> (4.5 <sup>5.1</sup> <sub>4.5</sub> )
nircam1-10087	0.31 <sup>0.32</sup> <sub>0.30</sub> (0.26 <sup>0.27</sup> <sub>0.26</sub> )	0.39 <sup>0.42</sup> <sub>0.37</sub> (0.31 <sup>0.32</sup> <sub>0.31</sub> )	0.23 <sup>0.24</sup> <sub>0.22</sub> (0.20 <sup>0.20</sup> <sub>0.20</sub> )	0.27 <sup>0.28</sup> <sub>0.26</sub> (0.22 <sup>0.22</sup> <sub>0.22</sub> )	13.6 <sup>14.0</sup> <sub>13.2</sub> (15.2 <sup>15.3</sup> <sub>15.1</sub> )	11.4 <sup>11.8</sup> <sub>10.9</sub> (13.4 <sup>13.6</sup> <sub>13.3</sub> )	16.6 <sup>17.0</sup> <sub>16.1</sub> (18.2 <sup>18.2</sup> <sub>18.1</sub> )	14.7 <sup>15.1</sup> <sub>14.3</sub> (17.1 <sup>17.2</sup> <sub>17.0</sub> )
nircam1-10163	0.71 <sup>0.73</sup> <sub>0.70</sub> (0.26 <sup>0.27</sup> <sub>0.25</sub> )	0.80 <sup>0.82</sup> <sub>0.78</sub> (0.32 <sup>0.34</sup> <sub>0.30</sub> )	0.67 <sup>0.68</sup> <sub>0.66</sub> (0.19 <sup>0.18</sup> <sub>0.18</sub> )	0.72 <sup>0.74</sup> <sub>0.70</sub> (0.21 <sup>0.22</sup> <sub>0.20</sub> )	7.3 <sup>7.4</sup> <sub>7.2</sub> (15.4 <sup>15.9</sup> <sub>15.0</sub> )	6.7 <sup>6.9</sup> <sub>6.6</sub> (13.1 <sup>13.8</sup> <sub>12.6</sub> )	7.7 <sup>7.8</sup> <sub>7.6</sub> (19.3 <sup>19.7</sup> <sub>19.0</sub> )	7.3 <sup>7.4</sup> <sub>7.4</sub> (17.6 <sup>18.2</sup> <sub>17.1</sub> )
nircam1-10234	1.01 <sup>1.18</sup> <sub>0.66</sub> (1.10 <sup>1.21</sup> <sub>0.92</sub> )	1.14 <sup>1.44</sup> <sub>0.82</sub> (1.40 <sup>1.50</sup> <sub>1.25</sub> )	0.79 <sup>1.03</sup> <sub>0.57</sub> (0.91 <sup>1.02</sup> <sub>0.77</sub> )	1.02 <sup>1.25</sup> <sub>0.68</sub> (1.21 <sup>1.32</sup> <sub>1.02</sub> )	5.6 <sup>7.7</sup> <sub>5.0</sub> (5.2 <sup>6.0</sup> <sub>4.9</sub> )	5.1 <sup>6.6</sup> <sub>4.2</sub> (4.3 <sup>4.7</sup> <sub>3.4</sub> )	6.8 <sup>8.6</sup> <sub>5.5</sub> (6.1 <sup>6.9</sup> <sub>5.6</sub> )	5.6 <sup>7.9</sup> <sub>4.7</sub> (4.8 <sup>5.6</sup> <sub>4.5</sub> )
nircam1-10398	0.56 <sup>0.63</sup> <sub>0.51</sub> (0.53 <sup>0.59</sup> <sub>0.49</sub> )	0.76 <sup>0.83</sup> <sub>0.69</sub> (0.71 <sup>0.78</sup> <sub>0.65</sub> )	0.53 <sup>0.59</sup> <sub>0.49</sub> (0.57 <sup>0.64</sup> <sub>0.52</sub> )	0.70 <sup>0.77</sup> <sub>0.64</sub> (0.77 <sup>0.85</sup> <sub>0.70</sub> )	8.8 <sup>9.4</sup> <sub>8.1</sub> (9.1 <sup>9.8</sup> <sub>8.4</sub> )	7.0 <sup>7.5</sup> <sub>6.5</sub> (7.4 <sup>7.9</sup> <sub>6.8</sub> )	9.2 <sup>9.8</sup> <sub>8.4</sub> (8.6 <sup>9.3</sup> <sub>8.0</sub> )	7.4 <sup>8.0</sup> <sub>6.9</sub> (6.9 <sup>7.4</sup> <sub>6.4</sub> )
nircam1-10564	1.45 <sup>1.57</sup> <sub>1.37</sub> (0.57 <sup>0.69</sup> <sub>0.48</sub> )	1.71 <sup>1.78</sup> <sub>1.64</sub> (0.89 <sup>1.09</sup> <sub>0.74</sub> )	1.00 <sup>1.09</sup> <sub>0.85</sub> (0.29 <sup>0.35</sup> <sub>0.25</sub> )	1.22 <sup>1.26</sup> <sub>1.17</sub> (0.35 <sup>0.42</sup> <sub>0.32</sub> )	4.2 <sup>4.3</sup> <sub>4.2</sub> (8.6 <sup>9.8</sup> <sub>7.5</sub> )	3.6 <sup>3.8</sup> <sub>3.5</sub> (6.2 <sup>7.3</sup> <sub>5.3</sub> )	5.6 <sup>6.4</sup> <sub>5.3</sub> (14.2 <sup>15.6</sup> <sub>12.4</sub> )	4.8 <sup>5.0</sup> <sub>4.7</sub> (11.6 <sup>13.3</sup> <sub>10.3</sub> )
nircam1-10634	1.39 <sup>1.56</sup> <sub>1.22</sub> (0.70 <sup>0.77</sup> <sub>0.63</sub> )	1.81 <sup>1.84</sup> <sub>1.64</sub> (0.95 <sup>1.06</sup> <sub>0.83</sub> )	1.28 <sup>1.48</sup> <sub>1.12</sub> (0.64 <sup>0.71</sup> <sub>0.58</sub> )	1.67 <sup>1.82</sup> <sub>1.49</sub> (0.84 <sup>0.94</sup> <sub>0.74</sub> )	4.3 <sup>4.8</sup> <sub>3.9</sub> (7.4 <sup>8.1</sup> <sub>6.9</sub> )	3.5 <sup>3.8</sup> <sub>3.3</sub> (5.9 <sup>6.5</sup> <sub>5.4</sub> )	4.6 <sup>5.2</sup> <sub>4.1</sub> (8.0 <sup>8.6</sup> <sub>7.4</sub> )	3.7 <sup>4.1</sup> <sub>3.5</sub> (6.5 <sup>7.2</sup> <sub>5.9</sub> )
nircam1-10770	1.43 <sup>1.46</sup> <sub>1.39</sub> (0.70 <sup>0.74</sup> <sub>0.65</sub> )	1.62 <sup>1.64</sup> <sub>1.59</sub> (0.94 <sup>0.98</sup> <sub>0.89</sub> )	1.13 <sup>1.19</sup> <sub>1.04</sub> (0.51 <sup>0.55</sup> <sub>0.47</sub> )	1.32 <sup>1.35</sup> <sub>1.26</sub> (0.67 <sup>0.72</sup> <sub>0.63</sub> )	4.2 <sup>4.2</sup> <sub>4.2</sub> (7.4 <sup>7.8</sup> <sub>7.1</sub> )	3.8 <sup>3.9</sup> <sub>3.8</sub> (5.9 <sup>6.2</sup> <sub>5.7</sub> )	5.1 <sup>5.5</sup> <sub>4.9</sub> (9.4 <sup>10.0</sup> <sub>8.9</sub> )	4.5 <sup>4.7</sup> <sub>4.4</sub> (7.7 <sup>8.1</sup> <sub>7.3</sub> )
nircam1-10795	1.44 <sup>1.59</sup> <sub>1.27</sub> (0.37 <sup>0.43</sup> <sub>0.33</sub> )	1.96 <sup>2.18</sup> <sub>1.78</sub> (0.54 <sup>0.61</sup> <sub>0.47</sub> )	1.49 <sup>1.66</sup> <sub>1.31</sub> (0.35 <sup>0.41</sup> <sub>0.31</sub> )	2.05 <sup>2.25</sup> <sub>1.84</sub> (0.51 <sup>0.59</sup> <sub>0.44</sub> )	4.2 <sup>4.2</sup> <sub>4.2</sub> (11.9 <sup>13.0</sup> <sub>10.7</sub> )	3.2 <sup>3.5</sup> <sub>3.2</sub> (9.0 <sup>10.0</sup> <sub>8.2</sub> )	4.1	



Table E.1: (Continued)

Galaxy name	$t_5$ [Gyr]	$t_{10}$ [Gyr]	$t_{5 \times 10^8 M_\odot}$ [Gyr]	$t_{10^9 M_\odot}$ [Gyr]	$z_5$	$z_{10}$	$z_{5 \times 10^8 M_\odot}$	$z_{10^9 M_\odot}$
nircam1-11036	2.19 <sup>+2.29</sup> <sub>-2.03</sub> (1.73 <sup>+1.91</sup> <sub>-1.41</sub> )	2.64 <sup>+2.70</sup> <sub>-2.56</sub> (2.53 <sup>+2.66</sup> <sub>-2.31</sub> )	1.72 <sup>+1.89</sup> <sub>-1.52</sub> (1.16 <sup>+1.39</sup> <sub>-0.94</sub> )	2.18 <sup>+2.29</sup> <sub>-2.05</sub> (1.90 <sup>+2.10</sup> <sub>-1.59</sub> )	2.93 <sup>+1</sup> <sub>-2.8</sub> (3.6 <sup>+4.3</sup> <sub>-3.3</sub> )	2.52 <sup>+5</sup> <sub>-2.4</sub> (2.6 <sup>+2.8</sup> <sub>-2.4</sub> )	3.64 <sup>+0</sup> <sub>-3.3</sub> (5.0 <sup>+5.9</sup> <sub>-4.3</sub> )	3.03 <sup>+1</sup> <sub>-2.8</sub> (3.3 <sup>+3.9</sup> <sub>-3.1</sub> )
nircam1-11038	0.63 <sup>+0.62</sup> <sub>-0.61</sub> (0.31 <sup>+0.32</sup> <sub>-0.31</sub> )	0.68 <sup>+0.69</sup> <sub>-0.67</sub> (0.37 <sup>+0.38</sup> <sub>-0.36</sub> )	0.59 <sup>+0.59</sup> <sub>-0.58</sub> (0.27 <sup>+0.27</sup> <sub>-0.26</sub> )	0.63 <sup>+0.64</sup> <sub>-0.63</sub> (0.31 <sup>+0.31</sup> <sub>-0.30</sub> )	8.28 <sup>+2</sup> <sub>-1.7</sub> (13.4 <sup>+13.5</sup> <sub>-13.2</sub> )	7.67 <sup>+7</sup> <sub>-6.6</sub> (11.9 <sup>+12.1</sup> <sub>-11.7</sub> )	8.58 <sup>+5</sup> <sub>-4.6</sub> (15.0 <sup>+15.1</sup> <sub>-14.8</sub> )	8.08 <sup>+1</sup> <sub>-1.7</sub> (13.6 <sup>+13.7</sup> <sub>-13.4</sub> )
nircam1-11048	0.75 <sup>+0.77</sup> <sub>-0.73</sub> (0.26 <sup>+0.28</sup> <sub>-0.25</sub> )	0.86 <sup>+0.91</sup> <sub>-0.83</sub> (0.33 <sup>+0.36</sup> <sub>-0.31</sub> )	0.69 <sup>+0.70</sup> <sub>-0.68</sub> (0.18 <sup>+0.18</sup> <sub>-0.18</sub> )	0.75 <sup>+0.73</sup> <sub>-0.73</sub> (0.20 <sup>+0.21</sup> <sub>-0.19</sub> )	7.17 <sup>+2</sup> <sub>-6.9</sub> (15.3 <sup>+15.8</sup> <sub>-14.7</sub> )	6.46 <sup>+6</sup> <sub>-6.1</sub> (12.9 <sup>+13.6</sup> <sub>-12.2</sub> )	7.67 <sup>+6</sup> <sub>-6.9</sub> (19.9 <sup>+20.2</sup> <sub>-19.6</sub> )	7.17 <sup>+2</sup> <sub>-6.9</sub> (18.5 <sup>+19.0</sup> <sub>-18.0</sub> )
nircam1-11082	0.49 <sup>+0.55</sup> <sub>-0.43</sub> (0.55 <sup>+0.61</sup> <sub>-0.49</sub> )	0.78 <sup>+0.87</sup> <sub>-0.68</sub> (0.97 <sup>+1.15</sup> <sub>-0.84</sub> )	0.31 <sup>+0.34</sup> <sub>-0.29</sub> (0.36 <sup>+0.39</sup> <sub>-0.33</sub> )	0.42 <sup>+0.47</sup> <sub>-0.38</sub> (0.50 <sup>+0.55</sup> <sub>-0.45</sub> )	9.81 <sup>+0.6</sup> <sub>-8.9</sub> (9.0 <sup>+9.7</sup> <sub>-8.2</sub> )	6.87 <sup>+6</sup> <sub>-5.2</sub> (5.8 <sup>+5.6</sup> <sub>-5.1</sub> )	13.4 <sup>+4.2</sup> <sub>-12.7</sub> (12.2 <sup>+12.9</sup> <sub>-11.5</sub> )	10.8 <sup>+1.7</sup> <sub>-10.0</sub> (9.6 <sup>+10.3</sup> <sub>-8.9</sub> )
nircam1-11242	0.89 <sup>+1.12</sup> <sub>-0.70</sub> (1.34 <sup>+1.48</sup> <sub>-1.16</sub> )	1.28 <sup>+1.47</sup> <sub>-1.06</sub> (1.71 <sup>+1.80</sup> <sub>-1.60</sub> )	0.88 <sup>+1.11</sup> <sub>-0.89</sub> (1.29 <sup>+1.45</sup> <sub>-1.10</sub> )	1.28 <sup>+1.46</sup> <sub>-1.10</sub> (1.67 <sup>+1.76</sup> <sub>-1.55</sub> )	6.25 <sup>+2</sup> <sub>-5.2</sub> (4.5 <sup>+4.5</sup> <sub>-4.1</sub> )	4.64 <sup>+2</sup> <sub>-3.9</sub> (3.6 <sup>+3.9</sup> <sub>-3.5</sub> )	6.37 <sup>+6</sup> <sub>-5.2</sub> (4.6 <sup>+4.2</sup> <sub>-4.2</sub> )	4.65 <sup>+4</sup> <sub>-4.3</sub> (3.7 <sup>+4.0</sup> <sub>-3.6</sub> )
nircam1-11292	1.14 <sup>+0.99</sup> <sub>-0.99</sub> (0.91 <sup>+1.13</sup> <sub>-0.76</sub> )	1.42 <sup>+1.57</sup> <sub>-1.30</sub> (1.46 <sup>+1.70</sup> <sub>-1.25</sub> )	1.02 <sup>+1.18</sup> <sub>-0.89</sub> (0.74 <sup>+0.94</sup> <sub>-0.61</sub> )	1.28 <sup>+1.42</sup> <sub>-1.10</sub> (1.12 <sup>+1.33</sup> <sub>-0.95</sub> )	5.15 <sup>+7</sup> <sub>-4.6</sub> (6.1 <sup>+7.0</sup> <sub>-5.1</sub> )	4.33 <sup>+9</sup> <sub>-3.9</sub> (4.2 <sup>+3.7</sup> <sub>-3.7</sub> )	5.66 <sup>+2</sup> <sub>-4.9</sub> (7.1 <sup>+8.2</sup> <sub>-5.9</sub> )	4.65 <sup>+2</sup> <sub>-4.3</sub> (5.2 <sup>+5.9</sup> <sub>-4.5</sub> )
nircam1-11387	0.55 <sup>+0.84</sup> <sub>-0.43</sub> (1.12 <sup>+1.35</sup> <sub>-0.93</sub> )	1.86 <sup>+2.08</sup> <sub>-1.32</sub> (1.67 <sup>+1.85</sup> <sub>-1.42</sub> )	0.62 <sup>+0.95</sup> <sub>-0.46</sub> (1.15 <sup>+1.38</sup> <sub>-0.92</sub> )	1.97 <sup>+2.22</sup> <sub>-1.55</sub> (1.70 <sup>+1.87</sup> <sub>-1.44</sub> )	8.91 <sup>+0.7</sup> <sub>-6.5</sub> (5.2 <sup>+6.0</sup> <sub>-4.4</sub> )	3.45 <sup>+5</sup> <sub>-3.1</sub> (3.7 <sup>+4.3</sup> <sub>-3.4</sub> )	8.21 <sup>+0.2</sup> <sub>-5.9</sub> (5.1 <sup>+6.0</sup> <sub>-4.4</sub> )	3.24 <sup>+0</sup> <sub>-2.9</sub> (3.7 <sup>+4.2</sup> <sub>-3.4</sub> )
nircam2-327	0.19 <sup>+0.12</sup> <sub>-0.11</sub> (0.65 <sup>+0.73</sup> <sub>-0.59</sub> )	0.19 <sup>+0.20</sup> <sub>-0.17</sub> (1.11 <sup>+1.12</sup> <sub>-1.11</sub> )	0.04 <sup>+0.04</sup> <sub>-0.04</sub> (0.31 <sup>+0.33</sup> <sub>-0.28</sub> )	0.06 <sup>+0.06</sup> <sub>-0.05</sub> (0.46 <sup>+0.51</sup> <sub>-0.43</sub> )	26.32 <sup>+3</sup> <sub>-18.6</sub> (7.88 <sup>+4.4</sup> <sub>-5.2</sub> )	19.32 <sup>+0.3</sup> <sub>-1.5</sub> (5.2 <sup>+5.2</sup> <sub>-4.5</sub> )	57.65 <sup>+9.1</sup> <sub>-56.2</sub> (13.6 <sup>+14.4</sup> <sub>-12.9</sub> )	44.64 <sup>+6.2</sup> <sub>-43.2</sub> (10.2 <sup>+10.8</sup> <sub>-9.4</sub> )
nircam2-526	0.35 <sup>+0.35</sup> <sub>-0.35</sub> (0.21 <sup>+0.21</sup> <sub>-0.21</sub> )	0.39 <sup>+0.40</sup> <sub>-0.39</sub> (0.27 <sup>+0.27</sup> <sub>-0.26</sub> )	0.32 <sup>+0.32</sup> <sub>-0.32</sub> (0.18 <sup>+0.18</sup> <sub>-0.18</sub> )	0.35 <sup>+0.35</sup> <sub>-0.35</sub> (0.21 <sup>+0.21</sup> <sub>-0.21</sub> )	12.41 <sup>+2.5</sup> <sub>-12.3</sub> (18.0 <sup>+17.8</sup> <sub>-14.9</sub> )	11.41 <sup>+1.5</sup> <sub>-11.3</sub> (15.1 <sup>+14.9</sup> <sub>-13.7</sub> )	13.21 <sup>+3.3</sup> <sub>-13.1</sub> (19.7 <sup>+19.6</sup> <sub>-19.6</sub> )	12.41 <sup>+2.5</sup> <sub>-12.3</sub> (17.6 <sup>+17.4</sup> <sub>-17.4</sub> )
nircam2-640	0.80 <sup>+0.80</sup> <sub>-0.79</sub> (0.27 <sup>+0.27</sup> <sub>-0.26</sub> )	0.85 <sup>+0.86</sup> <sub>-0.84</sub> (0.34 <sup>+0.35</sup> <sub>-0.33</sub> )	0.73 <sup>+0.73</sup> <sub>-0.73</sub> (0.18 <sup>+0.18</sup> <sub>-0.18</sub> )	0.75 <sup>+0.76</sup> <sub>-0.75</sub> (0.20 <sup>+0.21</sup> <sub>-0.20</sub> )	6.76 <sup>+8</sup> <sub>-6.7</sub> (15.1 <sup>+15.3</sup> <sub>-14.8</sub> )	6.46 <sup>+5</sup> <sub>-6.4</sub> (12.7 <sup>+12.9</sup> <sub>-12.4</sub> )	7.27 <sup>+2</sup> <sub>-7.2</sub> (19.6 <sup>+19.8</sup> <sub>-19.4</sub> )	7.07 <sup>+1</sup> <sub>-7.0</sub> (18.2 <sup>+18.3</sup> <sub>-18.0</sub> )
nircam2-739	1.24 <sup>+1.36</sup> <sub>-1.07</sub> (0.44 <sup>+0.49</sup> <sub>-0.39</sub> )	1.65 <sup>+1.75</sup> <sub>-1.53</sub> (0.64 <sup>+0.70</sup> <sub>-0.56</sub> )	0.89 <sup>+1.02</sup> <sub>-0.89</sub> (0.31 <sup>+0.35</sup> <sub>-0.26</sub> )	1.19 <sup>+1.33</sup> <sub>-1.03</sub> (0.43 <sup>+0.47</sup> <sub>-0.36</sub> )	4.85 <sup>+4</sup> <sub>-4.4</sub> (10.4 <sup>+11.4</sup> <sub>-9.7</sub> )	3.84 <sup>+0</sup> <sub>-3.6</sub> (7.9 <sup>+7.4</sup> <sub>-7.4</sub> )	6.27 <sup>+1</sup> <sub>-5.6</sub> (13.6 <sup>+15.3</sup> <sub>-12.4</sub> )	4.95 <sup>+5</sup> <sub>-4.5</sub> (10.7 <sup>+12.0</sup> <sub>-9.9</sub> )
nircam2-797	0.50 <sup>+0.50</sup> <sub>-0.49</sub> (0.34 <sup>+0.34</sup> <sub>-0.33</sub> )	0.55 <sup>+0.56</sup> <sub>-0.54</sub> (0.40 <sup>+0.41</sup> <sub>-0.40</sub> )	0.45 <sup>+0.45</sup> <sub>-0.45</sub> (0.30 <sup>+0.30</sup> <sub>-0.29</sub> )	0.49 <sup>+0.49</sup> <sub>-0.48</sub> (0.32 <sup>+0.32</sup> <sub>-0.32</sub> )	9.69 <sup>+7</sup> <sub>-8.9</sub> (12.7 <sup>+12.6</sup> <sub>-11.4</sub> )	8.90 <sup>+0</sup> <sub>-8.8</sub> (11.2 <sup>+11.4</sup> <sub>-11.4</sub> )	10.31 <sup>+0.4</sup> <sub>-10.3</sub> (14.0 <sup>+14.0</sup> <sub>-14.0</sub> )	9.79 <sup>+8</sup> <sub>-9.7</sub> (13.2 <sup>+13.3</sup> <sub>-13.2</sub> )
nircam2-887	0.23 <sup>+0.25</sup> <sub>-0.22</sub> (0.34 <sup>+0.39</sup> <sub>-0.39</sub> )	0.34 <sup>+0.37</sup> <sub>-0.31</sub> (0.46 <sup>+0.51</sup> <sub>-0.41</sub> )	0.13 <sup>+0.14</sup> <sub>-0.12</sub> (0.17 <sup>+0.21</sup> <sub>-0.14</sub> )	0.16 <sup>+0.18</sup> <sub>-0.15</sub> (0.23 <sup>+0.27</sup> <sub>-0.20</sub> )	16.71 <sup>+5</sup> <sub>-15.9</sub> (12.7 <sup>+13.9</sup> <sub>-12.0</sub> )	12.81 <sup>+3.7</sup> <sub>-11.5</sub> (10.2 <sup>+11.1</sup> <sub>-9.4</sub> )	25.02 <sup>+5.8</sup> <sub>-24.1</sub> (20.2 <sup>+23.4</sup> <sub>-17.9</sub> )	21.12 <sup>+2.2</sup> <sub>-19.9</sub> (16.7 <sup>+18.5</sup> <sub>-14.9</sub> )
nircam2-950	0.42 <sup>+0.42</sup> <sub>-0.41</sub> (0.26 <sup>+0.27</sup> <sub>-0.26</sub> )	0.47 <sup>+0.48</sup> <sub>-0.46</sub> (0.33 <sup>+0.34</sup> <sub>-0.32</sub> )	0.36 <sup>+0.36</sup> <sub>-0.35</sub> (0.21 <sup>+0.21</sup> <sub>-0.20</sub> )	0.38 <sup>+0.38</sup> <sub>-0.38</sub> (0.23 <sup>+0.23</sup> <sub>-0.22</sub> )	10.91 <sup>+0</sup> <sub>-10.0</sub> (15.1 <sup>+15.4</sup> <sub>-14.8</sub> )	10.10 <sup>+0</sup> <sub>-9.9</sub> (12.9 <sup>+13.2</sup> <sub>-12.6</sub> )	12.21 <sup>+2.3</sup> <sub>-12.1</sub> (18.0 <sup>+18.2</sup> <sub>-17.7</sub> )	11.71 <sup>+1.8</sup> <sub>-11.6</sub> (16.9 <sup>+17.0</sup> <sub>-16.7</sub> )
nircam2-1810	0.46 <sup>+0.47</sup> <sub>-0.45</sub> (0.45 <sup>+0.49</sup> <sub>-0.44</sub> )	0.53 <sup>+0.55</sup> <sub>-0.52</sub> (0.66 <sup>+0.66</sup> <sub>-0.60</sub> )	0.43 <sup>+0.44</sup> <sub>-0.42</sub> (0.42 <sup>+0.40</sup> <sub>-0.37</sub> )	0.49 <sup>+0.49</sup> <sub>-0.48</sub> (0.60 <sup>+0.67</sup> <sub>-0.54</sub> )	10.10 <sup>+0.3</sup> <sub>-10.0</sub> (10.3 <sup>+11.3</sup> <sub>-9.7</sub> )	9.13 <sup>+9</sup> <sub>-8.5</sub> (7.8 <sup>+7.3</sup> <sub>-7.7</sub> )	10.71 <sup>+0.8</sup> <sub>-10.6</sub> (10.9 <sup>+11.8</sup> <sub>-10.2</sub> )	9.89 <sup>+9</sup> <sub>-10.6</sub> (8.3 <sup>+9.0</sup> <sub>-7.7</sub> )
nircam2-1823	0.44 <sup>+0.46</sup> <sub>-0.41</sub> (0.40 <sup>+0.47</sup> <sub>-0.37</sub> )	0.59 <sup>+0.65</sup> <sub>-0.54</sub> (0.54 <sup>+0.59</sup> <sub>-0.49</sub> )	0.36 <sup>+0.37</sup> <sub>-0.34</sub> (0.27 <sup>+0.26</sup> <sub>-0.26</sub> )	0.43 <sup>+0.46</sup> <sub>-0.41</sub> (0.32 <sup>+0.30</sup> <sub>-0.30</sub> )	10.51 <sup>+0</sup> <sub>-10.1</sub> (11.2 <sup>+10.5</sup> <sub>-10.5</sub> )	8.57 <sup>+8</sup> <sub>-7.8</sub> (9.1 <sup>+8.5</sup> <sub>-8.5</sub> )	12.21 <sup>+1.9</sup> <sub>-11.9</sub> (15.0 <sup>+15.5</sup> <sub>-14.5</sub> )	10.61 <sup>+1.1</sup> <sub>-10.2</sub> (13.1 <sup>+13.8</sup> <sub>-12.5</sub> )
nircam2-2305	0.18 <sup>+0.20</sup> <sub>-0.16</sub> (0.51 <sup>+0.56</sup> <sub>-0.48</sub> )	0.30 <sup>+0.33</sup> <sub>-0.27</sub> (0.69 <sup>+0.74</sup> <sub>-0.64</sub> )	0.09 <sup>+0.10</sup> <sub>-0.08</sub> (0.33 <sup>+0.36</sup> <sub>-0.30</sub> )	0.13 <sup>+0.14</sup> <sub>-0.12</sub> (0.43 <sup>+0.47</sup> <sub>-0.40</sub> )	19.92 <sup>+1.2</sup> <sub>-18.3</sub> (9.4 <sup>+9.9</sup> <sub>-8.8</sub> )	14.04 <sup>+4.9</sup> <sub>-12.9</sub> (7.5 <sup>+7.9</sup> <sub>-7.1</sub> )	32.23 <sup>+4.5</sup> <sub>-30.2</sub> (12.8 <sup>+13.8</sup> <sub>-12.1</sub> )	24.62 <sup>+5.9</sup> <sub>-23.0</sub> (10.7 <sup>+11.3</sup> <sub>-10.0</sub> )
nircam2-2368	1.97 <sup>+2.06</sup> <sub>-1.80</sub> (0.72 <sup>+0.85</sup> <sub>-0.62</sub> )	2.32 <sup>+2.38</sup> <sub>-2.23</sub> (1.02 <sup>+1.19</sup> <sub>-0.90</sub> )	1.55 <sup>+1.69</sup> <sub>-1.36</sub> (0.53 <sup>+0.63</sup> <sub>-0.44</sub> )	1.91 <sup>+2.01</sup> <sub>-1.76</sub> (0.70 <sup>+0.82</sup> <sub>-0.60</sub> )	3.23 <sup>+5</sup> <sub>-3.1</sub> (7.2 <sup>+8.1</sup> <sub>-6.4</sub> )	2.82 <sup>+9</sup> <sub>-2.7</sub> (5.6 <sup>+6.2</sup> <sub>-4.9</sub> )	4.04 <sup>+4</sup> <sub>-3.7</sub> (9.2 <sup>+10.5</sup> <sub>-8.0</sub> )	3.33 <sup>+6</sup> <sub>-3.3</sub> (7.5 <sup>+8.4</sup> <sub>-6.6</sub> )
nircam2-2572	0.37 <sup>+0.37</sup> <sub>-0.37</sub> (0.22 <sup>+0.22</sup> <sub>-0.21</sub> )	0.41 <sup>+0.41</sup> <sub>-0.41</sub> (0.27 <sup>+0.27</sup> <sub>-0.26</sub> )	0.35 <sup>+0.35</sup> <sub>-0.35</sub> (0.20 <sup>+0.20</sup> <sub>-0.20</sub> )	0.39 <sup>+0.40</sup> <sub>-0.39</sub> (0.23 <sup>+0.23</sup> <sub>-0.23</sub> )	11.91 <sup>+2.0</sup> <sub>-11.9</sub> (17.5 <sup>+17.6</sup> <sub>-17.3</sub> )	11.01 <sup>+1.1</sup> <sub>-11.0</sub> (15.0 <sup>+15.2</sup> <sub>-14.8</sub> )	12.31 <sup>+2.3</sup> <sub>-12.2</sub> (18.5 <sup>+18.6</sup> <sub>-18.4</sub> )	11.41 <sup>+1.4</sup> <sub>-11.4</sub> (16.6 <sup>+16.8</sup> <sub>-16.3</sub> )
nircam2-2853	0.34 <sup>+0.35</sup> <sub>-0.33</sub> (0.27 <sup>+0.27</sup> <sub>-0.27</sub> )	0.40 <sup>+0.42</sup> <sub>-0.39</sub> (0.33 <sup>+0.34</sup> <sub>-0.32</sub> )	0.27 <sup>+0.27</sup> <sub>-0.27</sub> (0.20 <sup>+0.20</sup> <sub>-0.20</sub> )	0.29 <sup>+0.30</sup> <sub>-0.28</sub> (0.22 <sup>+0.22</sup> <sub>-0.21</sub> )	12.61 <sup>+2.8</sup> <sub>-12.4</sub> (14.9 <sup>+15.0</sup> <sub>-14.7</sub> )	11.21 <sup>+1.5</sup> <sub>-11.2</sub> (12.9 <sup>+13.1</sup> <sub>-12.7</sub> )	15.01 <sup>+5.1</sup> <sub>-4.8</sub> (18.6 <sup>+18.6</sup> <sub>-18.5</sub> )	14.21 <sup>+4.4</sup> <sub>-4.0</sub> (17.4 <sup>+17.6</sup> <sub>-17.2</sub> )
nircam2-2927	0.26 <sup>+0.30</sup> <sub>-0.22</sub> (0.39 <sup>+0.45</sup> <sub>-0.34</sub> )	0.37 <sup>+0.40</sup> <sub>-0.33</sub> (0.56 <sup>+0.67</sup> <sub>-0.46</sub> )	0.14 <sup>+0.19</sup> <sub>-0.11</sub> (0.33 <sup>+0.37</sup> <sub>-0.29</sub> )	0.22 <sup>+0.26</sup> <sub>-0.18</sub> (0.45 <sup>+0.52</sup> <sub>-0.40</sub> )	15.21 <sup>+7.3</sup> <sub>-13.8</sub> (11.5 <sup>+12.7</sup> <sub>-11.2</sub> )	11.91 <sup>+2.9</sup> <sub>-11.2</sub> (8.7 <sup>+9.7</sup> <sub>-7.7</sub> )	23.42 <sup>+7.2</sup> <sub>-19.4</sub> (12.9 <sup>+14.2</sup> <sub>-11.9</sub> )	17.12 <sup>+0.2</sup> <sub>-15.4</sub> (10.2 <sup>+11.2</sup> <sub>-9.3</sub> )
nircam2-3010	0.27 <sup>+0.30</sup> <sub>-0.25</sub> (0.27 <sup>+0.30</sup> <sub>-0.24</sub> )	0.37 <sup>+0.40</sup> <sub>-0.34</sub> (0.40 <sup>+0.46</sup> <sub>-0.36</sub> )	0.23 <sup>+0.24</sup> <sub>-0.21</sub> (0.28 <sup>+0.31</sup> <sub>-0.25</sub> )	0.30 <sup>+0.32</sup> <sub>-0.28</sub> (0.41 <sup>+0.46</sup> <sub>-0.37</sub> )	14.71 <sup>+5.6</sup> <sub>-14.0</sub> (15.0 <sup>+16.1</sup> <sub>-14.0</sub> )	12.01 <sup>+2.7</sup> <sub>-11.3</sub> (11.3 <sup>+12.1</sup> <sub>-10.6</sub> )	16.81 <sup>+7.5</sup> <sub>-16.0</sub> (14.6 <sup>+15.8</sup> <sub>-13.7</sub> )	13.81 <sup>+3.3</sup> <sub>-3.3</sub> (11.0 <sup>+11.8</sup> <sub>-10.2</sub> )
nircam2-3181	0.76 <sup>+0.84</sup> <sub>-0.62</sub> (0.24 <sup>+0.25</sup> <sub>-0.22</sub> )	0.91 <sup>+1.05</sup> <sub>-0.81</sub> (0.31 <sup>+0.34</sup> <sub>-0.29</sub> )	0.67 <sup>+0.74</sup> <sub>-0.41</sub> (0.18 <sup>+0.20</sup> <sub>-0.18</sub> )	0.78 <sup>+0.88</sup> <sub>-0.66</sub> (0.23 <sup>+0.24</sup> <sub>-0.22</sub> )	7.08 <sup>+2</sup> <sub>-5.3</sub> (16.4 <sup>+17.0</sup> <sub>-15.7</sub> )	6.16 <sup>+7</sup> <sub>-5.3</sub> (13.5 <sup>+14.2</sup> <sub>-12.7</sub> )	7.71 <sup>+1.1</sup> <sub>-18.6</sub> (19.5 <sup>+20.2</sup> <sub>-16.1</sub> )	6.87 <sup>+8</sup> <sub>-6.2</sub> (16.8 <sup>+17.4</sup> <sub>-16.1</sub> )
nircam2-3236	0.41 <sup>+0.43</sup> <sub>-0.40</sub> (0.18 <sup>+0.19</sup> <sub>-0.17</sub> )	0.51 <sup>+0.54</sup> <sub>-0.49</sub> (0.27 <sup>+0.28</sup> <sub>-0.25</sub> )	0.34 <sup>+0.35</sup> <sub>-0.33</sub> (0.13 <sup>+0.15</sup> <sub>-0.12</sub> )	0.39 <sup>+0.41</sup> <sub>-0.38</sub> (0.20 <sup>+0.21</sup> <sub>-0.18</sub> )	11.01 <sup>+1.3</sup> <sub>-11.0</sub> (19.6 <sup>+20.3</sup> <sub>-18.8</sub> )	9.49 <sup>+7</sup> <sub>-9.1</sub> (15.0 <sup>+15.6</sup> <sub>-14.4</sub> )	12.71 <sup>+3.0</sup> <sub>-12.4</sub> (24.3 <sup>+25.9</sup> <sub>-22.8</sub> )	11.41 <sup>+1.7</sup> <sub>-11.1</sub> (18.7 <sup>+19.6</sup> <sub>-17.9</sub> )
nircam2-3270	0.27 <sup>+0.28</sup> <sub>-0.27</sub> (1.02 <sup>+1.14</sup> <sub>-0.90</sub> )	0.33 <sup>+0.34</sup> <sub>-0.32</sub> (1.29 <sup>+1.39</sup> <sub>-1.22</sub> )	0.21 <sup>+0.22</sup> <sub>-0.21</sub> (0.85 <sup>+0.95</sup> <sub>-0.74</sub> )	0.25 <sup>+0.25</sup> <sub>-0.24</sub> (1.12 <sup>+1.23</sup> <sub>-1.07</sub> )	14.81 <sup>+3.1</sup> <sub>-14.6</sub> (5.6 <sup>+5.1</sup> <sub>-4.8</sub> )	12.81 <sup>+2.6</sup> <sub>-12.6</sub> (6.4 <sup>+5.9</sup> <sub>-5.1</sub> )	17.61 <sup>+7.7</sup> <sub>-6.1</sub> (6.4 <sup>+7.1</sup> <sub>-7.1</sub> )	16.01 <sup>+6.2</sup> <sub>-15.7</sub> (5.0 <sup>+5.3</sup> <sub>-4.8</sub> )
nircam2-4057	0.58 <sup>+0.65</sup> <sub>-0.52</sub> (0.36 <sup>+0.44</sup> <sub>-0.29</sub> )	0.75 <sup>+0.80</sup> <sub>-0.69</sub> (0.50 <sup>+0.60</sup> <sub>-0.42</sub> )	0.28 <sup>+0.25</sup> <sub>-0.25</sub> (0.16 <sup>+0.20</sup> <sub>-0.11</sub> )	0.34 <sup>+0.40</sup> <sub>-0.30</sub> (0.21 <sup>+0.27</sup> <sub>-0.20</sub> )	8.69 <sup>+3</sup> <sub>-7.8</sub> (12.2 <sup>+10.5</sup> <sub>-10.5</sub> )	7.07 <sup>+5</sup> <sub>-6.7</sub> (9.5 <sup>+10.9</sup> <sub>-8.3</sub> )	14.51 <sup>+5.6</sup> <sub>-13.4</sub> (21.6 <sup>+27.6</sup> <sub>-18.5</sub> )	12.61 <sup>+3.8</sup> <sub>-11.3</sub> (17.8 <sup>+20.7</sup> <sub>-14.8</sub> )
nircam2-4165	0.33 <sup>+0.34</sup> <sub>-0.32</sub> (0.36 <sup>+0.39</sup> <sub>-0.28</sub> )	0.39 <sup>+0.41</sup> <sub>-0.38</sub> (0.57 <sup>+0.80</sup> <sub>-0.53</sub> )	0.33 <sup>+0.34</sup> <sub>-0.33</sub> (0.43 <sup>+0.58</sup> <sub>-0.33</sub> )	0.40 <sup>+0.42</sup> <sub>-0.39</sub> (0.72 <sup>+0.90</sup> <sub>-0.54</sub> )	13.01 <sup>+3.2</sup> <sub>-12.7</sub> (12.2 <sup>+14.4</sup> <sub>-9.5</sub> )	11.51 <sup>+1.7</sup> <sub>-11.1</sub> (8.6 <sup>+10.6</sup> <sub>-6.7</sub> )	12.81 <sup>+3.0</sup> <sub>-12.5</sub> (10.7 <sup>+12.8</sup> <sub>-8.5</sub> )	11.21 <sup>+1.4</sup> <sub>-10.8</sub> (7.3 <sup>+9.1</sup> <sub>-7.1</sub> )
nircam2-4240	0.68 <sup>+0.69</sup> <sub>-0.67</sub> (0.53 <sup>+0.58</sup> <sub>-0.51</sub> )	0.83 <sup>+0.85</sup> <sub>-0.80</sub> (0.75 <sup>+0.79</sup> <sub>-0.71</sub> )	0.59 <sup>+0.59</sup> <sub>-0.58</sub> (0.36 <sup>+0.35</sup> <sub>-0.35</sub> )	0.65 <sup>+0.66</sup> <sub>-0.64</sub> (0.44 <sup>+0.46</sup> <sub>-0.43</sub> )	7.67 <sup>+5</sup> <sub>-7.5</sub> (9.1 <sup>+9.4</sup> <sub>-8.8</sub> )	6.66 <sup>+4</sup> <sub>-7.0</sub> (7.0 <sup>+7.3</sup> <sub>-6.8</sub> )	8.58 <sup>+5</sup> <sub>-5.4</sub> (12.0 <sup>+12.3</sup> <sub>-11.7</sub> )	7.98 <sup>+0</sup> <sub>-7.7</sub>

Table E.1: (Continued)

Galaxy name	$t_5^{\text{SB99(BC03)}}$ [Gyr]	$t_{10}^{\text{SB99(BC03)}}$ [Gyr]	$t_{5 \times 10^8 \text{ M}_\odot}^{\text{SB99(BC03)}}$ [Gyr]	$t_{10^9 \text{ M}_\odot}^{\text{SB99(BC03)}}$ [Gyr]	$z_5^{\text{SB99(BC03)}}$	$z_{10}^{\text{SB99(BC03)}}$	$z_{5 \times 10^8 \text{ M}_\odot}^{\text{SB99(BC03)}}$	$z_{10^9 \text{ M}_\odot}^{\text{SB99(BC03)}}$
nircam2-4406	0.63 <sup>+0.71</sup> <sub>-0.55</sub> (0.89 <sup>+1.05</sup> <sub>-0.79</sub> )	0.85 <sup>+0.95</sup> <sub>-0.76</sub> (1.28 <sup>+1.41</sup> <sub>-1.14</sub> )	0.72 <sup>+0.82</sup> <sub>-0.63</sub> (0.97 <sup>+1.13</sup> <sub>-0.86</sub> )	0.99 <sup>+1.10</sup> <sub>-0.87</sub> (1.38 <sup>+1.54</sup> <sub>-1.25</sub> )	8.0 <sup>+8.9</sup> <sub>-7.4</sub> (6.2 <sup>+6.8</sup> <sub>-5.4</sub> )	6.4 <sup>+7.0</sup> <sub>-5.8</sub> (4.7 <sup>+5.1</sup> <sub>-4.3</sub> )	7.3 <sup>+8.0</sup> <sub>-6.6</sub> (5.8 <sup>+6.4</sup> <sub>-5.1</sub> )	5.7 <sup>+6.3</sup> <sub>-5.2</sub> (4.4 <sup>+4.7</sup> <sub>-4.0</sub> )
nircam2-4491	2.29 <sup>+2.39</sup> <sub>-2.17</sub> (0.62 <sup>+0.72</sup> <sub>-0.55</sub> )	2.59 <sup>+2.51</sup> <sub>-2.22</sub> (0.90 <sup>+1.01</sup> <sub>-0.82</sub> )	1.98 <sup>+2.11</sup> <sub>-1.80</sub> (0.54 <sup>+0.63</sup> <sub>-0.47</sub> )	2.28 <sup>+2.38</sup> <sub>-2.15</sub> (0.70 <sup>+0.83</sup> <sub>-0.68</sub> )	2.8 <sup>+3.0</sup> <sub>-2.7</sub> (8.1 <sup>+9.3</sup> <sub>-7.9</sub> )	2.5 <sup>+2.6</sup> <sub>-2.5</sub> (6.1 <sup>+6.6</sup> <sub>-5.6</sub> )	3.2 <sup>+3.5</sup> <sub>-3.0</sub> (9.0 <sup>+10.0</sup> <sub>-8.1</sub> )	2.8 <sup>+3.0</sup> <sub>-2.7</sub> (7.0 <sup>+7.6</sup> <sub>-6.2</sub> )
nircam2-4610	0.86 <sup>+0.98</sup> <sub>-0.76</sub> (0.86 <sup>+0.95</sup> <sub>-0.77</sub> )	1.04 <sup>+1.12</sup> <sub>-0.96</sub> (1.10 <sup>+1.17</sup> <sub>-0.99</sub> )	0.73 <sup>+0.85</sup> <sub>-0.67</sub> (0.75 <sup>+0.87</sup> <sub>-0.67</sub> )	0.89 <sup>+1.00</sup> <sub>-0.80</sub> (0.93 <sup>+1.03</sup> <sub>-0.83</sub> )	6.3 <sup>+7.0</sup> <sub>-5.8</sub> (6.4 <sup>+6.9</sup> <sub>-5.9</sub> )	5.5 <sup>+5.8</sup> <sub>-5.2</sub> (5.3 <sup>+5.7</sup> <sub>-5.0</sub> )	7.2 <sup>+7.7</sup> <sub>-6.4</sub> (7.0 <sup>+7.1</sup> <sub>-6.5</sub> )	6.2 <sup>+6.7</sup> <sub>-5.6</sub> (6.0 <sup>+6.5</sup> <sub>-5.5</sub> )
nircam2-4650	1.11 <sup>+1.21</sup> <sub>-0.95</sub> (1.56 <sup>+1.66</sup> <sub>-1.42</sub> )	1.39 <sup>+1.48</sup> <sub>-1.28</sub> (1.89 <sup>+1.97</sup> <sub>-1.79</sub> )	1.00 <sup>+1.12</sup> <sub>-0.82</sub> (1.43 <sup>+1.51</sup> <sub>-1.26</sub> )	1.24 <sup>+1.35</sup> <sub>-1.13</sub> (1.73 <sup>+1.81</sup> <sub>-1.60</sub> )	5.2 <sup>+5.9</sup> <sub>-4.3</sub> (4.9 <sup>+5.3</sup> <sub>-3.7</sub> )	4.3 <sup>+4.6</sup> <sub>-4.1</sub> (3.3 <sup>+3.5</sup> <sub>-3.2</sub> )	5.7 <sup>+6.6</sup> <sub>-4.9</sub> (4.2 <sup>+4.7</sup> <sub>-4.0</sub> )	4.8 <sup>+5.1</sup> <sub>-4.5</sub> (3.6 <sup>+3.9</sup> <sub>-3.5</sub> )
nircam2-4680	0.84 <sup>+0.93</sup> <sub>-0.75</sub> (0.78 <sup>+0.88</sup> <sub>-0.69</sub> )	1.12 <sup>+1.20</sup> <sub>-1.04</sub> (1.28 <sup>+1.39</sup> <sub>-1.19</sub> )	0.85 <sup>+0.94</sup> <sub>-0.77</sub> (0.88 <sup>+0.98</sup> <sub>-0.79</sub> )	1.16 <sup>+1.21</sup> <sub>-1.07</sub> (1.45 <sup>+1.57</sup> <sub>-1.34</sub> )	6.5 <sup>+6.0</sup> <sub>-6.0</sub> (6.9 <sup>+6.5</sup> <sub>-6.3</sub> )	5.2 <sup>+5.5</sup> <sub>-4.9</sub> (4.6 <sup>+4.9</sup> <sub>-4.4</sub> )	6.4 <sup>+6.9</sup> <sub>-5.9</sub> (6.2 <sup>+6.8</sup> <sub>-5.8</sub> )	5.0 <sup>+5.4</sup> <sub>-4.9</sub> (4.2 <sup>+4.5</sup> <sub>-3.9</sub> )
nircam2-4733	2.41 <sup>+2.50</sup> <sub>-2.33</sub> (0.72 <sup>+0.79</sup> <sub>-0.63</sub> )	2.69 <sup>+2.74</sup> <sub>-2.65</sub> (0.96 <sup>+1.04</sup> <sub>-0.88</sub> )	1.61 <sup>+1.79</sup> <sub>-1.36</sub> (0.41 <sup>+0.47</sup> <sub>-0.35</sub> )	1.96 <sup>+2.11</sup> <sub>-1.80</sub> (0.52 <sup>+0.61</sup> <sub>-0.45</sub> )	2.7 <sup>+2.6</sup> <sub>-2.6</sub> (7.3 <sup>+8.0</sup> <sub>-6.8</sub> )	2.4 <sup>+2.4</sup> <sub>-2.4</sub> (5.8 <sup>+6.2</sup> <sub>-5.5</sub> )	3.8 <sup>+3.5</sup> <sub>-3.0</sub> (11.1 <sup>+12.4</sup> <sub>-10.0</sub> )	3.2 <sup>+3.0</sup> <sub>-3.0</sub> (9.2 <sup>+10.3</sup> <sub>-8.3</sub> )
nircam2-4789	0.30 <sup>+0.35</sup> <sub>-0.26</sub> (0.52 <sup>+0.58</sup> <sub>-0.47</sub> )	0.49 <sup>+0.54</sup> <sub>-0.43</sub> (0.69 <sup>+0.74</sup> <sub>-0.63</sub> )	0.14 <sup>+0.15</sup> <sub>-0.12</sub> (0.34 <sup>+0.40</sup> <sub>-0.30</sub> )	0.21 <sup>+0.24</sup> <sub>-0.18</sub> (0.44 <sup>+0.49</sup> <sub>-0.39</sub> )	13.7 <sup>+15.3</sup> <sub>-12.4</sub> (9.2 <sup>+10.9</sup> <sub>-8.6</sub> )	9.7 <sup>+10.7</sup> <sub>-9.0</sub> (7.5 <sup>+8.0</sup> <sub>-7.2</sub> )	24.1 <sup>+26.2</sup> <sub>-22.2</sub> (12.6 <sup>+13.7</sup> <sub>-11.2</sub> )	17.9 <sup>+20.0</sup> <sub>-16.3</sub> (10.5 <sup>+11.4</sup> <sub>-9.7</sub> )
nircam2-5041	0.53 <sup>+0.73</sup> <sub>-0.43</sub> (0.27 <sup>+0.34</sup> <sub>-0.21</sub> )	0.99 <sup>+1.27</sup> <sub>-0.79</sub> (0.40 <sup>+0.48</sup> <sub>-0.32</sub> )	0.28 <sup>+0.33</sup> <sub>-0.24</sub> (0.17 <sup>+0.22</sup> <sub>-0.13</sub> )	0.42 <sup>+0.53</sup> <sub>-0.35</sub> (0.25 <sup>+0.33</sup> <sub>-0.20</sub> )	9.1 <sup>+7.2</sup> <sub>-7.2</sub> (15.0 <sup>+17.9</sup> <sub>-12.7</sub> )	5.7 <sup>+6.8</sup> <sub>-4.7</sub> (11.2 <sup>+13.1</sup> <sub>-9.8</sub> )	14.6 <sup>+16.1</sup> <sub>-13.0</sub> (20.8 <sup>+24.9</sup> <sub>-17.1</sub> )	10.9 <sup>+12.4</sup> <sub>-9.1</sub> (15.6 <sup>+18.6</sup> <sub>-12.9</sub> )
nircam2-5342	0.23 <sup>+0.24</sup> <sub>-0.22</sub> (0.34 <sup>+0.36</sup> <sub>-0.33</sub> )	0.29 <sup>+0.30</sup> <sub>-0.28</sub> (0.41 <sup>+0.43</sup> <sub>-0.39</sub> )	0.19 <sup>+0.20</sup> <sub>-0.18</sub> (0.31 <sup>+0.30</sup> <sub>-0.28</sub> )	0.23 <sup>+0.24</sup> <sub>-0.18</sub> (0.35 <sup>+0.37</sup> <sub>-0.34</sub> )	16.7 <sup>+17.0</sup> <sub>-16.4</sub> (12.7 <sup>+13.0</sup> <sub>-11.4</sub> )	14.1 <sup>+14.5</sup> <sub>-13.7</sub> (11.0 <sup>+10.7</sup> <sub>-9.4</sub> )	19.1 <sup>+19.6</sup> <sub>-18.5</sub> (13.6 <sup>+14.0</sup> <sub>-13.3</sub> )	16.6 <sup>+17.1</sup> <sub>-16.2</sub> (12.3 <sup>+12.6</sup> <sub>-11.9</sub> )
nircam2-5418	0.26 <sup>+0.27</sup> <sub>-0.25</sub> (0.34 <sup>+0.36</sup> <sub>-0.32</sub> )	0.35 <sup>+0.36</sup> <sub>-0.34</sub> (0.50 <sup>+0.54</sup> <sub>-0.47</sub> )	0.15 <sup>+0.15</sup> <sub>-0.15</sub> (0.19 <sup>+0.20</sup> <sub>-0.18</sub> )	0.18 <sup>+0.18</sup> <sub>-0.17</sub> (0.25 <sup>+0.26</sup> <sub>-0.24</sub> )	15.3 <sup>+15.6</sup> <sub>-15.0</sub> (12.7 <sup>+13.3</sup> <sub>-12.1</sub> )	12.3 <sup>+12.7</sup> <sub>-12.1</sub> (9.6 <sup>+10.0</sup> <sub>-9.0</sub> )	22.3 <sup>+22.5</sup> <sub>-22.1</sub> (19.1 <sup>+19.9</sup> <sub>-18.5</sub> )	20.0 <sup>+20.3</sup> <sub>-19.6</sub> (15.6 <sup>+16.2</sup> <sub>-15.1</sub> )
nircam2-5904	0.57 <sup>+0.68</sup> <sub>-0.43</sub> (0.90 <sup>+1.06</sup> <sub>-0.76</sub> )	0.79 <sup>+0.90</sup> <sub>-0.68</sub> (1.26 <sup>+1.38</sup> <sub>-1.10</sub> )	0.46 <sup>+0.61</sup> <sub>-0.34</sub> (0.83 <sup>+0.99</sup> <sub>-0.69</sub> )	0.67 <sup>+0.78</sup> <sub>-0.56</sub> (1.15 <sup>+1.30</sup> <sub>-0.99</sub> )	8.7 <sup>+7.6</sup> <sub>-8.0</sub> (6.1 <sup>+6.5</sup> <sub>-5.4</sub> )	6.8 <sup>+7.6</sup> <sub>-6.1</sub> (4.7 <sup>+5.2</sup> <sub>-4.4</sub> )	10.1 <sup>+12.6</sup> <sub>-10.1</sub> (6.5 <sup>+7.5</sup> <sub>-5.7</sub> )	7.6 <sup>+8.8</sup> <sub>-6.9</sub> (5.1 <sup>+5.7</sup> <sub>-4.6</sub> )
nircam2-6479	0.49 <sup>+0.55</sup> <sub>-0.45</sub> (0.50 <sup>+0.54</sup> <sub>-0.46</sub> )	0.70 <sup>+0.75</sup> <sub>-0.64</sub> (0.73 <sup>+0.79</sup> <sub>-0.68</sub> )	0.36 <sup>+0.39</sup> <sub>-0.33</sub> (0.38 <sup>+0.41</sup> <sub>-0.35</sub> )	0.49 <sup>+0.53</sup> <sub>-0.44</sub> (0.54 <sup>+0.58</sup> <sub>-0.50</sub> )	9.7 <sup>+10.3</sup> <sub>-9.1</sub> (9.5 <sup>+10.1</sup> <sub>-9.0</sub> )	7.4 <sup>+8.0</sup> <sub>-7.4</sub> (7.2 <sup>+7.6</sup> <sub>-6.8</sub> )	12.1 <sup>+12.8</sup> <sub>-11.4</sub> (11.6 <sup>+12.3</sup> <sub>-11.0</sub> )	9.7 <sup>+10.5</sup> <sub>-9.2</sub> (9.0 <sup>+9.8</sup> <sub>-8.5</sub> )
nircam2-6539	0.56 <sup>+0.62</sup> <sub>-0.50</sub> (0.32 <sup>+0.35</sup> <sub>-0.30</sub> )	0.75 <sup>+0.84</sup> <sub>-0.68</sub> (0.46 <sup>+0.51</sup> <sub>-0.42</sub> )	0.49 <sup>+0.54</sup> <sub>-0.43</sub> (0.33 <sup>+0.36</sup> <sub>-0.33</sub> )	0.63 <sup>+0.69</sup> <sub>-0.56</sub> (0.49 <sup>+0.53</sup> <sub>-0.43</sub> )	8.8 <sup>+9.5</sup> <sub>-8.2</sub> (13.2 <sup>+14.0</sup> <sub>-12.3</sub> )	7.1 <sup>+7.6</sup> <sub>-6.5 (10.2<sup>+10.9</sup><sub>-9.5</sub>)</sub>	9.7 <sup>+10.6</sup> <sub>-9.0</sub> (12.8 <sup>+13.7</sup> <sub>-12.1</sub> )	8.1 <sup>+8.5</sup> <sub>-7.5</sub> (9.8 <sup>+10.7</sup> <sub>-9.1</sub> )
nircam2-7078	0.07 <sup>+0.07</sup> <sub>-0.07</sub> (0.08 <sup>+0.08</sup> <sub>-0.08</sub> )	0.11 <sup>+0.11</sup> <sub>-0.11</sub> (0.13 <sup>+0.13</sup> <sub>-0.13</sub> )	0.03 <sup>+0.03</sup> <sub>-0.03</sub> (0.04 <sup>+0.04</sup> <sub>-0.04</sub> )	0.04 <sup>+0.04</sup> <sub>-0.04</sub> (0.06 <sup>+0.06</sup> <sub>-0.06</sub> )	39.1 <sup>+39.2</sup> <sub>-39.0</sub> (33.8 <sup>+34.2</sup> <sub>-33.4</sub> )	27.9 <sup>+27.8</sup> <sub>-27.8</sub> (25.0 <sup>+25.2</sup> <sub>-24.8</sub> )	64.6 <sup>+64.8</sup> <sub>-64.4</sub> (56.2 <sup>+56.6</sup> <sub>-55.7</sub> )	51.6 <sup>+51.9</sup> <sub>-51.4</sub> (43.2 <sup>+43.6</sup> <sub>-42.7</sub> )
nircam2-7220	1.21 <sup>+1.38</sup> <sub>-1.06</sub> (0.33 <sup>+0.38</sup> <sub>-0.31</sub> )	1.64 <sup>+1.82</sup> <sub>-1.43</sub> (0.43 <sup>+0.50</sup> <sub>-0.39</sub> )	1.87 <sup>+2.11</sup> <sub>-1.64</sub> (0.39 <sup>+0.45</sup> <sub>-0.35</sub> )	2.99 <sup>+3.30</sup> <sub>-2.57</sub> (0.56 <sup>+0.63</sup> <sub>-0.47</sub> )	4.8 <sup>+4.4</sup> <sub>-4.4</sub> (12.9 <sup>+11.8</sup> <sub>-11.8</sub> )	3.8 <sup>+4.2</sup> <sub>-3.5</sub> (10.7 <sup>+9.6</sup> <sub>-9.6</sub> )	3.4 <sup>+3.8</sup> <sub>-3.0</sub> (11.5 <sup>+12.3</sup> <sub>-10.3</sub> )	2.2 <sup>+2.5</sup> <sub>-2.0</sub> (9.1 <sup>+10.0</sup> <sub>-8.1</sub> )
nircam2-7309	0.71 <sup>+0.81</sup> <sub>-0.63</sub> (0.56 <sup>+0.66</sup> <sub>-0.45</sub> )	0.96 <sup>+1.05</sup> <sub>-0.86</sub> (0.80 <sup>+0.90</sup> <sub>-0.69</sub> )	0.63 <sup>+0.73</sup> <sub>-0.55</sub> (0.53 <sup>+0.64</sup> <sub>-0.42</sub> )	0.83 <sup>+0.93</sup> <sub>-0.74</sub> (0.77 <sup>+0.87</sup> <sub>-0.63</sub> )	7.3 <sup>+8.0</sup> <sub>-7.6</sub> (8.8 <sup>+10.4</sup> <sub>-8.7</sub> )	5.8 <sup>+6.3</sup> <sub>-5.4</sub> (6.7 <sup>+8.2</sup> <sub>-6.2</sub> )	8.1 <sup>+8.9</sup> <sub>-7.2</sub> (9.1 <sup>+10.9</sup> <sub>-8.0</sub> )	6.6 <sup>+7.1</sup> <sub>-6.0</sub> (6.9 <sup>+8.0</sup> <sub>-6.3</sub> )
nircam2-7394	0.36 <sup>+0.38</sup> <sub>-0.35</sub> (0.27 <sup>+0.28</sup> <sub>-0.26</sub> )	0.48 <sup>+0.49</sup> <sub>-0.46</sub> (0.37 <sup>+0.38</sup> <sub>-0.35</sub> )	0.18 <sup>+0.18</sup> <sub>-0.17</sub> (0.14 <sup>+0.15</sup> <sub>-0.14</sub> )	0.22 <sup>+0.23</sup> <sub>-0.21</sub> (0.17 <sup>+0.18</sup> <sub>-0.16</sub> )	12.0 <sup>+12.4</sup> <sub>-11.6</sub> (14.9 <sup>+15.3</sup> <sub>-14.4</sub> )	9.9 <sup>+10.1</sup> <sub>-9.7</sub> (12.0 <sup>+12.3</sup> <sub>-11.7</sub> )	19.9 <sup>+20.4</sup> <sub>-19.5</sub> (23.5 <sup>+24.0</sup> <sub>-22.8</sub> )	17.3 <sup>+17.9</sup> <sub>-16.8</sub> (20.4 <sup>+21.1</sup> <sub>-19.6</sub> )
nircam2-7419	0.79 <sup>+0.92</sup> <sub>-0.64</sub> (1.09 <sup>+1.19</sup> <sub>-0.76</sub> )	1.18 <sup>+1.18</sup> <sub>-1.03</sub> (1.24 <sup>+1.28</sup> <sub>-1.12</sub> )	0.38 <sup>+0.42</sup> <sub>-0.35</sub> (0.52 <sup>+0.57</sup> <sub>-0.34</sub> )	0.49 <sup>+0.55</sup> <sub>-0.45</sub> (1.00 <sup>+1.05</sup> <sub>-0.53</sub> )	6.8 <sup>+7.9</sup> <sub>-6.6</sub> (5.3 <sup>+7.0</sup> <sub>-4.9</sub> )	5.0 <sup>+5.5</sup> <sub>-4.9</sub> (4.8 <sup>+5.2</sup> <sub>-4.6</sub> )	11.7 <sup>+12.4</sup> <sub>-10.8</sub> (9.2 <sup>+12.8</sup> <sub>-7.1</sub> )	9.7 <sup>+10.4</sup> <sub>-8.9</sub> (5.7 <sup>+9.2</sup> <sub>-5.4</sub> )
nircam2-7423	0.52 <sup>+0.52</sup> <sub>-0.52</sub> (0.29 <sup>+0.29</sup> <sub>-0.29</sub> )	0.57 <sup>+0.57</sup> <sub>-0.57</sub> (0.34 <sup>+0.35</sup> <sub>-0.33</sub> )	0.50 <sup>+0.51</sup> <sub>-0.50</sub> (0.28 <sup>+0.28</sup> <sub>-0.27</sub> )	0.54 <sup>+0.54</sup> <sub>-0.53</sub> (0.31 <sup>+0.31</sup> <sub>-0.30</sub> )	9.3 <sup>+9.2</sup> <sub>-9.3</sub> (14.1 <sup>+14.0</sup> <sub>-14.0</sub> )	8.7 <sup>+8.7</sup> <sub>-8.6</sub> (12.7 <sup>+12.5</sup> <sub>-12.5</sub> )	9.5 <sup>+9.5</sup> <sub>-9.5</sub> (14.7 <sup>+14.8</sup> <sub>-14.6</sub> )	9.1 <sup>+9.1</sup> <sub>-9.0</sub> (13.6 <sup>+13.8</sup> <sub>-13.5</sub> )
nircam2-7435	0.39 <sup>+0.42</sup> <sub>-0.36</sub> (0.34 <sup>+0.41</sup> <sub>-0.30</sub> )	0.49 <sup>+0.52</sup> <sub>-0.46</sub> (0.53 <sup>+0.63</sup> <sub>-0.46</sub> )	0.27 <sup>+0.28</sup> <sub>-0.25</sub> (0.20 <sup>+0.24</sup> <sub>-0.17</sub> )	0.31 <sup>+0.34</sup> <sub>-0.29</sub> (0.29 <sup>+0.35</sup> <sub>-0.25</sub> )	11.5 <sup>+12.1</sup> <sub>-10.9</sub> (12.6 <sup>+14.0</sup> <sub>-11.1</sub> )	9.7 <sup>+10.2</sup> <sub>-9.3</sub> (9.1 <sup>+10.1</sup> <sub>-8.1</sub> )	14.9 <sup>+15.6</sup> <sub>-14.4</sub> (18.2 <sup>+20.6</sup> <sub>-16.0</sub> )	13.4 <sup>+14.1</sup> <sub>-12.6</sub> (14.1 <sup>+15.9</sup> <sub>-12.5</sub> )
nircam2-7735	0.44 <sup>+0.46</sup> <sub>-0.42</sub> (0.45 <sup>+0.52</sup> <sub>-0.39</sub> )	0.57 <sup>+0.60</sup> <sub>-0.54</sub> (0.74 <sup>+0.82</sup> <sub>-0.66</sub> )	0.32 <sup>+0.34</sup> <sub>-0.31</sub> (0.31 <sup>+0.36</sup> <sub>-0.28</sub> )	0.40 <sup>+0.42</sup> <sub>-0.38</sub> (0.50 <sup>+0.58</sup> <sub>-0.44</sub> )	10.6 <sup>+10.9</sup> <sub>-10.1</sub> (10.4 <sup>+11.4</sup> <sub>-9.3</sub> )	8.7 <sup>+9.0</sup> <sub>-8.3</sub> (7.1 <sup>+7.8</sup> <sub>-6.6</sub> )	13.2 <sup>+13.6</sup> <sub>-12.6</sub> (13.4 <sup>+14.6</sup> <sub>-12.0</sub> )	11.2 <sup>+11.6</sup> <sub>-10.8</sub> (9.6 <sup>+10.5</sup> <sub>-8.5</sub> )
nircam2-7952	0.71 <sup>+0.82</sup> <sub>-0.64</sub> (0.88 <sup>+1.00</sup> <sub>-0.78</sub> )	1.15 <sup>+1.25</sup> <sub>-1.02</sub> (1.34 <sup>+1.51</sup> <sub>-1.19</sub> )	0.40 <sup>+0.41</sup> <sub>-0.39</sub> (0.38 <sup>+0.41</sup> <sub>-0.35</sub> )	0.48 <sup>+0.52</sup> <sub>-0.46</sub> (0.46 <sup>+0.52</sup> <sub>-0.43</sub> )	7.3 <sup>+8.0</sup> <sub>-6.6</sub> (6.2 <sup>+6.9</sup> <sub>-5.7</sub> )	5.1 <sup>+5.6</sup> <sub>-4.7</sub> (4.5 <sup>+4.9</sup> <sub>-4.1</sub> )	11.2 <sup>+11.5</sup> <sub>-10.9</sub> (11.6 <sup>+12.3</sup> <sub>-11.1</sub> )	9.8 <sup>+9.3</sup> <sub>-9.0</sub> (9.8 <sup>+9.6</sup> <sub>-9.3</sub> )
nircam2-8036	0.38 <sup>+0.40</sup> <sub>-0.36</sub> (0.40 <sup>+0.41</sup> <sub>-0.38</sub> )	0.51 <sup>+0.54</sup> <sub>-0.47</sub> (0.60 <sup>+0.65</sup> <sub>-0.56</sub> )	0.45 <sup>+0.48</sup> <sub>-0.42</sub> (0.38 <sup>+0.40</sup> <sub>-0.36</sub> )	0.68 <sup>+0.77</sup> <sub>-0.61</sub> (0.55 <sup>+0.60</sup> <sub>-0.52</sub> )	11.7 <sup>+12.1</sup> <sub>-11.3</sub> (11.3 <sup>+11.7</sup> <sub>-11.0</sub> )	9.5 <sup>+10.0</sup> <sub>-9.0</sub> (8.4 <sup>+8.8</sup> <sub>-7.9</sub> )	10.3 <sup>+10.8</sup> <sub>-9.9</sub> (11.7 <sup>+12.1</sup> <sub>-11.3</sub> )	7.6 <sup>+8.3</sup> <sub>-6.9</sub> (8.9 <sup>+9.2</sup> <sub>-8.4</sub> )
nircam2-8313	2.35 <sup>+2.44</sup> <sub>-2.21</sub> (2.11 <sup>+2.41</sup> <sub>-1.69</sub> )	2.62 <sup>+2.69</sup> <sub>-2.56</sub> (2.61 <sup>+2.71</sup> <sub>-2.41</sub> )	2.27 <sup>+2.41</sup> <sub>-2.12</sub> (2.00 <sup>+2.34</sup> <sub>-1.52</sub> )	2.57 <sup>+2.62</sup> <sub>-2.50</sub> (2.53 <sup>+2.66</sup> <sub>-2.26</sub> )	2.8 <sup>+2.9</sup> <sub>-2.8</sub> (3.0 <sup>+3.7</sup> <sub>-2.7</sub> )	2.5 <sup>+2.5</sup> <sub>-2.4</sub> (2.5 <sup>+2.7</sup> <sub>-2.4</sub> )	2.8 <sup>+3.0</sup> <sub>-2.5</sub> (3.2 <sup>+4.0</sup> <sub>-2.4</sub> )	2.5 <sup>+2.6</sup> <sub>-2.4</sub> (2.6 <sup>+2.9</sup> <sub>-2.4</sub> )
nircam2-8320	0.34 <sup>+0.35</sup> <sub>-0.33</sub> (0.26 <sup>+0.26</sup> <sub>-0.26</sub> )	0.40 <sup>+0.43</sup> <sub>-0.40</sub> (0.30 <sup>+0.30</sup> <sub>-0.30</sub> )	0.31 <sup>+0.32</sup> <sub>-0.30</sub> (0.23 <sup>+0.23</sup> <sub>-0.23</sub> )	0.36 <sup>+0.37</sup> <sub>-0.35</sub> (0.26 <sup>+0.26</sup> <sub>-0.25</sub> )	12.6 <sup>+12.8</sup> <sub>-12.3</sub> (15.4 <sup>+15.5</sup> <sub>-15.4</sub> )	11.2 <sup>+11.5</sup> <sub>-10.7</sub> (13.7 <sup>+13.8</sup> <sub>-13.7</sub> )	13.5 <sup>+13.7</sup> <sub>-13.1</sub> (16.5 <sup>+16.6</sup> <sub>-16.5</sub> )	12.2 <sup>+12.5</sup> <sub>-11.9</sub> (15.5 <sup>+15.6</sup> <sub>-15.5</sub> )
nircam2-8386	0.77 <sup>+0.89</sup> <sub>-0.68</sub> (1.19 <sup>+1.27</sup> <sub>-1.06</sub> )	1.15 <sup>+1.25</sup> <sub>-1.02</sub> (1.70 <sup>+1.79</sup> <sub>-1.60</sub> )	0.50 <sup>+0.60</sup> <sub>-0.44</sub> (0.88 <sup>+1.01</sup> <sub>-0.73</sub> )	0.68 <sup>+0.78</sup> <sub>-0.59</sub> (1.35 <sup>+1.44</sup> <sub>-1.25</sub> )	6.9 <sup>+7.6</sup> <sub>-6.2</sub> (4.9 <sup>+5.4</sup> <sub>-4.7</sub> )	5.1 <sup>+5.6</sup> <sub>-4.7</sub> (3.7 <sup>+3.9</sup> <sub>-3.3</sub> )	9.6 <sup>+10.4</sup> <sub>-8.3</sub> (6.2 <sup>+6.5</sup> <sub>-5.6</sub> )	7.6 <sup>+8.5</sup> <sub>-6.8</sub> (4.4 <sup>+4.7</sup> <sub>-4.2</sub> )
nircam2-8529	0.41 <sup>+0.44</sup> <sub>-0.38</sub> (0.71 <sup>+0.84</sup> <sub>-0.57</sub> )	0.54 <sup>+0.58</sup> <sub>-0.49</sub> (0.98 <sup>+1.01</sup> <sub>-0.93</sub> )	0.36 <sup>+0.38</sup> <sub>-0.33</sub> (0.72 <sup>+0.86</sup> <sub>-0.57</sub> )	0.45 <sup>+0.49</sup> <sub>-0.41</sub> (0.93 <sup>+1.01</sup> <sub>-0.94</sub> )	11.1 <sup>+11.7</sup> <sub>-10.5</sub> (7.4 <sup>+8.6</sup> <sub>-6.5</sub> )	9.1 <sup>+9.7</sup> <sub>-8.5</sub> (5.7 <sup>+6.0</sup> <sub>-5.6</sub> )	12.2 <sup>+13.0</sup> <sub>-11.6</sub> (7.3 <sup>+8.6</sup> <sub>-6.4</sub> )	10.3 <sup>+11.0</sup> <sub>-9.7</sub> (5.7 <sup>+6.0</sup> <sub>-5.6</sub> )
nircam2-8542	0.47 <sup>+0.48</sup> <sub>-0.47</sub> (0.40 <sup>+0.45</sup> <sub>-0.33</sub> )	0.55 <sup>+0.56</sup> <sub>-0.53</sub> (0.63 <sup>+0.72</sup> <sub>-0.52</sub> )	0.39 <sup>+0.39</sup> <sub>-0.38</sub> (0.18 <sup>+0.19</sup> <sub>-0.15</sub> )	0.40 <sup>+0.41</sup> <sub>-0.40</sub> (0.24 <sup>+0.27</sup> <sub>-0.20</sub> )	10.0 <sup>+10.1</sup> <sub>-9.8</sub> (11.2 <sup>+12.9</sup> <sub>-10.3</sub> )	9.0 <sup>+9.1</sup> <sub>-8</sub>		

Table E.1: (Continued)

Galaxy name	$t_5^{\text{SB99(BC03)}}$ [Gyr]	$t_{10}^{\text{SB99(BC03)}}$ [Gyr]	$t_{5 \times 10^8 M_\odot}^{\text{SB99(BC03)}}$ [Gyr]	$t_{10^9 M_\odot}^{\text{SB99(BC03)}}$ [Gyr]	$z_5^{\text{SB99(BC03)}}$	$z_{10}^{\text{SB99(BC03)}}$	$z_{5 \times 10^8 M_\odot}^{\text{SB99(BC03)}}$	$z_{10^9 M_\odot}^{\text{SB99(BC03)}}$
nircam2-9096	0.35 <sup>+0.33</sup> <sub>-0.30</sub> (0.16 <sup>+0.17</sup> <sub>-0.15</sub> )	0.41 <sup>+0.44</sup> <sub>-0.35</sub> (0.25 <sup>+0.28</sup> <sub>-0.23</sub> )	0.20 <sup>+0.21</sup> <sub>-0.20</sub> (0.06 <sup>+0.06</sup> <sub>-0.05</sub> )	0.23 <sup>+0.24</sup> <sub>-0.22</sub> (0.08 <sup>+0.09</sup> <sub>-0.07</sub> )	13.3 <sup>+13.8</sup> <sub>-12.8</sub> (21.7 <sup>+22.8</sup> <sub>-20.4</sub> )	11.0 <sup>+11.4</sup> <sub>-10.4</sub> (15.6 <sup>+16.5</sup> <sub>-14.5</sub> )	18.4 <sup>+18.6</sup> <sub>-18.0</sub> (43.5 <sup>+44.8</sup> <sub>-41.6</sub> )	16.9 <sup>+17.2</sup> <sub>-16.4</sub> (34.8 <sup>+36.3</sup> <sub>-32.7</sub> )
nircam2-9208	0.87 <sup>+1.00</sup> <sub>-0.77</sub> (0.60 <sup>+0.67</sup> <sub>-0.51</sub> )	1.12 <sup>+1.20</sup> <sub>-1.02</sub> (0.81 <sup>+0.88</sup> <sub>-0.72</sub> )	0.64 <sup>+0.69</sup> <sub>-0.40</sub> (0.44 <sup>+0.51</sup> <sub>-0.35</sub> )	0.82 <sup>+0.97</sup> <sub>-0.74</sub> (0.60 <sup>+0.68</sup> <sub>-0.52</sub> )	6.3 <sup>+6.9</sup> <sub>-5.6</sub> (8.4 <sup>+9.4</sup> <sub>-7.7</sub> )	5.2 <sup>+5.6</sup> <sub>-4.9</sub> (6.7 <sup>+7.2</sup> <sub>-6.2</sub> )	7.8 <sup>+7.5</sup> <sub>-7.5</sub> (10.5 <sup>+12.4</sup> <sub>-9.4</sub> )	6.6 <sup>+7.1</sup> <sub>-5.8</sub> (8.3 <sup>+9.3</sup> <sub>-7.6</sub> )
nircam2-9269	0.31 <sup>+0.35</sup> <sub>-0.28</sub> (0.33 <sup>+0.35</sup> <sub>-0.32</sub> )	0.49 <sup>+0.53</sup> <sub>-0.44</sub> (0.48 <sup>+0.50</sup> <sub>-0.45</sub> )	0.12 <sup>+0.13</sup> <sub>-0.11</sub> (0.19 <sup>+0.20</sup> <sub>-0.19</sub> )	0.16 <sup>+0.18</sup> <sub>-0.15</sub> (0.25 <sup>+0.26</sup> <sub>-0.24</sub> )	13.5 <sup>+14.5</sup> <sub>-12.5</sub> (12.8 <sup>+13.3</sup> <sub>-12.3</sub> )	9.7 <sup>+10.5</sup> <sub>-9.2</sub> (9.9 <sup>+10.4</sup> <sub>-9.5</sub> )	26.4 <sup>+27.9</sup> <sub>-24.9</sub> (18.9 <sup>+19.4</sup> <sub>-18.1</sub> )	21.1 <sup>+22.1</sup> <sub>-20.1</sub> (15.7 <sup>+16.2</sup> <sub>-15.2</sub> )
nircam2-9307	0.82 <sup>+0.89</sup> <sub>-0.77</sub> (0.76 <sup>+0.83</sup> <sub>-0.70</sub> )	1.05 <sup>+1.09</sup> <sub>-1.01</sub> (1.11 <sup>+1.20</sup> <sub>-1.03</sub> )	0.48 <sup>+0.50</sup> <sub>-0.45</sub> (0.48 <sup>+0.52</sup> <sub>-0.44</sub> )	0.61 <sup>+0.68</sup> <sub>-0.57</sub> (0.65 <sup>+0.71</sup> <sub>-0.59</sub> )	6.6 <sup>+6.9</sup> <sub>-6.5</sub> (7.0 <sup>+7.4</sup> <sub>-6.5</sub> )	5.5 <sup>+5.3</sup> <sub>-4.9</sub> (5.2 <sup>+5.5</sup> <sub>-4.9</sub> )	9.8 <sup>+10.2</sup> <sub>-9.1</sub> (9.9 <sup>+10.6</sup> <sub>-9.1</sub> )	8.2 <sup>+7.6</sup> <sub>-7.4</sub> (7.9 <sup>+8.4</sup> <sub>-7.4</sub> )
nircam2-9610	0.73 <sup>+0.87</sup> <sub>-0.59</sub> (0.50 <sup>+0.60</sup> <sub>-0.41</sub> )	0.98 <sup>+1.06</sup> <sub>-0.86</sub> (0.71 <sup>+0.82</sup> <sub>-0.66</sub> )	0.67 <sup>+0.82</sup> <sub>-0.54</sub> (0.55 <sup>+0.64</sup> <sub>-0.44</sub> )	0.91 <sup>+1.00</sup> <sub>-0.78</sub> (0.79 <sup>+0.92</sup> <sub>-0.66</sub> )	7.2 <sup>+8.4</sup> <sub>-6.3</sub> (9.6 <sup>+11.1</sup> <sub>-8.4</sub> )	5.8 <sup>+5.4</sup> <sub>-5.4</sub> (7.4 <sup>+8.3</sup> <sub>-6.6</sub> )	7.7 <sup>+9.0</sup> <sub>-6.6</sub> (9.0 <sup>+10.4</sup> <sub>-7.9</sub> )	6.1 <sup>+6.9</sup> <sub>-5.7</sub> (6.8 <sup>+7.8</sup> <sub>-6.1</sub> )
nircam2-9876	0.48 <sup>+0.58</sup> <sub>-0.40</sub> (0.55 <sup>+0.62</sup> <sub>-0.49</sub> )	0.71 <sup>+0.80</sup> <sub>-0.62</sub> (0.72 <sup>+0.78</sup> <sub>-0.65</sub> )	0.27 <sup>+0.41</sup> <sub>-0.21</sub> (0.43 <sup>+0.49</sup> <sub>-0.36</sub> )	0.41 <sup>+0.53</sup> <sub>-0.34</sub> (0.53 <sup>+0.61</sup> <sub>-0.47</sub> )	9.9 <sup>+11.2</sup> <sub>-8.6</sub> (8.9 <sup>+9.7</sup> <sub>-8.1</sub> )	7.3 <sup>+7.7</sup> <sub>-6.7</sub> (7.3 <sup>+7.9</sup> <sub>-6.8</sub> )	15.0 <sup>+17.7</sup> <sub>-11.1</sub> (10.8 <sup>+12.1</sup> <sub>-9.7</sub> )	11.0 <sup>+12.8</sup> <sub>-10.2</sub> (9.1 <sup>+8.3</sup> <sub>-8.3</sub> )
nircam2-10017	1.02 <sup>+1.09</sup> <sub>-0.97</sub> (1.45 <sup>+1.56</sup> <sub>-1.33</sub> )	1.90 <sup>+2.34</sup> <sub>-1.52</sub> (2.12 <sup>+2.22</sup> <sub>-2.01</sub> )	1.06 <sup>+1.13</sup> <sub>-1.00</sub> (1.34 <sup>+1.47</sup> <sub>-1.23</sub> )	2.18 <sup>+2.51</sup> <sub>-1.70</sub> (2.01 <sup>+2.12</sup> <sub>-1.88</sub> )	5.6 <sup>+5.8</sup> <sub>-5.3</sub> (4.2 <sup>+4.5</sup> <sub>-3.9</sub> )	3.3 <sup>+3.4</sup> <sub>-2.8</sub> (3.0 <sup>+3.2</sup> <sub>-2.9</sub> )	5.4 <sup>+5.6</sup> <sub>-5.1</sub> (4.5 <sup>+4.8</sup> <sub>-4.2</sub> )	3.0 <sup>+3.7</sup> <sub>-2.6</sub> (3.2 <sup>+3.4</sup> <sub>-3.0</sub> )
nircam2-10149	0.73 <sup>+0.82</sup> <sub>-0.56</sub> (0.29 <sup>+0.35</sup> <sub>-0.26</sub> )	0.89 <sup>+1.08</sup> <sub>-0.77</sub> (0.41 <sup>+0.50</sup> <sub>-0.35</sub> )	0.73 <sup>+0.84</sup> <sub>-0.57</sub> (0.29 <sup>+0.35</sup> <sub>-0.26</sub> )	0.91 <sup>+1.11</sup> <sub>-0.78</sub> (0.40 <sup>+0.49</sup> <sub>-0.34</sub> )	7.2 <sup>+8.7</sup> <sub>-6.6</sub> (14.0 <sup>+15.3</sup> <sub>-12.4</sub> )	6.2 <sup>+6.9</sup> <sub>-5.3</sub> (11.0 <sup>+12.4</sup> <sub>-9.6</sub> )	7.2 <sup>+7.7</sup> <sub>-6.5</sub> (14.1 <sup>+15.4</sup> <sub>-12.4</sub> )	6.1 <sup>+6.9</sup> <sub>-5.2</sub> (11.2 <sup>+12.6</sup> <sub>-9.7</sub> )
nircam2-10186	0.76 <sup>+0.87</sup> <sub>-0.66</sub> (0.52 <sup>+0.60</sup> <sub>-0.44</sub> )	1.02 <sup>+1.11</sup> <sub>-0.92</sub> (0.86 <sup>+1.00</sup> <sub>-0.76</sub> )	0.71 <sup>+0.83</sup> <sub>-0.63</sub> (0.55 <sup>+0.63</sup> <sub>-0.48</sub> )	0.95 <sup>+1.05</sup> <sub>-0.86</sub> (0.96 <sup>+1.16</sup> <sub>-0.81</sub> )	7.0 <sup>+7.7</sup> <sub>-6.3</sub> (9.3 <sup>+8.4</sup> <sub>-7.7</sub> )	5.6 <sup>+5.2</sup> <sub>-4.1</sub> (6.4 <sup>+7.0</sup> <sub>-5.7</sub> )	7.3 <sup>+8.0</sup> <sub>-6.6</sub> (8.9 <sup>+9.9</sup> <sub>-8.0</sub> )	5.9 <sup>+6.3</sup> <sub>-5.5</sub> (5.8 <sup>+6.0</sup> <sub>-5.0</sub> )
nircam2-10266	1.04 <sup>+1.13</sup> <sub>-0.98</sub> (0.70 <sup>+0.80</sup> <sub>-0.61</sub> )	1.43 <sup>+1.50</sup> <sub>-1.14</sub> (1.14 <sup>+1.27</sup> <sub>-1.00</sub> )	0.86 <sup>+0.95</sup> <sub>-0.79</sub> (0.57 <sup>+0.67</sup> <sub>-0.49</sub> )	1.15 <sup>+1.25</sup> <sub>-1.08</sub> (0.87 <sup>+1.00</sup> <sub>-0.77</sub> )	5.5 <sup>+5.8</sup> <sub>-5.1</sub> (7.5 <sup>+8.2</sup> <sub>-6.7</sub> )	4.2 <sup>+4.4</sup> <sub>-4.1</sub> (5.1 <sup>+5.7</sup> <sub>-4.7</sub> )	6.3 <sup>+6.8</sup> <sub>-5.9</sub> (8.6 <sup>+9.6</sup> <sub>-7.7</sub> )	5.0 <sup>+5.3</sup> <sub>-4.7</sub> (6.3 <sup>+6.9</sup> <sub>-5.7</sub> )
nircam2-10267	0.48 <sup>+0.48</sup> <sub>-0.48</sub> (0.25 <sup>+0.25</sup> <sub>-0.24</sub> )	0.57 <sup>+0.57</sup> <sub>-0.56</sub> (0.34 <sup>+0.35</sup> <sub>-0.33</sub> )	0.38 <sup>+0.38</sup> <sub>-0.38</sub> (0.13 <sup>+0.13</sup> <sub>-0.13</sub> )	0.40 <sup>+0.41</sup> <sub>-0.40</sub> (0.15 <sup>+0.15</sup> <sub>-0.15</sub> )	9.8 <sup>+9.9</sup> <sub>-8.9</sub> (15.8 <sup>+16.1</sup> <sub>-15.6</sub> )	8.7 <sup>+8.8</sup> <sub>-8.6</sub> (12.7 <sup>+12.9</sup> <sub>-12.3</sub> )	11.6 <sup>+11.6</sup> <sub>-11.6</sub> (24.6 <sup>+24.9</sup> <sub>-24.2</sub> )	11.2 <sup>+11.2</sup> <sub>-11.1</sub> (22.2 <sup>+22.3</sup> <sub>-22.0</sub> )
nircam2-10367	1.68 <sup>+1.75</sup> <sub>-1.59</sub> (1.87 <sup>+1.61</sup> <sub>-1.61</sub> )	2.02 <sup>+2.09</sup> <sub>-1.94</sub> (2.27 <sup>+2.15</sup> <sub>-2.15</sub> )	1.34 <sup>+1.45</sup> <sub>-1.24</sub> (1.39 <sup>+1.04</sup> <sub>-1.04</sub> )	1.65 <sup>+1.72</sup> <sub>-1.56</sub> (1.86 <sup>+2.04</sup> <sub>-1.57</sub> )	3.7 <sup>+3.9</sup> <sub>-3.6</sub> (3.4 <sup>+3.8</sup> <sub>-3.1</sub> )	3.2 <sup>+3.3</sup> <sub>-3.3</sub> (2.8 <sup>+3.0</sup> <sub>-2.8</sub> )	4.5 <sup>+4.8</sup> <sub>-4.4</sub> (4.3 <sup>+5.5</sup> <sub>-3.7</sub> )	3.8 <sup>+4.0</sup> <sub>-3.6</sub> (3.4 <sup>+3.9</sup> <sub>-3.1</sub> )
nircam2-10433	0.53 <sup>+0.58</sup> <sub>-0.49</sub> (0.70 <sup>+0.77</sup> <sub>-0.63</sub> )	0.77 <sup>+0.84</sup> <sub>-0.70</sub> (1.18 <sup>+1.26</sup> <sub>-1.08</sub> )	0.34 <sup>+0.37</sup> <sub>-0.31</sub> (0.38 <sup>+0.42</sup> <sub>-0.35</sub> )	0.47 <sup>+0.50</sup> <sub>-0.43</sub> (0.55 <sup>+0.60</sup> <sub>-0.51</sub> )	9.2 <sup>+9.7</sup> <sub>-8.5</sub> (7.4 <sup>+8.0</sup> <sub>-6.9</sub> )	6.9 <sup>+7.5</sup> <sub>-6.5</sub> (5.0 <sup>+5.3</sup> <sub>-4.7</sub> )	12.6 <sup>+13.5</sup> <sub>-12.0</sub> (11.6 <sup>+12.4</sup> <sub>-10.9</sub> )	10.1 <sup>+10.8</sup> <sub>-9.5</sub> (8.9 <sup>+9.5</sup> <sub>-8.4</sub> )
nircam2-10446	0.65 <sup>+0.70</sup> <sub>-0.61</sub> (0.32 <sup>+0.36</sup> <sub>-0.29</sub> )	0.89 <sup>+0.97</sup> <sub>-0.80</sub> (0.46 <sup>+0.51</sup> <sub>-0.42</sub> )	0.52 <sup>+0.54</sup> <sub>-0.50</sub> (0.22 <sup>+0.25</sup> <sub>-0.20</sub> )	0.62 <sup>+0.67</sup> <sub>-0.59</sub> (0.39 <sup>+0.34</sup> <sub>-0.27</sub> )	7.9 <sup>+8.3</sup> <sub>-7.5</sub> (13.3 <sup>+14.2</sup> <sub>-12.1</sub> )	6.2 <sup>+6.7</sup> <sub>-5.8</sub> (10.2 <sup>+10.9</sup> <sub>-9.4</sub> )	9.3 <sup>+9.6</sup> <sub>-9.0</sub> (17.1 <sup>+18.1</sup> <sub>-15.7</sub> )	8.1 <sup>+8.5</sup> <sub>-7.7</sub> (14.0 <sup>+14.8</sup> <sub>-12.5</sub> )
nircam2-10496	0.35 <sup>+0.39</sup> <sub>-0.28</sub> (0.57 <sup>+0.63</sup> <sub>-0.52</sub> )	0.52 <sup>+0.57</sup> <sub>-0.45</sub> (0.78 <sup>+0.84</sup> <sub>-0.71</sub> )	0.36 <sup>+0.40</sup> <sub>-0.30</sub> (0.64 <sup>+0.69</sup> <sub>-0.80</sub> )	0.56 <sup>+0.62</sup> <sub>-0.50</sub> (0.87 <sup>+0.93</sup> <sub>-0.80</sub> )	13.0 <sup>+14.7</sup> <sub>-11.5</sub> (8.6 <sup>+8.1</sup> <sub>-8.1</sub> )	9.3 <sup>+10.3</sup> <sub>-8.6</sub> (6.8 <sup>+6.5</sup> <sub>-6.5</sub> )	12.1 <sup>+13.8</sup> <sub>-10.9</sub> (8.0 <sup>+7.5</sup> <sub>-7.5</sub> )	8.8 <sup>+9.6</sup> <sub>-8.8</sub> (6.3 <sup>+6.7</sup> <sub>-6.0</sub> )
nircam2-10573	3.05 <sup>+3.06</sup> <sub>-3.04</sub> (2.71 <sup>+3.01</sup> <sub>-2.67</sub> )	3.11 <sup>+3.11</sup> <sub>-3.10</sub> (3.02 <sup>+2.92</sup> <sub>-2.92</sub> )	3.02 <sup>+3.03</sup> <sub>-3.01</sub> (1.45 <sup>+2.64</sup> <sub>-1.20</sub> )	3.05 <sup>+3.06</sup> <sub>-3.04</sub> (2.67 <sup>+2.56</sup> <sub>-1.56</sub> )	2.1 <sup>+2.2</sup> <sub>-2.1</sub> (2.4 <sup>+2.4</sup> <sub>-2.4</sub> )	2.1 <sup>+2.1</sup> <sub>-2.1</sub> (2.2 <sup>+2.2</sup> <sub>-2.2</sub> )	2.2 <sup>+2.2</sup> <sub>-2.2</sub> (4.2 <sup>+4.9</sup> <sub>-4.9</sub> )	2.1 <sup>+2.1</sup> <sub>-2.1</sub> (2.4 <sup>+2.4</sup> <sub>-2.4</sub> )
nircam2-10590	2.47 <sup>+2.62</sup> <sub>-2.23</sub> (1.19 <sup>+1.38</sup> <sub>-1.03</sub> )	3.02 <sup>+3.10</sup> <sub>-2.92</sub> (2.67 <sup>+2.69</sup> <sub>-2.43</sub> )	2.39 <sup>+2.55</sup> <sub>-2.06</sub> (0.96 <sup>+1.12</sup> <sub>-0.81</sub> )	2.95 <sup>+3.02</sup> <sub>-2.86</sub> (2.11 <sup>+2.50</sup> <sub>-1.53</sub> )	2.6 <sup>+2.9</sup> <sub>-2.5</sub> (4.9 <sup>+5.5</sup> <sub>-4.4</sub> )	2.2 <sup>+2.2</sup> <sub>-2.1</sub> (2.4 <sup>+2.4</sup> <sub>-2.4</sub> )	2.7 <sup>+3.1</sup> <sub>-2.5</sub> (5.9 <sup>+6.7</sup> <sub>-5.2</sub> )	2.2 <sup>+2.2</sup> <sub>-2.2</sub> (3.0 <sup>+4.0</sup> <sub>-2.6</sub> )
nircam2-10591	0.84 <sup>+0.99</sup> <sub>-0.68</sub> (0.87 <sup>+0.72</sup> <sub>-0.72</sub> )	1.14 <sup>+1.29</sup> <sub>-0.98</sub> (1.27 <sup>+1.46</sup> <sub>-1.08</sub> )	0.52 <sup>+0.72</sup> <sub>-0.38</sub> (0.58 <sup>+0.75</sup> <sub>-0.42</sub> )	0.74 <sup>+0.87</sup> <sub>-0.55</sub> (0.75 <sup>+0.93</sup> <sub>-0.59</sub> )	6.5 <sup>+7.6</sup> <sub>-5.4</sub> (6.3 <sup>+7.3</sup> <sub>-5.4</sub> )	5.1 <sup>+5.7</sup> <sub>-4.6</sub> (4.7 <sup>+5.3</sup> <sub>-4.2</sub> )	9.3 <sup>+11.7</sup> <sub>-7.3</sub> (8.5 <sup>+10.9</sup> <sub>-7.0</sub> )	7.1 <sup>+8.9</sup> <sub>-6.3</sub> (7.0 <sup>+8.4</sup> <sub>-6.0</sub> )
nircam2-10669	0.42 <sup>+0.44</sup> <sub>-0.39</sub> (0.31 <sup>+0.35</sup> <sub>-0.28</sub> )	0.57 <sup>+0.60</sup> <sub>-0.54</sub> (0.45 <sup>+0.50</sup> <sub>-0.40</sub> )	0.21 <sup>+0.21</sup> <sub>-0.20</sub> (0.11 <sup>+0.11</sup> <sub>-0.10</sub> )	0.22 <sup>+0.23</sup> <sub>-0.22</sub> (0.13 <sup>+0.14</sup> <sub>-0.12</sub> )	10.9 <sup>+11.4</sup> <sub>-10.5</sub> (13.4 <sup>+14.6</sup> <sub>-12.5</sub> )	8.7 <sup>+9.1</sup> <sub>-8.3</sub> (10.3 <sup>+11.2</sup> <sub>-9.5</sub> )	17.8 <sup>+18.1</sup> <sub>-17.7</sub> (28.5 <sup>+29.9</sup> <sub>-27.1</sub> )	17.1 <sup>+17.3</sup> <sub>-16.9</sub> (24.9 <sup>+26.7</sup> <sub>-23.1</sub> )
nircam2-10683	0.55 <sup>+0.61</sup> <sub>-0.50</sub> (0.67 <sup>+0.74</sup> <sub>-0.60</sub> )	0.77 <sup>+0.85</sup> <sub>-0.69</sub> (1.09 <sup>+1.20</sup> <sub>-0.97</sub> )	0.29 <sup>+0.30</sup> <sub>-0.28</sub> (0.26 <sup>+0.28</sup> <sub>-0.24</sub> )	0.33 <sup>+0.35</sup> <sub>-0.32</sub> (0.35 <sup>+0.38</sup> <sub>-0.31</sub> )	9.0 <sup>+9.6</sup> <sub>-8.2</sub> (7.7 <sup>+8.3</sup> <sub>-7.2</sub> )	6.9 <sup>+7.5</sup> <sub>-6.4</sub> (5.3 <sup>+5.8</sup> <sub>-4.9</sub> )	14.2 <sup>+14.6</sup> <sub>-13.7</sub> (15.3 <sup>+16.4</sup> <sub>-14.5</sub> )	12.8 <sup>+13.3</sup> <sub>-12.3</sub> (12.4 <sup>+13.4</sup> <sub>-11.7</sub> )
nircam3-64	1.12 <sup>+1.18</sup> <sub>-1.05</sub> (0.28 <sup>+0.28</sup> <sub>-0.27</sub> )	1.49 <sup>+1.55</sup> <sub>-1.40</sub> (0.34 <sup>+0.34</sup> <sub>-0.33</sub> )	0.64 <sup>+0.69</sup> <sub>-0.60</sub> (0.20 <sup>+0.20</sup> <sub>-0.20</sub> )	0.86 <sup>+0.96</sup> <sub>-0.76</sub> (0.22 <sup>+0.22</sup> <sub>-0.22</sub> )	5.2 <sup>+5.4</sup> <sub>-5.0</sub> (14.7 <sup>+14.8</sup> <sub>-14.5</sub> )	4.1 <sup>+4.3</sup> <sub>-4.0</sub> (12.8 <sup>+12.9</sup> <sub>-12.6</sub> )	7.9 <sup>+8.3</sup> <sub>-7.5</sub> (18.3 <sup>+18.4</sup> <sub>-18.2</sub> )	6.4 <sup>+7.0</sup> <sub>-5.9</sub> (17.2 <sup>+17.4</sup> <sub>-17.1</sub> )
nircam3-185	0.64 <sup>+0.72</sup> <sub>-0.56</sub> (0.53 <sup>+0.61</sup> <sub>-0.47</sub> )	0.94 <sup>+1.06</sup> <sub>-0.84</sub> (0.85 <sup>+1.02</sup> <sub>-0.75</sub> )	0.65 <sup>+0.74</sup> <sub>-0.58</sub> (0.56 <sup>+0.65</sup> <sub>-0.47</sub> )	0.96 <sup>+1.10</sup> <sub>-0.86</sub> (0.93 <sup>+1.17</sup> <sub>-0.81</sub> )	7.9 <sup>+8.8</sup> <sub>-7.3</sub> (9.2 <sup>+8.3</sup> <sub>-8.3</sub> )	5.9 <sup>+6.5</sup> <sub>-5.4</sub> (6.4 <sup>+7.1</sup> <sub>-6.3</sub> )	7.8 <sup>+7.6</sup> <sub>-7.8</sub> (6.8 <sup>+9.6</sup> <sub>-7.9</sub> )	5.8 <sup>+6.4</sup> <sub>-5.2</sub> (6.0 <sup>+6.6</sup> <sub>-5.0</sub> )
nircam3-254	0.44 <sup>+0.53</sup> <sub>-0.38</sub> (0.53 <sup>+0.59</sup> <sub>-0.48</sub> )	0.74 <sup>+0.86</sup> <sub>-0.59</sub> (0.78 <sup>+0.87</sup> <sub>-0.69</sub> )	0.34 <sup>+0.40</sup> <sub>-0.30</sub> (0.42 <sup>+0.47</sup> <sub>-0.39</sub> )	0.52 <sup>+0.65</sup> <sub>-0.43</sub> (0.58 <sup>+0.65</sup> <sub>-0.52</sub> )	10.5 <sup>+11.8</sup> <sub>-9.1</sub> (9.2 <sup>+9.9</sup> <sub>-8.4</sub> )	7.1 <sup>+8.4</sup> <sub>-6.4</sub> (6.8 <sup>+7.5</sup> <sub>-6.3</sub> )	12.6 <sup>+13.8</sup> <sub>-11.3</sub> (10.8 <sup>+11.5</sup> <sub>-10.0</sub> )	9.3 <sup>+10.7</sup> <sub>-7.9</sub> (8.6 <sup>+9.2</sup> <sub>-7.8</sub> )
nircam3-335	0.90 <sup>+1.00</sup> <sub>-0.79</sub> (0.66 <sup>+0.74</sup> <sub>-0.58</sub> )	1.18 <sup>+1.26</sup> <sub>-1.09</sub> (0.89 <sup>+0.96</sup> <sub>-0.82</sub> )	0.79 <sup>+0.90</sup> <sub>-0.68</sub> (0.61 <sup>+0.69</sup> <sub>-0.53</sub> )	1.05 <sup>+1.14</sup> <sub>-0.95</sub> (0.82 <sup>+0.90</sup> <sub>-0.74</sub> )	6.1 <sup>+6.8</sup> <sub>-5.7</sub> (7.8 <sup>+8.5</sup> <sub>-7.1</sub> )	4.9 <sup>+5.3</sup> <sub>-4.7</sub> (6.2 <sup>+6.8</sup> <sub>-5.8</sub> )	6.8 <sup>+7.6</sup> <sub>-6.1</sub> (8.2 <sup>+9.2</sup> <sub>-7.2</sub> )	5.5 <sup>+5.9</sup> <sub>-5.1</sub> (6.6 <sup>+7.1</sup> <sub>-6.2</sub> )
nircam3-395	0.75 <sup>+0.78</sup> <sub>-0.73</sub> (0.28 <sup>+0.27</sup> <sub>-0.27</sub> )	0.83 <sup>+0.88</sup> <sub>-0.80</sub> (0.33 <sup>+0.34</sup> <sub>-0.32</sub> )	0.77 <sup>+0.82</sup> <sub>-0.75</sub> (0.27 <sup>+0.26</sup> <sub>-0.26</sub> )	0.87 <sup>+0.96</sup> <sub>-0.83</sub> (0.33 <sup>+0.33</sup> <sub>-0.31</sub> )	7.1 <sup>+7.2</sup> <sub>-6.9</sub> (14.7 <sup>+14.8</sup> <sub>-14.4</sub> )	6.5 <sup>+6.7</sup> <sub>-6.2</sub> (12.9 <sup>+13.1</sup> <sub>-12.5</sub> )	6.9 <sup>+7.1</sup> <sub>-6.6</sub> (14.9 <sup>+15.2</sup> <sub>-14.7</sub> )	6.3 <sup>+6.5</sup> <sub>-6.5</sub> (13.2 <sup>+13.5</sup> <sub>-12.9</sub> )
nircam3-513	0.33 <sup>+0.33</sup> <sub>-0.32</sub> (0.22 <sup>+0.21</sup> <sub>-0.21</sub> )	0.40 <sup>+0.39</sup> <sub>-0.39</sub> (0.32 <sup>+0.30</sup> <sub>-0.30</sub> )	0.23 <sup>+0.23</sup> <sub>-0.23</sub> (0.09 <sup>+0.10</sup> <sub>-0.08</sub> )	0.24 <sup>+0.24</sup> <sub>-0.24</sub> (0.11 <sup>+0.12</sup> <sub>-0.10</sub> )	13.0 <sup>+13.2</sup> <sub>-12.9</sub> (17.0 <sup>+17.8</sup> <sub>-16.1</sub> )	11.3 <sup>+11.6</sup> <sub>-11.2</sub> (13.3 <sup>+13.8</sup> <sub>-12.7</sub> )	16.7 <sup>+16.7</sup> <sub>-16.7</sub> (31.5 <sup>+33.5</sup> <sub>-30.0</sub> )	16.4 <sup>+16.4</sup> <sub>-16.3</sub> (28.1 <sup>+29.0</sup> <sub>-26.6</sub> )
nircam3-515	0.35 <sup>+0.40</sup> <sub>-0.32</sub> (0.38 <sup>+0.43</sup> <sub>-0.35</sub> )	0.53 <sup>+0.59</sup> <sub>-0.48</sub> (0.68 <sup>+0.77</sup> <sub>-0.61</sub> )	0.18 <sup>+0.20</sup> <sub>-0.17</sub> (0.18 <sup>+0.20</sup> <sub>-0.17</sub> )	0.25 <sup>+0.29</sup> <sub>-0.23</sub> (0.25 <sup>+0.30</sup> <sub>-0.25</sub> )	12.3 <sup>+13.3</sup> <sub>-11.2</sub> (11.7 <sup>+12.4</sup> <sub>-10.8</sub> )	9.2 <sup>+9.9</sup> <sub>-8.5</sub> (7.6 <sup>+7.9</sup> <sub>-6.9</sub> )	19.8 <sup>+20.3</sup> <sub>-18.1</sub> (19.5 <sup>+20.7</sup> <sub>-18.3</sub> )	15.8 <sup>+16.9</sup> <sub>-14.2</sub> (14.6 <sup>+15.5</sup> <sub>-13.7</sub> )
nircam3-516	0.18 <sup>+0.18</sup> <sub>-0.18</sub> (0.16 <sup>+0.17</sup> <sub>-0.15</sub> )	0.23 <sup>+0.23</sup> <sub>-0.23</sub> (0.23 <sup>+0.24</sup> <sub>-0.22</sub> )	0.12 <sup>+0.12</sup> <sub>-0.12</sub> (0.09 <sup>+0.09</sup> <sub>-0.09</sub> )	0.15 <sup>+0.15</sup> <sub>-0.15</sub> (0.13 <sup>+0.13</sup> <sub>-0.12</sub> )	19.7 <sup>+19.8</sup> <sub>-19.6</sub> (21.7 <sup>+22.6</sup> <sub>-20.7</sub> )	16.7 <sup>+16.8</sup> <sub>-16.5</sub> (16.6 <sup>+16.0</sup> <sub>-16.0</sub> )	25.7 <sup>+25.8</sup> <sub>-25.6</sub> (31.7 <sup>+32.4</sup> <sub>-31.1</sub> )	22

Table E.1: (Continued)

Galaxy name	$t_5^{\text{SB99(BC03)}}$ [Gyr]		$t_{10}^{\text{SB99(BC03)}}$ [Gyr]		$t_{10^9 \text{M}_\odot}^{\text{SB99(BC03)}}$ [Gyr]		$z_5^{\text{SB99(BC03)}}$		$z_{5 \times 10^8 \text{M}_\odot}^{\text{SB99(BC03)}}$		$z_{10}^{\text{SB99(BC03)}}$		$z_{10^9 \text{M}_\odot}^{\text{SB99(BC03)}}$	
	$t_5$	$t_{10}$	$t_5$	$t_{10}$	$t_5$	$t_{10}$	$z_5$	$z_{10}$	$z_5$	$z_{10}$	$z_5$	$z_{10}$	$z_5$	$z_{10}$
nircam3-735	2.52 <sup>+0.57</sup> <sub>-0.44</sub> (0.84 <sup>+0.96</sup> <sub>-0.70</sub> )	2.76 <sup>+2.80</sup> <sub>-2.71</sub> (1.20 <sup>+1.33</sup> <sub>-1.05</sub> )	2.31 <sup>+2.42</sup> <sub>-2.19</sub> (0.72 <sup>+0.83</sup> <sub>-0.59</sub> )	2.58 <sup>+2.64</sup> <sub>-2.51</sub> (0.99 <sup>+1.14</sup> <sub>-0.84</sub> )	2.62 <sup>+7</sup> <sub>-5.8</sub> (6.5 <sup>+7.5</sup> <sub>-5.8</sub> )	2.42 <sup>+4</sup> <sub>-4.5</sub> (4.9 <sup>+5.5</sup> <sub>-4.5</sub> )	2.82 <sup>+9</sup> <sub>-2.7</sub> (7.3 <sup>+8.5</sup> <sub>-6.5</sub> )	2.52 <sup>+6</sup> <sub>-2.5</sub> (5.7 <sup>+6.4</sup> <sub>-5.1</sub> )						
nircam3-924	1.42 <sup>+1.44</sup> <sub>-1.29</sub> (1.29 <sup>+1.30</sup> <sub>-1.27</sub> )	1.61 <sup>+1.61</sup> <sub>-1.61</sub> (1.52 <sup>+1.54</sup> <sub>-1.46</sub> )	1.11 <sup>+1.11</sup> <sub>-1.10</sub> (1.08 <sup>+1.09</sup> <sub>-1.07</sub> )	1.24 <sup>+1.25</sup> <sub>-1.23</sub> (1.19 <sup>+1.21</sup> <sub>-1.18</sub> )	4.3 <sup>+4.2</sup> <sub>-4.6</sub> (4.6 <sup>+4.7</sup> <sub>-4.6</sub> )	3.8 <sup>+3.8</sup> <sub>-3.8</sub> (4.0 <sup>+4.0</sup> <sub>-4.0</sub> )	5.2 <sup>+5.3</sup> <sub>-5.2</sub> (5.3 <sup>+5.4</sup> <sub>-5.3</sub> )	4.8 <sup>+4.8</sup> <sub>-4.1</sub> (4.9 <sup>+4.9</sup> <sub>-4.9</sub> )						
nircam3-980	0.60 <sup>+0.62</sup> <sub>-0.59</sub> (0.42 <sup>+0.44</sup> <sub>-0.41</sub> )	0.68 <sup>+0.71</sup> <sub>-0.66</sub> (0.63 <sup>+0.67</sup> <sub>-0.60</sub> )	0.80 <sup>+0.87</sup> <sub>-0.75</sub> (0.36 <sup>+0.35</sup> <sub>-0.35</sub> )	1.23 <sup>+1.49</sup> <sub>-1.05</sub> (0.50 <sup>+0.52</sup> <sub>-0.47</sub> )	8.8 <sup>+8.4</sup> <sub>-8.2</sub> (10.8 <sup>+11.1</sup> <sub>-10.5</sub> )	7.6 <sup>+7.8</sup> <sub>-7.4</sub> (8.0 <sup>+8.2</sup> <sub>-7.7</sub> )	6.7 <sup>+6.3</sup> <sub>-6.3</sub> (12.0 <sup>+12.4</sup> <sub>-11.9</sub> )	4.8 <sup>+5.4</sup> <sub>-4.1</sub> (9.6 <sup>+10.0</sup> <sub>-9.3</sub> )						
nircam3-1033	0.43 <sup>+0.49</sup> <sub>-0.38</sub> (1.14 <sup>+1.32</sup> <sub>-0.93</sub> )	0.67 <sup>+0.73</sup> <sub>-0.59</sub> (1.62 <sup>+1.72</sup> <sub>-1.49</sub> )	0.26 <sup>+0.28</sup> <sub>-0.24</sub> (0.67 <sup>+0.82</sup> <sub>-0.54</sub> )	0.35 <sup>+0.39</sup> <sub>-0.31</sub> (1.01 <sup>+1.18</sup> <sub>-0.83</sub> )	10.7 <sup>+11.6</sup> <sub>-11.6</sub> (5.1 <sup>+6.0</sup> <sub>-4.5</sub> )	7.7 <sup>+7.5</sup> <sub>-7.2</sub> (3.8 <sup>+4.1</sup> <sub>-3.6</sub> )	15.4 <sup>+16.3</sup> <sub>-14.4</sub> (7.7 <sup>+9.0</sup> <sub>-6.6</sub> )	12.4 <sup>+13.4</sup> <sub>-11.4</sub> (5.6 <sup>+6.5</sup> <sub>-5.5</sub> )						
nircam3-1095	0.21 <sup>+0.23</sup> <sub>-0.19</sub> (0.33 <sup>+0.37</sup> <sub>-0.29</sub> )	0.31 <sup>+0.35</sup> <sub>-0.27</sub> (0.56 <sup>+0.64</sup> <sub>-0.46</sub> )	0.16 <sup>+0.18</sup> <sub>-0.14</sub> (0.25 <sup>+0.28</sup> <sub>-0.22</sub> )	0.23 <sup>+0.27</sup> <sub>-0.20</sub> (0.33 <sup>+0.44</sup> <sub>-0.34</sub> )	18.0 <sup>+19.2</sup> <sub>-16.6</sub> (13.0 <sup>+14.2</sup> <sub>-12.0</sub> )	13.5 <sup>+14.8</sup> <sub>-12.2</sub> (8.8 <sup>+9.7</sup> <sub>-7.3</sub> )	21.1 <sup>+23.3</sup> <sub>-19.5</sub> (15.9 <sup>+17.3</sup> <sub>-14.6</sub> )	16.7 <sup>+18.5</sup> <sub>-15.1</sub> (11.6 <sup>+12.6</sup> <sub>-10.6</sub> )						
nircam3-1143	0.84 <sup>+0.89</sup> <sub>-0.79</sub> (0.78 <sup>+0.88</sup> <sub>-0.70</sub> )	1.17 <sup>+1.22</sup> <sub>-1.12</sub> (1.30 <sup>+1.38</sup> <sub>-1.23</sub> )	0.52 <sup>+0.56</sup> <sub>-0.48</sub> (0.63 <sup>+0.71</sup> <sub>-0.57</sub> )	0.69 <sup>+0.74</sup> <sub>-0.65</sub> (1.09 <sup>+1.17</sup> <sub>-1.00</sub> )	6.5 <sup>+6.8</sup> <sub>-6.2</sub> (6.8 <sup>+7.4</sup> <sub>-6.3</sub> )	5.0 <sup>+5.2</sup> <sub>-4.8</sub> (4.6 <sup>+4.8</sup> <sub>-4.4</sub> )	9.3 <sup>+9.7</sup> <sub>-8.7</sub> (8.0 <sup>+8.7</sup> <sub>-7.3</sub> )	7.5 <sup>+7.9</sup> <sub>-7.1</sub> (5.3 <sup>+5.6</sup> <sub>-5.0</sub> )						
nircam3-1144	0.73 <sup>+0.73</sup> <sub>-0.73</sub> (0.22 <sup>+0.23</sup> <sub>-0.21</sub> )	0.77 <sup>+0.78</sup> <sub>-0.77</sub> (0.29 <sup>+0.31</sup> <sub>-0.27</sub> )	0.69 <sup>+0.69</sup> <sub>-0.69</sub> (0.16 <sup>+0.17</sup> <sub>-0.16</sub> )	0.71 <sup>+0.71</sup> <sub>-0.71</sub> (0.19 <sup>+0.19</sup> <sub>-0.18</sub> )	7.2 <sup>+7.2</sup> <sub>-7.2</sub> (17.1 <sup>+17.9</sup> <sub>-16.5</sub> )	6.9 <sup>+6.9</sup> <sub>-6.9</sub> (14.1 <sup>+14.8</sup> <sub>-13.4</sub> )	7.5 <sup>+7.5</sup> <sub>-7.3</sub> (21.3 <sup>+21.6</sup> <sub>-20.9</sub> )	7.3 <sup>+7.4</sup> <sub>-7.3</sub> (19.4 <sup>+19.8</sup> <sub>-18.9</sub> )						
nircam3-1481	0.50 <sup>+0.54</sup> <sub>-0.47</sub> (0.27 <sup>+0.29</sup> <sub>-0.24</sub> )	0.64 <sup>+0.69</sup> <sub>-0.59</sub> (0.39 <sup>+0.43</sup> <sub>-0.35</sub> )	0.47 <sup>+0.51</sup> <sub>-0.44</sub> (0.26 <sup>+0.29</sup> <sub>-0.23</sub> )	0.59 <sup>+0.65</sup> <sub>-0.55</sub> (0.38 <sup>+0.41</sup> <sub>-0.33</sub> )	9.5 <sup>+10.0</sup> <sub>-9.0</sub> (14.8 <sup>+16.1</sup> <sub>-13.8</sub> )	8.0 <sup>+8.4</sup> <sub>-7.5</sub> (11.4 <sup>+12.4</sup> <sub>-10.6</sub> )	9.9 <sup>+10.4</sup> <sub>-9.4</sub> (15.3 <sup>+16.7</sup> <sub>-14.3</sub> )	8.4 <sup>+8.9</sup> <sub>-7.9</sub> (11.8 <sup>+12.8</sup> <sub>-11.0</sub> )						
nircam3-1548	1.04 <sup>+1.04</sup> <sub>-1.03</sub> (0.97 <sup>+0.98</sup> <sub>-0.97</sub> )	1.12 <sup>+1.11</sup> <sub>-1.11</sub> (1.06 <sup>+1.06</sup> <sub>-1.06</sub> )	0.96 <sup>+0.96</sup> <sub>-0.96</sub> (0.89 <sup>+0.89</sup> <sub>-0.89</sub> )	0.99 <sup>+0.99</sup> <sub>-0.99</sub> (0.95 <sup>+0.96</sup> <sub>-0.95</sub> )	5.5 <sup>+5.5</sup> <sub>-5.5</sub> (5.8 <sup>+5.8</sup> <sub>-5.8</sub> )	5.2 <sup>+5.2</sup> <sub>-5.2</sub> (5.4 <sup>+5.4</sup> <sub>-5.4</sub> )	5.8 <sup>+5.9</sup> <sub>-5.8</sub> (6.2 <sup>+6.2</sup> <sub>-6.2</sub> )	5.7 <sup>+5.7</sup> <sub>-5.7</sub> (5.9 <sup>+5.9</sup> <sub>-5.9</sub> )						
nircam3-1668	0.65 <sup>+0.74</sup> <sub>-0.52</sub> (1.08 <sup>+1.26</sup> <sub>-0.90</sub> )	0.89 <sup>+1.04</sup> <sub>-0.79</sub> (1.59 <sup>+1.72</sup> <sub>-1.43</sub> )	0.56 <sup>+0.70</sup> <sub>-0.48</sub> (1.04 <sup>+1.23</sup> <sub>-0.86</sub> )	0.83 <sup>+0.96</sup> <sub>-0.72</sub> (1.53 <sup>+1.68</sup> <sub>-1.37</sub> )	8.2 <sup>+9.3</sup> <sub>-7.1</sub> (5.3 <sup>+6.1</sup> <sub>-4.7</sub> )	6.2 <sup>+6.8</sup> <sub>-5.5</sub> (3.9 <sup>+4.2</sup> <sub>-3.6</sub> )	8.8 <sup>+9.9</sup> <sub>-7.4</sub> (5.5 <sup>+6.4</sup> <sub>-4.8</sub> )	6.6 <sup>+7.3</sup> <sub>-5.9</sub> (4.0 <sup>+4.4</sup> <sub>-3.7</sub> )						
nircam3-1760	0.77 <sup>+0.79</sup> <sub>-0.75</sub> (0.54 <sup>+0.57</sup> <sub>-0.51</sub> )	1.02 <sup>+1.08</sup> <sub>-0.96</sub> (0.79 <sup>+0.86</sup> <sub>-0.73</sub> )	0.64 <sup>+0.65</sup> <sub>-0.64</sub> (0.33 <sup>+0.34</sup> <sub>-0.32</sub> )	0.75 <sup>+0.74</sup> <sub>-0.71</sub> (0.41 <sup>+0.42</sup> <sub>-0.38</sub> )	6.9 <sup>+7.1</sup> <sub>-6.8</sub> (9.1 <sup>+9.5</sup> <sub>-8.7</sub> )	5.6 <sup>+5.8</sup> <sub>-5.3</sub> (6.8 <sup>+7.2</sup> <sub>-6.6</sub> )	7.9 <sup>+8.0</sup> <sub>-7.7</sub> (11.1 <sup>+11.6</sup> <sub>-10.8</sub> )	7.2 <sup>+7.3</sup> <sub>-7.3</sub> (11.1 <sup>+11.6</sup> <sub>-10.8</sub> )						
nircam3-1779	0.25 <sup>+0.21</sup> <sub>-0.20</sub> (0.44 <sup>+0.39</sup> <sub>-0.39</sub> )	0.39 <sup>+0.47</sup> <sub>-0.35</sub> (0.70 <sup>+0.62</sup> <sub>-0.61</sub> )	0.14 <sup>+0.16</sup> <sub>-0.12</sub> (0.27 <sup>+0.25</sup> <sub>-0.25</sub> )	0.20 <sup>+0.23</sup> <sub>-0.17</sub> (0.37 <sup>+0.34</sup> <sub>-0.34</sub> )	15.9 <sup>+18.1</sup> <sub>-13.9</sub> (10.4 <sup>+11.5</sup> <sub>-9.5</sub> )	11.5 <sup>+13.2</sup> <sub>-10.1</sub> (7.4 <sup>+8.3</sup> <sub>-6.6</sub> )	23.9 <sup>+26.0</sup> <sub>-21.8</sub> (14.9 <sup>+15.9</sup> <sub>-13.7</sub> )	18.7 <sup>+20.5</sup> <sub>-16.5</sub> (11.8 <sup>+12.7</sup> <sub>-10.8</sub> )						
nircam3-1787	0.69 <sup>+1.35</sup> <sub>-0.45</sub> (0.17 <sup>+0.21</sup> <sub>-0.15</sub> )	1.85 <sup>+2.37</sup> <sub>-1.08</sub> (0.27 <sup>+0.32</sup> <sub>-0.23</sub> )	0.60 <sup>+1.10</sup> <sub>-0.40</sub> (0.09 <sup>+0.11</sup> <sub>-0.08</sub> )	1.64 <sup>+2.13</sup> <sub>-0.84</sub> (0.13 <sup>+0.17</sup> <sub>-0.11</sub> )	7.5 <sup>+10.3</sup> <sub>-4.5</sub> (20.2 <sup>+22.7</sup> <sub>-17.8</sub> )	3.4 <sup>+5.2</sup> <sub>-2.7</sub> (15.0 <sup>+16.9</sup> <sub>-13.3</sub> )	8.4 <sup>+11.2</sup> <sub>-5.2</sub> (31.6 <sup>+34.5</sup> <sub>-20.9</sub> )	3.8 <sup>+6.5</sup> <sub>-3.0</sub> (24.4 <sup>+27.4</sup> <sub>-20.9</sub> )						
nircam3-2119	0.20 <sup>+0.22</sup> <sub>-0.19</sub> (0.17 <sup>+0.17</sup> <sub>-0.16</sub> )	0.31 <sup>+0.33</sup> <sub>-0.28</sub> (0.24 <sup>+0.25</sup> <sub>-0.23</sub> )	0.17 <sup>+0.18</sup> <sub>-0.16</sub> (0.13 <sup>+0.14</sup> <sub>-0.13</sub> )	0.24 <sup>+0.26</sup> <sub>-0.22</sub> (0.18 <sup>+0.19</sup> <sub>-0.18</sub> )	18.2 <sup>+19.1</sup> <sub>-17.2</sub> (20.8 <sup>+21.3</sup> <sub>-20.3</sub> )	13.6 <sup>+14.5</sup> <sub>-12.8</sub> (16.1 <sup>+16.5</sup> <sub>-15.6</sub> )	21.0 <sup>+21.8</sup> <sub>-20.0</sub> (24.2 <sup>+25.0</sup> <sub>-23.5</sub> )	16.3 <sup>+17.2</sup> <sub>-15.3</sub> (19.6 <sup>+20.2</sup> <sub>-19.1</sub> )						
nircam3-2161	0.34 <sup>+0.33</sup> <sub>-0.30</sub> (0.46 <sup>+0.38</sup> <sub>-0.38</sub> )	0.39 <sup>+0.40</sup> <sub>-0.39</sub> (0.64 <sup>+0.72</sup> <sub>-0.52</sub> )	0.29 <sup>+0.29</sup> <sub>-0.29</sub> (0.32 <sup>+0.37</sup> <sub>-0.37</sub> )	0.32 <sup>+0.31</sup> <sub>-0.31</sub> (0.43 <sup>+0.49</sup> <sub>-0.35</sub> )	12.7 <sup>+12.8</sup> <sub>-12.5</sub> (10.2 <sup>+11.7</sup> <sub>-9.1</sub> )	11.4 <sup>+11.2</sup> <sub>-11.2</sub> (8.0 <sup>+9.3</sup> <sub>-7.3</sub> )	14.3 <sup>+14.4</sup> <sub>-14.2</sub> (13.1 <sup>+14.9</sup> <sub>-11.9</sub> )	13.3 <sup>+13.5</sup> <sub>-13.1</sub> (10.7 <sup>+12.3</sup> <sub>-9.6</sub> )						
nircam3-2223	3.04 <sup>+3.04</sup> <sub>-3.04</sub> (3.02 <sup>+3.02</sup> <sub>-3.02</sub> )	3.09 <sup>+3.09</sup> <sub>-3.08</sub> (3.03 <sup>+3.03</sup> <sub>-3.03</sub> )	3.03 <sup>+3.03</sup> <sub>-3.03</sub> (3.01 <sup>+3.01</sup> <sub>-3.01</sub> )	3.06 <sup>+3.06</sup> <sub>-3.05</sub> (3.02 <sup>+3.02</sup> <sub>-3.02</sub> )	2.1 <sup>+2.1</sup> <sub>-2.1</sub> (2.2 <sup>+2.2</sup> <sub>-2.2</sub> )	2.1 <sup>+2.1</sup> <sub>-2.1</sub> (2.2 <sup>+2.2</sup> <sub>-2.2</sub> )	2.2 <sup>+2.2</sup> <sub>-2.2</sub> (2.2 <sup>+2.2</sup> <sub>-2.2</sub> )	2.1 <sup>+2.1</sup> <sub>-2.1</sub> (2.2 <sup>+2.2</sup> <sub>-2.2</sub> )						
nircam3-2238	0.45 <sup>+0.55</sup> <sub>-0.36</sub> (0.22 <sup>+0.24</sup> <sub>-0.21</sub> )	0.73 <sup>+0.83</sup> <sub>-0.62</sub> (0.36 <sup>+0.39</sup> <sub>-0.33</sub> )	0.23 <sup>+0.28</sup> <sub>-0.19</sub> (0.12 <sup>+0.11</sup> <sub>-0.11</sub> )	0.37 <sup>+0.46</sup> <sub>-0.29</sub> (0.17 <sup>+0.19</sup> <sub>-0.16</sub> )	10.3 <sup>+12.2</sup> <sub>-8.9</sub> (17.0 <sup>+18.0</sup> <sub>-16.2</sub> )	7.2 <sup>+8.1</sup> <sub>-6.5</sub> (12.2 <sup>+13.9</sup> <sub>-11.5</sub> )	16.7 <sup>+19.1</sup> <sub>-14.6</sub> (25.9 <sup>+27.3</sup> <sub>-24.9</sub> )	11.9 <sup>+14.0</sup> <sub>-10.2</sub> (20.4 <sup>+21.4</sup> <sub>-19.3</sub> )						
nircam3-2387	0.49 <sup>+0.61</sup> <sub>-0.43</sub> (0.40 <sup>+0.43</sup> <sub>-0.38</sub> )	0.71 <sup>+0.84</sup> <sub>-0.61</sub> (0.55 <sup>+0.61</sup> <sub>-0.50</sub> )	0.34 <sup>+0.40</sup> <sub>-0.32</sub> (0.31 <sup>+0.30</sup> <sub>-0.30</sub> )	0.43 <sup>+0.53</sup> <sub>-0.39</sub> (0.39 <sup>+0.42</sup> <sub>-0.36</sub> )	9.7 <sup>+8.2</sup> <sub>-8.2</sub> (11.2 <sup>+11.8</sup> <sub>-10.6</sub> )	7.4 <sup>+8.3</sup> <sub>-6.5</sub> (8.9 <sup>+9.5</sup> <sub>-8.3</sub> )	12.6 <sup>+13.3</sup> <sub>-11.3</sub> (13.4 <sup>+13.8</sup> <sub>-12.9</sub> )	10.7 <sup>+11.4</sup> <sub>-9.2</sub> (11.5 <sup>+12.1</sup> <sub>-10.9</sub> )						
nircam3-2521	0.52 <sup>+0.53</sup> <sub>-0.51</sub> (0.28 <sup>+0.28</sup> <sub>-0.28</sub> )	0.59 <sup>+0.60</sup> <sub>-0.57</sub> (0.35 <sup>+0.36</sup> <sub>-0.34</sub> )	0.45 <sup>+0.45</sup> <sub>-0.45</sub> (0.21 <sup>+0.21</sup> <sub>-0.21</sub> )	0.47 <sup>+0.47</sup> <sub>-0.46</sub> (0.23 <sup>+0.23</sup> <sub>-0.23</sub> )	9.2 <sup>+9.4</sup> <sub>-9.4</sub> (14.5 <sup>+14.7</sup> <sub>-14.2</sub> )	8.5 <sup>+8.6</sup> <sub>-8.3</sub> (12.4 <sup>+12.7</sup> <sub>-12.1</sub> )	10.4 <sup>+10.4</sup> <sub>-10.3</sub> (18.0 <sup>+18.2</sup> <sub>-17.8</sub> )	10.1 <sup>+10.1</sup> <sub>-10.0</sub> (16.8 <sup>+16.6</sup> <sub>-16.6</sub> )						
nircam3-2527	0.68 <sup>+0.74</sup> <sub>-0.65</sub> (0.43 <sup>+0.46</sup> <sub>-0.41</sub> )	0.82 <sup>+0.92</sup> <sub>-0.76</sub> (0.55 <sup>+0.60</sup> <sub>-0.50</sub> )	0.58 <sup>+0.61</sup> <sub>-0.56</sub> (0.34 <sup>+0.36</sup> <sub>-0.33</sub> )	0.64 <sup>+0.69</sup> <sub>-0.61</sub> (0.41 <sup>+0.44</sup> <sub>-0.39</sub> )	7.6 <sup>+7.9</sup> <sub>-7.1</sub> (10.7 <sup>+11.3</sup> <sub>-10.1</sub> )	6.6 <sup>+7.0</sup> <sub>-6.0</sub> (8.9 <sup>+9.5</sup> <sub>-8.4</sub> )	8.6 <sup>+8.8</sup> <sub>-8.3</sub> (12.6 <sup>+13.0</sup> <sub>-12.0</sub> )	8.0 <sup>+8.2</sup> <sub>-7.5</sub> (11.0 <sup>+11.5</sup> <sub>-10.5</sub> )						
nircam3-2552	0.80 <sup>+1.04</sup> <sub>-0.64</sub> (0.36 <sup>+0.41</sup> <sub>-0.29</sub> )	1.10 <sup>+1.41</sup> <sub>-0.84</sub> (0.59 <sup>+0.72</sup> <sub>-0.46</sub> )	0.60 <sup>+0.76</sup> <sub>-0.49</sub> (0.21 <sup>+0.25</sup> <sub>-0.18</sub> )	0.87 <sup>+1.18</sup> <sub>-0.68</sub> (0.39 <sup>+0.37</sup> <sub>-0.26</sub> )	6.7 <sup>+8.0</sup> <sub>-5.5</sub> (12.2 <sup>+14.3</sup> <sub>-11.0</sub> )	5.3 <sup>+5.5</sup> <sub>-4.3</sub> (8.4 <sup>+10.1</sup> <sub>-7.3</sub> )	8.4 <sup>+9.7</sup> <sub>-7.0</sub> (17.8 <sup>+20.0</sup> <sub>-15.9</sub> )	6.3 <sup>+6.5</sup> <sub>-5.0</sub> (13.2 <sup>+15.3</sup> <sub>-11.8</sub> )						
nircam3-2578	0.34 <sup>+0.42</sup> <sub>-0.30</sub> (1.26 <sup>+1.07</sup> <sub>-0.74</sub> )	0.54 <sup>+0.65</sup> <sub>-0.45</sub> (1.64 <sup>+1.51</sup> <sub>-1.51</sub> )	0.25 <sup>+0.30</sup> <sub>-0.22</sub> (1.12 <sup>+0.92</sup> <sub>-0.92</sub> )	0.37 <sup>+0.46</sup> <sub>-0.31</sub> (1.50 <sup>+1.61</sup> <sub>-1.34</sub> )	12.6 <sup>+14.0</sup> <sub>-10.9</sub> (4.7 <sup>+4.3</sup> <sub>-4.3</sub> )	9.0 <sup>+9.4</sup> <sub>-8.3</sub> (3.8 <sup>+3.6</sup> <sub>-3.6</sub> )	15.6 <sup>+17.4</sup> <sub>-13.8</sub> (5.2 <sup>+6.0</sup> <sub>-4.6</sub> )	11.9 <sup>+13.5</sup> <sub>-10.2</sub> (4.1 <sup>+4.5</sup> <sub>-3.8</sub> )						
nircam3-2598	0.38 <sup>+0.38</sup> <sub>-0.37</sub> (0.30 <sup>+0.34</sup> <sub>-0.27</sub> )	0.44 <sup>+0.45</sup> <sub>-0.43</sub> (0.51 <sup>+0.62</sup> <sub>-0.44</sub> )	0.26 <sup>+0.26</sup> <sub>-0.26</sub> (0.07 <sup>+0.08</sup> <sub>-0.06</sub> )	0.27 <sup>+0.27</sup> <sub>-0.27</sub> (0.09 <sup>+0.09</sup> <sub>-0.08</sub> )	11.8 <sup>+12.0</sup> <sub>-11.6</sub> (13.8 <sup>+15.1</sup> <sub>-12.6</sub> )	10.5 <sup>+10.7</sup> <sub>-10.2</sub> (9.4 <sup>+10.5</sup> <sub>-8.2</sub> )	15.2 <sup>+15.2</sup> <sub>-15.1</sub> (39.7 <sup>+42.3</sup> <sub>-36.1</sub> )	14.8 <sup>+14.8</sup> <sub>-14.7</sub> (32.6 <sup>+33.7</sup> <sub>-31.1</sub> )						
nircam3-2789	0.19 <sup>+0.20</sup> <sub>-0.18</sub> (0.27 <sup>+0.29</sup> <sub>-0.25</sub> )	0.26 <sup>+0.27</sup> <sub>-0.24</sub> (0.37 <sup>+0.40</sup> <sub>-0.35</sub> )	0.14 <sup>+0.14</sup> <sub>-0.13</sub> (0.22 <sup>+0.24</sup> <sub>-0.20</sub> )	0.18 <sup>+0.19</sup> <sub>-0.17</sub> (0.30 <sup>+0.32</sup> <sub>-0.28</sub> )	19.1 <sup>+19.7</sup> <sub>-18.6</sub> (14.9 <sup>+15.7</sup> <sub>-14.0</sub> )	15.5 <sup>+16.0</sup> <sub>-15.0</sub> (11.8 <sup>+12.3</sup> <sub>-11.2</sub> )	23.8 <sup>+24.4</sup> <sub>-23.1</sub> (17.4 <sup>+18.2</sup> <sub>-16.4</sub> )	19.5 <sup>+20.2</sup> <sub>-18.8</sub> (13.9 <sup>+14.7</sup> <sub>-13.2</sub> )						
nircam3-2885	1.00 <sup>+1.18</sup> <sub>-0.82</sub> (0.66 <sup>+0.79</sup> <sub>-0.55</sub> )	1.37 <sup>+1.52</sup> <sub>-1.25</sub> (1.12 <sup>+1.35</sup> <sub>-0.88</sub> )	1.15 <sup>+1.35</sup> <sub>-0.99</sub> (0.96 <sup>+1.15</sup> <sub>-0.76</sub> )	1.56 <sup>+1.69</sup> <sub>-1.44</sub> (1.63 <sup>+1.86</sup> <sub>-1.39</sub> )	5.7 <sup>+6.6</sup> <sub>-4.9</sub> (7.7 <sup>+8.9</sup> <sub>-6.8</sub> )	4.4 <sup>+4.8</sup> <sub>-4.4</sub> (5.2 <sup>+6.2</sup> <sub>-4.4</sub> )	5.1 <sup>+5.7</sup> <sub>-4.4</sub> (5.9 <sup>+7.0</sup> <sub>-5.0</sub> )	4.0 <sup>+4.2</sup> <sub>-3.7</sub> (3.8 <sup>+4.3</sup> <sub>-3.4</sub> )						
nircam3-2944	0.28 <sup>+0.28</sup> <sub>-0.27</sub> (0.44 <sup>+0.50</sup> <sub>-0.41</sub> )	0.33 <sup>+0.33</sup> <sub>-0.32</sub> (0.72 <sup>+0.78</sup> <sub>-0.65</sub> )	0.20 <sup>+0.20</sup> <sub>-0.20</sub> (0.15 <sup>+0.15</sup> <sub>-0.13</sub> )	0.21 <sup>+0.21</sup> <sub>-0.21</sub> (0.21 <sup>+0.24</sup> <sub>-0.19</sub> )	14.7 <sup>+14.8</sup> <sub>-14.6</sub> (10.5 <sup>+11.1</sup> <sub>-9.6</sub> )	12.9 <sup>+13.1</sup> <sub>-12.8</sub> (7.3 <sup>+7.9</sup> <sub>-6.8</sub> )	18.5 <sup>+18.6</sup> <sub>-18.5</sub> (22.1 <sup>+24.3</sup> <sub>-20.0</sub> )	18.0 <sup>+18.1</sup> <sub>-18.0</sub> (17.6 <sup>+18.8</sup> <sub>-16.2</sub> )						
nircam3-2956	0.47 <sup>+0.55</sup> <sub>-0.42</sub> (0.35 <sup>+0.40</sup> <sub>-0.30</sub> )	0.67 <sup>+0.74</sup> <sub>-0.60</sub> (0.51 <sup>+0.56</sup> <sub>-0.45</sub> )	0.34 <sup>+0.38</sup> <sub>-0.31</sub> (0.24 <sup>+0.28</sup> <sub>-0.19</sub> )	0.44 <sup>+0.50</sup> <sub>-0.40</sub> (0.36 <sup>+0.41</sup> <sub>-0.29</sub> )	10.0 <sup>+10.8</sup> <sub>-9.0</sub> (12.4 <sup>+14.0</sup> <sub>-11.2</sub> )	7.7 <sup>+8.4</sup> <sub>-7.1</sub> (9.5 <sup>+10.4</sup> <sub>-8.8</sub> )	12.7 <sup>+13.4</sup> <sub>-11.8</sub> (16.3 <sup>+18.9</sup> <sub>-14.4</sub> )	10.5 <sup>+11.3</sup> <sub>-9.6</sub> (12.2 <sup>+14.1</sup> <sub>-11.1</sub> )						
nircam3-3069	0.94 <sup>+1.00</sup> <sub>-0.88</sub> (0.49 <sup>+0.55</sup> <sub>-0.43</sub> )	1.19 <sup>+1.24</sup> <sub>-1.13</sub> (0.70 <sup>+0.77</sup> <sub>-0.62</sub> )	0.80 <sup>+0.87</sup> <sub>-0.74</sub> (0.42 <sup>+0.48</sup> <sub>-0.37</sub> )	1.01 <sup>+1.07</sup> <sub>-0.94</sub> (0.50 <sup>+0.56</sup> <sub>-0.50</sub> )	5.9 <sup>+6.3</sup> <sub>-5.6</sub> (9.7 <sup>+10.8</sup> <sub>-8.8</sub> )	4.9 <sup>+5.4</sup> <sub>-4.8</sub> (7.4 <sup>+8.2</sup> <sub>-6.9</sub> )	6.7 <sup>+7.1</sup> <sub>-6.3</sub> (10.9 <sup>+12.0</sup> <sub>-9.8</sub> )	5.6 <sup>+5.9</sup> <sub>-5.4</sub> (8.5 <sup>+9</sup>						

Table E.1: (Continued)

Galaxy name	$t_5^{\text{SB99(BC03)}}$ [Gyr]	$t_{10}^{\text{SB99(BC03)}}$ [Gyr]	$t_{5 \times 10^8 \text{ M}_\odot}^{\text{SB99(BC03)}}$ [Gyr]	$t_{10^9 \text{ M}_\odot}^{\text{SB99(BC03)}}$ [Gyr]	$z_5^{\text{SB99(BC03)}}$	$z_{10}^{\text{SB99(BC03)}}$	$z_{5 \times 10^8 \text{ M}_\odot}^{\text{SB99(BC03)}}$	$z_{10^9 \text{ M}_\odot}^{\text{SB99(BC03)}}$
nircam3-3217	0.75 <sup>+0.83</sup> <sub>-0.66</sub> (0.98 <sup>+1.13</sup> <sub>-0.82</sub> )	1.04 <sup>+1.10</sup> <sub>-0.94</sub> (1.38 <sup>+1.48</sup> <sub>-1.23</sub> )	0.53 <sup>+0.62</sup> <sub>-0.48</sub> (0.75 <sup>+0.90</sup> <sub>-0.61</sub> )	0.73 <sup>+0.81</sup> <sub>-0.64</sub> (1.09 <sup>+1.21</sup> <sub>-0.90</sub> )	7.1 <sup>+7.8</sup> <sub>-6.5</sub> (5.7 <sup>+6.6</sup> <sub>-5.1</sub> )	5.5 <sup>+5.9</sup> <sub>-4.4</sub> (4.4 <sup>+4.8</sup> <sub>-4.1</sub> )	9.1 <sup>+10.9</sup> <sub>-8.1</sub> (7.1 <sup>+8.3</sup> <sub>-6.2</sub> )	7.2 <sup>+7.9</sup> <sub>-6.7</sub> (5.3 <sup>+6.2</sup> <sub>-4.9</sub> )
nircam3-3243	0.78 <sup>+0.90</sup> <sub>-0.60</sub> (0.63 <sup>+0.70</sup> <sub>-0.54</sub> )	1.10 <sup>+1.26</sup> <sub>-0.94</sub> (1.08 <sup>+0.96</sup> <sub>-0.96</sub> )	0.90 <sup>+1.04</sup> <sub>-0.79</sub> (0.62 <sup>+0.71</sup> <sub>-0.54</sub> )	1.30 <sup>+1.47</sup> <sub>-1.12</sub> (1.07 <sup>+1.24</sup> <sub>-0.89</sub> )	6.9 <sup>+7.7</sup> <sub>-6.2</sub> (8.1 <sup>+7.4</sup> <sub>-7.4</sub> )	5.2 <sup>+6.0</sup> <sub>-4.7</sub> (5.3 <sup>+4.7</sup> <sub>-4.7</sub> )	6.1 <sup>+6.8</sup> <sub>-5.5</sub> (8.1 <sup>+7.4</sup> <sub>-7.4</sub> )	4.6 <sup>+5.2</sup> <sub>-4.1</sub> (5.4 <sup>+6.2</sup> <sub>-4.8</sub> )
nircam3-3339	0.14 <sup>+0.14</sup> <sub>-0.13</sub> (0.14 <sup>+0.14</sup> <sub>-0.14</sub> )	0.18 <sup>+0.18</sup> <sub>-0.18</sub> (0.19 <sup>+0.19</sup> <sub>-0.18</sub> )	0.09 <sup>+0.09</sup> <sub>-0.09</sub> (0.09 <sup>+0.09</sup> <sub>-0.09</sub> )	0.10 <sup>+0.10</sup> <sub>-0.10</sub> (0.11 <sup>+0.11</sup> <sub>-0.11</sub> )	24.2 <sup>+24.1</sup> <sub>-24.1</sub> (23.5 <sup>+23.7</sup> <sub>-23.4</sub> )	19.8 <sup>+19.8</sup> <sub>-19.7</sub> (19.4 <sup>+19.5</sup> <sub>-19.3</sub> )	31.5 <sup>+31.5</sup> <sub>-31.5</sub> (31.1 <sup>+31.1</sup> <sub>-31.0</sub> )	28.9 <sup>+28.9</sup> <sub>-28.9</sub> (28.5 <sup>+28.5</sup> <sub>-28.4</sub> )
nircam3-3461	0.52 <sup>+0.65</sup> <sub>-0.47</sub> (0.34 <sup>+0.40</sup> <sub>-0.28</sub> )	0.76 <sup>+1.09</sup> <sub>-0.64</sub> (0.56 <sup>+0.64</sup> <sub>-0.48</sub> )	0.43 <sup>+0.50</sup> <sub>-0.40</sub> (0.19 <sup>+0.24</sup> <sub>-0.16</sub> )	0.55 <sup>+0.72</sup> <sub>-0.49</sub> (0.30 <sup>+0.37</sup> <sub>-0.24</sub> )	9.4 <sup>+10.0</sup> <sub>-7.8</sub> (12.6 <sup>+14.4</sup> <sub>-11.2</sub> )	7.0 <sup>+8.0</sup> <sub>-5.3</sub> (8.8 <sup>+9.9</sup> <sub>-6.1</sub> )	10.7 <sup>+11.3</sup> <sub>-9.5</sub> (19.2 <sup>+22.0</sup> <sub>-16.1</sub> )	8.9 <sup>+9.6</sup> <sub>-7.3</sub> (13.7 <sup>+16.0</sup> <sub>-11.8</sub> )
nircam3-3539	0.19 <sup>+0.19</sup> <sub>-0.19</sub> (0.14 <sup>+0.14</sup> <sub>-0.14</sub> )	0.23 <sup>+0.24</sup> <sub>-0.23</sub> (0.19 <sup>+0.18</sup> <sub>-0.18</sub> )	0.13 <sup>+0.13</sup> <sub>-0.13</sub> (0.08 <sup>+0.08</sup> <sub>-0.08</sub> )	0.14 <sup>+0.14</sup> <sub>-0.14</sub> (0.08 <sup>+0.08</sup> <sub>-0.08</sub> )	19.1 <sup>+19.2</sup> <sub>-19.1</sub> (23.6 <sup>+23.9</sup> <sub>-23.1</sub> )	16.5 <sup>+16.5</sup> <sub>-16.4</sub> (19.3 <sup>+19.5</sup> <sub>-18.9</sub> )	25.2 <sup>+25.3</sup> <sub>-25.2</sub> (35.8 <sup>+36.1</sup> <sub>-35.6</sub> )	23.8 <sup>+23.9</sup> <sub>-23.7</sub> (33.8 <sup>+33.9</sup> <sub>-33.6</sub> )
nircam3-3544	0.42 <sup>+0.46</sup> <sub>-0.39</sub> (0.32 <sup>+0.33</sup> <sub>-0.31</sub> )	0.56 <sup>+0.64</sup> <sub>-0.37</sub> (0.38 <sup>+0.39</sup> <sub>-0.37</sub> )	0.30 <sup>+0.32</sup> <sub>-0.28</sub> (0.25 <sup>+0.25</sup> <sub>-0.25</sub> )	0.34 <sup>+0.37</sup> <sub>-0.32</sub> (0.27 <sup>+0.27</sup> <sub>-0.26</sub> )	10.9 <sup>+10.2</sup> <sub>-10.2</sub> (13.2 <sup>+13.4</sup> <sub>-13.0</sub> )	8.8 <sup>+8.9</sup> <sub>-7.9</sub> (11.7 <sup>+11.9</sup> <sub>-11.4</sub> )	13.9 <sup>+14.5</sup> <sub>-13.3</sub> (15.8 <sup>+15.9</sup> <sub>-15.7</sub> )	12.6 <sup>+13.1</sup> <sub>-11.9</sub> (15.0 <sup>+15.1</sup> <sub>-14.8</sub> )
nircam3-3622	2.38 <sup>+2.62</sup> <sub>-1.94</sub> (2.09 <sup>+2.31</sup> <sub>-1.82</sub> )	3.07 <sup>+3.11</sup> <sub>-3.03</sub> (2.79 <sup>+2.94</sup> <sub>-2.59</sub> )	1.92 <sup>+2.30</sup> <sub>-1.47</sub> (1.85 <sup>+2.11</sup> <sub>-1.56</sub> )	2.97 <sup>+3.03</sup> <sub>-2.89</sub> (2.54 <sup>+2.74</sup> <sub>-2.31</sub> )	2.7 <sup>+3.3</sup> <sub>-2.5</sub> (3.1 <sup>+3.4</sup> <sub>-2.8</sub> )	2.1 <sup>+2.2</sup> <sub>-2.1</sub> (2.3 <sup>+2.5</sup> <sub>-2.2</sub> )	3.3 <sup>+3.4</sup> <sub>-3.0</sub> (3.4 <sup>+3.9</sup> <sub>-3.0</sub> )	2.2 <sup>+2.3</sup> <sub>-2.2</sub> (2.6 <sup>+2.8</sup> <sub>-2.4</sub> )
nircam3-3679	0.32 <sup>+0.35</sup> <sub>-0.30</sub> (0.38 <sup>+0.42</sup> <sub>-0.34</sub> )	0.52 <sup>+0.56</sup> <sub>-0.48</sub> (0.72 <sup>+0.82</sup> <sub>-0.64</sub> )	0.07 <sup>+0.08</sup> <sub>-0.07</sub> (0.09 <sup>+0.10</sup> <sub>-0.08</sub> )	0.10 <sup>+0.10</sup> <sub>-0.09</sub> (0.15 <sup>+0.16</sup> <sub>-0.13</sub> )	13.3 <sup>+14.0</sup> <sub>-12.5</sub> (11.7 <sup>+12.7</sup> <sub>-10.9</sub> )	9.3 <sup>+8.8</sup> <sub>-7.5</sub> (7.3 <sup>+8.0</sup> <sub>-6.6</sub> )	36.5 <sup>+37.4</sup> <sub>-35.6</sub> (32.0 <sup>+34.2</sup> <sub>-30.2</sub> )	30.5 <sup>+31.6</sup> <sub>-29.3</sub> (23.0 <sup>+25.0</sup> <sub>-21.7</sub> )
nircam3-3864	0.44 <sup>+0.48</sup> <sub>-0.41</sub> (0.31 <sup>+0.28</sup> <sub>-0.28</sub> )	0.59 <sup>+0.66</sup> <sub>-0.55</sub> (0.42 <sup>+0.45</sup> <sub>-0.38</sub> )	0.31 <sup>+0.30</sup> <sub>-0.30</sub> (0.18 <sup>+0.20</sup> <sub>-0.17</sub> )	0.36 <sup>+0.38</sup> <sub>-0.35</sub> (0.24 <sup>+0.26</sup> <sub>-0.21</sub> )	10.5 <sup>+11.0</sup> <sub>-9.8</sub> (13.5 <sup>+14.5</sup> <sub>-12.6</sub> )	8.4 <sup>+8.9</sup> <sub>-7.8</sub> (10.9 <sup>+11.7</sup> <sub>-10.3</sub> )	13.6 <sup>+13.9</sup> <sub>-13.1</sub> (19.5 <sup>+20.4</sup> <sub>-18.2</sub> )	12.1 <sup>+12.5</sup> <sub>-11.6</sub> (16.4 <sup>+17.7</sup> <sub>-15.3</sub> )
nircam3-4244	2.22 <sup>+2.61</sup> <sub>-1.44</sub> (1.67 <sup>+1.79</sup> <sub>-1.51</sub> )	3.09 <sup>+3.16</sup> <sub>-2.91</sub> (2.14 <sup>+2.21</sup> <sub>-2.06</sub> )	0.57 <sup>+0.65</sup> <sub>-0.48</sub> (0.72 <sup>+0.85</sup> <sub>-0.61</sub> )	1.00 <sup>+1.41</sup> <sub>-0.68</sub> (1.16 <sup>+1.37</sup> <sub>-0.99</sub> )	2.9 <sup>+2.5</sup> <sub>-2.5</sub> (3.7 <sup>+4.0</sup> <sub>-3.5</sub> )	2.1 <sup>+2.2</sup> <sub>-2.1</sub> (3.0 <sup>+3.1</sup> <sub>-2.9</sub> )	8.7 <sup>+9.9</sup> <sub>-7.9</sub> (7.3 <sup>+8.2</sup> <sub>-6.4</sub> )	5.6 <sup>+7.6</sup> <sub>-4.3</sub> (5.0 <sup>+5.7</sup> <sub>-4.4</sub> )
nircam3-4581	0.29 <sup>+0.32</sup> <sub>-0.26</sub> (0.24 <sup>+0.27</sup> <sub>-0.23</sub> )	0.39 <sup>+0.44</sup> <sub>-0.35</sub> (0.33 <sup>+0.36</sup> <sub>-0.30</sub> )	0.31 <sup>+0.36</sup> <sub>-0.28</sub> (0.29 <sup>+0.32</sup> <sub>-0.27</sub> )	0.43 <sup>+0.49</sup> <sub>-0.38</sub> (0.41 <sup>+0.45</sup> <sub>-0.37</sub> )	14.3 <sup>+15.3</sup> <sub>-13.1</sub> (16.0 <sup>+16.9</sup> <sub>-15.1</sub> )	11.4 <sup>+12.3</sup> <sub>-10.4</sub> (12.9 <sup>+13.7</sup> <sub>-12.0</sub> )	13.5 <sup>+14.6</sup> <sub>-12.3</sub> (14.1 <sup>+15.0</sup> <sub>-13.1</sub> )	10.6 <sup>+11.6</sup> <sub>-9.7</sub> (11.0 <sup>+11.8</sup> <sub>-10.2</sub> )
nircam3-4769	0.96 <sup>+0.86</sup> <sub>-0.64</sub> (0.42 <sup>+0.49</sup> <sub>-0.36</sub> )	1.24 <sup>+1.14</sup> <sub>-1.33</sub> (0.62 <sup>+0.71</sup> <sub>-0.53</sub> )	0.99 <sup>+0.90</sup> <sub>-0.90</sub> (0.50 <sup>+0.57</sup> <sub>-0.43</sub> )	1.27 <sup>+1.36</sup> <sub>-1.18</sub> (0.79 <sup>+0.67</sup> <sub>-0.60</sub> )	5.8 <sup>+5.4</sup> <sub>-5.6</sub> (10.8 <sup>+12.1</sup> <sub>-9.8</sub> )	4.8 <sup>+4.5</sup> <sub>-4.4</sub> (8.2 <sup>+9.7</sup> <sub>-7.4</sub> )	5.7 <sup>+5.3</sup> <sub>-4.4</sub> (9.6 <sup>+10.7</sup> <sub>-8.6</sub> )	4.7 <sup>+5.0</sup> <sub>-4.4</sub> (6.8 <sup>+7.7</sup> <sub>-6.1</sub> )
nircam3-5478	0.54 <sup>+0.54</sup> <sub>-0.54</sub> (0.37 <sup>+0.38</sup> <sub>-0.35</sub> )	0.60 <sup>+0.60</sup> <sub>-0.59</sub> (0.54 <sup>+0.57</sup> <sub>-0.51</sub> )	0.56 <sup>+0.56</sup> <sub>-0.56</sub> (0.28 <sup>+0.29</sup> <sub>-0.27</sub> )	0.63 <sup>+0.64</sup> <sub>-0.62</sub> (0.37 <sup>+0.38</sup> <sub>-0.35</sub> )	9.0 <sup>+9.1</sup> <sub>-9.0</sub> (12.0 <sup>+12.3</sup> <sub>-11.7</sub> )	8.4 <sup>+8.5</sup> <sub>-8.3</sub> (9.0 <sup>+9.7</sup> <sub>-8.7</sub> )	8.8 <sup>+8.8</sup> <sub>-8.8</sub> (14.5 <sup>+14.9</sup> <sub>-14.3</sub> )	8.0 <sup>+8.1</sup> <sub>-8.0</sub> (11.9 <sup>+12.3</sup> <sub>-11.6</sub> )
nircam3-5633	0.45 <sup>+0.49</sup> <sub>-0.42</sub> (0.17 <sup>+0.18</sup> <sub>-0.16</sub> )	0.60 <sup>+0.69</sup> <sub>-0.54</sub> (0.25 <sup>+0.26</sup> <sub>-0.23</sub> )	0.31 <sup>+0.32</sup> <sub>-0.30</sub> (0.10 <sup>+0.10</sup> <sub>-0.10</sub> )	0.35 <sup>+0.37</sup> <sub>-0.33</sub> (0.19 <sup>+0.12</sup> <sub>-0.11</sub> )	10.3 <sup>+10.9</sup> <sub>-9.7</sub> (20.5 <sup>+21.3</sup> <sub>-19.6</sub> )	8.4 <sup>+9.1</sup> <sub>-7.5</sub> (15.8 <sup>+16.5</sup> <sub>-15.1</sub> )	13.5 <sup>+13.8</sup> <sub>-13.1</sub> (30.1 <sup>+30.6</sup> <sub>-29.5</sub> )	12.4 <sup>+12.8</sup> <sub>-11.9</sub> (26.3 <sup>+27.0</sup> <sub>-25.5</sub> )
nircam3-5757	0.60 <sup>+0.65</sup> <sub>-0.55</sub> (0.69 <sup>+0.83</sup> <sub>-0.58</sub> )	0.81 <sup>+0.86</sup> <sub>-0.74</sub> (1.26 <sup>+1.55</sup> <sub>-1.04</sub> )	0.49 <sup>+0.53</sup> <sub>-0.45</sub> (0.75 <sup>+0.66</sup> <sub>-0.66</sub> )	0.63 <sup>+0.68</sup> <sub>-0.57</sub> (1.40 <sup>+1.24</sup> <sub>-1.24</sub> )	8.3 <sup>+8.9</sup> <sub>-7.1</sub> (7.5 <sup>+8.6</sup> <sub>-6.6</sub> )	6.7 <sup>+7.1</sup> <sub>-6.3</sub> (4.7 <sup>+5.5</sup> <sub>-4.0</sub> )	9.7 <sup>+10.4</sup> <sub>-9.2</sub> (7.1 <sup>+8.4</sup> <sub>-6.4</sub> )	8.1 <sup>+8.6</sup> <sub>-7.6</sub> (4.3 <sup>+4.8</sup> <sub>-3.8</sub> )
nircam3-5848	0.23 <sup>+0.26</sup> <sub>-0.22</sub> (0.36 <sup>+0.42</sup> <sub>-0.32</sub> )	0.33 <sup>+0.37</sup> <sub>-0.31</sub> (0.55 <sup>+0.63</sup> <sub>-0.48</sub> )	0.20 <sup>+0.22</sup> <sub>-0.19</sub> (0.34 <sup>+0.30</sup> <sub>-0.30</sub> )	0.28 <sup>+0.31</sup> <sub>-0.26</sub> (0.50 <sup>+0.45</sup> <sub>-0.45</sub> )	16.5 <sup>+17.3</sup> <sub>-15.4</sub> (12.2 <sup>+13.3</sup> <sub>-10.9</sub> )	12.8 <sup>+13.5</sup> <sub>-11.9</sub> (8.9 <sup>+8.0</sup> <sub>-8.0</sub> )	18.2 <sup>+19.1</sup> <sub>-17.3</sub> (12.8 <sup>+11.5</sup> <sub>-11.5</sub> )	14.4 <sup>+15.4</sup> <sub>-13.6</sub> (9.6 <sup>+10.4</sup> <sub>-8.6</sub> )
nircam3-6288	0.25 <sup>+0.30</sup> <sub>-0.21</sub> (0.31 <sup>+0.39</sup> <sub>-0.23</sub> )	0.40 <sup>+0.51</sup> <sub>-0.33</sub> (0.51 <sup>+0.64</sup> <sub>-0.37</sub> )	0.16 <sup>+0.19</sup> <sub>-0.14</sub> (0.21 <sup>+0.27</sup> <sub>-0.16</sub> )	0.24 <sup>+0.29</sup> <sub>-0.20</sub> (0.39 <sup>+0.41</sup> <sub>-0.24</sub> )	15.8 <sup>+17.6</sup> <sub>-13.8</sub> (13.4 <sup>+16.6</sup> <sub>-11.4</sub> )	11.2 <sup>+12.8</sup> <sub>-9.4</sub> (9.4 <sup>+12.0</sup> <sub>-8.0</sub> )	21.6 <sup>+23.6</sup> <sub>-19.3</sub> (17.6 <sup>+21.6</sup> <sub>-14.9</sub> )	16.2 <sup>+18.1</sup> <sub>-14.3</sub> (13.1 <sup>+16.1</sup> <sub>-11.0</sub> )
nircam3-6437	0.26 <sup>+0.30</sup> <sub>-0.22</sub> (0.34 <sup>+0.38</sup> <sub>-0.30</sub> )	0.37 <sup>+0.42</sup> <sub>-0.33</sub> (0.45 <sup>+0.53</sup> <sub>-0.40</sub> )	0.14 <sup>+0.17</sup> <sub>-0.11</sub> (0.28 <sup>+0.32</sup> <sub>-0.25</sub> )	0.21 <sup>+0.26</sup> <sub>-0.17</sub> (0.37 <sup>+0.42</sup> <sub>-0.33</sub> )	15.4 <sup>+17.4</sup> <sub>-13.8</sub> (12.7 <sup>+13.9</sup> <sub>-11.7</sub> )	11.9 <sup>+13.0</sup> <sub>-10.9</sub> (10.3 <sup>+11.2</sup> <sub>-9.2</sub> )	23.5 <sup>+27.1</sup> <sub>-20.4</sub> (14.4 <sup>+15.6</sup> <sub>-13.1</sub> )	18.0 <sup>+20.5</sup> <sub>-15.4</sub> (11.9 <sup>+12.9</sup> <sub>-10.8</sub> )
nircam3-6471	1.41 <sup>+1.49</sup> <sub>-1.32</sub> (1.81 <sup>+1.92</sup> <sub>-1.68</sub> )	1.77 <sup>+1.83</sup> <sub>-1.70</sub> (2.21 <sup>+2.28</sup> <sub>-2.13</sub> )	1.03 <sup>+1.11</sup> <sub>-0.93</sub> (1.23 <sup>+1.41</sup> <sub>-1.07</sub> )	1.31 <sup>+1.41</sup> <sub>-1.20</sub> (1.66 <sup>+1.77</sup> <sub>-1.49</sub> )	4.3 <sup>+4.5</sup> <sub>-4.1</sub> (3.3 <sup>+3.3</sup> <sub>-3.3</sub> )	3.5 <sup>+3.7</sup> <sub>-3.4</sub> (2.9 <sup>+3.0</sup> <sub>-2.8</sub> )	5.5 <sup>+6.0</sup> <sub>-5.2</sub> (4.8 <sup>+5.4</sup> <sub>-4.3</sub> )	4.6 <sup>+4.9</sup> <sub>-4.3</sub> (3.7 <sup>+4.1</sup> <sub>-3.5</sub> )
nircam3-6517	1.07 <sup>+1.15</sup> <sub>-1.00</sub> (1.09 <sup>+1.16</sup> <sub>-1.01</sub> )	1.37 <sup>+1.43</sup> <sub>-1.29</sub> (1.46 <sup>+1.47</sup> <sub>-1.39</sub> )	0.83 <sup>+0.89</sup> <sub>-0.79</sub> (0.79 <sup>+0.86</sup> <sub>-0.71</sub> )	1.06 <sup>+1.13</sup> <sub>-1.01</sub> (1.10 <sup>+1.16</sup> <sub>-1.00</sub> )	5.4 <sup>+5.6</sup> <sub>-5.0</sub> (5.3 <sup>+5.6</sup> <sub>-5.0</sub> )	4.4 <sup>+4.6</sup> <sub>-4.2</sub> (4.2 <sup>+4.5</sup> <sub>-4.1</sub> )	6.5 <sup>+6.8</sup> <sub>-6.2</sub> (6.8 <sup>+7.4</sup> <sub>-6.3</sub> )	5.4 <sup>+5.6</sup> <sub>-5.1</sub> (5.3 <sup>+5.6</sup> <sub>-5.0</sub> )
nircam3-6621	0.83 <sup>+0.96</sup> <sub>-0.74</sub> (0.44 <sup>+0.58</sup> <sub>-0.24</sub> )	1.08 <sup>+1.22</sup> <sub>-0.92</sub> (0.71 <sup>+0.98</sup> <sub>-0.42</sub> )	0.69 <sup>+0.77</sup> <sub>-0.65</sub> (0.30 <sup>+0.40</sup> <sub>-0.15</sub> )	0.81 <sup>+0.94</sup> <sub>-0.73</sub> (0.48 <sup>+0.62</sup> <sub>-0.25</sub> )	6.6 <sup>+7.1</sup> <sub>-5.8</sub> (10.5 <sup>+16.1</sup> <sub>-8.5</sub> )	5.3 <sup>+6.0</sup> <sub>-4.2</sub> (7.3 <sup>+10.8</sup> <sub>-5.8</sub> )	7.6 <sup>+7.9</sup> <sub>-6.7</sub> (13.8 <sup>+22.0</sup> <sub>-11.3</sub> )	6.7 <sup>+7.2</sup> <sub>-6.7</sub> (9.1 <sup>+15.9</sup> <sub>-9.1</sub> )
nircam3-6644	0.30 <sup>+0.31</sup> <sub>-0.30</sub> (0.19 <sup>+0.20</sup> <sub>-0.18</sub> )	0.38 <sup>+0.39</sup> <sub>-0.37</sub> (0.27 <sup>+0.28</sup> <sub>-0.26</sub> )	0.24 <sup>+0.24</sup> <sub>-0.23</sub> (0.14 <sup>+0.14</sup> <sub>-0.13</sub> )	0.28 <sup>+0.28</sup> <sub>-0.28</sub> (0.20 <sup>+0.19</sup> <sub>-0.19</sub> )	13.8 <sup>+14.0</sup> <sub>-13.6</sub> (18.9 <sup>+19.6</sup> <sub>-18.4</sub> )	11.8 <sup>+12.0</sup> <sub>-11.5</sub> (15.0 <sup>+15.5</sup> <sub>-14.5</sub> )	16.4 <sup>+16.6</sup> <sub>-16.2</sub> (23.9 <sup>+24.7</sup> <sub>-23.0</sub> )	14.5 <sup>+14.7</sup> <sub>-15.4</sub> (18.7 <sup>+19.2</sup> <sub>-18.1</sub> )
nircam3-6739	0.69 <sup>+0.77</sup> <sub>-0.56</sub> (1.22 <sup>+1.36</sup> <sub>-0.99</sub> )	0.98 <sup>+1.17</sup> <sub>-0.87</sub> (1.66 <sup>+1.76</sup> <sub>-1.52</sub> )	0.56 <sup>+0.67</sup> <sub>-0.45</sub> (1.05 <sup>+1.20</sup> <sub>-0.84</sub> )	0.82 <sup>+0.93</sup> <sub>-0.70</sub> (1.51 <sup>+1.62</sup> <sub>-1.32</sub> )	7.6 <sup>+8.8</sup> <sub>-6.9</sub> (4.8 <sup>+5.7</sup> <sub>-4.4</sub> )	5.8 <sup>+6.3</sup> <sub>-5.2</sub> (3.7 <sup>+4.0</sup> <sub>-3.6</sub> )	8.8 <sup>+10.4</sup> <sub>-7.7</sub> (5.4 <sup>+6.5</sup> <sub>-4.5</sub> )	6.6 <sup>+7.5</sup> <sub>-6.0</sub> (4.1 <sup>+4.5</sup> <sub>-3.5</sub> )
nircam3-7007	0.30 <sup>+0.31</sup> <sub>-0.30</sub> (0.27 <sup>+0.29</sup> <sub>-0.26</sub> )	0.37 <sup>+0.38</sup> <sub>-0.36</sub> (0.41 <sup>+0.44</sup> <sub>-0.38</sub> )	0.22 <sup>+0.22</sup> <sub>-0.22</sub> (0.09 <sup>+0.10</sup> <sub>-0.09</sub> )	0.23 <sup>+0.24</sup> <sub>-0.23</sub> (0.13 <sup>+0.13</sup> <sub>-0.12</sub> )	13.7 <sup>+13.8</sup> <sub>-13.5</sub> (14.8 <sup>+15.5</sup> <sub>-14.2</sub> )	11.9 <sup>+12.0</sup> <sub>-11.7</sub> (11.1 <sup>+11.6</sup> <sub>-10.5</sub> )	17.3 <sup>+17.3</sup> <sub>-17.2</sub> (31.0 <sup>+31.9</sup> <sub>-30.2</sub> )	16.6 <sup>+16.7</sup> <sub>-16.4</sub> (25.2 <sup>+26.2</sup> <sub>-24.3</sub> )
nircam3-7412	1.38 <sup>+1.48</sup> <sub>-1.24</sub> (0.58 <sup>+0.71</sup> <sub>-0.49</sub> )	1.69 <sup>+1.79</sup> <sub>-1.50</sub> (0.85 <sup>+1.01</sup> <sub>-0.71</sub> )	1.31 <sup>+1.39</sup> <sub>-1.10</sub> (0.51 <sup>+0.63</sup> <sub>-0.43</sub> )	1.56 <sup>+1.61</sup> <sub>-1.49</sub> (0.70 <sup>+0.86</sup> <sub>-0.60</sub> )	4.4 <sup>+4.8</sup> <sub>-4.4</sub> (8.5 <sup>+9.7</sup> <sub>-7.4</sub> )	3.7 <sup>+3.5</sup> <sub>-3.5</sub> (6.4 <sup>+5.6</sup> <sub>-5.6</sub> )	4.5 <sup>+5.2</sup> <sub>-4.3</sub> (9.4 <sup>+10.7</sup> <sub>-8.1</sub> )	4.0 <sup>+4.3</sup> <sub>-3.7</sub> (7.5 <sup>+8.4</sup> <sub>-6.4</sub> )
nircam3-7579	0.76 <sup>+0.88</sup> <sub>-0.65</sub> (0.81 <sup>+0.92</sup> <sub>-0.71</sub> )	1.05 <sup>+1.16</sup> <sub>-0.94</sub> (1.15 <sup>+1.29</sup> <sub>-1.01</sub> )	0.54 <sup>+0.61</sup> <sub>-0.41</sub> (0.61 <sup>+0.68</sup> <sub>-0.52</sub> )	0.70 <sup>+0.81</sup> <sub>-0.59</sub> (0.79 <sup>+0.89</sup> <sub>-0.70</sub> )	7.0 <sup>+7.9</sup> <sub>-6.2</sub> (6.6 <sup>+7.4</sup> <sub>-6.0</sub> )	5.5 <sup>+5.9</sup> <sub>-5.0</sub> (5.1 <sup>+5.6</sup> <sub>-4.6</sub> )	9.1 <sup>+11.0</sup> <sub>-8.2</sub> (8.3 <sup>+9.3</sup> <sub>-7.6</sub> )	7.4 <sup>+8.5</sup> <sub>-6.6</sub> (6.8 <sup>+7.4</sup> <sub>-6.2</sub> )
nircam3-7695	0.53 <sup>+0.59</sup> <sub>-0.49</sub> (0.84 <sup>+0.96</sup> <sub>-0.72</sub> )	0.74 <sup>+0.84</sup> <sub>-0.67</sub> (1.06 <sup>+1.09</sup> <sub>-0.81</sub> )	0.42 <sup>+0.46</sup> <sub>-0.40</sub> (0.66 <sup>+0.60</sup> <sub>-0.55</sub> )	0.55 <sup>+0.60</sup> <sub>-0.51</sub> (0.97 <sup>+1.03</sup> <sub>-0.87</sub> )	9.1 <sup>+9.7</sup> <sub>-8.5</sub> (6.5 <sup>+7.3</sup> <sub>-5.8</sub> )	7.2 <sup>+7.7</sup> <sub>-6.5</sub> (5.4 <sup>+5.3</sup> <sub>-4.6</sub> )	10.8 <sup>+11.3</sup> <sub>-10.1</sub> (7.9 <sup>+9.0</sup> <sub>-6.7</sub> )	8.9 <sup>+8.4</sup> <sub>-8.4</sub> (5.8 <sup>+6.3</sup> <sub>-5.5</sub> )
nircam3-7701	0.71 <sup>+0.78</sup> <sub>-0.63</sub> (0.37 <sup>+0.41</sup> <sub>-0.33</sub> )	0.88 <sup>+0.94</sup> <sub>-0.83</sub> (0.54 <sup>+0.61</sup> <sub>-0.46</sub> )	0.50 <sup>+0.56</sup> <sub>-0.41</sub> (0.24 <sup>+0.27</sup> <sub>-0.22</sub> )	0.62 <sup>+0.69</sup> <sub>-0.53</sub> (0.33 <sup>+0.30</sup> <sub>-0.30</sub> )	7.4 <sup>+8.1</sup> <sub>-6.9</sub> (11.9 <sup>+12.9</sup> <sub>-11.0</sub> )	6.2 <sup>+6.6</sup> <sub>-5.9</sub> (9		

Table E.1: (Continued)

Galaxy name	$t_5^{\text{SB99(BC03)}}$ [Gyr]	$t_{10}^{\text{SB99(BC03)}}$ [Gyr]	$t_{5 \times 10^8 \text{ M}_\odot}^{\text{SB99(BC03)}}$ [Gyr]	$t_{10^9 \text{ M}_\odot}^{\text{SB99(BC03)}}$ [Gyr]	$z_5^{\text{SB99(BC03)}}$	$z_{10}^{\text{SB99(BC03)}}$	$z_{5 \times 10^8 \text{ M}_\odot}^{\text{SB99(BC03)}}$	$z_{10^9 \text{ M}_\odot}^{\text{SB99(BC03)}}$
nircam3-8098	1.54 <sup>+1.66</sup> <sub>-1.37</sub> (1.59 <sup>+1.42</sup> <sub>-1.42</sub> )	1.85 <sup>+2.01</sup> <sub>-1.70</sub> (2.12 <sup>+2.25</sup> <sub>-1.98</sub> )	1.32 <sup>+1.49</sup> <sub>-1.17</sub> (1.31 <sup>+1.49</sup> <sub>-1.10</sub> )	1.64 <sup>+1.76</sup> <sub>-1.45</sub> (1.83 <sup>+1.97</sup> <sub>-1.63</sub> )	4.0 <sup>+4.4</sup> <sub>-3.7</sub> (3.9 <sup>+4.3</sup> <sub>-3.6</sub> )	3.4 <sup>+3.7</sup> <sub>-2.9</sub> (3.0 <sup>+3.2</sup> <sub>-2.9</sub> )	4.5 <sup>+5.0</sup> <sub>-4.1</sub> (4.6 <sup>+5.3</sup> <sub>-4.1</sub> )	3.8 <sup>+4.2</sup> <sub>-3.6</sub> (3.4 <sup>+3.8</sup> <sub>-3.2</sub> )
nircam3-8401	0.58 <sup>+0.65</sup> <sub>-0.50</sub> (0.37 <sup>+0.34</sup> <sub>-0.34</sub> )	0.86 <sup>+0.94</sup> <sub>-0.79</sub> (0.65 <sup>+0.73</sup> <sub>-0.57</sub> )	0.19 <sup>+0.23</sup> <sub>-0.17</sub> (0.14 <sup>+0.16</sup> <sub>-0.13</sub> )	0.29 <sup>+0.35</sup> <sub>-0.25</sub> (0.19 <sup>+0.22</sup> <sub>-0.18</sub> )	8.6 <sup>+9.6</sup> <sub>-8.7</sub> (11.8 <sup>+12.7</sup> <sub>-10.9</sub> )	6.4 <sup>+6.8</sup> <sub>-5.9</sub> (7.9 <sup>+7.2</sup> <sub>-6.9</sub> )	18.2 <sup>+20.3</sup> <sub>-16.5</sub> (23.2 <sup>+24.8</sup> <sub>-21.9</sub> )	14.3 <sup>+15.7</sup> <sub>-12.4</sub> (18.9 <sup>+20.1</sup> <sub>-17.4</sub> )
nircam3-8558	1.10 <sup>+1.16</sup> <sub>-1.04</sub> (0.56 <sup>+0.62</sup> <sub>-0.49</sub> )	1.32 <sup>+1.27</sup> <sub>-0.78</sub> (0.87 <sup>+0.98</sup> <sub>-0.74</sub> )	0.98 <sup>+1.04</sup> <sub>-0.91</sub> (0.50 <sup>+0.55</sup> <sub>-0.42</sub> )	1.17 <sup>+1.22</sup> <sub>-1.11</sub> (0.75 <sup>+0.83</sup> <sub>-0.65</sub> )	5.2 <sup>+5.5</sup> <sub>-5.0</sub> (8.8 <sup>+7.2</sup> <sub>-6.3</sub> )	4.5 <sup>+4.7</sup> <sub>-4.4</sub> (6.3 <sup>+7.1</sup> <sub>-5.7</sub> )	5.8 <sup>+6.1</sup> <sub>-5.5</sub> (9.5 <sup>+10.6</sup> <sub>-8.9</sub> )	5.0 <sup>+5.2</sup> <sub>-4.8</sub> (7.1 <sup>+7.9</sup> <sub>-6.5</sub> )
nircam3-8596	0.99 <sup>+1.06</sup> <sub>-0.91</sub> (0.48 <sup>+0.53</sup> <sub>-0.43</sub> )	1.15 <sup>+1.19</sup> <sub>-1.10</sub> (0.70 <sup>+0.77</sup> <sub>-0.64</sub> )	0.83 <sup>+0.92</sup> <sub>-0.72</sub> (0.37 <sup>+0.42</sup> <sub>-0.34</sub> )	0.96 <sup>+1.04</sup> <sub>-0.88</sub> (0.51 <sup>+0.57</sup> <sub>-0.46</sub> )	5.7 <sup>+6.1</sup> <sub>-5.4</sub> (9.8 <sup>+10.6</sup> <sub>-9.1</sub> )	5.1 <sup>+5.3</sup> <sub>-4.9</sub> (7.5 <sup>+8.0</sup> <sub>-6.9</sub> )	6.6 <sup>+7.3</sup> <sub>-6.1</sub> (11.9 <sup>+12.8</sup> <sub>-10.9</sub> )	5.8 <sup>+6.3</sup> <sub>-5.5</sub> (9.4 <sup>+10.1</sup> <sub>-8.7</sub> )
nircam3-8852	0.15 <sup>+0.16</sup> <sub>-0.14</sub> (0.25 <sup>+0.23</sup> <sub>-0.23</sub> )	0.21 <sup>+0.22</sup> <sub>-0.21</sub> (0.39 <sup>+0.44</sup> <sub>-0.36</sub> )	0.08 <sup>+0.09</sup> <sub>-0.08</sub> (0.13 <sup>+0.14</sup> <sub>-0.11</sub> )	0.11 <sup>+0.11</sup> <sub>-0.11</sub> (0.19 <sup>+0.21</sup> <sub>-0.18</sub> )	22.5 <sup>+23.2</sup> <sub>-21.8</sub> (15.8 <sup>+16.9</sup> <sub>-14.6</sub> )	17.6 <sup>+18.1</sup> <sub>-17.1</sub> (11.4 <sup>+12.2</sup> <sub>-10.4</sub> )	33.6 <sup>+34.2</sup> <sub>-32.9</sub> (25.4 <sup>+27.2</sup> <sub>-23.4</sub> )	27.9 <sup>+28.7</sup> <sub>-27.1</sub> (19.0 <sup>+20.1</sup> <sub>-17.8</sub> )
nircam3-8980	0.57 <sup>+0.69</sup> <sub>-0.45</sub> (0.15 <sup>+0.16</sup> <sub>-0.13</sub> )	0.81 <sup>+0.93</sup> <sub>-0.71</sub> (0.23 <sup>+0.25</sup> <sub>-0.22</sub> )	0.33 <sup>+0.46</sup> <sub>-0.25</sub> (0.08 <sup>+0.09</sup> <sub>-0.07</sub> )	0.53 <sup>+0.65</sup> <sub>-0.41</sub> (0.12 <sup>+0.13</sup> <sub>-0.12</sub> )	8.7 <sup>+10.2</sup> <sub>-10.2</sub> (23.0 <sup>+24.2</sup> <sub>-21.8</sub> )	6.6 <sup>+7.3</sup> <sub>-6.0</sub> (16.5 <sup>+17.5</sup> <sub>-15.7</sub> )	13.1 <sup>+15.8</sup> <sub>-10.1</sub> (34.8 <sup>+36.8</sup> <sub>-32.8</sub> )	9.1 <sup>+11.0</sup> <sub>-7.8</sub> (25.7 <sup>+26.8</sup> <sub>-24.6</sub> )
nircam3-9142	0.41 <sup>+0.44</sup> <sub>-0.39</sub> (0.42 <sup>+0.47</sup> <sub>-0.38</sub> )	0.51 <sup>+0.55</sup> <sub>-0.48</sub> (0.60 <sup>+0.67</sup> <sub>-0.54</sub> )	0.38 <sup>+0.40</sup> <sub>-0.36</sub> (0.43 <sup>+0.49</sup> <sub>-0.39</sub> )	0.46 <sup>+0.50</sup> <sub>-0.43</sub> (0.62 <sup>+0.69</sup> <sub>-0.55</sub> )	11.0 <sup>+11.4</sup> <sub>-10.5</sub> (10.8 <sup>+11.7</sup> <sub>-10.0</sub> )	9.4 <sup>+9.8</sup> <sub>-8.9</sub> (8.3 <sup>+9.0</sup> <sub>-7.7</sub> )	11.7 <sup>+12.2</sup> <sub>-11.2</sub> (10.6 <sup>+11.5</sup> <sub>-9.8</sub> )	10.2 <sup>+10.6</sup> <sub>-9.6</sub> (8.1 <sup>+8.9</sup> <sub>-7.5</sub> )
nircam3-9199	1.04 <sup>+1.11</sup> <sub>-0.98</sub> (0.81 <sup>+0.76</sup> <sub>-0.66</sub> )	1.35 <sup>+1.28</sup> <sub>-1.15</sub> (1.22 <sup>+1.29</sup> <sub>-1.15</sub> )	0.69 <sup>+0.74</sup> <sub>-0.65</sub> (0.45 <sup>+0.48</sup> <sub>-0.42</sub> )	0.88 <sup>+0.93</sup> <sub>-0.82</sub> (0.59 <sup>+0.63</sup> <sub>-0.55</sub> )	5.5 <sup>+5.7</sup> <sub>-5.2</sub> (6.7 <sup>+7.0</sup> <sub>-6.3</sub> )	4.5 <sup>+4.6</sup> <sub>-4.3</sub> (4.8 <sup>+5.1</sup> <sub>-4.6</sub> )	7.5 <sup>+7.8</sup> <sub>-7.1</sub> (10.3 <sup>+10.8</sup> <sub>-9.8</sub> )	6.3 <sup>+6.6</sup> <sub>-6.0</sub> (8.4 <sup>+8.9</sup> <sub>-8.1</sub> )
nircam3-9667	1.04 <sup>+1.11</sup> <sub>-0.94</sub> (0.57 <sup>+0.60</sup> <sub>-0.50</sub> )	1.20 <sup>+1.25</sup> <sub>-1.13</sub> (0.76 <sup>+0.85</sup> <sub>-0.69</sub> )	0.88 <sup>+0.97</sup> <sub>-0.74</sub> (0.52 <sup>+0.59</sup> <sub>-0.45</sub> )	1.02 <sup>+1.09</sup> <sub>-0.91</sub> (0.69 <sup>+0.76</sup> <sub>-0.61</sub> )	5.5 <sup>+5.9</sup> <sub>-5.2</sub> (8.7 <sup>+9.5</sup> <sub>-7.9</sub> )	4.9 <sup>+5.1</sup> <sub>-4.7</sub> (7.0 <sup>+7.5</sup> <sub>-6.4</sub> )	6.3 <sup>+7.1</sup> <sub>-5.8</sub> (9.3 <sup>+10.3</sup> <sub>-8.5</sub> )	5.6 <sup>+5.3</sup> <sub>-5.3</sub> (7.5 <sup>+7.0</sup> <sub>-6.7</sub> )
nircam3-9784	0.68 <sup>+0.79</sup> <sub>-0.58</sub> (0.21 <sup>+0.23</sup> <sub>-0.20</sub> )	0.96 <sup>+1.04</sup> <sub>-0.87</sub> (0.36 <sup>+0.39</sup> <sub>-0.33</sub> )	0.63 <sup>+0.72</sup> <sub>-0.51</sub> (0.19 <sup>+0.21</sup> <sub>-0.18</sub> )	0.87 <sup>+0.97</sup> <sub>-0.75</sub> (0.31 <sup>+0.35</sup> <sub>-0.29</sub> )	7.6 <sup>+8.5</sup> <sub>-6.8</sub> (17.6 <sup>+18.7</sup> <sub>-16.6</sub> )	5.8 <sup>+6.3</sup> <sub>-5.5</sub> (12.2 <sup>+13.0</sup> <sub>-11.4</sub> )	8.1 <sup>+9.5</sup> <sub>-7.3</sub> (18.9 <sup>+20.2</sup> <sub>-17.7</sub> )	6.3 <sup>+7.1</sup> <sub>-5.8</sub> (13.4 <sup>+14.2</sup> <sub>-12.4</sub> )
nircam3-9865	0.14 <sup>+0.14</sup> <sub>-0.14</sub> (0.10 <sup>+0.10</sup> <sub>-0.09</sub> )	0.18 <sup>+0.18</sup> <sub>-0.18</sub> (0.15 <sup>+0.16</sup> <sub>-0.15</sub> )	0.09 <sup>+0.09</sup> <sub>-0.09</sub> (0.06 <sup>+0.06</sup> <sub>-0.06</sub> )	0.10 <sup>+0.10</sup> <sub>-0.10</sub> (0.07 <sup>+0.08</sup> <sub>-0.07</sub> )	23.6 <sup>+23.9</sup> <sub>-23.2</sub> (30.1 <sup>+29.9</sup> <sub>-29.2</sub> )	20.0 <sup>+20.2</sup> <sub>-19.7</sub> (22.4 <sup>+22.9</sup> <sub>-21.8</sub> )	33.1 <sup>+33.2</sup> <sub>-33.0</sub> (43.4 <sup>+44.0</sup> <sub>-42.6</sub> )	30.1 <sup>+30.2</sup> <sub>-30.0</sub> (36.7 <sup>+37.4</sup> <sub>-35.9</sub> )
nircam3-9866	0.75 <sup>+0.79</sup> <sub>-0.70</sub> (0.65 <sup>+0.70</sup> <sub>-0.59</sub> )	0.97 <sup>+0.93</sup> <sub>-0.93</sub> (1.12 <sup>+1.19</sup> <sub>-1.05</sub> )	0.27 <sup>+0.25</sup> <sub>-0.25</sub> (0.14 <sup>+0.16</sup> <sub>-0.13</sub> )	0.33 <sup>+0.37</sup> <sub>-0.31</sub> (0.21 <sup>+0.22</sup> <sub>-0.19</sub> )	7.1 <sup>+7.4</sup> <sub>-6.8</sub> (7.9 <sup>+8.5</sup> <sub>-7.4</sub> )	5.8 <sup>+6.0</sup> <sub>-5.7</sub> (5.2 <sup>+5.4</sup> <sub>-4.9</sub> )	15.0 <sup>+15.7</sup> <sub>-14.1</sub> (23.2 <sup>+25.1</sup> <sub>-21.8</sub> )	13.0 <sup>+13.6</sup> <sub>-12.0</sub> (18.1 <sup>+19.2</sup> <sub>-17.2</sub> )
nircam3-10039	0.56 <sup>+0.65</sup> <sub>-0.47</sub> (0.67 <sup>+0.86</sup> <sub>-0.49</sub> )	0.78 <sup>+0.86</sup> <sub>-0.71</sub> (1.11 <sup>+1.34</sup> <sub>-0.81</sub> )	0.28 <sup>+0.35</sup> <sub>-0.24</sub> (0.39 <sup>+0.49</sup> <sub>-0.25</sub> )	0.42 <sup>+0.53</sup> <sub>-0.35</sub> (0.57 <sup>+0.74</sup> <sub>-0.37</sub> )	8.8 <sup>+10.1</sup> <sub>-7.9</sub> (7.7 <sup>+10.4</sup> <sub>-6.3</sub> )	6.9 <sup>+7.4</sup> <sub>-6.4</sub> (5.2 <sup>+6.9</sup> <sub>-4.5</sub> )	14.4 <sup>+16.1</sup> <sub>-12.4</sub> (11.4 <sup>+15.7</sup> <sub>-9.8</sub> )	10.9 <sup>+12.4</sup> <sub>-9.2</sub> (8.6 <sup>+11.9</sup> <sub>-7.1</sub> )
nircam3-10103	0.64 <sup>+0.73</sup> <sub>-0.53</sub> (0.92 <sup>+1.07</sup> <sub>-0.78</sub> )	0.87 <sup>+0.97</sup> <sub>-0.76</sub> (1.26 <sup>+1.38</sup> <sub>-1.12</sub> )	0.37 <sup>+0.40</sup> <sub>-0.29</sub> (0.64 <sup>+0.76</sup> <sub>-0.49</sub> )	0.58 <sup>+0.68</sup> <sub>-0.45</sub> (0.88 <sup>+1.01</sup> <sub>-0.73</sub> )	7.9 <sup>+9.2</sup> <sub>-7.2</sub> (6.0 <sup>+6.9</sup> <sub>-5.4</sub> )	6.3 <sup>+7.0</sup> <sub>-5.8</sub> (4.7 <sup>+5.2</sup> <sub>-4.4</sub> )	11.8 <sup>+14.1</sup> <sub>-9.3</sub> (8.0 <sup>+9.7</sup> <sub>-7.0</sub> )	8.6 <sup>+10.3</sup> <sub>-7.6</sub> (6.3 <sup>+7.2</sup> <sub>-5.6</sub> )
nircam3-10226	0.67 <sup>+0.71</sup> <sub>-0.62</sub> (0.20 <sup>+0.21</sup> <sub>-0.19</sub> )	0.85 <sup>+0.88</sup> <sub>-0.82</sub> (0.27 <sup>+0.29</sup> <sub>-0.26</sub> )	0.74 <sup>+0.78</sup> <sub>-0.70</sub> (0.23 <sup>+0.25</sup> <sub>-0.22</sub> )	0.94 <sup>+0.97</sup> <sub>-0.91</sub> (0.34 <sup>+0.36</sup> <sub>-0.32</sub> )	7.7 <sup>+7.4</sup> <sub>-7.2</sub> (18.7 <sup>+19.3</sup> <sub>-17.8</sub> )	6.4 <sup>+6.6</sup> <sub>-6.3</sub> (14.8 <sup>+15.4</sup> <sub>-14.1</sub> )	7.1 <sup>+7.4</sup> <sub>-6.8</sub> (16.5 <sup>+17.2</sup> <sub>-15.6</sub> )	5.9 <sup>+6.1</sup> <sub>-5.8</sub> (12.8 <sup>+13.3</sup> <sub>-12.2</sub> )
nircam3-10290	1.84 <sup>+1.89</sup> <sub>-1.79</sub> (0.88 <sup>+1.03</sup> <sub>-0.72</sub> )	2.01 <sup>+2.03</sup> <sub>-1.98</sub> (1.24 <sup>+1.37</sup> <sub>-1.12</sub> )	1.76 <sup>+1.81</sup> <sub>-1.70</sub> (0.83 <sup>+0.98</sup> <sub>-0.67</sub> )	1.94 <sup>+1.96</sup> <sub>-1.90</sub> (1.17 <sup>+1.32</sup> <sub>-1.04</sub> )	3.4 <sup>+3.5</sup> <sub>-3.3</sub> (6.2 <sup>+7.3</sup> <sub>-5.5</sub> )	3.2 <sup>+3.2</sup> <sub>-3.1</sub> (4.8 <sup>+5.2</sup> <sub>-4.4</sub> )	3.6 <sup>+3.7</sup> <sub>-3.2</sub> (6.5 <sup>+7.7</sup> <sub>-5.7</sub> )	3.3 <sup>+3.2</sup> <sub>-3.2</sub> (5.0 <sup>+5.5</sup> <sub>-4.5</sub> )
nircam3-10630	0.25 <sup>+0.26</sup> <sub>-0.25</sub> (0.38 <sup>+0.40</sup> <sub>-0.35</sub> )	0.33 <sup>+0.34</sup> <sub>-0.32</sub> (0.56 <sup>+0.61</sup> <sub>-0.52</sub> )	0.16 <sup>+0.16</sup> <sub>-0.16</sub> (0.14 <sup>+0.15</sup> <sub>-0.14</sub> )	0.18 <sup>+0.18</sup> <sub>-0.18</sub> (0.19 <sup>+0.20</sup> <sub>-0.18</sub> )	15.6 <sup>+15.8</sup> <sub>-15.4</sub> (11.7 <sup>+12.4</sup> <sub>-11.2</sub> )	13.0 <sup>+13.2</sup> <sub>-12.8</sub> (8.7 <sup>+9.3</sup> <sub>-8.2</sub> )	21.6 <sup>+21.7</sup> <sub>-21.4</sub> (23.1 <sup>+23.8</sup> <sub>-22.5</sub> )	19.9 <sup>+20.1</sup> <sub>-19.6</sub> (19.0 <sup>+19.7</sup> <sub>-18.2</sub> )
nircam3-10688	1.77 <sup>+1.84</sup> <sub>-1.44</sub> (0.65 <sup>+0.72</sup> <sub>-0.58</sub> )	1.89 <sup>+1.97</sup> <sub>-1.76</sub> (0.92 <sup>+1.05</sup> <sub>-0.81</sub> )	1.76 <sup>+1.84</sup> <sub>-1.42</sub> (0.63 <sup>+0.70</sup> <sub>-0.56</sub> )	1.89 <sup>+1.96</sup> <sub>-1.75</sub> (0.86 <sup>+0.98</sup> <sub>-0.77</sub> )	3.5 <sup>+3.4</sup> <sub>-3.4</sub> (7.8 <sup>+8.5</sup> <sub>-7.3</sub> )	3.3 <sup>+3.2</sup> <sub>-3.2</sub> (6.0 <sup>+6.6</sup> <sub>-5.4</sub> )	3.6 <sup>+3.4</sup> <sub>-3.4</sub> (8.1 <sup>+8.8</sup> <sub>-7.4</sub> )	3.3 <sup>+3.6</sup> <sub>-3.2</sub> (6.3 <sup>+6.9</sup> <sub>-5.7</sub> )
nircam3-10755	0.56 <sup>+0.58</sup> <sub>-0.55</sub> (0.29 <sup>+0.30</sup> <sub>-0.29</sub> )	0.66 <sup>+0.70</sup> <sub>-0.63</sub> (0.34 <sup>+0.35</sup> <sub>-0.34</sub> )	0.51 <sup>+0.53</sup> <sub>-0.50</sub> (0.25 <sup>+0.26</sup> <sub>-0.25</sub> )	0.58 <sup>+0.60</sup> <sub>-0.56</sub> (0.28 <sup>+0.28</sup> <sub>-0.27</sub> )	8.8 <sup>+9.0</sup> <sub>-8.5</sub> (14.1 <sup>+14.0</sup> <sub>-14.0</sub> )	7.8 <sup>+8.0</sup> <sub>-7.4</sub> (12.6 <sup>+12.7</sup> <sub>-12.5</sub> )	9.4 <sup>+9.5</sup> <sub>-9.2</sub> (15.5 <sup>+15.6</sup> <sub>-15.4</sub> )	8.5 <sup>+8.7</sup> <sub>-8.3</sub> (14.7 <sup>+14.8</sup> <sub>-14.6</sub> )
nircam3-10791	0.88 <sup>+1.15</sup> <sub>-0.64</sub> (0.24 <sup>+0.31</sup> <sub>-0.20</sub> )	1.72 <sup>+1.45</sup> <sub>-1.31</sub> (0.39 <sup>+0.47</sup> <sub>-0.33</sub> )	0.23 <sup>+0.20</sup> <sub>-0.20</sub> (0.08 <sup>+0.10</sup> <sub>-0.07</sub> )	0.34 <sup>+0.44</sup> <sub>-0.28</sub> (0.11 <sup>+0.14</sup> <sub>-0.09</sub> )	6.2 <sup>+6.8</sup> <sub>-5.1</sub> (16.0 <sup>+18.1</sup> <sub>-13.4</sub> )	3.6 <sup>+4.2</sup> <sub>-3.3</sub> (11.5 <sup>+13.0</sup> <sub>-10.0</sub> )	16.5 <sup>+18.4</sup> <sub>-10.5</sub> (35.2 <sup>+37.7</sup> <sub>-30.8</sub> )	12.7 <sup>+14.5</sup> <sub>-10.5</sub> (28.2 <sup>+31.3</sup> <sub>-23.4</sub> )
nircam3-11158	0.79 <sup>+0.88</sup> <sub>-0.70</sub> (1.01 <sup>+1.13</sup> <sub>-0.89</sub> )	1.04 <sup>+1.11</sup> <sub>-0.94</sub> (1.33 <sup>+1.42</sup> <sub>-1.21</sub> )	0.71 <sup>+0.79</sup> <sub>-0.62</sub> (0.94 <sup>+1.07</sup> <sub>-0.83</sub> )	0.93 <sup>+1.02</sup> <sub>-0.83</sub> (1.25 <sup>+1.37</sup> <sub>-1.12</sub> )	6.8 <sup>+7.5</sup> <sub>-6.8</sub> (5.6 <sup>+6.2</sup> <sub>-5.1</sub> )	5.5 <sup>+5.9</sup> <sub>-5.2</sub> (4.5 <sup>+4.9</sup> <sub>-4.3</sub> )	7.3 <sup>+8.1</sup> <sub>-6.8</sub> (5.9 <sup>+6.6</sup> <sub>-5.4</sub> )	6.0 <sup>+6.6</sup> <sub>-5.5</sub> (4.7 <sup>+5.2</sup> <sub>-4.4</sub> )
nircam3-11245	0.25 <sup>+0.25</sup> <sub>-0.24</sub> (0.30 <sup>+0.31</sup> <sub>-0.29</sub> )	0.30 <sup>+0.30</sup> <sub>-0.30</sub> (0.45 <sup>+0.48</sup> <sub>-0.43</sub> )	0.17 <sup>+0.17</sup> <sub>-0.17</sub> (0.14 <sup>+0.14</sup> <sub>-0.14</sub> )	0.18 <sup>+0.18</sup> <sub>-0.18</sub> (0.16 <sup>+0.16</sup> <sub>-0.16</sub> )	15.9 <sup>+16.0</sup> <sub>-15.8</sub> (13.7 <sup>+14.2</sup> <sub>-13.4</sub> )	13.9 <sup>+14.1</sup> <sub>-13.8</sub> (10.3 <sup>+10.7</sup> <sub>-9.9</sub> )	20.6 <sup>+20.6</sup> <sub>-20.5</sub> (23.8 <sup>+24.0</sup> <sub>-23.6</sub> )	19.9 <sup>+20.0</sup> <sub>-19.8</sub> (21.6 <sup>+21.8</sup> <sub>-21.2</sub> )
nircam3-11248	0.69 <sup>+0.70</sup> <sub>-0.68</sub> (0.37 <sup>+0.45</sup> <sub>-0.35</sub> )	0.75 <sup>+0.77</sup> <sub>-0.74</sub> (0.53 <sup>+0.66</sup> <sub>-0.44</sub> )	0.68 <sup>+0.70</sup> <sub>-0.67</sub> (0.27 <sup>+0.31</sup> <sub>-0.25</sub> )	0.74 <sup>+0.77</sup> <sub>-0.72</sub> (0.34 <sup>+0.41</sup> <sub>-0.30</sub> )	7.6 <sup>+7.6</sup> <sub>-7.1</sub> (11.9 <sup>+13.4</sup> <sub>-10.4</sub> )	7.1 <sup>+7.1</sup> <sub>-6.9</sub> (9.1 <sup>+10.4</sup> <sub>-7.7</sub> )	7.6 <sup>+7.7</sup> <sub>-7.5</sub> (15.0 <sup>+16.0</sup> <sub>-13.5</sub> )	7.1 <sup>+7.3</sup> <sub>-6.9</sub> (12.6 <sup>+13.9</sup> <sub>-11.0</sub> )
nircam3-11615	1.18 <sup>+1.37</sup> <sub>-1.01</sub> (0.82 <sup>+0.94</sup> <sub>-0.72</sub> )	1.50 <sup>+1.68</sup> <sub>-1.30</sub> (1.11 <sup>+1.23</sup> <sub>-0.97</sub> )	1.20 <sup>+1.40</sup> <sub>-1.01</sub> (0.84 <sup>+0.98</sup> <sub>-0.73</sub> )	1.50 <sup>+1.70</sup> <sub>-1.33</sub> (1.14 <sup>+1.27</sup> <sub>-0.99</sub> )	5.0 <sup>+5.6</sup> <sub>-4.6</sub> (6.6 <sup>+7.3</sup> <sub>-5.9</sub> )	4.1 <sup>+4.6</sup> <sub>-3.7</sub> (5.2 <sup>+5.8</sup> <sub>-4.8</sub> )	4.9 <sup>+5.6</sup> <sub>-4.3</sub> (6.5 <sup>+7.2</sup> <sub>-5.7</sub> )	4.1 <sup>+4.5</sup> <sub>-3.7</sub> (5.1 <sup>+5.7</sup> <sub>-4.7</sub> )
nircam3-11637	0.25 <sup>+0.20</sup> <sub>-0.20</sub> (0.18 <sup>+0.19</sup> <sub>-0.17</sub> )	0.30 <sup>+0.33</sup> <sub>-0.28</sub> (0.25 <sup>+0.27</sup> <sub>-0.24</sub> )	0.18 <sup>+0.20</sup> <sub>-0.17</sub> (0.19 <sup>+0.20</sup> <sub>-0.18</sub> )	0.26 <sup>+0.28</sup> <sub>-0.23</sub> (0.27 <sup>+0.29</sup> <sub>-0.25</sub> )	17.5 <sup>+18.7</sup> <sub>-17.5</sub> (19.8 <sup>+20.7</sup> <sub>-19.0</sub> )	13.7 <sup>+14.5</sup> <sub>-12.8</sub> (15.6 <sup>+16.4</sup> <sub>-14.8</sub> )	19.7 <sup>+20.8</sup> <sub>-18.5</sub> (19.2 <sup>+20.0</sup> <sub>-18.2</sub> )	15.4 <sup>+16.6</sup> <sub>-14.4</sub> (14.9 <sup>+15.6</sup> <sub>-14.2</sub> )
nircam6-444	0.89 <sup>+1.10</sup> <sub>-0.79</sub> (0.21 <sup>+0.23</sup> <sub>-0.20</sub> )	1.14 <sup>+1.20</sup> <sub>-1.03</sub> (0.29 <sup>+0.32</sup> <sub>-0.27</sub> )	0.72 <sup>+0.83</sup> <sub>-0.68</sub> (0.14 <sup>+0.15</sup> <sub>-0.13</sub> )	0.86 <sup>+0.98</sup> <sub>-0.77</sub> (0.15 <sup>+0.19</sup> <sub>-0.17</sub> )	6.2 <sup>+6.8</sup> <sub>-5.2</sub> (17.7 <sup>+18.3</sup> <sub>-16.8</sub> )	5.1 <sup>+5.5</sup> <sub>-4.9</sub> (14.1 <sup>+14.8</sup> <sub>-13.3</sub> )	7.3 <sup>+7.6</sup> <sub>-6.6</sub> (23.8 <sup>+24.5</sup> <sub>-23.0</sub> )	6.3 <sup>+6.9</sup> <sub>-5.3</sub> (19.9 <sup>+20.3</sup> <sub>-19.3</sub> )
nircam6-575	0.32 <sup>+0.33</sup> <sub>-0.32</sub> (0.35 <sup>+0.38</sup> <sub>-0.33</sub> )	0.41 <sup>+0.42</sup> <sub>-0.40</sub> (0.55 <sup>+0.60</sup> <sub>-0.51</sub> )	0.24 <sup>+0.24</sup> <sub>-0.24</sub> (0.17 <sup>+0.18</sup> <sub>-0.16</sub> )	0.27 <sup>+0.28</sup> <sub>-0.27</sub> (0.24 <sup>+0.26</sup> <sub>-0.23</sub> )	13.1 <sup>+13.3</sup> <sub>-12.9</sub> (12.3 <sup>+13.0</sup> <sub>-11.8</sub> )	11.1 <sup>+11.3</sup> <sub>-10.9</sub> (8.9 <sup>+9.4</sup> <sub>-8.4</sub> )	16.3 <sup>+16.4</sup> <sub>-16.2</sub> (20.4 <sup>+21.1</sup> <sub>-19.6</sub> )	14.8 <sup>+14.9</sup> <sub>-14.7</sub> (16.1 <sup>+16.8</sup> <sub>-15.5</sub> )
nircam6-660	0.48 <sup>+0.55</sup> <sub>-0.44</sub> (0.41 <sup>+0.49</sup> <sub>-0.32</sub> )	0.61 <sup>+0.71</sup> <sub>-0.56</sub> (0.62 <sup>+0.73</sup> <sub>-0.49</sub> )	0.37 <sup>+0.39</sup> <sub>-0.35</sub> (0.24 <sup>+0.30</sup> <sub>-0.18</sub> )	0.43 <sup>+0.47</sup> <sub>-0.40</sub> (0.34 <sup>+0.41</sup> <sub>-0.26</sub> )	9.9 <sup>+10.4</sup> <sub>-9.9</sub> (11.0<			

Table E.1: (Continued)

Galaxy name	$t_5^{\text{SB99(BC03)}}$ [Gyr]	$t_{10}^{\text{SB99(BC03)}}$ [Gyr]	$t_{5 \times 10^8 \text{ M}_\odot}^{\text{SB99(BC03)}}$ [Gyr]	$t_{10^9 \text{ M}_\odot}^{\text{SB99(BC03)}}$ [Gyr]	$z_5^{\text{SB99(BC03)}}$	$z_{10}^{\text{SB99(BC03)}}$	$z_{5 \times 10^8 \text{ M}_\odot}^{\text{SB99(BC03)}}$	$z_{10^9 \text{ M}_\odot}^{\text{SB99(BC03)}}$
nircam6-775	2.31 <sup>+2.79</sup> <sub>-1.83</sub> (0.97 <sup>+1.29</sup> <sub>-0.70</sub> )	2.86 <sup>+3.05</sup> <sub>-2.35</sub> (1.40 <sup>+1.72</sup> <sub>-1.02</sub> )	1.99 <sup>+2.60</sup> <sub>-1.26</sub> (0.90 <sup>+1.26</sup> <sub>-0.64</sub> )	2.57 <sup>+2.90</sup> <sub>-1.35</sub> (1.33 <sup>+1.67</sup> <sub>-0.93</sub> )	2.83 <sup>+4</sup> <sub>-2.3</sub> (5.8 <sup>+7.4</sup> <sub>-4.6</sub> )	2.32 <sup>+8</sup> <sub>-2.1</sub> (4.3 <sup>+5.5</sup> <sub>-3.6</sub> )	3.24 <sup>+7</sup> <sub>-2.5</sub> (6.1 <sup>+8.0</sup> <sub>-4.7</sub> )	2.53 <sup>+1</sup> <sub>-2.3</sub> (4.5 <sup>+6.0</sup> <sub>-3.7</sub> )
nircam6-939	1.46 <sup>+1.70</sup> <sub>-1.19</sub> (0.14 <sup>+0.15</sup> <sub>-0.13</sub> )	1.98 <sup>+2.11</sup> <sub>-1.81</sub> (0.22 <sup>+0.23</sup> <sub>-0.20</sub> )	0.69 <sup>+0.87</sup> <sub>-0.54</sub> (0.07 <sup>+0.07</sup> <sub>-0.05</sub> )	1.13 <sup>+1.38</sup> <sub>-0.72</sub> (0.10 <sup>+0.10</sup> <sub>-0.09</sub> )	4.24 <sup>+9</sup> <sub>-7.0</sub> (23.5 <sup>+24.9</sup> <sub>-22.2</sub> )	3.23 <sup>+5</sup> <sub>-3.0</sub> (17.5 <sup>+18.5</sup> <sub>-16.4</sub> )	7.59 <sup>+0</sup> <sub>-6.3</sub> (36.8 <sup>+38.0</sup> <sub>-35.4</sub> )	5.16 <sup>+1</sup> <sub>-4.4</sub> (30.5 <sup>+32.0</sup> <sub>-28.8</sub> )
nircam6-968	0.68 <sup>+0.71</sup> <sub>-0.66</sub> (0.22 <sup>+0.26</sup> <sub>-0.19</sub> )	0.81 <sup>+0.88</sup> <sub>-0.76</sub> (0.32 <sup>+0.37</sup> <sub>-0.27</sub> )	0.62 <sup>+0.65</sup> <sub>-0.60</sub> (0.12 <sup>+0.15</sup> <sub>-0.11</sub> )	0.70 <sup>+0.74</sup> <sub>-0.67</sub> (0.17 <sup>+0.20</sup> <sub>-0.15</sub> )	7.67 <sup>+8</sup> <sub>-7.3</sub> (17.3 <sup>+19.3</sup> <sub>-15.2</sub> )	6.7 <sup>+6.2</sup> <sub>-6.2</sub> (13.3 <sup>+14.9</sup> <sub>-11.8</sub> )	8.1 <sup>+3</sup> <sub>-3</sub> (25.6 <sup>+28.0</sup> <sub>-22.8</sub> )	7.47 <sup>+7</sup> <sub>-7.1</sub> (20.8 <sup>+22.5</sup> <sub>-18.7</sub> )
nircam6-1029	1.17 <sup>+1.36</sup> <sub>-1.01</sub> (0.81 <sup>+0.98</sup> <sub>-0.68</sub> )	2.40 <sup>+2.50</sup> <sub>-2.20</sub> (2.09 <sup>+2.44</sup> <sub>-1.55</sub> )	0.44 <sup>+0.48</sup> <sub>-0.42</sub> (0.28 <sup>+0.33</sup> <sub>-0.23</sub> )	0.59 <sup>+0.68</sup> <sub>-0.54</sub> (0.42 <sup>+0.45</sup> <sub>-0.35</sub> )	5.0 <sup>+5.6</sup> <sub>-4.6</sub> (6.6 <sup>+7.6</sup> <sub>-5.8</sub> )	2.72 <sup>+9</sup> <sub>-2.6</sub> (3.1 <sup>+4.0</sup> <sub>-2.7</sub> )	10.5 <sup>+0.9</sup> <sub>-0.9</sub> (14.5 <sup>+16.5</sup> <sub>-12.9</sub> )	8.5 <sup>+0.9</sup> <sub>-0.9</sub> (10.9 <sup>+12.4</sup> <sub>-9.8</sub> )
nircam6-1177	1.51 <sup>+1.69</sup> <sub>-1.35</sub> (0.25 <sup>+0.26</sup> <sub>-0.24</sub> )	2.44 <sup>+2.30</sup> <sub>-2.56</sub> (0.35 <sup>+0.37</sup> <sub>-0.34</sub> )	0.67 <sup>+0.69</sup> <sub>-1.01</sub> (0.11 <sup>+0.11</sup> <sub>-0.13</sub> )	0.76 <sup>+0.80</sup> <sub>-1.59</sub> (0.10 <sup>+0.12</sup> <sub>-0.21</sub> )	4.14 <sup>+4</sup> <sub>-3.7</sub> (15.7 <sup>+16.2</sup> <sub>-11.6</sub> )	2.72 <sup>+8</sup> <sub>-2.5</sub> (12.3 <sup>+12.7</sup> <sub>-11.9</sub> )	7.7 <sup>+7.8</sup> <sub>-4.1</sub> (27.9 <sup>+28.1</sup> <sub>-24.3</sub> )	7.0 <sup>+7.2</sup> <sub>-3.3</sub> (26.1 <sup>+26.4</sup> <sub>-15.8</sub> )
nircam6-1868	2.18 <sup>+2.04</sup> <sub>-2.04</sub> (0.34 <sup>+0.39</sup> <sub>-0.30</sub> )	2.56 <sup>+2.61</sup> <sub>-2.51</sub> (0.58 <sup>+0.65</sup> <sub>-0.50</sub> )	1.26 <sup>+1.49</sup> <sub>-1.01</sub> (0.15 <sup>+0.17</sup> <sub>-0.13</sub> )	1.82 <sup>+1.95</sup> <sub>-1.59</sub> (0.23 <sup>+0.27</sup> <sub>-0.21</sub> )	2.9 <sup>+2.8</sup> <sub>-2.8</sub> (12.7 <sup>+13.9</sup> <sub>-11.6</sub> )	2.52 <sup>+6</sup> <sub>-2.6</sub> (8.5 <sup>+9.5</sup> <sub>-7.8</sub> )	4.7 <sup>+5.6</sup> <sub>-4.1</sub> (22.4 <sup>+24.3</sup> <sub>-20.2</sub> )	3.5 <sup>+3.9</sup> <sub>-3.3</sub> (16.7 <sup>+18.1</sup> <sub>-15.0</sub> )
nircam6-1890	0.32 <sup>+0.33</sup> <sub>-0.31</sub> (0.31 <sup>+0.34</sup> <sub>-0.29</sub> )	0.39 <sup>+0.41</sup> <sub>-0.38</sub> (0.42 <sup>+0.47</sup> <sub>-0.37</sub> )	0.35 <sup>+0.36</sup> <sub>-0.34</sub> (0.22 <sup>+0.24</sup> <sub>-0.21</sub> )	0.45 <sup>+0.48</sup> <sub>-0.43</sub> (0.27 <sup>+0.29</sup> <sub>-0.25</sub> )	13.3 <sup>+13.5</sup> <sub>-13.0</sub> (13.4 <sup>+14.2</sup> <sub>-12.6</sub> )	11.5 <sup>+11.8</sup> <sub>-11.0</sub> (10.9 <sup>+11.8</sup> <sub>-10.0</sub> )	12.4 <sup>+12.8</sup> <sub>-12.0</sub> (17.1 <sup>+17.6</sup> <sub>-16.4</sub> )	10.4 <sup>+10.8</sup> <sub>-9.9</sub> (15.0 <sup>+15.7</sup> <sub>-14.0</sub> )
nircam6-1959	1.36 <sup>+1.51</sup> <sub>-1.18</sub> (0.14 <sup>+0.14</sup> <sub>-0.13</sub> )	1.81 <sup>+1.92</sup> <sub>-1.60</sub> (0.20 <sup>+0.21</sup> <sub>-0.19</sub> )	0.98 <sup>+1.14</sup> <sub>-0.78</sub> (0.10 <sup>+0.10</sup> <sub>-0.09</sub> )	1.35 <sup>+1.49</sup> <sub>-1.15</sub> (0.19 <sup>+0.12</sup> <sub>-0.11</sub> )	4.45 <sup>+0</sup> <sub>-4.1</sub> (23.7 <sup>+24.2</sup> <sub>-23.1</sub> )	3.53 <sup>+9</sup> <sub>-3.3</sub> (18.4 <sup>+18.9</sup> <sub>-17.9</sub> )	5.8 <sup>+6.8</sup> <sub>-5.1</sub> (30.5 <sup>+31.0</sup> <sub>-26.3</sub> )	4.5 <sup>+4.1</sup> <sub>-4.1</sub> (27.0 <sup>+27.5</sup> <sub>-26.3</sub> )
nircam6-2317	0.39 <sup>+0.45</sup> <sub>-0.34</sub> (1.32 <sup>+1.43</sup> <sub>-1.20</sub> )	0.59 <sup>+0.67</sup> <sub>-0.50</sub> (1.81 <sup>+1.91</sup> <sub>-1.70</sub> )	0.31 <sup>+0.36</sup> <sub>-0.27</sub> (1.23 <sup>+1.34</sup> <sub>-1.10</sub> )	0.45 <sup>+0.53</sup> <sub>-0.38</sub> (1.70 <sup>+1.80</sup> <sub>-1.59</sub> )	11.5 <sup>+12.8</sup> <sub>-10.4</sub> (4.5 <sup>+4.9</sup> <sub>-4.3</sub> )	8.4 <sup>+9.5</sup> <sub>-7.7</sub> (3.5 <sup>+3.7</sup> <sub>-3.3</sub> )	13.5 <sup>+14.9</sup> <sub>-12.2</sub> (4.8 <sup>+5.2</sup> <sub>-4.5</sub> )	10.4 <sup>+11.7</sup> <sub>-9.2</sub> (3.7 <sup>+3.9</sup> <sub>-3.5</sub> )
nircam6-2347	0.26 <sup>+0.27</sup> <sub>-0.26</sub> (0.18 <sup>+0.19</sup> <sub>-0.18</sub> )	0.32 <sup>+0.32</sup> <sub>-0.32</sub> (0.26 <sup>+0.27</sup> <sub>-0.25</sub> )	0.20 <sup>+0.20</sup> <sub>-0.20</sub> (0.10 <sup>+0.10</sup> <sub>-0.10</sub> )	0.21 <sup>+0.22</sup> <sub>-0.21</sub> (0.19 <sup>+0.12</sup> <sub>-0.12</sub> )	15.2 <sup>+15.3</sup> <sub>-15.1</sub> (19.5 <sup>+19.9</sup> <sub>-19.1</sub> )	13.2 <sup>+13.3</sup> <sub>-13.1</sub> (15.3 <sup>+15.6</sup> <sub>-15.0</sub> )	18.4 <sup>+18.5</sup> <sub>-18.3</sub> (29.5 <sup>+29.7</sup> <sub>-29.3</sub> )	17.5 <sup>+17.5</sup> <sub>-17.5</sub> (26.0 <sup>+26.3</sup> <sub>-25.7</sub> )
nircam6-2383	0.92 <sup>+1.12</sup> <sub>-0.75</sub> (0.22 <sup>+0.24</sup> <sub>-0.22</sub> )	1.56 <sup>+1.65</sup> <sub>-1.45</sub> (0.33 <sup>+0.35</sup> <sub>-0.31</sub> )	0.67 <sup>+0.82</sup> <sub>-0.55</sub> (0.18 <sup>+0.19</sup> <sub>-0.17</sub> )	1.20 <sup>+1.40</sup> <sub>-0.98</sub> (0.24 <sup>+0.26</sup> <sub>-0.23</sub> )	6.0 <sup>+7.1</sup> <sub>-5.2</sub> (17.0 <sup>+17.5</sup> <sub>-16.1</sub> )	4.04 <sup>+2</sup> <sub>-3.8</sub> (13.0 <sup>+13.5</sup> <sub>-12.3</sub> )	7.7 <sup>+8.9</sup> <sub>-4.3</sub> (20.1 <sup>+20.5</sup> <sub>-19.3</sub> )	4.9 <sup>+5.8</sup> <sub>-4.3</sub> (16.4 <sup>+16.9</sup> <sub>-15.5</sub> )
nircam6-2762	0.47 <sup>+0.51</sup> <sub>-0.41</sub> (0.48 <sup>+0.54</sup> <sub>-0.42</sub> )	0.63 <sup>+0.68</sup> <sub>-0.56</sub> (0.70 <sup>+0.80</sup> <sub>-0.61</sub> )	0.39 <sup>+0.44</sup> <sub>-0.30</sub> (0.46 <sup>+0.50</sup> <sub>-0.41</sub> )	0.51 <sup>+0.56</sup> <sub>-0.46</sub> (0.60 <sup>+0.72</sup> <sub>-0.59</sub> )	10.1 <sup>+11.1</sup> <sub>-9.4</sub> (9.8 <sup>+9.9</sup> <sub>-9.5</sub> )	8.1 <sup>+8.8</sup> <sub>-7.6</sub> (7.4 <sup>+8.3</sup> <sub>-7.5</sub> )	11.5 <sup>+12.7</sup> <sub>-10.5</sub> (10.1 <sup>+11.1</sup> <sub>-9.5</sub> )	9.4 <sup>+10.2</sup> <sub>-8.8</sub> (7.8 <sup>+8.5</sup> <sub>-7.5</sub> )
nircam6-2958	0.18 <sup>+0.18</sup> <sub>-0.17</sub> (0.20 <sup>+0.22</sup> <sub>-0.19</sub> )	0.26 <sup>+0.27</sup> <sub>-0.25</sub> (0.30 <sup>+0.33</sup> <sub>-0.28</sub> )	0.12 <sup>+0.13</sup> <sub>-0.12</sub> (0.10 <sup>+0.11</sup> <sub>-0.10</sub> )	0.17 <sup>+0.17</sup> <sub>-0.16</sub> (0.15 <sup>+0.15</sup> <sub>-0.14</sub> )	20.0 <sup>+20.5</sup> <sub>-19.5</sub> (18.4 <sup>+19.3</sup> <sub>-17.3</sub> )	15.2 <sup>+15.7</sup> <sub>-14.8</sub> (13.8 <sup>+14.6</sup> <sub>-13.0</sub> )	26.2 <sup>+27.0</sup> <sub>-25.4</sub> (28.9 <sup>+30.1</sup> <sub>-27.6</sub> )	21.0 <sup>+21.5</sup> <sub>-20.4</sub> (23.0 <sup>+24.1</sup> <sub>-22.1</sub> )
nircam6-2991	0.42 <sup>+0.42</sup> <sub>-0.42</sub> (0.20 <sup>+0.21</sup> <sub>-0.19</sub> )	0.47 <sup>+0.47</sup> <sub>-0.46</sub> (0.25 <sup>+0.27</sup> <sub>-0.24</sub> )	0.43 <sup>+0.43</sup> <sub>-0.43</sub> (0.20 <sup>+0.21</sup> <sub>-0.20</sub> )	0.47 <sup>+0.48</sup> <sub>-0.47</sub> (0.26 <sup>+0.28</sup> <sub>-0.24</sub> )	10.9 <sup>+10.9</sup> <sub>-10.8</sub> (18.4 <sup>+18.8</sup> <sub>-17.8</sub> )	10.1 <sup>+10.1</sup> <sub>-10.0</sub> (15.7 <sup>+16.1</sup> <sub>-14.9</sub> )	10.7 <sup>+10.8</sup> <sub>-10.6</sub> (18.2 <sup>+18.7</sup> <sub>-17.6</sub> )	9.9 <sup>+10.0</sup> <sub>-9.8</sub> (15.5 <sup>+16.1</sup> <sub>-14.7</sub> )
nircam6-3216	0.44 <sup>+0.52</sup> <sub>-0.39</sub> (0.52 <sup>+0.60</sup> <sub>-0.44</sub> )	0.60 <sup>+0.68</sup> <sub>-0.51</sub> (0.72 <sup>+0.80</sup> <sub>-0.64</sub> )	0.31 <sup>+0.34</sup> <sub>-0.29</sub> (0.27 <sup>+0.27</sup> <sub>-0.25</sub> )	0.38 <sup>+0.43</sup> <sub>-0.34</sub> (0.40 <sup>+0.48</sup> <sub>-0.32</sub> )	10.5 <sup>+11.5</sup> <sub>-9.3</sub> (9.3 <sup>+10.5</sup> <sub>-9.3</sub> )	8.3 <sup>+8.6</sup> <sub>-7.6</sub> (7.3 <sup>+8.0</sup> <sub>-7.2</sub> )	13.4 <sup>+14.0</sup> <sub>-12.5</sub> (14.7 <sup>+17.3</sup> <sub>-12.3</sub> )	11.8 <sup>+12.7</sup> <sub>-11.0</sub> (11.3 <sup>+13.1</sup> <sub>-10.8</sub> )
nircam6-3217	0.28 <sup>+0.30</sup> <sub>-0.26</sub> (1.12 <sup>+1.33</sup> <sub>-0.98</sub> )	0.41 <sup>+0.45</sup> <sub>-0.38</sub> (1.34 <sup>+1.36</sup> <sub>-1.32</sub> )	0.19 <sup>+0.20</sup> <sub>-0.19</sub> (0.55 <sup>+0.65</sup> <sub>-0.46</sub> )	0.25 <sup>+0.27</sup> <sub>-0.24</sub> (0.89 <sup>+0.78</sup> <sub>-0.78</sub> )	14.4 <sup>+15.1</sup> <sub>-13.7</sub> (5.2 <sup>+5.8</sup> <sub>-4.8</sub> )	11.0 <sup>+11.6</sup> <sub>-10.3</sub> (4.5 <sup>+4.5</sup> <sub>-4.4</sub> )	18.8 <sup>+19.2</sup> <sub>-18.3</sub> (8.9 <sup>+9.8</sup> <sub>-7.8</sub> )	15.6 <sup>+16.2</sup> <sub>-15.0</sub> (6.2 <sup>+6.8</sup> <sub>-5.6</sub> )
nircam6-3231	0.39 <sup>+0.40</sup> <sub>-0.39</sub> (0.28 <sup>+0.31</sup> <sub>-0.25</sub> )	0.45 <sup>+0.45</sup> <sub>-0.44</sub> (0.40 <sup>+0.46</sup> <sub>-0.36</sub> )	0.33 <sup>+0.33</sup> <sub>-0.33</sub> (0.14 <sup>+0.15</sup> <sub>-0.12</sub> )	0.34 <sup>+0.34</sup> <sub>-0.34</sub> (0.19 <sup>+0.21</sup> <sub>-0.16</sub> )	11.4 <sup>+11.4</sup> <sub>-11.3</sub> (14.5 <sup>+15.8</sup> <sub>-13.5</sub> )	10.4 <sup>+10.4</sup> <sub>-10.3</sub> (11.2 <sup>+12.1</sup> <sub>-10.2</sub> )	13.0 <sup>+13.0</sup> <sub>-13.0</sub> (24.1 <sup>+25.6</sup> <sub>-22.3</sub> )	12.7 <sup>+12.6</sup> <sub>-11.3</sub> (19.4 <sup>+21.3</sup> <sub>-17.9</sub> )
nircam6-3604	1.39 <sup>+1.48</sup> <sub>-1.28</sub> (1.58 <sup>+1.64</sup> <sub>-1.51</sub> )	1.69 <sup>+1.75</sup> <sub>-1.62</sub> (1.86 <sup>+1.91</sup> <sub>-1.81</sub> )	1.36 <sup>+1.45</sup> <sub>-1.25</sub> (1.69 <sup>+1.75</sup> <sub>-1.62</sub> )	1.65 <sup>+1.72</sup> <sub>-1.57</sub> (1.97 <sup>+2.02</sup> <sub>-1.93</sub> )	4.34 <sup>+6</sup> <sub>-4.1</sub> (3.9 <sup>+4.0</sup> <sub>-3.8</sub> )	3.73 <sup>+3.8</sup> <sub>-3.6</sub> (3.4 <sup>+3.5</sup> <sub>-3.3</sub> )	4.4 <sup>+4.7</sup> <sub>-4.2</sub> (3.7 <sup>+3.8</sup> <sub>-3.6</sub> )	3.8 <sup>+3.9</sup> <sub>-3.6</sub> (3.2 <sup>+3.3</sup> <sub>-3.2</sub> )
nircam6-3650	0.33 <sup>+0.31</sup> <sub>-0.31</sub> (0.19 <sup>+0.18</sup> <sub>-0.18</sub> )	0.41 <sup>+0.43</sup> <sub>-0.37</sub> (0.25 <sup>+0.27</sup> <sub>-0.24</sub> )	0.25 <sup>+0.25</sup> <sub>-0.24</sub> (0.15 <sup>+0.16</sup> <sub>-0.14</sub> )	0.27 <sup>+0.28</sup> <sub>-0.26</sub> (0.18 <sup>+0.17</sup> <sub>-0.17</sub> )	12.9 <sup>+13.5</sup> <sub>-12.6</sub> (19.0 <sup>+19.9</sup> <sub>-18.1</sub> )	11.1 <sup>+11.9</sup> <sub>-10.7</sub> (15.6 <sup>+16.2</sup> <sub>-15.0</sub> )	15.8 <sup>+16.1</sup> <sub>-15.7</sub> (22.6 <sup>+23.4</sup> <sub>-21.9</sub> )	15.0 <sup>+15.3</sup> <sub>-14.7</sub> (19.5 <sup>+20.4</sup> <sub>-18.5</sub> )
nircam6-3730	0.29 <sup>+0.33</sup> <sub>-0.26</sub> (0.31 <sup>+0.35</sup> <sub>-0.27</sub> )	0.42 <sup>+0.46</sup> <sub>-0.38</sub> (0.52 <sup>+0.62</sup> <sub>-0.45</sub> )	0.24 <sup>+0.29</sup> <sub>-0.21</sub> (0.31 <sup>+0.36</sup> <sub>-0.28</sub> )	0.35 <sup>+0.40</sup> <sub>-0.31</sub> (0.53 <sup>+0.63</sup> <sub>-0.46</sub> )	14.2 <sup>+15.4</sup> <sub>-12.8</sub> (13.7 <sup>+14.8</sup> <sub>-12.4</sub> )	10.9 <sup>+11.7</sup> <sub>-10.2</sub> (9.3 <sup>+10.4</sup> <sub>-8.2</sub> )	16.1 <sup>+17.7</sup> <sub>-14.3</sub> (13.5 <sup>+14.6</sup> <sub>-12.1</sub> )	12.4 <sup>+13.5</sup> <sub>-11.3</sub> (9.2 <sup>+10.2</sup> <sub>-8.0</sub> )
nircam6-3995	0.66 <sup>+0.67</sup> <sub>-0.66</sub> (0.13 <sup>+0.13</sup> <sub>-0.12</sub> )	0.71 <sup>+0.71</sup> <sub>-0.71</sub> (0.19 <sup>+0.20</sup> <sub>-0.18</sub> )	0.62 <sup>+0.62</sup> <sub>-0.62</sub> (0.08 <sup>+0.08</sup> <sub>-0.07</sub> )	0.65 <sup>+0.65</sup> <sub>-0.64</sub> (0.10 <sup>+0.10</sup> <sub>-0.09</sub> )	7.77 <sup>+8</sup> <sub>-7.7</sub> (25.2 <sup>+26.2</sup> <sub>-24.5</sub> )	7.4 <sup>+7.4</sup> <sub>-7.3</sub> (19.2 <sup>+20.1</sup> <sub>-18.7</sub> )	8.1 <sup>+8.1</sup> <sub>-8.1</sub> (34.9 <sup>+36.6</sup> <sub>-29.7</sub> )	7.9 <sup>+7.9</sup> <sub>-7.9</sub> (30.2 <sup>+31.0</sup> <sub>-29.7</sub> )
nircam6-4042	0.53 <sup>+0.63</sup> <sub>-0.45</sub> (1.30 <sup>+1.47</sup> <sub>-1.05</sub> )	0.81 <sup>+0.91</sup> <sub>-0.73</sub> (1.80 <sup>+1.94</sup> <sub>-1.57</sub> )	0.36 <sup>+0.43</sup> <sub>-0.30</sub> (0.98 <sup>+1.15</sup> <sub>-0.75</sub> )	0.57 <sup>+0.67</sup> <sub>-0.49</sub> (1.40 <sup>+1.58</sup> <sub>-1.16</sub> )	9.1 <sup>+10.2</sup> <sub>-8.0</sub> (4.6 <sup>+4.1</sup> <sub>-4.1</sub> )	6.7 <sup>+6.7</sup> <sub>-6.1</sub> (3.5 <sup>+3.9</sup> <sub>-3.3</sub> )	12.2 <sup>+13.3</sup> <sub>-12.0</sub> (6.7 <sup>+7.0</sup> <sub>-6.4</sub> )	8.7 <sup>+9.8</sup> <sub>-7.7</sub> (4.3 <sup>+4.9</sup> <sub>-3.9</sub> )
nircam6-4751	1.66 <sup>+1.76</sup> <sub>-1.49</sub> (1.28 <sup>+1.52</sup> <sub>-1.00</sub> )	2.07 <sup>+2.16</sup> <sub>-1.95</sub> (1.98 <sup>+2.18</sup> <sub>-1.63</sub> )	1.52 <sup>+1.68</sup> <sub>-1.38</sub> (1.25 <sup>+1.53</sup> <sub>-0.98</sub> )	1.94 <sup>+2.05</sup> <sub>-1.82</sub> (1.93 <sup>+2.17</sup> <sub>-1.57</sub> )	3.74 <sup>+4.1</sup> <sub>-3.6</sub> (4.7 <sup>+5.7</sup> <sub>-4.0</sub> )	3.1 <sup>+3.2</sup> <sub>-3.0</sub> (3.2 <sup>+3.8</sup> <sub>-2.9</sub> )	4.0 <sup>+4.4</sup> <sub>-3.7</sub> (4.7 <sup>+5.7</sup> <sub>-4.0</sub> )	3.3 <sup>+3.5</sup> <sub>-3.0</sub> (3.3 <sup>+3.9</sup> <sub>-3.0</sub> )
nircam6-4891	0.29 <sup>+0.34</sup> <sub>-0.27</sub> (0.33 <sup>+0.37</sup> <sub>-0.30</sub> )	0.41 <sup>+0.49</sup> <sub>-0.36</sub> (0.44 <sup>+0.49</sup> <sub>-0.39</sub> )	0.20 <sup>+0.22</sup> <sub>-0.18</sub> (0.24 <sup>+0.25</sup> <sub>-0.22</sub> )	0.25 <sup>+0.27</sup> <sub>-0.23</sub> (0.29 <sup>+0.32</sup> <sub>-0.26</sub> )	14.1 <sup>+14.9</sup> <sub>-14.9</sub> (12.8 <sup>+13.9</sup> <sub>-12.0</sub> )	11.1 <sup>+12.0</sup> <sub>-9.6</sub> (10.4 <sup>+11.4</sup> <sub>-9.7</sub> )	18.6 <sup>+19.5</sup> <sub>-17.5</sub> (16.3 <sup>+17.3</sup> <sub>-15.6</sub> )	15.9 <sup>+16.9</sup> <sub>-14.9</sub> (14.2 <sup>+15.2</sup> <sub>-13.1</sub> )
nircam6-5284	0.21 <sup>+0.20</sup> <sub>-0.20</sub> (0.47 <sup>+0.58</sup> <sub>-0.41</sub> )	0.29 <sup>+0.31</sup> <sub>-0.28</sub> (0.89 <sup>+1.15</sup> <sub>-0.73</sub> )	0.13 <sup>+0.13</sup> <sub>-0.13</sub> (0.30 <sup>+0.35</sup> <sub>-0.27</sub> )	0.16 <sup>+0.17</sup> <sub>-0.16</sub> (0.49 <sup>+0.59</sup> <sub>-0.43</sub> )	17.9 <sup>+18.3</sup> <sub>-17.3</sub> (10.1 <sup>+11.1</sup> <sub>-10.6</sub> )	14.1 <sup>+14.6</sup> <sub>-13.6</sub> (6.2 <sup>+7.2</sup> <sub>-6.5</sub> )	25.0 <sup>+25.4</sup> <sub>-24.3</sub> (13.8 <sup>+14.8</sup> <sub>-12.3</sub> )	21.1 <sup>+21.7</sup> <sub>-20.3</sub> (9.7 <sup>+10.6</sup> <sub>-8.5</sub> )
nircam6-5398	0.18 <sup>+0.18</sup> <sub>-0.17</sub> (0.16 <sup>+0.15</sup> <sub>-0.15</sub> )	0.24 <sup>+0.25</sup> <sub>-0.23</sub> (0.25 <sup>+0.28</sup> <sub>-0.23</sub> )	0.16 <sup>+0.17</sup> <sub>-0.16</sub> (0.15 <sup>+0.16</sup> <sub>-0.14</sub> )	0.21 <sup>+0.22</sup> <sub>-0.20</sub> (0.23 <sup>+0.25</sup> <sub>-0.22</sub> )	20.1 <sup>+20.6</sup> <sub>-19.6</sub> (21.3 <sup>+22.5</sup> <sub>-20.1</sub> )	16.7 <sup>+16.7</sup> <sub>-15.6</sub> (15.7 <sup>+16.8</sup> <sub>-14.7</sub> )	21.5 <sup>+21.8</sup> <sub>-20.9</sub> (22.2 <sup>+23.4</sup> <sub>-21.2</sub> )	17.8 <sup>+18.3</sup> <sub>-17.1</sub> (16.6 <sup>+17.4</sup> <sub>-15.7</sub> )
nircam6-5655	0.45 <sup>+0.48</sup> <sub>-0.42</sub> (0.57 <sup>+0.63</sup> <sub>-0.52</sub> )	0.62 <sup>+0.66</sup> <sub>-0.58</sub> (0.84 <sup>+0.89</sup> <sub>-0.78</sub> )	0.25 <sup>+0.26</sup> <sub>-0.24</sub> (0.23 <sup>+0.26</sup> <sub>-0.21</sub> )	0.29 <sup>+0.30</sup> <sub>-0.28</sub> (0.33 <sup>+0.36</sup> <sub>-0.29</sub> )	10.3 <sup>+10.8</sup> <sub>-9.9</sub> (8.6 <sup>+9.3</sup> <sub>-8.0</sub> )	8.2 <sup>+8.6</sup> <sub>-6.2</sub> (6.5 <sup>+6.9</sup> <sub>-6.2</sub> )	15.6 <sup>+16.0</sup> <sub>-15.2</sub> (16.5 <sup>+18.0</sup> <sub>-15.2</sub> )	14.2 <sup>+14.5</sup> <sub>-13.9</sub> (13.0 <sup>+14.0</sup> <sub>-12.1</sub> )
nircam6-5662	0.07 <sup>+0.07</sup> <sub>-0.07</sub> (0.28 <sup>+0.37</sup> <sub>-0.27</sub> )	0.12 <sup>+0.12</sup> <sub>-0.12</sub> (0.34 <sup>+0.34</sup> <sub>-0.33</sub> )	0.01 <sup>+0.01</sup> <sub>-0.01</sub> (0.19 <sup>+0.19</sup> <sub>-0.19</sub> )	0.01 <sup>+0.01</sup> <sub>-0.01</sub> (0.20 <sup>+0.20</sup> <sub>-0.20</sub> )	37.0 <sup>+37.1</sup> <sub>-36.8</sub> (14.6 <sup>+14.8</sup> <sub>-14.4</sub> )	26.7 <sup>+26.8</sup> <sub>-26.5</sub> (12.7 <sup>+12.9</sup> <sub>-12.5</sub> )	202.3 <sup>+204.0</sup> <sub>-199.9</sub> (19.1 <sup>+19.1</sup> <sub>-19.0</sub> )	129.1 <sup>+130.2</sup> <sub>-127.6</sub> (18.6 <sup>+18.7</sup> <sub>-18.6</sub> )
nircam6-5824	1.35 <sup>+1.46</sup> <sub>-1.26</sub> (0.32 <sup>+0.35</sup> <sub>-0.30</sub> )	1.79 <sup>+1.88</sup> <sub>-1.70</sub> (0.47 <sup>+0.50</sup> <sub>-0</sub>						

Table E.1: (Continued)

Galaxy name	$t_5^{\text{SB99(BC03)}}$ [Gyr]	$t_{10}^{\text{SB99(BC03)}}$ [Gyr]	$t_{5 \times 10^8 M_{\odot}}^{\text{SB99(BC03)}}$ [Gyr]	$t_{10^9 M_{\odot}}^{\text{SB99(BC03)}}$ [Gyr]	$z_5^{\text{SB99(BC03)}}$	$z_{10}^{\text{SB99(BC03)}}$	$z_{5 \times 10^8 M_{\odot}}^{\text{SB99(BC03)}}$	$z_{10^9 M_{\odot}}^{\text{SB99(BC03)}}$
nircam6-5946	0.71 <sup>+0.77</sup> <sub>-0.63</sub> (0.94 <sup>+0.95</sup> <sub>-0.85</sub> )	0.89 <sup>+0.92</sup> <sub>-1.05</sub> (1.05 <sup>+1.06</sup> <sub>-1.04</sub> )	0.64 <sup>+0.71</sup> <sub>-0.95</sub> (0.95 <sup>+0.96</sup> <sub>-0.94</sub> )	0.82 <sup>+0.87</sup> <sub>-0.76</sub> (1.06 <sup>+1.07</sup> <sub>-1.05</sub> )	7.38 <sup>+0.6</sup> <sub>-5.9</sub> (5.96 <sup>+6.0</sup> <sub>-5.9</sub> )	6.26 <sup>+4.7</sup> <sub>-6.0</sub> (5.55 <sup>+5.5</sup> <sub>-5.4</sub> )	8.08 <sup>+9.9</sup> <sub>-7.3</sub> (5.9 <sup>+5.9</sup> <sub>-5.9</sub> )	6.67 <sup>+5.4</sup> <sub>-5.4</sub> (5.45 <sup>+5.4</sup> <sub>-5.4</sub> )
nircam6-6491	0.78 <sup>+0.87</sup> <sub>-0.71</sub> (0.32 <sup>+0.38</sup> <sub>-0.28</sub> )	0.98 <sup>+1.02</sup> <sub>-0.90</sub> (0.46 <sup>+0.52</sup> <sub>-0.41</sub> )	0.57 <sup>+0.65</sup> <sub>-0.20</sub> (0.20 <sup>+0.25</sup> <sub>-0.17</sub> )	0.71 <sup>+0.78</sup> <sub>-0.64</sub> (0.28 <sup>+0.34</sup> <sub>-0.24</sub> )	6.97 <sup>+4.4</sup> <sub>-11.8</sub> (13.1 <sup>+14.5</sup> <sub>-11.8</sub> )	5.86 <sup>+16.1</sup> <sub>-6.3</sub> (10.1 <sup>+11.0</sup> <sub>-11.0</sub> )	8.79 <sup>+20.5</sup> <sub>-9.3</sub> (18.6 <sup>+20.5</sup> <sub>-19.5</sub> )	7.47 <sup>+16.0</sup> <sub>-6.9</sub> (14.6 <sup>+16.0</sup> <sub>-16.0</sub> )
nircam6-6558	0.74 <sup>+0.76</sup> <sub>-0.71</sub> (0.26 <sup>+0.28</sup> <sub>-0.25</sub> )	0.83 <sup>+0.87</sup> <sub>-0.73</sub> (0.34 <sup>+0.36</sup> <sub>-0.31</sub> )	0.68 <sup>+0.70</sup> <sub>-0.67</sub> (0.19 <sup>+0.20</sup> <sub>-0.21</sub> )	0.74 <sup>+0.76</sup> <sub>-0.71</sub> (0.22 <sup>+0.23</sup> <sub>-0.21</sub> )	7.27 <sup>+3.3</sup> <sub>-7.0</sub> (15.2 <sup>+15.8</sup> <sub>-14.5</sub> )	6.58 <sup>+18.6</sup> <sub>-6.3</sub> (12.8 <sup>+13.6</sup> <sub>-12.1</sub> )	7.67 <sup>+19.5</sup> <sub>-7.0</sub> (19.1 <sup>+19.5</sup> <sub>-18.6</sub> )	7.27 <sup>+17.9</sup> <sub>-7.0</sub> (17.2 <sup>+17.9</sup> <sub>-16.5</sub> )
nircam6-6710	0.56 <sup>+0.70</sup> <sub>-0.47</sub> (0.40 <sup>+0.51</sup> <sub>-0.34</sub> )	0.80 <sup>+0.92</sup> <sub>-0.72</sub> (0.61 <sup>+0.76</sup> <sub>-0.49</sub> )	0.37 <sup>+0.46</sup> <sub>-0.32</sub> (0.30 <sup>+0.37</sup> <sub>-0.25</sub> )	0.52 <sup>+0.67</sup> <sub>-0.44</sub> (0.41 <sup>+0.51</sup> <sub>-0.33</sub> )	8.84 <sup>+10.0</sup> <sub>-11.4</sub> (11.2 <sup>+12.4</sup> <sub>-9.4</sub> )	6.77 <sup>+11.9</sup> <sub>-10.2</sub> (8.2 <sup>+9.7</sup> <sub>-7.0</sub> )	12.0 <sup>+13.1</sup> <sub>-10.2</sub> (13.8 <sup>+15.5</sup> <sub>-11.9</sub> )	9.3 <sup>+10.5</sup> <sub>-7.7</sub> (11.1 <sup>+12.8</sup> <sub>-9.4</sub> )
nircam6-6741	0.49 <sup>+0.56</sup> <sub>-0.42</sub> (0.83 <sup>+0.99</sup> <sub>-0.70</sub> )	1.37 <sup>+2.12</sup> <sub>-1.04</sub> (1.14 <sup>+1.32</sup> <sub>-1.06</sub> )	0.28 <sup>+0.30</sup> <sub>-0.25</sub> (0.64 <sup>+0.75</sup> <sub>-0.53</sub> )	0.46 <sup>+0.53</sup> <sub>-0.40</sub> (0.83 <sup>+1.00</sup> <sub>-0.70</sub> )	9.7 <sup>+10.8</sup> <sub>-8.8</sub> (6.6 <sup>+5.7</sup> <sub>-5.4</sub> )	4.4 <sup>+5.5</sup> <sub>-3.0</sub> (5.1 <sup>+4.5</sup> <sub>-4.5</sub> )	14.6 <sup>+15.8</sup> <sub>-13.7</sub> (8.0 <sup>+9.1</sup> <sub>-7.1</sub> )	10.2 <sup>+11.3</sup> <sub>-9.1</sub> (6.5 <sup>+7.4</sup> <sub>-5.7</sub> )
nircam6-6830	1.35 <sup>+1.45</sup> <sub>-1.24</sub> (0.71 <sup>+0.80</sup> <sub>-0.64</sub> )	1.68 <sup>+1.76</sup> <sub>-1.58</sub> (0.99 <sup>+1.11</sup> <sub>-0.89</sub> )	1.12 <sup>+1.24</sup> <sub>-1.02</sub> (0.63 <sup>+0.73</sup> <sub>-0.56</sub> )	1.41 <sup>+1.51</sup> <sub>-1.29</sub> (0.80 <sup>+0.98</sup> <sub>-0.77</sub> )	4.4 <sup>+4.8</sup> <sub>-4.2</sub> (7.3 <sup>+8.0</sup> <sub>-6.7</sub> )	3.7 <sup>+3.9</sup> <sub>-3.6</sub> (5.7 <sup>+6.2</sup> <sub>-5.2</sub> )	5.2 <sup>+5.6</sup> <sub>-4.8</sub> (8.0 <sup>+8.8</sup> <sub>-7.2</sub> )	4.3 <sup>+4.6</sup> <sub>-4.1</sub> (6.3 <sup>+6.9</sup> <sub>-5.7</sub> )
nircam6-6832	0.76 <sup>+0.87</sup> <sub>-0.69</sub> (0.94 <sup>+1.06</sup> <sub>-0.82</sub> )	1.02 <sup>+1.10</sup> <sub>-0.95</sub> (1.28 <sup>+1.37</sup> <sub>-1.17</sub> )	0.66 <sup>+0.74</sup> <sub>-0.58</sub> (0.84 <sup>+0.96</sup> <sub>-0.74</sub> )	0.88 <sup>+0.98</sup> <sub>-0.78</sub> (1.14 <sup>+1.25</sup> <sub>-1.02</sub> )	7.0 <sup>+7.9</sup> <sub>-6.3</sub> (5.9 <sup>+6.6</sup> <sub>-5.4</sub> )	5.6 <sup>+6.9</sup> <sub>-5.2</sub> (4.6 <sup>+5.0</sup> <sub>-4.4</sub> )	7.8 <sup>+8.5</sup> <sub>-7.1</sub> (6.5 <sup>+7.2</sup> <sub>-5.8</sub> )	6.3 <sup>+6.8</sup> <sub>-5.8</sub> (5.1 <sup>+5.5</sup> <sub>-4.7</sub> )
nircam6-7113	0.53 <sup>+0.57</sup> <sub>-0.49</sub> (0.52 <sup>+0.69</sup> <sub>-0.40</sub> )	0.73 <sup>+0.79</sup> <sub>-0.68</sub> (1.13 <sup>+1.33</sup> <sub>-0.69</sub> )	0.26 <sup>+0.29</sup> <sub>-0.25</sub> (0.23 <sup>+0.27</sup> <sub>-0.18</sub> )	0.32 <sup>+0.36</sup> <sub>-0.30</sub> (0.33 <sup>+0.40</sup> <sub>-0.26</sub> )	9.2 <sup>+9.7</sup> <sub>-8.7</sub> (9.3 <sup>+11.3</sup> <sub>-10.4</sub> )	7.2 <sup>+7.6</sup> <sub>-6.8</sub> (5.1 <sup>+7.5</sup> <sub>-4.5</sub> )	15.3 <sup>+15.9</sup> <sub>-14.1</sub> (16.8 <sup>+19.7</sup> <sub>-14.9</sub> )	13.3 <sup>+13.9</sup> <sub>-12.1</sub> (12.9 <sup>+15.5</sup> <sub>-11.2</sub> )
nircam6-7223	1.26 <sup>+1.15</sup> <sub>-1.15</sub> (0.35 <sup>+0.42</sup> <sub>-0.30</sub> )	1.58 <sup>+1.67</sup> <sub>-1.46</sub> (0.54 <sup>+0.62</sup> <sub>-0.45</sub> )	1.02 <sup>+1.11</sup> <sub>-0.89</sub> (0.24 <sup>+0.26</sup> <sub>-0.20</sub> )	1.20 <sup>+1.33</sup> <sub>-1.10</sub> (0.37 <sup>+0.45</sup> <sub>-0.30</sub> )	4.7 <sup>+5.1</sup> <sub>-4.3</sub> (12.4 <sup>+14.3</sup> <sub>-10.8</sub> )	3.9 <sup>+4.2</sup> <sub>-3.3</sub> (9.0 <sup>+10.3</sup> <sub>-8.2</sub> )	5.6 <sup>+5.2</sup> <sub>-4.5</sub> (16.1 <sup>+18.3</sup> <sub>-13.3</sub> )	4.9 <sup>+5.3</sup> <sub>-4.5</sub> (11.8 <sup>+13.7</sup> <sub>-10.3</sub> )
nircam6-7384	1.84 <sup>+1.88</sup> <sub>-1.81</sub> (0.74 <sup>+0.83</sup> <sub>-0.66</sub> )	1.97 <sup>+2.09</sup> <sub>-1.95</sub> (0.99 <sup>+1.08</sup> <sub>-0.92</sub> )	1.72 <sup>+1.76</sup> <sub>-1.67</sub> (0.69 <sup>+0.79</sup> <sub>-0.62</sub> )	1.85 <sup>+1.88</sup> <sub>-1.82</sub> (0.94 <sup>+1.02</sup> <sub>-0.85</sub> )	3.4 <sup>+3.5</sup> <sub>-3.4</sub> (7.2 <sup>+7.8</sup> <sub>-6.3</sub> )	3.2 <sup>+3.3</sup> <sub>-3.2</sub> (5.7 <sup>+6.0</sup> <sub>-5.3</sub> )	3.6 <sup>+3.7</sup> <sub>-3.4</sub> (7.5 <sup>+8.2</sup> <sub>-6.8</sub> )	3.4 <sup>+3.5</sup> <sub>-3.4</sub> (5.9 <sup>+6.4</sup> <sub>-5.6</sub> )
nircam6-7452	1.12 <sup>+1.20</sup> <sub>-1.02</sub> (0.67 <sup>+0.78</sup> <sub>-0.58</sub> )	1.44 <sup>+1.54</sup> <sub>-1.34</sub> (1.10 <sup>+1.30</sup> <sub>-0.92</sub> )	1.38 <sup>+1.48</sup> <sub>-1.28</sub> (0.95 <sup>+1.16</sup> <sub>-0.80</sub> )	1.82 <sup>+1.89</sup> <sub>-1.72</sub> (1.92 <sup>+2.11</sup> <sub>-1.64</sub> )	5.2 <sup>+5.6</sup> <sub>-4.9</sub> (7.7 <sup>+8.6</sup> <sub>-6.9</sub> )	4.2 <sup>+4.5</sup> <sub>-4.0</sub> (5.3 <sup>+6.0</sup> <sub>-4.6</sub> )	4.4 <sup>+4.7</sup> <sub>-4.1</sub> (5.9 <sup>+6.7</sup> <sub>-5.0</sub> )	3.5 <sup>+3.6</sup> <sub>-3.3</sub> (3.3 <sup>+3.8</sup> <sub>-3.0</sub> )
nircam6-7600	0.78 <sup>+0.94</sup> <sub>-0.65</sub> (1.19 <sup>+0.96</sup> <sub>-0.94</sub> )	1.11 <sup>+1.25</sup> <sub>-0.93</sub> (1.54 <sup>+1.65</sup> <sub>-1.36</sub> )	0.78 <sup>+0.93</sup> <sub>-0.64</sub> (1.16 <sup>+0.93</sup> <sub>-0.93</sub> )	1.09 <sup>+1.24</sup> <sub>-0.91</sub> (1.51 <sup>+1.35</sup> <sub>-1.35</sub> )	6.8 <sup>+7.9</sup> <sub>-6.5</sub> (9.4 <sup>+9.5</sup> <sub>-4.5</sub> )	5.2 <sup>+6.0</sup> <sub>-4.7</sub> (4.0 <sup>+3.8</sup> <sub>-4.5</sub> )	6.9 <sup>+7.9</sup> <sub>-6.6</sub> (5.0 <sup>+5.9</sup> <sub>-4.5</sub> )	5.3 <sup>+6.1</sup> <sub>-4.8</sub> (4.0 <sup>+4.4</sup> <sub>-3.8</sub> )
nircam6-7645	0.42 <sup>+0.48</sup> <sub>-0.38</sub> (0.27 <sup>+0.36</sup> <sub>-0.20</sub> )	0.56 <sup>+0.69</sup> <sub>-0.49</sub> (0.42 <sup>+0.56</sup> <sub>-0.32</sub> )	0.31 <sup>+0.33</sup> <sub>-0.30</sub> (0.18 <sup>+0.26</sup> <sub>-0.15</sub> )	0.37 <sup>+0.39</sup> <sub>-0.35</sub> (0.27 <sup>+0.36</sup> <sub>-0.22</sub> )	10.9 <sup>+11.6</sup> <sub>-9.8</sub> (14.7 <sup>+18.2</sup> <sub>-12.3</sub> )	8.9 <sup>+7.5</sup> <sub>-7.5</sub> (10.8 <sup>+13.1</sup> <sub>-8.8</sub> )	13.5 <sup>+13.8</sup> <sub>-13.0</sub> (19.5 <sup>+23.0</sup> <sub>-15.5</sub> )	12.0 <sup>+12.3</sup> <sub>-11.3</sub> (14.8 <sup>+17.3</sup> <sub>-12.2</sub> )
nircam6-7670	1.39 <sup>+1.44</sup> <sub>-1.31</sub> (0.56 <sup>+0.63</sup> <sub>-0.49</sub> )	1.70 <sup>+1.73</sup> <sub>-1.67</sub> (0.95 <sup>+1.02</sup> <sub>-0.86</sub> )	0.70 <sup>+0.79</sup> <sub>-0.61</sub> (0.30 <sup>+0.34</sup> <sub>-0.26</sub> )	1.03 <sup>+1.14</sup> <sub>-0.95</sub> (0.47 <sup>+0.53</sup> <sub>-0.42</sub> )	4.3 <sup>+4.6</sup> <sub>-4.2</sub> (8.8 <sup>+9.6</sup> <sub>-7.7</sub> )	3.7 <sup>+3.7</sup> <sub>-3.6</sub> (5.9 <sup>+6.4</sup> <sub>-5.6</sub> )	7.4 <sup>+8.3</sup> <sub>-6.8</sub> (13.8 <sup>+15.3</sup> <sub>-12.7</sub> )	5.5 <sup>+5.9</sup> <sub>-5.1</sub> (9.9 <sup>+10.9</sup> <sub>-9.2</sub> )
nircam6-7699	0.53 <sup>+0.54</sup> <sub>-0.52</sub> (0.25 <sup>+0.24</sup> <sub>-0.24</sub> )	0.61 <sup>+0.63</sup> <sub>-0.60</sub> (0.31 <sup>+0.32</sup> <sub>-0.31</sub> )	0.42 <sup>+0.42</sup> <sub>-0.41</sub> (0.15 <sup>+0.15</sup> <sub>-0.15</sub> )	0.42 <sup>+0.43</sup> <sub>-0.42</sub> (0.16 <sup>+0.16</sup> <sub>-0.16</sub> )	9.2 <sup>+9.3</sup> <sub>-9.1</sub> (15.8 <sup>+16.0</sup> <sub>-15.7</sub> )	8.3 <sup>+8.4</sup> <sub>-8.1</sub> (13.4 <sup>+13.2</sup> <sub>-13.2</sub> )	10.9 <sup>+10.8</sup> <sub>-10.9</sub> (22.3 <sup>+22.4</sup> <sub>-22.3</sub> )	10.8 <sup>+10.8</sup> <sub>-10.8</sub> (21.3 <sup>+21.4</sup> <sub>-21.2</sub> )
nircam6-7837	0.14 <sup>+0.18</sup> <sub>-0.12</sub> (0.24 <sup>+0.20</sup> <sub>-0.20</sub> )	0.23 <sup>+0.30</sup> <sub>-0.20</sub> (0.35 <sup>+0.44</sup> <sub>-0.29</sub> )	0.13 <sup>+0.16</sup> <sub>-0.11</sub> (0.17 <sup>+0.15</sup> <sub>-0.15</sub> )	0.21 <sup>+0.26</sup> <sub>-0.18</sub> (0.24 <sup>+0.20</sup> <sub>-0.20</sub> )	23.2 <sup>+25.7</sup> <sub>-20.0</sub> (16.2 <sup>+18.3</sup> <sub>-13.9</sub> )	16.5 <sup>+18.4</sup> <sub>-14.0</sub> (12.3 <sup>+14.2</sup> <sub>-10.4</sub> )	25.1 <sup>+27.7</sup> <sub>-21.5</sub> (20.3 <sup>+22.1</sup> <sub>-17.6</sub> )	18.0 <sup>+19.8</sup> <sub>-15.4</sub> (16.3 <sup>+18.3</sup> <sub>-13.8</sub> )
nircam6-7928	2.03 <sup>+2.14</sup> <sub>-1.88</sub> (1.26 <sup>+1.59</sup> <sub>-1.03</sub> )	2.34 <sup>+2.42</sup> <sub>-2.24</sub> (1.86 <sup>+2.12</sup> <sub>-1.50</sub> )	1.64 <sup>+1.80</sup> <sub>-1.36</sub> (1.00 <sup>+1.29</sup> <sub>-0.80</sub> )	1.94 <sup>+2.07</sup> <sub>-1.78</sub> (1.37 <sup>+1.72</sup> <sub>-1.08</sub> )	3.1 <sup>+3.4</sup> <sub>-3.0</sub> (4.7 <sup>+5.5</sup> <sub>-3.9</sub> )	2.8 <sup>+2.9</sup> <sub>-2.7</sub> (3.4 <sup>+4.1</sup> <sub>-3.0</sub> )	3.8 <sup>+4.4</sup> <sub>-3.1</sub> (5.6 <sup>+6.7</sup> <sub>-4.6</sub> )	3.3 <sup>+3.5</sup> <sub>-3.1</sub> (4.5 <sup>+5.3</sup> <sub>-3.6</sub> )
nircam6-8012	0.64 <sup>+0.80</sup> <sub>-0.57</sub> (0.22 <sup>+0.24</sup> <sub>-0.21</sub> )	0.89 <sup>+1.00</sup> <sub>-0.76</sub> (0.30 <sup>+0.33</sup> <sub>-0.28</sub> )	0.50 <sup>+0.56</sup> <sub>-0.47</sub> (0.17 <sup>+0.17</sup> <sub>-0.16</sub> )	0.61 <sup>+0.72</sup> <sub>-0.54</sub> (0.20 <sup>+0.22</sup> <sub>-0.19</sub> )	8.0 <sup>+8.6</sup> <sub>-6.7</sub> (17.0 <sup>+18.0</sup> <sub>-16.1</sub> )	6.2 <sup>+7.0</sup> <sub>-5.6</sub> (13.8 <sup>+14.6</sup> <sub>-12.9</sub> )	9.5 <sup>+10.0</sup> <sub>-8.8</sub> (21.0 <sup>+21.7</sup> <sub>-20.4</sub> )	8.3 <sup>+9.0</sup> <sub>-7.3</sub> (18.2 <sup>+19.1</sup> <sub>-17.3</sub> )
nircam6-8094	1.10 <sup>+1.18</sup> <sub>-1.01</sub> (0.46 <sup>+0.52</sup> <sub>-0.41</sub> )	1.31 <sup>+1.36</sup> <sub>-1.24</sub> (0.65 <sup>+0.71</sup> <sub>-0.58</sub> )	1.00 <sup>+1.08</sup> <sub>-0.88</sub> (0.40 <sup>+0.46</sup> <sub>-0.36</sub> )	1.20 <sup>+1.27</sup> <sub>-1.12</sub> (0.50 <sup>+0.63</sup> <sub>-0.50</sub> )	5.2 <sup>+5.6</sup> <sub>-5.0</sub> (10.2 <sup>+11.0</sup> <sub>-9.3</sub> )	4.6 <sup>+4.8</sup> <sub>-4.4</sub> (7.9 <sup>+8.5</sup> <sub>-7.3</sub> )	5.7 <sup>+6.3</sup> <sub>-5.3</sub> (11.2 <sup>+12.2</sup> <sub>-10.2</sub> )	4.9 <sup>+5.2</sup> <sub>-4.7</sub> (8.8 <sup>+9.6</sup> <sub>-8.1</sub> )
nircam6-8103	0.90 <sup>+0.97</sup> <sub>-0.83</sub> (0.93 <sup>+1.06</sup> <sub>-0.81</sub> )	1.31 <sup>+1.37</sup> <sub>-1.25</sub> (1.56 <sup>+1.72</sup> <sub>-1.43</sub> )	0.67 <sup>+0.75</sup> <sub>-0.57</sub> (0.52 <sup>+0.61</sup> <sub>-0.46</sub> )	0.96 <sup>+1.03</sup> <sub>-0.89</sub> (0.77 <sup>+0.89</sup> <sub>-0.66</sub> )	6.1 <sup>+6.5</sup> <sub>-5.8</sub> (6.0 <sup>+6.7</sup> <sub>-5.4</sub> )	4.6 <sup>+4.7</sup> <sub>-4.4</sub> (3.9 <sup>+4.2</sup> <sub>-3.6</sub> )	7.7 <sup>+8.7</sup> <sub>-7.1</sub> (9.2 <sup>+10.1</sup> <sub>-8.3</sub> )	5.8 <sup>+6.2</sup> <sub>-5.5</sub> (6.9 <sup>+7.8</sup> <sub>-6.2</sub> )
nircam6-8159	0.43 <sup>+0.47</sup> <sub>-0.33</sub> (0.33 <sup>+0.37</sup> <sub>-0.29</sub> )	0.56 <sup>+0.64</sup> <sub>-0.48</sub> (0.46 <sup>+0.52</sup> <sub>-0.40</sub> )	0.47 <sup>+0.54</sup> <sub>-0.38</sub> (0.45 <sup>+0.53</sup> <sub>-0.39</sub> )	0.66 <sup>+0.75</sup> <sub>-0.54</sub> (0.75 <sup>+1.11</sup> <sub>-0.62</sub> )	10.9 <sup>+12.8</sup> <sub>-9.9</sub> (12.9 <sup>+14.2</sup> <sub>-11.9</sub> )	8.8 <sup>+9.8</sup> <sub>-8.0</sub> (10.2 <sup>+11.2</sup> <sub>-9.2</sub> )	10.1 <sup>+11.6</sup> <sub>-9.0</sub> (10.3 <sup>+11.5</sup> <sub>-9.1</sub> )	7.8 <sup>+9.0</sup> <sub>-7.1</sub> (7.0 <sup>+8.2</sup> <sub>-5.2</sub> )
nircam6-8295	0.80 <sup>+0.82</sup> <sub>-0.68</sub> (1.18 <sup>+0.95</sup> <sub>-0.95</sub> )	1.11 <sup>+1.20</sup> <sub>-0.99</sub> (1.59 <sup>+1.69</sup> <sub>-1.45</sub> )	0.71 <sup>+0.81</sup> <sub>-0.56</sub> (1.06 <sup>+1.25</sup> <sub>-0.85</sub> )	0.97 <sup>+1.09</sup> <sub>-0.83</sub> (1.47 <sup>+1.28</sup> <sub>-1.28</sub> )	6.7 <sup>+7.6</sup> <sub>-6.1</sub> (5.0 <sup>+5.9</sup> <sub>-4.5</sub> )	5.2 <sup>+5.7</sup> <sub>-4.4</sub> (3.9 <sup>+4.7</sup> <sub>-3.7</sub> )	7.4 <sup>+8.7</sup> <sub>-6.7</sub> (5.4 <sup>+6.4</sup> <sub>-4.7</sub> )	5.8 <sup>+6.5</sup> <sub>-5.3</sub> (4.1 <sup>+4.6</sup> <sub>-3.9</sub> )
nircam6-8355	0.52 <sup>+0.55</sup> <sub>-0.48</sub> (0.43 <sup>+0.36</sup> <sub>-0.36</sub> )	0.72 <sup>+0.78</sup> <sub>-0.67</sub> (0.83 <sup>+1.03</sup> <sub>-0.64</sub> )	0.27 <sup>+0.27</sup> <sub>-0.27</sub> (0.08 <sup>+0.09</sup> <sub>-0.07</sub> )	0.29 <sup>+0.30</sup> <sub>-0.28</sub> (0.13 <sup>+0.15</sup> <sub>-0.11</sub> )	9.3 <sup>+9.8</sup> <sub>-8.9</sub> (10.7 <sup>+12.1</sup> <sub>-9.6</sub> )	7.2 <sup>+7.7</sup> <sub>-6.8</sub> (6.6 <sup>+8.0</sup> <sub>-5.9</sub> )	14.9 <sup>+15.0</sup> <sub>-14.0</sub> (34.3 <sup>+37.2</sup> <sub>-30.9</sub> )	14.2 <sup>+14.4</sup> <sub>-14.0</sub> (25.3 <sup>+28.2</sup> <sub>-22.3</sub> )
nircam6-8473	0.75 <sup>+0.83</sup> <sub>-0.68</sub> (0.27 <sup>+0.28</sup> <sub>-0.25</sub> )	1.01 <sup>+1.08</sup> <sub>-0.94</sub> (0.41 <sup>+0.43</sup> <sub>-0.39</sub> )	0.41 <sup>+0.43</sup> <sub>-0.40</sub> (0.11 <sup>+0.11</sup> <sub>-0.11</sub> )	0.47 <sup>+0.50</sup> <sub>-0.44</sub> (0.14 <sup>+0.13</sup> <sub>-0.13</sub> )	7.1 <sup>+7.6</sup> <sub>-6.5</sub> (15.0 <sup>+15.5</sup> <sub>-14.5</sub> )	5.6 <sup>+5.9</sup> <sub>-5.3</sub> (11.0 <sup>+10.6</sup> <sub>-10.6</sub> )	11.0 <sup>+11.3</sup> <sub>-10.7</sub> (28.1 <sup>+28.5</sup> <sub>-27.7</sub> )	10.0 <sup>+10.4</sup> <sub>-10.0</sub> (24.1 <sup>+24.6</sup> <sub>-23.6</sub> )
nircam6-8572	1.11 <sup>+1.06</sup> <sub>-1.10</sub> (0.72 <sup>+0.77</sup> <sub>-0.66</sub> )	1.37 <sup>+1.52</sup> <sub>-1.26</sub> (0.93 <sup>+0.99</sup> <sub>-0.87</sub> )	0.72 <sup>+0.75</sup> <sub>-0.70</sub> (0.42 <sup>+0.46</sup> <sub>-0.38</sub> )	0.90 <sup>+0.93</sup> <sub>-0.87</sub> (0.52 <sup>+0.55</sup> <sub>-0.46</sub> )	5.2 <sup>+5.4</sup> <sub>-4.6</sub> (7.3 <sup>+7.8</sup> <sub>-6.8</sub> )	4.4 <sup>+4.7</sup> <sub>-4.0</sub> (6.0 <sup>+6.7</sup> <sub>-5.7</sub> )	7.3 <sup>+7.5</sup> <sub>-7.1</sub> (10.8 <sup>+11.7</sup> <sub>-10.2</sub> )	6.1 <sup>+6.3</sup> <sub>-5.4</sub> (9.3 <sup>+10.1</sup> <sub>-8.9</sub> )
nircam6-8691	1.56 <sup>+1.67</sup> <sub>-1.44</sub> (0.68 <sup>+0.79</sup> <sub>-0.59</sub> )	1.87 <sup>+1.95</sup> <sub>-1.79</sub> (1.03 <sup>+1.20</sup> <sub>-0.87</sub> )	0.95 <sup>+1.05</sup> <sub>-0.81</sub> (0.37 <sup>+0.44</sup> <sub>-0.32</sub> )	1.15 <sup>+1.29</sup> <sub>-1.03</sub> (0.48 <sup>+0.56</sup> <sub>-0.41</sub> )	3.9 <sup>+4.2</sup> <sub>-3.7</sub> (7.6 <sup>+8.5</sup> <sub>-6.8</sub> )	3.4 <sup>+3.5</sup> <sub>-3.3</sub> (5.5 <sup>+6.3</sup> <sub>-4.9</sub> )	5.9 <sup>+6.6</sup> <sub>-5.4</sub> (12.0 <sup>+13.2</sup> <sub>-10.5</sub> )	5.1 <sup>+5.5</sup> <sub>-4.6</sub> (9.9 <sup>+11.0</sup> <sub>-8.8</sub> )
nircam6-8778	0.62 <sup>+0.66</sup> <sub>-0.60</sub> (0.35 <sup>+0.36</sup> <sub>-0.34</sub> )	0.73 <sup>+0.81</sup> <sub>-0.69</sub> (0.43 <sup>+0.45</sup> <sub>-0.41</sub> )	0.57 <sup>+0.59</sup> <sub>-0.55</sub> (0.29 <sup>+0.30</sup> <sub>-0.29</sub> )	0.64 <sup>+0.68</sup> <sub>-0.61</sub> (0.34 <sup>+0.35</sup> <sub>-0.33</sub> )	8.2 <sup>+8.4</sup> <sub>-6.7</sub> (12.5 <sup>+12.7</sup> <sub>-12.1</sub> )	7.2 <sup>+7.5</sup> <sub>-6.7</sub> (10.7 <sup>+11.0</sup> <sub>-10.3</sub> )	8.7 <sup>+8.9</sup> <sub>-8.4</sub> (14.1 <sup>+14.3</sup> <sub>-13.9</sub> )	8.0 <sup>+8.3</sup> <sub>-7.6</sub> (12.7 <sup>+13.0</sup> <sub>-12.4</sub> )
nircam6-8796	0.58 <sup>+0.65</sup> <sub>-0.52</sub> (0.79 <sup>+0.92</sup> <sub>-0.68</sub> )	0.81 <sup>+0.88</sup> <sub>-0.72</sub> (1.33 <sup>+1.53</sup> <sub>-1.21</sub> )	0.43 <sup>+0.47</sup> <sub>-0.39</sub> (0.52 <sup>+0.61</sup> <sub>-0.46</sub> )	0.56 <sup>+0.62</sup> <sub>-0.50</sub> (0.80 <sup>+0.93</sup> <sub>-0.75</sub> )	8.6 <sup>+9.3</sup> <sub>-8.0</sub> (6.8 <sup>+7.6</sup> <sub>-6.0</sub> )	6.7 <sup>+7.3</sup> <sub>-6.2</sub> (4.5 <sup>+4.0</sup> <sub>-4.0</sub> )	10.7 <sup>+11.4</sup> <sub>-10.0</sub> (9.2 <sup>+10.2</sup> <sub>-8.3</sub> )	8.8 <sup>+9.5</sup> <sub>-8.1</sub> (6.3 <sup>+7.1</sup> <sub>-5.7</sub> )
nircam6-8878	0.95 <sup>+1.02</sup> <sub>-0.89</sub> (0.17 <sup>+0.19</sup> <sub>-0.16</sub> )	1.18 <sup>+1.12</sup> <sub>-1.12</sub> (0.26 <sup>+0.28</sup> <sub>-0.24</sub> )	0.73 <sup>+0.76</sup> <sub>-0.70</sub> (0.09 <sup>+0.09</sup> <sub>-0.09</sub> )	0.83 <sup>+0.88</sup> <sub>-0.78</sub> (0.13 <sup>+0.12</sup> <sub>-0.1</sub>				



Table E.1: (Continued)

Galaxy name	$t_5^{SB99(BC03)}$ [Gyr]	$t_{10}^{SB99(BC03)}$ [Gyr]	$t_{10}^{SB99(BC03)}$ $z_5 \times 10^8 M_\odot$	$t_{10^9 M_\odot}^{SB99(BC03)}$ [Gyr]	$z_5^{SB99(BC03)}$	$z_{10}^{SB99(BC03)}$	$z_{5 \times 10^8 M_\odot}^{SB99(BC03)}$	$z_{10^9 M_\odot}^{SB99(BC03)}$
nircam6-9375	$1.51_{-0.37}^{+0.66}$ (1.42, 1.49)	$1.89_{-1.75}^{+0.98}$ (1.69, 1.76)	$1.25_{-1.09}^{+0.37}$ (1.05, 1.18)	$1.47_{-1.29}^{+0.60}$ (1.37, 1.45)	$4.0_{-3.7}^{+4.4}$ (4.3, 4.5)	$3.3_{-3.2}^{+3.6}$ (3.7, 3.8)	$4.7_{-4.4}^{+5.3}$ (5.4, 6.1)	$4.1_{-4.2}^{+4.6}$ (4.4, 4.8)
nircam6-9559	$0.66_{-0.48}^{+0.78}$ (1.48, 1.61)	$0.90_{-0.73}^{+0.06}$ (1.75, 1.61)	$0.54_{-0.40}^{+0.70}$ (1.39, 1.54)	$0.77_{-0.61}^{+0.92}$ (1.65, 1.49)	$7.8_{-6.9}^{+9.8}$ (4.1, 3.8)	$6.1_{-5.4}^{+7.2}$ (3.6, 3.4)	$9.0_{-7.5}^{+11.3}$ (4.3, 4.0)	$6.9_{-6.0}^{+8.2}$ (3.8, 3.5)
nircam6-10556	$0.28_{-0.28}^{+0.29}$ (0.35, 0.36)	$0.35_{-0.34}^{+0.37}$ (0.46, 0.49)	$0.18_{-0.18}^{+0.18}$ (0.18, 0.18)	$0.19_{-0.19}^{+0.19}$ (0.19, 0.20)	$14.4_{-14.1}^{+14.7}$ (12.4, 12.9)	$12.3_{-11.9}^{+12.5}$ (10.1, 9.8)	$19.8_{-19.8}^{+19.8}$ (19.8, 20.0)	$19.3_{-19.2}^{+19.4}$ (18.7, 19.0)
nircam6-10988	$0.57_{-0.48}^{+0.64}$ (0.82, 0.99)	$0.77_{-0.69}^{+0.84}$ (1.18, 1.06)	$0.34_{-0.28}^{+0.46}$ (0.60, 0.67)	$0.53_{-0.44}^{+0.61}$ (0.85, 0.91)	$8.7_{-7.9}^{+9.8}$ (6.6, 6.2)	$6.9_{-6.4}^{+7.5}$ (5.0, 5.4)	$12.6_{-10.2}^{+14.7}$ (8.4, 8.4)	$9.1_{-8.2}^{+10.6}$ (6.5, 6.1)
nircam6-11098	$1.24_{-1.11}^{+1.33}$ (0.16, 0.15)	$1.48_{-1.44}^{+1.54}$ (0.23, 0.22)	$0.81_{-0.55}^{+0.93}$ (0.09, 0.08)	$0.96_{-0.79}^{+1.06}$ (0.11, 0.10)	$4.8_{-4.5}^{+5.2}$ (21.5, 22.0)	$4.1_{-4.0}^{+4.2}$ (16.6, 16.2)	$6.7_{-6.0}^{+8.9}$ (32.8, 32.0)	$5.8_{-5.4}^{+6.8}$ (28.4, 28.0)
nircam6-11125	$1.33_{-1.23}^{+1.41}$ (0.56, 0.65)	$1.82_{-1.67}^{+1.93}$ (0.79, 0.68)	$1.71_{-1.56}^{+1.82}$ (0.56, 0.47)	$2.33_{-2.22}^{+2.43}$ (0.80, 0.94)	$4.5_{-4.3}^{+4.8}$ (8.8, 7.9)	$3.5_{-3.3}^{+3.7}$ (6.8, 6.1)	$3.6_{-3.5}^{+3.9}$ (8.8, 8.1)	$2.8_{-2.7}^{+2.9}$ (6.7, 6.6)
nircam6-11371	$1.38_{-0.96}^{+1.58}$ (0.46, 0.55)	$2.10_{-1.87}^{+2.26}$ (0.70, 0.60)	$0.44_{-0.38}^{+0.52}$ (0.27, 0.23)	$0.71_{-0.55}^{+1.04}$ (0.35, 0.43)	$4.5_{-3.9}^{+5.9}$ (10.1, 11.3)	$3.0_{-2.9}^{+3.4}$ (7.4, 8.3)	$10.5_{-9.3}^{+11.6}$ (15.0, 16.6)	$7.4_{-5.9}^{+8.9}$ (12.3, 13.8)
nircam6-11443	$0.19_{-0.19}^{+0.20}$ (0.85, 0.73)	$0.26_{-0.25}^{+0.27}$ (1.20, 1.34)	$0.16_{-0.16}^{+0.17}$ (0.72, 0.60)	$0.22_{-0.21}^{+0.22}$ (1.01, 1.14)	$18.7_{-18.3}^{+19.1}$ (6.4, 7.2)	$15.2_{-14.9}^{+15.5}$ (4.9, 5.3)	$21.4_{-20.9}^{+21.9}$ (7.3, 8.4)	$17.5_{-17.1}^{+18.0}$ (5.6, 6.3)
nircam6-11480	$1.54_{-1.22}^{+1.81}$ (0.56, 0.46)	$2.03_{-1.80}^{+2.16}$ (0.78, 0.66)	$1.14_{-0.77}^{+1.45}$ (0.39, 0.33)	$1.55_{-1.21}^{+1.81}$ (0.50, 0.42)	$4.0_{-3.5}^{+4.8}$ (8.8, 7.4)	$3.1_{-3.0}^{+3.5}$ (6.8, 5.9)	$5.1_{-4.2}^{+6.9}$ (11.4, 9.4)	$4.0_{-3.5}^{+4.9}$ (9.5, 9.9)
nircam6-11797	$0.18_{-0.16}^{+0.20}$ (0.12, 0.12)	$0.28_{-0.25}^{+0.32}$ (0.17, 0.17)	$0.09_{-0.08}^{+0.10}$ (0.06, 0.06)	$0.13_{-0.12}^{+0.15}$ (0.09, 0.09)	$19.7_{-18.1}^{+21.2}$ (26.6, 27.3)	$14.4_{-13.1}^{+15.8}$ (20.9, 21.3)	$31.8_{-29.2}^{+34.1}$ (40.7, 41.4)	$24.4_{-22.7}^{+25.8}$ (33.0, 33.9)
nircam6-11812	$0.45_{-0.40}^{+0.49}$ (0.36, 0.32)	$0.68_{-0.60}^{+0.75}$ (0.52, 0.46)	$0.41_{-0.37}^{+0.46}$ (0.42, 0.38)	$0.60_{-0.53}^{+0.67}$ (0.66, 0.74)	$10.4_{-9.6}^{+11.2}$ (12.2, 13.1)	$7.6_{-7.1}^{+8.3}$ (9.3, 10.1)	$11.1_{-10.1}^{+12.0}$ (10.8, 11.6)	$8.3_{-7.7}^{+9.1}$ (7.8, 8.6)
nircam6-11843	$0.85_{-0.75}^{+0.96}$ (0.43, 0.39)	$1.07_{-0.98}^{+1.14}$ (0.58, 0.53)	$0.68_{-0.62}^{+0.77}$ (0.35, 0.41)	$0.85_{-0.75}^{+0.95}$ (0.47, 0.42)	$6.4_{-5.8}^{+7.1}$ (10.7, 11.5)	$5.4_{-5.1}^{+5.8}$ (8.5, 9.2)	$7.6_{-6.9}^{+8.2}$ (12.3, 13.4)	$6.4_{-5.9}^{+7.1}$ (10.9, 10.9)
nircam6-11936	$1.38_{-1.21}^{+1.62}$ (0.68, 0.89)	$1.70_{-1.53}^{+1.81}$ (1.05, 1.31)	$1.52_{-1.32}^{+1.71}$ (0.88, 1.10)	$1.83_{-1.70}^{+1.96}$ (1.34, 1.61)	$4.4_{-3.8}^{+4.9}$ (7.6, 6.2)	$3.7_{-3.5}^{+4.0}$ (5.4, 6.6)	$4.0_{-3.6}^{+4.5}$ (6.2, 7.7)	$3.4_{-3.2}^{+3.7}$ (4.5, 5.3)
nircam6-12061	$0.35_{-0.34}^{+0.35}$ (1.01, 1.01)	$0.45_{-0.44}^{+0.47}$ (1.04, 1.03)	$0.28_{-0.28}^{+0.29}$ (0.64, 0.77)	$0.34_{-0.34}^{+0.35}$ (1.01, 1.01)	$12.5_{-12.3}^{+12.7}$ (5.6, 5.9)	$10.2_{-10.0}^{+10.5}$ (5.5, 5.5)	$14.4_{-14.2}^{+14.6}$ (8.0, 6.9)	$12.5_{-12.4}^{+12.8}$ (5.6, 5.6)



# List of research publications

---

## Core publications:

- **García-Argumánez, Á.**, Pérez-González, P. G., Gil de Paz, A., et al. 2023, *Probing the Earliest Phases in the Formation of Massive Galaxies with Simulated HST+JWST Imaging Data from Illustris*, *Astrophys. J.*, 944, 3, doi:10.3847/1538-4357/aca8ff

## Related publications:

- Annunziatella, M., Pérez-González, P. G., **García-Argumánez, Á.**, et al. 2023, *Lack of influence of the environment in the earliest stages of massive galaxy formation*, *Mon. Not. R. Astron. Soc.*, 519, 1476, doi:10.1093/mnras/stac2731
- Mérida, R.M., Pérez-González, P.G., Sánchez-Blázquez, P., **García-Argumánez, Á.**, et al. 2023. *Probing the Star Formation Main Sequence down to  $10^8 M_{\odot}$  at  $1 < z < 3$* , *Astrophys. J.*, 950, 125, doi:10.3847/1538-4357/acc7a3
- Pérez-González, P.G., Barro, G., Annunziatella, M., Costantin, L., **García-Argumánez, Á.**, et al. 2023, *CEERS Key Paper. IV. A Triality in the Nature of HST-dark Galaxies*, *Astrophys. J. Lett.*, 946, L16, doi:10.3847/2041-8213/acb3a5
- Pérez-González, P.G., Costantin, L., Langeroodi, D., Rinaldi, P., Annunziatella, M., Ilbert, O., Colina, L., Nørgaard-Nielsen, H.U., Greve, T.R., Östlin, G., Wright, G., Alonso-Herrero, A., Álvarez-Márquez, J., Caputi, K., Eckart, A., Le Fèvre, O., Labiano, Á., García-Marín, M., Hjorth, J., Kendrew, S., Pye, J.P., Tikkanen, T., van der Werf, P., Walter, F., Ward, M., Bik, A., Boogaard, L., Bosman, S.E.I., Gómez, A.C., Gillman, S., Iani, E., Jermann, I., Melinder, J., Meyer, R.A., Moutard, T., van Dishoek, E., Henning, T., Lagage, P-O., Guedel, M., Peissker, F., Ray, T., Vandenbussche, B., **García-Argumánez, Á.**, and Mérida, R.M. 2023, *Life beyond 30: Probing the  $-20 < M_{UV} < -17$  Luminosity Function at  $8 < z < 13$  with the NIRCam Parallel Field of the MIRI Deep Survey*, *Astrophys. J. Lett.*, 951, L1, doi:10.3847/2041-8213/acd9d0



# Acronyms

---

<b>2D</b>	Two dimensions
<b>2D SEDs</b>	Spectral Energy Distributions in two dimensions
<b>2D SPS</b>	Stellar Population Synthesis in two dimensions
<b>2dFGRS</b>	two-degree-Field Galaxy Redshift Survey
<b>ACS</b>	Advanced Camera for Surveys
<b>AEGIS</b>	All-Wavelength Extended Groth Strip International Survey
<b>AGB</b>	Asymptotic Giant Branch
<b>AGHAST</b>	A Grism H-Alpha SpecTroscopic (survey)
<b>AGN</b>	Active Galactic Nucleus
<b>ALMA</b>	Atacama Large Millimeter/submillimeter Array
<b>BC</b>	Blue Cloud
<b>BC03</b>	Bruzual & Charlot (2003)
<b>CANDELS</b>	Cosmic Assembly Near-infrared Deep Extragalactic Legacy Survey
<b>CDM</b>	Cold Dark Matter
<b>CEERS</b>	Cosmic Evolution Early Release Science
<b>CFHT</b>	Canada–France–Hawaii Telescope
<b>CFHTLS</b>	CFHT Legacy Survey
<b>CMB</b>	Cosmic Microwave Background
<b>COS</b>	Cosmic Origins Spectrograph
<b>COSMOS</b>	Cosmic Evolution Survey
<b>COSTAR</b>	Corrective Optics Space Telescope Axial Replacement
<b>CSA</b>	Canadian Space Agency
<b>CSP</b>	Composite Stellar Population
<b>DB</b>	Database
<b>DD-ERS</b>	Directors Discretionary Early Release Science
<b>EAGLE</b>	Evolution and Assembly of GaLaxies and their Environments
<b>EGS</b>	Extended Groth Strip
<b>ERO</b>	Early Release Observations
<b>ERS</b>	Early Release Science
<b>ESA</b>	European Space Agency

---

<b>ESO</b>	European Southern Observatory
<b>ETG</b>	Early-Type Galaxy
<b>EW</b>	Equivalent Width
<b>FGS</b>	Fine Guidance Sensor
<b>FIR</b>	Far-Infrared
<b>FOC</b>	Faint Object Camera
<b>FUV</b>	Far-Ultraviolet
<b>FWHM</b>	Full Width at Half Maximum
<b>FoF</b>	Friends-of-Friends
<b>GEMS</b>	Galaxy Evolution from Morphologies and SEDs
<b>GLASS</b>	Grism Lens-Amplified Survey from Space
<b>GLF</b>	Galaxy Luminosity Function
<b>GO1</b>	Cycle 1 Guest Observers
<b>GOODS</b>	Great Observatories Origins Deep Surveys
<b>GOODS-N</b>	GOODS-North
<b>GOODS-S</b>	GOODS-South
<b>GSMF</b>	Galaxy Stellar Mass Function
<b>GTC</b>	Gran Telescopio de Canarias
<b>GTO</b>	Guaranteed Time Observations
<b>GV</b>	Green Valley
<b>HAWK-I</b>	High Acuity Wide field K-band Imager
<b>HDF</b>	Hubble Deep Field
<b>HDFN</b>	Hubble Deep Field North
<b>HDFS</b>	Hubble Deep Field South
<b>HMF</b>	Halo Mass Function
<b>HR</b>	Hertzsprung-Russell
<b>HRC</b>	High Resolution Channel
<b>HST</b>	Hubble Space Telescope
<b>HUDF</b>	Hubble Ultra Deep Field
<b>HUDF09</b>	Hubble Ultra Deep Field 2009
<b>HUGS</b>	HAWK-I UDS and GOODS Survey
<b>IFU</b>	Integral Field Unit
<b>IGM</b>	Intergalactic Medium
<b>IMF</b>	Initial Mass Function
<b>IR</b>	Infrared

---

<b>IRAC</b>	Infrared Array Camera
<b>ISAAC</b>	Infrared Spectrometer and Array Camera
<b>ISIM</b>	Integrated Science Instrument Module
<b>ISM</b>	Interstellar Medium Model
<b>IllustrisTNG</b>	Illustris The Next Generation
<b>JADES</b>	JWST Advanced Deep Extragalactic Survey
<b>JWST</b>	James Webb Space Telescope
<b>L2</b>	Second Sun-Earth Lagrange point
<b>LAE</b>	Lyman Alpha Emitter
<b>LBG</b>	Lyman Break Galaxy
<b>LCM</b>	Large Magellanic Cloud
<b>LW</b>	Long Wavelength
<b>MAST</b>	Mikulski Archive for Space Telescopes
<b>MC</b>	Monte Carlo
<b>MILES</b>	Medium resolution Isaac Newton Telescope Library of Empirical Spectra
<b>MIR</b>	Mid-Infrared
<b>MIRI</b>	Mid-Infrared Instrument
<b>MODS</b>	MOIRCS Deep Survey
<b>MOIRCS</b>	Multi-Object InfraRed Camera and Spectrograph
<b>MOS</b>	Multi-Object Spectroscopy
<b>MOSDEF</b>	MOSFIRE Deep Evolution Field (survey)
<b>MSA</b>	Microshutter Assembly (MSA)
<b>MW</b>	Milky Way
<b>NASA</b>	National Aeronautics and Space Administration
<b>NEWFIRM</b>	NOAO Extremely Wide-Field Infrared Imager
<b>NGST</b>	Next Generation Space Telescope
<b>NIC3</b>	NICMOS Camera 3
<b>NICMOS</b>	Near Infrared Camera and Multi-Object Spectrometer
<b>NIR</b>	Near-Infrared
<b>NIRCam</b>	Near-Infrared Camera
<b>NIRISS</b>	Near-Infrared Slitless Spectrograph
<b>NIRSpec</b>	Near-Infrared Spectrograph
<b>NMBS</b>	NEWFIRM Medium-Band Survey
<b>NOAO</b>	National Optical Astronomy Observatory
<b>OTE</b>	Optical Telescope Element

---

<b>PAHs</b>	Polycyclic Aromatic Hydrocarbons
<b>PI</b>	Principal Investigator
<b>PRIMER</b>	Public Release IMaging for Extragalactic Research
<b>PSF</b>	Point Spread Function
<b>RS</b>	Red Sequence
<b>S-CANDELS</b>	Spitzer-Cosmic Assembly Deep Near-infrared Extragalactic Legacy Survey
<b>SB99</b>	STARBURST99
<b>SBC</b>	Solar Blind Channel
<b>SDSS</b>	Sloan Digital Sky Survey
<b>SED</b>	Spectral Energy Distribution
<b>SEDS</b>	Spitzer Extended Deep Survey
<b>SF</b>	Star Formation
<b>SFH</b>	Star Formation History
<b>SFMS</b>	Star Forming Main Sequence
<b>SFR</b>	Star Formation Rate
<b>SFRD</b>	Star Formation Rate Density
<b>SHARDS</b>	Survey for High-z Absorption Red and Dead Sources
<b>SM</b>	Servicing Mission
<b>SMBH</b>	Super-Massive Black Hole
<b>SN</b>	Supernova
<b>SNII</b>	Type II Supernova
<b>SNIa</b>	Type Ia Supernova
<b>SNR</b>	Signal-to-Noise Ratio
<b>SPS</b>	Stellar Population Synthesis
<b>SSP</b>	Single Stellar Population
<b>STIS</b>	Space Telescope Imaging Spectrograph
<b>STScI</b>	Space Telescope Science Institute
<b>SVO</b>	Spanish Virtual Observatory
<b>SW</b>	Short Wavelength
<b>SpUDS</b>	Spitzer UKIDSS Ultra Deep Survey
<b>TEMPLATES</b>	Targeting Extremely Magnified Panchromatic Lensed Arcs and Their Extended Star Formation
<b>TMA</b>	Three-Mirror Anastigmat
<b>TP-AGB</b>	Thermally Pulsing Asymptotic Giant Branch
<b>UDS</b>	UKIDSS Ultra Deep Survey
<b>UKIDSS</b>	UKIRT Infrared Deep Sky Survey



---

<b>UKIRT</b>	United Kingdom Infrared Telescope
<b>UV</b>	Ultraviolet
<b>UltraVISTA</b>	Ultra Deep Survey with the VISTA telescope
<b>VIMOS</b>	Visible Multi-Object Spectrograph
<b>VISTA</b>	Visible and Infrared Survey Telescope for Astronomy
<b>VLT</b>	Very Large Telescope
<b>WFC</b>	Wide Field Channel
<b>WFC3</b>	Wide Field Camera 3
<b>WFI</b>	Wide-Field Instrument
<b>WFPC1</b>	Wide Field Planetary Camera 1
<b>WFPC2</b>	Wide Field Planetary Camera 2
<b>WFSS</b>	Wide Field Slitless Spectroscopy
<b>WIMP</b>	Weakly Interacting Massive Particle
<b>WIRCam</b>	Wide-field InfraRed Camera
<b>WIRDS</b>	WIRCam Deep Survey
<b>WLM</b>	Wolf–Lundmark–Melotte
<b>WMAP</b>	Wilkinson Microwave Anisotropy Probe
<b>XDF</b>	Hubble eXtreme Deep Field
<b>sSFR</b>	Specific Star Formation Rate



# Bibliography

---

- Abdurro'uf, Lin, Y.-T., Hirashita, H., Morishita, T., Tacchella, S., Akiyama, M., Takeuchi, T. T., and Wu, P.-F.: 2022, *ApJ* **926**(1), 81
- Adams, N. J., Conselice, C. J., Ferreira, L., Austin, D., Trussler, J. A. A., Juodžbalis, I., Wilkins, S. M., Caruana, J., Dayal, P., Verma, A., and Vijayan, A. P.: 2023, *MNRAS* **518**(3), 4755
- Akhshik, M., Whitaker, K. E., Leja, J., Richard, J., Spilker, J. S., Song, M., Brammer, G., Bezanson, R., Ebeling, H., Gallazzi, A. R., Mahler, G., Mowla, L. A., Nelson, E. J., Pacifici, C., Sharon, K., Toft, S., Williams, C. C., Wright, L., and Zabl, J.: 2022, *arXiv e-prints* p. arXiv:2203.04979
- Alcalde Pampliega, B., Pérez-González, P. G., Barro, G., Domínguez Sánchez, H., Eliche-Moral, M. C., Cardiel, N., Hernán-Caballero, A., Rodríguez-Muñoz, L., Sánchez Blázquez, P., and Esquej, P.: 2019, *ApJ* **876**(2), 135
- Alongi, M., Bertelli, G., Bressan, A., Chiosi, C., Fagotto, F., Greggio, L., and Nasi, E.: 1993, *A&AS* **97**, 851
- Anders, P. and Fritze-v. Alvensleben, U.: 2003, *A&A* **401**, 1063
- Angulo, R. E. and Hahn, O.: 2022, *Living Reviews in Computational Astrophysics* **8**(1), 1
- Angulo, R. E., Springel, V., White, S. D. M., Jenkins, A., Baugh, C. M., and Frenk, C. S.: 2012, *MNRAS* **426**(3), 2046
- Ashby, M. L. N., Willner, S. P., Fazio, G. G., Dunlop, J. S., Egami, E., Faber, S. M., Ferguson, H. C., Grogin, N. A., Hora, J. L., Huang, J. S., Koekemoer, A. M., Labbé, I., and Wang, Z.: 2015, *ApJS* **218**(2), 33
- Ashby, M. L. N., Willner, S. P., Fazio, G. G., Huang, J. S., Arendt, R., Barmby, P., Barro, G., Bell, E. F., Bouwens, R., Cattaneo, A., Croton, D., Davé, R., Dunlop, J. S., Egami, E., Faber, S., Finlator, K., Grogin, N. A., Guhathakurta, P., Hernquist, L., Hora, J. L., Illingworth, G., Kashlinsky, A., Koekemoer, A. M., Koo, D. C., Labbé, I., Li, Y., Lin, L., Moseley, H., Nandra, K., Newman, J., Noeske, K., Ouchi, M., Peth, M., Rigopoulou, D., Robertson, B., Sarajedini, V., Simard, L., Smith, H. A., Wang, Z., Wechsler, R., Weiner, B., Wilson, G., Wuyts, S., Yamada, T., and Yan, H.: 2013, *ApJ* **769**(1), 80
- Atek, H., Shuntov, M., Furtak, L. J., Richard, J., Kneib, J.-P., Mahler, G., Zitrin, A., McCracken, H. J., Charlot, S., Chevillard, J., and Chemerynska, I.: 2023, *MNRAS* **519**(1), 1201
- Bagley, M. B., Finkelstein, S. L., Koekemoer, A. M., Ferguson, H. C., Arrabal Haro, P., Dickinson, M., Kartaltepe, J. S., Papovich, C., Pérez-González, P. G., Pirzkal, N., Somerville, R. S., Willmer, C. N. A., Yang, G., Yung, L. Y. A., Fontana, A., Grazian, A., Grogin, N. A., Hirschmann, M., Kewley, L. J., Kirkpatrick, A., Kocevski, D. D., Lotz, J. M., Medrano, A., Morales, A. M., Pentericci, L., Ravindranath, S., Trump, J. R., Wilkins, S. M., Calabrò, A., Cooper, M. C., Costantin, L., de la Vega, A., Hilbert, B., Hutchison, T. A., Larson, R. L., Lucas, R. A., McGrath, E. J., Ryan, R., Wang, X., and Wuyts, S.: 2023, *ApJ* **946**(1), L12

- Bagley, M. B., Finkelstein, S. L., Koekemoer, A. M., Ferguson, H. C., Arrabal Haro, P., Dickinson, M., Kartaltepe, J. S., Papovich, C., Pérez-González, P. G., Pirzkal, N., Somerville, R. S., Willmer, C. N. A., Yang, G., Yung, L. Y. A., Fontana, A., Grazian, A., Grogin, N. A., Hirschmann, M., Kewley, L. J., Kirkpatrick, A., Kocevski, D. D., Lotz, J. M., Medrano, A., Morales, A. M., Pentericci, L., Ravindranath, S., Trump, J. R., Wilkins, S. M., Calabrò, A., Cooper, M. C., Costantin, L., de la Vega, A., Hutchison, T. A., Lucas, R. A., McGrath, E. J., Wang, X., and Wuyts, S.: 2022, *arXiv e-prints* p. arXiv:2211.02495
- Barkana, R. and Loeb, A.: 2001, *Phys. Rep.* **349(2)**, 125
- Barro, G., Faber, S. M., Pérez-González, P. G., Koo, D. C., Williams, C. C., Kocevski, D. D., Trump, J. R., Mozena, M., McGrath, E., van der Wel, A., Wuyts, S., Bell, E. F., Croton, D. J., Ceverino, D., Dekel, A., Ashby, M. L. N., Cheung, E., Ferguson, H. C., Fontana, A., Fang, J., Gialalisco, M., Grogin, N. A., Guo, Y., Hathi, N. P., Hopkins, P. F., Huang, K.-H., Koekemoer, A. M., Kartaltepe, J. S., Lee, K.-S., Newman, J. A., Porter, L. A., Primack, J. R., Ryan, R. E., Rosario, D., Somerville, R. S., Salvato, M., and Hsu, L.-T.: 2013, *ApJ* **765(2)**, 104
- Barro, G., Faber, S. M., Pérez-González, P. G., Pacifici, C., Trump, J. R., Koo, D. C., Wuyts, S., Guo, Y., Bell, E., Dekel, A., Porter, L., Primack, J., Ferguson, H., Ashby, M. L. N., Caputi, K., Ceverino, D., Croton, D., Fazio, G. G., Gialalisco, M., Hsu, L., Kocevski, D., Koekemoer, A., Kurczynski, P., Kollipara, P., Lee, J., McIntosh, D. H., McGrath, E., Moody, C., Somerville, R., Papovich, C., Salvato, M., Santini, P., Tal, T., van der Wel, A., Williams, C. C., Willner, S. P., and Zolotov, A.: 2014, *ApJ* **791(1)**, 52
- Barro, G., Pérez-González, P. G., Cava, A., Brammer, G., Pandya, V., Eliche Moral, C., Esquej, P., Domínguez-Sánchez, H., Alcalde Pampliega, B., Guo, Y., Koekemoer, A. M., Trump, J. R., Ashby, M. L. N., Cardiel, N., Castellano, M., Conselice, C. J., Dickinson, M. E., Dolch, T., Donley, J. L., Espino Briones, N., Faber, S. M., Fazio, G. G., Ferguson, H., Finkelstein, S., Fontana, A., Galametz, A., Gardner, J. P., Gawiser, E., Gialalisco, M., Grazian, A., Grogin, N. A., Hathi, N. P., Hemmati, S., Hernán-Caballero, A., Kocevski, D., Koo, D. C., Kodra, D., Lee, K.-S., Lin, L., Lucas, R. A., Mobasher, B., McGrath, E. J., Nandra, K., Nayyeri, H., Newman, J. A., Pforr, J., Peth, M., Rafelski, M., Rodríguez-Munoz, L., Salvato, M., Stefanon, M., van der Wel, A., Willner, S. P., Wiklind, T., and Wuyts, S.: 2019, *ApJS* **243(2)**, 22
- Bastian, N., Covey, K. R., and Meyer, M. R.: 2010, *ARA&A* **48**, 339
- Beckwith, S. V. W., Stiavelli, M., Koekemoer, A. M., Caldwell, J. A. R., Ferguson, H. C., Hook, R., Lucas, R. A., Bergeron, L. E., Corbin, M., Jogee, S., Panagia, N., Robberto, M., Royle, P., Somerville, R. S., and Sosey, M.: 2006a, *AJ* **132(5)**, 1729
- Beckwith, S. V. W., Stiavelli, M., Koekemoer, A. M., Caldwell, J. A. R., Ferguson, H. C., Hook, R., Lucas, R. A., Bergeron, L. E., Corbin, M., Jogee, S., Panagia, N., Robberto, M., Royle, P., Somerville, R. S., and Sosey, M.: 2006b, *AJ* **132(5)**, 1729
- Behroozi, P., Wechsler, R. H., Hearin, A. P., and Conroy, C.: 2019, *MNRAS* **488(3)**, 3143
- Behroozi, P. S. and Silk, J.: 2015, *ApJ* **799(1)**, 32
- Behroozi, P. S., Wechsler, R. H., and Conroy, C.: 2013, *ApJ* **770(1)**, 57
- Beichman, C. A., Rieke, M., Eisenstein, D., Greene, T. P., Krist, J., McCarthy, D., Meyer, M., and Stansberry, J.: 2012, in M. C. Clampin, G. G. Fazio, H. A. MacEwen, and J. Oschmann, Jacobus M. (eds.), *Space Telescopes and Instrumentation 2012: Optical, Infrared, and Millimeter Wave*, Vol. 8442 of *Society of Photo-Optical Instrumentation Engineers (SPIE) Conference Series*, p. 84422N
- Bell, E. F., McIntosh, D. H., Katz, N., and Weinberg, M. D.: 2003, *ApJS* **149(2)**, 289
- Bellardini, M. A., Wetzel, A., Loebman, S. R., and Bailin, J.: 2022, *MNRAS* **514(3)**, 4270

- Belleville, M.: 2022, *Hubble Fast Facts*, <https://www.nasa.gov/content/about-facts-hubble-fast-facts>, Accessed: 2022-01-23
- Bernardi, M., Meert, A., Sheth, R. K., Fischer, J. L., Huertas-Company, M., Maraston, C., Shankar, F., and Vikram, V.: 2017, *MNRAS* **467**(2), 2217
- Bertelli, G., Bressan, A., Chiosi, C., Fagotto, F., and Nasi, E.: 1994, *A&AS* **106**, 275
- Bertin, E. and Arnouts, S.: 1996, *A&AS* **117**, 393
- Bertone, G., Hooper, D., and Silk, J.: 2005, *Phys. Rep.* **405**(5-6), 279
- Biagetti, M., Franciolini, G., and Riotto, A.: 2023, *ApJ* **944**(2), 113
- Bielby, R., Hudelot, P., McCracken, H. J., Ilbert, O., Daddi, E., Le Fèvre, O., Gonzalez-Perez, V., Kneib, J. P., Marmo, C., Mellier, Y., Salvato, M., Sanders, D. B., and Willott, C. J.: 2012, *A&A* **545**, A23
- Blanton, M. R. and Moustakas, J.: 2009, *ARA&A* **47**(1), 159
- Bond, J. R., Cole, S., Efstathiou, G., and Kaiser, N.: 1991, *ApJ* **379**, 440
- Bond, J. R., Kofman, L., and Pogosyan, D.: 1996, *Nature* **380**(6575), 603
- Bouwens, R. J., Illingworth, G. D., Blakeslee, J. P., Broadhurst, T. J., and Franx, M.: 2004, *ApJ* **611**(1), L1
- Bouwens, R. J., Illingworth, G. D., Oesch, P. A., Labbé, I., Trenti, M., van Dokkum, P., Franx, M., Stiavelli, M., Carollo, C. M., Magee, D., and Gonzalez, V.: 2011, *ApJ* **737**(2), 90
- Bouwens, R. J., Illingworth, G. D., Oesch, P. A., Stiavelli, M., van Dokkum, P., Trenti, M., Magee, D., Labbé, I., Franx, M., Carollo, C. M., and Gonzalez, V.: 2010, *ApJ* **709**(2), L133
- Bouwens, R. J., Illingworth, G. D., Oesch, P. A., Trenti, M., Labbé, I., Bradley, L., Carollo, M., van Dokkum, P. G., Gonzalez, V., Holwerda, B., Franx, M., Spitler, L., Smit, R., and Magee, D.: 2015, *ApJ* **803**(1), 34
- Boylan-Kolchin, M.: 2023, *Nature Astronomy*
- Boylan-Kolchin, M., Springel, V., White, S. D. M., Jenkins, A., and Lemson, G.: 2009, *MNRAS* **398**(3), 1150
- Bradley, L. D., Coe, D., Brammer, G., Furtak, L. J., Larson, R. L., Andrade-Santos, F., Bhatavdekar, R., Bradac, M., Broadhurst, T., Carnall, A., Conselice, C. J., Diego, J. M., Frye, B., Fujimoto, S., Y. -Y Hsiao, T., Hutchison, T. A., Jung, I., Mahler, G., McCandliss, S., Oguri, M., Postman, M., Sharon, K., Trenti, M., Vanzella, E., Welch, B., Windhorst, R. A., and Zitrin, A.: 2022, *arXiv e-prints* p. arXiv:2210.01777
- Brammer, G. B., van Dokkum, P. G., and Coppi, P.: 2008, *ApJ* **686**(2), 1503
- Brammer, G. B., van Dokkum, P. G., Franx, M., Fumagalli, M., Patel, S., Rix, H.-W., Skelton, R. E., Kriek, M., Nelson, E., Schmidt, K. B., Bezanson, R., da Cunha, E., Erb, D. K., Fan, X., Förster Schreiber, N., Illingworth, G. D., Labbé, I., Leja, J., Lundgren, B., Magee, D., Marchesini, D., McCarthy, P., Momcheva, I., Muzzin, A., Quadri, R., Steidel, C. C., Tal, T., Wake, D., Whitaker, K. E., and Williams, A.: 2012, *ApJS* **200**(2), 13
- Bressan, A., Fagotto, F., Bertelli, G., and Chiosi, C.: 1993, *A&AS* **100**, 647
- Brocklehurst, M.: 1971, *MNRAS* **153**, 471
- Bromm, V.: 2013, *Reports on Progress in Physics* **76**(11), 112901

- Bromm, V., Coppi, P. S., and Larson, R. B.: 2002, *ApJ* **564**(1), 23
- Bromm, V., Ferrara, A., Coppi, P. S., and Larson, R. B.: 2001, *MNRAS* **328**(3), 969
- Bromm, V. and Yoshida, N.: 2011, *ARA&A* **49**(1), 373
- Bruce, V. A., Dunlop, J. S., McLure, R. J., Cirasuolo, M., Buitrago, F., Bowler, R. A. A., Targett, T. A., Bell, E. F., McIntosh, D. H., Dekel, A., Faber, S. M., Ferguson, H. C., Grogin, N. A., Hartley, W., Kocevski, D. D., Koekemoer, A. M., Koo, D. C., and McGrath, E. J.: 2014, *MNRAS* **444**(2), 1001
- Bruzual, G.: 1983, *ApJ* **273**, 105
- Bruzual, G. and Charlot, S.: 1993, *ApJ* **405**, 538
- Bruzual, G. and Charlot, S.: 2003, *MNRAS* **344**(4), 1000
- Calzetti, D., Armus, L., Bohlin, R. C., Kinney, A. L., Koornneef, J., and Storchi-Bergmann, T.: 2000, *ApJ* **533**(2), 682
- Cameron, A. J., Katz, H., Rey, M. P., and Saxena, A.: 2023, *MNRAS* **523**(3), 3516
- Cardelli, J. A., Clayton, G. C., and Mathis, J. S.: 1989, *ApJ* **345**, 245
- Carnall, A. C., McLeod, D. J., McLure, R. J., Dunlop, J. S., Begley, R., Cullen, F., Donnan, C. T., Hamadouche, M. L., Jewell, S. M., Jones, E. W., Pollock, C. L., and Wild, V.: 2023, *MNRAS*
- Carnall, A. C., Walker, S., McLure, R. J., Dunlop, J. S., McLeod, D. J., Cullen, F., Wild, V., Amorin, R., Bolzonella, M., Castellano, M., Cimatti, A., Cucciati, O., Fontana, A., Gargiulo, A., Garilli, B., Jarvis, M. J., Pentericci, L., Pozzetti, L., Zamorani, G., Calabro, A., Hathi, N. P., and Koekemoer, A. M.: 2020, *MNRAS* **496**(1), 695
- Carollo, C. M., Bschorr, T. J., Renzini, A., Lilly, S. J., Capak, P., Cibinel, A., Ilbert, O., Onodera, M., Scoville, N., Cameron, E., Mobasher, B., Sanders, D., and Taniguchi, Y.: 2013, *ApJ* **773**(2), 112
- Castellano, M., Fontana, A., Treu, T., Santini, P., Merlin, E., Leethochawalit, N., Trenti, M., Vanzella, E., Mestric, U., Bonchi, A., Belfiori, D., Nonino, M., Paris, D., Polenta, G., Roberts-Borsani, G., Boyett, K., Bradač, M., Calabrò, A., Glazebrook, K., Grillo, C., Mascia, S., Mason, C., Mercurio, A., Morishita, T., Nanayakkara, T., Pentericci, L., Rosati, P., Vulcani, B., Wang, X., and Yang, L.: 2022, *ApJ* **938**(2), L15
- Catalán-Torrecilla, C., Gil de Paz, A., Castillo-Morales, A., Méndez-Abreu, J., Falcón-Barroso, J., Bekeraitė, S., Costantin, L., de Lorenzo-Cáceres, A., Florido, E., García-Benito, R., Husemann, B., Iglesias-Páramo, J., Kennicutt, R. C., Mast, D., Pascual, S., Ruiz-Lara, T., Sánchez-Menguiano, L., Sánchez, S. F., Walcher, C. J., Bland-Hawthorn, J., Duarte Puertas, S., Marino, R. A., Masegosa, J., Sánchez-Blázquez, P., and CALIFA Collaboration: 2017, *ApJ* **848**(2), 87
- Chabrier, G.: 2003, *PASP* **115**(809), 763
- Chamorro-Cazorla, M., Gil de Paz, A., Castillo-Morales, A., Dullo, B. T., Gallego, J., Carrasco, E., Iglesias-Páramo, J., Cedazo, R., García-Vargas, M. L., Pascual, S., Cardiel, N., Pérez-Calpena, A., Gómez-Álvarez, P., Martínez-Delgado, I., and Catalán-Torrecilla, C.: 2022, *A&A* **657**, A95
- Charbonneau, P.: 1995, *ApJS* **101**, 309
- Charlot, S. and Bruzual, G.: 1991, *ApJ* **367**, 126
- Charlot, S. and Fall, S. M.: 2000, *ApJ* **539**(2), 718

- Chary, R. and Elbaz, D.: 2001, *ApJ* **556**(2), 562
- Chiosi, C., Bertelli, G., and Bressan, A.: 1988, *A&A* **196**, 84
- Cimatti, A., Fraternali, F., and Nipoti, C.: 2020, *Introduction to galaxy formation and evolution: from primordial gas to present-day galaxies*
- Cirasuolo, M., McLure, R. J., Dunlop, J. S., Almaini, O., Foucaud, S., Smail, I., Sekiguchi, K., Simpson, C., Eales, S., Dye, S., Watson, M. G., Page, M. J., and Hirst, P.: 2007, *MNRAS* **380**(2), 585
- Clark, P. C., Glover, S. C. O., and Klessen, R. S.: 2008, *ApJ* **672**(2), 757
- Clark, P. C., Glover, S. C. O., Klessen, R. S., and Bromm, V.: 2011, *ApJ* **727**(2), 110
- Coelho, P., Barbu, B., Meléndez, J., Schiavon, R. P., and Castilho, B. V.: 2005, *A&A* **443**(2), 735
- Conroy, C.: 2013, *ARA&A* **51**(1), 393
- Cook, B. A., Conroy, C., Pillepich, A., Rodriguez-Gomez, V., and Hernquist, L.: 2016, *ApJ* **833**(2), 158
- Cooray, A., Aguirre, J., Ali-Haïmoud, Y., Alvarez, M., Appleton, P., Armus, L., Becker, G., Bock, J., Bowler, R., Bowman, J., Bradford, M., Breyse, P., Bromm, V., Burns, J., Caputi, K., Castellano, M., Chang, T.-C., Chary, R., Chiang, H., Cohn, J., Conselice, C., Cuby, J.-G., Davies, F., Dayal, P., Dore, O., Farrah, D., Ferrara, A., Finkelstein, S., Furlanetto, S., Hazelton, B., Heneka, C., Hutter, A., Jacobs, D., Koopmans, L., Kovetz, E., La Plante, P., Le Fevre, O., Liu, A., Ma, J., Ma, Y.-Z., Malhotra, S., Mao, Y., Marrone, D., Masui, K., McQuinn, M., Mirocha, J., Mortlock, D., Murphy, E., Nayyeri, H., Natarajan, P., Nithyanandan, T., Parsons, A., Pello, R., Pope, A., Rhoads, J., Rhodes, J., Riechers, D., Robertson, B., Scarlata, C., Serjeant, S., Saliwanchik, B., Salvaterra, R., Schneider, R., Silva, M., Sahlén, M., Santos, M. G., Switzer, E., Temi, P., Trac, H., Venkatesan, A., Visbal, E., Zaldarriaga, M., Zemcov, M., and Zheng, Z.: 2019, *BAAS* **51**(3), 48
- Cordier, D., Pietrinferni, A., Cassisi, S., and Salaris, M.: 2007, *AJ* **133**(2), 468
- Costantin, L., Pérez-González, P. G., Méndez-Abreu, J., Huertas-Company, M., Dimauro, P., Alcalde-Pampliega, B., Buitrago, F., Ceverino, D., Daddi, E., Domínguez-Sánchez, H., Espino-Briones, N., Hernán-Caballero, A., Koekemoer, A. M., and Rodighiero, G.: 2021, *ApJ* **913**(2), 125
- Costantin, L., Pérez-González, P. G., Méndez-Abreu, J., Huertas-Company, M., Pampliega, B. A., Balcells, M., Barro, G., Ceverino, D., Dimauro, P., Sánchez, H. D., Espino-Briones, N., and Koekemoer, A. M.: 2022, *ApJ* **929**(2), 121
- Couchman, H. M. P. and Rees, M. J.: 1986, *MNRAS* **221**, 53
- Cowie, L. L., Songaila, A., Hu, E. M., and Cohen, J. G.: 1996, *AJ* **112**, 839
- Crain, R. A., Schaye, J., Bower, R. G., Furlong, M., Schaller, M., Theuns, T., Dalla Vecchia, C., Frenk, C. S., McCarthy, I. G., Helly, J. C., Jenkins, A., Rosas-Guevara, Y. M., White, S. D. M., and Trayford, J. W.: 2015, *MNRAS* **450**(2), 1937
- da Cunha, E., Charlot, S., and Elbaz, D.: 2008, *MNRAS* **388**(4), 1595
- Daddi, E., Renzini, A., Pirzkal, N., Cimatti, A., Malhotra, S., Stiavelli, M., Xu, C., Pasquali, A., Rhoads, J. E., Brusa, M., di Serego Alighieri, S., Ferguson, H. C., Koekemoer, A. M., Moustakas, L. A., Panagia, N., and Windhorst, R. A.: 2005, *ApJ* **626**(2), 680

- Dahlen, T., Mobasher, B., Faber, S. M., Ferguson, H. C., Barro, G., Finkelstein, S. L., Finlator, K., Fontana, A., Gruetzbauch, R., Johnson, S., Pforr, J., Salvato, M., Wiklind, T., Wuyts, S., Acquaviva, V., Dickinson, M. E., Guo, Y., Huang, J., Huang, K.-H., Newman, J. A., Bell, E. F., Conselice, C. J., Galametz, A., Gawiser, E., Giavalisco, M., Grogin, N. A., Hathi, N., Kocevski, D., Koekemoer, A. M., Koo, D. C., Lee, K.-S., McGrath, E. J., Papovich, C., Peth, M., Ryan, R., Somerville, R., Weiner, B., and Wilson, G.: 2013, *ApJ* **775(2)**, 93
- Davé, R., Anglés-Alcázar, D., Narayanan, D., Li, Q., Rafieferantsoa, M. H., and Appleby, S.: 2019, *MNRAS* **486(2)**, 2827
- Davis, M., Efstathiou, G., Frenk, C. S., and White, S. D. M.: 1985, *ApJ* **292**, 371
- Davis, M., Guhathakurta, P., Konidaris, N. P., Newman, J. A., Ashby, M. L. N., Biggs, A. D., Barmby, P., Bundy, K., Chapman, S. C., Coil, A. L., Conselice, C. J., Cooper, M. C., Croton, D. J., Eisenhardt, P. R. M., Ellis, R. S., Faber, S. M., Fang, T., Fazio, G. G., Georgakakis, A., Gerke, B. F., Goss, W. M., Gwyn, S., Harker, J., Hopkins, A. M., Huang, J. S., Ivison, R. J., Kassin, S. A., Kirby, E. N., Koekemoer, A. M., Koo, D. C., Laird, E. S., Le Floch, E., Lin, L., Lotz, J. M., Marshall, P. J., Martin, D. C., Metevier, A. J., Moustakas, L. A., Nandra, K., Noeske, K. G., Papovich, C., Phillips, A. C., Rich, R. M., Rieke, G. H., Rigopoulou, D., Salim, S., Schiminovich, D., Simard, L., Smail, I., Small, T. A., Weiner, B. J., Willmer, C. N. A., Willner, S. P., Wilson, G., Wright, E. L., and Yan, R.: 2007, *ApJ* **660(1)**, L1
- Davison, T. A., Norris, M. A., Pfeffer, J. L., Davies, J. J., and Crain, R. A.: 2020, *MNRAS* **497(1)**, 81
- Dayal, P. and Ferrara, A.: 2018, *Phys. Rep.* **780**, 1
- De Lucia, G. and Blaizot, J.: 2007, *MNRAS* **375(1)**, 2
- Dekel, A. and Burkert, A.: 2014, *MNRAS* **438(2)**, 1870
- Di Matteo, P., Haywood, M., Combes, F., Semelin, B., and Snaith, O. N.: 2013, *A&A* **553**, A102
- Di Matteo, T., Springel, V., and Hernquist, L.: 2005, *Nature* **433(7026)**, 604
- Dickinson, M., Bergeron, J., Casertano, S., Cesarsky, C., Chary, R.-R., Cristiani, S., Eisenhardt, P., Elbaz, D., Elston, R., Fall, S. M., Ferguson, H. C., Fosbury, R., Giacomini, R., Giavalisco, M., Grogin, N., Hauser, M., Hanisch, R., Hook, R., J  rgensen, I., Koekemoer, A., Ledlow, M., Livio, M., Mobasher, B., Padovani, P., Papovich, C., Primack, J., Rauscher, B., Reach, W., Renzini, A., Rieke, M., Rosati, P., Roth, K., Roy, J.-R., Schreier, E., Stern, D., Stiavelli, M., Takamiya, M., Tollestrup, E., Urry, M., Williams, R., Winge, C., and Wright, E. L.: 2003, *Great Observatories Origins Deep Survey (GOODS) Validation Observations*, Spitzer Proposal ID 196
- Diego, J. M.: 2019, *A&A* **625**, A84
- Diemand, J., Kuhlen, M., Madau, P., Zemp, M., Moore, B., Potter, D., and Stadel, J.: 2008, *Nature* **454(7205)**, 735
- Dolag, K., Borgani, S., Murante, G., and Springel, V.: 2009, *MNRAS* **399(2)**, 497
- Dom  nguez S  nchez, H., P  rez-Gonz  lez, P. G., Esquej, P., Eliche-Moral, M. C., Barro, G., Cava, A., Koekemoer, A. M., Alcalde Pampliega, B., Alonso Herrero, A., Bruzual, G., Cardiel, N., Cenarro, J., Ceverino, D., Charlot, S., and Hern  n Caballero, A.: 2016, *MNRAS* **457(4)**, 3743
- Donnan, C. T., McLeod, D. J., Dunlop, J. S., McLure, R. J., Carnall, A. C., Begley, R., Cullen, F., Hamadouche, M. L., Bowler, R. A. A., Magee, D., McCracken, H. J., Milvang-Jensen, B., Moneti, A., and Targett, T.: 2023, *MNRAS* **518(4)**, 6011



- Doyon, R., Hutchings, J. B., Beaulieu, M., Albert, L., Lafrenière, D., Willott, C., Touahri, D., Rowlands, N., Maszkiewicz, M., Fullerton, A. W., Volk, K., Martel, A. R., Chayer, P., Sivaramakrishnan, A., Abraham, R., Ferrarese, L., Jayawardhana, R., Johnstone, D., Meyer, M., Pipher, J. L., and Sawicki, M.: 2012, in M. C. Clampin, G. G. Fazio, H. A. MacEwen, and J. Oschmann, Jacobus M. (eds.), *Space Telescopes and Instrumentation 2012: Optical, Infrared, and Millimeter Wave*, Vol. 8442 of *Society of Photo-Optical Instrumentation Engineers (SPIE) Conference Series*, p. 84422R
- Draine, B. T. and Li, A.: 2007, *ApJ* **657**(2), 810
- Dressel, L.: 2022, in *WFC3 Instrument Handbook for Cycle 30 v. 14*, Vol. 14, p. 14
- Dubois, Y., Peirani, S., Pichon, C., Devriendt, J., Gavazzi, R., Welker, C., and Volonteri, M.: 2016, *MNRAS* **463**(4), 3948
- Dubois, Y., Pichon, C., Welker, C., Le Borgne, D., Devriendt, J., Laigle, C., Codis, S., Pogosyan, D., Arnouts, S., Benabed, K., Bertin, E., Blaizot, J., Bouchet, F., Cardoso, J. F., Colombi, S., de Lapparent, V., Desjacques, V., Gavazzi, R., Kassin, S., Kimm, T., McCracken, H., Milliard, B., Peirani, S., Prunet, S., Rouberol, S., Silk, J., Slyz, A., Sousbie, T., Teyssier, R., Tresse, L., Treyer, M., Vibert, D., and Volonteri, M.: 2014, *MNRAS* **444**(2), 1453
- Dunlop, J. S., Abraham, R. G., Ashby, M. L. N., Bagley, M., Best, P. N., Bongiorno, A., Bouwens, R., Bowler, R. A. A., Brammer, G., Bremer, M., Calabro', A., Carnall, A., Castellano, M., Cirasuolo, M., Conselice, C., Cullen, F., Dave, R., Dayal, P., Dekel, A., Dickinson, M., Duncan, K. J., Elbaz, D., Ellis, R. S., Ferguson, H. C., Ferrara, A., Finkelstein, S. L., Fontana, A., Furlanetto, S., Fynbo, J. P. U., Gallerani, S., Gardner, J. P., Giavalisco, M., Grazian, A., Grogin, N., Harikane, Y., Hopkins, P. F., Ilbert, O., Illingworth, G. D., Juneau, S., Jung, I., Kartaltepe, J., Kassin, S., Kauffmann, O. B., Khochfar, S., Kirkpatrick, A., Kocevski, D. D., Koekemoer, A. M., Labbe, I., Laporte, N., Larson, R. L., Lucas, R. A., Magee, D. K., Mason, C., McCracken, H. J., McLeod, D., McLure, R., Merlin, E., Mesinger, A., Milvang-Jensen, B., Newman, J. A., Oesch, P., Ouchi, M., Pacifici, C., Papovich, C., Peacock, J., Peeples, M., Pentericci, L., Perez-Gonzalez, P. G., Pirzkal, N., Pope, A., Pye, J. P., Reddy, N. A., Robertson, B., Salvato, M., Santini, P., Schaerer, D., Shapley, A. E., Simons, R., Smit, R., Smith, B. D., Snyder, G., Somerville, R. S., Stanway, E. R., Stefanon, M., Tasca, L., Tikkanen, T., Tresse, L., Trump, J. R., Whitaker, K. E., Wilkins, S. M., Wright, G., Wyithe, J. S. B., van Dokkum, P., and van der Werf, P.: 2021, *PRIMER: Public Release IMaging for Extragalactic Research*, JWST Proposal. Cycle 1, ID. #1837
- Elias, L. M., Sales, L. V., Creasey, P., Cooper, M. C., Bullock, J. S., Rich, R. M., and Hernquist, L.: 2018, *MNRAS* **479**(3), 4004
- Ellis, R. S., McLure, R. J., Dunlop, J. S., Robertson, B. E., Ono, Y., Schenker, M. A., Koekemoer, A., Bowler, R. A. A., Ouchi, M., Rogers, A. B., Curtis-Lake, E., Schneider, E., Charlot, S., Stark, D. P., Furlanetto, S. R., and Cirasuolo, M.: 2013a, *ApJ* **763**(1), L7
- Ellis, R. S., McLure, R. J., Dunlop, J. S., Robertson, B. E., Ono, Y., Schenker, M. A., Koekemoer, A., Bowler, R. A. A., Ouchi, M., Rogers, A. B., Curtis-Lake, E., Schneider, E., Charlot, S., Stark, D. P., Furlanetto, S. R., and Cirasuolo, M.: 2013b, *ApJ* **763**(1), L7
- Erb, D. K., Shapley, A. E., Pettini, M., Steidel, C. C., Reddy, N. A., and Adelberger, K. L.: 2006, *ApJ* **644**(2), 813
- Erfanianfar, G., Finoguenov, A., Furnell, K., Popesso, P., Biviano, A., Wuyts, S., Collins, C. A., Mirkazemi, M., Comparat, J., Khosroshahi, H., Nandra, K., Capasso, R., Rykoff, E., Wilman, D., Merloni, A., Clerc, N., Salvato, M., Chitham, J. I., Kelvin, L. S., Gozaliasl, G., Weijmans, A., Brownstein, J., Egami, E., Pereira, M. J., Schneider, D. P., Kirkpatrick, C., Damsted, S., and Kukkola, A.: 2019, *A&A* **631**, A175

- Espino-Briones, N., Pérez-González, P. G., Zamorano, J., and Rodríguez-Muñoz, L.: 2022, *MNRAS* **513**(1), 1175
- Faber, S. M.: 1972, *A&A* **20**, 361
- Fagotto, F., Bressan, A., Bertelli, G., and Chiosi, C.: 1994a, *A&AS* **104**, 365
- Fagotto, F., Bressan, A., Bertelli, G., and Chiosi, C.: 1994b, *A&AS* **105**, 29
- Faucher-Giguère, C.-A., Lidz, A., Zaldarriaga, M., and Hernquist, L.: 2009, *ApJ* **703**(2), 1416
- Ferland, G. J.: 1980, *PASP* **92**, 596
- Ferland, G. J., Porter, R. L., van Hoof, P. A. M., Williams, R. J. R., Abel, N. P., Lykins, M. L., Shaw, G., Henney, W. J., and Stancil, P. C.: 2013, *Rev. Mexicana Astron. Astrofis.* **49**, 137
- Ferré-Mateu, A., Mezcuca, M., Trujillo, I., Balcells, M., and van den Bosch, R. C. E.: 2015, *ApJ* **808**(1), 79
- Ferré-Mateu, A., Trujillo, I., Martín-Navarro, I., Vazdekis, A., Mezcuca, M., Balcells, M., and Domínguez, L.: 2017, *MNRAS* **467**(2), 1929
- Finkelstein, S. L., Bagley, M., Song, M., Larson, R., Papovich, C., Dickinson, M., Finkelstein, K. D., Koekemoer, A. M., Pirzkal, N., Somerville, R. S., Yung, L. Y. A., Behroozi, P., Ferguson, H., Giavalisco, M., Grogin, N., Hathi, N., Hutchison, T. A., Jung, I., Kocevski, D., Kawinwanichakij, L., Rojas-Ruiz, S., Ryan, R., Snyder, G. F., and Tacchella, S.: 2022a, *ApJ* **928**(1), 52
- Finkelstein, S. L., Bagley, M. B., Arrabal Haro, P., Dickinson, M., Ferguson, H. C., Kartaltepe, J. S., Papovich, C., Burgarella, D., Kocevski, D. D., Huertas-Company, M., Iyer, K. G., Koekemoer, A. M., Larson, R. L., Pérez-González, P. G., Rose, C., Tacchella, S., Wilkins, S. M., Chworowsky, K., Medrano, A., Morales, A. M., Somerville, R. S., Yung, L. Y. A., Fontana, A., Giavalisco, M., Grazian, A., Grogin, N. A., Kewley, L. J., Kirkpatrick, A., Kurczynski, P., Lotz, J. M., Pentericci, L., Pirzkal, N., Ravindranath, S., Ryan, R. E., Trump, J. R., Yang, G., Almaini, O., Amorín, R. O., Annunziatella, M., Backhaus, B. E., Barro, G., Behroozi, P., Bell, E. F., Bhatawdekar, R., Bisigello, L., Bromm, V., Buat, V., Buitrago, F., Calabrò, A., Casey, C. M., Castellano, M., Chávez Ortiz, Ó. A., Ciesla, L., Cleri, N. J., Cohen, S. H., Cole, J. W., Cooke, K. C., Cooper, M. C., Cooray, A. R., Costantin, L., Cox, I. G., Croton, D., Daddi, E., Davé, R., de La Vega, A., Dekel, A., Elbaz, D., Estrada-Carpenter, V., Faber, S. M., Fernández, V., Finkelstein, K. D., Freundlich, J., Fujimoto, S., García-Argumánuez, Á., Gardner, J. P., Gawiser, E., Gómez-Guijarro, C., Guo, Y., Hamblin, K., Hamilton, T. S., Hathi, N. P., Holwerda, B. W., Hirschmann, M., Hutchison, T. A., Jaskot, A. E., Jha, S. W., Jogee, S., Juneau, S., Jung, I., Kassin, S. A., Le Bail, A., Leung, G. C. K., Lucas, R. A., Magnelli, B., Mantha, K. B., Matharu, J., McGrath, E. J., McIntosh, D. H., Merlin, E., Mobasher, B., Newman, J. A., Nicholls, D. C., Pandya, V., Rafelski, M., Ronayne, K., Santini, P., Seillé, L.-M., Shah, E. A., Shen, L., Simons, R. C., Snyder, G. F., Stanway, E. R., Straughn, A. N., Teplitz, H. I., Vanderhoof, B. N., Vega-Ferrero, J., Wang, W., Weiner, B. J., Willmer, C. N. A., Wuyts, S., Zavala, J. A., and CEERS Team: 2022b, *ApJ* **940**(2), L55
- Finkelstein, S. L., Bagley, M. B., Ferguson, H. C., Wilkins, S. M., Kartaltepe, J. S., Papovich, C., Yung, L. Y. A., Haro, P. A., Behroozi, P., Dickinson, M., Kocevski, D. D., Koekemoer, A. M., Larson, R. L., Le Bail, A., Morales, A. M., Pérez-González, P. G., Burgarella, D., Davé, R., Hirschmann, M., Somerville, R. S., Wuyts, S., Bromm, V., Casey, C. M., Fontana, A., Fujimoto, S., Gardner, J. P., Giavalisco, M., Grazian, A., Grogin, N. A., Hathi, N. P., Hutchison, T. A., Jha, S. W., Jogee, S., Kewley, L. J., Kirkpatrick, A., Long, A. S., Lotz, J. M., Pentericci, L., Pierel, J. D. R., Pirzkal, N., Ravindranath, S., Ryan, R. E., Trump, J. R., Yang, G., Bhatawdekar, R., Bisigello, L., Buat, V., Calabrò, A., Castellano, M., Cleri, N. J., Cooper, M. C., Croton, D., Daddi, E., Dekel, A., Elbaz, D., Franco, M., Gawiser, E., Holwerda, B. W., Huertas-Company, M., Jaskot, A. E., Leung, G. C. K., Lucas, R. A., Mobasher, B., Pandya, V., Tacchella, S., Weiner, B. J., and Zavala, J. A.: 2023, *ApJ* **946**(1), L13

- Finkelstein, S. L., Dickinson, M., Ferguson, H. C., Grazian, A., Grogin, N., Kartaltepe, J., Kewley, L., Kocevski, D. D., Koekemoer, A. M., Lotz, J., Papovich, C., Pentericci, L., Perez-Gonzalez, P. G., Pirzkal, N., Ravindranath, S., Somerville, R. S., Trump, J. R., and Wilkins, S. M.: 2017, *The Cosmic Evolution Early Release Science (CEERS) Survey*, JWST Proposal ID 1345. Cycle 0 Early Release Science
- Finkelstein, S. L., Papovich, C., Dickinson, M., Song, M., Tilvi, V., Koekemoer, A. M., Finkelstein, K. D., Mobasher, B., Ferguson, H. C., Giavalisco, M., Reddy, N., Ashby, M. L. N., Dekel, A., Fazio, G. G., Fontana, A., Grogin, N. A., Huang, J. S., Kocevski, D., Rafelski, M., Weiner, B. J., and Willner, S. P.: 2013, *Nature* **502(7472)**, 524
- Fioc, M. and Rocca-Volmerange, B.: 1997, *A&A* **326**, 950
- Flury, S. R., Jaskot, A. E., Ferguson, H. C., Worseck, G., Makan, K., Chisholm, J., Saldana-Lopez, A., Schaerer, D., McCandliss, S., Wang, B., Ford, N. M., Heckman, T., Ji, Z., Giavalisco, M., Amorin, R., Atek, H., Blaizot, J., Borthakur, S., Carr, C., Castellano, M., Cristiani, S., De Barros, S., Dickinson, M., Finkelstein, S. L., Fleming, B., Fontanot, F., Garel, T., Grazian, A., Hayes, M., Henry, A., Mauerhofer, V., Micheva, G., Oey, M. S., Ostlin, G., Papovich, C., Pentericci, L., Ravindranath, S., Rosdahl, J., Rutkowski, M., Santini, P., Scarlata, C., Teplitz, H., Thuan, T., Trebitsch, M., Vanzella, E., Verhamme, A., and Xu, X.: 2022, *ApJS* **260(1)**, 1
- Fontana, A., Dunlop, J. S., Paris, D., Targett, T. A., Boutsia, K., Castellano, M., Galametz, A., Grazian, A., McLure, R., Merlin, E., Pentericci, L., Wuyts, S., Almaini, O., Caputi, K., Chary, R. R., Cirasuolo, M., Conselice, C. J., Cooray, A., Daddi, E., Dickinson, M., Faber, S. M., Fazio, G., Ferguson, H. C., Giallongo, E., Giavalisco, M., Grogin, N. A., Hathi, N., Koekemoer, A. M., Koo, D. C., Lucas, R. A., Nonino, M., Rix, H. W., Renzini, A., Rosario, D., Santini, P., Scarlata, C., Sommariva, V., Stark, D. P., van der Wel, A., Vanzella, E., Wild, V., Yan, H., and Zibetti, S.: 2014, *A&A* **570**, A11
- Forrest, B., Annunziatella, M., Wilson, G., Marchesini, D., Muzzin, A., Cooper, M. C., Marsan, Z. C., McConachie, I., Chan, J. C. C., Gomez, P., Kado-Fong, E., L Barbera, F., Labbé, I., Lange-Vagle, D., Nantais, J., Nonino, M., Peña, T., Saracco, P., Stefanon, M., and van der Burg, R. F. J.: 2020a, *ApJ* **890(1)**, L1
- Forrest, B., Marsan, Z. C., Annunziatella, M., Wilson, G., Muzzin, A., Marchesini, D., Cooper, M. C., Chan, J. C. C., McConachie, I., Gomez, P., Kado-Fong, E., La Barbera, F., Lange-Vagle, D., Nantais, J., Nonino, M., Saracco, P., Stefanon, M., and van der Burg, R. F. J.: 2020b, *ApJ* **903(1)**, 47
- Fu, H., Cooray, A., Feruglio, C., Ivison, R. J., Riechers, D. A., Gurwell, M., Bussmann, R. S., Harris, A. I., Altieri, B., Aussel, H., Baker, A. J., Bock, J., Boylan-Kolchin, M., Bridge, C., Calanog, J. A., Casey, C. M., Cava, A., Chapman, S. C., Clements, D. L., Conley, A., Cox, P., Farrah, D., Frayer, D., Hopwood, R., Jia, J., Magdis, G., Marsden, G., Martínez-Navajas, P., Negrello, M., Neri, R., Oliver, S. J., Omont, A., Page, M. J., Pérez-Fournon, I., Schulz, B., Scott, D., Smith, A., Vaccari, M., Valtchanov, I., Vieira, J. D., Viero, M., Wang, L., Wardlow, J. L., and Zemcov, M.: 2013, *Nature* **498(7454)**, 338
- Fukugita, M., Hogan, C. J., and Peebles, P. J. E.: 1998, *ApJ* **503(2)**, 518
- Furusawa, H., Kosugi, G., Akiyama, M., Takata, T., Sekiguchi, K., Tanaka, I., Iwata, I., Kajisawa, M., Yasuda, N., Doi, M., Ouchi, M., Simpson, C., Shimasaku, K., Yamada, T., Furusawa, J., Morokuma, T., Ishida, C. M., Aoki, K., Fuse, T., Imanishi, M., Iye, M., Karoji, H., Kobayashi, N., Kodama, T., Komiyama, Y., Maeda, Y., Miyazaki, S., Mizumoto, Y., Nakata, F., Noumaru, J., Ogasawara, R., Okamura, S., Saito, T., Sasaki, T., Ueda, Y., and Yoshida, M.: 2008, *ApJS* **176(1)**, 1
- Galametz, A., Grazian, A., Fontana, A., Ferguson, H. C., Ashby, M. L. N., Barro, G., Castellano, M., Dahlen, T., Donley, J. L., Faber, S. M., Grogin, N., Guo, Y., Huang, K.-H., Kocevski, D. D., Koekemoer, A. M., Lee, K.-S., McGrath, E. J., Peth, M., Willner, S. P., Almaini, O., Cooper, M., Cooray, A., Conselice, C. J., Dickinson, M., Dunlop, J. S., Fazio, G. G., Foucaud, S., Gardner, J. P., Giavalisco, M., Hathi, N. P.,

- Hartley, W. G., Koo, D. C., Lai, K., de Mello, D. F., McLure, R. J., Lucas, R. A., Paris, D., Pentericci, L., Santini, P., Simpson, C., Sommariva, V., Targett, T., Weiner, B. J., Wuyts, S., and CANDELS Team: 2013, *ApJS* **206**(2), 10
- Gallazzi, A., Charlot, S., Brinchmann, J., White, S. D. M., and Tremonti, C. A.: 2005, *MNRAS* **362**(1), 41
- Gallego, J., Zamorano, J., Rego, M., Alonso, O., and Vitores, A. G.: 1996, *A&AS* **120**, 323
- Gao, L., Navarro, J. F., Frenk, C. S., Jenkins, A., Springel, V., and White, S. D. M.: 2012, *MNRAS* **425**(3), 2169
- García-Argumánuez, Á., Pérez-González, P. G., de Paz, A. G., Snyder, G. F., Haro, P. A., Bagley, M. B., Finkelstein, S. L., Kartaltepe, J. S., Koekemoer, A., Papovich, C., Pirzkal, N., Ferguson, H. C., Yung, L. Y. A., Annunziatella, M., Cleri, N. J., Cooper, M. C., Costantin, L., Holwerda, B. W., Mérida, R. M., Rose, C., Giavalisco, M., Grogin, N. A., and Kocevski, D. D.: 2023, *ApJ* **944**(1), 3
- Gardner, J. P., Mather, J. C., Clampin, M., Doyon, R., Greenhouse, M. A., Hammel, H. B., Hutchings, J. B., Jakobsen, P., Lilly, S. J., Long, K. S., Lunine, J. I., McCaughrean, M. J., Mountain, M., Nella, J., Rieke, G. H., Rieke, M. J., Rix, H.-W., Smith, E. P., Sonneborn, G., Stiavelli, M., Stockman, H. S., Windhorst, R. A., and Wright, G. S.: 2006, *Space Sci. Rev.* **123**(4), 485
- Garner, R.: 2019, *Hubble's Mirror Flaw*, <https://www.nasa.gov/content/hubbles-mirror-flaw>, Accessed: 2022-01-23
- Garner, R.: 2022a, *Hubble History Timeline*, <https://www.nasa.gov/content/goddard/hubble-history-timeline>, Accessed: 2022-01-23
- Garner, R.: 2022b, *Hubble's Observatory - Optics*, <https://www.nasa.gov/content/goddard/hubble-space-telescope-optics-system>, Accessed: 2022-01-24
- Garner, R.: 2022c, *Hubble's Observatory - Pointing Control*, <https://www.nasa.gov/content/goddard/hubble-space-telescope-pointing-control-system>, Accessed: 2022-01-24
- Garrison-Kimmel, S., Boylan-Kolchin, M., Bullock, J. S., and Lee, K.: 2014, *MNRAS* **438**(3), 2578
- Gavazzi, G., Bonfanti, C., Sanvito, G., Boselli, A., and Scodreggio, M.: 2002, *ApJ* **576**(1), 135
- Genel, S., Vogelsberger, M., Nelson, D., Sijacki, D., Springel, V., and Hernquist, L.: 2013, *MNRAS* **435**(2), 1426
- Genel, S., Vogelsberger, M., Springel, V., Sijacki, D., Nelson, D., Snyder, G., Rodriguez-Gomez, V., Torrey, P., and Hernquist, L.: 2014, *MNRAS* **445**(1), 175
- Giavalisco, M., Ferguson, H. C., Koekemoer, A. M., Dickinson, M., Alexander, D. M., Bauer, F. E., Bergeron, J., Biagetti, C., Brandt, W. N., Casertano, S., Cesarsky, C., Chatzichristou, E., Conselice, C., Cristiani, S., Da Costa, L., Dahlen, T., de Mello, D., Eisenhardt, P., Erben, T., Fall, S. M., Fassnacht, C., Fosbury, R., Fruchter, A., Gardner, J. P., Grogin, N., Hook, R. N., Hornschemeier, A. E., Idzi, R., Joglee, S., Kretchmer, C., Laidler, V., Lee, K. S., Livio, M., Lucas, R., Madau, P., Mobasher, B., Moustakas, L. A., Nonino, M., Padovani, P., Papovich, C., Park, Y., Ravindranath, S., Renzini, A., Richardson, M., Riess, A., Rosati, P., Schirmer, M., Schreier, E., Somerville, R. S., Spinrad, H., Stern, D., Stiavelli, M., Strolger, L., Urry, C. M., Vandame, B., Williams, R., and Wolf, C.: 2004, *ApJ* **600**(2), L93
- Gil de Paz, A. and Madore, B. F.: 2002, *AJ* **123**(4), 1864
- Girardi, L., Bertelli, G., Bressan, A., Chiosi, C., Groenewegen, M. A. T., Marigo, P., Salasnich, B., and Weiss, A.: 2002, *A&A* **391**, 195

- Girardi, L., Bressan, A., Bertelli, G., and Chiosi, C.: 2000, *A&AS* **141**, 371
- Girardi, L., Bressan, A., Chiosi, C., Bertelli, G., and Nasi, E.: 1996, *A&AS* **117**, 113
- Glazebrook, K., Schreiber, C., Labbé, I., Nanayakkara, T., Kacprzak, G. G., Oesch, P. A., Papovich, C., Spitler, L. R., Straatman, C. M. S., Tran, K.-V. H., and Yuan, T.: 2017, *Nature* **544(7648)**, 71
- Grand, R. J. J., Gómez, F. A., Marinacci, F., Pakmor, R., Springel, V., Campbell, D. J. R., Frenk, C. S., Jenkins, A., and White, S. D. M.: 2017, *MNRAS* **467(1)**, 179
- Greif, T. H.: 2015, *Computational Astrophysics and Cosmology* **2**, 3
- Greif, T. H., Bromm, V., Clark, P. C., Glover, S. C. O., Smith, R. J., Klessen, R. S., Yoshida, N., and Springel, V.: 2012, *MNRAS* **424(1)**, 399
- Greif, T. H., Glover, S. C. O., Bromm, V., and Klessen, R. S.: 2010, *ApJ* **716(1)**, 510
- Greif, T. H., Johnson, J. L., Klessen, R. S., and Bromm, V.: 2008, *MNRAS* **387(3)**, 1021
- Grogin, N. A., Kocevski, D. D., Faber, S. M., Ferguson, H. C., Koekemoer, A. M., Riess, A. G., Acquaviva, V., Alexander, D. M., Almaini, O., Ashby, M. L. N., Barden, M., Bell, E. F., Bournaud, F., Brown, T. M., Caputi, K. I., Casertano, S., Cassata, P., Castellano, M., Challis, P., Chary, R.-R., Cheung, E., Cirasuolo, M., Conselice, C. J., Roshan Cooray, A., Croton, D. J., Daddi, E., Dahlen, T., Davé, R., de Mello, D. F., Dekel, A., Dickinson, M., Dolch, T., Donley, J. L., Dunlop, J. S., Dutton, A. A., Elbaz, D., Fazio, G. G., Filippenko, A. V., Finkelstein, S. L., Fontana, A., Gardner, J. P., Garnavich, P. M., Gawiser, E., Giavalisco, M., Grazian, A., Guo, Y., Hathi, N. P., Häussler, B., Hopkins, P. F., Huang, J.-S., Huang, K.-H., Jha, S. W., Kartaltepe, J. S., Kirshner, R. P., Koo, D. C., Lai, K., Lee, K.-S., Li, W., Lotz, J. M., Lucas, R. A., Madau, P., McCarthy, P. J., McGrath, E. J., McIntosh, D. H., McLure, R. J., Mobasher, B., Moustakas, L. A., Mozena, M., Nandra, K., Newman, J. A., Niemi, S.-M., Noeske, K. G., Papovich, C. J., Pentericci, L., Pope, A., Primack, J. R., Rajan, A., Ravindranath, S., Reddy, N. A., Renzini, A., Rix, H.-W., Robaina, A. R., Rodney, S. A., Rosario, D. J., Rosati, P., Salimbeni, S., Scarlata, C., Siana, B., Simard, L., Smidt, J., Somerville, R. S., Spinrad, H., Straughn, A. N., Strolger, L.-G., Telford, O., Teplitz, H. I., Trump, J. R., van der Wel, A., Villforth, C., Wechsler, R. H., Weiner, B. J., Wiklind, T., Wild, V., Wilson, G., Wuyts, S., Yan, H.-J., and Yun, M. S.: 2011, *ApJS* **197(2)**, 35
- Groves, B. A., Dopita, M. A., and Sutherland, R. S.: 2004, *ApJS* **153(1)**, 9
- Guedes, J., Callegari, S., Madau, P., and Mayer, L.: 2011, *ApJ* **742(2)**, 76
- Guo, Y., Ferguson, H. C., Giavalisco, M., Barro, G., Willner, S. P., Ashby, M. L. N., Dahlen, T., Donley, J. L., Faber, S. M., Fontana, A., Galametz, A., Grazian, A., Huang, K.-H., Kocevski, D. D., Koekemoer, A. M., Koo, D. C., McGrath, E. J., Peth, M., Salvato, M., Wuyts, S., Castellano, M., Cooray, A. R., Dickinson, M. E., Dunlop, J. S., Fazio, G. G., Gardner, J. P., Gawiser, E., Grogin, N. A., Hathi, N. P., Hsu, L.-T., Lee, K.-S., Lucas, R. A., Mobasher, B., Nandra, K., Newman, J. A., and van der Wel, A.: 2013, *ApJS* **207(2)**, 24
- Gwyn, S. D. J.: 2012, *AJ* **143(2)**, 38
- Hainline, K. N., Johnson, B. D., Robertson, B., Tacchella, S., Helton, J. M., Sun, F., Eisenstein, D. J., Simmonds, C., Topping, M. W., Whitler, L., Willmer, C. N. A., Rieke, M., Suess, K. A., Hviding, R. E., Cameron, A. J., Alberts, S., Baker, W. M., Bhatawdekar, R., Boyett, K., Bunker, A. J., Carniani, S., Charlot, S., Chen, Z., Curti, M., Curtis-Lake, E., D'Eugenio, F., Egami, E., Endsley, R., Hausen, R., Ji, Z., Looser, T. J., Lyu, J., Maiolino, R., Nelson, E., Puskas, D., Rawle, T., Sandles, L., Saxena, A., Smit, R., Stark, D. P., Williams, C. C., Willott, C., and Witstok, J.: 2023, *arXiv e-prints* p. arXiv:2306.02468

- Harikane, Y., Ouchi, M., Oguri, M., Ono, Y., Nakajima, K., Isobe, Y., Umeda, H., Mawatari, K., and Zhang, Y.: 2022, *arXiv e-prints* p. arXiv:2208.01612
- Harikane, Y., Ouchi, M., Oguri, M., Ono, Y., Nakajima, K., Isobe, Y., Umeda, H., Mawatari, K., and Zhang, Y.: 2023, *ApJS* **265**(1), 5
- Hartwig, T., Magg, M., Chen, L.-H., Tarumi, Y., Bromm, V., Glover, S. C. O., Ji, A. P., Klessen, R. S., Latif, M. A., Volonteri, M., and Yoshida, N.: 2022, *ApJ* **936**(1), 45
- Haslbauer, M., Kroupa, P., Zonoozi, A. H., and Haghi, H.: 2022, *ApJ* **939**(2), L31
- Heavens, A., Panter, B., Jimenez, R., and Dunlop, J.: 2004, *Nature* **428**(6983), 625
- Henriques, B. M. B., White, S. D. M., Lemson, G., Thomas, P. A., Guo, Q., Marleau, G.-D., and Overzier, R. A.: 2012, *MNRAS* **421**(4), 2904
- Hillier, D. J. and Miller, D. L.: 1998, *ApJ* **496**(1), 407
- Hinshaw, G., Larson, D., Komatsu, E., Spergel, D. N., Bennett, C. L., Dunkley, J., Nolte, M. R., Halpern, M., Hill, R. S., Odegard, N., Page, L., Smith, K. M., Weiland, J. L., Gold, B., Jarosik, N., Kogut, A., Limon, M., Meyer, S. S., Tucker, G. S., Wollack, E., and Wright, E. L.: 2013, *ApJS* **208**(2), 19
- Hirano, S., Hosokawa, T., Yoshida, N., Omukai, K., and Yorke, H. W.: 2015, *MNRAS* **448**(1), 568
- Hirano, S., Hosokawa, T., Yoshida, N., Umeda, H., Omukai, K., Chiaki, G., and Yorke, H. W.: 2014, *ApJ* **781**(2), 60
- Ho, I. T., Meidt, S. E., Kudritzki, R.-P., Groves, B. A., Seibert, M., Madore, B. F., Schinnerer, E., Rich, J. A., Kobayashi, C., and Kewley, L. J.: 2018, *A&A* **618**, A64
- Höfner, S., Loidl, R., Aringer, B., Jørgensen, U. G., and Hron, J.: 2000, in A. Salama, M. F. Kessler, K. Leech, and B. Schulz (eds.), *ISO Beyond the Peaks: The 2nd ISO Workshop on Analytical Spectroscopy*, Vol. 456 of *ESA Special Publication*, p. 299
- Hsu, L.-T., Lin, L., Dickinson, M., Yan, H., Bau-Ching, H., Wang, W.-H., Lee, C.-H., Yan, C.-H., Scott, D., Willner, S. P., Ouchi, M., Ashby, M. L. N., Chen, Y.-W., Daddi, E., Elbaz, D., Fazio, G. G., Foucaud, S., Huang, J., Koo, D. C., Morrison, G., Owen, F., Pannella, M., Pope, A., Simard, L., and Wang, S.-Y.: 2019, *ApJ* **871**(2), 233
- Hutchison, T. A., Papovich, C., Finkelstein, S. L., Dickinson, M., Jung, I., Zitrin, A., Ellis, R., Malhotra, S., Rhoads, J., Roberts-Borsani, G., Song, M., and Tilvi, V.: 2019, *ApJ* **879**(2), 70
- Illingworth, G. D., Magee, D., Oesch, P. A., Bouwens, R. J., Labbé, I., Stiavelli, M., van Dokkum, P. G., Franx, M., Trenti, M., Carollo, C. M., and Gonzalez, V.: 2013a, *ApJS* **209**(1), 6
- Illingworth, G. D., Magee, D., Oesch, P. A., Bouwens, R. J., Labbé, I., Stiavelli, M., van Dokkum, P. G., Franx, M., Trenti, M., Carollo, C. M., and Gonzalez, V.: 2013b, *ApJS* **209**(1), 6
- Isobe, Y., Ouchi, M., Tominaga, N., Watanabe, K., Nakajima, K., Umeda, H., Yajima, H., Harikane, Y., Fukushima, H., Xu, Y., Ono, Y., and Zhang, Y.: 2023, *arXiv e-prints* p. arXiv:2307.00710
- Iyer, K. G., Tacchella, S., Genel, S., Hayward, C. C., Hernquist, L., Brooks, A. M., Caplar, N., Davé, R., Diemer, B., Forbes, J. C., Gawiser, E., Somerville, R. S., and Starkenburg, T. K.: 2020, *MNRAS* **498**(1), 430

- Jakobsen, P., Ferruit, P., Alves de Oliveira, C., Arribas, S., Bagnasco, G., Barho, R., Beck, T. L., Birkmann, S., Böker, T., Bunker, A. J., Charlot, S., de Jong, P., de Marchi, G., Ehrenwinkler, R., Falcolini, M., Fels, R., Franx, M., Franz, D., Funke, M., Giardino, G., Gnata, X., Holota, W., Honnen, K., Jensen, P. L., Jentsch, M., Johnson, T., Jollet, D., Karl, H., Kling, G., Köhler, J., Kolm, M. G., Kumari, N., Lander, M. E., Lemke, R., López-Caniego, M., Lützgendorf, N., Maiolino, R., Manjavacas, E., Marston, A., Maschmann, M., Maurer, R., Messerschmidt, B., Moseley, S. H., Mosner, P., Mott, D. B., Muzerolle, J., Pirzkal, N., Pittet, J. F., Plitzke, A., Posselt, W., Rapp, B., Rauscher, B. J., Rawle, T., Rix, H. W., Rödel, A., Rumler, P., Sabbi, E., Salvignol, J. C., Schmid, T., Sirianni, M., Smith, C., Strada, P., te Plate, M., Valenti, J., Wettemann, T., Wiehe, T., Wiesmayer, M., Willott, C. J., Wright, R., Zeidler, P., and Zincke, C.: 2022, *A&A* **661**, A80
- Ji, Z. and Giavalisco, M.: 2023, *ApJ* **943**(1), 54
- Johnson, B. D., Leja, J., Conroy, C., and Speagle, J. S.: 2021, *ApJS* **254**(2), 22
- Johnston, E. J., Häußler, B., and Jegatheesan, K.: 2022, *MNRAS* **514**(4), 6120
- Jonsson, P.: 2006, *MNRAS* **372**(1), 2
- Jonsson, P., Groves, B. A., and Cox, T. J.: 2010, *MNRAS* **403**(1), 17
- JWST: 2016, *JWST User Documentation (JDox)*, JWST User Documentation Website
- Kajisawa, M., Ichikawa, T., Tanaka, I., Konishi, M., Yamada, T., Akiyama, M., Suzuki, R., Tokoku, C., Uchimoto, Y. K., Yoshikawa, T., Ouchi, M., Iwata, I., Hamana, T., and Onodera, M.: 2009, *ApJ* **702**(2), 1393
- Katz, N., Weinberg, D. H., and Hernquist, L.: 1996, *ApJS* **105**, 19
- Kennicutt, Robert C., J.: 1989, *ApJ* **344**, 685
- Khandai, N., Di Matteo, T., Croft, R., Wilkins, S., Feng, Y., Tucker, E., DeGraf, C., and Liu, M.-S.: 2015, *MNRAS* **450**(2), 1349
- Kirby, E. N., Cohen, J. G., Guhathakurta, P., Cheng, L., Bullock, J. S., and Gallazzi, A.: 2013, *ApJ* **779**(2), 102
- Kitzbichler, M. G. and White, S. D. M.: 2007, *MNRAS* **376**(1), 2
- Klessen, R. S. and Glover, S. C. O.: 2023, *arXiv e-prints* p. arXiv:2303.12500
- Klypin, A. A., Trujillo-Gomez, S., and Primack, J.: 2011, *ApJ* **740**(2), 102
- Koekemoer, A. M., Ellis, R. S., McLure, R. J., Dunlop, J. S., Robertson, B. E., Ono, Y., Schenker, M. A., Ouchi, M., Bowler, R. A. A., Rogers, A. B., Curtis-Lake, E., Schneider, E., Charlot, S., Stark, D. P., Furlanetto, S. R., Cirasuolo, M., Wild, V., and Targett, T.: 2013a, *ApJS* **209**(1), 3
- Koekemoer, A. M., Ellis, R. S., McLure, R. J., Dunlop, J. S., Robertson, B. E., Ono, Y., Schenker, M. A., Ouchi, M., Bowler, R. A. A., Rogers, A. B., Curtis-Lake, E., Schneider, E., Charlot, S., Stark, D. P., Furlanetto, S. R., Cirasuolo, M., Wild, V., and Targett, T.: 2013b, *ApJS* **209**(1), 3
- Koekemoer, A. M., Faber, S. M., Ferguson, H. C., Grogin, N. A., Kocevski, D. D., Koo, D. C., Lai, K., Lotz, J. M., Lucas, R. A., McGrath, E. J., Ogaz, S., Rajan, A., Riess, A. G., Rodney, S. A., Strolger, L., Casertano, S., Castellano, M., Dahlen, T., Dickinson, M., Dolch, T., Fontana, A., Giavalisco, M., Grazian, A., Guo, Y., Hathi, N. P., Huang, K.-H., van der Wel, A., Yan, H.-J., Acquaviva, V., Alexander, D. M., Almaini, O., Ashby, M. L. N., Barden, M., Bell, E. F., Bournaud, F., Brown, T. M., Caputi, K. I., Cassata,

- P., Challis, P. J., Chary, R.-R., Cheung, E., Cirasuolo, M., Conselice, C. J., Roshan Cooray, A., Croton, D. J., Daddi, E., Davé, R., de Mello, D. F., de Ravel, L., Dekel, A., Donley, J. L., Dunlop, J. S., Dutton, A. A., Elbaz, D., Fazio, G. G., Filippenko, A. V., Finkelstein, S. L., Frazer, C., Gardner, J. P., Garnavich, P. M., Gawiser, E., Gruetzbauch, R., Hartley, W. G., Häußler, B., Herrington, J., Hopkins, P. F., Huang, J.-S., Jha, S. W., Johnson, A., Kartaltepe, J. S., Khostovan, A. A., Kirshner, R. P., Lani, C., Lee, K.-S., Li, W., Madau, P., McCarthy, P. J., McIntosh, D. H., McLure, R. J., McPartland, C., Mobasher, B., Moreira, H., Mortlock, A., Moustakas, L. A., Mozena, M., Nandra, K., Newman, J. A., Nielsen, J. L., Niemi, S., Noeske, K. G., Papovich, C. J., Pentericci, L., Pope, A., Primack, J. R., Ravindranath, S., Reddy, N. A., Renzini, A., Rix, H.-W., Robaina, A. R., Rosario, D. J., Rosati, P., Salimbeni, S., Scarlata, C., Siana, B., Simard, L., Smidt, J., Snyder, D., Somerville, R. S., Spinrad, H., Straughn, A. N., Telford, O., Teplitz, H. I., Trump, J. R., Vargas, C., Villforth, C., Wagner, C. R., Wandro, P., Wechsler, R. H., Weiner, B. J., Wiklind, T., Wild, V., Wilson, G., Wuyts, S., and Yun, M. S.: 2011, *ApJS* **197**(2), 36
- Korsch, D.: 1972, *Appl. Opt.* **11**(12), 2986
- Kriek, M., Shapley, A. E., Reddy, N. A., Siana, B., Coil, A. L., Mobasher, B., Freeman, W. R., de Groot, L., Price, S. H., Sanders, R., Shivaee, I., Brammer, G. B., Momcheva, I. G., Skelton, R. E., van Dokkum, P. G., Whitaker, K. E., Aird, J., Azadi, M., Kassis, M., Bullock, J. S., Conroy, C., Davé, R., Kereš, D., and Krumholz, M.: 2015, *ApJS* **218**(2), 15
- Kroupa, P.: 2001, *MNRAS* **322**(2), 231
- Kubo, J. M., Stebbins, A., Annis, J., Dell’Antonio, I. P., Lin, H., Khiabani, H., and Frieman, J. A.: 2007, *ApJ* **671**(2), 1466
- Labbé, I., van Dokkum, P., Nelson, E., Bezanson, R., Suess, K. A., Leja, J., Brammer, G., Whitaker, K., Mathews, E., Stefanon, M., and Wang, B.: 2023, *Nature* **616**(7956), 266
- Lacey, C. and Cole, S.: 1994, *MNRAS* **271**, 676
- Larson, R. B.: 1985, *MNRAS* **214**, 379
- Lawrence, A., Warren, S. J., Almaini, O., Edge, A. C., Hambly, N. C., Jameson, R. F., Lucas, P., Casali, M., Adamson, A., Dye, S., Emerson, J. P., Foucaud, S., Hewett, P., Hirst, P., Hodgkin, S. T., Irwin, M. J., Lodiéu, N., McMahan, R. G., Simpson, C., Smail, I., Mortlock, D., and Folger, M.: 2007, *MNRAS* **379**(4), 1599
- Le Bertre, T.: 1997, *A&A* **324**, 1059
- Le Borgne, J. F., Bruzual, G., Pelló, R., Lançon, A., Rocca-Volmerange, B., Sanahuja, B., Schaerer, D., Soubiran, C., and Vílchez-Gómez, R.: 2003, *A&A* **402**, 433
- Le Sidaner, P. and Le Bertre, T.: 1996, *A&A* **314**, 896
- Lee, J. and Yi, S. K.: 2013, *ApJ* **766**(1), 38
- Lee, J. and Yi, S. K.: 2017, *ApJ* **836**(2), 161
- Lee, S.-K., Ferguson, H. C., Somerville, R. S., Wiklind, T., and Giavalisco, M.: 2010, *ApJ* **725**(2), 1644
- Leitherer, C., Ekström, S., Meynet, G., Schaerer, D., Agienko, K. B., and Levesque, E. M.: 2014, *ApJS* **212**(1), 14
- Leitherer, C., Ortiz Otálvaro, P. A., Bresolin, F., Kudritzki, R.-P., Lo Faro, B., Pauldrach, A. W. A., Pettini, M., and Rix, S. A.: 2010, *ApJS* **189**(2), 309



- Leitherer, C., Schaerer, D., Goldader, J. D., Delgado, R. M. G., Robert, C., Kune, D. F., de Mello, D. F., Devost, D., and Heckman, T. M.: 1999, *ApJS* **123**(1), 3
- Leja, J., Johnson, B. D., Conroy, C., van Dokkum, P. G., and Byler, N.: 2017, *ApJ* **837**(2), 170
- Licquia, T. C. and Newman, J. A.: 2015, *ApJ* **806**(1), 96
- Madau, P. and Dickinson, M.: 2014, *ARA&A* **52**, 415
- Maeder, A. and Meynet, G.: 1987, *A&A* **182**, 243
- Maiolino, R., Nagao, T., Grazian, A., Cocchia, F., Marconi, A., Mannucci, F., Cimatti, A., Pipino, A., Ballero, S., Calura, F., Chiappini, C., Fontana, A., Granato, G. L., Matteucci, F., Pastorini, G., Pentericci, L., Risaliti, G., Salvati, M., and Silva, L.: 2008, *A&A* **488**(2), 463
- Mannucci, F., Cresci, G., Maiolino, R., Marconi, A., Pastorini, G., Pozzetti, L., Gnerucci, A., Risaliti, G., Schneider, R., Lehnert, M., and Salvati, M.: 2009, *MNRAS* **398**(4), 1915
- Maraston, C.: 2005, *MNRAS* **362**(3), 799
- Maraston, C., Pforr, J., Renzini, A., Daddi, E., Dickinson, M., Cimatti, A., and Tonini, C.: 2010, *MNRAS* **407**(2), 830
- Marigo, P., Girardi, L., Bressan, A., Groenewegen, M. A. T., Silva, L., and Granato, G. L.: 2008, *A&A* **482**(3), 883
- Marinacci, F., Vogelsberger, M., Pakmor, R., Torrey, P., Springel, V., Hernquist, L., Nelson, D., Weinberger, R., Pillepich, A., Naiman, J., and Genel, S.: 2018, *MNRAS* **480**(4), 5113
- Marsan, Z. C., Muzzin, A., Marchesini, D., Stefanon, M., Martis, N., Annunziatella, M., Chan, J. C. C., Cooper, M. C., Forrest, B., Gomez, P., McConachie, I., and Wilson, G.: 2022, *ApJ* **924**(1), 25
- Martins, L. P., González Delgado, R. M., Leitherer, C., Cerviño, M., and Hauschildt, P.: 2005, *MNRAS* **358**(1), 49
- McCracken, H. J., Milvang-Jensen, B., Dunlop, J., Franx, M., Fynbo, J. P. U., Le Fèvre, O., Holt, J., Caputi, K. I., Goranova, Y., Buitrago, F., Emerson, J., Freudling, W., Herent, O., Hudelot, P., López-Sanjuan, C., Magnard, F., Muzzin, A., Mellier, Y., Møller, P., Nilsson, K. K., Sutherland, W., Tasca, L., and Zabl, J.: 2013, *The Messenger* **154**, 29
- McElwain, M. W., Feinberg, L. D., Perrin, M. D., Clampin, M., Mountain, C. M., Lallo, M. D., Lajoie, C.-P., Kimble, R. A., Bowers, C. W., Stark, C. C., Acton, D. S., Aiello, K., Atkinson, C., Barinek, B., Barto, A., Basinger, S., Beck, T., Bergkoetter, M. D., Bluth, M., Boucarut, R. A., Brady, G. R., Brooks, K. J., Brown, B., Byard, J., Carey, L., Carrasquilla, M., Celeste, S., Chae, D., Chaney, D., Chayer, P., Chonis, T., Cohen, L., Cole, H. J., Comeau, T. M., Coon, M., Coppock, E., Coyle, L., Davis, R., Dean, B. H., Dziak, K. J., Eisenhower, M., Flagey, N., Franck, R., Gallagher, B., Gilman, L., Glassman, T., Golnik, G., Green, J. J., Grieco, J., Haase, S., Hadjimichael, T. J., Hagopian, J. G., Hahn, W. G., Hartig, G. F., Havey, K. A., Hayden, W. L., Hellekson, R., Hicks, B., Holfeltz, S. T., Howard, J. M., Huguet, J. A., Jahne, B., Johnson, L. A., Johnston, J. D., Jurling, A. S., Kegley, J. R., Kennard, S., Keski-Kuha, R. A., Knight, J. S., Kulp, B. A., Levi, J. S., Levine, M. B., Lightsey, P., Luetgens, R. A., Mather, J. C., Matthews, G. W., McKay, A. G., Mehalick, K. I., Meléndez, M., Messer, T., Mosier, G. E., Murphy, J., Nelan, E. P., Niedner, M. B., Noël, D. M., Ohara, C. M., Ohl, R. G., Olczak, E., Osborne, S. B., Park, S., Patton, K., Perrygo, C., Pueyo, L., Quesnel, L., Ranck, D., Redding, D. C., Regan, M. W., Reynolds, P., Rifelli, R., Rigby, J. R., Sabatke, D., Saif, B. N., Scorse, T. R., Seo, B.-J., Shi, F., Sigrist, N., Smith, K., Smith, J. S., Smith, E. C., Sohn, S. T., Spina, J., Stahl, H. P., Telfer, R., Terlecki, T., Texter, S. C., Van Buren, D., Van Campen, J. M., Vila, B., Voyton, M. F., Waldman, M., Walker, C. B., Weiser, N., Wells,

- C., West, G., Whitman, T. L., Wick, E., Wolf, E., Young, G., and Zielinski, T. P.: 2023, *arXiv e-prints* p. arXiv:2301.01779
- Méndez-Abreu, J., de Lorenzo-Cáceres, A., and Sánchez, S. F.: 2021, *MNRAS* **504**(2), 3058
- Mérida, R. M., Pérez-González, P. G., Sánchez-Blázquez, P., García-Argumánez, Á., Annunziatella, M., Costantin, L., Lumbreras-Calle, A., Alcalde-Pampliega, B., Barro, G., Espino-Briones, N., and Koekoemoer, A. M.: 2023, *arXiv e-prints* p. arXiv:2303.16234
- Meynet, G. and Maeder, A.: 2000, *A&A* **361**, 101
- Moster, B. P., Somerville, R. S., Maulbetsch, C., van den Bosch, F. C., Macciò, A. V., Naab, T., and Oser, L.: 2010, *ApJ* **710**(2), 903
- Murphy, L. J., Groh, J. H., Farrell, E., Meynet, G., Ekström, S., Tsiatsiou, S., Hackett, A., and Martinet, S.: 2021, *MNRAS* **506**(4), 5731
- Naab, T., Johansson, P. H., and Ostriker, J. P.: 2009, *ApJ* **699**(2), L178
- Naidu, R. P., Oesch, P. A., van Dokkum, P., Nelson, E. J., Suess, K. A., Brammer, G., Whitaker, K. E., Illingworth, G., Bouwens, R., Tacchella, S., Matthee, J., Allen, N., Bezanson, R., Conroy, C., Labbe, I., Leja, J., Leonova, E., Magee, D., Price, S. H., Setton, D. J., Strait, V., Stefanon, M., Toft, S., Weaver, J. R., and Weibel, A.: 2022, *ApJ* **940**(1), L14
- Naiman, J. P., Pillepich, A., Springel, V., Ramirez-Ruiz, E., Torrey, P., Vogelsberger, M., Pakmor, R., Nelson, D., Marinacci, F., Hernquist, L., Weinberger, R., and Genel, S.: 2018, *MNRAS* **477**(1), 1206
- Nayyeri, H., Hemmati, S., Mobasher, B., Ferguson, H. C., Cooray, A., Barro, G., Faber, S. M., Dickinson, M., Koekoemoer, A. M., Peth, M., Salvato, M., Ashby, M. L. N., Darvish, B., Donley, J., Durbin, M., Finkelstein, S., Fontana, A., Grogin, N. A., Gruetzbauch, R., Huang, K., Khostovan, A. A., Kocevski, D., Kodra, D., Lee, B., Newman, J., Pacifici, C., Pforr, J., Stefanon, M., Wiklind, T., Willner, S. P., Wuyts, S., Castellano, M., Conselice, C., Dolch, T., Dunlop, J. S., Galametz, A., Hathi, N. P., Lucas, R. A., and Yan, H.: 2017, *ApJS* **228**(1), 7
- Nelson, D., Pillepich, A., Genel, S., Vogelsberger, M., Springel, V., Torrey, P., Rodriguez-Gomez, V., Sijacki, D., Snyder, G. F., Griffen, B., Marinacci, F., Blecha, L., Sales, L., Xu, D., and Hernquist, L.: 2015, *Astronomy and Computing* **13**, 12
- Nelson, D., Pillepich, A., Springel, V., Weinberger, R., Hernquist, L., Pakmor, R., Genel, S., Torrey, P., Vogelsberger, M., Kauffmann, G., Marinacci, F., and Naiman, J.: 2018, *MNRAS* **475**(1), 624
- Nelson, E., van Dokkum, P., Franx, M., Brammer, G., Momcheva, I., Förster Schreiber, N., da Cunha, E., Tacconi, L., Bezanson, R., Kirkpatrick, A., Leja, J., Rix, H.-W., Skelton, R., van der Wel, A., Whitaker, K., and Wuyts, S.: 2014, *Nature* **513**(7518), 394
- Nelson, E. J., van Dokkum, P. G., Förster Schreiber, N. M., Franx, M., Brammer, G. B., Momcheva, I. G., Wuyts, S., Whitaker, K. E., Skelton, R. E., Fumagalli, M., Hayward, C. C., Kriek, M., Labbé, I., Leja, J., Rix, H.-W., Tacconi, L. J., van der Wel, A., van den Bosch, F. C., Oesch, P. A., Dickey, C., and Ulf Lange, J.: 2016, *ApJ* **828**(1), 27
- Nonino, M., Dickinson, M., Rosati, P., Grazian, A., Reddy, N., Cristiani, S., Giavalisco, M., Kuntschner, H., Vanzella, E., Daddi, E., Fosbury, R. A. E., and Cesarsky, C.: 2009, *ApJS* **183**(2), 244
- Norgaard-Nielsen, H. U. and Perez-Gonzalez, P. G.: 2017, *The MIRI HUDF Deep Imaging Survey*, JWST Proposal. Cycle 1, ID. #1283

- O'Donnell, J. E.: 1994, *ApJ* **422**, 158
- Oesch, P. A., Bouwens, R. J., Carollo, C. M., Illingworth, G. D., Trenti, M., Stiavelli, M., Magee, D., Labbé, I., and Franx, M.: 2010a, *ApJ* **709**(1), L21
- Oesch, P. A., Bouwens, R. J., Illingworth, G. D., Carollo, C. M., Franx, M., Labbé, I., Magee, D., Stiavelli, M., Trenti, M., and van Dokkum, P. G.: 2010b, *ApJ* **709**(1), L16
- Oesch, P. A., Bouwens, R. J., Illingworth, G. D., Carollo, C. M., Franx, M., Labbé, I., Magee, D., Stiavelli, M., Trenti, M., and van Dokkum, P. G.: 2010c, *ApJ* **709**(1), L16
- Oesch, P. A., Bouwens, R. J., Illingworth, G. D., Labbé, I., Smit, R., Franx, M., van Dokkum, P. G., Momcheva, I., Ashby, M. L. N., Fazio, G. G., Huang, J. S., Willner, S. P., Gonzalez, V., Magee, D., Trenti, M., Brammer, G. B., Skelton, R. E., and Spitler, L. R.: 2014, *ApJ* **786**(2), 108
- Oesch, P. A., Bouwens, R. J., Illingworth, G. D., Labbé, I., and Stefanon, M.: 2018, *ApJ* **855**(2), 105
- Oesch, P. A., Brammer, G., van Dokkum, P. G., Illingworth, G. D., Bouwens, R. J., Labbé, I., Franx, M., Momcheva, I., Ashby, M. L. N., Fazio, G. G., Gonzalez, V., Holden, B., Magee, D., Skelton, R. E., Smit, R., Spitler, L. R., Trenti, M., and Willner, S. P.: 2016, *ApJ* **819**(2), 129
- Oke, J. B. and Gunn, J. E.: 1983, *ApJ* **266**, 713
- Omukai, K. and Palla, F.: 2003, *ApJ* **589**(2), 677
- Ono, Y., Ouchi, M., Curtis-Lake, E., Schenker, M. A., Ellis, R. S., McLure, R. J., Dunlop, J. S., Robertson, B. E., Koekemoer, A. M., Bowler, R. A. A., Rogers, A. B., Schneider, E., Charlot, S., Stark, D. P., Shimasaku, K., Furlanetto, S. R., and Cirasuolo, M.: 2013, *ApJ* **777**(2), 155
- Oser, L., Naab, T., Ostriker, J. P., and Johansson, P. H.: 2013, in D. Thomas, A. Pasquali, and I. Ferreras (eds.), *The Intriguing Life of Massive Galaxies*, Vol. 295, pp 204–207
- Oser, L., Ostriker, J. P., Naab, T., Johansson, P. H., and Burkert, A.: 2010, *ApJ* **725**(2), 2312
- Osterbrock, D. E.: 1989, *Astrophysics of gaseous nebulae and active galactic nuclei*
- Pacifici, C., Kassin, S. A., Weiner, B., Charlot, S., and Gardner, J. P.: 2013, *ApJ* **762**(1), L15
- Pauldrach, A. W. A., Hoffmann, T. L., and Lennon, M.: 2001, *A&A* **375**, 161
- Peebles, P. J. E. and Dicke, R. H.: 1968, *ApJ* **154**, 891
- Peng, Y.-j., Lilly, S. J., Kovač, K., Bolzonella, M., Pozzetti, L., Renzini, A., Zamorani, G., Ilbert, O., Knobel, C., Iovino, A., Maier, C., Cucciati, O., Tasca, L., Carollo, C. M., Silverman, J., Kampczyk, P., de Ravel, L., Sanders, D., Scoville, N., Contini, T., Mainieri, V., Scodreggio, M., Kneib, J.-P., Le Fèvre, O., Bardelli, S., Bongiorno, A., Caputi, K., Coppa, G., de la Torre, S., Franzetti, P., Garilli, B., Lamareille, F., Le Borgne, J.-F., Le Brun, V., Mignoli, M., Perez Montero, E., Pello, R., Ricciardelli, E., Tanaka, M., Tresse, L., Vergani, D., Welikala, N., Zucca, E., Oesch, P., Abbas, U., Barnes, L., Bordoloi, R., Bottini, D., Cappi, A., Cassata, P., Cimatti, A., Fumana, M., Hasinger, G., Koekemoer, A., Leauthaud, A., Maccagni, D., Marinoni, C., McCracken, H., Memeo, P., Meneux, B., Nair, P., Porciani, C., Presotto, V., and Scaramella, R.: 2010, *ApJ* **721**(1), 193
- Pérez-González, P. G., Barro, G., Annunziatella, M., Costantin, L., García-Argumánuez, Á., McGrath, E. J., Mérida, R. M., Zavala, J. A., Arrabal Haro, P., Bagley, M. B., Backhaus, B. E., Behroozi, P., Bell, E. F., Buat, V., Calabrò, A., Casey, C. M., Cleri, N. J., Coogan, R. T., Cooper, M. C., Cooray, A. R., Dekel, A., Dickinson, M., Elbaz, D., Ferguson, H. C., Finkelstein, S. L., Fontana, A., Franco, M., Gardner, J. P.,

- Giavalisco, M., Gómez-Guijarro, C., Grazian, A., Grogin, N. A., Guo, Y., Jogee, S., Kartaltepe, J. S., Kewley, L. J., Kirkpatrick, A., Kocevski, D. D., Koekemoer, A. M., Long, A. S., Lotz, J. M., Lucas, R. A., Papovich, C., Pirzkal, N., Ravindranath, S., Somerville, R. S., Tacchella, S., Trump, J. R., Wang, W., Wilkins, S. M., Wuyts, S., Yang, G., and Yung, L. Y. A.: 2022, *arXiv e-prints* p. arXiv:2211.00045
- Pérez-González, P. G., Cava, A., Barro, G., Villar, V., Cardiel, N., Ferreras, I., Rodríguez-Espinosa, J. M., Alonso-Herrero, A., Balcells, M., Cenarro, J., Cepa, J., Charlot, S., Cimatti, A., Conselice, C. J., Daddi, E., Donley, J., Elbaz, D., Espino, N., Gallego, J., Gobat, R., González-Martín, O., Guzmán, R., Hernán-Caballero, A., Muñoz-Tuñón, C., Renzini, A., Rodríguez-Zaurín, J., Tresse, L., Trujillo, I., and Zamorano, J.: 2013, *ApJ* **762**(1), 46
- Pérez-González, P. G., Costantin, L., Langeroodi, D., Rinaldi, P., Annunziatella, M., Ilbert, O., Colina, L., Noorgaard-Nielsen, H. U., Greve, T., Ostlin, G., Wright, G., Alonso-Herrero, A., Álvarez-Márquez, J., Caputi, K. I., Eckart, A., Le Fèvre, O., Labiano, Á., García-Marín, M., Hjorth, J., Kendrew, S., Pye, J. P., Tikkanen, T., van der Werf, P., Walter, F., Ward, M., Bosman, S. E. I., Gillman, S., García-Argumánuez, Á., and María Mérida, R.: 2023a, *arXiv e-prints* p. arXiv:2302.02429
- Pérez-González, P. G., Costantin, L., Langeroodi, D., Rinaldi, P., Annunziatella, M., Ilbert, O., Colina, L., Nørgaard-Nielsen, H. U., Greve, T. R., Östlin, G., Wright, G., Alonso-Herrero, A., Álvarez-Márquez, J., Caputi, K. I., Eckart, A., Le Fèvre, O., Labiano, Á., García-Marín, M., Hjorth, J., Kendrew, S., Pye, J. P., Tikkanen, T., van der Werf, P., Walter, F., Ward, M., Bik, A., Boogaard, L., Bosman, S. E. I., Gómez, A. C., Gillman, S., Iani, E., Jermann, I., Melinder, J., Meyer, R. A., Moutard, T., van Dishoek, E., Henning, T., Lagage, P.-O., Guedel, M., Peissker, F., Ray, T., Vandenbussche, B., García-Argumánuez, Á., and María Mérida, R.: 2023b, *ApJ* **951**(1), L1
- Pérez-González, P. G., Gil de Paz, A., Zamorano, J., Gallego, J., Alonso-Herrero, A., and Aragón-Salamanca, A.: 2003, *MNRAS* **338**(2), 508
- Pérez-González, P. G., Rieke, G. H., Egami, E., Alonso-Herrero, A., Dole, H., Papovich, C., Blaylock, M., Jones, J., Rieke, M., Rigby, J., Barmby, P., Fazio, G. G., Huang, J., and Martin, C.: 2005, *ApJ* **630**(1), 82
- Pérez-González, P. G., Rieke, G. H., Villar, V., Barro, G., Blaylock, M., Egami, E., Gallego, J., Gil de Paz, A., Pascual, S., Zamorano, J., and Donley, J. L.: 2008, *ApJ* **675**(1), 234
- Pfarr, J., Maraston, C., and Tonini, C.: 2012, *MNRAS* **422**(4), 3285
- Pietrinferni, A., Cassisi, S., Salaris, M., and Castelli, F.: 2004, *ApJ* **612**(1), 168
- Pillepich, A., Nelson, D., Hernquist, L., Springel, V., Pakmor, R., Torrey, P., Weinberger, R., Genel, S., Naiman, J. P., Marinacci, F., and Vogelsberger, M.: 2018a, *MNRAS* **475**(1), 648
- Pillepich, A., Nelson, D., Hernquist, L., Springel, V., Pakmor, R., Torrey, P., Weinberger, R., Genel, S., Naiman, J. P., Marinacci, F., and Vogelsberger, M.: 2018b, *MNRAS* **475**(1), 648
- Pillepich, A., Springel, V., Nelson, D., Genel, S., Naiman, J., Pakmor, R., Hernquist, L., Torrey, P., Vogelsberger, M., Weinberger, R., and Marinacci, F.: 2018c, *MNRAS* **473**(3), 4077
- Planck Collaboration, Aghanim, N., Akrami, Y., Ashdown, M., Aumont, J., Baccigalupi, C., Ballardini, M., Banday, A. J., Barreiro, R. B., Bartolo, N., Basak, S., Battye, R., Benabed, K., Bernard, J. P., Bersanelli, M., Bielewicz, P., Bock, J. J., Bond, J. R., Borrill, J., Bouchet, F. R., Boulanger, F., Bucher, M., Burigana, C., Butler, R. C., Calabrese, E., Cardoso, J. F., Carron, J., Challinor, A., Chiang, H. C., Chluba, J., Colombo, L. P. L., Combet, C., Contreras, D., Crill, B. P., Cuttaia, F., de Bernardis, P., de Zotti, G., Delabrouille, J., Delouis, J. M., Di Valentino, E., Diego, J. M., Doré, O., Douspis, M., Ducout, A., Dupac, X., Dusini, S., Efstathiou, G., Elsner, F., Enßlin, T. A., Eriksen, H. K., Fantaye, Y., Farhang,

- M., Fergusson, J., Fernandez-Cobos, R., Finelli, F., Forastieri, F., Frailis, M., Fraisse, A. A., Franceschi, E., Frolov, A., Galeotta, S., Galli, S., Ganga, K., Génova-Santos, R. T., Gerbino, M., Ghosh, T., González-Nuevo, J., Górski, K. M., Gratton, S., Gruppuso, A., Gudmundsson, J. E., Hamann, J., Handley, W., Hansen, F. K., Herranz, D., Hildebrandt, S. R., Hivon, E., Huang, Z., Jaffe, A. H., Jones, W. C., Karakci, A., Keihänen, E., Keskitalo, R., Kiiveri, K., Kim, J., Kisner, T. S., Knox, L., Krachmalnicoff, N., Kunz, M., Kurki-Suonio, H., Lagache, G., Lamarre, J. M., Lasenby, A., Lattanzi, M., Lawrence, C. R., Le Jeune, M., Lemos, P., Lesgourgues, J., Levrier, F., Lewis, A., Liguori, M., Lilje, P. B., Lilley, M., Lindholm, V., López-Cañiego, M., Lubin, P. M., Ma, Y. Z., Macías-Pérez, J. F., Maggio, G., Maino, D., Mandolesi, N., Mangilli, A., Marcos-Caballero, A., Maris, M., Martin, P. G., Martinelli, M., Martínez-González, E., Matarrese, S., Mauri, N., McEwen, J. D., Meinhold, P. R., Melchiorri, A., Mennella, A., Migliaccio, M., Millea, M., Mitra, S., Miville-Deschênes, M. A., Molinari, D., Montier, L., Morgante, G., Moss, A., Natoli, P., Nørgaard-Nielsen, H. U., Pagano, L., Paoletti, D., Partridge, B., Patanchon, G., Peiris, H. V., Perrotta, F., Pettorino, V., Piacentini, F., Polastri, L., Polenta, G., Puget, J. L., Rachen, J. P., Reinecke, M., Remazeilles, M., Renzi, A., Rocha, G., Rosset, C., Roudier, G., Rubiño-Martín, J. A., Ruiz-Granados, B., Salvati, L., Sandri, M., Savelainen, M., Scott, D., Shellard, E. P. S., Sirignano, C., Sirri, G., Spencer, L. D., Sunyaev, R., Suur-Uski, A. S., Tauber, J. A., Tavagnacco, D., Tenti, M., Toffolatti, L., Tomasi, M., Trombetti, T., Valenziano, L., Valiviita, J., Van Tent, B., Vibert, L., Vielva, P., Villa, F., Vittorio, N., Wandelt, B. D., Wehus, I. K., White, M., White, S. D. M., Zacchei, A., and Zonca, A.: 2020, *A&A* **641**, A6
- Pontoppidan, K. M., Barrientes, J., Blome, C., Braun, H., Brown, M., Carruthers, M., Coe, D., DePasquale, J., Espinoza, N., Marin, M. G., Gordon, K. D., Henry, A., Hustak, L., James, A., Jenkins, A., Koekemoer, A. M., LaMassa, S., Law, D., Lockwood, A., Moro-Martin, A., Mullally, S. E., Pagan, A., Player, D., Proffitt, C., Pulliam, C., Ramsay, L., Ravindranath, S., Reid, N., Robberto, M., Sabbi, E., Ubeda, L., Balogh, M., Flanagan, K., Gardner, J., Hasan, H., Meinke, B., and Nota, A.: 2022, *ApJ* **936**(1), L14
- Pontoppidan, K. M., Pickering, T. E., Laidler, V. G., Gilbert, K., Sontag, C. D., Slocum, C., Sienkiewicz, M. J., Hanley, C., Earl, N. M., Pueyo, L., Ravindranath, S., Karakla, D. M., Robberto, M., Noriega-Crespo, A., and Barker, E. A.: 2016, in A. B. Peck, R. L. Seaman, and C. R. Benn (eds.), *Observatory Operations: Strategies, Processes, and Systems VI*, Vol. 9910 of *Society of Photo-Optical Instrumentation Engineers (SPIE) Conference Series*, p. 991016
- Press, W. H. and Schechter, P.: 1974, *ApJ* **187**, 425
- Pulsoni, C., Gerhard, O., Arnaboldi, M., Pillepich, A., Rodriguez-Gomez, V., Nelson, D., Hernquist, L., and Springel, V.: 2021, *A&A* **647**, A95
- Rahmati, A., Pawlik, A. H., Raičević, M., and Schaye, J.: 2013, *MNRAS* **430**(3), 2427
- Reddy, N. A., Kriek, M., Shapley, A. E., Freeman, W. R., Siana, B., Coil, A. L., Mobasher, B., Price, S. H., Sanders, R. L., and Shivaee, I.: 2015, *ApJ* **806**(2), 259
- Reddy, N. A., Pettini, M., Steidel, C. C., Shapley, A. E., Erb, D. K., and Law, D. R.: 2012, *ApJ* **754**(1), 25
- Rees, M. J. and Ostriker, J. P.: 1977, *MNRAS* **179**, 541
- Remus, R.-S. and Forbes, D. A.: 2022, *ApJ* **935**(1), 37
- Renzini, A.: 2006, *ARA&A* **44**(1), 141
- Retzlaff, J., Rosati, P., Dickinson, M., Vandame, B., Rit e, C., Nonino, M., Cesarsky, C., and GOODS Team: 2010, *A&A* **511**, A50
- Ricciardelli, E., Trujillo, I., Buitrago, F., and Conselice, C. J.: 2010, *MNRAS* **406**(1), 230

- Rieke, G. H., Wright, G. S., Böker, T., Bouwman, J., Colina, L., Glasse, A., Gordon, K. D., Greene, T. P., Güdel, M., Henning, T., Justtanont, K., Lagage, P. O., Meixner, M. E., Nørgaard-Nielsen, H. U., Ray, T. P., Ressler, M. E., van Dishoeck, E. F., and Waelkens, C.: 2015, *PASP* **127**(953), 584
- Rieke, M., Arribas, S., Bunker, A., Charlot, S., Finkelstein, S., Maiolino, R., Robertson, B., Willott, C., Windhorst, R., Eisenstein, D., Nelson, E., Tacchella, S., Egami, E., Endsley, R., Frye, B., Hainline, K., Hviding, R., Rieke, G., Williams, C., Willmer, C., and Woodrum, C.: 2019, *BAAS* **51**(3), 45
- Rieke, M., Kelly, D., Horner, S., and NIRCcam Team: 2005, in *American Astronomical Society Meeting Abstracts*, Vol. 207 of *American Astronomical Society Meeting Abstracts*, p. 115.09
- Rieke, M. J., Baum, S. A., Beichman, C. A., Crampton, D., Doyon, R., Eisenstein, D., Greene, T. P., Hodapp, K.-W., Horner, S. D., Johnstone, D., Lesyna, L., Lilly, S., Meyer, M., Martin, P., McCarthy, Donald W., J., Rieke, G. H., Roellig, T. L., Stauffer, J., Trauger, J. T., and Young, E. T.: 2003, in J. C. Mather (ed.), *IR Space Telescopes and Instruments*, Vol. 4850 of *Society of Photo-Optical Instrumentation Engineers (SPIE) Conference Series*, pp 478–485
- Rigby, J., Perrin, M., McElwain, M., Kimble, R., Friedman, S., Lallo, M., Doyon, R., Feinberg, L., Ferruit, P., Glasse, A., Rieke, M., Rieke, G., Wright, G., Willott, C., Colon, K., Milam, S., Neff, S., Stark, C., Valenti, J., Abell, J., Abney, F., Abul-Huda, Y., Acton, D. S., Adams, E., Adler, D., Aguilar, J., Ahmed, N., Albert, L., Alberts, S., Aldridge, D., Allen, M., Altenburg, M., Alvarez Marquez, J., Alves de Oliveira, C., Andersen, G., Anderson, H., Anderson, S., Argyriou, I., Armstrong, A., Arribas, S., Artigau, E., Arvai, A., Atkinson, C., Bacon, G., Bair, T., Banks, K., Barrientes, J., Barringer, B., Bartosik, P., Bast, W., Baudoz, P., Beatty, T., Bechtold, K., Beck, T., Bergeron, E., Bergkoetter, M., Bhatawdekar, R., Birkmann, S., Blazek, R., Blome, C., Boccaletti, A., Boeker, T., Boia, J., Bonaventura, N., Bond, N., Bosley, K., Boucarut, R., Bourque, M., Bouwman, J., Bower, G., Bowers, C., Boyer, M., Bradley, L., Brady, G., Braun, H., Breda, D., Bresnahan, P., Bright, S., Britt, C., Bromenschenkel, A., Brooks, B., Brooks, K., Brown, B., Brown, M., Brown, P., Bunker, A., Burger, M., Bushouse, H., Cale, S., Cameron, A., Cameron, P., Canipe, A., Caplinger, J., Caputo, F., Cara, M., Carey, L., Carniani, S., Carrasquilla, M., Carruthers, M., Case, M., Catherine, R., Chance, D., Chapman, G., Charlot, S., Charlow, B., Chayer, P., Chen, B., Cherinka, B., Chichester, S., Chilton, Z., Chonis, T., Clampin, M., Clark, C., Clark, K., Coe, D., Coleman, B., Comber, B., Comeau, T., Connolly, D., Cooper, J., Cooper, R., Coppock, E., Correnti, M., Cossou, C., Coulais, A., Coyle, L., Cracraft, M., Curti, M., Cuturic, S., Davis, K., Davis, M., Dean, B., DeLisa, A., deMeester, W., Dencheva, N., Dencheva, N., DePasquale, J., Deschenes, J., Hunor Detre, Ö., Diaz, R., Dicken, D., DiFelice, A., Dillman, M., Dixon, W., Doggett, J., Donaldson, T., Douglas, R., DuPrie, K., Dupuis, J., Durning, J., Easmin, N., Eck, W., Edeani, C., Egami, E., Ehrenwinkler, R., Eisenhamer, J., Eisenhower, M., Elie, M., Elliott, J., Elliott, K., Ellis, T., Engesser, M., Espinoza, N., Etienne, O., Etxaluze, M., Falini, P., Feeney, M., Ferry, M., Filippazzo, J., Fincham, B., Fix, M., Flagey, N., Florian, M., Flynn, J., Fontanella, E., Ford, T., Forshay, P., Fox, O., Franz, D., Fu, H., Fullerton, A., Galkin, S., Galyer, A., Garcia Marin, M., Gardner, J., Gardner, L., Garland, D., Garrett, B., Gasman, D., Gaspar, A., Gaudreau, D., Gauthier, P., Geers, V., Geithner, P., Gennaro, M., Giardino, G., Girard, J., Giuliano, M., Glassmire, K., Glauser, A., Glazer, S., Godfrey, J., Golimowski, D., Gollnitz, D., Gong, F., Gonzaga, S., Gordon, M., Gordon, K., Goudfrooij, P., Greene, T., Greenhouse, M., Grimaldi, S., Groebner, A., Grundy, T., Guillard, P., Gutman, I., Ha, K. Q., Haderlein, P., Hagedorn, A., Hainline, K., Haley, C., Hami, M., Hamilton, F., Hammel, H., Hansen, C., Harkins, T., Harr, M., Hart, J., Hart, Q., Hartig, G., Hashimoto, R., Haskins, S., Hathaway, W., Havey, K., Hayden, B., Hecht, K., Heller-Boyer, C., Henriques, C., Henry, A., Hermann, K., Hernandez, S., Hesman, B., Hicks, B., Hilbert, B., Hines, D., Hoffman, M., Holfeltz, S., Holler, B. J., Hoppa, J., Hott, K., Howard, J., Howard, R., Hunter, A., Hunter, D., Hurst, B., Husemann, B., Hustak, L., Ilinca Ignat, L., Illingworth, G., Irish, S., Jackson, W., Jahromi, A., Jakobsen, P., James, L., James, B., Januszewski, W., Jenkins, A., Jirdeh, H., Johnson, P., Johnson, T., Jones, V., Jones, R., Jones, D., Jones, O., Jordan, I., Jordan, M., Jurczyk, S., Jurling, A., Kaleida, C., Kalmanson, P., Kammerer, J., Kang, H., Kao, S.-H., Karakla, D., Kavanagh, P., Kelly, D., Kendrew, S., Kennedy, H., Kenny, D., Keski-kuha, R., Keyes, C., Kidwell, R., Kinzel, W., Kirk, J.,

- Kirkpatrick, M., Kirshenblat, D., Klaassen, P., Knapp, B., Knight, J. S., Knollenberg, P., Koehler, R., Koekemoer, A., Kovacs, A., Kulp, T., Kumari, N., Kyprianou, M., La Massa, S., Labrador, A., Labiano Ortega, A., Lagage, P.-O., Lajoie, C.-P., Lallo, M., Lam, M., Lamb, T., Lambros, S., Lampenfield, R., Langston, J., Larson, K., Law, D., Lawrence, J., Lee, D., Leisenring, J., Lepo, K., Leveille, M., Levenson, N., Levine, M., Levy, Z., Lewis, D., Lewis, H., Libralato, M., Lightsey, P., Link, M., Liu, L., Lo, A., Lockwood, A., Logue, R., Long, C., Long, D., Loomis, C., Lopez-Caniego, M., Alvarez, J. L., Love-Pruitt, J., Lucy, A., Luetzgendorf, N., Maghami, P., Maiolino, R., Major, M., Malla, S., Malumuth, E., Manjavacas, E., Mannfolk, C., Marrione, A., Marston, A., Martel, A., Maschmann, M., Masci, G., Masciarelli, M., Maszkiewicz, M., Mather, J., McKenzie, K., McLean, B., McMaster, M., Melbourne, K., Meléndez, M., Menzel, M., Merz, K., Meyett, M., Meza, L., Miskey, C., Misselt, K., Moller, C., Morrison, J., Morse, E., Moseley, H., Mosier, G., Mountain, M., Mueckay, J., Mueller, M., Mullally, S., Murphy, J., Murray, K., Murray, C., Mustelier, D., Muzerolle, J., Mycroft, M., Myers, R., Myrick, K., Nanavati, S., Nance, E., Nayak, O., Naylor, B., Nelan, E., Nickson, B., Nielson, A., Nieto-Santisteban, M., Nikolov, N., Noriega-Crespo, A., O’Shaughnessy, B., O’Sullivan, B., Ochs, W., Ogle, P., Oleszczuk, B., Olmsted, J., Osborne, S., Ottens, R., Owens, B., Pacifici, C., Pagan, A., Page, J., Park, S., Parrish, K., Patapis, P., Paul, L., Pauly, T., Pavlovsky, C., Pedder, A., Peek, M., Pena-Guerrero, M., Pennanen, K., Perez, Y., Perna, M., Perriello, B., Phillips, K., Pietraszkiwicz, M., Pinaud, J.-P., Pirzkal, N., Pitman, J., Piwowar, A., Platais, V., Player, D., Plesha, R., Pollizi, J., Polster, E., Pontoppidan, K., Porterfield, B., Proffitt, C., Pueyo, L., Pulliam, C., Qirt, B., Quispe Neira, I., Ramos Alarcon, R., Ramsay, L., Rapp, G., Rapp, R., Rauscher, B., Ravindranath, S., Rawle, T., Regan, M., Reichard, T. A., Reis, C., Ressler, M. E., Rest, A., Reynolds, P., Rhue, T., Richon, K., Rickman, E., Ridgeway, M., Ritchie, C., Rix, H.-W., Robberto, M., Robinson, G., Robinson, M., Robinson, O., Rock, F., Rodriguez, D., Rodriguez Del Pino, B., Roellig, T., Rohrbach, S., Roman, A., Romelfanger, F., Rose, P., Roteliuk, A., Roth, M., Rothwell, B., Rowlands, N., Roy, A., Royer, P., Royle, P., Rui, C., Rumler, P., Runnels, J., Russ, M., Rustamkulov, Z., Ryden, G., Ryer, H., Sabata, M., Sabatke, D., Sabbi, E., Samuelson, B., Sapp, B., Sappington, B., Sargent, B., Sauer, A., Scheithauer, S., Schlawin, E., Schlitz, J., Schmitz, T., Schneider, A., Schreiber, J., Schulze, V., Schwab, R., Scott, J., Sembach, K., Shanahan, C., Shaughnessy, B., Shaw, R., Shawger, N., Shay, C., Sheehan, E., Shen, S., Sherman, A., Shiao, B., Shih, H.-Y., Shivaie, I., Sienkiewicz, M., Sing, D., Sirianni, M., Sivaramakrishnan, A., Skipper, J., Sloan, G., Slocum, C., Slowinski, S., Smith, E., Smith, E., Smith, D., Smith, C., Snyder, G., Soh, W., Sohn, T., Soto, C., Spencer, R., Stallcup, S., Stansberry, J., Starr, C., Starr, E., Stewart, A., Stiavelli, M., Straughn, A., Strickland, D., Stys, J., Summers, F., Sun, F., Sunnquist, B., Swade, D., Swam, M., Swaters, R., Swoish, R., Taylor, J. M., Taylor, R., Te Plate, M., Tea, M., Teague, K., Telfer, R., Temim, T., Thatte, D., Thompson, C., Thompson, L., Thomson, S., Tikkanen, T., Tippet, W., Todd, C., Toolan, S., Tran, H., Trejo, E., Truong, J., Tsukamoto, C., Tustain, S., Tyra, H., Ubeda, L., Underwood, K., Uzzo, M., Van Campen, J., Vandal, T., Vandenbussche, B., Vila, B., Volk, K., Wahlgren, G., Waldman, M., Walker, C., Wander, M., Warfield, C., Warner, G., Wasiak, M., Watkins, M., Weaver, A., Weilert, M., Weiser, N., Weiss, B., Weissman, S., Welty, A., West, G., Wheate, L., Wheatley, E., Wheeler, T., White, R., Whiteaker, K., Whitehouse, P., Whiteleather, J., Whitman, W., Williams, C., Willmer, C., Willoughby, S., Wilson, A., Wirth, G., Wislowski, E., Wolf, E., Wolfe, D., Wolff, S., Workman, B., Wright, R., Wu, C., Wu, R., Wymer, K., Yates, K., Yeager, C., Yeates, J., Yerger, E., Yoon, J., Young, A., Yu, S., Zak, D., Zeidler, P., Zhou, J., Zielinski, T., Zincke, C., and Zonak, S.: 2022a, *arXiv e-prints* p. arXiv:2207.05632
- Rigby, J. R., Lightsey, P. A., García Marín, M., Bowers, C. W., Smith, E. C., Glasse, A., McElwain, M. W., Rieke, G. H., Chary, R.-R., Liu, X., Clampin, M., Kinzel, W., Laidler, V., Mehalick, K. I., Noriega-Crespo, A., Shivaie, I., Stark, C., Temim, T., Wei, Z., and Willott, C. J.: 2022b, *arXiv e-prints* p. arXiv:2211.09890
- Rix, H.-W., Barden, M., Beckwith, S. V. W., Bell, E. F., Borch, A., Caldwell, J. A. R., Häussler, B., Jahnke, K., Joglee, S., McIntosh, D. H., Meisenheimer, K., Peng, C. Y., Sanchez, S. F., Somerville, R. S., Wisotzki, L., and Wolf, C.: 2004, *ApJS* **152**(2), 163
- Robertson, B. E.: 2022, *ARA&A* **60**, 121

- Rodighiero, G., Bisigello, L., Iani, E., Marasco, A., Grazian, A., Sinigaglia, F., Cassata, P., and Gruppioni, C.: 2023, *MNRAS* **518**(1), L19
- Rodriguez-Gomez, V., Genel, S., Vogelsberger, M., Sijacki, D., Pillepich, A., Sales, L. V., Torrey, P., Snyder, G., Nelson, D., Springel, V., Ma, C.-P., and Hernquist, L.: 2015, *MNRAS* **449**(1), 49
- Rodriguez-Gomez, V., Pillepich, A., Sales, L. V., Genel, S., Vogelsberger, M., Zhu, Q., Wellons, S., Nelson, D., Torrey, P., Springel, V., Ma, C.-P., and Hernquist, L.: 2016, *MNRAS* **458**(3), 2371
- Rydberg, C.-E., Zackrisson, E., Lundqvist, P., and Scott, P.: 2013, *MNRAS* **429**(4), 3658
- Ryon, J. E.: 2022, in *ACS Instrument Handbook for Cycle 30 v. 21.0*, Vol. 21, p. 21
- Sales, L. V., Vogelsberger, M., Genel, S., Torrey, P., Nelson, D., Rodriguez-Gomez, V., Wang, W., Pillepich, A., Sijacki, D., Springel, V., and Hernquist, L.: 2015, *MNRAS* **447**, L6
- Salpeter, E. E.: 1955, *ApJ* **121**, 161
- Sánchez-Blázquez, P., Peletier, R. F., Jiménez-Vicente, J., Cardiel, N., Cenarro, A. J., Falcón-Barroso, J., Gorgas, J., Selam, S., and Vazdekis, A.: 2006, *MNRAS* **371**(2), 703
- Sánchez-Menguiano, L., Sánchez, S. F., Pérez, I., Ruiz-Lara, T., Galbany, L., Anderson, J. P., and Kuncarayakti, H.: 2020, *MNRAS* **492**(3), 4149
- Sandage, A.: 1986, *A&A* **161**, 89
- Sanders, D. B., Salvato, M., Aussel, H., Ilbert, O., Scoville, N., Surace, J. A., Frayer, D. T., Sheth, K., Helou, G., Brooke, T., Bhattacharya, B., Yan, L., Kartaltepe, J. S., Barnes, J. E., Blain, A. W., Calzetti, D., Capak, P., Carilli, C., Carollo, C. M., Comastri, A., Daddi, E., Ellis, R. S., Elvis, M., Fall, S. M., Franceschini, A., Giavalisco, M., Hasinger, G., Impey, C., Koekemoer, A., Le Fèvre, O., Lilly, S., Liu, M. C., McCracken, H. J., Mobasher, B., Renzini, A., Rich, M., Schinnerer, E., Shopbell, P. L., Taniguchi, Y., Thompson, D. J., Urry, C. M., and Williams, J. P.: 2007, *ApJS* **172**(1), 86
- Santini, P., Ferguson, H. C., Fontana, A., Mobasher, B., Barro, G., Castellano, M., Finkelstein, S. L., Grazian, A., Hsu, L. T., Lee, B., Lee, S. K., Pforr, J., Salvato, M., Wiklind, T., Wuyts, S., Almaini, O., Cooper, M. C., Galametz, A., Weiner, B., Amorin, R., Boutsia, K., Conselice, C. J., Dahlen, T., Dickinson, M. E., Giavalisco, M., Grogin, N. A., Guo, Y., Hathi, N. P., Kocevski, D., Koekemoer, A. M., Kurczynski, P., Merlin, E., Mortlock, A., Newman, J. A., Paris, D., Pentericci, L., Simons, R., and Willner, S. P.: 2015, *ApJ* **801**(2), 97
- Saslaw, W. C. and Zipoy, D.: 1967, *Nature* **216**(5119), 976
- Savaglio, S., Glazebrook, K., Le Borgne, D., Juneau, S., Abraham, R. G., Chen, H. W., Crampton, D., McCarthy, P. J., Carlberg, R. G., Marzke, R. O., Roth, K., Jørgensen, I., and Murowinski, R.: 2005, *ApJ* **635**(1), 260
- Sawala, T., Frenk, C. S., Fattahi, A., Navarro, J. F., Bower, R. G., Crain, R. A., Dalla Vecchia, C., Furlong, M., Helly, J. C., Jenkins, A., Oman, K. A., Schaller, M., Schaye, J., Theuns, T., Trayford, J., and White, S. D. M.: 2016, *MNRAS* **457**(2), 1931
- Schaller, G., Schaerer, D., Meynet, G., and Maeder, A.: 1992, *A&AS* **96**, 269
- Schauer, A. T. P., Glover, S. C. O., Klessen, R. S., and Ceverino, D.: 2019, *MNRAS* **484**(3), 3510
- Schaye, J., Crain, R. A., Bower, R. G., Furlong, M., Schaller, M., Theuns, T., Dalla Vecchia, C., Frenk, C. S., McCarthy, I. G., Helly, J. C., Jenkins, A., Rosas-Guevara, Y. M., White, S. D. M., Baes, M., Booth, C. M., Camps, P., Navarro, J. F., Qu, Y., Rahmati, A., Sawala, T., Thomas, P. A., and Trayford, J.: 2015, *MNRAS* **446**(1), 521



- Schneider, R., Ferrara, A., Natarajan, P., and Omukai, K.: 2002, *ApJ* **571**(1), 30
- Scoville, N., Abraham, R. G., Aussel, H., Barnes, J. E., Benson, A., Blain, A. W., Calzetti, D., Comastri, A., Capak, P., Carilli, C., Carlstrom, J. E., Carollo, C. M., Colbert, J., Daddi, E., Ellis, R. S., Elvis, M., Ewald, S. P., Fall, M., Franceschini, A., Giavalisco, M., Green, W., Griffiths, R. E., Guzzo, L., Hasinger, G., Impey, C., Kneib, J. P., Koda, J., Koekemoer, A., Lefevre, O., Lilly, S., Liu, C. T., McCracken, H. J., Massey, R., Mellier, Y., Miyazaki, S., Mobasher, B., Mould, J., Norman, C., Refregier, A., Renzini, A., Rhodes, J., Rich, M., Sanders, D. B., Schiminovich, D., Schinnerer, E., Scodreggio, M., Sheth, K., Shopbell, P. L., Taniguchi, Y., Tyson, N. D., Urry, C. M., Van Waerbeke, L., Vettolani, P., White, S. D. M., and Yan, L.: 2007, *ApJS* **172**(1), 38
- Searle, L., Sargent, W. L. W., and Bagnuolo, W. G.: 1973, *ApJ* **179**, 427
- Siana, B., Teplitz, H. I., Ferguson, H. C., Brown, T. M., Giavalisco, M., Dickinson, M., Chary, R.-R., de Mello, D. F., Conselice, C. J., Bridge, C. R., Gardner, J. P., Colbert, J. W., and Scarlata, C.: 2010, *ApJ* **723**(1), 241
- Sijacki, D., Springel, V., Di Matteo, T., and Hernquist, L.: 2007, *MNRAS* **380**(3), 877
- Silk, J.: 1977, *ApJ* **211**, 638
- Skelton, R. E., Whitaker, K. E., Momcheva, I. G., Brammer, G. B., van Dokkum, P. G., Labbé, I., Franx, M., van der Wel, A., Bezanson, R., Da Cunha, E., Fumagalli, M., Förster Schreiber, N., Kriek, M., Leja, J., Lundgren, B. F., Magee, D., Marchesini, D., Maseda, M. V., Nelson, E. J., Oesch, P., Pacifici, C., Patel, S. G., Price, S., Rix, H.-W., Tal, T., Wake, D. A., and Wuyts, S.: 2014, *ApJS* **214**(2), 24
- Skillman, S. W., Warren, M. S., Turk, M. J., Wechsler, R. H., Holz, D. E., and Sutter, P. M.: 2014, *arXiv e-prints* p. arXiv:1407.2600
- Skinner, D. and Wise, J. H.: 2020, *MNRAS* **492**(3), 4386
- Smail, I., Ivison, R. J., and Blain, A. W.: 1997, *ApJ* **490**(1), L5
- Smith, R. J.: 2020, *ARA&A* **58**, 577
- Snyder, G. F., Lotz, J. M., Rodriguez-Gomez, V., Guimarães, R. d. S., Torrey, P., and Hernquist, L.: 2017, *MNRAS* **468**(1), 207
- Snyder, G. F., Torrey, P., Lotz, J. M., Genel, S., McBride, C. K., Vogelsberger, M., Pillepich, A., Nelson, D., Sales, L. V., Sijacki, D., Hernquist, L., and Springel, V.: 2015, *MNRAS* **454**(2), 1886
- Song, M., Finkelstein, S. L., Ashby, M. L. N., Grazian, A., Lu, Y., Papovich, C., Salmon, B., Somerville, R. S., Dickinson, M., Duncan, K., Faber, S. M., Fazio, G. G., Ferguson, H. C., Fontana, A., Guo, Y., Hathi, N., Lee, S.-K., Merlin, E., and Willner, S. P.: 2016, *ApJ* **825**(1), 5
- Sparre, M., Hayward, C. C., Springel, V., Vogelsberger, M., Genel, S., Torrey, P., Nelson, D., Sijacki, D., and Hernquist, L.: 2015, *MNRAS* **447**(4), 3548
- Sparre, M. and Springel, V.: 2016, *MNRAS* **462**(3), 2418
- Spiniello, C., Tortora, C., D'Ago, G., Napolitano, N. R., and Inspire Team: 2021, *The Messenger* **184**, 26
- Spinrad, H. and Taylor, B. J.: 1971, *ApJS* **22**, 445
- Springel, V.: 2010, *MNRAS* **401**(2), 791
- Springel, V., Di Matteo, T., and Hernquist, L.: 2005a, *MNRAS* **361**(3), 776

- Springel, V., Frenk, C. S., and White, S. D. M.: 2006, *Nature* **440(7088)**, 1137
- Springel, V. and Hernquist, L.: 2003, *MNRAS* **339(2)**, 289
- Springel, V., Pakmor, R., Pillepich, A., Weinberger, R., Nelson, D., Hernquist, L., Vogelsberger, M., Genel, S., Torrey, P., Marinacci, F., and Naiman, J.: 2018, *MNRAS* **475(1)**, 676
- Springel, V., Wang, J., Vogelsberger, M., Ludlow, A., Jenkins, A., Helmi, A., Navarro, J. F., Frenk, C. S., and White, S. D. M.: 2008, *MNRAS* **391(4)**, 1685
- Springel, V., White, M., and Hernquist, L.: 2001, *ApJ* **549(2)**, 681
- Springel, V., White, S. D. M., Jenkins, A., Frenk, C. S., Yoshida, N., Gao, L., Navarro, J., Thacker, R., Croton, D., Helly, J., Peacock, J. A., Cole, S., Thomas, P., Couchman, H., Evrard, A., Colberg, J., and Pearce, F.: 2005b, *Nature* **435(7042)**, 629
- Stacy, A., Bromm, V., and Lee, A. T.: 2016, *MNRAS* **462(2)**, 1307
- Stacy, A., Greif, T. H., and Bromm, V.: 2010, *MNRAS* **403(1)**, 45
- Stadel, J., Potter, D., Moore, B., Diemand, J., Madau, P., Zemp, M., Kuhlen, M., and Quilis, V.: 2009, *MNRAS* **398(1)**, L21
- Stark, D. P.: 2016, *ARA&A* **54**, 761
- Stefanon, M., Yan, H., Mobasher, B., Barro, G., Donley, J. L., Fontana, A., Hemmati, S., Koekemoer, A. M., Lee, B., Lee, S.-K., Nayyeri, H., Peth, M., Pforr, J., Salvato, M., Wiklind, T., Wuyts, S., Ashby, M. L. N., Castellano, M., Conselice, C. J., Cooper, M. C., Cooray, A. R., Dolch, T., Ferguson, H., Galametz, A., Giavalisco, M., Guo, Y., Willner, S. P., Dickinson, M. E., Faber, S. M., Fazio, G. G., Gardner, J. P., Gawiser, E., Grazian, A., Grogin, N. A., Kocevski, D., Koo, D. C., Lee, K.-S., Lucas, R. A., McGrath, E. J., Nandra, K., Newman, J. A., and van der Wel, A.: 2017, *ApJS* **229(2)**, 32
- Swinbank, A. M., Chapman, S. C., Smail, I., Lindner, C., Borys, C., Blain, A. W., Ivison, R. J., and Lewis, G. F.: 2006, *MNRAS* **371(1)**, 465
- Szomoru, D., Franx, M., and van Dokkum, P. G.: 2012, *ApJ* **749(2)**, 121
- Tacchella, S., Carollo, C. M., Förster Schreiber, N. M., Renzini, A., Dekel, A., Genzel, R., Lang, P., Lilly, S. J., Mancini, C., Onodera, M., Tacconi, L. J., Wuyts, S., and Zamorani, G.: 2018, *ApJ* **859(1)**, 56
- Tacchella, S., Carollo, C. M., Renzini, A., Förster Schreiber, N. M., Lang, P., Wuyts, S., Cresci, G., Dekel, A., Genzel, R., Lilly, S. J., Mancini, C., Newman, S., Onodera, M., Shapley, A., Tacconi, L., Woo, J., and Zamorani, G.: 2015, *Science* **348(6232)**, 314
- Tacchella, S., Dekel, A., Carollo, C. M., Ceverino, D., DeGraf, C., Lapiner, S., Mandelker, N., and Primack, J. R.: 2016, *MNRAS* **458(1)**, 242
- Tacchella, S., Diemer, B., Hernquist, L., Genel, S., Marinacci, F., Nelson, D., Pillepich, A., Rodriguez-Gomez, V., Sales, L. V., Springel, V., and Vogelsberger, M.: 2019, *MNRAS* **487(4)**, 5416
- Tacconi, L. J., Genzel, R., Smail, I., Neri, R., Chapman, S. C., Ivison, R. J., Blain, A., Cox, P., Omont, A., Bertoldi, F., Greve, T., Förster Schreiber, N. M., Genel, S., Lutz, D., Swinbank, A. M., Shapley, A. E., Erb, D. K., Cimatti, A., Daddi, E., and Baker, A. J.: 2008, *ApJ* **680(1)**, 246
- Taniguchi, Y., Scoville, N., Murayama, T., Sanders, D. B., Mobasher, B., Aussel, H., Capak, P., Ajiki, M., Miyazaki, S., Komiyama, Y., Shioya, Y., Nagao, T., Sasaki, S. S., Koda, J., Carilli, C., Giavalisco, M., Guzzo, L., Hasinger, G., Impey, C., LeFevre, O., Lilly, S., Renzini, A., Rich, M., Schinnerer, E., Shopbell, P., Kaifu, N., Karoji, H., Arimoto, N., Okamura, S., and Ohta, K.: 2007, *ApJS* **172(1)**, 9

- Taylor, E. N., Franx, M., Glazebrook, K., Brinchmann, J., van der Wel, A., and van Dokkum, P. G.: 2010, *ApJ* **720**(1), 723
- Tegmark, M., Silk, J., Rees, M. J., Blanchard, A., Abel, T., and Palla, F.: 1997, *ApJ* **474**, 1
- Tinker, J., Kravtsov, A. V., Klypin, A., Abazajian, K., Warren, M., Yepes, G., Gottlöber, S., and Holz, D. E.: 2008, *ApJ* **688**(2), 709
- Tinsley, B. M.: 1968, *ApJ* **151**, 547
- Tinsley, B. M. and Gunn, J. E.: 1976, *ApJ* **203**, 52
- Tomczak, A. R., Quadri, R. F., Tran, K.-V. H., Labbé, I., Straatman, C. M. S., Papovich, C., Glazebrook, K., Allen, R., Brammer, G. B., Kacprzak, G. G., Kawinwanichakij, L., Kelson, D. D., McCarthy, P. J., Mehrtens, N., Monson, A. J., Persson, S. E., Spitler, L. R., Tilvi, V., and van Dokkum, P.: 2014, *ApJ* **783**(2), 85
- Topping, M. W., Shapley, A. E., Stark, D. P., Endsley, R., Robertson, B., Greene, J. E., Furlanetto, S. R., and Tang, M.: 2021, *ApJ* **917**(2), L36
- Torrey, P., Snyder, G. F., Vogelsberger, M., Hayward, C. C., Genel, S., Sijacki, D., Springel, V., Hernquist, L., Nelson, D., Kriek, M., Pillepich, A., Sales, L. V., and McBride, C. K.: 2015, *MNRAS* **447**(3), 2753
- Tremmel, M., Karcher, M., Governato, F., Volonteri, M., Quinn, T. R., Pontzen, A., Anderson, L., and Bellovary, J.: 2017, *MNRAS* **470**(1), 1121
- Trujillo, I., Cenarro, A. J., de Lorenzo-Cáceres, A., Vazdekis, A., de la Rosa, I. G., and Cava, A.: 2009, *ApJ* **692**(2), L118
- Trujillo, I., Conselice, C. J., Bundy, K., Cooper, M. C., Eisenhardt, P., and Ellis, R. S.: 2007, *MNRAS* **382**(1), 109
- Trujillo, I., Ferré-Mateu, A., Balcells, M., Vazdekis, A., and Sánchez-Blázquez, P.: 2014, *ApJ* **780**(2), L20
- Valentino, F., Tanaka, M., Davidzon, I., Toft, S., Gómez-Guijarro, C., Stockmann, M., Onodera, M., Brammer, G., Ceverino, D., Faisst, A. L., Gallazzi, A., Hayward, C. C., Ilbert, O., Kubo, M., Magdis, G. E., Selsing, J., Shimakawa, R., Sparre, M., Steinhardt, C., Yabe, K., and Zabl, J.: 2020, *ApJ* **889**(2), 93
- van der Wel, A., Franx, M., van Dokkum, P. G., Skelton, R. E., Momcheva, I. G., Whitaker, K. E., Brammer, G. B., Bell, E. F., Rix, H. W., Wuyts, S., Ferguson, H. C., Holden, B. P., Barro, G., Koekemoer, A. M., Chang, Y.-Y., McGrath, E. J., Häussler, B., Dekel, A., Behroozi, P., Fumagalli, M., Leja, J., Lundgren, B. F., Maseda, M. V., Nelson, E. J., Wake, D. A., Patel, S. G., Labbé, I., Faber, S. M., Grogin, N. A., and Kocevski, D. D.: 2014, *ApJ* **788**(1), 28
- van Dokkum, P. G., Bezanson, R., van der Wel, A., Nelson, E. J., Momcheva, I., Skelton, R. E., Whitaker, K. E., Brammer, G., Conroy, C., Förster Schreiber, N. M., Fumagalli, M., Kriek, M., Labbé, I., Leja, J., Marchesini, D., Muzzin, A., Oesch, P., and Wuyts, S.: 2014, *ApJ* **791**(1), 45
- van Dokkum, P. G., Franx, M., Kriek, M., Holden, B., Illingworth, G. D., Magee, D., Bouwens, R., Marchesini, D., Quadri, R., Rudnick, G., Taylor, E. N., and Toft, S.: 2008, *ApJ* **677**(1), L5
- van Dokkum, P. G., Whitaker, K. E., Brammer, G., Franx, M., Kriek, M., Labbé, I., Marchesini, D., Quadri, R., Bezanson, R., Illingworth, G. D., Muzzin, A., Rudnick, G., Tal, T., and Wake, D.: 2010, *ApJ* **709**(2), 1018
- Vassiliadis, E. and Wood, P. R.: 1993, *ApJ* **413**, 641

- Vassiliadis, E. and Wood, P. R.: 1994, *ApJS* **92**, 125
- Vázquez, G. A. and Leitherer, C.: 2005, *ApJ* **621(2)**, 695
- Vogelsberger, M., Genel, S., Sijacki, D., Torrey, P., Springel, V., and Hernquist, L.: 2013, *MNRAS* **436(4)**, 3031
- Vogelsberger, M., Genel, S., Springel, V., Torrey, P., Sijacki, D., Xu, D., Snyder, G., Bird, S., Nelson, D., and Hernquist, L.: 2014a, *Nature* **509(7499)**, 177
- Vogelsberger, M., Genel, S., Springel, V., Torrey, P., Sijacki, D., Xu, D., Snyder, G., Nelson, D., and Hernquist, L.: 2014b, *MNRAS* **444(2)**, 1518
- Vogelsberger, M., Marinacci, F., Torrey, P., and Puchwein, E.: 2020, *Nature Reviews Physics* **2(1)**, 42
- Vogelsberger, M., Sijacki, D., Kereš, D., Springel, V., and Hernquist, L.: 2012, *MNRAS* **425(4)**, 3024
- Walcher, J., Groves, B., Budavári, T., and Dale, D.: 2011, *Ap&SS* **331**, 1
- Wang, J., Bose, S., Frenk, C. S., Gao, L., Jenkins, A., Springel, V., and White, S. D. M.: 2020, *Nature* **585(7823)**, 39
- Wang, L., Dutton, A. A., Stinson, G. S., Macciò, A. V., Penzo, C., Kang, X., Keller, B. W., and Wadsley, J.: 2015, *MNRAS* **454(1)**, 83
- Wang, W., Faber, S. M., Liu, F. S., Guo, Y., Pacifici, C., Koo, D. C., Kassin, S. A., Mao, S., Fang, J. J., Chen, Z., Koekemoer, A. M., Kocevski, D. D., and Ashby, M. L. N.: 2017, *MNRAS* **469(4)**, 4063
- Westera, P., Lejeune, T., Buser, R., Cuisinier, F., and Bruzual, G.: 2002, *A&A* **381**, 524
- Wetzell, A. R., Hopkins, P. F., Kim, J.-h., Faucher-Giguère, C.-A., Kereš, D., and Quataert, E.: 2016, *ApJ* **827(2)**, L23
- Whitaker, K. E., Labbé, I., van Dokkum, P. G., Brammer, G., Kriek, M., Marchesini, D., Quadri, R. F., Franx, M., Muzzin, A., Williams, R. J., Bezanson, R., Illingworth, G. D., Lee, K.-S., Lundgren, B., Nelson, E. J., Rudnick, G., Tal, T., and Wake, D. A.: 2011, *ApJ* **735(2)**, 86
- Whitaker, K. E., van Dokkum, P. G., Brammer, G., and Franx, M.: 2012, *ApJ* **754(2)**, L29
- Whitaker, K. E., van Dokkum, P. G., Brammer, G., Momcheva, I. G., Skelton, R., Franx, M., Kriek, M., Labbé, I., Fumagalli, M., Lundgren, B. F., Nelson, E. J., Patel, S. G., and Rix, H.-W.: 2013, *ApJ* **770(2)**, L39
- White, S. D. M. and Frenk, C. S.: 1991, *ApJ* **379**, 52
- Williams, C. C., Curtis-Lake, E., Hainline, K. N., Chevallard, J., Robertson, B. E., Charlot, S., Endsley, R., Stark, D. P., Willmer, C. N. A., Alberts, S., Amorin, R., Arribas, S., Baum, S., Bunker, A., Carniani, S., Crandall, S., Egami, E., Eisenstein, D. J., Ferruit, P., Husemann, B., Maseda, M. V., Maiolino, R., Rawle, T. D., Rieke, M., Smit, R., Tacchella, S., and Willott, C. J.: 2018, *ApJS* **236(2)**, 33
- Williams, C. C., Giavalisco, M., Cassata, P., Tundo, E., Wiklind, T., Guo, Y., Lee, B., Barro, G., Wuyts, S., Bell, E. F., Conselice, C. J., Dekel, A., Faber, S. M., Ferguson, H. C., Grogin, N., Hathi, N., Huang, K.-H., Kocevski, D., Koekemoer, A., Koo, D. C., Ravindranath, S., and Salimbeni, S.: 2014, *ApJ* **780(1)**, 1

- Williams, R. E., Baum, S., Bergeron, L. E., Bernstein, N., Blacker, B. S., Boyle, B. J., Brown, T. M., Carollo, C. M., Casertano, S., Covarrubias, R., de Mello, D. F., Dickinson, M. E., Espey, B. R., Ferguson, H. C., Fruchter, A., Gardner, J. P., Gonnella, A., Hayes, J., Hewett, P. C., Heyer, I., Hook, R., Irwin, M., Jones, D., Kaiser, M. E., Levay, Z., Lubenow, A., Lucas, R. A., Mack, J., MacKenty, J. W., Madau, P., Makidon, R. B., Martin, C. L., Mazzuca, L., Mutchler, M., Norris, R. P., Perriello, B., Phillips, M. M., Postman, M., Royle, P., Sahu, K., Savaglio, S., Sherwin, A., Smith, T. E., Stiavelli, M., Suntzeff, N. B., Teplitz, H. I., van der Marel, R. P., Walker, A. R., Weymann, R. J., Wiggs, M. S., Williger, G. M., Wilson, J., Zacharias, N., and Zurek, D. R.: 2000, *AJ* **120**(6), 2735
- Williams, R. E., Blacker, B., Dickinson, M., Dixon, W. V. D., Ferguson, H. C., Fruchter, A. S., Giavalisco, M., Gilliland, R. L., Heyer, I., Katsanis, R., Levay, Z., Lucas, R. A., McElroy, D. B., Petro, L., Postman, M., Adorf, H.-M., and Hook, R.: 1996, *AJ* **112**, 1335
- Windhorst, R. A., Cohen, S. H., Hathi, N. P., McCarthy, P. J., Ryan, Russell E., J., Yan, H., Baldry, I. K., Driver, S. P., Frogel, J. A., Hill, D. T., Kelvin, L. S., Koekemoer, A. M., Mechtley, M., O'Connell, R. W., Robotham, A. S. G., Rutkowski, M. J., Seibert, M., Straughn, A. N., Tuffs, R. J., Balick, B., Bond, H. E., Bushouse, H., Calzetti, D., Crockett, M., Disney, M. J., Dopita, M. A., Hall, D. N. B., Holtzman, J. A., Kaviraj, S., Kimble, R. A., MacKenty, J. W., Mutchler, M., Paresce, F., Saha, A., Silk, J. I., Trauger, J. T., Walker, A. R., Whitmore, B. C., and Young, E. T.: 2011, *ApJS* **193**(2), 27
- Wise, J. H. and Abel, T.: 2007, *ApJ* **665**(2), 899
- Wise, J. H. and Abel, T.: 2008, *ApJ* **685**(1), 40
- Wise, J. H., Demchenko, V. G., Halicek, M. T., Norman, M. L., Turk, M. J., Abel, T., and Smith, B. D.: 2014, *MNRAS* **442**(3), 2560
- Woo, J., Courteau, S., and Dekel, A.: 2008, *MNRAS* **390**(4), 1453
- Worthey, G., Faber, S. M., Gonzalez, J. J., and Burstein, D.: 1994, *ApJS* **94**, 687
- Wright, G. S., Wright, D., Goodson, G. B., Rieke, G. H., Aitink-Kroes, G., Amiaux, J., Aricha-Yanguas, A., Azzollini, R., Banks, K., Barrado-Navascues, D., Belenguer-Davila, T., Bloemmart, J. A. D. L., Bouchet, P., Brandl, B. R., Colina, L., Detre, Ö., Diaz-Catala, E., Eccleston, P., Friedman, S. D., García-Marín, M., Güdel, M., Glasse, A., Glauser, A. M., Greene, T. P., Groezinger, U., Grundy, T., Hastings, P., Henning, T., Hofferbert, R., Hunter, F., Jessen, N. C., Justtanont, K., Karnik, A. R., Khorrami, M. A., Krause, O., Labiano, A., Lagage, P. O., Langer, U., Lemke, D., Lim, T., Lorenzo-Alvarez, J., Mazy, E., McGowan, N., Meixner, M. E., Morris, N., Morrison, J. E., Müller, F., rgaard-Nielson, H. U. N., Olofsson, G., O'Sullivan, B., Pel, J. W., Penanen, K., Petach, M. B., Pye, J. P., Ray, T. P., Renotte, E., Renouf, I., Ressler, M. E., Samara-Ratna, P., Scheithauer, S., Schneider, A., Shaughnessy, B., Stevenson, T., Sukhatme, K., Swinyard, B., Sykes, J., Thatcher, J., Tikkanen, T., van Dishoeck, E. F., Waelkens, C., Walker, H., Wells, M., and Zhender, A.: 2015, *PASP* **127**(953), 595
- Wuyts, S., Förster Schreiber, N. M., Lutz, D., Nordon, R., Berta, S., Altieri, B., Andreani, P., Aussel, H., Bongiovanni, A., Cepa, J., Cimatti, A., Daddi, E., Elbaz, D., Genzel, R., Koekemoer, A. M., Magnelli, B., Maiolino, R., McGrath, E. J., Pérez García, A., Poglitsch, A., Popesso, P., Pozzi, F., Sanchez-Portal, M., Sturm, E., Tacconi, L., and Valtchanov, I.: 2011, *ApJ* **738**(1), 106
- Xu, G.: 1995, *ApJS* **98**, 355
- Yan, H., Ma, Z., Ling, C., Cheng, C., and Huang, J.-S.: 2023, *ApJ* **942**(1), L9
- Yang, G., Papovich, C., Bagley, M., Ferguson, H., Finkelstein, S., Koekemoer, A., Pérez-González, P., Arrabal Haro, P., Bisigello, L., Caputi, K., Cheng, Y., Costantin, L., Dickinson, M., Fontana, A., Gardner, J., Grazian, A., Grogin, N., Harish, S., Holwerda, B., Iani, E., Kartaltepe, J., Kewley, L., Kirkpatrick,

- A., Kocevski, D., Kokorev, V., Lotz, J. M., Lucas, R., Navarro-Carrera, R., Pentericci, L., Pirzkal, N., Ravindranath, S., Rinaldi, P., Shen, L., Somerville, R., Trump, J., de la Vega, A., Wilkins, S., and Yung, L. Y. A.: 2023, *arXiv e-prints* p. arXiv:2307.14509
- Yoshida, N., Abel, T., Hernquist, L., and Sugiyama, N.: 2003, *ApJ* **592**(2), 645
- Zahid, H. J., Kewley, L. J., and Bresolin, F.: 2011, *ApJ* **730**(2), 137
- Zahid, H. J., Torrey, P., Vogelsberger, M., Hernquist, L., Kewley, L., and Davé, R.: 2014, *Ap&SS* **349**(2), 873
- Zaroubi, S.: 2013, in T. Wiklind, B. Mobasher, and V. Bromm (eds.), *The First Galaxies*, Vol. 396 of *Astrophysics and Space Science Library*, p. 45
- Zavala, J. A., Buat, V., Casey, C. M., Finkelstein, S. L., Burgarella, D., Bagley, M. B., Ciesla, L., Daddi, E., Dickinson, M., Ferguson, H. C., Franco, M., Jiménez-Andrade, E. F., Kartaltepe, J. S., Koekemoer, A. M., Le Bail, A., Murphy, E. J., Papovich, C., Tacchella, S., Wilkins, S. M., Aretxaga, I., Behroozi, P., Champagne, J. B., Fontana, A., Giavalisco, M., Grazian, A., Grogin, N. A., Kewley, L. J., Kocevski, D. D., Kirkpatrick, A., Lotz, J. M., Pentericci, L., Pérez-González, P. G., Pirzkal, N., Ravindranath, S., Somerville, R. S., Trump, J. R., Yang, G., Aaron Yung, L. Y., Almaini, O., Amorín, R. O., Annunziatella, M., Haro, P. A., Backhaus, B. E., Barro, G., Bell, E. F., Bhatawdekar, R., Bisigello, L., Buitrago, F., Calabrò, A., Castellano, M., Chávez Ortiz, Ó. A., Chworowsky, K., Cleri, N. J., Cohen, S. H., Cole, J. W., Cooke, K. C., Cooper, M. C., Cooray, A. R., Costantin, L., Cox, I. G., Croton, D., Davé, R., de La Vega, A., Dekel, A., Elbaz, D., Estrada-Carpenter, V., Fernández, V., Finkelstein, K. D., Freundlich, J., Fujimoto, S., García-Argumán, Á., Gardner, J. P., Gawiser, E., Gómez-Guijarro, C., Guo, Y., Hamilton, T. S., Hathi, N. P., Holwerda, B. W., Hirschmann, M., Huertas-Company, M., Hutchison, T. A., Iyer, K. G., Jaskot, A. E., Jha, S. W., Jogee, S., Juneau, S., Jung, I., Kassin, S. A., Kurczynski, P., Larson, R. L., Leung, G. C. K., Long, A. S., Lucas, R. A., Magnelli, B., Mantha, K. B., Matharu, J., McGrath, E. J., McIntosh, D. H., Medrano, A., Merlin, E., Mobasher, B., Morales, A. M., Newman, J. A., Nicholls, D. C., Pandya, V., Rafelski, M., Ronayne, K., Rose, C., Ryan, R. E., Santini, P., Seillé, L.-M., Shah, E. A., Shen, L., Simons, R. C., Snyder, G. F., Stanway, E. R., Straughn, A. N., Teplitz, H. I., Vanderhoof, B. N., Vega-Ferrero, J., Wang, W., Weiner, B. J., Willmer, C. N. A., Wuyts, S., and Ceers Team: 2023, *ApJ* **943**(2), L9
- Zolotov, A., Dekel, A., Mandelker, N., Tweed, D., Inoue, S., DeGraf, C., Ceverino, D., Primack, J. R., Barro, G., and Faber, S. M.: 2015, *MNRAS* **450**(3), 2327